NBS SPECIAL PUBLICATION 435

U.S. DEPARTMENT OF COMMERCE / National Bureau of Standards

Laser Induced Damage in Optical Materials: 1975

ASTM

STP 1604

NATIONAL BUREAU OF STANDARDS

The National Bureau of Standards[1] was established by an act of Congress March 3, 1901. The Bureau's overall goal is to strengthen and advance the Nation's science and technology and facilitate their effective application for public benefit. To this end, the Bureau conducts research and provides: (1) a basis for the Nation's physical measurement system, (2) scientific and technological services for industry and government, (3) a technical basis for equity in trade, and (4) technical services to promote public safety. The Bureau consists of the Institute for Basic Standards, the Institute for Materials Research, the Institute for Applied Technology, the Institute for Computer Sciences and Technology, and the Office for Information Programs.

THE INSTITUTE FOR BASIC STANDARDS provides the central basis within the United States of a complete and consistent system of physical measurement; coordinates that system with measurement systems of other nations; and furnishes essential services leading to accurate and uniform physical measurements throughout the Nation's scientific community, industry, and commerce. The Institute consists of the Office of Measurement Services, the Office of Radiation Measurement and the following Center and divisions:

Applied Mathematics — Electricity — Mechanics — Heat — Optical Physics — Center for Radiation Research: Nuclear Sciences; Applied Radiation — Laboratory Astrophysics[2] — Cryogenics[2] — Electromagnetics[2] — Time and Frequency[2].

THE INSTITUTE FOR MATERIALS RESEARCH conducts materials research leading to improved methods of measurement, standards, and data on the properties of well-characterized materials needed by industry, commerce, educational institutions, and Government; provides advisory and research services to other Government agencies; and develops, produces, and distributes standard reference materials. The Institute consists of the Office of Standard Reference Materials, the Office of Air and Water Measurement, and the following divisions:

Analytical Chemistry — Polymers — Metallurgy — Inorganic Materials — Reactor Radiation — Physical Chemistry.

THE INSTITUTE FOR APPLIED TECHNOLOGY provides technical services to promote the use of available technology and to facilitate technological innovation in industry and Government; cooperates with public and private organizations leading to the development of technological standards (including mandatory safety standards), codes and methods of test; and provides technical advice and services to Government agencies upon request. The Institute consists of the following divisions and Centers:

Standards Application and Analysis — Electronic Technology — Center for Consumer Product Technology: Product Systems Analysis; Product Engineering — Center for Building Technology: Structures, Materials, and Life Safety; Building Environment; Technical Evaluation and Application — Center for Fire Research: Fire Science; Fire Safety Engineering.

THE INSTITUTE FOR COMPUTER SCIENCES AND TECHNOLOGY conducts research and provides technical services designed to aid Government agencies in improving cost effectiveness in the conduct of their programs through the selection, acquisition, and effective utilization of automatic data processing equipment; and serves as the principal focus within the executive branch for the development of Federal standards for automatic data processing equipment, techniques, and computer languages. The Institute consists of the following divisions:

Computer Services — Systems and Software — Computer Systems Engineering — Information Technology.

THE OFFICE FOR INFORMATION PROGRAMS promotes optimum dissemination and accessibility of scientific information generated within NBS and other agencies of the Federal Government; promotes the development of the National Standard Reference Data System and a system of information analysis centers dealing with the broader aspects of the National Measurement System; provides appropriate services to ensure that the NBS staff has optimum accessibility to the scientific information of the world. The Office consists of the following organizational units:

Office of Standard Reference Data — Office of Information Activities — Office of Technical Publications — Library — Office of International Relations — Office of International Standards.

---

[1] Headquarters and Laboratories at Gaithersburg, Maryland, unless otherwise noted; mailing address Washington, D.C. 20234.

[2] Located at Boulder, Colorado 80302.

Laser Induced Damage In Optical Materials: 1975

Proceedings of a Symposium Sponsored by:
National Bureau of Standards
American Society for Testing and Materials
Office of Naval Research
Energy Research and Development Administration

July 29-31, 1975
NBS Boulder, Colorado 80302

Edited by

Alexander J. Glass
Lawrence Livermore Laboratory
Livermore, California 94550

and

Arthur H. Guenther
Air Force Weapons Laboratory
Kirtland AFB, New Mexico 87117

U.S. DEPARTMENT OF COMMERCE, Elliot L. Richardson, *Secretary*

James A. Baker, III, *Under Secretary*

Dr. Betsy Ancker-Johnson, *Assistant Secretary for Science and Technology*

NATIONAL BUREAU OF STANDARDS, Ernest Ambler, *Acting Director*

Issued April 1976

Library of Congress Cataloging in Publication Data

Symposium on Laser Damage in Optical Materials, 7th, Boulder, Colo., 1975.
Laser induced damage in optical materials, 1975.

(NBS special publication; 435)
1. Optical materials—Defects—Congresses. 2. Optical materials, Effect of radiation on—Congresses. 3. Laser materials—Defects—Congresses. 4. Laser materials, Effect of radiation on—Congresses. I. Glass, Alexander, J. 1933- . II. Guenther, Arthur Henry, 1931- . III. United States. National Bureau of Standards. IV. Title. V. Series: United States. National Bureau of Standards. Special publication; 435.
QC100.U57 No. 435 [QC374] 602'.1s [621.36'6'028]
76-4985

National Bureau of Standards Special Publication 435

Nat. Bur. Stand. (U.S.), Spec. Publ. 435, 437 pages (Apr. 1976)

CODEN: XNBSAV

U.S. GOVERNMENT PRINTING OFFICE
WASHINGTON: 1976

For sale by the Superintendent of Documents, U.S. Government Printing Office
Washington, D.C. 20402 - Price $5.60

Foreword

These proceedings report in detail the formal papers presented at the 7th Annual Symposium on Laser Damage in Optical Materials held at the National Bureau of Standards, Boulder, Colorado, July 29-31, 1975. This meeting was jointly sponsored by the Office of Naval Research, National Bureau of Standards, the Energy Research and Development Administration, and the American Society of Testing and Materials. The major topics covered were optical fabrication, use of metal mirrors for high power lasers, window materials for infrared lasers, measurement of laser induced damage in the infrared, damage in dielectric film and at exposed surfaces, avalanche ionization, and multiphoton absorption as a damage mechanism.

The Co-chairperson, Dr. Alexander J. Glass of Lawrence Livermore Laboratory, Livermore, California, and Dr. A. H. Guenther of the Air Force Weapons Laboratory, Kirtland AFB, New Mexico, take full responsibility for the summary, conclusions, and recommendations contained in this report, as well as the summaries of the discussions at the conclusion of each presentation. It is suggested that individuals interested in the subject of this meeting obtain copies of those publications referenced in the bibliography contained in the summary and conclusions.

It is our intention to convene another symposium next year in Boulder, July 13-15, 1976, to update and document the state of the art of Laser Damage in Optical Materials at that time. This meeting will cover the subject historically presented at these symposia with additional emphasis on thin film and surface damage, machined optics, the problem of cleaning optical materials and components, as well as address ourselves to the subject of avalanche and multiphoton processes particularly as they relate to short wavelength application. Hopefully, additional reports relating to very short pulses, short wavelengths, and multipulse damage effects will be heard. We wish to encourage the reader to contact us on matters pertinent to the intent of these conferences.

A. H. Guenther

CONTENTS

IR DAMAGE TESTS

DAMAGE IN DIELECTRIC FILMS AND AT EXPOSED SURFACES

AVALANCHE IONIZATION and MULTIPHOTON PROCESSES

APPENDIX I

Laser Induced Damage in Optical Materials
7th ASTM Symposium
July 29-31, 1975

The Seventh ERDA-ASTM-ONR-NBS Symposium on Laser Induced Damage in Optical Materials was held at the National Bureau of Standards in Boulder, Colorado, on July 29-31 of this year. These Symposia are held as part of the activities in Subcommittee II on Lasers and Laser Materials, of the ASTM. Subcommittee II is charged with the responsibilities of formulating standards and test procedures for laser materials, components, and devices. The Chairperson of Subcommittee II is Haynes Lee, of Owens-Illinois, Inc. Co-chairpersons for the Damage Symposia are Dr. Arthur Guenther, Chief Scientist of the Air Force Weapons Laboratory, and Dr. Alexander J. Glass, Head, Theoretical Studies, Y Division, Lawrence Livermore Laboratory.

Over 150 attendees at the Symposium heard 42 papers on topics relating fabrication procedures to laser induced damage in optical materials; on metal mirrors; in infrared window materials; the multipulse, wavelength and pulse length dependence of damage thresholds; damage in dielectric films and at exposed surfaces; as well as theoretical discussions on avalanche ionization and multiphoton processes of importance at shorter wavelengths. Of particular importance was the sealing relations developed from several parametric studies relating fundamental properties (refractive index, surface roughness, etc.) to the damage threshold. This year many of the extrinsic influences tending to reduce a material damage resistance were isolated such that a measure of its egregious nature could be quantified. Unfortunately, it was evident that much still needs to be accomplished to improve processing and fabrication procedures to allow a measurable approach to a materials intrinsic strength to be demonstrated.

Key words: Avalanche ionization; IR windows and mirrors; laser damage; laser materials; multiphoton processes; self-focusing; thin films.

1. Principal Conclusions

The seventh consecutive Symposium on Damage in Laser Materials was held at the National Bureau of Standards in Boulder, Colorado, on July 29-31, 1975. This symposium, held each year since 1969, was jointly sponsored by the National Bureau of Standards, the Office of Naval Research and the Energy Research and Development Administration, and is an activity of Subcommittee II of the American Society of Testing and Materials, on Lasers and Laser Materials. The symposium co-persons are Dr. Arthur H. Guenther, Chief Scientist of the Air Force Weapons Laboratory, and Dr. Alexander J. Glass, Head of the Theory and Design Analysis Group in Y-Program at the Lawrence Livermore Laboratory. The symposium was attended by about 150 scientists who heard papers on a variety of subjects relating to the suitability of various materials and components for high-power laser applications. Primary interest was concentrated on problems attendant to large glass lasers for fusion research, and large gas lasers operating in the infrared, for military and industrial applications. Forty-five papers were presented during the two and one-half day symposium, representing research efforts at twenty-five institutions in the US, France, and Australia. Next year's symposium will be held at the National Bureau of Standards in Boulder, Colorado, on July 13 to 15, 1976.

The topics discussed at this year's symposium included details on techniques of optical fabrication, use of metal mirrors for high power lasers, window materials for IR lasers, measurement of laser induced damage in the IR, damage in dielectric films and at exposed surfaces, avalanche ionization, and multiphoton absorption as a damage mechanism. The sessions on metal mirrors and fabrication were moderated by Capt. T. A. Saito of the Air Force Weapons Laboratory, who is currently at the Lawrence Livermore Laboratory. The increasing use of metal mirrors for both IR gas and Nd-glass lasers is due primarily to improved fabrication methods, especially diamond-turning or micomachining. In fact, diamond-turned metal mirrors are now being employed for high level laser fusion illumination systems. Experimental results indicate that damage thresholds on quality diamond-turned metal surfaces are comparable to dielectric surface values, and as expected in excess of those seen with dielectric coated metal surfaces.

Where the reflectivity of the bare metal is sufficiently high, diamond turning offers an attractive means of mirror generation, especially for spherical, ellipsoidal, or other non-planar geometries. Enhancing the performance of metal mirrors, however, by dielectric coatings, is hard to achieve without lowering the damage threshold. This is due to poorer adhesions of coatings, and to the multitude of problems associated with the use of dielectric coatings at high power levels, as detailed below in this article. In the micromachining process itself, machine control is still a problem, especially for large, non-planar figures. Inspection techniques need considerable improvement, especially for fast optics.

Similar considerations apply to the fabrication of large transmitting elements, such as laser disks, and gas laser windows. Detailed understanding is emerging of the influence of the fabrication process on the damage threshold of the element, and in many cases, the preferred processes have been identified. To be useful, however, these processes must be suitable for volume production of large pieces. Similarly, inspection techniques must advance correspondingly, and must be capable of identifying those features to which the damage process is sensitive, such as micro-irregularities and particulate impurities.

In infrared window materials, surface absorption is seen to play a limiting role in establishing the damage threshold. Damage in most cases results not from thermal fracture of the element, but from thermal distortion. New methods of surface preparation have been developed, especially for alkali halides, to decrease surface absorption. Surface cleaning, with acid etching, ion-beam polishing, or even flame polishing, can increase the damage resistance of surfaces, by removing impurities, but can also alter the optical character of the surface. Prolonged ultrasonic cleaning can expose imperfect sub-surface features, yielding a lower damage threshold. Fundamental measurements of material properties relevant to thermal damage are beginning to be tabulated. These include values of thermal diffusivity, bulk absorption, surface absorption, the refractive index and its temperature variation, and photoelastic constants. These measurements provide the necessary data base for the evaluation of material performance. Care must be taken in both obtaining and applying the measured values of parameters like absorption coefficients, due to the strong effect of impurities.

Several laboratories have established dedicated facilities for damage testing. These include the Michelson Laboratory at the Naval Weapons Center in China Lake, the Air Force Weapons Laboratory, Avco-Everett Research Laboratory, and Lawrence Livermore Laboratory. All laser fusion laboratories are perforce damage testing facilities, as was evidenced by the paper presented by C. E. Thomas of KMS Fusion.

Present systems are primarily limited by failure at optical surfaces. It was pointed out at this year's symposium that surface damage, especially where coated surfaces and multi-layer dielectrics are involved, is a complicated phenomenon dependent on many parameters of the system. Thus, in high repetition rate CO_2 lasers, surface damage via plasma formation shows hysteresis effects, with plasma formation and damage on successive pulses being dependent on conditions created by previous pulses. Plasma shielding of surfaces is seen, and plasma propagation toward the laser is observed. In thermal failure, coated elements exhibit lower damage thresholds, due to the poor thermal conductivity across the interface between coating and substrate.

Nowhere is the complexity of damage phenomena more evident than in multilayer dielectric coatings. These film materials are variable in structure, depending on the process by which they are deposited. Their morphology is seen to change, after deposition, due to residual stress, thermal cycling during a laser pulse, or even on the shelf. Thin film damage is seen to depend on substrate roughness, even down to rms roughness values of less than 100 Å, on interlayer roughness, standing wave intensity, and residual stress. Empirical relations are emerging, however, which allow one to isolate the damage dependence on each separate variable, in order to assess the relative importance of each of the contributing factors. The dependence of surface breakdown electric field E^{th} on surface roughness, for example, is found to take the form $E^{th} \sim \sigma^{-m}$, where σ is the rms roughness, and $m \sim 0.5$. This expression appears to be valid for 10 Å $< \sigma <$ 300 Å, although a complete theoretical justification is yet unavailable.

The dependence on surface roughness is an example of the cycle of improvement of optical materials. The relation between the process of fabrication and the measured parameters, in this case, the roughness, is established via careful measurement. The relation between the measured parameters and the damage threshold is elucidated by careful experiment, and then summarized in an empirical relationship of convenient

simplicity. Thus the fabrication process is linked directly to the performance characteristics via an intermediate scientific hypothesis. The laser user can specify to the vendor the required fabrication method, and can measure the resultant character of the element involved. Unless this cycle is complete, specification of high power laser components is essentially impossible.

An observation emerging from the investigations of several laboratories concern the use of ZrO_2 vs. TiO_2 for the high index layer of multilayer film. Although ZrO_2 has a slightly lower index than TiO_2, its damage level, in thin film form, is consistently lower. This is attributed to poorer homogeneity and purity in this material. Some evidence is emerging of multiphoton absorption in ZrO_2 films, even though the band structure of the material would seem to preclude this effect. A preference for TiO_2 over ZrO_2 has been indicated by several manufacturers and purchasers of thin films for high power use.

Whenever thin films are involved, it is of great importance to distinguish between bulk properties of the material and thin film properties. Fundamental characteristics of optical materials, such as refractive index, are seen to vary significantly from bulk values depending on the nature of the film deposition process, the substrate, the thermal environments, and other variables of the coating process. All properties of thin films are severely affected by impurities, particulate inclusions, and defects, both in the films and at the film-substrate interface.

The ultimate failure mode of dielectric surfaces in short pulses is by avalanche ionization. Evidence is accumulating that this process is more complicated than previously thought. The process whereby the avalanche is initiated, by impurity ionization, multiphoton ionization, or excitation of electrons from shallow traps and color centers, is seen to play a large role in determining the threshold for avalanche ionization, the statistical character of the avalanche, and the wavelength dependence of the breakdown threshold. Avalanche ionization in solids, and at dielectric surfaces, will be a subject of continuing, vigorous investigation.

Interest in uv lasers has spurred renewed investigation of multiphoton processes. Here again, the theoretical picture is uncertain, and accurate experimental data are just beginning to appear. As more powerful short wavelength lasers are developed, multiphoton processes will be more clearly revealed.

A vital lesson can be learned from the series of symposia on laser damage, one that may not be fully appreciated. At present, optical material development retains an empirical flavor, and lacks the underlying base of continuing scientific support the field requires. The tendency is to attack problems as they arise in the engineering development of large systems, rather than attempting to develop the base of scientific understanding. This is a consequence of the way funds are allocated, rather than the proclivities of the research community. In the long run, the absence of an underlying scientific program in optical materials development will increase the cost and decrease the performance and reliability of large laser systems. It is fervently hoped that this situation can be remedied in the not-too-distant future.

2.0 Summary of Papers

The papers presented at the 1975 Symposium were organized under six topics: Fabrication; Metal Mirrors; IR Window Materials, IR Damage Tests; Damage in Dielectric Films and at Exposed Surfaces, and Avalanche Ionization and Multiphoton Processes. Because of the large number of papers submitted and an intent to avoid concurrent sessions, several papers were presented by title only. These papers have been inserted and summarized under the most appropriate topical heading. As in the previous years, the purpose of these summaries is to provide the reader with a concise overview of the conference papers and to direct his attention to those papers of greatest interest to him.

2.1 Fabrication

The influence of fabrication procedures on resultant optical quality and damage resistance was described in four papers in the initial session of the Symposium. These early presentations stressed the processes and test employed at four organizations involved in the generation of high power optical components for use from 1.06 μm to 10.6 μm. It is obvious to most knowledgeable laser specialists that fabrication variation is the largest contributing factor in the non-reproducibility and ultimate damage resistance of high power optical elements.

To lead off the session on Fabrication, N. J. Brown of the Lawrence Livermore Laboratory discussed the procedures and techniques presently employed at LLL in the fabrication of laser optics. Techniques developed at LLL for laser optics fabrication are strongly tied to the stringent requirements of figure control, geometric (parallelism) control, and cosmetic quality for both dielectric and metallic elements. Details relating to the importance of temperature stability and component blocking were presented in light of $\lambda/10$ figure and 2-3 seconds of parallelism tolerances.

For example, polishing elliptically shaped laser disks to good figure is difficult because of fluctuating thermal gradients across the disk. A typical radius to thickness ratio of 4 at λ 6328 Å in BK7 leads to about 4 1/2 fringes/degree for a 20 cm diameter workpiece. Thus it is easily seen that very small thermal gradients can indeed cause considerable difficulty in fabricating good figure elements, particularly if the workpiece is removed from the lap for intermittent testing and placed in a slightly different temperature environment. Many other fabrication concerns and limits were described.

W. J. Spawr of Spawr Optical Research, Inc., discussed standard industrial polishing procedures employed at his company. His message stressed the major importance of the skilled and careful optician who through experience or knowledge of the fabrication process can produce high quality optics in a timely manner. In the case of metal mirrors, they have essentially eliminated the grinding process by the use of standard machine tools. Machining to a $\sqrt[32]{}$ finish allows the grinding step to be eliminated. The component proceeds directly to the polishing operation. This procedure has consistenly yielded damage resistant elements.

Ion polishing has been employed in several cases to improve the surface finish of optical materials, most notably glasses, metals and hard crystalline substances such as sapphire. R. A. Hoffman, W. J. Lange and W. J. Choyke of Westinghouse have explored this technique on single crystal NaCl, using low energy grazing incidence Xe ions. The main purpose of this study was not only improving surface finish but to evaluate the adhesion of films to ion planed vs. conventionally finished surfaces. Results indicated that ion planing and coating (As_2S_3) in situ of NaCl surfaces minimizes contamination at the film-substrate interface, greatly improves film adherence and protects NaCl substrates against moisture attack. While previously introduced surface scratches were removed, they were replaced by other raised surface features, which may be the result of different sputtering rates at dislocations introduced in the grinding phase or from contaminates. This area requires further study.

Surface aborption, optical figure and optical scatter from alkali-halide windows are particularly important in high average power 10.6 μm lasers. These factors were considered from a polishing standpoint in a paper by M. J. Soileau, H. E. Bennett, J. M. Bethke, and J. Shaffer of the Michelson Lab at the Naval Weapons Center. Through a chemical-mechanical surface finishing technique they have developed alkali-halide surfaces which have less than 1×10^{-4} surface absorption, are parallel to < 3 seconds of arc and flat to better than $\lambda/4$ in the visible and achieve scatter levels below 10^{-4} at 10.6 μm. While the recommended procedure is too lengthy to detail here, it involves first removal of all surface contamination and mechanical damage by etching in concentrated HCl. The requisite optical figure is then produced with a minimum of surface working. In this procedure, the surface is initially ground to approximate flatness by various controlled grinding with different grit sizes (20 → 5 μm) of Al_2O_3 in kerosene on a Pyrex plate. The sample is then etched for 3 minutes and rinsed in ethanol, then blown dry with nitrogen. Thence, several steps proceed to the final polishing and cleaning state. If the sample does not reach the desired figure in 4 hours of polishing it is best to re-etch and then repolish again. This procedure allows the fabrication of alkali halide surfaces of acceptably high quality. Several important ancillary conclusions were drawn from this work. They are: (1) scratches significantly increase IR scattering in KCl windows as well as resulting in lower damage thresholds; (2) in the absence of scratches scattering above 5×10^{-4} is determined by microirregularities, while below this by particulates; (3) components used in reflection (mirrors) are much more sensitive to microirregularities than low-index materials used in transmission (windows). For example, surface σ values of 80 to 100 Å rms can be tolerated on windows while σ values of 20 Å rms or less are desirable for mirrors; and finally (4) the magnitude of backscattering from windows is approximately equal to the magnitude of forward scattering.

2.2 Metal Mirrors

The growing interest in metal mirrors for both high peak power and high average power applications was evident in the second topical session. Results of damage testing under these two conditions was reported along with detailed optical measurements of diamond turned surfaces. Problems relating to the actual turning and cleaning of micromachined surfaces were revealed. These two areas are in need of further emphasis if damage resistant coatings for enhanced reflectivity of high optical quality metal mirrors are to be achieved.

Although metal substrate mirror development is generally driven by high average power infrared applications (primarily because of better thermal conductivity and evidenced high reflectivity of these elements), they may as well offer considerable advantages as laser fusion system components as well. In this vain, the damage resistance of diamond turned and polished metal mirrors to 150 psec, 1.06 μm laser pulses was the subject of a report by T. T. Saito, D. Milam, P. Baker and G. Murphy of the Lawrence Livermore Laboratory. Several diamond turned, diamond turned/polished and polished copper and silver mirrors were evaluated both at near normal and 45° angles of incidence. As a corollary to the experimental damage assessments a one-dimensional heat flow treatment was developed. In this case to attain satisfactory agreement between theory and experiment, it was deemed necessary to include the heat of fusion into the computed damage threshold. From the experimental observations, diamond turned surfaces had the highest damage threshold of the types of surfaces tested, with silver (4 J/cm^2) being the best. Similar to other reports at this symposium an increased damage resistance at a 45° angle of incidence for s polarization was found. Thus these elements compare favorably with dielectric mirrors. This work demonstrated that various defects introduced during fabrication degrade the damage resistance of silver. A multiplicative degradation factor D was estimated for each effect. A reduction of the theoretical damage threshold was observed as follows: (a) slight electroplating defects (D=0.8); (b) diamond turning marks (D=0.7); (c) scratches introduced during cleaning (D=0.5); and (d) final polishing (D=0.1→0.2).

Threshold damage measurements on a variety of polished bulk copper and thin gold film reflectors were reported by I. Goldstein and D. Bua of Raytheon and F. A. Horrigan of Science Applications. The laser employed was a Nd:YAG system operating in the TEM_{00} mode with a pulse width of 11 nsec FWHM. Experimental results agreed quite well with a simple thermal model assuming a critical surface temperature at damage threshold. From their results a figure of merit (FOM) for the selection of metal mirrors materials useful in pulsed laser applications was tendered. This FOM was equal to $\frac{\Delta T_c \sqrt{KC}}{1 - R}$, where ΔT_c = critical temperature rise at the surface, K the thermal conductivity in watt/cm ∿ °K, C is the specific heat per area, in joules/cm^2, and R the reflectivity of the surface. Based upon this analysis, the ranking of normally used materials shows copper to be the optimum, followed by silver and gold. Sample tests were performed to validate the suggested analytical approach, together with damage measurements as a function of angle of incidence and polarization. They found damage thresholds as high as 44 j/cm^{2}at a 70° angle of incidence. Furthermore, increasing the reflecting film thickness also causes an increase damage resistance until a thickness of about 1 μm is reached. A basic conclusion of this study was that use of reflecting metal mirrors at large angles of incidence, such as in toric optics, can lead to greater throughput power/operative area than more normal incidence focusing configuration.

The group at the Michelson Laboratories, Naval Weapon Center, have applied their extensive array of optical evaluation facilities to assess diamond turned mirrors. H. E. Bennett, M. J. Soileau, and P. C. Archibald investigated the surface figure, scattering characteristics, reflectivity, laser damage resistance and environmental resistance of several high quality micromachined elements. Generally, optical figure better than λ/20 at 10.6 μm for ∿ 4 cm diameter samples and one wave for 10 cm samples was noted on a large number of samples from the Y-12 plant at Oak Ridge. Scattered light levels in the infrared as low as 2 x 10^{-5} were noted, comparable to values of good conventionally polished mirrors. Typical roughness was 20-30 Å rms with one sample showing only a 12 Å rms level from scattering measurements. In addition, infrared reflection values as high or higher than those of conventional evaporated or sputtered metallic coatings have been achieved and one mirror exhibited an absorption of only 0.006 at 10.6 μm. It is conjectured that the damage threshold of micromachined mirrors may well be higher than those produced by other techniques. This specific area as well as environmental durability and coatability of these surfaces requires further assessment.

R. E. Sladky and R. H. Dean of the Oak Ridge Y-12 plant discussed optical measurements on high-quality, large diamond-turned mirrors. They pointed out that in order to produce acceptable super finished metal mirrors by single point turning, five requirements must be met. They are: (1) precise machine movements; (2) complete static and dynamic vibration analysis; (3) dynamic balancing; (4) temperature control; and finally (5) sharp diamond tools. However, after the component is fabricated, testing is necessary to insure that it meets specification as well as allowing immediate diagnostic information to be made available to the machine tool engineer. A most important test has been surface finish and surface figure. A recently fabricated flat 15.5 x 25.75 inch, elliptical mirror, made of copper electroplated on an aluminum substrate was inspected by both a Leitz interference miroscope and a Davidson plano interferometer. Average deviation from flatness was 77 microinches (saddle-shaped). This result is thought to be due to the shape of the mirror, and its blocking resulting in mirror flexing during fabrication. Spherical mirrors are normally tested with the classic Foucault knife-edge test. For a 15" diameter spherical mirror with a radius of curvature of 133 inches, a maximum error of 31 μinch ($\lambda/13$ at 10.6 μm) was obtained. Other measurements frequently made are blur circle testing, scattering and diffraction. Diamond turned surfaces are quite similar to a circular diffraction grating. A typical cusp spacing might be 0.001 inch resulting in a $\sim$ 1.2 μinch finish. Further studies are under way to assess the utility of diffraction testing of these surfaces as an indication of mirror quality.

Because of the outstanding potential of diamond turned metal mirrors as high average power laser elements, an obvious possibility for improved performance and durability would be to enhance their reflectivity and protect them against environmental degradation by dielectric coatings. Thus, the damage resistance of coated diamond turned mirrors to a CW CO_2 laser beam was evaluated by J. R. Buckmelter, T. T. Saito and R. Esposito of the Air Force Weapons Laboratory and L. R. Mott and R. Strundlund of Optical Coating Laboratory. While the samples tested are too numerous to describe in this review, certain major conclusions can be stated. The initial results of multilayer 10.6 μm dielectric coatings on diamond turned mirrors demonstrated serious problems of coating adhesion. Auger analysis has shown the presence of hydrocarbon contamination probably as residuals from cutting fluids. Furthermore, stress relief of electroplated/diamond turned surfaces contributes to coating adhesion problems. CW laser damage tests at 10.6 μm demonstrated threshold only up to 46 KW/cm^2, which is considerably less than the damage threshold of similar coatings on polished bare substrates. Adhesion problems are identified by peeling and erratic (non-uniform) optical properties. This problem bears further study if present metal mirror reflectivities of 99.3% are to be raised to levels of 99.9%, typical of good multilayer dielectric enhanced surfaces. Generally this initial endeavor into dielectric coating of metal mirrors was disappointing. This is usually the case, when dielectric coatings are employed in new situations. However, if coatings could be deposited on diamond-machined elements without defects such as pinholes, inclusions, absorption and with good adherence, laser damage thresholds of these elements can be expected to increase substantially.

An obvious concern in machined optics is the introduction of systematic or random out-of-tolerance variations by the machine tool itself. The degradation of resulting component quality from slide position errors was treated by J. B. Arnold, P. J. Sleger and R. R. Burleson of the Y-12 plant. After reviewing the important criteria for diamond turning, they described various inspection techniques which are suitable for identifying error sources in the drive train. As a consequence of this procedure, the stepping motors employed in setting the slide position was identified as a prime culprit in causing poor quality mirror surfaces. This source of error has been greatly reduced by employing encoded DC torque motors. It is intended that a further reduction in this source of error will be achieved by the use of laser interferometry to set the slide position accurately. The correction of these errors must be accomplished before contoured surface finishes comparable to present-day flat and cylindrical surface quality can be fabricated by diamond machining techniques.

Several individuals, including Ted Saito of LLL, R. House, J. Bettis, and A. Guenther of AFWL, and W. E. K. Gibbs and A. D. McLachlan of the Material Research Laboratory, Department of Defense, Commonwealth of Australia, have recently noted the degradation of polished optical surfaces by ultrasonic cleaning. In a communication from the last two authors, surfaces of OFHC copper, beryllium/copper, zirconium/copper, stainless steel, kanigen, and fused quartz were investigated using Nomarski microscopy. In all cases somewhat mild ultrasonic cleaning caused a discernible degradation of surface finish after periods of 45 or 90 minutes in the cleaning bath. Subsurface structures, obviously introduced during the grinding process, were subsequently revealed for fused quartz after ultrasonic cleaning, and several of the metallic reflectors exhibited enhanced grain boundaries and the appearance of imperfections similar to etch pits.

2.3 IR Window Materials

As might be expected, a large number of presentations addressed the multi-faceted subject of laser windows. Topics ranged from fundamental thermophysical and optical properties of materials, to pulsed and CW damage and distortion studies. Several improved instruments for making fundamental measurements were described together with a novel technique for ascertaining surface absorption, a subject of growing importance.

Physical parameters such as the thermal diffusivity, thermal conductivity, optical absorption coefficient, thermal expansion coefficient, critical rupture stress and Young's modulus are all important characteristics in the thermally induced failure of optical components. R. Doussain and H. P. LeBodo of the Laboratoire National D'Essais, Paris, France, reported on careful measurements of the thermal diffusivity of germanium, gallium arsenide and cadmium telluride over the temperature range 80°K - 900°K. Their experimental procedure employed a laser flash technique in which a thin, disk-shaped specimen was uniformly irradiated by a pulsed (0.5 - 1.3 msec) Nd-glass laser system. The resultant temperature at the rear surface of the sample was recorded and analyzed to produce the thermal diffusivity values. As a check of this procedure, Armco iron and OFHC copper were also investigated. Typical values for the thermal diffusivity @ 300°K were 0.195 for Armco iron; 1.14 for OFHC copper; 0.340 for germanium; 0.225 for gallium arsenide and 0.046 for cadmium telluride all in units of cm^2/sec. Estimated accuracy was better than ± 8%.

In another attempt at finding a suitable damage indicator, K. M. Leung, M. Bass, and A. G. J. Balbin-Villeverde of the University of Southern California employed a comparison of the incident and transmitted laser pulse waveforms to exhibit the on set and type of laser induced damage to several 10.6 μm window materials. Employing a TEM_{00}, CO_2 TEA laser emitting up to 100 mj in a FWHM gain switched pulse of ∿ 92 nsec, they reported results on improved ZnSe, commercial and RAP Grown KCl, and commercial NaCl. The self mode-locked output typically consisted of twenty-three pulses of duration < 2.5 nsec, separated by 8 nsec. From previous work, indications were that variations in the transmitted pulse shape through a window under test can be used to identify either intrinsic, electron avalanche or extrinsic, inclusion dominated damage. A summary of their results based on survival times (before damage) or bulk breakdown on the tested materials led to the conclusions that the NaCl damage was intrinsic in nature but that the failure of the KCl and ZnSe samples were inclusion dominated. The NaCl samples, polished conventionally, damaged between an axial peak power density of 840 and 1600 MW/cm^2 on the surface and between 3900 and 6100 MW/cm^2 in the bulk. Conventionally polished RAP grown KCl samples damaged at 460 MW/cm^2 on the surface and bulk between 1500 and 4600 MW/cm^2, while conventionally polished commercial KCL damaged at 560 MW/cm^2 on the surface and from < 190 to 650 MW/cm^2 in the bulk. For conventionally polished ZnSe, surface damage was 270 MW/cm^2, diamond polished 350 MW/cm^2 and super polished also 350 MW/cm^2. Bulk values ranged from 230 MW/cm^2 for an old sample to 460 MW/cm^2 for more recently produced ZnSe. Obviously, for several of the samples the surface values were controlled by contamination.

Continuing laser induced damage studies on alkali halides at 10.6 μm by V. Wang, C. R. Giuliano, S. D. Allen, and R. C. Pastor have again stressed the dominant role played by material purity and processing variables in limiting the damage resistance of KBr, KCl, and NaCl exposed to pulsed CO_2 TEA lasers. Large variations in threshold were observed for samples grown by different methods. Unfortunately it was not possible to ascertain whether the large fluctuations observed were due to spatial inhomogeneities or from purely statistical processes. In essentially all cases the performance of RAP grown samples was superior to the commercially available materials. The highest observed breakdown fields (in Mv/cm) for KBr, KCl, and NaCl at 0.6 μsec and 4 μsec were 0.8/0.94, 0.42/0.44; 1.8/2.7, 1.03; and 2.5/2.9, > 1.08.

Inasmuch as most present-day candidate window materials for high power 10.6 μm CW laser application exhibit sufficient strength to preclude their fracture before unacceptable laser induced optical distortion, J. S. Loomis of the Air Force Weapons Laboratory and E. Bernal of Honeywell have performed a detailed analysis and experimental verification of optical distortion as a function of incident power and material properties of ZnSe, KCl, NaCl, CaF_2, SrF_2 and BaF_2 windows. Changes in interferometric patterns were attributed to: (a) isotropic phase shifts resulting from local temperature rises; (b) anisotropic effects due to induced birefrigence, and (c) localized phase shifts at the entrance and exit points due to surface absorption. The effects of thermally induced birefringence are shown to be dominant in the case of alkaline earth fluorides. For KCl, NaCl and ZnSe relative shifts in fringes/watt were in the ratio of 1:1.11:6.30 with KCl and NaCl displaying negative lensing and ZnSe positive. Again in this research bare windows performed better than coated elements because of decreased surface absorption.

To arrive at a quantitative understanding of the ultimate concern in windows used in high average power laser systems, J. A. Detrio and R. D. Petty of the University of Dayton evaluated the thermal distortion in ZnSe windows by measuring variations in the far field irradiance of a 10.6 μm laser beam as a function of input power and absorption coefficient. Results were compared to theoretical predictions based on a figure of merit analysis previously proposed by Sparks. This analysis treats two modes of failure, the first being a mechanical fracture due to thermally induced stresses and the second failure due to unacceptable optical distortions resulting in a reduction in far field intensity. The latter mode was the concern of this paper. It was not possible to make an exact comparison between theory and experiments, since experimental conditions did not conform to the assumptions of the theory. It was concluded that ZnSe fails primarily in the optical distortion mode, however.

D. L. Stierwalt of the Naval Electronics Laboratory Center has continued his program on the accurate measurement of the spectral emittances of laser window materials. Until the present time, the sensitivity of his measurements was limited by background noise caused by thermal fluctuations in the temperature of the total instrument. To reduce this limitation a new instrument was constructed allowing operation at 77°K. Through this reduction in background level, new measurements were reported for NaF, NaCl, and KBr over the ranges 200°K to 373°K in temperature, and 2.5 to 14 μm in wavelength with a spectral resolution of 1.5%. The noise equivalent absorption coefficient was estimated to 10^{-6} cm^{-1} at 10.6 μm and about 10^{-5} cm^{-1} at 5.0 μm. A number of new previously unreported bands were observed in the above materials.

In a report describing a rather elegant technique for measuring surface absorption as a function of depth, J. H. Parks and D. A. Rockwell of the University of Southern California discussed the use of acoustic probe techniques to evaluate absorption levels down to 1×10^{-4} in thin surface layers of bulk KCl polished by different procedures. It was pointed out that while infrared absorption measurement techniques are available which avoid surface contributions, no sensitive method has been devised which allowed the direct assessment of surface absorption (1 - 10 μm depths) as might be modified from the bulk value by environmental or finishing processes. Consideration was given to any non uniform temperature gradient over the surface wave penetration depth, which could produce dispersive effects in the surface wave propagation. These considerations are generally arrived at through recorded phase changes. A principal conclusion of initial studies on KCl indicated that chemical etching can reduce surface absorption by a factor of 3-4 over that of conventionally polished surfaces.

In their continuing DARPA sponsored program on the precise measurement of the optical and thermal properties of optical materials, A. Feldman, D. Horowitz, and R. m. Waxler of the National Bureau of Standards reported on the determination of photoelastic constants (importance in birefrigence considerations) of Ge, RAP grown KCl and KCl doped with KI. Present techniques employ null methods using Twymann-Green and/or Fizeau interferometers. These procedures have several advantages over previous techniques which were not independent of the intensity fluctuations frequently present in the radiant thermal source. From the evaluation of the various combinations of photo-elastic coefficients, q_{ij}'s, several elasto-optic coefficients, p_{ij}'s, were computed. For germanium, q_{ij}'s at 10.6 μm were determined and for KCl at 10.6, 0.644, and 0.633 μm.

Another paper dealing with fundamental material properties was presented by M. J. Dodge and I. H. Malitson also of the National Bureau of Standards. In their work, the refractive index of CVD zinc selenide and its temperature coefficient was investigated. Measurements of the refractive index of this important window material were accomplished over the range 0.5086 to 18.2 μm by the normal minimum deviation method employing prismatic samples. For the evaluation of the temperature coefficient of index change, data were obtained at 20°C and 34°C and subsequently fit to a three term Sellmeir-type dispersion equation. For two samples investigated the index of refraction ranged from 2.67544 at 0.54 μm to 2.32781 at 18.2 μm and was 2.40778 at 10.6 μm. For the temperature coefficient of refractive index at 10.6 μm values ranged from a low of 6.2×10^{-5}/°C to a high of 10.0×10^{-5}/°C. The average of all reported values being 7.8×10^{-5}/°C. Agreement between their measurement and those of several other published values was good. Any differences between reported values are undoubtedly due in large part to differences in the test materials, as well as some possible instrumental factors.

In a paper, "by title only," J. L. Zar of the Arco-Everett Research Laboratory communicated information concerning the establishment of a test facility specifically constructed for testing laser window materials at high power levels. Among several available lasers the facility primarily utilizes a smooth intensity profile focusable 15 KW CW laser operating at 10.6 μm, with provisions for cooling of windows and evaluation of the mechanical and optical response of test objects. Another laser is available for testing with 80 j at 10.6 μm in 100 μsec pulses. In an initial experimental sequence of tests, forty-seven diamonds were evaluated to attempt a correlation between the UV absorption spectrum, the IR absorption spectrum, and the absorption coefficient β at 10.6 μm. Preliminary results indicate a rough correlation between β at 10.6 μm and the sample transparency at 0.253 μm. This correlation is only a rough guide, since impurities, in the form of interstitial nitrogen in diamond, have a profound effect in the IR transmission. In materials with greater tolerance for impurities, it is expected that infrared absorption will be only weakly correlated with uv absorption.

2.4 IR Damage Tests

Three very interesting papers discussed various aspects of optical material damage. For the first time, information on the repetivitively pulsed damage response of components was heard, as well as IR wavelength dependent studies at HF, DF, and CO_2 wavelengths. Both these presentations portend greater emphasis in these areas in the future.

A very comprehensive set of CW 10 μm damage tests on a large variety of optical components was reported by C. A. Hugeley and J. S. Loomis of the Air Force Weapons Laboratory. In their experiment they subjected several samples to the output of a 1000-watt gas transport laser for periods 2 or 30 seconds at discrete power levels of 120, 240, 360, 480 and 600 watts on 1 mm diameter spots. These included seventeen coated and uncoated windows of ZnSe and KCl, eleven abraded and varying absorptance KCl windows twelve coated mirrors and eleven gratings. Briefly, in almost all cases, samples exhibiting higher absorption failed at low incident laser powers as expected. Materials with opaque coatings of Ge or CdTe did not exhibit a high damage resistance. These materials are low-band gap semiconductors and damage is most probably caused by thermal runaway. Results from the abraded KCl samples suggest that some damage to coated KCl windows may be due to higher absorption at the substrate surface and consequent failure at the surface, rather than the failure of the coating producing subsequent failure of the substrate. From the mirror tests it was obvious that damage resistance was apparently more a factor of who prepared the sample than the sample's composition and structure. This again points out the dominance of processing variables in ultimate damage resistance of fabricated optical components. For the samples tested, one can conclude that under CW irradiation dielectric coated mirrors can survive intensity levels comparable to bare metal mirrors; however, extrinsic factors are more likely to be present in coated elements. Finally gratings damaged in a manner similar to metal mirrors, but with damage levels generally at or above 150 KW/cm^2.

For the first time in this symposium series, results on the laser induced damage of components subjected toa rapidly pulsed high energy 10.6 μm laser were reported. The results reported by A. B. Callender of the Air Force Weapons Laboratory clearly indicated that high rate multi-exposure damage thresholds differ considerably from single shot values primarily due to the formation of breakdown plasmas in the vicinity of the component surface after several repetitive irradiations. Repetitive pulsing is an interesting region of damage testing intermediate between single high peak power exposures and the high average power situation. As was pointed out, under the conditions of this experiment, a new laser parameter must be introduced, namely the duty cycle, to evaluate the damage mechanism properly. Depending on the specific conditions of the test, other factors may also play a role. They are primarily the environmental flow rate over the component under test, and its thermal time constant. The laser employed in this study was an electric discharge laser (EDL) emitting 60 joule pulses of 20 μsec duration at rates up to 150 pps over sufficiently large areas. The pulse shape consisted of a leading 100 nsec pulse followed by a 20 μsec duration flat topped pulse, the initial peak being between two and four times the average power. In this study consideration was given to surface temperature rises during an experimental run to determine if substantial vapor was released to aid plasma formation. Calculations indicated that this situation was unlikely unless influences such as evaporation at surface irregularities come into play, which they can if the pulses are short enough, i.e., transition from thermal to electrical breakdown behavior. The variation of surface temperature rise was investigated experimentally by controlling the firing rate. Generally, conclusions from the test results were encouraging for mirrors and somewhat discouraging for windows. Bare copper samples exhibited surface plasmas for low repetition rate loading above 200 J/cm^2 ($\sim$ 10 mW/cm^2) but no permanent visible

damage to 290 J/cm^2. Dielectric coated mirrors showed much lower thresholds as can be expected in that the dielectric film was evaporated producing a visible substrate degradation. Window tests were carried out in a strongly focused beam. Bubble tracks were observed for impurity-doped alkali halide samples, but not for undoped KCl, NaCl or ZnSe. The author attributes these tracks to self-focusing in the samples, but in light of the low value of n_2 for these materials, and its susceptibility to impurities, this explanation seems unlikely.

J. O. Porteus, M. J. Soileau and H. E. Bennett of the Michelson Laboratories, Naval Weapons Center, reported on the establishment of a new well instrumented test facility at China Lake. Optical samples are mounted in a bakeable ultra-high vacuum chamber. In situ measurements of the response of the test object is accomplished by scanning electron imaging, optical microscopy, a profiling Auger system and charged particle collectors. The output and focused characteristics of the test lasers are well controlled. Typical laser outputs are 1.5 J at 10.6 μm (CO_2) in 100 nsec and 0.5 J at 2.8 μm or 3.8 μm (HF, DF) in a range of pulse widths from 200 to 800 nsec. Preliminary results using machined Al or Al coated mirrors have been performed. At 10.6 μm polished or machined 2024Al damaged at ∿ 14 J/cm^2 while DC sputtered Al (1500 Å thick) on an aluminum substrate damaged at 8 J/cm^2, DC sputtered Al (1500 Å), RF sputtered Al (2000 Å) and UHV evaporated Al (1400 Å) deposited on high quality quartz substrates (σ < 20 Å rms) failed at 7, 6 and 4 J/cm^2 respectively. At 3.8 μm polished 2024 Al failed at 63 J/cm^2. These threshold damage levels correspond to the observance of visible pitting. Even though the coated elements have a greater surface purity, uniformity and reflectance than the bare Al substrates, it is seen that coated elements have considerably lower damage thresholds. This was attributed to the coating -- substrate interface which acts as a barrier to heat flow. We look forward to more results from this facility in the future.

2.5 Damage in Dielectric Films and at Exposed Surfaces

As can be expected the most populated session of the 1975 Damage Symposium was concerned with damage at bare and coated surfaces. It is well known that this is the area where the major extrinsic damage initiating features are introduced. Looking for guidelines and scaling relationships, several parametric studies addressed the influence of the following variables: materials, aging, mode structure, spot size, pulse length, wavelength, temperature, environment, reflectance, coating design, refractive index, and surface roughness. Both pulsed and CW high power tests from 1.06 μm to 10.6 μm were reported. Several very important results were obtained as a consequence of these efforts.

Investigation of damage in ZnSe/ThF_4 multilayer dielectric enhanced reflectors (∿ 99.8%) as a function of mode structure, spot size, and pulse duration were reported by V. Wang, C. R. Giuliano, and G. Garcia of the Hughes Research Laboratory. This parametric study, using a 10.6 μm CO_2 TEA laser operated in either a single or multi-longitudinal mode over the temporal domain from 0.6 μsec to 6 μsec and over spot sizes from 50 μm to 255 μm, was performed to elucidate the appropriate damage mechanism of dielectric coated reflectors under the conditions of the experiment. In tests on samples placed in an evacuated (∿ 20 m torr) chamber to avoid extraneous dust or air breakdown processes, it was observed that ZnSe/ThF_4 dielectric coatings deposited on silver overcoated molybdenum substrates displayed an essentially constant damaging energy threshold for pulses of 0.6, 1.0, 4.0, and 6.0 μsec duration. These results are in agreement with a thermal damage mechanism as opposed to an electric field dominated breakdown processes. By performing additional pulsed (6.0 μsec) irradiations over 50, 72, 140, and 255 μm diameter spot sizes, and using an analysis similar to that previously reported by DeShazer, et al., the average inclusion spacing was ∿ 25 μm with 90 J/cm^2 being the defect limited threshold, with an intrinsic level of 4.4 kj/cm^2, it being the highest threshold recorded. Thus, for this class of optical elements tested under the above conditions, it was concluded that performance is limited by the presence of localized absorbing defects.

It is surprising to note that despite the considerable concern for thermal distortion and damage to high average power windows and mirrors, no one had performed a thermal sensitivity study of the changes in optical properties of enchanced reflectivity coatings as a function of temperature. However, this year D. L. Decker of the Michelson Laboratories accomplished a careful evaluation of the temperature and wavelength dependence of the reflectance of multilayer dielectric mirrors for use in the infrared. It is well known that the absorptance of an optical element in high average power application controls both the thermal heat load and the

associated distortion. Thus one must evaluate this property both at room temperature and under operating conditions to assess adequately the performance of the total system as well as of the individual component. Thus data are needed on the change in absorptance and/or reflectivity with temperature, together with any wavelength dependence for broad band reflectors. Employing an instrument of his own design capable of detecting changes in reflectivity and temperature with a precision of better than 7×10^{-5} over the temperature range 25°C to 125°C, Decker analyzed several commercially available dielectric multilayer designs as well as a thin film Ag coating. The multilayer designs (R's) included $ZnS/ThF_4/Ag(R_1)$ $ZnSe/ThF_4/Ag(R_3)$ and $Si/SiOx/Ag(R_4)$ coatings on ULE glass with the bulk of the measurements being made around 3.8 μm. Results are given in terms of absolute reflectance as a function of temperature for the original film, after storage for one year under nitrogen and after cycling to 120°C. Design R_1 was much less stable than designs R_3 or R_4. The observed change in reflectivity was strongly wavelength dependent. The variation in reflectivity could not be associated to any degree with changes in scattering and this was thus eliminated as a reason for the observations. From a critical analysis of possible causes it was concluded that since design R_1 produced an irreversible variation in mirror performance with temperature, the dominant mechanism was a change in structure of composition as a result of possible intra or inter-layer diffusion producing a concurrent index change. The total change was also highly wavelength dependent. In the case of design R_4 the variation with temperature was nearly wavelength independent with a value of $dR/dT \sim +3 \times 10^{-5}$/°C. Decker pointed out, in an additional experiment, that an analysis of the behavior of a metal coated mirror would be instructive in corroborating the results. Theory predicts a dR/dT of -1.5×10^{-5}/°C in the near infrared for silver at temperatures near room temperature and indeed at 10 μm a value of -1×10^{-5}/°C was observed. This is in agreement with electron-phonon scattering considerations. At 4.0 μm, however, results obtained did not agree either in magnitude or sign. No unambiguous explanation of this unexpected result is presently available and thus it warrants further study. Summarizing Decker's results, design R_3 was clearly superior since it exhibited the smallest reversible temperature dependency and lowest apparent absorption, leading to highest damage thresholds. It is obvious that temperature dependent studies such as those reported by Decker are not only welcome but strongly suggested for other future investigations.

In an attempt to find isotropic, homogeneous, stable, and suitably damage resistant coatings for 10.6 μm windows, A. Golubovic, W. Ewing, R. Bradbury, I. Berman, J. Bruce, and J. J. Comer of the Air Force Cambridge Research Laboratories investigated the ZnS/CeF_3 bi-layer anti-reflection coating. The study investigated both preparation effects and a damage evaluation of the finished coating on well characterized RAP grown KCl substrates. Both sublimed and sputtered ZnS layers were first deposited with CeF_3 layers thermally evaporated on both bare and ZnS coated KCl. From a large variety of instrumental investigations they were able to analyze the resulting films as a function of deposition conditions. Sputtered films of ZnS on KCl were identified as being in the cubic form with a preferred {111} orientation regardless of substrate orientation providing the rate of deposition was > 1 Å/sec. Surface roughness of the coating is strongly dependent on deposition rate, e.g., there is a decrease in grain size with increased deposition rate from 2.5 to 6.5 A°/sec. Evaporated ZnS films displayed preferred orientation of [110] planes parallel to the substrate, and tended to be smoother than sputtered films, but had a greater tendency to vary in crystallinity and orientation. CeF_3 coatings on KCl were also crystalline, being hexagonal with a preferred orientation of [100], fairly smooth and fine grained (< 300 Å). For CeF_3 on ZnS coated KCl, the films were polycrystalline with no preferred orientation. All the anti-reflection coatings were found to be environmentally stable, adhering well to the substrate. Damage tests were accomplished on the samples employing a 65 mj, 100 nsec FWHM, TEM_{00}, 1 PPS CO_2 TEA laser focused to a 180 μs spot size. Single CeF_3 and single evaporated ZnS coatings both damaged at $\sim$ 35 j/cm^2. Sputtered single films of ZnS damaged from 40 to 65 J/cm^2 depending on deposition rate, and the CeF_3-sputtered ZnS AR coatings failed over a range from 5 to 13 J/cm^2 depending on ZnS deposition rate while the CeF_3-evaporated ZnS failed at < 6 J/cm^2. The results of this paper point out that the mechanical properties of both substrate and individual coatings must be considered (particularly stress) and that interface topography may contribute significantly to the total absorption of the coating stack.

As_2S_3 coatings are frequently considered for infrared applications because of their ability to withstand high levels of laser power, while offering the added advantage of environmental durability. A. D. Bear, T. M. Donovan, and M. J. Soileau of the Michelson Laboratories reported on their studies of the effects of various deposition procedures on the quality and optical characteristics of As_2S_3 coatings applied to KCl substrates. Taking a lead from previously reported results that the stoichiometric behavior of KCl surfaces was probably a distinct function of temperature, they concentrated their efforts on an evaluation of this point for both KCl and fused quartz by applying thermally evaporated As_2S_3 coatings on substrates at different temperatures. The conclusions of these studies were as follows. The stoichiometry of KCl surfaces under electron bombardment is a function of temperature. As Golubovic previously had reported for room temperature KCl surfaces coated by either sputtering or e-beam evaporation, they have a K-rich layer. Coatings deposited on windows held at 80°C are more durable and less absorbing than those on 22°C substrates. Bulk absorption of As_2S_3 is 1.1 cm^{-1}, while for As_2S_3 coatings on 22°C KCl substrates it is 2.9 - 11 cm^{-1}, while for As_2S_3 coatings on 80° KCl substrates it is $\sim$ 1.7 cm^{-1}, and the film index is more nearly that of the bulk. Little difference was noted on fused quartz at two temperatures. The index of refraction of the As_2S_3 coating is a function of the substrate temperature for KCl, but not for quartz, with the coating on quartz having a higher index than either the 22°C or 80°C coatings on KCl.

A. L. Bloom and V. R. Costich, of Coherent Radiation, described the sensitivity of high power coating performance to structural design and materials parameters. They analyzed the influence of thermal conductivity, thermal expansivity, intrinsic stress, and Young's modulus on the damage resistance of metal, metal-dielectric, and dielectric multilayer coatings. The main points put forward in regard to the short pulse performance of multilayer dielectric films were as follows. The stress in a coating before illumination is the sum of the intrinsic stresses of the components, which can be either tensile or compressive, and the thermal stress. The latter arises due to the differences in thermal expansivity between the coating components and the substrate, which produces additional stress upon cooling from the deposition temperature to the ambient temperature. Upon illumination, the coating is further compressed by heating from the laser pulse.

Calculations were presented for TiO_2/SiO_2 coatings on quartz and glass substrates. The SiO_2 film is expected to be less resistant to damage, since it is under compressive stress before illumination, and is further compressed during illumination, while the TiO_2 film is tensile. This analysis is consistent with experimental results presented at an earlier damage symposium by Austin and Guenther, on damage threshold as a function of residual stress.

Due to its high thermal conductivity, silver would seem a good coating material for mirror use at 10.6 μm. However, its performance degrades at 100°C, so that gold and copper are competitive, if not clearly superior. At 1.06 μm, TiO_2/SiO_2 on fused silica seems the best coating. ZnS/ThF_4 is too compressive to resist damage, while ZrO_2 is so non-reproducible that the authors state that it is no longer used for good quality, high power optics.

Another aspect of coating design was emphasis by B. E. Newnam, D. H. Gill and G. Faulkner of the Los Alamos Scientific Laboratory. They showed that the standing wave pattern established in a dielectric film influences the observed damage threshold. Experiments were carried out on films of TiO_2, ZrO_2, SiO_2, and MgF_2, deposited by electron-gun evaporation on substrates of BK-7 glass. The thresholds observed for TiO_2 films of odd quarter-wave thickness were generally greater than those observed for even quarter-wave thickness, as expected from the internal field distributions. ZrO_2 also showed the same trend, but with much greater scatter in the data. SiO_2 and MgF_2 films showed little effect, as expected from their low indices.

The variability of ZrO_2 has already been discussed in connection with the previous paper. An overall observation concerning the data presented on these film damage thresholds is in order. For each coating, i.e., of a given thickness, of a given material, on a given substrate, tbe reported damage thresholds varied by a factor of 1.5 to 2. In previous damage symposia, both Newnam and A. Leppelmeier, of the Lawrence Livermore Laboratory, have reported on the large variation of damage resistance from vendor to vendor for the same film design. It is therefore not prudent to attach absolute significance to the actual damage levels reported in any given study; and intercomparison is especially unreliable.

Newnam, et al., did study the variation of threshold on individual samples as a function of various parameters. In most cases, no difference was seen in damage threshold for films illuminated from the coating side or the substrate side. This is not consistent with the standing wave picture. The authors attribute this discrepancy to the presence of absorbing inclusions in the films masking out the standing wave effects. In another study, they looked for differences in threshold between linear and circularly polarized light, as evidence of multi-photon absorption. No significant difference was seen except for ZrO_2 films. (Other evidence for two-photon absorption in ZrO_2 films has been reported in the following paper at this symposium.) No clear cut dependence on the plane of polarization of light obliquely incident on the film was seen in any sample, indicating that photoemission plays a minimal role in film damage.

It should be noted that in this work, no consideration was given to film stress effects, which were discussed in the previous paper. Three aspects of thin film damage which have been emphasized in these proceedings over the years are a) the large number of significant variables, b) the wide variation in sample quality, and c) the "Achilles heel" aspect of the damage process, which always finds the weakest point in the structure. Due to these factors, damage studies in thin films are much harder to interpret than studies in bulk materials or even at surfaces. Careful studies such as those carried out in this paper, where an attempt is made to isolate individual variables, are of great value in unraveling a very complicated situation.

A careful study of thin film damage was reported by R. H. Picard and R. A. Bradbury of the Air Force Cambridge Research Laboratories, J. C. C. Fan of the Lincoln Laboratory, and D. Milam of the Lawrence Livermore Laboratory. They measured the time to the appearance of damage in single-layer SiO_2, Al_2O_3 and ZrO_2 films; RF sputtered on glass substrates. Damage was generated using a 20-30 nsec ruby laser producing a rectangular temporal waveform described in last year's proceedings. Thus, the damage is created at a constant power level, and the time to survival is a linear measure of the deposited energy density.

In this paper the authors tested two hypotheses. They restricted their investigations to samples which exhibited homogeneous absorption, rather than defect or inclusion damage. They first tested the effect of heat conduction out of the film, and found that the observations were consistent with uniform heating only when heat conduction to the substrate was taken into account. Secondly, they tested the hypotheses that two-photon absorption plays a role in thin-film damage. Here the results were somewhat more ambiguous. The data for ZrO_2 films seem to show a clear two-photon dependence, with a nonlinear absorption coefficient of 2.4 to 2.8 cm/GW. This number is remarkably high, especially for a material in which the energy gap exceeds twice the photon energy, as is discussed in the papers at the end of this proceedings. Furthmore, they found evidence of two-photon absorption in some (but not all) SiO_2 samples.

Thus, we have two reports of possible two-photon absorption in thin film structure, in materials in which two-photon absorption is not expected in the bulk material. Clearly, this effect will require further study and experimental observation before the physics is made clear.

It has come to be accepted that laser induced scattering (LIS) provides a sensitive probe for detecting laser damage. N. Alyassini and J. H. Parks of the University of Southern California reported on a technique of damage detection more sensitive than conventional LIS. In this method, a He-Ne probe laser is focused in the region to be illuminated by a pulsed ruby laser. The probe laser is internally incident on the interface between a thin film and substrate. The films were quarter-wave ZnS and MgF_2, a half-wave MgF_2 on a quarter-wave ZnS, and a 17 layer ZnS/ThF_4 multilayer stack. All films were thermally deposited on BSC-2 Dove prisms.

Observations of changes of the reflected intensity of the probe beam were compared to spark observation and transmission changes in the ruby laser beam. The probe reflection was detected with a temporal resolution of less than 1 nsec. Changes in probe reflection were observed in cases where no visible spark or ruby laser attenuation was observed. It was also noted that the probe signal often followed the damaging laser pulse by as much as 25 nsec.

The probe scattering signal is associated with morphological changes in the film structure, either through melting or cracking due to thermal stresses. In the case of pronounced delay, it would appear that time was required for the stress to reach a critical value at some weak point in the film, which served as an initiation point for crack propagation. In a later paper, discussed below, the probe technique was applied to the study of avalanche initiation, providing a means of detecting the build-up of the conduction electron concentration in the damage area.

J. R. Bettis, R. A. House, and A. H. Guenther, of the Air Force Weapons Laboratory, along with R. R. Austin of Perkin-Elmer, presented data on the dependence of surface damage in both vacuum-deposited thin films and bare surfaces on material parameters and method of preparation. The research presented represented a continuation of earlier work by the authors, attempting to develop a description of the dependence of the breakdown field strengths on such variables as surface roughness, number density and refractive index of the material. A Nd-doped glass laser, generating approximately 400 mj in 40 nsec was used in these experiments. The laser was carefully mode-selected to give single-mode output. Half-wave films of ZrO_2, MgF_2, LiF and ThF_4 were deposited on various substrates, including fused silica, sapphire and BK-7. Al_2O_3 on sapphire, and ZnSe on ZnSe substrate were also tested.

The data obtained were fit to the form empirically derived earlier by Bettis, which predicts that the threshold field for damage should vary like $N/(n^2-1)$ where N is the number density, and n the refractive index of the material. Half-wave films were used, to produce a controlled standing-wave effect. The effect of surface roughness as discussed in a later paper by these same authors was found to modify the threshold field and the threshold field was found to vary as σ^{-m}, where $0.5 < m < 0.75$. These empirical relations apply over a broad range of variables, except in cases where extrinsic factors, such as imperfections or inclusions in the film lower the damage threshold. The presence of OH radicals, indicated by spectrophotometric measurements, was found to have an overriding influencing effect on thin film performance, completely dominating standing wave effects produced by alterations in stack geometry. It was generally found that "good" films exhibit higher damage thresholds than "bad" films, where good and bad refer to scattering by inhomogeneities. Application of these expressions, using experimental intrinsic bulk damage levels for several materials of varying index from LiF to ZnSe gave excellent agreement. However, when applied to these materials in thin film form, agreement was also good except in the case of inhomogeneous films or films of low packing factor (generally the fluorides of Li, Mg, Ba, Sr). There variations from the bulk performance are process related. Through these relationships it is possible to estimate the intrinsic damage level of materials and determine, for example, how much improvement can be made in a marginally performing fabricated component (thin film device, etc.). Again the isolation of individual variables, carefully done, is of great service in uncovering salient factors affecting the laser induced damage of thin film devices.

The primary motivation of laser damage studies at 1.06 μm is the development of large Nd-glass lasers for fusion research. The laboratories currently active in laser fusion are the major consumers of coated elements for high power operation at this wavelength. They also are active in supporting developmental efforts in the coating industry to improve the quality of hard coatings for fusion lasers. An excellent example of the cooperative effort between consumer and producer in the coating area was provided in the paper given by C. E. Thomas, B. Guscott, K. Moncur, S. Hildum, and R. Sigler of KMS Fusion.

The authors first reviewed the main attributes of the KMSF laser system. To stress the importance of coated elements, they pointed out that in its present configuration their system includes 91 dielectric coatings (mirrors, AR coatings, beam-splitters, and polarizers) in the main beam. The laser produces a series of pulses of 30 psec FWHM, 40 psec apart. Generally, 6 pulses comprise the total laser output. Damage tests were carred out with a beam of 90 mm diameter, the spatially filtered output of the final CGE rod amplifier. The beam is focused with a 25 cm focal length lens for damage testing, and samples are placed in the converging beam at diameters of 10, 20, or 40 mm. Due to temporal and spatial variations in the beam, the peak power density is typically 10 to 12 dB above the average.

Damage tests were carried out on high power mirrors, polarizers, and AR coating. Samples tested included full-sized pieces (production coatings) up to 30 cm in diameter, and test pieces (developmental coatings) of 5 cm diameter. Samples were obtained from four of the leading vendors of high power coatings. As would be expected, there was significant variation from vendor to vendor on the relative merit of given coating designs and on the absolute performance of individual compositions and designs. Nevertheless, some fairly general conclusions were drawn.

In mirror coatings, TiO_2/SiO_2 coatings were generally better than ZrO_2/SiO_2 coatings. One of the four vendors, however, consistently produced higher damage thresholds for ZiO_2/SiO_2 than TiO_2/SiO_2. Higher damage thresholds were obtained for TiO_2 coatings on Pyrex than on BK-7, which would seem to follow the stress analysis given previously by Bloom and Costich. Note that in polarizers, this effect was not observed. As expected for short-pulse applications, mirror damage levels were not affected by predeposition substrate cleaning.

Polarizers exhibited lower thresholds than mirrors. A serious problem encountered with polarizers is a dimensional shift with age. Thus a polarizer designed for optimum "p" transmission at 60° fell from 90% transmission at that angle to 78% in five months, and the optimum angle shifted from 60° to 64°. The same effect was observed whether the coating was exposed to laser radiation or remained on the shelf. With AR coatings, the damage levels were higher than most polarizers, and predeposition cleaning seemed to improve performance.

In general, coatings with higher thresholds exhibited less scattering. Some exceptions were noted. One vendor consistently produced mirrors with relatively high scattering, but high damage thresholds. Analysis of damage threshold vs. pulse length for pulse durations from 80 to 48 psec showed neither constant-energy nor constant-power behavior. As is pointed out above, in the paper of Picard, et al., this effect requires detailed analysis, and is currently not satisfactorily understood. The authors conclude that polarizers are the most vulnerable elements in the system, with AR coatings the next most vulnerable. Other laboratories with fusion lasers have reported similar observations.

It is important to distinguish between parametric studies of specially prepared coatings, such as those reported by the other authors in this session, and acceptance testing of production coatings or testing of developmental coatings, such as the KMSF authors reported. The former studies advance the understanding of the detailed physics of damage phenomena, but the latter aid the industry in process improvement, and provide an operational test of coating quality where it counts, in the actual system in which it is intended to operate.

A further study of damage dependence on structural properties and preparation techniques in optical glasses was presented by R.A. House, J. R. Bettis and A. H. Guenther of the Air Force Weapons Laboratory, and R. R. Austin of Perkin-Elmer. Materials investigated included fused silica, BK-7, ED-2, ED-4, and Cer-Vit. Samples were prepared using controlled grinding, chemical etching, overcoating, conventional polishing, ion polishing, bowl-feed polishing, and flame polishing. The laser used for the investigation was the same one previously described by the authors in a paper discussed above.

Four methods of damage detection were used, listed here in order of increasing sensitivity. These were laser-induced scattering, phase contrast detection of scattered light, visible observation of the luminous plasma, and the breath test.

The damage threshold electric field was found to vary as σ^m, where σ is the rms surface roughness, and $0.4 < m < 0.6$ for conventionally polished fused silica, SiO_2-overcoated fused silica, and MgF_2-overcoated fused silica. The relation was observed to hold for σ-values from 335 Å to 13.75 Å. For reputed bulk damage thresholds, a value of σ equal to the lattice spacing (3.57 Å) was seen to fit the general curve. Etched samples were not found to obey the relation $E \sim \sigma^m$, although the trend for lower thresholds on rougher surfaces was observed.

Among the general observations reported in this paper were the following. Nitric acid etching resulted in a 21% improvement of breakdown field strength, for all samples. Flame polishing greatly increased the damage threshold, raising the breakdown field strength to eight times its former value, but generally destroyed the optical figure of the surface. Overcoating by vacuum deposition caused a marked reduction in damage level, for both SiO_2 and MgF_2. Ion polishing yielded a higher damage threshold, when surface roughness was taken into account. As other reports at this Symposium have indicated, prolonged ultrasonic cleaning resulted in a decrease in surface damage threshold.

The conclusions one can draw from a systematic study such as reported here are fairly general. Increased surface smoothness yields a higher damage level. Absence of impurities on the surface yields higher damage levels. Thin films damage more easily than does bulk material. The damage value is sensitive to properties on the exposed surface of the material, not in the subsurface layers. The success of empirical relation $E_{th} \sim \sigma^m$ for a broad range of surface roughness values prepared by different processes is surprising, especially for $\sigma < 100$ Å. It was pointed out, however, that even for $\sigma < 100$ Å surfaces there are many features > 100 Å in dimension. In the present work, the relation was extended to bulk damage values with σ equal to the lattice spacing. This implies that the damage threshold is responding to the short range order or periodicity of the surface material, probably through variation of electron mobility near the surface. This last point warrants continuing investigations. The above relationship and m value should be of great utility in selecting the most appropriate finishing procedure. It also allows an estimate of the increase in damage resistance as a function of surface roughness level, which frequently is economic in nature.

2.6 Avalanche Ionization and Multi-photon Processes

In short-pulse laser operation, performance is limited by the creation of high concentrations ($> 10^{18}$ cm^{-3}) of conduction electrons in nominally transparent dielectrics. Since window and laser host materials are generally chosen to exhibit a band gap far in excess of the photon energy, this internal plasma formation must arise either through a relatively improbable multiphoton ionization process, or through the repeated absorption of energy from the optical field by the few conduction electrons already present, until these electrons are sufficiently energetic to cause secondary ionization to occur. This latter process is called avalanche ionization or optical breakdown. Both multi-photon ionization and avalanche ionization have been extensively studied for a long time, there are still serious questions concerning the accuracy of the existing theories, and the significance of reported measurements. For this reason, the final session of the Symposium was devoted to these two topics.

M. Sparks, of Xonics, Inc., provided a critical review of existing theories of avalanche ionization. He first outlined the basic tenets of avalanche theory, that the threshold field is determined by equating the electron energy gain to its loss, and that the effective ionization rate is determined by the amount by which the intensity exceeds the threshold value. He also reviewed the assumptions concerning frequency dependence and necessary electron concentration. He further reviewed the "lucky electron" theory of Schockley, and its extension to optical frequencies by Bass. He showed at every step that inconsistencies appear in the theory, which cannot be resolved simply by adjustment of parameters. The main points at issue were the origin of the initiating electrons, and the role of collisions in controlling the rate at which conduction electrons can gain energy from the field.

Sparks then proposed a new theory, in which electrons gain energy from the light field continuously, through electron-phonon-photon collisions. This process, just proposed by Wolstein, is essentially a three-body collision, in which the presence of the phonon allows the electron to gain a large amount of energy from the photon, while still conserving momentum. In this sense, the concept of a quasi-free electron is abandoned, in favor of an electron continuously interacting with the lattice. This theory is most attractive for polar crystals, where longitudinal optical phonons do interact strongly with conduction electrons, forming polarons. It is also in these materials that the intermittent collision model is least satisfactory, since the collision mean free paths one arrives at are comparable to the lattice spacing.

Sparks further proposed that the starting electrons are generated by a variety of multi-photon process, either across the gap directly or from impurities, depending on the incident optical frequency. In this way, the lack of a strong frequency dependence observed in many experiments can be understood. A few cases were presented in which good agreement between theory and experiment was obtained without adjusting parameters. Dr. Sparks indicated, however, that this success of the revised theory must be viewed as tentative, if encouraging, until further tests can be made.

Much of the difficulty encountered in understanding avalanche ionization at optical frequencies arises from the paucity of reliable data, particularly, comparative data for families of materials. This situation has been remedied somewhat by the continuing efforts of the Harvard group. W. L. Smith, J. H. Bechtel, and N. Bloembergen presented an account of breakdown studies carried out in alkali halides using 30 psec pulses from a well-characterized Nd:YAG laser.

An interesting feature of this study was the simultaneous measurement of breakdown field and index nonlinearity. The laser output was focused into the sample using a lens of given power. In the focal region, however, self-focusing alters the intensity distribution, and it is this altered distribution which must be analyzed to determine the breakdown threshold. From the constant shape approximation for weak self-focusing, the effective focal area is given by $A_o(1-P/P_{CR})$, where A_o is the low-power focal area, P_{CR} is the Talanov critical power for the medium. The peak intensity at the final focus, I_m, is then simply given in terms of total power P and critical power P_{CR} by the relation, $P^{-1} = I_o^{-1}A_o^{-1} + P_{CR}^{-1}$. By varying the lens power and recording the laser power at which breakdown occurs, assuming that no other factors, such as focal spot size are important, both the breakdown field and critical power can be determined. The latter yields a value of the index nonlinearity, n_2.

The authors reported values of breakdown fields for 14 materials, including 9 alkali halides, fused silica, ED-4 glass, YAG, CaF_2 and KDP. Breakdown field strengths varied from 3.4 MV/cm for RbI to 22.3 MV/cm for KDP. Index nonlinearity values, which were only determined to ± 50%, ranged from 10^{-12} to 10^{-13} esu for all materials tested. Agreement with other measurements of n_2 was generally consistent with the accuracy quoted for this measurement, but some exceptions were observed.

A significant difference exists between breakdown investigations using picosecond pulses and those using nanosecond pulses. In the latter case, damage occurs early in the pulse, and the rest of the laser energy goes into excavating the damage site. In the former case, the damage site morphology is more nearly representative of the geometry in which the breakdown initially occurred. Thus, post-mortem investigations can yield information about the breakdown process in the picosecond case. The authors reported the observation of isolated, discrete damage loci, which they identify as arising from individual electron avalanches, at a density of about 2×10^{11} cm^{-3} in NaCl. This number is consistent with current estimates of "starting electron" densities. (The reader should note the comments concerning the previous paper in this regard, however.) Further evidence from the size of the damage sites attested to the identification of the damage process as avalanche ionization, and not heating of absorbing impurities.

Damage via avalanche ionization is expected to be a statistical process. If a sample is irradiated n times at a given power level, damage will occur in some fraction of cases. This fraction, the probability of damage, goes from zero at low power to unity at very high power. The probability of survival, given by one minus the damage probability, decreases monotonically from unity at low power to zero at high power. The lucky electron theory of avalanche ionization predicts that the logarithm of the survival probability, after irradiation for a given time at a given field strength, E, should decay exponentially, like exp(-K/E), where K depends on the material and laser frequency.

D. Milam, of the Lawrence Livermore Laboratory, and R. A. Bradbury and R. H. Picard, of the Air Force Cambridge Research Laboratories, had noted in the past that damage statistics in solid dielectrics did not obey the predictions of the lucky electron theory. They decided to examine the survival time statistics in gas breakdown to see if similar discrepancies appeared.

Gas breakdown survival statistics were reported for argon at pressures from 20 ps: to 500 psi, and N_2 at 150 psi, with and without an added DC field of one-half the breakdown value. As the argon pressure was increased, a marked variation in survival statistics occurred. At low pressure, the breakdown was almost causal, i.e., at a given power level, breakdown occurred over a very small range of times for many trials. As the pressure was increased, and correspondingly the breakdown field decreased, the time of breakdown became less and less well defined, and the survival statistics took on the character of those similar for solid dielectric breakdown. The authors attribute this behavior to the fact that as the pressure increases and the field at which the breakdown occurs decreases, the rate of photoionization, which starts the avalanche is reduced. Thus the statistics which are observed reflect the statistical character of the initiation process rather than the avalanche process, and do not reflect the lucky electron hypothesis. In the case of an added DC field, electrons are swept out of the volume as ionization occurs, and correspondingly, the spread in breakdown times is increased. The data reported in N_2 gas agree with this model.

Among the crucial parameters of any avalanche ionization theory is the density of electrons formed in the process. N. Alyassini and J. Parks of the University of Southern California reported a measurement of the build up of the electron concentration at the surface of a glass sample under ruby laser illumination. The electron density was probed by observing variation in the reflectivity of a He-Ne probe beam reflected at the critical angle in internal reflection. This method is sensitive to changes in index of the order of 10^{-5} to 10^{-4}, corresponding to electron concentrations of 10^{17} to 10^{18}. The refractive index change was observed to precede the attenuation of the ruby laser beam by as much as 2.4 nsec. This delay time is associated with the build up of an absorbing plasma in the solid. Build up times varied from one to two nsec in duration.

In a short contribution by P. Braunlich of the Bendix Research Laboratories and the Research Institute for Engineering Sciences at Wayne State University, and P. Kelly of the National Research Council, further evidence was put forward that breakdown thresholds are sensitive to the process of initiation as well as the process of build up. The authors show that recent results of Penzkover, in which multi-pulse damage thresholds were systematically lower than single pulse thresholds, are entirely explicable from avalanche ionization theory, if appropriate source terms for conduction electron generation are included. The model neglected any diffusion of conduction electrons out of the irradiated volume, which was consistent with the spot size and pulse duration employed in the experiments. It was shown that as much as a ten-fold reduction in the peak power density required for damage resulted from using a train of ten pulses instead of a single pulse. The authors cautioned against the interpretation of multi-pulse damage threshold values as being single-pulse values. They conclude that no extrinsic mechanism, such as inclusion damage, is required to explain Penzkover's results.

A series of papers relating to multi-photon processes in dielectric solids was presented at the Symposium. A Schmidt, P. Braunlich, and P. Rol of the Research Institute for Engineering Sciences, at Wayne State, and of the Bendix Research Laboratories, reported a hitherto unobserved phenomenon in laser-irradiated alkali halides. The effect proceeds as follows. By multi-photon absorption of laser light, a negative halide ion is generated. This ion subsequently forms a negatively charged F-center, or self-trapped exciton. The exciton decays nonradiatively, launching a Pooley-Hersh collision chain along those directions in the crystal, [211] and [110], in which a chain of halide atoms occurs. If this chain lies near the surface, a halide atom is ejected from the surface. In KCl, in which the absorption is via four photons, as many as 10^{16} chloride atoms have been detected at incident laser fluxes well below the damage threshold. The authors report cases in which surface damage occurred, not due to plasma formation, but instead due to concentrated energy of these collision chains at the crystal surface.

R. A. Shatas, S. S. Mitra, and L. M. Narducci of the Physical Sciences Directorate of the U.S. Army Missile Command offered a critical review of the theory of multi-photon absorption in direct-band semiconductors. A comparison was made of theoretical perturbation calculations of Braunstein and Ockman, and Basov, and the empirical theory of Keldysh, which employed "dressed" states to represent the effect of the applied field on the states of the system. The Braunstein and Ockman theory assumes a model of transitions between the valence band and the lowest-lying conduction band, with an intermediate state in a higher-lying conduction band, while the Basov model assumes that only intraband transitions enter in the intermediate state. Comparison of the three calculations with experimental results for GaAs and InSb show that the Basov model leads to a substantial overestimate of the two-photon absorption, while the Braunstein and Ockman model leads to an underestimate. The Keldysh model, however, provides surprisingly good agreement with experiment. It also gives good agreement for band-edge absorption, without parameter adjustment. Furthermore, the Keldysh model allows the calculation of higher-order multi-photon effects more directly than is possible via perturbation theory. For a large class of II-VI and III-V semiconductors, two-photon absorption coefficients at wavelengths near 1 μm are of the order of 10^{-8} cm/watt.

Another paper, read by title only, also dealt with multi-photon absorption, and the validity of the Keldysh theory. In this paper, by R. P. Benedict and A. H. Guenther of the Air Force Weapons Laboratory, the effect of electroabsorption (the Franz-Keldysh effect) as possible damage mechanism was considered. The authors conclude that the important manifestation of electroabsorption at optical frequencies is just multi-photon absorption. They further conclude that, for IR materials, multi-photon absorption is not important as a damage mechanism, being less probable than avalanche ionization except for extremely short pulses. For lasers in the visible and uv, two-photon absorption can be the limiting phenomenon.

Benedict and Guenther agree with the previous paper in their evaluation of the applicability of the Keldysh formulation to two- and three-photon absorption. Like Shatas et al., they found the Keldysh theory to be within an order of magnitude of experimental results for several materials. They gave several sample calculations for materials used both in the IR and visible region of the spectrum.

Two-photon absorption as a limiting damage mechanism for vacuum uv laser components was considered by C. J. Duthler and M. Sparks, of Xonics, Inc. They estimated the two-photon absorption coefficient from the theoretical perturbation expression of Braunstein, referenced above. They examined in detail the implications of two-photon absorption for the performance of an uv laser with a photon energy of 7.2 eV, with windows of LiF, which has a band gap of 13.0 eV, less than twice the photon energy. The authors list a number of other possible uv window materials, all of which exhibit smaller band gap energies than LiF.

The authors first discuss the use of metallic reflectors in the vacuum uv. Aluminum, which has the best reflecting properties at photon energies above 6 eV, is found to have a melting threshold of 20 MW/cm^2, too low for practical use at high power density. Multilayer dielectric mirrors will be severely limited for vacuum wavelengths. The authors conclude that the most damaging consequence of two-photon absorption is optical distortion due to the creation of free carriers. The threshold for avalanche ionization is estimated to be an order of magnitude higher than that for free carrier production. Other effects, such as bulk heating from two-photon absorption, valence electron contributions to the nonlinear refractive index, and stimulated scattering processes, are also considered.

In light of considerations put forth in the preceding papers, the estimate of the two-photon transition probability in this paper is only to be interpreted as a qualitative estimate. Shatas et al. have shown that discrepancies greater than two orders of magnitude can arise from different choices of models for two-photon processes. Nevertheless, Duthler and Sparks have reemphasized the fact that two-photon absorption is the most severe limitation for short wavelength laser operation.

3. Recommendations

The recommendations forthcoming from this year's discussion are not substantially different from those of previous years. The problems of optical surface preparation, coating and evaluation continue to be of great interest and importance. Advances have been made in scientific understanding and fabrication processes, but much improvement can still be gained. We shall attempt to set down a subjective view of the subjects of great interest and the areas of greatest potential advance.

Fabrication processes continue to play a dominant role in determining the damage sensitivity and mechanisms of exposed optical surfaces. In order for a process to be useful commercially it must be reproducible, suitable for volume production, and capable of uniformaly preparing large size elements economically. Quality assurance requires suitable test procedures for monitoring the process. Process development, both for the preparation of bulk materials and for preparation and finishing of surfaces must continue in close association with the advance of characterization techniques and damage studies. Economic factors will become important in many instances and thus damage resistance versus process cost will have to be determined.

As lasers evolve with different operating characteristics such as new wavelengths or different pulse durations, new materials become attractive for specific laser applications. These in turn require new approaches for fabrication. A prime example is the recent interest in diamond-turned metal mirrors for 1.06 μm optics. We can look for a similar upsurge in interest in low index optical materials for use with uv lasers and with 1.06 μm lasers, the latter to reduce the index nonlinearity in passive optics. Techniques for the fabrication, coating, and testing of large aperture optics made from crystalline flourides, for example, to meet high power laser specifications deserve greater attention and emphasis than they have been receiving, particularly since in many cases flouride coatings tend to exhibit considerably different optical properties than bulk flouride characteristics. What is obviously needed besides an accurate tabulation of bulk optical and physical properties is a tabulation of optical and physical properties of materials in thin film form as a function of process variables.

Diamond turning itself is still far from a closed subject. The turning of non-planar surfacess such as ellopsoids and paraboloids require further development. The application of micromachining techniques to non-metallic materials requires further development. The question of coatings for metal mirrors must be clarified with particular attention to substrate preparation techniques and the problem of the differential expansion of the metal substrate and dielectric coating. For high average power application, cleaning procedures must be developed to completely remove all traces of contaminates introduced in the machining process, such as cutting oils, before sufficiently adhering coatings can be applied.

Similar problems remain in the area of window materials and their preparation. Presently the residual absorption in these materials is dominated by surface impurities. Further development of surface treatment is required, including chemical etching, ultrasonic cleaning, and optical finishing. The chemical basis of surface absorption is still not clear and requires elucidation. A quantitative evaluation of the efficacy of ultrasonic cleaning is necessary. This study should relate material type, duration of cleaning, pH, and type of bath, power and frequency with the resultant surface characterization for surfaces prepared by different methods.

Great strides have been made in understanding damage processes. The empirical scaling laws recently evolved relating damage levels to observable characteristics of the material, such as index, dispersion, or surface topography, have provided a very useful guide to the user in choosing materials and processes. These results are a powerful incentive to the research scientist to understand surface damage phenomena better. Further work along this line is needed. The temperature dependence of damage thresholds is of great interest, as revealing the role of phonon processes, especially in electron avalanches. Data collection on samples of high purity and known and well characterized impurity levels should be undertaken to evaluate the impurity role in damage, again with emphasis on avalanche ionization, then existing scaling relations can be placed on a firmer scientific basis.

No where is the potential for improvement as great as in the area of thin films. Studies reported in this year's symposium show the successive isolation of several factors which determine the performance of a coating. These include the substrate material and preparation, method of deposition, temperature, coating design, field configuration, residual stress, structure, density, and others. Scattering continues to be a valuable measure of quality in films, but low scattering and high quality are not always correlated. Roughness and impurity effects need further elucidation. The problem of dimensional changes in the coating apparently associated with the coalescing of minute crystalline regions emerged from this year's discussion as an important consideration. This is part of the general problem of film stability which is of great impact. The relative importance of surface absorption vis a vis bulk absorption for high average power bare and coated elements needs further study as relates to its response at high levels of irradiation.

Finally, it is appropriate to remind ourselves of the purpose of this series of symposia. These meetings and their consequent publications are designed to provide a forum for the transfer of information regarding optical materials for lasers from the research scientist to the practical user, to stimulate the collection of data regarding these materials, and to tabulate, organize, and explain those data where possible. By providing a forum and a mechanism for this exchange of information we can hopefully avoid the expense and pain of relearning old truths in new guise each time a new material or laser emerges.

4. Acknowledgment

The editors would like to thank Capt. T. A. Saito of the U.S. Air Force for his kind service as moderator of the sessions on fabrication and metal mirrors, areas with which he is intimately familiar. We would like to acknowledge the invaluable assistance of Dr. Harold S. Boyne, Mr. Wilbur Anson, and Mrs. Florence M. Indorf of the National Bureau of Standards in Boulder, Colorado, for their interest, support, and untiring efforts in the operation of this Symposium and in the preparation and publication of the proceedings. We would like to take special note of Sue A. DiLullo and Paula J. Chukoski, who added measurably to the conference operation particularly during the discussion periods following the formal presentations. The continued success of the Damage Symposia would not have been possible without the support of those named above.

5. Bibliography

[1] "Damage in Laser Glass," A. J. Glass and A. H. Guenther, Editors, ASTM Special Technical Publication 469, ASTM, Philadelphia, PA (1969).

[2] "Damage in Laser Materials," A. J. Glass and A. H. Guenther, Editors, NBS Special Publication 341, U. S. Government Printing Office, Washington, D.C. (1970).

[3] "Fundamentals of Damage in Laser Glass," N. Bloembergen, National Materials Advisory Board Publication NMAB-271, National Academy of Sciences, Washington, D.C. (1970).

[4] "Damage in Laser Materials: 1971," A. J. Glass and A. H. Guenther, Editors, NBS Special Publication 356, U. S. Government Printing Office, Washington, D.C. (1971).

[5] "High Power Infrared Laser Windows," N. Bloembergen, National Materials Advisory Board Publication NMAB-292, National Academy of Sciences, Washington, D.C. (1972).

[6] Proceedings of the Conference on High Power Infrared Laser Window Materials, (October 1971). C. S. Sahagian and C. A. Pitha, Editors, Special Report No. 127, Air Force Cambridge Research Laboratories (1971).

[7] "Laser Induced Damage in Optical Materials: 1972," A. J. Glass and A. H. Guenther, Editors, NBS Special Publication 372, U. S. Government Printing Office, Washington, D.C. (1972).

[8] "Laser Induced Damage of Optical Elements, A Status Report," A. J. Glass and A. H. Guenther, Applied Optics 12, pp. 637-649 (1973).

[9] "Laser Induced Damage in Optical Materials: 1973," A. J. Glass and A. H. Guenther, Editors, NBS Special Publication 387, U. S. Government Printing Office, Washington, D.C. (1973).

[10] "Laser Induced Damage to Optical Materials, 1973: a Conference Report," A. J. Glass and A. H. Guenther, Applied Optics, 14, pp. 74-88 (1974).

[11] "Laser Induced Damage in Optical Materials: 1974," A. J. Glass and A. H. Guenther, Editors, NBS Special Publication 414, U. S. Government Printing Office, Washington, D.C. (1974).

[12] "Laser Induced Damage in Optical Materials: 6th ASTM Symposium," A. J. Glass and A. H. Guenther, Applied Optics, 14, pp. 698-715 (1975).

0.1 Opening Remarks

Arthur H. Guenther

Kirtland Air Force Base, New Mexico 87117

Unfortunately this year Haynes Lee, Chairperson of Subcommittee 2 on Lasers of the ASTM, could not be with us to personally open the conference. He has asked me to express his regrets, but he is sure that the conference will carry on in its characteristic manner. I am sure he would want me to mention that the ASTM looks to this conference for the technical details concerning proposed and possible standards for evaluating the damage sensitivity of optical components and materials used in conjunction with high power lasers. In particular, the ASTM finds the damage symposium most useful as a sounding board for evaluating diagnostic techniques and instruments which can be transferred to viable standards, procedures and recommended practices. Of course, the prime goal is non-destructive testing methods if possible.

Speaking for Alex Glass and myself, we would like to welcome you to the Seventh Annual Symposium on Damage in Laser Materials. As you can see from the program, there has been an increase in the number of sponsoring agencies. We have already covered the interest of the ASTM and its role in supplying the initiative for these meetings. Certainly these meetings would not have achieved their prominence without the excellent support and facilities made available to us by the National Bureau of Standards here at Boulder. We particularly wish to express our appreciation to Dr. Hal Boyne, Chief of the Electromagnetic Division, for sponsoring our annual conclave. Furthermore, this year we have the benefit of Mrs. Florence Indorf who is now filling the role formerly held by Pauline Smith. Mrs. Indorf works for Mr. Wilbur Anson who has marshalled the resources for the operation of the meeting, including Paula Chukoski, and Sue Dilullo who will carry our roving microphones. Of course, we are most grateful that the Office of Naval Research has again supported us financially to help defray the cost of publishing the Symposium proceedings. I imagine because of our popularity and success, this year the Energy Research and Development Administration has also seen fit to aid us financially. We are glad to add them to our list of sponsors.

We would also like to issue a warm welcome to our international attendees from Canada, Great Britain and France.

In the event that we remain to receive support from these, as well as possibly from other agencies, we are finding it somewhat of a tongue twister to refer to this as the Seventh Annual ASTM-ERDA-NBS-ONR Symposium on Damage in Laser Materials. So to preclude this from becoming known as the alphabet conference, I suggest that in the future we simply refer to this conference as the Boulder Meeting on Laser Damage.

Each year we wonder if there will be enough interest for another meeting the following year, but our experience has been that each year more papers and more attendees have been the general rule. In fact, this year we received in excess of fifty submitted papers. Because of our past emphasis on damage in optical components used in high power laser systems, we found it necessary to reject several papers dealing more with engineering and ancillary component damage, such as photo-detectors, since there are already several meetings for which these papers would be likely candidates. In addition, we found several papers of high interest, but because of the press of the limited duration of our meeting, as well as our desire to avoid concurrent sessions, we have accepted several papers by title only. The abstracts of these papers will be found in your handouts. It is our intention that these papers be published in full in the Symposium proceedings. Even after these two courses of action, we found that to present the remaining papers while allotting sufficient time for discussion we had to extend the meeting an additional half day.

The success of this meeting I believe primarily stems from our flexibility in changing the emphasis each year to concentrate on the major accomplishments and near-term large-scale efforts. These major programs today are obviously the high peak power laser systems of the fusion program primarily at 1.06 μm and 10.6 μm and the numerous government and industrial applications of high average power lasers, to date mainly in the infrared region. Of course, we would expect both of these areas to move to shorter wavelengths for a variety of technical and engineering reasons. This will come about as soon as the several large efforts underway in the search for new efficient short wavelength lasers bear fruit.

From the program you will note that the meeting has been organized into sessions on Fabrication, Metal Mirrors, IR Window Materials, IR Damage Tests, Damage in Dielectric Films and at Exposed Surfaces and finally Avalanche Ionization. Thus the subjects of interest to the high average power

community come early in the conference, while the high peak power subjects conclude our meeting with the dielectric film and surface papers forming a bridge between the far extremes. We do hope, however, that you will see fit to attend the full two and one-half days.

This year there is little or no in-depth discussion of bulk and self-focusing laser-induced damage. These concerns have either been successfully eliminated by improved processing procedures or sufficiently understood theoretically to allow us to design around them. This situation fortunately is complemented by a considerable tabulation of salient material properties which allow the necessary assessment of their import in high power laser system design and performance.

This year we have elevated the subject of metal mirrors from the workshop sessions held last year to a formal session here at the Symposium and have enlisted the services of Captain Ted Saito who, besides being concerned with the Air Force high energy laser program, is presently on assignment to Lawrence Livermore Laboratory to aid in coordinating the metal mirror activities which bear on both major program areas.

Several years ago the deleterious effects of rouge were identified as a damage initiator. This situation led to the most widely used rule of thumb in specifying optics to be used in high power lasers and that is the total avoidance of rouge polishing. This year several discussions may center on yet another process which may possibly degrade the damage resistance of optical elements and that is ultrasonic cleaning, particularly as it applies to metal mirrors. I am sure several discussions will concern themselves with this topic during the next two and one-half days. In addition, this meeting will identify many other important processing variables which control factors that can be identified as damage indicators. Therefore, this correlation is useful in both an analytic and an engineering sense.

But we should remember that the prime reason for this forum is the transfer of information relative to the development of standards by which proper specifications can be written and optimum processes identified together with the development of diagnostic techniques suitable as a non-destructive test. This year sees several papers dealing with the collation of these several factors.

1.1 Fabrication of Laser Optics at Lawrence Livermore Laboratory*

Norman J. Brown

Lawrence Livermore Laboratory
Box 808
Livermore, California 94550

This paper summarizes fabrication techniques in use at Lawrence Livermore Laboratory for laser discs, windows, and mirrors, and polishing techniques used with metal surfaces.

Key words: Chamfering; continuous polishing; grinding; metal polishing; optical fabrication.

1. Introduction

To achieve a near diffraction-limited beam in a laser chain composed of dozens of elements requires optical components having surfaces that are ultra flat, parallel and of high cosmetic quality. This paper summarizes the results of studies conducted by LLL to determine methods for fabrication production quantities of these components.

There are seven basic steps in plano-parallel glass fabrication:

1. The flat surfaces are rough ground with bonded diamond.
2. An edge chamfer is ground and polished.
3. One surface is ground flat to a few fringes in several steps of free abrasive.
4. The second surface is similarly ground, with some blocking or fixturing technique to obtain parallelism in the second range.
5. Both sides are prepolished or greyed out.
6. The first side is polished flat to specification.
7. The second side is polished to a figure consistent with specified transmission figure with special care to maintain parallelism.

These processes will be described in inverse order.

2. Figure Control

The 20 cm diameter flat shown in the interferogram (figure 1) is one of eight that were brought to $\lambda/20$ (at 633 nm) peak-to-valley figure. Two flats were processed at a time, four times in succession, with a total polishing time of six hours per pair. Both the figure and the low edge roll are typical. The material is fused silica; this is the only material for which we can regard the above performance as routine, but it does establish the fact that the polishing process can be controlled.

Our processing is done on a 48" single planetary lap consisting of a pitch covered annulus whose width is one-third the lap diameter. A two-foot low expansion glass tool continuously trues the pitch which passes at 2 to 3 rpm under 3 workrings. Slurry is composed of rare earth oxide in a water vehicle. Tool, rings and lap are independently driven, usually at the same rpm. Lap figure is controlled by moving the tool in the radial direction, the outermost position producing a convex lap and the innermost producing a concave lap. Material removal rates are near one-tenth micron per minute, and workpieces can range in size up to 1/2 to 2/3 of the lap annular width.

When we attempted to polish elliptically shaped laser glass we found that half wave surfaces were easily-obtained,but 1/10 to 1/20 wave surfaces were approached erratically. It soon became obvious that the erratic results were due to a fluctuating thermal gradient across the disc. The sag for a circular disc of radius r and thickness t in terms of coefficient of thermal expansion α and temperature gradient ΔT is given by

$$\delta = \frac{r^2 \alpha \Delta T}{2T} = \left(\frac{r}{2t}\right) r \alpha \Delta T. \qquad (1)$$

Assuming BK7 glass, a typical radius-to-thickness ratio of 4 and a wavelength of 633 nm, the expression becomes:

$$\delta/(\lambda \Delta T) = .224r, \qquad (2)$$

or about 4-1/2 fringes per degree C for a 20 cm diameter workpiece.

* Work performed under the auspices of the U. S. Energy Research and Development Administration.

It is easily seen that fluctuating gradients of 1/50 to 1/100 degree C can be troublesome. Identically shaped pieces of different materials that are simultaneously polished tend to come off the lap with residual curvatures a linear function of their coefficients of thermal expansion. The thermal gradients due to polishing action appear to be quite small, most of the heat being removed by the slurry. The real culprit is a fluctuating temperature difference between air and slurry.

We attempt to control this to 0.1°C. It is difficult to assess the effectiveness of this control but two independent estimates in our shop after six months experience agree that it decreases the polishing time by at least one-half. There are a number of ways to control this temperature difference. We enclose the lap in a plastic cover. The air above the lap is slightly warmer than that outside the cover due to heat from the polishing. We raise the temperature of the slurry to match this within 0.1°C. The slurry control consists of a thermistor in one leg of a Wheatstone bridge, a commerical unit costing under $100. This operates either a 750 watt immersion heater or a solenoid valve permitting chilled water to flow through a 50 ft. length of 1/2 inch copper tubing. Heater and chiller buck each other in a typical cycle of 5 seconds heat and 15 seconds cool.

There are several less obvious sources of thermal error. One is the transient effect occurring when a part is moved from one environment to another. An examination of various slab transient temperature solutions shows that for most common initial distributions where one side is suddenly fixed and the other insulated, the distribution will decay to a near linear distribution with the insulated side 10% of the initial difference between the fixed and insulated sides at a time θ when the Fourier number $(K\theta/(\rho Cpt^2))$ approaches unity [1][1]. Assuming BK7 glass and a typical radius-to-thickness ratio of 4, the time θ to accomplish this change in minutes is approximately

$$\theta \approx r^2/5 \qquad (r \text{ in cm}). \tag{3}$$

Thus a 20 cm workpiece has a relaxation time of 20 minutes or so. Assume such a workpiece is returned to the lap after a brief test at a temperature only a half a degree different from the lap. Almost immediately upon contact with the slurry, it will bow several fringes. The direction of bowing will depend on whether the temperature difference is positive or negative. During the tens of minutes for this to relax to equilibrium, several microns of material will be removed from the disc in its deformed shape. Thus, the figure of a part nearing completion can be completely destroyed in the last minutes.

We monitor the lap figure constantly with Cervit discs, removing the workpieces as seldom as possible. On return to the lap in final stages of polishing, the part should be brought to equilibrium by a brief soak in lap air at least, and preferably in the lap slurry.

Another source of thermal error is the power supply in the base of most commercial plano interferometers. Placing the work to be examined on an insulating pad can reduce this effect considerably. Attempts to compensate for significant thermal gradients by adjusting the curvature of the lap are never completely satisfactory. There are always variations in thermal gradients at the edges of the workpieces. A flat figure obtained with varying edge gradients will relax into a different shape, and smoothly upturned edges are sometimes seen. This problem is more pronounced in elliptical and sharp-cornered workpieces. Note that the interferogram for the fused silica rounds show a remarkable lack of turned edges, and this is quite characteristic of materials such as fused silica which have a low coefficient of expansion.

Another source of figure variation is a ground glass surface on the opposite side. A ground surface is a mass of subsurface fractures which tend to expand the surface. Moisture complicates this behavior as capillary pressures further expand the surface in different areas in a manner which can vary with time. In addition, there is a strong tensile stress developed in a polished surface. It is an old optician's trick to bring in the figure of small or medium mirrors by judicious polishing of the back surface. Final figuring should not be attempted until both surfaces are thoroughly greyed out. In the case of thin parts, the edge should also be etched prior to final figuring since an expanding edge scallops and leads to potato chipping. Etching should also be considered for the back of thin mirrors.

Another source of figure errors is lack of rotational synchronism. Consider a circular disc rotated on a stationary flat plate. The velocity and resulting wear at any point is a function of the radius; the edges will wear at a faster rate than the center. Only pure translation will result in even wear. Rotation during translation will also result in a wear pattern that increases from the center of rotation. Consider the wear along two axes, one parallel to the direction of translation and one normal to it. Along the normal there will be wear variations that are linear across the diameter, canceling out on a full revolution. Along the axis parallel to the direction of translation there will be a vectorial addition of velocities that does not cancel out. In the case of a part resting on a rotating lap, it can be shown that the radial variations in wear are proportional to the absolute value of the angular velocity difference between the part and the lap. This can easily be verified by observing the synchronous rotation that occurs when a part, pinned at the center of gravity of area, is free to rotate on a rotating lap. This point is crucial to the understanding of planetary lapping.

1. Figures in brackets indicate the literature references at the end of the paper.

The large circular tool will tend to rotate in synchronization if it is free, but if it is not separately driven, extreme care must be taken to see that its restraints are truly frictionless. In the case of workrings, these should either be driven, or kept loaded such that they rotate as much as possible about the center of gravity of their loads; the latter method is not too feasible as different pieces may have different weights and may suck down on the lap with different pressures during their processing. Synchronization is especially important in the case of odd shaped parts restrained from independent rotation within the workring, but even circular parts free to rotate tend to be dragged around at higher angular velocity than the lap by contact with the edges of the workring or inserts.

3. Parallelism Control

This results both in a figure effect and in a parallelism effect. There is a second parallelism effect due to lack of synchronization that is very pronounced. Polishing results in a shearing pressure at the interface between part and lap. This is reacted by a load above the surface resulting in a moment supported by a linearly varying pressure distribution across the interface. This pressure variation is in opposite directions relative to the disc as it rotates in the workring. At synchronous velocity these wear distribution variations cancel out resulting in even wear over one revolution. At nonsynchronous rotation they can result in up to 10 seconds of wedge per hour for 1% - 2% angular velocity difference.

So far we have discussed maintaining parallelism in the polishing operation. This parallelism is initially set up in the free abrasive grinding operation. The traditional methods of achieving this are by contact or color blocking parts to a larger plate. This does not work too well with laser glasses due to their combination of high expansion, low strength, and softness. Contact blocking is particularly unsuitable since it usually results in material being pulled out of the glass. We have devised a very simple mechanical fixture to supplant this method. This is a vacuum chuck free to rotate within a lapmaster workring. The chuck is held in a precision sleeve precisely oriented orthogonal to the ring face. A workring was first lapped parallel. The bearing assembly was rough machined and a final cut was taken on the sleeve and bearing assembly face in a precision lathe. The chuck was then inserted and its face lapped parallel to the ring face. We grind the glass on one face and apply this to the chuck face. A five-minute grind in the finest grit generally reduces wedge to 2 - 3 seconds of arc.

4. Cosmetic Quality

Most of our surfaces are of 10/5 scratch/dig quality and the majority are probably nearer 5/2. This is achieved by keeping the lap under a filter hood supposedly good to class 100 conditions. There is a second plastic thermal barrier over the lap. Even with this we found scratches. We traced most of these occurring on the lap to breakout from the edge chamfer. With soft laser glass in particular we find that a finely ground and polished edge chamfer is a necessity. These materials grind rapidly. If the chamfer is lost in this operation, the edge will break away on striking the edges of lap facets, whether they are metal or pitch. Polishing the chamfers results in very few breakouts and reduces polishing time 2 to 4 hours per disc.

There was another class of scratches we found resulting from grinding laps which were cast iron. We began picking inclusions out of the cast iron. The scratches were not immediately visible in the ground surface, but became visible as the surface was polished out. These are readily distinguishable from scratches started in polishing since the latter tend to be clean and continuous while the former tend to be a series of irregularly shaped pits.

We had one other problem with grinding laps that was peculiar to laser glasses, glazing or premature fusing during the grinding operation. These glasses are gummy and soft and grind very fast. When the abrasive size is decreased below a certain point the material is not flushed out rapidly enough and burnishing of the glass against its own frit and glazing takes place. Observations of this glazing material filling pits of known size lead us to conclude that this layer is microns thick. It is very hard to polish through and there is a danger that figure may be achieved before polishing into the base material. This fused material contains particles of grinding compound and scrapings of the lap material, iron, which can lead to laser damage.

In addition to iron, we have tried copper, tin, aluminum, brass, and ceramic. These were not exhaustive tests, but we believe brass is giving us our best results. It is more uniform than iron and we find we can go to 5 micron silicon carbide abrasive without encountering glazing. The brass requires much more care than iron. It has a tendency to pick up and imbed grit, so it should only be used with a single size abrasive unless resurfacing tools (e.g., coarse diamond faced rings) are available.

Due to the fast grinding action on soft laser glasses we grind in only two free abrasive stages, 30 micron and 5 micron. Five minutes on 30 micron is usually sufficient. We then go to 5 micron abrasive for 15 to 20 minutes removing initially about two microns of stock per minute. The first 10 minutes remove the bulk of the coarse grind and the second 10 minutes show a stock removal rate of about one-half of a micron per minute.

Ceramic tile laps work almost as well, seldom causing glazing and showing removal rates about half those of brass. They do, however, show a greater tendency to scratch.

In addition to the problem of eliminating scratches and digs, we must detect those that are present. The inspection illumination scheme used in most shops is usually that of MIL-O-13830A. This was designed for clear glass and is insufficient to show up the scratches and digs of the same spec in colored laser glass. We illuminate the glass with a high intensity projection lamp while looking through the glass at a dark background with a 5 - 8 power eye loop or binocular magnifier. Dust is a problem and anti-static or laminar flow-filtered air equipment is a great help. It should be emphasized that this is not the overly stringent test that it appears. It is an attempt to overcome the absorption of the glass.

The attention to cleanliness is important. The combination of the filtered hood and recirculating slurry leads to surfaces that are almost superpolished. Under conditions of extreme cleanliness we are able to use the slurry for a period of weeks gradually breaking it down and approaching the conditions of a bowl feed process. We recently examined a cylindrical lens that we fabricated and coated on both sides. The lens was later damaged by beam hot spots. The front cylindrical surface had been polished on a conventional cylindrical lap with normal attention to cleanliness. It was a good surface with a 30 to 40 Å finish viewed on the Nomarski microscope. The back surface was polished flat on the continuous lap under the hood. The front surface shows damage clearly originating in sleeks and shows these literally burned out. The back surface showed a completely different kind of damage. There is no indication of propagation along sleek lines indicating a surface of uniform damage resistance. This was obviously not a controlled test, but presumably the back surface saw higher fields due to the exit effect and some self-focusing.

5. Metal Finishing

We have recently been working gold, copper, silver, aluminum and nickel material using diamond and low viscosity silicon oils. We have used pitch and beeswax, both separately and covered with fine unsized silk. We have had excellent results, copper showing consistent reflectivities in the 99.2% to 99.3% range uncoated at 10.6 micron. We have had our best results with 1/4 micron natural diamond and 1 centistoke silicon oil using pitch and silk. The opticians prefer the silicon oil to other vehicles with the diamond finding that although cutting may be slower, there is very little tendency for the lap to work through the fluid and grab the metal surface. The oil protects the surfaces without the need for chemical buffers. We find sleeking is always a problem,but that it can be significantly reduced by working under a plastic tent fitted over the quill. The use of small powered polishing pads keeps a thicker film of oil between lap and workpiece and also reduces sleeking. To date these surfaces have a bulk reflectivity at 10 μm that is equivalent to surface turned with a single-point diamond tool but their damage threshold is lower than that of the turned surfaces by a factor of about four.

6. Acknowledgments

The author gratefully acknowledges the many helpful suggestions of Mr. Frank Cooke of Frank Cooke, Inc., by Mr. Saul Laufer and the staff of Zygo Inc., manufacturers of the LLL continuous polisher, and the skill of Messrs. Procknow, Baker, Stolcis, Blackman, Whistler,and Gillespie of the LLL Optical Fabrication Facility.

7. References

[1] Carslaw, H. S. and V. C. Jaeger, "Conduction of Heat in Solids," 2nd ed, Chap. 3 (Oxford Univ. Press, London and New York, 1959).

NOTE: Micron(s) as used in this paper expresses micrometer(s).

8. Figures

Figure 1. Typical figure of 8" fused silica round after six hours of polish.

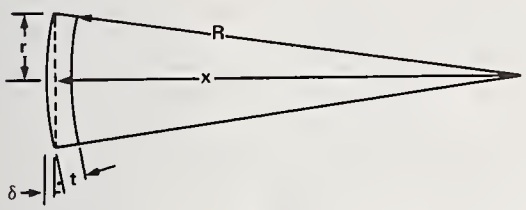

$r^2 = R^2 - x^2 = (R + x)(R - x) = 2R\delta$

$\Delta R/R = t/R = \alpha\Delta T$

$R = r^2/2\delta = t/\alpha\Delta T$

$\delta = \frac{r^2\alpha\Delta T}{2t} = \left(\frac{r}{2t}\right) r\alpha\Delta T$

Assume BK7, λ = 633 nm, r/t = 4

$\delta/\lambda = .224\ r$ (r in cm) $\Delta T = 1°C$

Figure 3. Curvature induced by thermal gradients through flatware.

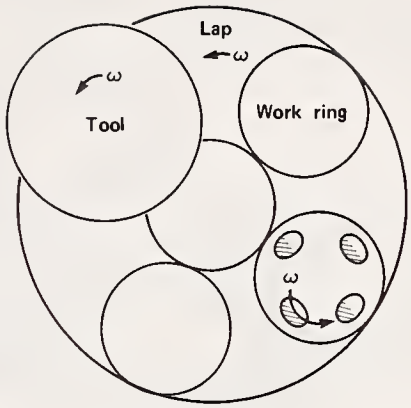

Figure 2. Typical lap geometry for continuous polishing.

Figure 4. Continuous ring polisher in clean booth.

TEMPERATURE CONTROL SYSTEM

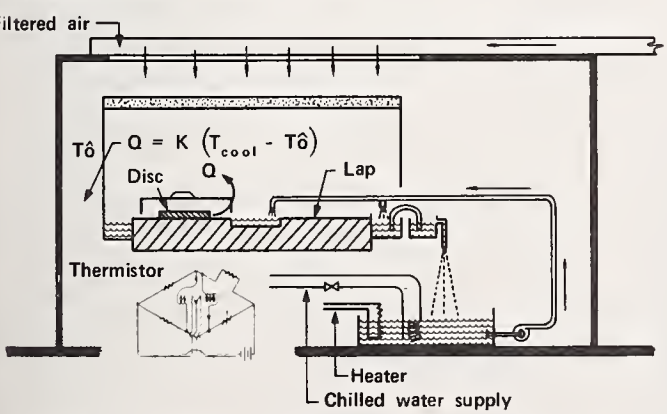

Figure 5. Temperature control scheme in use at Lawrence Livermore Laboratory.

TRANSIENT BEHAVIOR

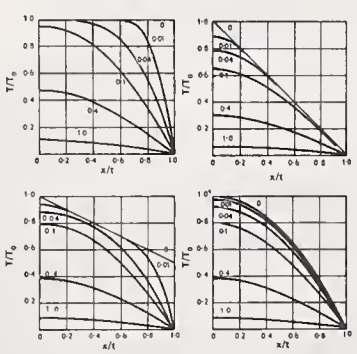

Note that for a Fourier Number approaching unity, each solution approaches a linear gradient with T/To (0) → 0.1

$\xi = \frac{K\theta}{\rho C_p t^2}$

For BK7 & $\xi \rightarrow 1.0$

θ(minutes) = 3.22 t^2

Assume r/t = 4

$\theta \approx r^2/5$

From Carslaw & Jaeger, Conduction of Heat in Solids

Figure 6. Thermal transient decay for flatware.

Figure 7. Ring insert for small laser discs. Note rabbited edges and cutout for monitoring disc.

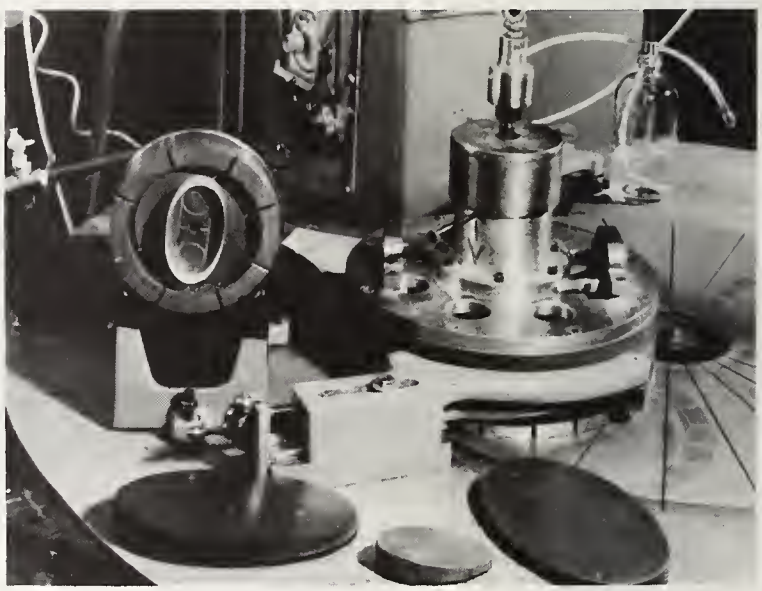

Figure 8. Two mechanical fixtures that yield 2 - 3 seconds parallelism.

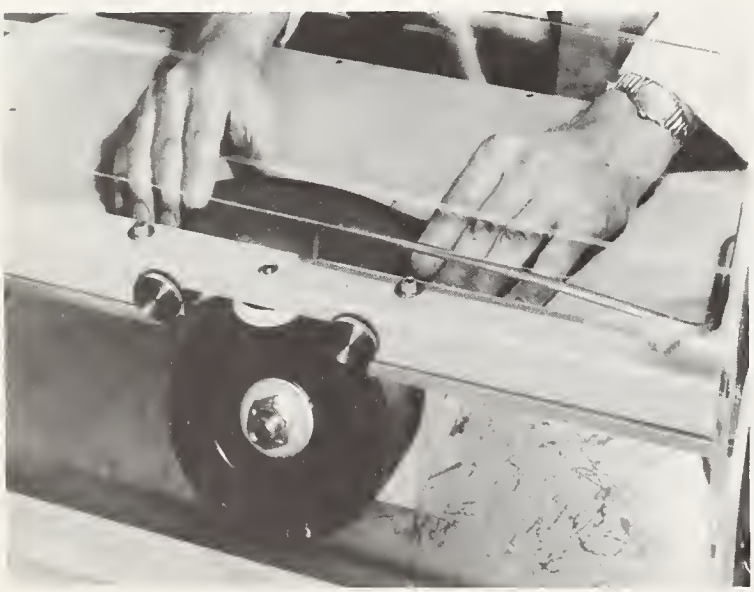

Figure 9. Lawrence Livermore Laboratory chamfering fixture.

Figure 10. Typical chamfers (600x) generated by mutal bonded diamond, and by 15 micron diamond belt followed by buff polishing.

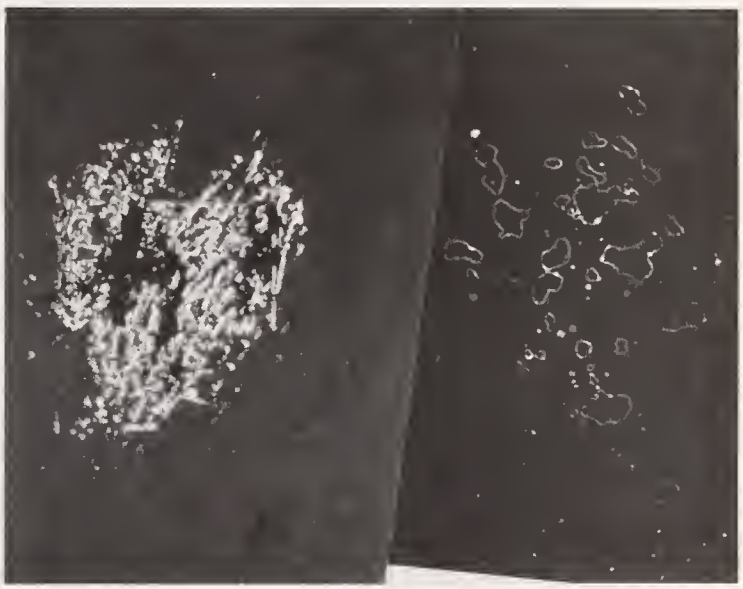

Figure 11. Coating damage on front and back surfaces (500x & 600 x) of cylindrical lens. Front surface (Nomarski photo) shows sleek damage initiation.

NO COMMENTS ON PAPER BY BROWN

1.2 STANDARD INDUSTRIAL POLISHING OF HIGH ENERGY LASER OPTICS

Walter J. Spawr
SPAWR Optical Research, Inc.
Corona, California 91720

The polishing and figuring of optical materials to produce state-of-the-art surface quality is truly an art, a scientific art, but an art nonetheless.

To attain success, the optician must have a clear mental model of the processes and associated techniques, and use this model as his most important tool. Second only to that is the combination of discipline and determination that no harmful or deleterious influences are allowed to effect the processes. New sophisticated polishing machines used in "Metrology Laboratory" environments are of little or no assistance. Polishing machines built 50 years ago work as well as the latest designs.

Today, moderately skilled technicians routinely produce 30Å RMS surfaces on copper, molybdenum, and zinc selenide. These surfaces are free of orange peel, scratches, and digs; and are produced on conventional polishing machinery. Such surfaces are shown [3][1] to exhibit exceedingly high laser damage thresholds from 1.06μm to 10.6μm. This is accomplished on a daily basis in a time frame comparable to the commercial polishing of ordinary optical glasses.

Key words: Copper; molybdenum; optician; polishing; surfaces; zinc selenide.

Introduction

The limitations in polishing state-of-the-art surfaces in any type of material are primarily imposed only by the optician. The present standard materials, environments, and polishing machines are of sufficient quality to produce high energy laser (HEL) components, provided the optician understands the techniques involved.

Polishing

An optician is not necessarily limited to any specific type of material. Both very hard and very soft polycrystalline materials can be polished to super-smooth (scratch free) surfaces. The highest damage resistant surfaces can be produced using the standard polishing techniques established many years ago [1]. State-of-the-art surfaces of various geometries are produced on a daily schedule in our optical polishing lab. This demonstrates that new technological breakthroughs are not necessarily required for many present requirements that have been considered unattainable in the industry.

Photo No. 1 shows a 10" diameter molybdenum (bulk material) mirror and a 2.2" diameter zinc selenide (CVD) window. The molybdenum mirror was polished flat to $\lambda/2$ (λ = 5461Å) with a surface quality (or smoothness) of 30Å RMS. The zinc selenide window in the foreground was polished (both sides) flat to $\lambda/4$ (λ = 5461Å) with 20Å RMS surface smoothness. Both the molybdenum mirror and the zinc selenide window were fabricated in 1972.

Photo No. 2 is a Nomarski photograph[5] of the surface of the zinc selenide (shown in photo No. 1) using 98X.

Multiple element blocks, which is a standard practice in the industry, can also be used to meet high volume production requirements for copper and molybdenum without sacrificing optical surface figure or damage threshold [1].

We have also found that experienced opticians are not limited to polishing simple geometries.

1. Figures in brackets indicate the literature references at the end of the paper.

Photo No. 3 is of a water-cooled copper elliptical mirror with a large output coupling hole. Mirrors of this geometrical configuration are normally considered to be very costly because of the extra detailed work involved in mounting a plug for the central hole, and "fill material" for the surrounding area. When this coupler was fabricated we chose to use no plugs or polishing aids (fill material) of any kind. The mirror was polished flat to 3 fringes overall with a 3 fringe rolloff extending <0.050" out from the hole. This was well within the design tolerances specified for this mirror.

Aspheric configurations including parabolic cylinders and toric surfaces can also be produced. Photo No. 4 illustrates interference fringes for a cylindrical figure in a water-cooled molybdenum mirror. This mirror was accurate to $\lambda/8$ (NaD). The surface quality was $\leq$35Å RMS and <60/40 scratch and dig per MIL-O-13830A. Though this was the first of its kind, research and development was not required to produce it.

Based on the results of diamond turning experiments [2], we decided to obtain better surfaces from machine tools (lathes and mills) to cut down on the grinding and polishing time for copper mirrors. We found that with surfaces no better than a $\sqrt[32]{}$ machine finish as illustrated in photo No. 5, the entire grinding process could be eliminated. We can now take machined surfaces (in copper) from the machine shop and go right into the polishing operation.

The polishing processes used by opticians in our lab do not seem to be limited to small sizes. They have fabricated several 12" and 16" diameter copper mirrors polished to <35Å RMS, 40/20 scratch and dig, and flat to 5500Å. The largest mirrors fabricated to date measured 25.5" x 15.5" and offered no additional problems to polish [1].

The reported [3,4] reflectance and damage threshold values for polished copper surfaces are $\geq$0.99 and >250 J/cm^2 @ 600 nsec, respectively. Molybdenum reflectance and damage threshold is reported [3,4] to be $\geq$0.98 and >200 KW/cm^2 CW for 10 sec. uncooled.

Summary

When copper or molybdenum is properly polished it offers high damage thresholds [3]. The opticians in our lab are taught that the basic limitations in polishing and figuring HEL optical components is with their understanding. An optician's technical capability is a direct function of the optical figure and damage threshold achieved.

References

[1] Spawr, W. J., "The Art of Metal Polishing," presented at SPIE, August 1975.

[2] Saito, T. T., APPL. OPT. 14, 1973.

[3] Spawr, W. J. and Pierce, R. L., "Metal Mirror Selection Guide," SOR Report No. 74-004, Spawr Optical Research, Inc., Corona, CA.

[4] Saito, T. T., "Microinch Machining of Optical Components for Infrared Optics," Air Force Weapons Laboratory Tech Report AFWL-TR-73-290, Air Force Weapons Laboratory, Kirtland Air Force Base, NM (February 1974).

[5] Compliments Capt. R. Selleck, Kirtland Air Force Base, NM.

Figures

Photo No. 1 - Molybdenum Mirror and Zinc Selenide Window

Photo No. 2 - Zinc Selenide Surface 98X Nomarski

Photo No. 3 - Copper Laser Coupling Mirror

Photo No. 4 - Interference Fringes of a Cylindrical Mirror

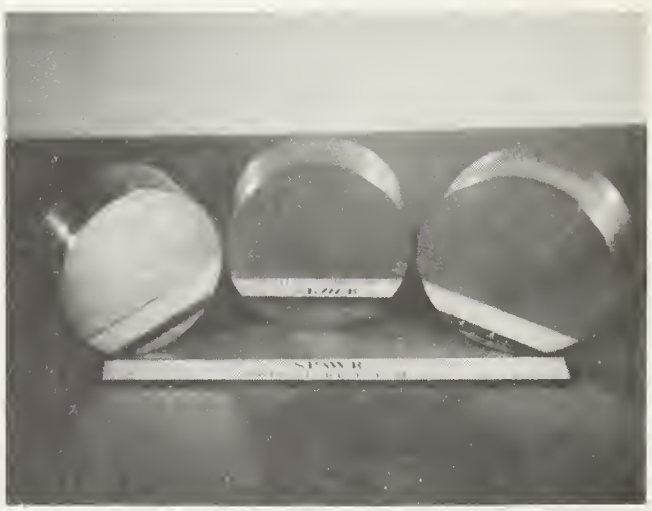

Photo No. 5 - Machined Surfaces of Copper Mirrors

COMMENTS ON PAPER BY SPAWR

The speaker maintained that in his experience mirrors prepared by this technique have not damaged in regular use at illumination levels up to four or five joules per square centimeter. Variations in reflectivity have been noted in copper mirrors prepared by the method described. These variations are attributed to details of the proprietary polishing process. Surface roughness is monitored using a visual observation of light scattering. An accuracy of ± 2 Å was claimed. The technique of inspection was described.

1.3 Ion Planing and Coating of Sodium Chloride

R. A. Hoffman, W. J. Lange and W. J. Choyke

Westinghouse Electric Corp.
Research Laboratories
Pittsburgh, Pennsylvania 15235

Ion planing of single crystal sodium chloride, using low energy Xe ions at grazing incidence, is effective in removing scratches from surfaces when the sample is rotated. Surface features which develop, probably due to defects such as polishing grit and dislocations, can be minimized and the scratches eliminated by optimizing the amount of material removed. Ion planing and depositing overcoating films "in situ" greatly improves film adherence and protection of sodium chloride substrates against moisture attack.

Key words: Arsenic trisulphide; ion planing; protective films; moisture resistance; sodium chloride.

1. Introduction

Several studies have indicated that ion planing of optical components can produce beneficial results. In a previous paper [1][1] we have shown that the combination of ion planing and vacuum annealing of single crystal copper samples results in a smoother surface with significantly lower optical absorption at 10.6 μm. Giuliano [2] has demonstrated that ion planing of sapphire yielded samples with improved laser damage threshold. Finally, Bruce and co-workers [3] have reported that ion planing of alkali-halide windows results in a better surface finish with lower optical absorption. The object of this study is to demonstrate another use for ion planing, namely, the improvement in film adherence and protection afforded by the combination of ion planing and depositing overcoating films "in situ." Ion planing and overcoating "in situ" offers great potential for producing more durable laser components. In addition to a better surface finish, the technique should yield a clean film-substrate interface free from contamination, thus giving rise to improved film adhesion, lower absorptance, and increased laser damage threshold. This is especially true for alkali-halide laser windows where surface preparation and film adhesion are major problems because of substrate hardness and moisture sensitivity. Hence, it was decided first to investigate the effects of ion planing on the surface morphology of single crystal NaCl and then to study the influence of ion planing and overcoating "in situ" on film adhesion and moisture protection.

2. Experimental Procedures

The ion planing apparatus was constructed to provide an experimental laboratory facility for removing material from surfaces in a controlled manner. The apparatus, which is fully described elsewhere [1], is shown schematically in figure 1 along with typical operating conditions. Briefly, the planer employs sputtering by a focused beam of relatively low energy Xe ions incident on the sample surface at glancing angle, 12° from the plane of surface. The beam is rastered across the surface and the sample is rotated to produce uniform removal of material. The combination of low ion energy, glancing angle of incidence, rastering, and sample rotation are expected to produce a smoothing of the surface features while minimizing damage to the surface. Figure 2 depicts the sample chamber of the ion planer in the configuration for depositing overcoating films. Shown in the figure are a basket evaporation source with shutter, a quartz crystal film thickness monitor, a neutralization filament used when planing insulating samples, and a phosphor screen used for focusing and positioning the ion beam. In practice, ion planing at a low removal rate is continued during film deposition to minimize contamination at the interface and in the film, while sample rotation provides better film thickness uniformity over the sample.

One series of experiments was performed using a commercial "Microetch" unit purchased from the Veeco Corporation. A sample holder has been added to this equipment to provide sample rotation and variable angle of incidence of the ions which form a broad area beam. Typical operating conditions used 950 eV Xe ions incident on the rotating sample at 40° from the normal. The removal rate, using either apparatus, was determined by masking a portion of the sample during planing, and then using a profilometer to measure the amount of material removed.

Two instruments were used to examine the surfaces of the NaCl samples: an optical microscope with an interference contrast attachment and magnification up to 500X, and a scanning electron microscope having magnification up to 20,000X. Of course, insulating samples such as NaCl must be coated with a conducting film, gold for example, before the surface can be examined in the SEM which limits the usefulness of this instrument.

The humidity test chamber consisted of a bell jar containing dishes of water, a humidity meter, and a thermometer. A small opening was provided under the bell jar rim to permit some circulation and prevent the relative humidity from reaching 100%. During testing, the relative humidity was typically in the range 90-95%.

1. Figures in brackets indicate the literature references at the end of the paper.

3. Ion Planing Results

The samples used in this study were single crystal NaCl disks, 2.54 cm in diameter, which were first mechanically polished. Most of the sample faces had a crystallographic orientation close to (100) except for those especially prepared with (110) and (111) faces for the orientation dependence study. These samples were selected because NaCl represented a typical laser window material with polishing and moisture sensitivity problems, they were readily available, and it was felt that the results on single crystal material would be less complicated and easier to interpret. A typical surface, which was ion planed to remove about 3 μm and then coated with about 400Å of Au, is shown in the scanning electron micrograph in figure 3. The surface shown in the left hand side of the figure was masked off during ion planing while that on the right hand side was ion planed. It is seen that the surface is drastically different after ion planing with all the scratches removed and raised features (hummocks) appearing predominantly along previous polishing scratches. Figure 4 shows scanning electron micrographs of the same area of the ion planed surface, but with higher magnifications. Several different types of hummocks can be seen in these photographs, ranging from those with pointed tops to those with a broad rounded profile. The hummocks are caused by regions with a lower sputtering yield than the surrounding area and emerge out of the background as it is sputtered away. One can speculate that polishing grit having a lower sputtering yield and trapped in the surface would evolve into a pointed feature while dislocations, induced by mechanical polishing of the surface, might lead to the rounded features that predominate along polishing scratches.

The change in surface morphology with the amount of material removed by ion planing is shown in figure 5 which consists of interference contrast micrographs of NaCl surfaces with 0.4, 1.5, 4.1, and 7 μm removed. It can be seen that as more material is removed from the surface the scratches disappear and the number and size of the hummocks grow until for large amounts of material removed the entire surface is covered with them. This suggests that there is an optimum amount of material to be removed which would eliminate the scratches and damage layer and minimize the growth of hummocks. The crystallographic orientation of the sample with 1.5 μm removed was (110) while the other samples had (100) orientation. It is seen that the growth of hummocks is similar for both orientations, but the background texture appears to be different. These same observations can be made from examination of figure 6 which shows interference contrast micrographs of (100), (110) and (111) samples which were ion planed to remove about 4 μm. It must be noted that the quality of the surface before ion planing was worse for the (110) and (111) orientations since mechanical polishing of these orientations was found to be more difficult.

It was observed that the density of the hummocks varied dramatically over some of the ion planed surfaces. This is seen in figure 7 which shows interference contrast micrographs of two areas of a (110) NaCl crystal which was ion planed to remove about 4 μm. The hummock density was much greater near the edge of the sample (left-hand photograph) than in the center of the sample (right-hand photograph). It is possible that hummock growth is related to damage in the sample induced by mechanical polishing which can be greater at the sample edges. Davisson [4] reported that damage which resulted from mechanical polishing of NaCl windows had to be annealed out before chemical polishing would give satisfactory surfaces. Therefore, a NaCl sample was annealed at 650°C for 1/2 hour in air prior to ion planing, but the surface both before and after ion planing seemed worse after annealing. It is not known what happened to this sample, but the effects of annealing prior to ion planing should be investigated further.

Several samples were ion planed, with the Xe ion beam incident at 40° from the surface normal, using the commercial apparatus described previously. Typical surfaces obtained with this equipment are shown in interference contrast micrographs in figure 8. By comparing figures 5 and 8, it is seen that for similar amounts of material removed, ion planing at 40° is not as effective as that at 78° (from the surface normal) in removing scratches from the surface. Also the raised features on the surface, although they have similar density and disposition in both cases, seem sharper in the former case. Hence, we conclude that ion planing at glancing angles results in a smoother surface than obtained by planing at more normal incidence.

Finally, the interference contrast micrographs of figure 9 show the effects of not rotating the sample. On the left hand side, the NaCl sample was not rotated and the scanned beam was incident in the horizontal direction in the photograph. The surface in the top half of the photograph was masked off during ion planing which removed about 3 μm from the lower portion of the sample. It is seen that the scratches that run perpendicular to the ion beam direction are "washed out" while those running in the direction of the ion beam are still sharp. The right hand photograph of figure 9 shows a sample that was planed with the ion beam scan narrower than the sample width in one direction; thus, the edges of the sample were struck by ions traveling predominantly in one direction. In the photograph the surface features are elongated in the direction of the ion beam. It can be concluded that sample rotation during ion planing is necessary for obtaining smooth, scratch-free surfaces.

4. Ion Planing and Overcoating "In Situ"

The principal purpose of this work was to determine what effect ion planing of NaCl and overcoating "in situ" had on film adherence and protection. First, two NaCl disks with a rough mechanical polish were coated on one face and edges with a 3.7 μm thick film of As_2S_3. The uncoated face of one sample was ion planed and after removing about 7 μm, a 2.2 μm thick film of As_2S_3 was deposited on both samples in the ion planer at the same time. Both samples were subjected to the humidity test previously described with the relative humidity at about 95%. Interference contrast micrographs of the surfaces of the two samples after 7 hours in the humidity test are shown in figure 10. The As_2S_3 film is cracked and lifting off the sample that was not ion polished (left hand photograph), while the ion polished surface appeared to have a deposit on it (light areas in the photograph), but the film remained intact. The samples were returned to the humidity test chamber and after several hours it was observed that small water droplets were condensing on the surface of the ion polished sample, while it looked as if moisture had penetrated the film on the sample that was not ion polished. This is shown in figure 11 which is a photograph of the samples in the humidity chamber after 39 hours of test. The As_2S_3 film on the sample on the left, not ion planed, appears to be floating on water, while the surface of the ion planed sample on the right has condensed water droplets on the film surface predominantly along the remnants of two large polishing scratches. Figure 12 shows interference contrast micrographs of the two samples after the 39 hours of humidity testing. The film on the sample that was not ion polished was badly blistered and lifting making it difficult to photograph. The ion polished sample had what appeared to be NaCl crystals on the film surface as shown in the right-hand side of figure 12. This probably indicates that moisture had penetrated the As_2S_3 coating through film defects in discrete spots, but the film was still intact and flat even in the vicinity of the defect. Therefore, we conclude that ion planing and coating "in situ" does markedly improve film adherence and protection of NaCl substrates against moisture, and that even better protection of alkali-halide windows can be expected if the film can be made free from defects, perhaps by the proper combination of mechanical polishing and ion planing.

5. Conclusions

We conclude that ion planing, using low energy inert gas ions incident at a glancing angle on a rotating sample, is effective in removing scratches in single crystal NaCl. The influence of the raised surface features that develop, probably due to defects such as polishing grit and dislocations, can be minimized by optimizing the amount of material removed and could possibly be eliminated by proper annealing prior to ion planing. Ion planing and depositing overcoating films "in situ", which minimizes contamination at the film-substrate interface, greatly improves film adherence and protection of NaCl substrates against moisture attack and offers promise of increased laser damage thresholds.

6. References

[1] Hoffman, R. A., Lange, W. J. and Choyke, W. J., To be published Appl. Opt. Aug. (1975).

[2] Giuliano, C. R., Appl. Phys. Lett. 21, 39 (1972).

[3] Bruce, J. A., Comer, J. J., Collins, C. V., and Lipson, H. G., Proc. Third Laser Window Conf. AFCRL-TR-74-0085(111), 757 (1974).

[4] Davisson, J. W., Proc. Second Laser Window Conf. AFCRL-TR-73-0372(11), 525 (1973).

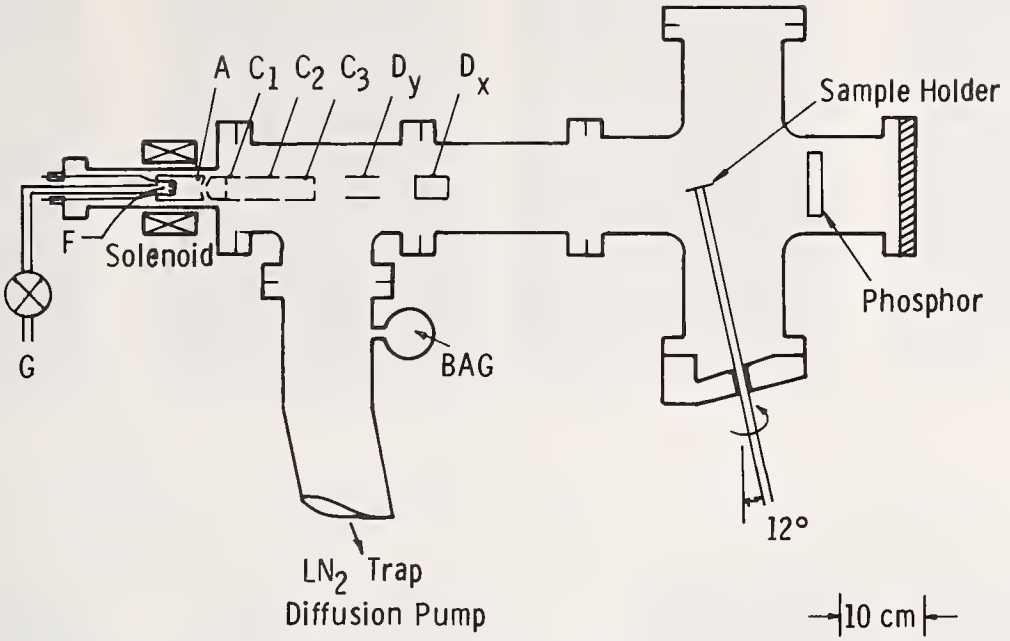

Figure 1. Ion polishing apparatus. The vacuum envelope, except for the large glass cross on the right, is stainless steel at ground potential. The LN_2-trapped, oil diffusion pump provides a base pressure measured by the ion gauge (BAG) of $\leq 5 \times 10^{-8}$ Torr (6×10^{-6} Pa). The system is inclined to the horizontal at 12°, so that the sample is held on the rotatable holder by gravity alone. Electrons supplied by the filament, F, maintain a discharge in the anode, A, into which gas, G, is admitted to maintain a pressure of $\sim 1 \times 10^{-3}$ Torr, some 500 times that in the remainder of the system. Cylinders C_1, C_2, and C_3 comprise the ion lens. Two pairs of plates, D_x and D_y, provide deflection of the beam in the x and y directions; for rastering, frequencies of 1000 and 50 Hz, respectively, are used on D_x and D_y. Typical operating conditions using Xe as the sputtering gas are: filament at +3975 V, anode at +4000 V, C_1 at -2000 V, C_2 at +2600 V, C_3 at ground, target at ground, ion current 10 μA, sample rotated at 6 rpm.

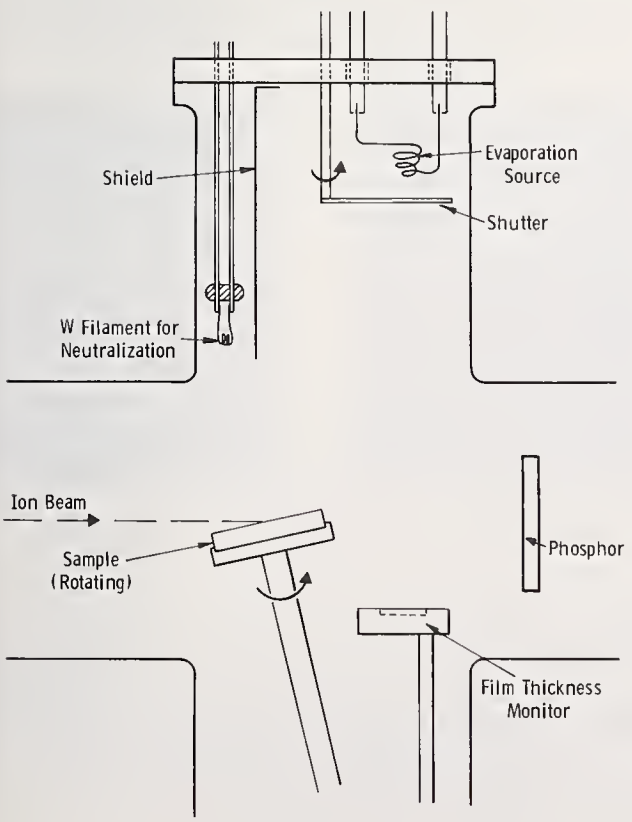

Figure 2. Apparatus for depositing overcoating films in ion planer.

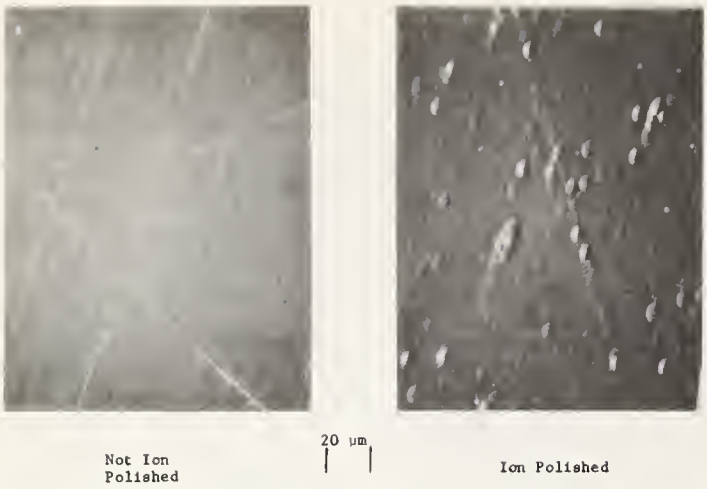

Figure 3. SEM photomicrographs of sodium chloride. Right-hand side was ion planed to remove 3 µm.

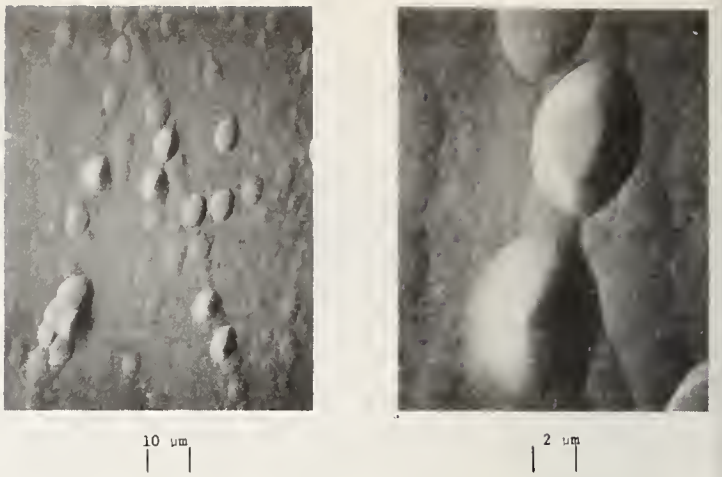

Figure 4. SEM photomicrographs of sodium chloride which was ion planed to remove 3 µm.

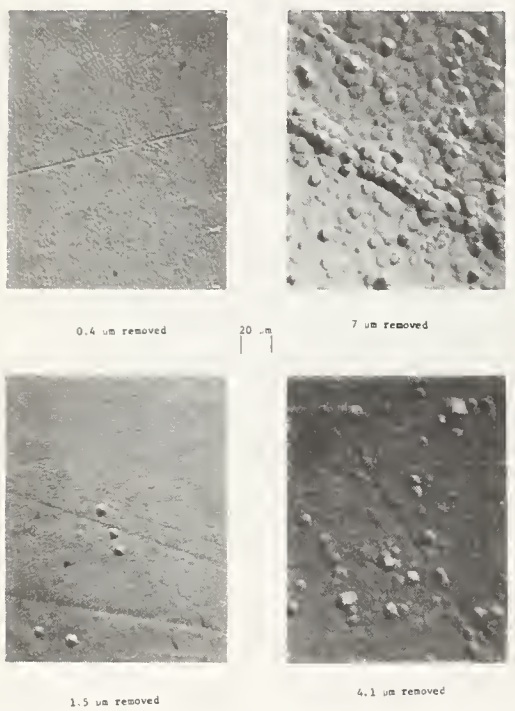

Figure 5. Interference contrast photomicrographs of sodium chloride showing dependence on amount of material removed by ion planing.

Figure 6. Interference contrast photomicrographs of ion planed sodium chloride showing dependence on crystallographic orientation.

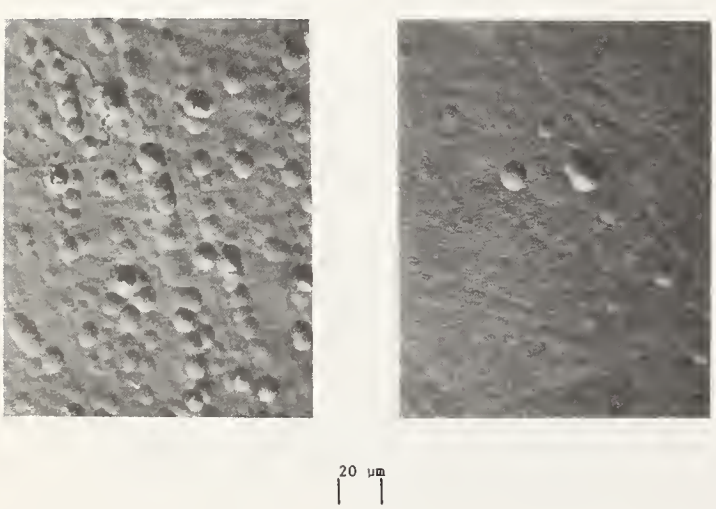

Figure 7. Interference contrast photomicrographs of two areas of ion planed sodium chloride sample. Left side is near edge and right side is in center.

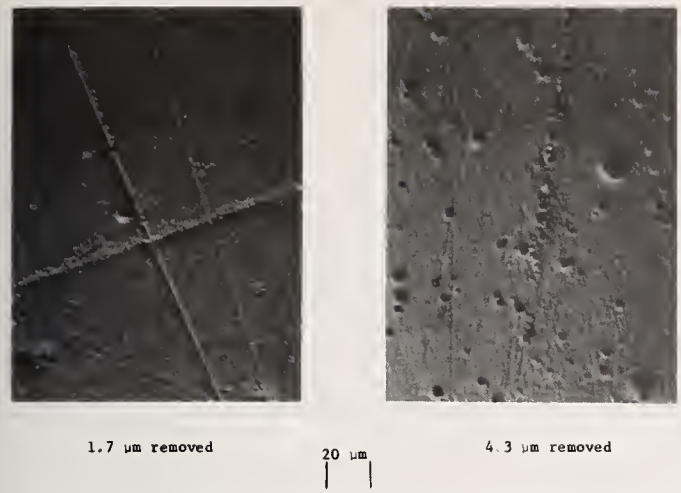

Figure 8. Interference contrast photomicrographs of sodium chloride which was ion planed at 40° from the surface normal.

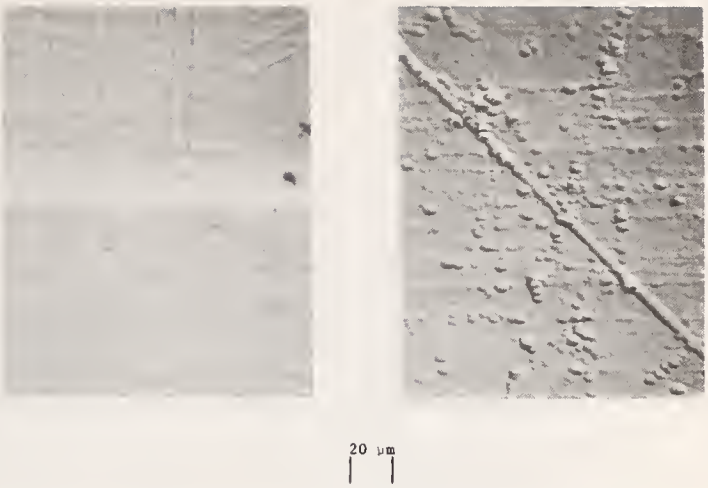

Figure 9. Interference contrast photomicrographs of sodium chloride showing effects of not rotating the sample during ion planing. Sample on left was not rotated, on right was partially rotated.

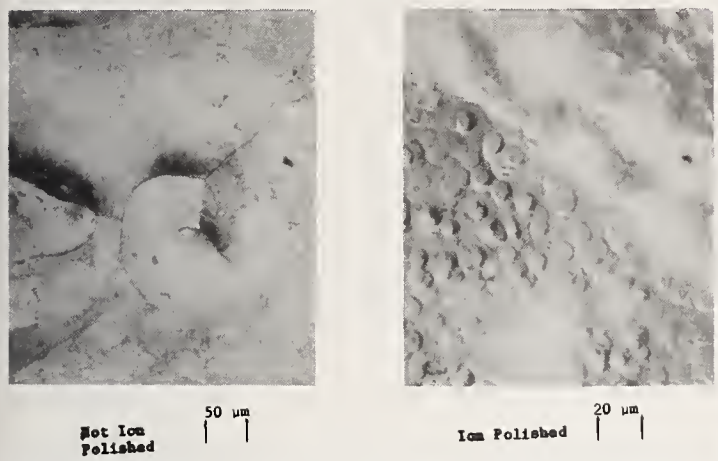

Figure 10. Interference contrast photomicrographs of sodium chloride coated with As_2S_3 after 7 hours of humidity testing.

Figure 11. Photograph of sodium chloride coated with As_2S_3 after 39 hours of humidity testing. Sample on right was ion planed, that on left was not.

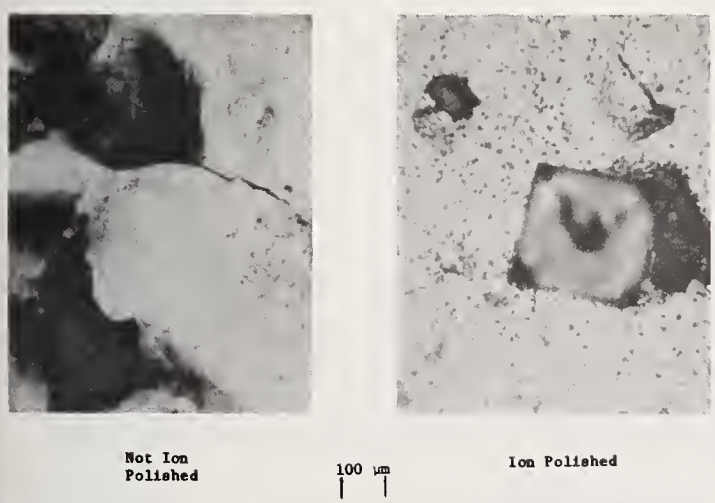

Figure 12. Interference contrast photomicrographs of sodium chloride coated with As_2S_3 after 39 hours of humidity testing.

COMMENTS ON PAPER BY HOFFMAN, *et al*

The speaker was asked if surface figure was maintained during the polishing process. He replied that surface figure itself was not monitored, but that uniformity of removal was monitored and a variation of up to 10% was observed over the surface with a total removal of four micrometers of material. The pattern of removal was designed to be essentially random. Heating of the sample was not thought to be a serious problem. The question of bubble formation due to subsurface penetration of the ion beam was discussed and it was concluded that the ion range at the energy used was not sufficient to cause significant subsurface penetration and consequent bubble formation.

1.4 Polishing Studies and Backscatter Measurements on Alkali-Halide Windows

M. J. Soileau, H. E. Bennett, J. M. Bethke, and J. Shaffer

Michelson Laboratories, Naval Weapons Center
China Lake, California 93555

Surface absorption, optical figure, and optical scatter from windows are particularly important in high energy lasers. Surface absorption can result in window failure due to thermal distortion and in some cases catastrophic failure. Excellent optical figure is required for each component in the laser system optical train in order to maintain maximum on axis intensity of the focused laser beam. Backscatter from windows and other optical components can cause depumping of the active medium, and in the case of amplified chains, catastrophic damage to the laser amplifiers. A technique for polishing alkali-halide and quantitative measurements of backscatter for alkali-halide windows from the visible to 10.6 μm will be presented. This polishing procedure produces alkali-halide surfaces which have less than 1×10^{-4} surface absorption, are parallel to less than 3 seconds of arc and are flat to better than a quarter wave in the visible. Scattering levels below 10^{-4} at 10.6 μm have been achieved.

Key words: Alkali-halide; KCl; laser windows; optical figure; polishing; scattered light; surface absorption.

1. Introduction

A technique has been developed for producing HEL window surfaces which have low surface absorption, low scatter, excellent optical figure, and are parallel. This procedure, which employs a combination chemical-mechanical polish, has been successfully applied to pure KCl (single and polycrystalline), KCl alloys (single and polycrystalline), and NaCl windows. Surfaces which have less than 1×10^{-4} surface absorption, total backscatter below 1×10^{-4} at 10.6 μm, are parallel to less than 3 seconds of arc and are flat to better than $\lambda/4$ have been achieved. The details of the polishing procedure, experimental results on a variety of alkali-halide laser windows and backscatter and absorption measurements will be discussed.

2. Polishing Technique for Alkali-Halide Windows

We have developed a technique for polishing alkali-halide windows with less than 1×10^{-4} surface absorption, parallel to less than 3 seconds of arc and flat to better than a quarter wave in the visible. This technique is a hybrid of the mechanical procedure previously reported by Michelson Laboratory [1][1], and the chemical etch procedure reported by the Naval Research Laboratory and Hughes Research Laboratory [2,3].

Previously we described a technique which yielded well-figured KCl which has surface roughness a factor of four less than conventional polished KCl [1]. This technique employed a pitch lap, Al_2O_3 abrasive, and triacetin as a polishing vehicle. Initial measurements of the 10.6-μm absorptance of KCl polished using this technique indicated significant surface absorption. Previous results by Davisson and Allen have shown that the mechanical polishing damage and surface contamination, which give rise to surface absorption, can be removed by careful etching [2,3]. The primary difficulty with etching is that material is removed at a high rate, thus making figure control extremely difficult.

The basic idea of the technique reported here is to first remove all surface contamination and mechanical damage by etching in concentrated HCl, and then produce the optical figure with a minimum working of the surface (usually no more than 4 hours polishing on each side). In practice the specimen is ground to approximate flatness and wedge using 20-, 11-, and 5-μm Al_2O_3 grit in kerosene on a Pyrex plate. After grinding, the specimen is etched for 3 minutes in concentrated HCl and rinsed in reagent-grade ethanol in the manner described by Davisson. When the specimen is removed from the ethanol it is blown dry with clean, dry nitrogen. Boil-off from liquid nitrogen is used in conjunction with a deionizing nozzle to minimize buildup of static charges, thus minimizing dust accumulation on the surface.

The etching procedure sometimes results in enhanced grain boundaries (particularly in fine grain polycrystalline materials) and sharp edges. If visual inspection reveals any such edges the specimen is buffed on a Polytex cloth using 0.3-μm Al_2O_3 in triacetin until the surface is smooth enough to reveal optical figure. This usually takes 1 to 2 minutes and is done only when indicated by visual inspection. If sharp edges are present and are not removed damage to the polishing lap will result.

The specimen is then blocked by taping it to a felt-covered metal disc of the same diameter. The part is then polished on a paraffin lap with 0.3-μm Al_2O_3 abrasive in a triacetin vehicle. The specimen is polished until desired figure is obtained and optimum surface quality (determined by inspection

1. Figures in brackets indicate the literature references at the end of the paper.

with a Nomarski microscope) is achieved. Experience has shown that if the desired figure and surface quality are not achieved after approximately 4 hours of polishing, it is best to re-etch the specimen and repolish it. When the desired surface finish and figure are obtained the sample is cleaned with benzene. A soft tissue is saturated with benzene and *gently* rubbed over the specimen until the residual polishing material has been removed.

After cleaning, the polished side is coated with Carbofilm and the specimen is blocked as previously described. The polishing process is repeated for the second side. The procedures are summarized in tables 1 and 2, and are illustrated in figures 1 and 2.

Table 1. General Procedure for Polishing Alkali-Halide Windows.

Rough grind	Flat glass lap, Al_2O_3 abrasive (20, 11, and 5 μm), kerosene vehicle.
Chemical etch	3 minutes in concentrated HCl, rinse in ethanol, dry with clean, dry N_2 gas.
Cloth buff	Polytex cloth, 0.3-μm Al_2O_3 abrasive, triacetin vehicle.
Block	Coat one side with Carbofilm and tape to felt covered metal plate.
Polish	Paraffin lap, 0.3-μm Al_2O_3 abrasive, triacetin vehicle, bowl feed or fresh feed.

Table 2. Details of Polishing Procedure.

Lap	Paraffin, pressed flat, cut to form 1/2-in. squares with approximately 1/8-in. spacing.
Polish	Spindle speed 28-30 rpm, arm speed 1/4 spindle speed, 1 to 1.5 lb/in^2 load, bowl feed with paddle in continuously or fresh feed by brushing on slurry, avoid polishing more than 4 hours per side.
Clean	Wipe clean with soft tissue saturated with reagent-grade benzene.

3. Surface Microroughness Requirements for KCl and NaCl

Although we have demonstrated that it is possible to polish KCl and NaCl surfaces using the pitch-lap, triacetin-polish technique to rms roughness values under 30 Å rms, we have not succeeded in producing surfaces with low surface absorption which are this smooth. The goal to achieve roughnesses under 20 Å rms was set by analogy with roughness requirements for mirrors. Infrared absorption of silver coatings increases rapidly with roughness for rms values above 20 Å. This anomalous absorption may result from a resonant dipole phenomenon [4], from limitation of the electronic mean free path by surface irregularities with lateral dimensions in the 100 Å range [5], or possibly by some other phenomenon, such as two-carrier absorption. None of these mechanisms should cause surface absorption in dielectrics.

Another reason for minimizing surface roughness is to increase the threshold for damage resistance. Scratches and other gross surface imperfections increase the local field in dielectrics, resulting in a lowered threshold for dielectric breakdown. The minimum size of irregularities for which this mechanism is estimated to be important in the infrared is about 100 Å [6].

The final reason for minimizing surface roughness on polished dielectric surfaces is to minimize scattered light. Both forward and backscattering are important in a high energy beam. In addition, light scattered at the surface into the dielectric at angles larger than the critical angle will be trapped and eventually absorbed in the window and its mounting. For low absorption surfaces a significant fraction of the apparent "surface absorption" may result from this mechanism. However, as discussed in a later section of this paper, the dominant scattering mechanism at 10.6 μm is not necessarily surface microroughness. If the contribution to scattered light from microirregularities is below about 10^{-5}, other scattering mechanisms dominate. The fraction of the light incident externally on the surface which is scattered by microirregularities is

$$\frac{\Delta R}{I_o} = \frac{R_o}{I_o}\left(\frac{4\pi\delta}{\lambda}\right)^2 ,$$

where ΔR is the fraction of the reflected light R_o which is scattered, I_o is the incident intensity, δ is the rms height of surface irregularities, and λ is the wavelength. For KCl and NaCl at 10.6 μm, $R_o = 0.04$ so that

$$\frac{\Delta R}{I_o} < 10^{-5} \text{ for } \delta < 130 \text{ Å}.$$

We thus conclude that although the criterion that surface microirregularities be under 20 Å rms is a valid objective for mirrors used in HEL systems, it is unnecessarily severe for NaCl and KCl windows and may be relaxed. A requirement that the microroughness be under 100 Å seems adequate for HEL windows made from these materials.

4. Experimental Results

4.1 Single Crystal KCl

Initial efforts were directed at polishing pure KCl and emphasis was placed on obtaining very smooth flat surfaces. This approach proved successful and yielded surfaces flat to one-eighth wave in the visible and with surface microroughness of less than 30 Å rms. The next step was to determine the effects of the polishing procedure on surface absorption. A laser calorimeter was assembled for measuring absorptance of the polished material. A schematic diagram of this calorimeter is shown in figure 3. The calorimeter and the method of data reduction are based on earlier work by John Loomis [7,8].

The first absorptance measurement on a triacetin-polished single crystal KCl yielded total absorptance of 0.0062 to 0.014 (measurements at different spots) on a 5-mm-thick piece. Hope that the measurements were wrong was vanquished by measurements on a similar specimen polished by Harshaw which indicated total absorptance of 0.0011. Since the specimen with the high absorptance had been polished for weeks in order to try to optimize surface finish, the logical thing to assume was that extensive surface damage had resulted and the surface had been contaminated.

This theory was tested by etching the high absorptance specimen. After 3 minutes of etching the total absorptance was reduced to 0.00077, thus indicating surface absorptance in the polished piece on the order of 0.005 per surface. This high surface absorptance cast serious doubts as to the usefulness of the polishing technique. However, as we were to discover, the technique could be used successfully if polishing time could be restricted to less than 8 hours and preferably 4 hours per surface.

After etch, the specimen discussed above was polished until flat to one-half wave in the visible. The absorptance was measured after polish and found to be 0.00053. Since this value was less than that of the freshly etched piece, it seemed that all the surface contamination was not removed in the 3-minute etch. The specimen was etched again for 3 minutes and the absorptance went down to 0.00041. The specimen was polished again on both sides to a flatness of less than $\lambda/2$ in the visible on each surface. The specimen was polished a total of 8 hours using fresh feed and the total absorptance was 0.00066, indicating surface absorptance on the order of 1.2×10^{-4} per surface. These results are summarized in table 3.

Table 3. Polishing Results on Single Crystal KCl. This specimen was pure KCl from Harshaw. The specimen was 1.5 inches in diameter and 5 mm thick.

Surface treatment	Optical figure	Total absorptance at 10.6 μm
Several weeks of triacetin polish using bowl feed	$\lambda/8^a$	0.0062-0.014
3 min HCl etch	none	0.00077
6 hours triacetin polish using fresh feed	$\lambda/2$	0.00053
3 min HCl etch	none	0.00041
8 hours triacetin polish using fresh feed	$\lambda/2$	0.00066

[a] λ is in the visible.

4.2 KCl Alloys

The results obtained on single crystal, pure KCl were applied to Eu^{++} and RbCl doped KCl in single and polycrystalline form. This material was provided by the Air Force Weapons Laboratory. The single crystal material was grown by Harshaw and was hot pressed by the Honeywell Ceramics Center [9].

At this point the NWC technique consisted of etching in HCl and polishing with the triacetin slurry using fresh feed. Bowl feed polishing sometimes produced severe scratching. We later found that this was caused by "tearing" or "chipping" of the lap by sharp edges produced in the etching process. These pieces of lap material were then thrown back in the lap by the stirring action of the paddle in the bowl. This problem was eliminated by buffing the part on a Polytex cloth for approximately 1 minute to remove the sharp edges. This buffing procedure should only be performed if visual inspection indicates the presence of sharp edges, since any handling of the KCl is likely to cause some surface contamination and increased absorptance.

Excellent results have been achieved in polishing the KCl alloy materials using the technique outlined in section 2 with bowl feed and fresh feed. Single crystal and polycrystalline specimens have been polished to a good optical figure, while keeping the total surface absorption in the 1×10^{-4} range. Figure 4 summarizes the results obtained on polycrystalline Eu^{++} doped KCl. The total absorptance of this specimen after being polished to $\lambda/4$ in the visible was only 7×10^{-5} more than the absorptance after chemical etching. Thus, the increase in surface absorptance by the mechanical polishing was only 3.5×10^{-5} per surface. Similar results have been obtained on single crystal Eu doped single and polycrystalline RbCl/KCl alloy material. The results of our efforts to polish polycrystalline alloy materials are summarized in table 4.

Table 4. KCl Alloy Polishing Results.

Optical figure	$\lambda/8$
Surface absorption	$< 1 \times 10^{-4}$ per surface
Surface roughness	27 Å rms
Scale-up	6 in. diameter
Wedge	< 3 sec

Although the results obtained to date have been encouraging, several problems remain to be solved. First, even in best case results some increased absorptance is caused by the optical figuring process. The origin of this residual absorption is not well understood and will be subject to further research. Second, there appears to be a serious problem with the "coatability" of polished surfaces. The absorptance of coatings deposited on the polished surfaces is as much as a factor of 10 higher than that of chemically etched surfaces. We are presently pursuing this problem. Two possible mechanisms for the higher coating absorptance are (1) inadequate cleaning of the polished surface, and (2) enhanced trapping of scattered light by the addition of a quarter-wave optical thickness, high index coating (in this case As_2S_3).

4.3 Polycrystalline NaCl

The procedures developed for polishing KCl were applied to Harshaw "Polytran" provided to us by Dr. Walter Reichelt of Los Alamos Scientific Laboratory (LASL). In general, the NaCl was easier to polish than the KCl. Both figure and surface quality were easier to control; however, the problem of "coatability" discussed in the previous paragraph is as serious for NaCl as for KCl.

The results of the work on NaCl surfaces are shown in table 5 and figure 5. The value of the absorptance of the NWC-polished specimen presented in table 5 indicates no increase over that for the chemically etched surface. However, since the total absorptance is so high (0.0016) it would be difficult to detect increases in absorptance on the order of 1×10^{-4}. Thus, one cannot conclude from this data that no surface absorptance is introduced by the optical figuring process. The absolute accuracy of the calorimeter used to measure the absorptance is on the order of $\pm 10\%$, thus one can conclude that the total induced absorptance is less than 3×10^{-4}, i.e., less than 1.5×10^{-4} per surface.

Table 5. Results of NaCl Polishing.

Absorptance of etched NaCl (1 cm thick)	0.0016
Absorptance after NWC polish	0.0016
Optical figure	$\lambda/8^a$
Surface roughness	26 Å rms

$^a\lambda$ is in the visible.

5. Backscattering From Alkali Halide Windows

Backscattering from windows and other optical components is particularly important in high energy lasers, since it can cause depumping of the active medium, and in the case of amplified chains, catastrophic damage to the laser amplifiers. The surface microirregularities for both NaCl and KCl have been shown by FECO interferometry to have Gaussian height distribution functions [10], so scattering levels from this source should fall exponentially with increasing wavelength and exhibit a $1/\lambda^2$ dependence. Scattering from scratches would be expected to show little wavelength dependence. Particulate scattering was investigated previously for mirrors [11] and also showed little wavelength dependence. To our knowledge, quantitative measurements for alkali halide windows have not been previously reported.

To obtain an approximate value of the level of backscattering to be expected from single crystal and polycrystalline KCl windows, measurements were made on the Optical Evaluation Facility (OEF) [12] using a conical absorber mounted approximately 10 cm behind the window to prevent light transmitted through the window from reaching the scattered light detector. The contribution from light scattered from the back surface of the transparent sample was determined by measuring the apparent scattering level from a mirror surface as the mirror was moved back from the Coblentz sphere focus. For a window of 1 cm thickness with index of refraction of 1.5, the effective air path would be 1/1.5 = 6.67 mm and the signal from the back side at that effective distance was determined to be 0.79th of that from the front surface. The scattered light results reported are total values observed on the OEF, and hence are 1.79 times the values from a single surface. However, the roughness values quoted are obtained by dividing the observed scattering levels by 1.790 to correct for back surface reflection.

The first sample measured was polycrystalline KCl doped with Eu and hot forged by Honeywell. It had been polished commercially, was heavily scratched, and had a figure of about 5 fringes across its 38-mm diameter. The observed backscattering is given by the circles in figure 6 and follows an exponential curve, indicated by the dashed line. The slope of the dashed line is less than would be predicted for microirregularities, probably because of the scratches, which result in scattering levels with little wavelength dependence [11]. Forward scattering from this sample was also measured at a wavelength of 6328 Å on the Optical Functional Tester [13] and was in excellent agreement with the backscattering values. This result is important since it suggests that forward and backscattering values for windows may often be nearly identical.

After the initial measurements the KCl sample was given an NWC polish, described in section 2 of this paper, and had a figure of about 1/2 fringe before etching. It was etched for 3 minutes as described in section 2 of this paper and then remeasured. The results are shown by the square points in figure 6. The scatter in the visible region is reduced by over a factor of 2, and falls more rapidly in the infrared region than did the commercially polished sample. It fits the theoretical line for scattering from microirregularities of height 183 Å rms very well both in the visible and infrared regions. Under a Nomarski microscope the etched surface appeared virtually free from scratches, suggesting that microirregularities should be the dominant scattering mechanism.

The difference in scattering from polycrystalline and single-crystal surfaces is shown in figure 7. Both Eu-doped samples were etched for 3 minutes in HCl. The polycrystalline surface scatters in a manner similar to the polycrystalline surface in figure 6. However, scattering from the single-crystal surface is lower by a factor of 3 in the visible and near infrared. At longer wavelengths, scattering from the single-crystal surface departs from the theoretical predictions for scattering from microirregularities and is a factor of 4 higher than that from the polycrystalline surface at 10 μm. Since Eu is a much larger atom than K and will cause significant distortion of the lattice, the same experiment was carried out with another dopant, Rb. The results are shown in figure 8. Again the single-crystal surface scattered much less than did the polycrystalline one in the visible region. Again scattering from the single-crystal surface departed from the theoretical predictions at about 5×10^{-4} scattering level. This time, however, the polycrystalline surface scattering also departed from theory and virtually coincided with that from the single-crystal surface in the 3-10 μm wavelength region.

The average deviation in scattering from various points on the surface is also plotted in figure 8. The circles correspond to the polycrystalline sample and the squares to the single-crystal sample. In the case of the single-crystal sample, the average deviation in the points is almost independent of wavelength. Scatter in the polycrystalline points is about an order of magnitude lower than the

scattering values in the visible region, and decreases with wavelength until it reaches the single-crystal values, at which point it also becomes independent of wavelength. A similar behavior has been observed for mirrors; when the scattering values reach the 10^{-4} region they tend to stabilize and do not decrease further. We suspect that the variations from point-to-point are caused largely by scattering from particulates, such as dust, or possibly microscopic salt protuberances, rather than from microirregularities. If the scattering is from dust, then surface finishing beyond a certain point is not productive and the scattering level of the component will be determined by the environment in which it is used, rather than by the way in which it is polished. Work is continuing on this question.

6. Conclusions

A technique has been developed at Michelson Laboratory for producing HEL window surfaces which have low surface absorption (1×10^{-4} per surface or less), excellent optical figure ($\lambda/8$ in the visible), and are parallel (less than 3 seconds of wedge). The major problems remaining are the coatability of these surfaces, improvements in surface quality, and scale-up to larger sizes.

Our tentative conclusions regarding scattering from halide windows are: (1) Scratches can significantly increase the infrared scattering level in KCl windows as well as presumably lower the damage threshold and should be minimized; (2) In the absence of scratches scattering above about 5×10^{-4} is determined by microirregularities and below this value may be governed by particulates. In the 10 μm wavelength region particulate scattering may well be the dominant scattering mechanism; (3) Since the index of refraction and hence the reflection coefficient from the surface is low, requirements on microirregularities for window surfaces are much lower than for mirror surfaces. For example, a window with a reflection coefficient of 4% can have surface irregularities with rms values four to five times those permissible for a good mirror surface scattering the same amount of light. Thus as far as scattered light goes, surfaces of 80-100 Å rms can be tolerated for windows, whereas roughnesses of 20 Å rms or less are desirable for mirrors; (4) The magnitude of backscattering from windows is approximately equal to the magnitude of forward scattering.

7. Acknowledgments

The authors wish to acknowledge the support of the following agencies and individuals: ARPA, Dr. C. Martin Stickley, program monitor; AFWL, Major James Stapp, program monitor; ERDA, Dr. Walter Reichelt of LASL, program monitor.

8. References

[1] Shaffer, J., et al., "High Energy Laser Mirrors and Windows," (Semi-Annual Report No. 4, ARPA Order 2175, Naval Weapons Center, March 1974), pp. 103-109.

[2] Davisson, J. W., Conference on High Power IR Laser Window Materials, Oct. 30, 31 and Nov. 1, 1972, Vol. 2, AFCRL, June 1973, pp. 525-534.

[3] Allen, S. D., M. Braunstein, C. Giuliano, and V. Wang, "Laser Induced Damage in Optical Materials: 1974," NBS Spec. Publ. 414 (1974), pp. 66-75.

[4] Decker, D. L., "High Energy Laser Mirrors and Windows," (Semi-Annual Report No. 4, ARPA Order 2175, Naval Weapons Center, March 1974), pp. 66-83.

[5] Tinkham, M., "Report of the Materials Research Council (1974)," (ARPA Order 2341, University of Michigan, December 1974), p. 37.

[6] Bloembergen, N., Appl. Opt. 12, 661 (1973).

[7] Loomis, J., Appl. Opt. 12, 877 (1973).

[8] Loomis, J., "Laser Division Digest, Spring 1972," (Air Force Special Weapons Center, Kirtland AFB, N. M., TR LRD-72-1, 1972), pp. 29-41.

[9] Harrison, W. B., et al., Fourth Annual Conference on Infrared Laser Window Materials, ARPA, Jan. 1975, pp. 599-610.

[10] Bennett, J. M., "Laser Induced Damage in Optical Materials: 1974," NBS Spec. Publ. 414 (1974), pp. 157-162.

[11] Bennett, H. E. and M. J. Soileau, "High Energy Laser Mirrors and Windows," (Semi-Annual Report No. 6, ARPA Order 2175, Naval Weapons Center, May 1975), pp. 156-172.

[12] Bennett, H. E. and P. C. Archibald, ibid., pp. 145-155.

[13] Soileau, M. J. and H. E. Bennett, "Laser Induced Damage in Optical Materials: 1974," NBS Spec. Publ. 414 (1974), pp. 149-156.

1(a)

1(b)

Figure 1. Bowl feed polishing of alkali-halide windows. (a) A 1.5" diameter piece of KCl is being polished using a submerged paraffin lap and the blocking procedure described in the text. (b) The "paddle" can be seen; in this case a paintbrush is used to stir the slurry. Solid paddles are also used and give similar results.

Figure 2. Blocking procedure. A piece of polished KCl is resting on the felt-covered blocking plate. The side of the KCl adjacent to its blocking plate is coated with carbofilm prior to blocking.

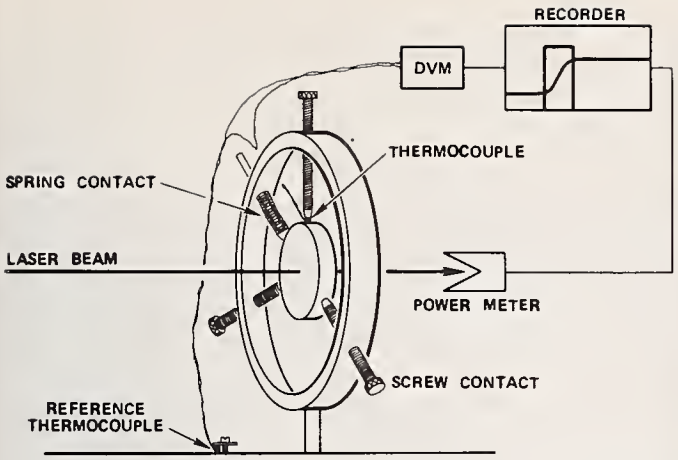

Figure 3. Window calorimeter. This is a schematic of the calorimeter used to measure 10.6 μm absorptance in alkali-halide materials. Copper-constantan thermocouples are used. Pressure contact by a plastic-tipped screw is used to attach the thermocouple to the specimen. The thermocouple voltage is read by a digital voltmeter (DVM) and displayed, along with the transmitted laser power, on a strip chart recorder. The laser source is a Coherent Radiation Model 41 CO_2 laser with continuous wave output up to 250 watts.

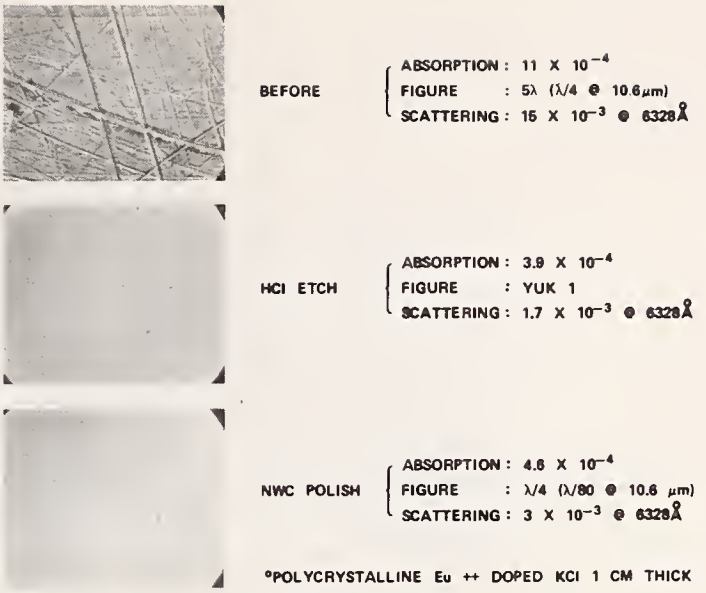

Figure 4. Polished Eu^{++} doped KCl. The polished surfaces exhibit only a slight increase in absorptance as compared to chemically etched surface. Similar results have been obtained on single crystal Eu doped material and single and polycrystalline RbCl alloy material. The magnification of the micrographs is 360X.

Figure 5. NWC polished NaCl. The picture on the right is a 360X Nomarski micrograph of a NaCl specimen polished for 4 hours using the NWC triacetin slurry. The picture on the left is an interferogram of the optical figure of this specimen. The interferogram was taken with a YZGO interferometer with a He-Ne laser source (λ = 6328 Å).

NOTE: Microns as expressed in figure 5 expresses micrometers.

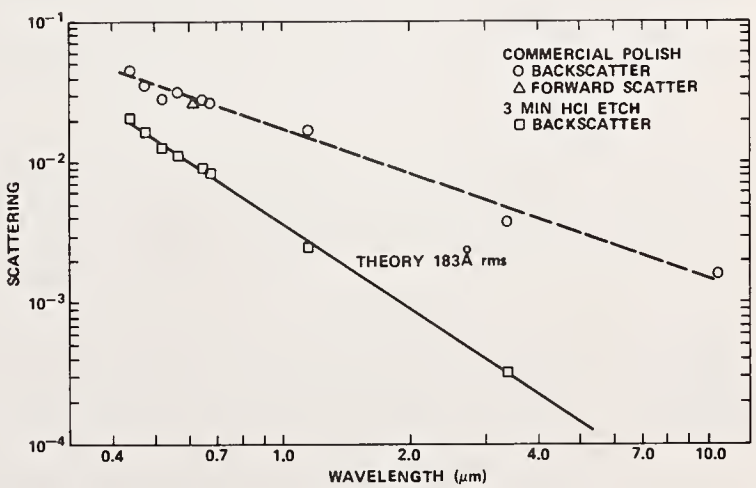

Figure 6. Backscatter from Eu-doped KCl after commercial polish and after 3-minute HCl etch.

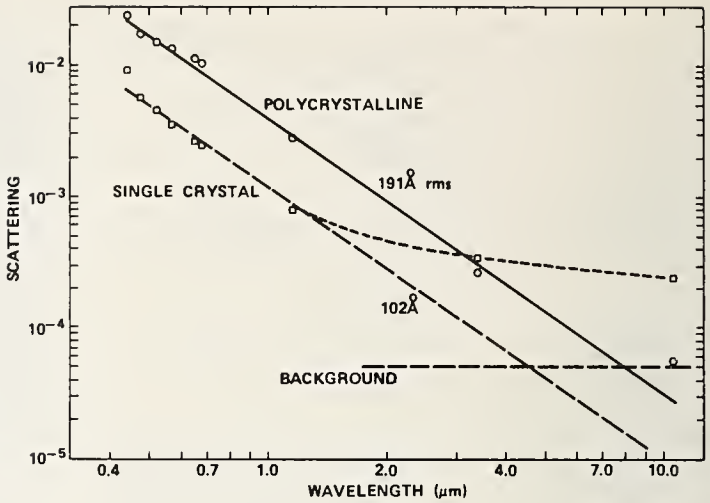

Figure 7. Backscatter from etched, Eu-doped KCl for polycrystalline and single crystal samples.

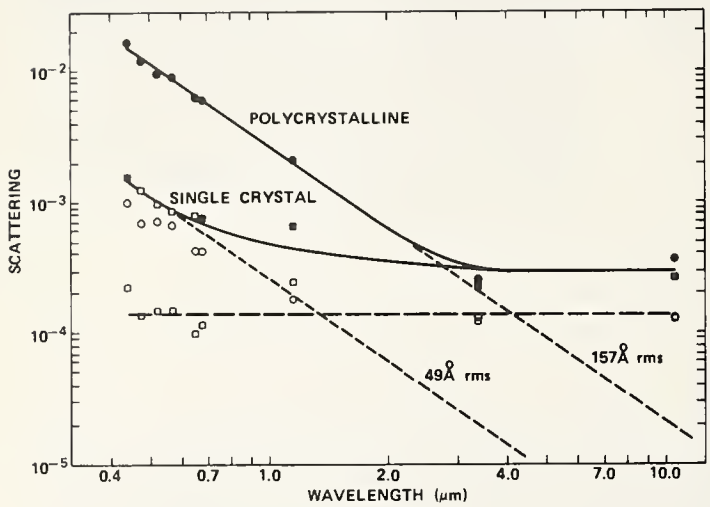

Figure 8. Backscatter from etched, Rb-doped for polycrystalline and single crystal samples. The open circles and squares represent the average deviation in scattering from different points on the surface of the polycrystalline and single-crystal samples, respectively.

COMMENTS ON PAPER BY SOILEAU, et al

In response to a question concerning the polishing of doped alkali-halides vs pure alkali-halides the speaker indicated that the same technique was used for both classes of materials. He also indicated that because in this method the polished surface is submerged the environmental variation observed in other polishing techniques, for example, the susceptibility to atmospheric humidity was greatly reduced by this process. It was further commented that because the final figuring of the surface is performed after the etching degradation of surface figure is minimized.

2.1 1.06μm 150 psec Laser Damage Study of Diamond Turned, Diamond Turned/Polished and Polished Metal Mirrors

T. T. Saito*, D. Milam, P. Baker, and G. Murphy, Lawrence Livermore Laboratory
Livermore, California 94550

Using a well characterized 1.06 μm 150 psec glass laser pulse we have studied the damage characteristics for diamond turned, diamond turned/polished, and polished copper and silver mirrors less than 5 cm diameter. Although most samples were tested with a normal angle of incidence, some were tested at 45° with different linear polarization showing an increase in damage threshold for S polarization. Different damage mechanisms observed will be discussed. Laser damage is related to residual surface influences of the fabrication process. Our first attempts to polish diamond turned surfaces resulted in a significant decrease in laser damage threshold. The importance of including the heat of fusion in the one dimensional heat analysis of the theoretical damage threshold and how close our samples came to the theoretical damage threshold will be discussed.

Key words: Copper mirror; damage threshold; dark field photography; diamond turned optics; 1.06 μm polishing.

1. Introduction

Metal mirrors are of interest to the high power pulsed laser programs because of the high reflectivity and good thermal conductivity. Diamond [1][1] turning of metals offers expanded design flexibility to incorporate fast parabolas or unusual shapes such as compound axicons or ellipses. In addition, diamond turning may offer considerable cost benefits over dielectrics for large diameter optics which will require refinishing due to laser damage.

This paper presents our study of laser damage on metal mirrors. We shall discuss the experimental arrangement, preparation of the samples, and demonstrate the degradation effects of polishing or even rubbing/cleaning diamond turned silver. Comparisons of our results to other studies of polished copper at different wavelength and pulse length indicate that a similar damage mechanism is present for less than 500 nsec pulses.

2. Experimental Apparatus

A schematic of the damage facility in the laboratory is shown in figure 1. The source consists of a mode-locked oscillator and pulse selector, two YAG preamps, and two glass rod amplifiers. Fast diodes A and B monitor waveforms of the pulse train and of the switched-out pulse. Integrating diodes C and D measure the energy of the switched-out pulse before and after amplification. The output energy is controlled by setting the amplification. Typical beam parameters in a plane normal to the beam at the test sample's surface are:

Energy	-	.0 - 0.5 joules
Beam profile	-	nearly Gaussian
Beam diameter	-	∿ mm at 1/e level
Pulse duration	-	150 ± 25 psec

The damage experiment is also shown in figure 1. A Galilean telescope is adjusted to serve as a focusing element with the beam waist being 4-8 meters distant as required. The reflection from the front surface of a bare BK-7 wedge is centered on an aperture placed in front of the calorimeter. The aperture is chosen to correspond to the approximate diameter of the beam at the e^{-2} intensity level, and the centering of the aperture is photographically certified at the beginning of each day of operation. This calorimeter serves as the fundamental monitor of pulse energy.

The reflection from the rear surface of the BK-7 wedge is incident on a 40% - 100% mirror pair used to form multiple replicas of the beam profile existent in the sample plane. The images are recorded on polaroid film so that the results of each firing can be viewed immediately thereby avoiding the possibility of operating with significant undetected problems with the beam profile. The poloroid photos also furnish an instant estimate of the incident energy density. We have found these estimates to be reproducible to 20% as substantiated with much more ellaborate methods.

The replicas are also recorded on 1-Z plates. From five to nine firings can be recorded on each plate. The most intensely exposed of these is reduced using the Photocal routine [2]. That serves to calibrate absolutely the exposure vs. film density curve for that particular plate. The film densities resulting from the remaining shots recorded on the same plate can then be interpreted without recourse to Photocal.

*Detached duty from the Air Force Weapons Laboratory, Laser Division, Kirtland AFB, NM 87117

1. Figures in brackets indicate the literature references at the end of the paper.

Photocal is a sophisticated generalized computer routine developed by our colleague, Dr. Joe Weaver, for providing the energy density on the sample. After the exposure versus film density (i.e., the H & D curve) for the plate is determined, a hundred by hundred matrix of optical density versus position is established by repeated scans of a spot. The optical density and H & D curves are used to yield the relative intensity as a function of position in the sample plane and a three-dimensional computer picture is produced. Using the total energy measurements from the calorimeter the program can then calculate the peak energy density taking into consideration intensity spikes and other departures from true Gaussian profiles.

Values obtained from the reduction of 1-Z plates are qualitatively compared with the poloroid beam photographs to insure that no significant data reduction errors have been made. The incident energy densities of a set of firings can be ranked from least to greatest by simply counting the number of replicas recorded on poloroid film for each firing. The reduction of 1-Z data should yield the same ranking.

Since the Gunn calorimeters appear to be accurate to within about 3-5%,energy densities determined in these experiments should mirror that accuracy. Estimates of the energy made from the same 1-Z plate, but without the 100 x 100 matrix are accurate to 10%. The estimates of energy density from just the poloroid pictures are accurate to 20%.

The pulse width is determined by using a streak camera. We did not measure the pulse width for each shot. We have many thousands of laser firings, and have periodically measured the pulse width to be 150 ± 25 psec.

3. Experimental Technique

Sample Preparation. The diamond turned samples were all electroplated on copper or brass substrates. Lea Ronal[a] silver and copper pyrophosphate electroplating were used. Most of the samples were heat treated by placing them in a beaker with oil and slowly raising the temperature to 150° C, maintaining 150° C for one hour, and then removing the beaker from the heat source and allowing the beaker/oil/mirror blank to cool to room temperature. The heat treating process was used to relieve the residual stresses from the electroplating [3]. The samples were then diamond turned. Some of the samples were diamond turned simultaneously in batches of 18. After they are diamond turned and while the spindle is spinning, isopropyl alcohol is used to rinse the cutting oil off the samples.

Some of the diamond turned samples were polished using techniques which will be described in detail elsewhere [4]. Based on the success of others [5, 6] in using india ink, we used suspended carbon particles (Acqua Dag) to polish some of our samples. Other samples were polished with diamond and silicon oil. Our lap was made of pitch, bees wax, and silk.

Immediately before the laser damage test, the samples were rinsed with various solvents in an attempt to remove the residual film. Eastman lens cleaner left such a bad residue on some parts that they were not tested. We found the best results came from rinsing the samples first with acetone, and then removing the residual acetone film with alcohol. Further studies of cleaning of diamond turned optics are being planned.

Laser Damage Testing. Unless specified, all tests were performed at a nominally normal angle of incidence. Experiments were also performed with a 45° (±2°) angle of incidence with p or s polarization. The sample was placed on a stage which had translation stages in directions perpendicular to the direction of laser propagation. Each shot number and the corresponding coordinates of illumination were recorded along with any observations made before firing, during firing (viewed through laser safety glasses), or after firing. We found small emissions of light could be seen during the firing without seeing any damage using a dark field illumination technique. Before and after the firing we inspected the surface by dimming the room lights and illuminating the sample with a bright (white) microscope light. Residue films from the cleaning process, scratches as well as laser damage could be easily seen. Newnam has reported that the most sensitive technique in his experiments was the visual determination of scattering of an auxilary low power cw laser [7]. Similar to Newnam, we found light scattering to be the best technique for determining damage.

Dark Field Illumination Photographs. We have adapted Hizney's photographic technique to present the surface defects which we saw during the laser tests [8,9]. The simple experimental set-up is shown in figure 2. A white light source illuminates the sample such that the specular beam misses the camera which photographs the scattered light. Figure 3 is a series of photographs taken in sequence. A diamond turned copper mirror was photographed as received from the diamond turning lab as shown in figure 3a. Figures 3c and 3d were taken immediately after 3b, but by increasing the exposure time. This technique has several advantages:

a. Produced by Sel-Rex Corporation, Nutley, N.J.

1. It is easy and economical to set up.
2. It may lend itself to an easily describable, and therefore, reproducible technique.
3. It can give 100 % part inspection.
4. It presents artifacts (especially residual films) which are not easily observed with even Nomarski microscopy.

We plan further investigations of this technique with the possibility of establishing a quantitative technique for measuring cleanliness.

It was very difficult to find the laser damage sites when using a microscope, even with a Nomarski differential interference contrast accessory. The best success in doing optical microscopy was to place the sample on the translation stage while illuminating it from the side with the high intensity white light source. We could then see the laser damage spot and translate the sample until the light from the microscope coincided with the site of interest. Simply scanning the sample with normal observation usually resulted in overlooking the damage sites because of the very small differences in the background surface and laser damage in some sites.

4. Theoretical Calculations

Since our 150 psec pulse length is so short, a one-dimensional heat transfer model is adequate for calculating the damage threshold. The laser light is absorbed and heats a cylinder whose base is the same as the cross section of the laser on the mirror and whose height is $(\pi\alpha t/4)^{1/2}$ where t is the pulse length and α is the thermal diffusivity in cm^2/sec. The incident laser energy density, E_1, with pulse width t needed for a temperature rise, ΔT, to the melting temperature is a function of the density ρ, the specific heat s, and the absorption A of the laser light as given by eq. (1).

$$E_1 = \frac{\Delta T \rho s}{2A} (\pi\alpha t)^{1/2} . \qquad (1)$$

In order to change phase from a solid to a liquid, the heat of fusion H must be included requiring additional energy E_2.

$$E_2 = \frac{H\rho}{2A} (\pi\alpha t)^{1/2} . \qquad (2)$$

We have not included the heat of vaporization because we are calculating the threshold energy density, E_{th}, which is the sum of E_1 and E_2. (It is not necessary to vaporize the mirror in order to see a change in the surface.)

$$E_{th} = \frac{(\pi\alpha t)^{1/2}}{2A} (\Delta TS + H) . \qquad (3)$$

This calculation assumes a uniform intensity beam, but is valid for our experiment since the $1/e^2$ radius is so much greater than the thermal diffusion length. Note the $t^{1/2}$ time dependance of the damage threshold.

Theoretical damage thresholds are calculated for various metals and are presented in table 1 using typical absorption for 1 μm. These absorption values are based on Goldstein's work, 1 μm reflectivity and light scattering measurements [10].

The requirement for including the heat of fusion has been demonstrated by our experiments as silver samples have been illuminated at 4 j/cm^2 without exhibiting laser damage.

If copper, gold, and silver mirrors each had the same absorption, copper would have the highest theoretical damage threshold. Copper is theoretically better than silver or gold because of the higher specific heat and heat of fusion. Gold has the lowest theoretical damage threshold of the three.

Table 1. Theoretical Prediction of Damage Threshold for 150 psec 1 μm Pulse

Material	A	α cm^2/sec	ρ gm/cm^3	ΔT °C	S j/gm °C	E_1 j/cm^2	H j/gm	E_2 j/cm2	E_{th} j/cm2
Aluminum	0.06	0.86	2.70	635	0.899	0.26	396	0.18	0.44
Copper	0.011	1.18	8.97	1058	0.384	3.9	212	2.0	5.9
Gold	0.016	1.14	19.3	1038	0.13	1.9	67.5	0.94	2.8
Silver	0.011	1.71	10.5	936	0.23	2.9	104	1.4	4.3

5. Results and Discussion

Figure 4 is a dark field photograph of the Spawr copper. The damage sites are clearly visible along the edge of the mirror. Figure 5a is a regular micrograph of a damage site illuminated at 2 j/cm^2 on the Spawr mirror. Figure 5b and 5c are dark-field illumination photomicrographs at the same magnification as 5a at the center and edge respectively, demonstrating the laser enhanced scratches in the damaged area. Figure 5d is a Nomarski photomicrograph taken at about twice the magnification of 5a demonstrating that many small laser enhanced scratches are evident as well as some pitting. These scratches are very similar in appearance to what Brown reported observing laser damage of an anti-reflection coated cylindrical lens [11].

The effect of scratches on damage threshold is further demonstrated in figure 6 for sample LLL-Ag-5. LLL-Ag-5,6, and 7' were all diamond turned simultaneously in a fixture which can hold eighteen mirrors. Sample 5 was cleaned with alcohol and optical tissue by lightly wiping the surface. Fig. 6a is the dark field illumination photograph of the mirror which shows the (mainly) uni-directional scratches from the cleaning. Figures 6b and 6c are Nomarski photomicrographs taken at the same magnification of the same place,but by rotating the part so as to emphasize the diamond turning marks in 6b and show the background in 6c. The damage of site 793 has clearly been initiated along the scratches of the cleaning process and at one-half the threshold for just diamond turned silver as discussed below.

Electroplating defects can effect the laser damage threshold as shown in figure 7. The pox marks are evident across all the surface,but are more pronounced in the area where the laser damage occurs. This Nomarski photomicrograph was taken with the background contrast such that only the laser effected pox marks showed.

Diamond turning marks and electroplating defects in silver are shown in Fig. 8. Fig. 8a is a dark field illumination of the mirror taken at about the same time as 6a and with identical illumination and camera settings. Attempts were made to rinse the mirror clean with acetone and alcohol, blowing off the residual solvent with canned methane or freon. The residual film on LLL-Ag-7' has been removed in some spots by the laser without damaging the surface. We inspected the surface with the light scattering technique and with the Nomarski microscope without finding damage. We plan to investigate these sites with a double objective two beam (Linnick) micro-interferometer to see if we can detect any changes in the surface. Site 837 shown in Fig. 9 on LLL-Ag-7', illuminated at 3.9 j/cm^2, demonstrates damage along the diamond turning lines. I translated the sample and followed one of the heavier damage lines into an undamaged region where I could see that the diamond turning mark was one of the darker lines in the field of view. Light scattering may offer a quantitative measure of the important parameters of the particular diamond turning marks which seem to create damage at a lower threshold. Fig. 9 shows damage similar to that of the copper mirror in Fig. 7. These small marks are felt to be due to electroplating defects.

Table 2 summarizes our findings. We have listed the lowest level energy density, E_d, which caused damage and the highest level at which laser damage was not observed, E_{nd}. Due to inhomogeneities in the laser damage threshold across the surface, E_d can be less than E_{nd} as for LLL-Cu-78. The 1 μm absorption is estimated from the 1 μm reflectivity which we measured [12],and estimating the scattering as 0.001-0.002 for the diamond turned mirrors and for as much as 0.004 for the polished mirrors. Qualitatively we know the diamond turned mirrors scatter much less than the polished mirrors, because during the reflectivity measurements an S-1 diode "sniperscope" was used to view the 1 μm 0.5 cm diameter, 100 mw, cw laser beam. The scattering from the polished sample was readily observable,but we could see no 1 μm scattering from the diamond turned samples. Diamond turned samples have given some of the lowest light scattering of metal mirrors,with the exception of one super-polished piece of kanigen [3,13].

One of the most encouraging results is the 4.0 j/cm^2 damage threshold for diamond turned silver, which is 80% of the theoretical damage threshold. Higher damage thresholds may possibly be achieved by better cleaning procedures, as well as improvements in electroplating surface defects. Goldstein and co-workers have demonstrated that with 1μm 11 ns pulses the damage thresholds appear to follow absorption [10].

The results for copper are especially disappointing. The damage threshold of about 2.5 j/cm^2 is only about 40% of the theoretical value. We do not know why the threshold is proportionally so much lower than for the case of silver. Studies of optical properties at 10.6 μm have indicated that Cubath (a) has given the highest reflectivity by as much as 0.004. We plan to test Selrex Cubath in the future.

(a) Produced by Sel-Rex Corporation, Nutley, N.J.

Table 2. Summary of Laser Damage Threshold

Sample	A	E_{dam} j/cm^2	$E_{no\ dam}$ j/cm^2	E_{theory} j/cm^2	Comments
			Silver		
LLL-Ag-7'	0.010	4.0[c]	4.0[c]	4.8	EP/HT/DT/R
		3.9[b]	1.6[b]		45° P polarization
		5.4[a]	4.8[b]		45° S polarization
LLL-Ag-5	0.009	2.2[b]	2.2[b]	5.3	EP/HT/DT/R/cleaned
LLL-Ag-6	0.020	0.43[b]	0.24[b]	2.4	EP/HT/DT/R/P/cleaned
			Copper		
LLL-Cu-78	0.01	2.0[c]	2.6[c]	6.5	EP/HT/DT/R
		2.0[b]	1.6[b]		45° R polarization
		5.9[b]	4.9[b]		45° S polarization
LLL-Cu-44	0.042	0.16[b]	None	1.4	EP/DT/R/C/P/cleaned
Baker 10	0.026	0.7[b]	0.4[b]	2.5	P
Spawr Cu	0.018	0.39[b]	0.41[b]	3.6	P

a = ± 5%
b = ± 10%
c = ± 20%

EP = Electroplate
DT = Diamond Turned
R = Rinsed

P = Polished
c = Coated

We have not optimized our polishing parameters and hope to improve laser damage threshold for polished smaples. LLL-Ag-6 and LLL-Cu-44 were both polished with suspended carbon particles. The especially high absorption for LLL-Cu-44 coupled with its damage threshold so low that we could not determine it with this experimental arrangement has led us to conclude that our technique with carbon particles will not yield good high power metal laser components. The results for Baker 10, polished with diamond and silicon oil, compare favorably with damage data on other polished copper.

Based on the work of Goldstein, et al., [10] we tested some samples at 45° angle of incidence using first p and then s polarization. Similar to Goldstein we found an improvement in the damage threshold for s polarization. This improvement is due to the decreased absorption as well as the increased area of illumination. The values given in table 2 are the energy density in the beam measured in a plane perpendicular to the laser propagation direction. We concur with Goldstein's findings that use of metal turning mirrors may be very competitive with dielectrics in terms of laser damage. In the case of diamond turning, the initial fabrication cost and especially the refinishing cost would be better than for dielectrics.

It may be possible to take advantage of the periodic nature of the surface finish of a dimaond turned mirror. Although the total amount of scattering is low (less than 0.002), the mirror may serve as a low efficiency diffraction grating and the diffracted beam be used for beam diagnostics.

Comparison of laser damage thresholds at different wavelengths and pulse lengths can be compared to our results using eq. (3). Table 3 normalizes results for other polished copper reported mainly by Spawr and Pierce [14] and one from Stewart [15] of 10.6 μm, 470 ns pulsed study. The values have been normalized to our values of 0.018 absorption and 150 psec. Our results seem to be consistent with others except for the pulses longer than 500 ns. There is a possibility that at the longer pulse length, a different mechanism is associated with the damage than with the shorter pulse lengths.

It is now tempting to speculate on the cause of the lower damage threshold around micro-scratches. Bloembergen has discussed the effects of pits and scratches enhancing the electric field and lowering laser damage [16]. It may be possible that scratches have a higher absorption to pulses than is measured by low power cw methods, and therefore the scratches have lower damage thresholds than the theoretical value.

Table 3. Polished Copper Laser Damage Data Normalized to A = 0.018 5 - 150 psec

Testor	λ μm	t nsec	A %	E_{exp} j/cm2	$E_{normalized}$ u/cm2	Ref.
Our Data	1.06	0.15	1.8	0.4 - 0.6	0.4 - 0.6	-
Cincinnati Electronics	1.06	17	∿ 2	2 - 4	0.3	13
Raytheon	1.06	11	1.4	2.9	0.3	8
Los Alamos	1.06	0.05	∿ 2	0.4	0.7	13
Los Alamos	3	50	∿ 1.8	10	0.6	13
Northrop	5	10^5	∿ 1.5	1000	1	13
Los Alamos	10.6	1	∿ 0.9	> 4	>0.3	13
Battelle NW	10.6	470	1.7	35	0.6	14
Hughes Research	10.6	600	∿ 0.9	260	2.1	13

6. Conclusions

Diamond turned metals have the highest laser damage threshold for metal mirrors which we have tested. Diamond turned silver competes favorably with dielectric mirrors especially for turning S polarized beams.

Our work has demonstrated that various fabrication effects degrade the laser damage of silver. The degradation factor, D, is estimated and presented in table 4. One can estimate the damage threshold due to the effect by multiplying the theoretical damage threshold by D.

Table 4. Fabrication Degradation Factor for Silver

Fabrication Effect	D
Slight Electroplating Defects	0.8
Diamond Turning Marks	0.7
Scratches During Cleaning	0.5
Polishing	0.1 - 0.2

In contrast to Stewart [14] we were unsuccessful in polishing with suspended carbon particles in that although we achieved smooth surfaces low damage threshold resulted.

7. Acknowledgment

We are grateful for the donation of a sample and helpful discussions with Mr. Walter Spawr, the advanced use of the data of Dr. Irv Goldstein, and the assistance of our colleague Mr. Wayne Whistler in making the reflectivity measurements.

8. References

[1] T. T. Saito, "Machining of Optics: An Introduction" to be published in Appl Opt 14:1773 (1975)

[2] J. Weaver, G. Sommargren, and E. Bliss, "Self Calibration and Analysis of Image Formation in the Sub-nanosecond Domain" Proceedings of the Society of Photo-Optical Engineers, 18th Annual Technical Meeting 48: p-63.

[3] T. T. Saito "Characterizations of Diamond Turned Optics" to be published AF Weapons Laboratory Technical Report.

[4] P. Baker, J. Sonderman, and T. T. Saito, "Finishing of Precision Generated Optical Components" to be presented to the Soc. Photo-Optical Instrumentation Eng. Symposium on the "Design, Manufacture and Application of Metal Optics" San Diego, Aug. 1975.

[5] F. Twyman, "Prism and Lens Making", 2nd Edition, Hilger & Watts Ltd., London p-46.(1952_

[6] R. W. Stewart "Investigate Materials Systems for Mirrors Used in High Power CO & CO_2 Lasers," Technical Report ARPA Order No. 2175 Battelle Pacific Northwest Laboratories, Richland, Washington (Dec. 1972).

[7] B. E. Newnam "Damage Resistance of Dielectric Reflectors for Picosecond Pulses" in Laser Induced Damage in Optical Materials 1974, A. Glass and A. H. Guenther Editors, National Bureau of Standards Special Publication 414, 1974.

[8] J. Hizny"(Characterization of Low Scatter Optics" given at ASTM Mini-Symposium "The Possibility of Using Light Scattering to Establish a Surface Characterization Standard" Dallas, Tex, Jan. 1975.

[9] J. Z. Hizny "Substrate Throughprint in Low Scatter Mirrors" Society of Photo-Optical Instrumentation Engineers Symposium "The Design, Manufacture and Application of Metal Optics" at San Diego, August, 1975.

[10] I. Goldstein, D. Bua, and F. A. Horrigan "Pulsed Laser Damage to Uncoated Metallic Reflectors" 7th Annual Laser Induced Damage in Optical Materials, 1975.

[11] N. J. Brown "Fabrication of Laser Optics at Lawrence Livermore Laboratory" 7th Laser Induced Damage in Optical Materials Symposium, 1975.

[12] T. T. Saito, "1.06 μm Reflectivity Measurements of Metal Optics" UCID 16815, Lawrence Livermore Laboratory, Livermore, CA 1975.

[13] H. E. Bennett "High Energy Laser Mirrors and Windows" Semi-Annual Report No. 6, ARPS Order 2175, Michelson Laboratory, Naval Weapons Center, China Lake, CA March 1975.

[14] W. J. Spawr and R. L. Pierce, Metal Mirror Selection Guide, SOR Report #74-004, 30 Dec 74, published in part as "Guide to Metal Mirrors" Laser Focus, March, 1975, p-37 (1975)

[15] R. W. Stewart, "Investigate Material Systems for Mirrors Used in High Power CO and CO_2 Lasers" Semiannual Technical Report, August 1973, ARPA Order No. 2175, Battelle Pacific Northwest Laboratories, Richland, Washington

[16] N. Boemberger, "Role of Cracks, Pores, and Absorbing Inclusions on Laser Damage Threshold at Surfaces of Transparent Dielectrics" Appl Opt 12:661 (1973)

8. Figures

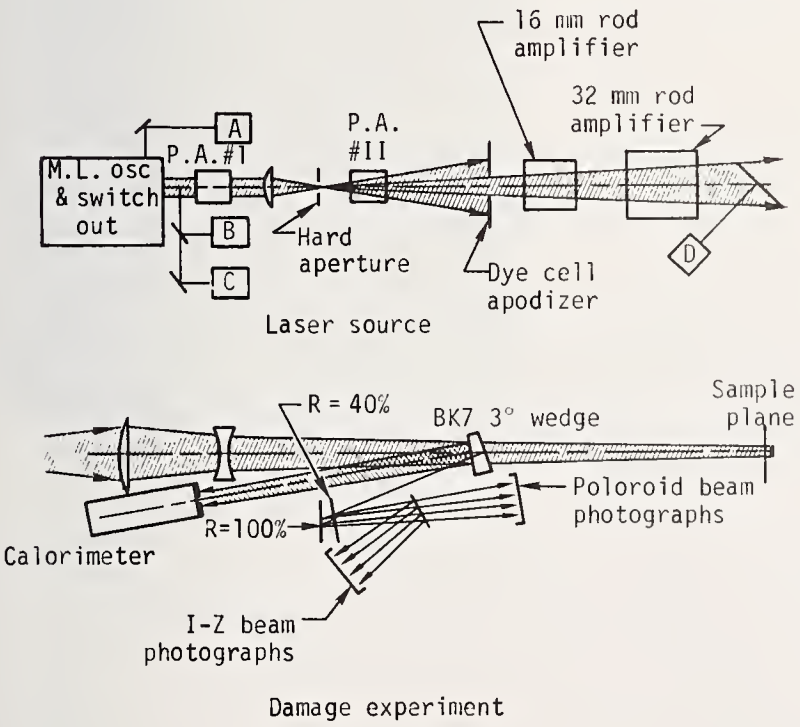

Figure 1. Schematic of experimental apparatus showing the mode locked oscillator which generates the 150 psec pulse. Diagnostics include calorimeters, 1-Z photographic plates, and polaroid pictures.

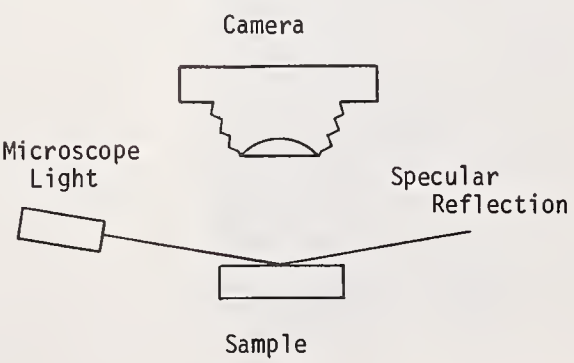

Figure 2. Schematic for the dark field photographic scheme for investigating laser damage specimen.

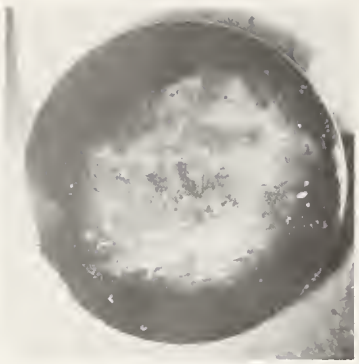

a. No cleoning
(t = 1/8 sec)

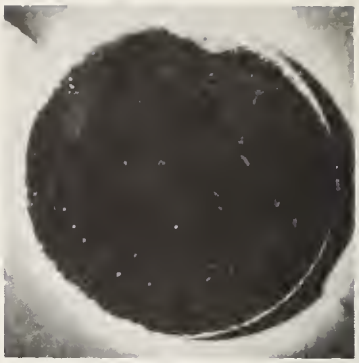

b. 90 sec cleaning
(t = 1/8 sec)

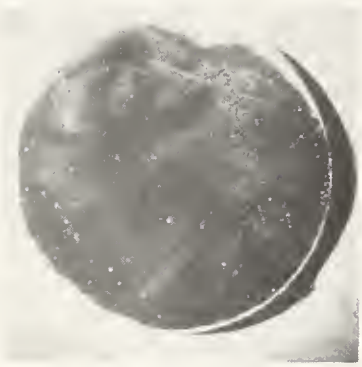

c. 90 sec cleoning
(t = 1/4 sec)

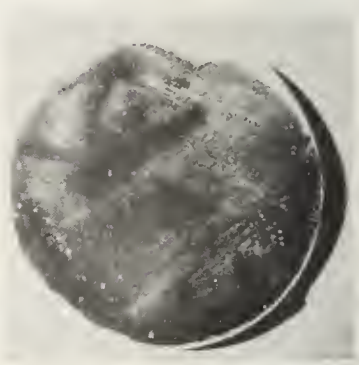

d. 90 sec cleaning
(t = 1/2 sec)

Figure 3. The dark field photographs were taken of a diamond turned copper mirror (a) as received from our diamond turning laboratory, and (b,c,d) after 90 seconds of cleaning in a vapor degreaser using TF freon at 50°C. Figure a and b were taken at the same photographic conditions. Figure c and d were taken at longer exposure times to demonstrate the residue on the mirror which still has not been removed.

Figure 4. Dark field photograph of the Spawr copper demonstrating the rows of laser damage spots along the bottom.

SPAWR COPPER

SITE 793

A 100 μm

B 100 μm

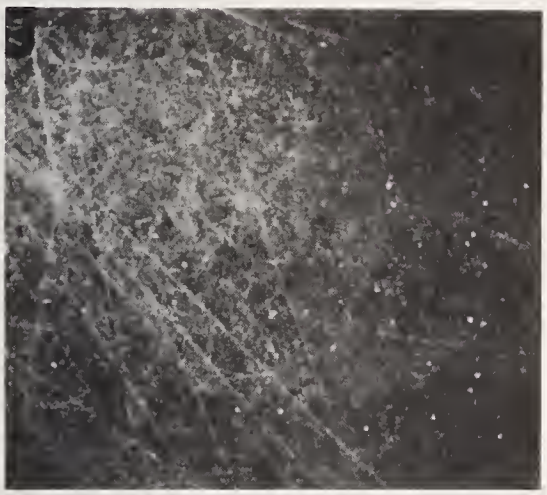

C 100 μm

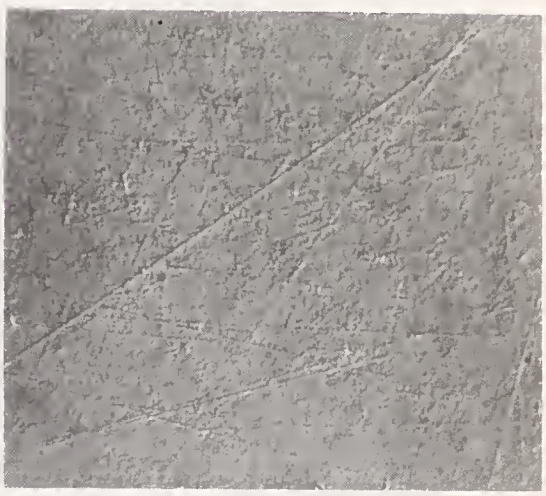

D 50 μm

Figure 5. Site 793 on the Spawr copper was illuminated at 2 j/cm^2. The laser damage is manifested by the enhanced scratches shown in (a) which is a regular photomicrograph and (b) which is taken using dark field illumination. (c) shows the edge of the damage area and the background smoothness of the undamaged area. (d) is a Nomarski photomicrograph of site 793.

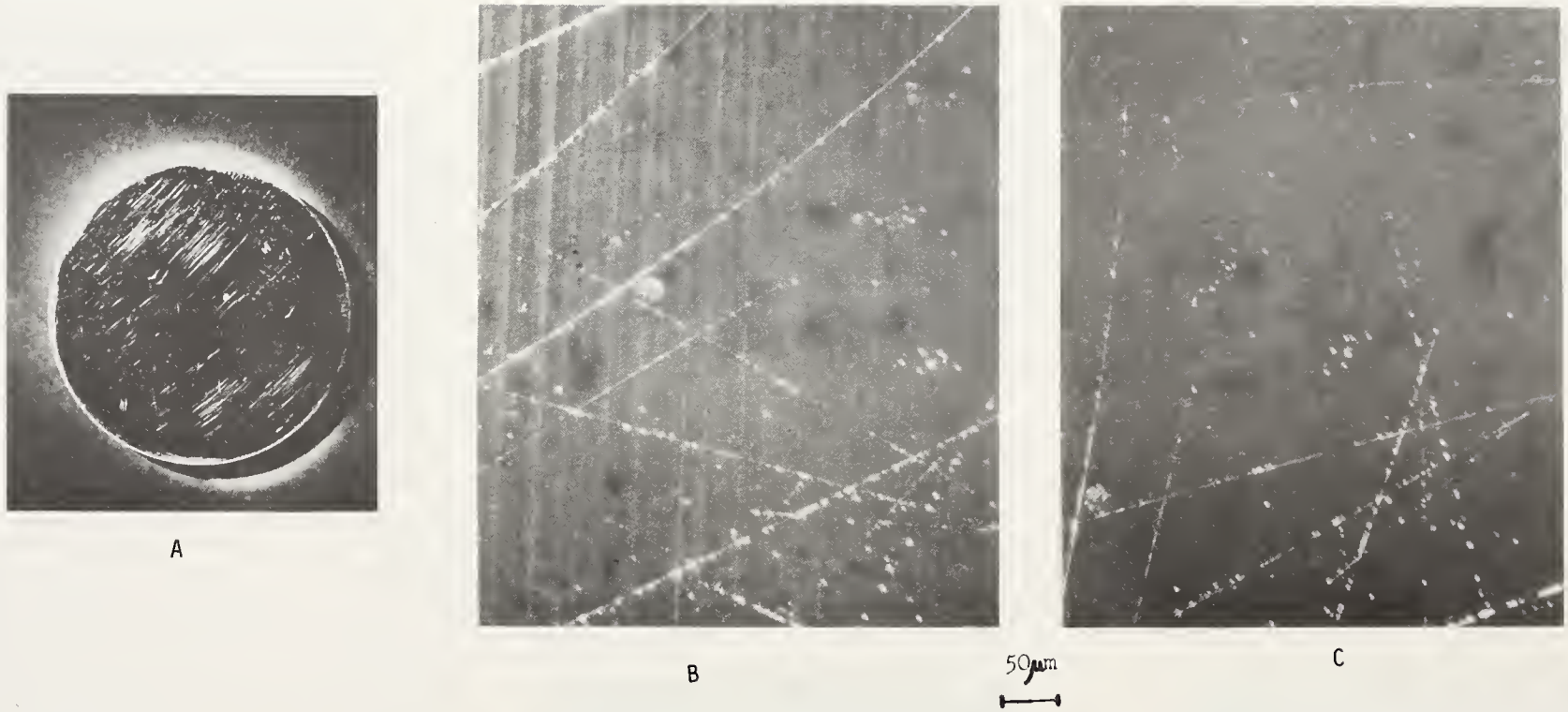

Figure 6. The scratches caused by the cleaning are visible in the dark field photograph of LLL-Ag-5 which is a diamond turned silver sample. The laser damage along the scratches is shown in (b) and (c) which are Nomarski micrographs of the same place with the sample oriented to show the diamond turning marks (b) and to show the background smoothness (c).

Figure 7. The damage on the diamond turned copper is due to electroplating artifacts which appear as pox marks in this Nomarski photomicrograph.

(a)

(b)

Figure 8. The removal without any apparent damage of the residual film from the diamond turned silver LLL-Ag-7 sample is shown in the dark field photograph (a). The damage in the slight electroplating defects is shown in (b).

Figure 9. Laser damage along the diamond turning marks of the silver sample LLL-Ag-7' is shown in the Nomarski photomicrograph.

COMMENTS ON PAPER BY SAITO, et al

(See comments on paper by Goldstein, et al which follows)

2.2 Pulsed Laser Damage to Uncoated Metallic Reflectors

Irving Goldstein
Raytheon Co. Missile Systems Division, Bedford, Mass.

Don Bua
Raytheon Research Division, Waltham, Mass.

Frank A. Horrigan
Science Applications, Inc., Bedford, Mass.

Threshold damage measurements were made on a variety of polished bulk copper and thin gold film reflectors using a TEM_{00} mode Q-switched Nd:YAG laser. Results correlate well with a simple thermal model based on the assumed existence of a critical surface temperature. Direct confirmation of this thermal model was obtained through systematic variations of the polarization and angle of incidence of the incident laser beam and calorimetric measurements of the surface optical absorption coefficients. The "Damage Threshold" was defined through a careful procedure of attenuating the incident beam and varying all parameters (e.g., focus, position on the surface) until the sample no longer could be "damaged" as assessed visually with a microscope. In one striking case the damage threshold of two "identical" samples was shown to correlate with the measured surface absorption and not with the visual surface quality.

The implications of these results to the design of high power optical systems which use large angles of incidence (e.g., axicon or toric optical elements) are discussed. In particular, for the polarization associated with Brewster's phenomenon the damage threshold was found to remain constant over wide variations of the angle of incidence, e.g., from 0 to 70° or 80°.

Key words: Angle of incidence; polarization; pulsed laser damage; thermal model.

1. Introduction and Summary

The purpose of this work was to determine the feasibility of using metal mirrors with a high energy, pulse laser at $\lambda = 1.06\mu m$ for axicon or toric optical systems. As a consequence, a program was set up at Raytheon to measure both the absorption and pulse (t = 11 nanosec) damage threshold of a series of sample mirrors at varying incidence angles. Damage thresholds on Cu mirrors have been measured in the range of 44 to 70 joules/cm^2 at an incidence angle of 80° for and 11 nanosec pulse. It was found that the damage threshold did follow the pattern of absorption.

2. Technical Approach

Initially there was a selection of the different metals to be tested in the program and figure of merit (FOM) was assigned to each material. This FOM derived below from the Surface Heating Relationship which is eq. (1).

$$\Delta T = \frac{2\,(1 - R)\, I_o \sqrt{t}}{\sqrt{\pi K C}} \qquad (1)$$

where
- I_o = watts/cm^2 in the laser beam
- t = Pulse width in sec.
- R = Reflectivity of the surface
- K = Thermal conductivity watt/cm°K
- C = joules/cm^2°K = watt, sec/cm^2°K
- ΔT = Temperature rise at the surface.

Regrouping eq. (1) into laser variables and material variables resulted in the following definition of a Figure of Merit (FOM) as the material parameter of equation (1)

$$FOM = \frac{\Delta T_c \sqrt{KC}}{1 - R}. \qquad (2)$$

With appropriate values put into eq. (2) the following bar chart (figure 0) indicates the ranking of the materials with copper being the optimum followed by silver and gold. Experiments were performed on a number of these metals.

Next the absorption change with incidence angle was investigated and one of the key results obtained was that two polarizations have to be considered for the metal mirrors that we were testing for the following reasons:

In a toric optical system, for example, let the input polarization vector be vertical as shown in figure 1.

There will be regions in plane (A-A) and plane (B-B) where the absorption will be different for polarization vector E. The following diagram (figure 2) should help clarify the meaning of the terms to be used namely, $E_{||}$ and $E_{\perp}$. $E_{\perp}$ is defined as the electric field vector which is perpendicular to the plane orthogonal to the mirror surface, and $E_{||}$ is defined as the electric field vector parallel to plane orthogonal to the mirror surface. Figure 3 shows the absorption versus polarization and angle of incidence for a mirror surface incidentally where $\beta_{\perp}$ and $\beta_{||}$ are defined as the absorption coefficients for the different polarizations as previously defined. The circles and squares indicate the experimental data points and the solid and dashed lines the computed values. As can be seen, there is a reasonably good agreement between the expected and measured points and the theoretical curves of absorption are based on a solution of the Fresnel reflection formulas with complex index of refraction and absorption.

Next, the damage thresholds for the two different polarizations have been calculated as shown in figure 4. The interesting curve is $E_{||}$ in which the increase in mirror area is directly compensated by the increase in absorption ($\beta_{||}$) with incidence angle.

Experimental results are shown in figure 5. This data was taken on a gold plated mirror with a poor surface finish. Next threshold damage data was taken on two Cu mirrors purchased from Spawr Optical Company in California. The specifications on the mirrors were very good optical finish with little attenation paid to optical figure, since the damage would be confined to 70μ diameter spot.

Schematic of the experimental laser damage set up is shown in figures 6 and 7. The sample was placed on a stage which has a number of degrees of freedom of movement and the reason for this was that the Damage Measurement Procedure shown in figure 8 required such freedom in order to make meaningful measurements at the grazing angle. For each threshold damage point there are at least 5 or 6 measurements made. The laser parameters are shown in figure 9, and figure 10 shows the Intensity distribution of the YAG laser used. The absorption values for the different mirrors were obtained from measurements that were made on a set up shown in figure 11.

The results of the tests on the two Spawr samples are shown in figures 12 and 13. For mirror #1 a damage threshold of 44 joules/cm^2 was observed for an incidence angle of 80°, for mirror #2 damage thresholds of 43 joules/cm^2, and 69 joules/cm^2 for incidence angles of 75° and 80°, respectively. Photomicrographs were taken on both these mirrors as shown in figure 14. Note that the finish of Spawr mirror #1 appears to be better than Spawr mirror #2, and yet mirror #2 has a higher threshold of damage level. We attribute this to the absorption of the mirror surface rather than the optical finish,

á la the Bloembergen criteria. At 0° angle of incidence the absorption of Spawr #1 and Spawr #2 was 2.1% and 1.42%, respectively, and the damage for Spawr #1 and #2 was 2.12 joules/cm^2 and 2.86 joules/cm^2, respectively.

Figure 15 is interesting since the simple thermal model correlates well with the experimental data and surface finish does not play a significant role in determining damage threshold. This finding was also corroborated by the damage data taken on the two copper Spawr mirrors.

Since the competing technique to the use of metal mirrors are dielectric coatings either on refractive or reflective optics, the damage threshold obtained at Raytheon was compared to the results obtained by other workers. Figure 16 indicates the typical data obtained on other materials [1,2,3] for different pulse widths. The slope of damage threshold versus pulse width was obtained from the reference sighted and agrees quite well with a proportionality to $\sqrt{\text{pulse width}}$. The Raytheon data for 80° incidence angle - when extrapolated to the picosecond range from the nanosec, indicate definite promise of being able to achieve damage threshold at least equal, if not better, than the dielectric materials.

Now let us reexamine the meaning of the input polarization vector for a toric symmetrical mirror (see figure 1). It can be seen that there will be portions of the input mirror when the $\beta_{||}$ absorption coefficient will increase and $\beta_{\perp}$ absorption coefficient will decrease with incidence angle. Hence, for a high power CW case there will be potential distortion problem with parts of the mirror and as to the pulse case, there are the problems of different damage thresholds because the different values of $\beta_{\perp}$ and $\beta_{||}$ previously described. The asymmetrical toric optical design provides a solution to the varying absorption of the symmetric case, provided an operating point is assigned to the mirrors in the asymmetrical system. Figure 17 indicates an operating point for an asymmetrical derived from the threshold damage data taken to date, and it is a ratio $E_{\perp}/E_{||} \geq 20$ for an incidence angle in the range of 75° to 80°.

3. Conclusions

There are a number of conclusions that can be drawn from this program and these are as follows:

1) Damage threshold appears to follow absorption.

2) Metal mirrors at grazing angles can be used with pulsewidths in the nanosec range at $\lambda = 1.06\mu$. Toric Optics can provide this grazing angle very conveniently.

3) Metal mirrors at grazing angles can be expected to show acceptable damage thresholds in the picosec pulsewidth range.

4) The incidence angle has not been optimized.

5) Reflecting surface thicknesses of 1μm or greater are sufficient for good mirror performance.

6) The operating point for an asymmetrical toric optical system has been prescribed.

4. References

[1] "Dielectric mirror damage by laser radiation over a range of pulse durations and beam radii," Applied Optics 12, no. 4 (April 1973).

[2] Milam, D., Lawrence Livermore Lab, Private communication.

[3] Saito, T., Lawrence Livermore Lab, Private communication.

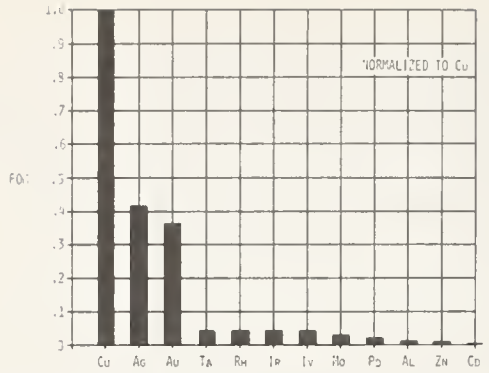

Figure 0. Figure of merit for different metals at λ = 1.06μ.

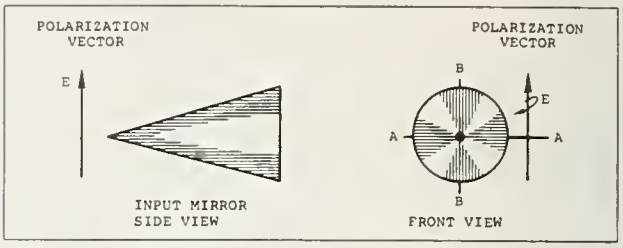

Figure 1. Toric or axicon mirror.

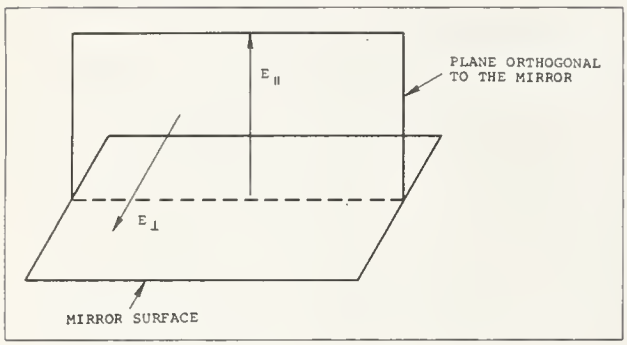

Figure 2. Definition of polarization vectors.

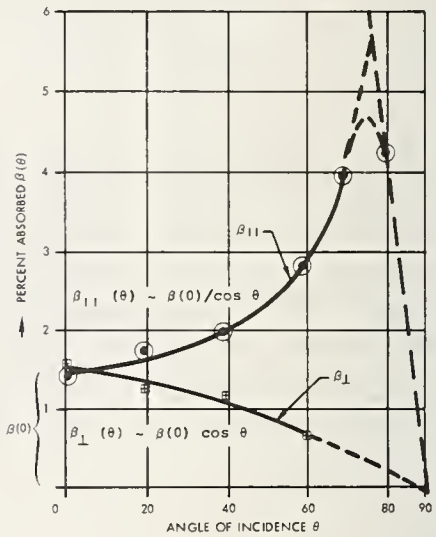

Figure 3. Absorption at 1.06μm polarization and angle of incidence copper mirror (LLL).

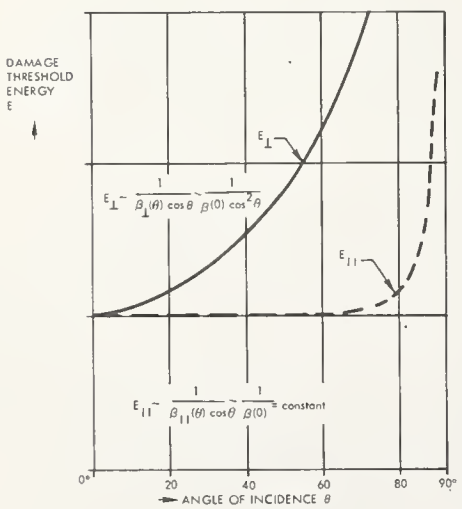

Figure 4. Anticipated variation of damage threshold energy for a simple thermal failure model.

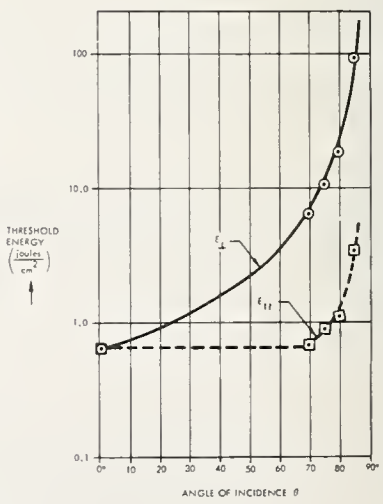

Figure 5. Experimental damage threshold energies vs polarization and angle of incidence.

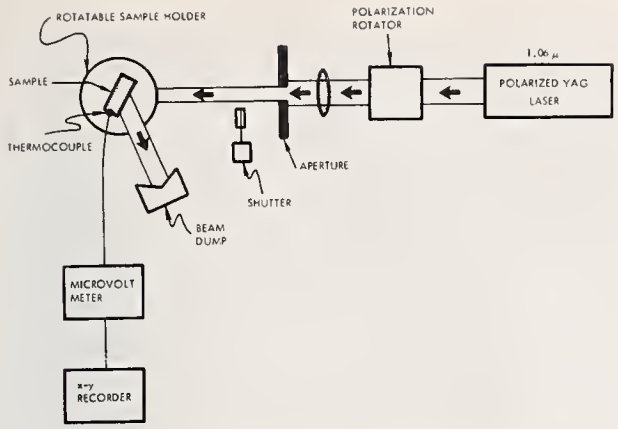

Figure 6. Laser damage experiment.

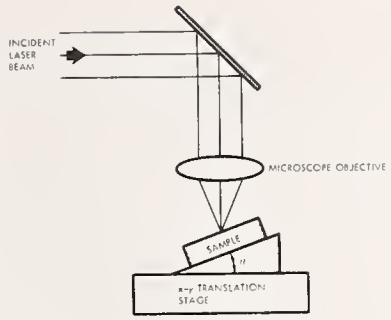

Figure 7. Experimental setup.

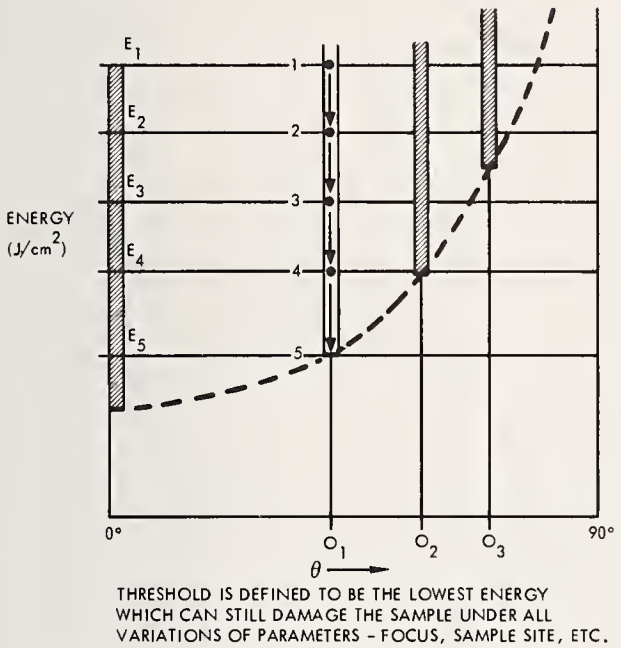

Figure 8. Damage measurement procedure.

WAVELENGTH	NO:YAG 1.06 μM
ENERGY TEM_{00} MOOE	≈1.5 MILLIJOULES
BEAM OIAMETER AT OUTPUT MIRROR TEM_{00} MOOE	0.8 MM
POLARIZATION	LINEAR
PULSE REPETITION RATE	1 PPS
PULSE OURATION IN TEM_{00} MOOE	≈11 NSEC (FWHP)
PULSE-TO-PULSE ENERGY REPROOUCIBILITY	± 7 PERCENT

Figure 9. Laser parameters.

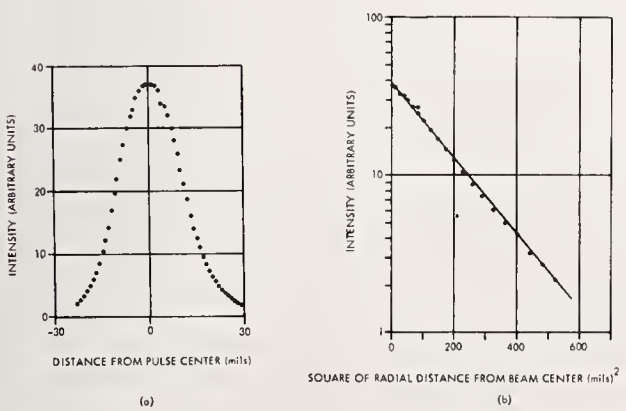

Figure 10. Intensity distribution of the YAG laser.

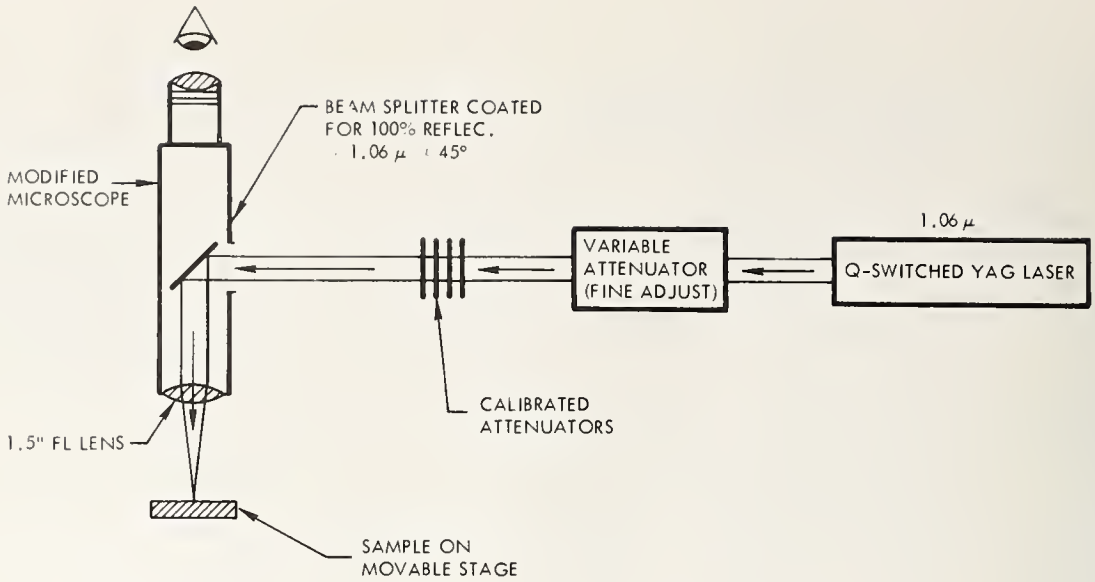

Figure 11. Absorption measurements test setup.

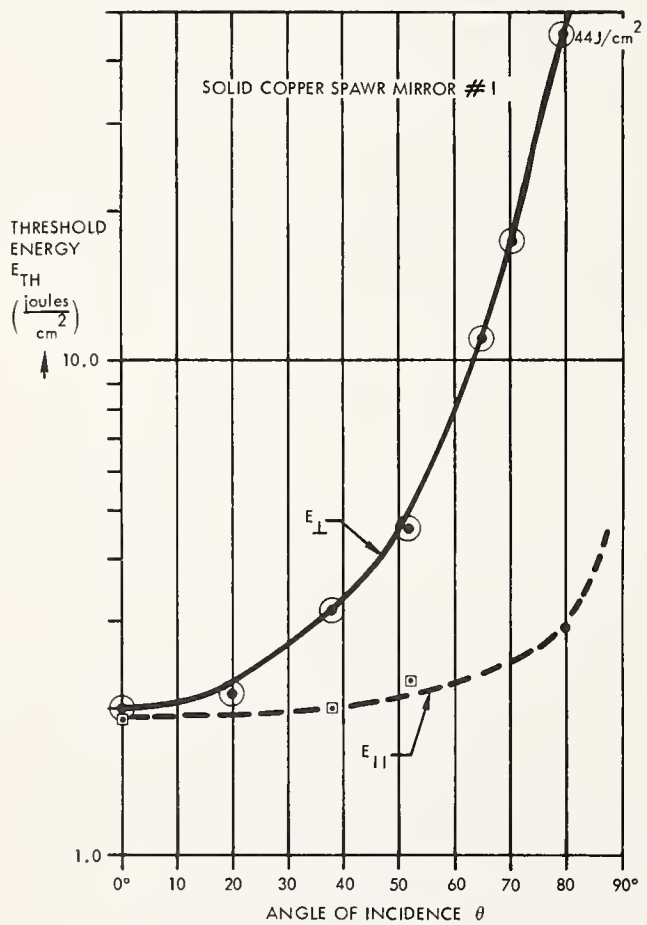

Figure 12. Experimental damage threshold energies vs. polarization and angle of incidence (#1).

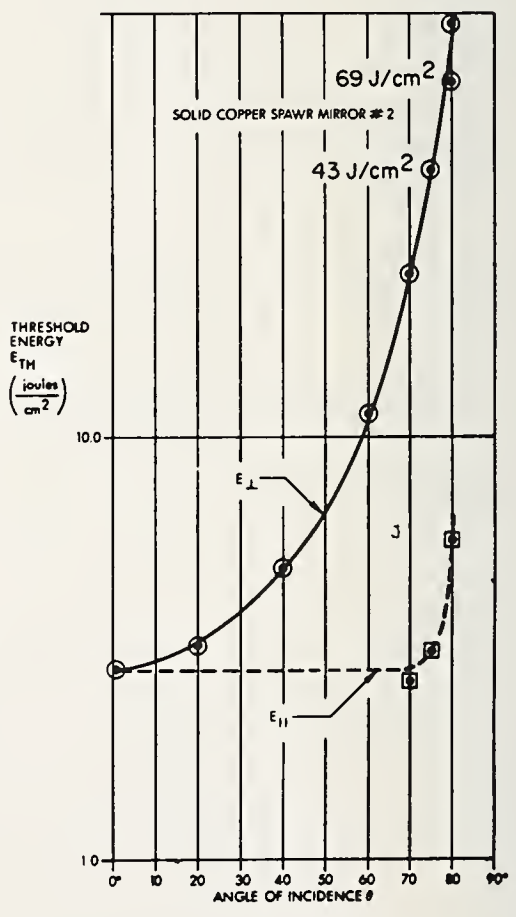

Figure 13. Experimental damage threshold energies vs polarization and angle of incidence (#2).

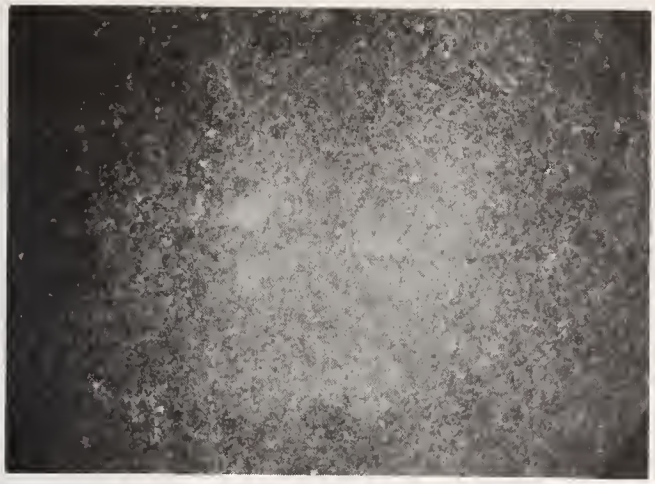

SPAWR #1

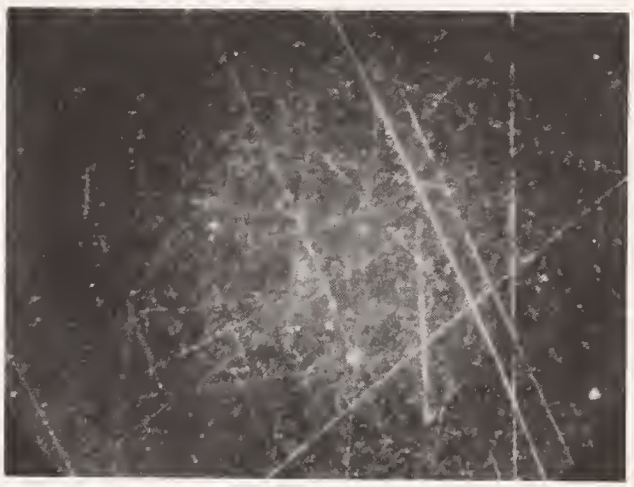

SPAWR #2

Figure 14. Photomicrographs of two solid copper mirrors polished by SPAWR.

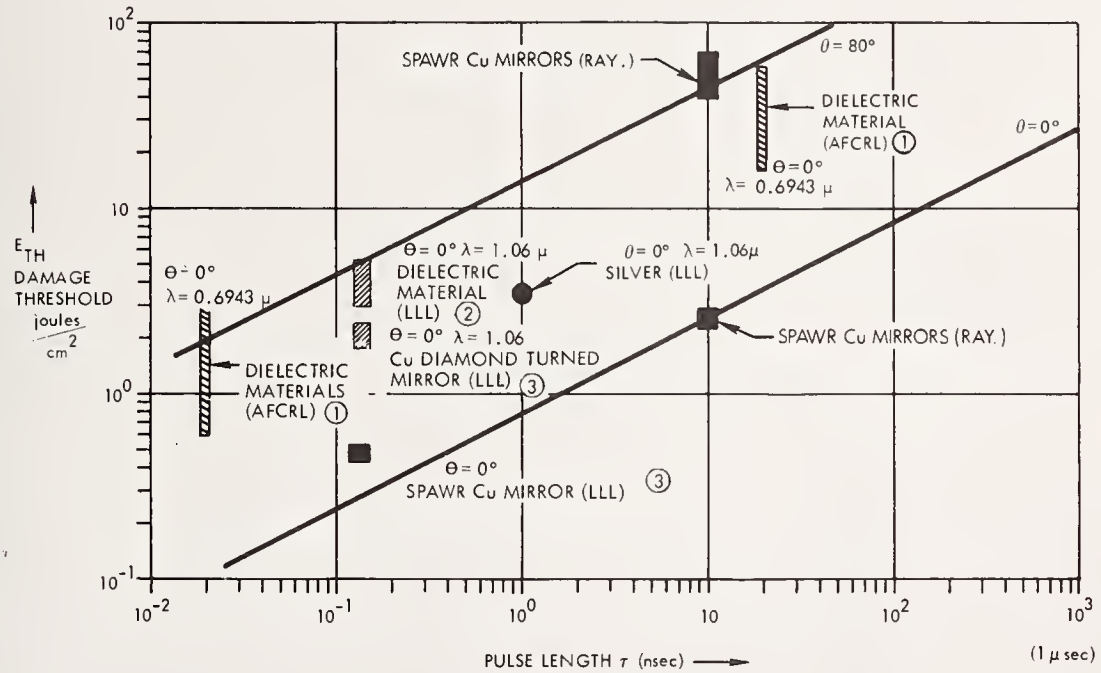

Figure 15. Theroetical curve and experimental points.

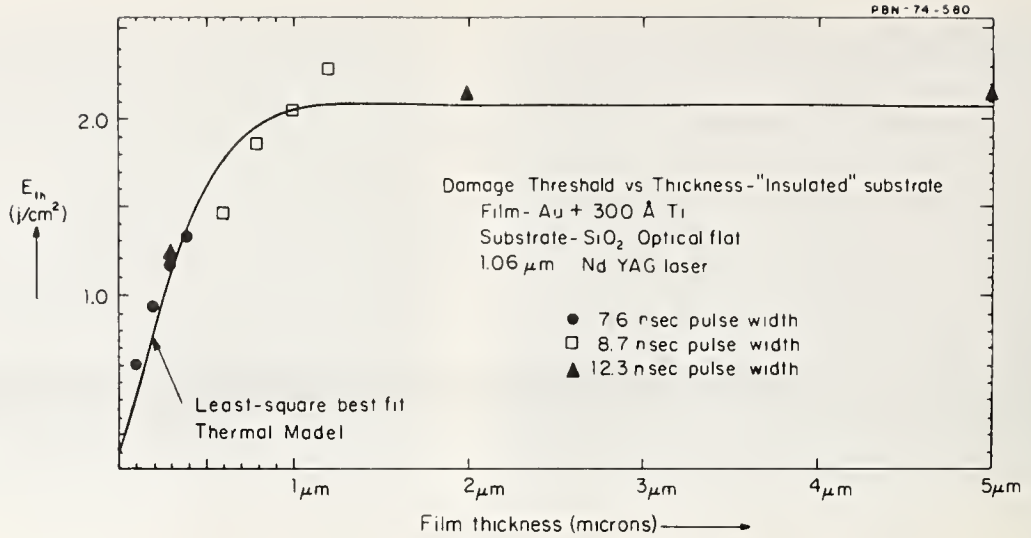

Figure 16. Comparison of damage threshold for metal and dielectrics vs pulse width.

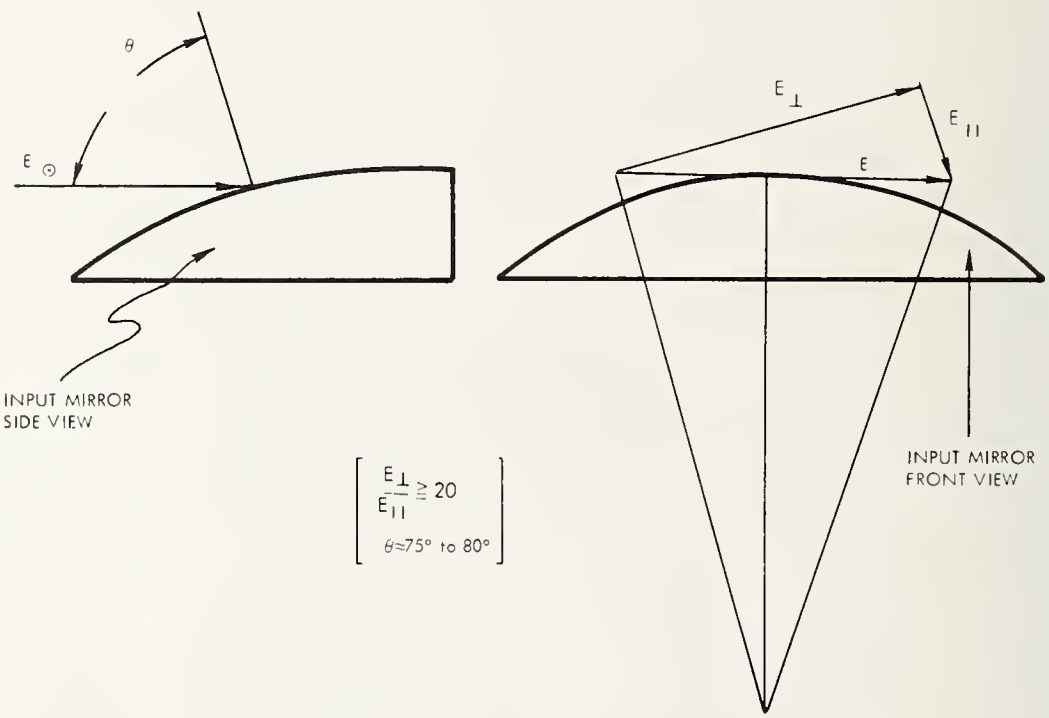

Figure 17. Operating point data for an asymmetrical system.

COMMENT ON PAPERS BY SAITO, *et al* and GOLDSTEIN, *et al*

It was emphasized that the damage threshold is dominated by surface absorption rather than the total reflectivity. The latter is also sensitive to scattering. However, scratches on the surface may influence both scattering and the damage threshold since both the electric field and electron scattering in the subsurface material are increased in the vicinity of the scratch.

2.3 Diamond-Turned Mirrors

H. E. Bennett, M. J. Soileau, and P. C. Archibald

Michelson Laboratories, Naval Weapons Center
China Lake, California 93555

Diamond-turned, micromachined metal mirrors offer a new approach to optical fabrication and may have significant advantages for use as laser components. A laser mirror must have (1) excellent optical figure, (2) low scattered light, (3) high reflectance, (4) high damage threshold, and (5) good environmental resistance. We have measured optical figures as good as 1/20th wave over a 3.86-cm diameter sample and better than a wave over a 10.2-cm diameter sample on micromachined mirrors produced by Oak Ridge National Laboratories. Scattered light levels in the infrared can be as low or lower than those obtained on conventional mirrors and values as low as 2×10^{-5} have been observed at a wavelength of 10.6 μm. Infrared reflectance values as high or higher than those of conventional evaporated or sputtered coatings have been achieved and one mirror had an absorption at 10.6 μm of 0.006. The laser damage threshold of micromachined mirrors may well be higher than that obtainable by other techniques, but this question and the environmental resistance and "coatability" of a micromachined surface require further investigation.

Key words: Diamond turning; laser damage; metal mirrors; micromachining; optical figure; scattered light.

Introduction

Diamond-turned optics represent a relatively new development in precision optics manufacture. The potential of this method is not yet clear, partly because improvements are still being made at a rapid rate. However, the outlook for this production technique is very favorable and it could conceivably displace the more established methods for high quality and economical metal mirror fabrication. Mirrors for use in laser systems must satisfy the following requirements: (1) good optical figure, (2) low scattered light, and hence both minimum surface microroughness and minimum scratches and other macroirregularities, (3) high reflectance, (4) high damage threshold, and (5) good environmental resistance. Let us consider how diamond-turned metal optics meet these objectives.

We have now measured 23 different 3.86-cm diameter, diamond-turned test samples and four larger aluminum mirrors. All but one of the mirrors were made at Y-12 Division of Oak Ridge National Laboratories. Most of the small mirrors were machined on platings deposited on brass substrates. The larger mirrors were all machined from solid aluminum. Of the 23 test samples, 10 were copper coated, 5 were silvered, 3 were gold coated, 2 coatings were of unknown composition, and 3 were machined out of solid copper. We have measured optical figure, surface microroughness, scattered light, and reflectance. The general conclusions to be drawn from this study so far are: (1) Extremely smooth, low scatter surfaces can be prepared by diamond turning. Typical surfaces have equivalent optical rms roughness values in the 20-30 Å range. These values are in good agreement with those determined interferometrically [1][1]. The best sample we have seen had an average roughness of 12 Å rms. This sample scattered only 1.1×10^{-5} of the reflected light at 10.6 μm and is nearly as low at this wavelength as the best conventional mirror we have measured. (2) The infrared absorption of diamond-turned mirrors is much lower than that of typical optically polished metal surfaces, and in the best cases it approaches the minimum theoretical absorption. At 10.6 μm absorption values as low as 6×10^{-3} have been observed. (3) The major problem with diamond-machined mirrors until recently was figure control. Typical values on the earlier samples were 6-8 fringes across a 3.86-cm diameter. Recently, considerable effort has been spent in improving figure control, and we have measured figures as good as 1/10th fringe across a 3.86-cm diameter flat and less than 2 fringes across a 10.2-cm diameter flat. Since diamond turning is a relatively new technique, even further improvement may be anticipated.

Measurement Techniques

Optical figure, surface topography, equivalent roughness of the optical surface, and scattering level as a function of wavelength were measured in this study. The figure measurements were made on a Zygo Model GH Interferometer System and the initial surface topographic measurements on a Zeiss Differential Interference Contrast (Nomarski) microscope. To determine the equivalent surface roughness and scattering level we used the Optical Evaluation Facility described below.

A schematic diagram of the Optical Evaluation Facility (OEF) used to measure scattered light is shown in figure 1 and an overall view in figure 2. Light from one of five lasers is focused on sample S_1 at nearly normal incidence. An angle of incidence of 20 min is usually used to prevent instabilities in the CO_2 and HeCd lasers caused by reflected light reentering the laser cavity. All turning mirrors used with the CO_2 and DF lasers are 50 mm or more in projected diameter to minimize edge effects.

1. Figures in brackets indicate the literature references at the end of the paper.

An aperture d of 9.5 mm diameter is mounted directly in front of the beveled hole in the Coblentz sphere, also 9.5 mm in diameter, to act as a beam trap for oblique rays. A blackened conical mask of the same inner diameter is mounted inside the 114 mm radius of curvature sphere to ensure that the wings of the reflected beam are either absorbed or reflected back outside the hole in the sphere. The mask subtends 11° at the sample surface.

Light scattered by the sample is imaged by the Coblentz sphere on pyroelectric detector D_1, which is blackened and mounted inside a spherical BaF_2 dome to minimize the angular sensitivity of detector response. A second pyroelectric detector is mounted at D_2 together with a silicon detector on a movable arm to measure scatter as a function of angle both in the incident and reflected beams. D_2 registered less than 10^{-8} of the incident flux at angles greater than 11°, the angle subtended by the outer edge of the mask inside the Coblentz sphere, for all wavelengths except the CO_2 laser line, which was about 10^{-7} at the mask angle. Most of the diffracted light which did not pass back through the hole in the sphere was thus trapped by the cone and did not reach the detector.

The OEF was calibrated at 4416 Å by measuring the scattering level of an aluminized spray-painted glass sample. The angular distribution function of this sample was measured and found to be very nearly Lambertian with virtually no specular component. Knowing the reflectance of the aluminum thus gave the desired calibration. As a check, an optically polished DF2 glass was measured using this calibration and found to have a scatter of 10.6×10^{-3}. The measured scattering level of this sample on the NWC visible light scatterometer [1] at 4358 Å was 9.3×10^{-3}. The measurements made on slightly different points of the sample at slightly different wavelengths using two entirely different instruments thus agreed to within 13%.

To compare measurements made at different wavelengths, it is necessary to know the wavelength dependence of the ratio of the signal from detector D_1 to D_3, the reference detector. Since both are pyroelectric detectors of similar design, they should be wavelength independent. However, to reduce the signal of D_3 to manageable proportions, a screen transmitting approximately 2.9% of the incident energy and a CaF_2 filter for reducing the 10.6 μm signal were used. The wavelength dependence of this combination was determined by comparing the signal from D_3 to that from a Scientech Model 3610 power meter which employs an optical cavity and thus has a response which is nearly independent of wavelength.

Origins of Scattered Light

Light scattering may be caused by various mechanisms. In high quality optics scattered light in the visible region results primarily from surface microirregularities only a few tens of angstroms in height, but extending over the entire surface area. If the height distribution function for these microirregularities is Gaussian, as is nearly always the case to a good approximation, the total integrated scatter in all directions (TIS) should fall off inversely as the square of the wavelength of incident light. In the visible region these predictions are usually in good agreement with theory. Infrared scattered light measurements have been few in number and plagued by experimental uncertainties, but have indicated that in the infrared the experimental TIS values usually do not obey the theory. Often the TIS stops decreasing in the near infrared and approaches a nearly constant value. An example is given in figure 3. In the visible region the experimental scattering values for this relatively rough aluminized dense flint glass mirror fit the theoretical predictions (straight dashed line) quite well. However, in the infrared they reach a nearly constant value and at 10.6 μm were about 20 times higher than the theoretical predictions. The squares indicate the difference between the average and minimum values of scattered light at a given wavelength as determined from measurements at ten points across the mirror surface each separated by 1 mm. This difference value is nearly independent of wavelength, and when the total scatter value reaches the difference value it stops decreasing and becomes nearly constant. Under microscopic examination numerous particulates were observed on the mirror surface and by examining the surface under a microscope in dark field using grazing incidence illumination many more scattering centers could be detected. The total particulate count was about 10^3 particles/mm^2 and the particles ranged in size from several micrometers in diameter to submicroscopic. They could not be removed by a jet of ionized air and many of them may have been deposited during the coating process. The small bump, in the neighborhood of 1 μm, is often seen. Increased scattering at this wavelength would be expected if many of the particulates were about 1 μm in diameter. Dust is about this size. Dust particles are used as optical spacers between our FECO interferometer plates and the minimum order of interference, which is normally obtained in our laboratory, four, corresponds to a one micron diameter particle.

Scattering From Micromachined Mirrors

The scattering behavior of micromachined mirrors in the infrared is typically somewhat different from that of the evaporated coating shown in figure 3. The scattered light does deviate from the theoretical curve for microirregularities having a Gaussian height distribution as shown in figure 4, but the average deviation in the scattered light from point to point on the surface is not independent of wavelength. Instead it has the same shape as the scattering curve. This behavior suggests that particulate scattering is not as important as for the evaporated film shown in figure 3. Microscopic examination reveals there are almost no large particulates on the micromachined surface, although many were visible on the evaporated film surface of figure 3. How then to explain the deviation of the

infrared scattering from the theoretical curve in the case of the micromachined surface? Scanning FECO interferometry may furnish an answer. The height distribution functions of microirregularities can be determined by this technique. Usually the distribution function is quite close to a Gaussian. However, for micromachined surfaces the measured height distribution in the wings is higher than for a Gaussian function. There are thus more large irregularities than would be predicted on a Gaussian model and hence the infrared scattering, which should be most sensitive to these large microirregularity heights, would be expected to be somewhat larger than for a purely Gaussian surface. Qualitatively this explanation is in agreement with the experimental data. Quantitative analysis has not yet been performed. If this explanation is correct, however, it suggests that by controlling the tool shape and machining parameters the infrared scattering from micromachined mirrors might be reduced even further.

Solid Copper Mirrors

The most recent 3.86-cm diameter Y-12 mirrors we have measured were machined from massive copper on a new Moore diamond point turning machine. The three we measured were part of a set of 18 which were potted on a large plate with PPR rubber and machined simultaneously [2]. Figure control was excellent, the best samples were flat to about 1/10th fringe or 1/20th wave, which compares favorably with the best optical figures normally obtainable on glass or quartz using conventional optical polishing techniques. In addition, unlike conventionally polished optics there is no rounded edge on any of the diamond turned samples we have examined. An interferogram and a Nomarski micrograph of one of the optical surfaces is shown in figure 5. The reflectance of this sample is shown as a function of wavelength in figure 6. It is significantly higher than typical polished, sputtered, or evaporated copper films and is as high at 10.6 μm as the best copper surfaces we have measured. The equivalent rms roughness of this surface was 21.0 Å and its scattering behavior as a function of wavelength is shown in figure 4.

Copper-Coated Mirrors

Most of the mirrors tested thus far have been machined from brass blanks coated with electrolytically deposited copper. The coated samples were received in two batches. In most cases the effective rms roughness, defined as the value obtained from scattering measurements made in the visible region, ranged from 20 to 25 Å rms. However, one copper-plated sample had a value of 117 Å, and thus a visible scattering level 20 times that of the other samples. The smoothest copper-plated sample averaged 16 Å rms. However, its absorption at 10.6 μm was 2.6 times that of the best sample. When the same plating technique was repeated on another sample the same low infrared reflectance was achieved. The mechanical condition of the sample during plating may also be important. For example, one sample was peened on the plated surface as it was being plated. This sample has reflectance and short wavelength scattering values which were comparable to the others, but the scattering level at 10.6 μm was an order of magnitude higher, possibly because of the increased sensitivity at longer infrared wavelengths to long range irregularities.

Based on the evidence we have, it would appear that low infrared absorption, low scatter surfaces can be obtained by using either a solid copper blank or copper plating from either a high copper concentration, low acid concentration bath, or a low copper, high acid bath. Absorption values at 10.6 μm as low as those for the best evaporated copper films and very close to the theoretical value of 0.0065 calculated from the Drude-Zener theory [3] can be obtained on plated diamond-point-machined copper surfaces. The surfaces obtained are quite uniform, with average deviations in scattering from point-to-point an order of magnitude lower than the scattered light level even at 10.6 μm.

Silver-Coated Mirrors

Five silver, diamond-point machined mirrors were tested. Four of these were machined by Y-12 and one by Lawrence Livermore Laboratory (L^3). The lowest scatter diamond-turned mirror yet tested, sample 9, was in this group. It had an equivalent roughness of 12 Å rms and scattered 2×10^{-5} of the reflected light at 10.6 μm. Its absorption at 10.6 μm was 0.008, about twice the theoretical value of 0.0040 calculated from the Drude-Zener theory [4]. The machine marks were still evident in this sample (figure 7), but it was quite uniform in scattering level at successive points on the surface even at 10.6 μm where the average deviation in scattering was about 1×10^{-5}. This sample was measured before and after being coated with "Carbofilm", a strippable protective coating manufactured by the American Drug and Chemical Company and useful for removing dust from optical surfaces without damaging them. Only a very slight improvement in scattering levels at 10.6 μm was observed.

None of the other silver samples had surface roughnesses comparable to sample 9, although all of the silvered Y-12 samples were somewhat better than the plated copper samples. The silver mirror micromachined at Lawrence Livermore Laboratory (L^3) had an equivalent roughness value of 85 Å, four times as rough as most of the silver Y-12 samples and seven times as rough as sample 9. The scattering level goes as the square of the roughness so that the scattering level of the L^3 sample was 16 to 50 times as high as the Y-12 samples in the visible region and possibly in the infrared also. Unfortunately, the scattering level at 10.6 μm of this sample could not be measured before it was returned to Y-12. The reflectance at 10.6 μm was measured, however, and was as high or higher than any of the coated Y-12

samples and the figure was more uniform. Since this sample was machined we have heard that additional improvements have been made in the diamond turning technique at L^3, although we have not measured any of their newer samples.

Gold-Coated Mirrors

Three gold-coated mirrors were measured. Gold [4] has a theoretical absorption at 10.6 μm of 0.0059, but only one sample was within a factor of two of this value. It, however, had nearly as low absorption as any sample tested. Scattering levels for this sample were equal to or better than those of most of the other samples tested, but were six times as high at 10.6 μm as those measured for silver sample 9. Gold has the definite advantage that unlike both silver and copper it does not form a heavy tarnish film upon exposure to air and thus may not require a protective coating. Gold coatings frequently have much lower reflectance than would be expected theoretically. However, good diamond-point-machined mirror surfaces have been demonstrated on gold-coated mirrors and the fabrication of such mirrors appear to hold considerable promise.

Operational Size Mirrors

The micromachined surfaces discussed above have been all 3.86-cm diameter laboratory samples. In many applications mirrors significantly larger in diameter than this will be required. Surface uniformity and figure control are more difficult to achieve in any optical fabrication process as mirror size increases, but significant achievements are being made in micromachining medium size mirrors as well as laboratory samples. Figure 8 shows the figure and surface character of two such mirrors. Both are 10.2-cm in diameter and were turned from solid aluminum. The best one has a figure of better than one wave across its entire surface. The other one is a two wave surface but, the figure is quite uniform, the surface is smoother and the machining marks are less pronounced. The depth of the final cut on the smoother surface was only one ten thousandth of an inch, which illustrates the type of precision required for micromachining operations.

Damage Threshold and Tarnish Resistance

The properties of diamond turned surfaces have as yet not been extensively explored. Preliminary measurements indicate [5] that the laser damage threshold for micromachined surfaces is as high or higher than that of any type of coated mirror. Tarnish resistance and environmental stability are also unclear. It has been suggested that micromachined silver mirrors tarnish much less readily than do other silver coated mirrors. However, preliminary studies of chemically deposited silver layers which had been micromachined indicate [6] that the initial rate of tarnish formation is the same as that on evaporated silver coatings. Protective overcoatings can presumably halt, or at least greatly inhibit, tarnish formation on micromachined surfaces. However, since cutting oil is normally used in the machining process and some of it may penetrate the microcracks in the metal surface and be difficult to remove, the "coatability" of micromachined surfaces is at present unclear and should be explored.

Conclusions

Diamond turned micromachined surfaces offer a new approach to optical fabrication. Mirrors used in lasers must have (1) excellent optical figure, (2) low scattered light, (3) high reflectance, (4) a high damage threshold, and (5) good environmental resistance. At present, micromachined mirrors can be produced which are better than a wave over a 10.2-cm diameter and 1/20th wave over a 3.86-cm diameter. Infrared scattered light levels as low as those obtained on conventional mirrors have been demonstrated, and because of the uniformity of the machining process there is hope that even lower infrared scattering levels may be achieved. Infrared reflectance values as high or higher than those obtained by conventional evaporation or sputtered coatings have been demonstrated and the laser damage threshold of micromachined mirrors may well be higher than that obtainable by any coating technique. The damage threshold, environmental resistance, and "coatability" of micromachined surfaces, however, require further investigation.

Acknowledgment

The authors are grateful to Mr. R. E. Sladky of Oak Ridge National Laboratory, Y-12 Division, for furnishing the micromachined samples for evaluation and to Dr. W. Reichelt of the Los Alamos Scientific Laboratory for encouragement and project support. This program was sponsored by LASL under ERDA Order LS-75-4.

References

[1] Bennett, H. E., J. L. Stanford, and J. M. Bennett, in *Space Optics* (National Academy of Sciences, Washington, D. C., 1974), pp. 717-738.

[2] Sladky, R., Y-12 Division, Oak Ridge National Laboratory (private communication).

[3] Bennett, H. E., in *Symposium on Thermal Radiation in Solids*, S. Katzoff, ed. (National Aeronautics and Space Administration, Washington, D. C., 1965), pp. 145-152.

[4] Bennett, H. E. and J. M. Bennett, in *Optical Properties and Electronic Structure of Metals and Alloys*, F. Abelès, ed. (North-Holland Publishing Co., Amsterdam, 1966), pp. 175-188.

[5] Soileau, M. J. and V. Wang, Appl. Opt. 13, 1286 (1974).

[6] Burge, D. K., in *High Energy Laser Mirrors and Windows* (Semi-Annual Report No. 6, ARPA Order 2175, Naval Weapons Center, May 1975), pp. 63-67.

Tables and Figures

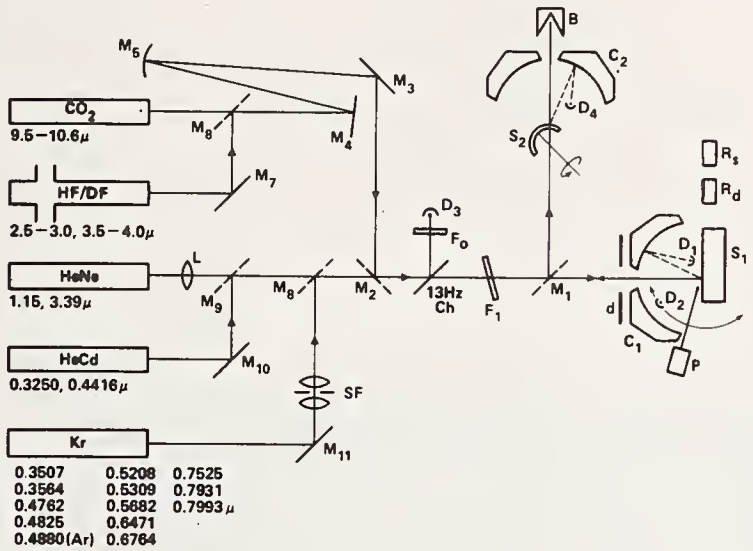

Figure 1. Schematic of optical evaluation facility.

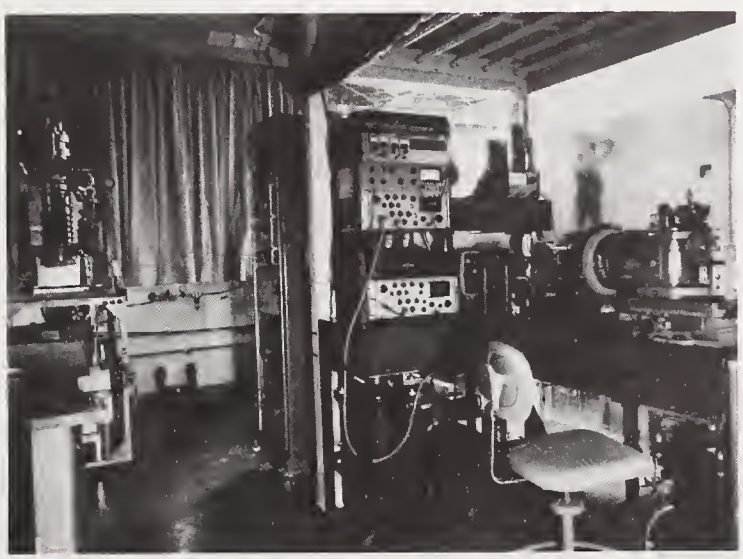

Figure 2. View of optical evaluation facility.

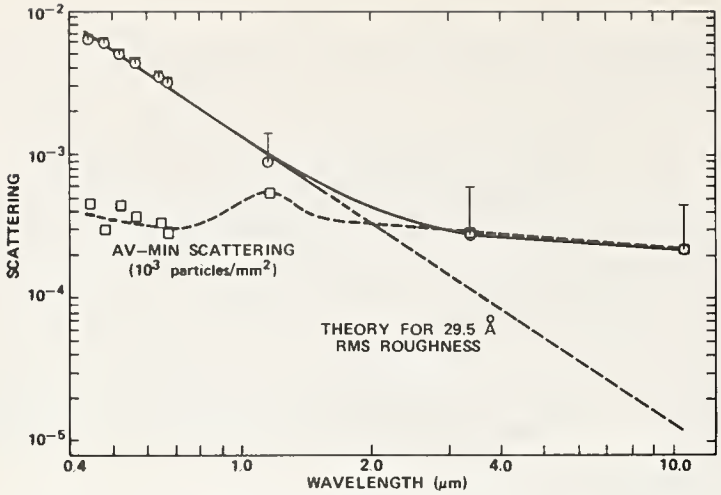

Figure 3. Scattering from an aluminized dense flint glass (DF2) mirror.

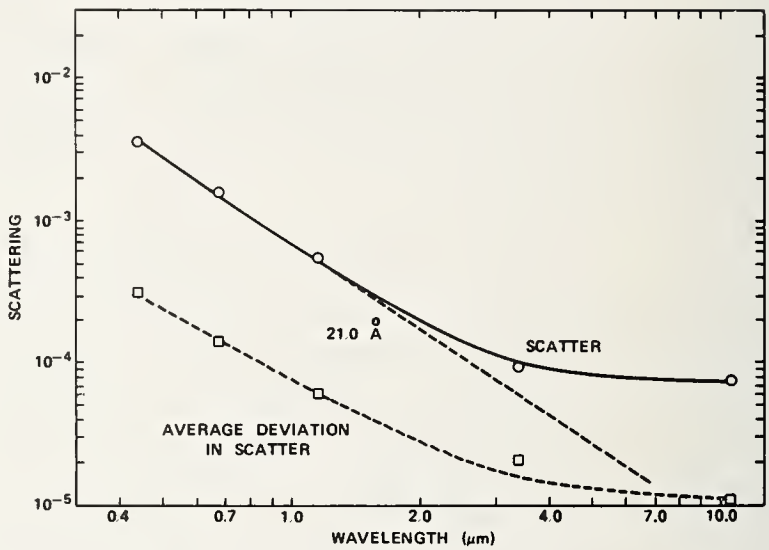

Figure 4. Scattering from diamond-turned, solid copper mirror.

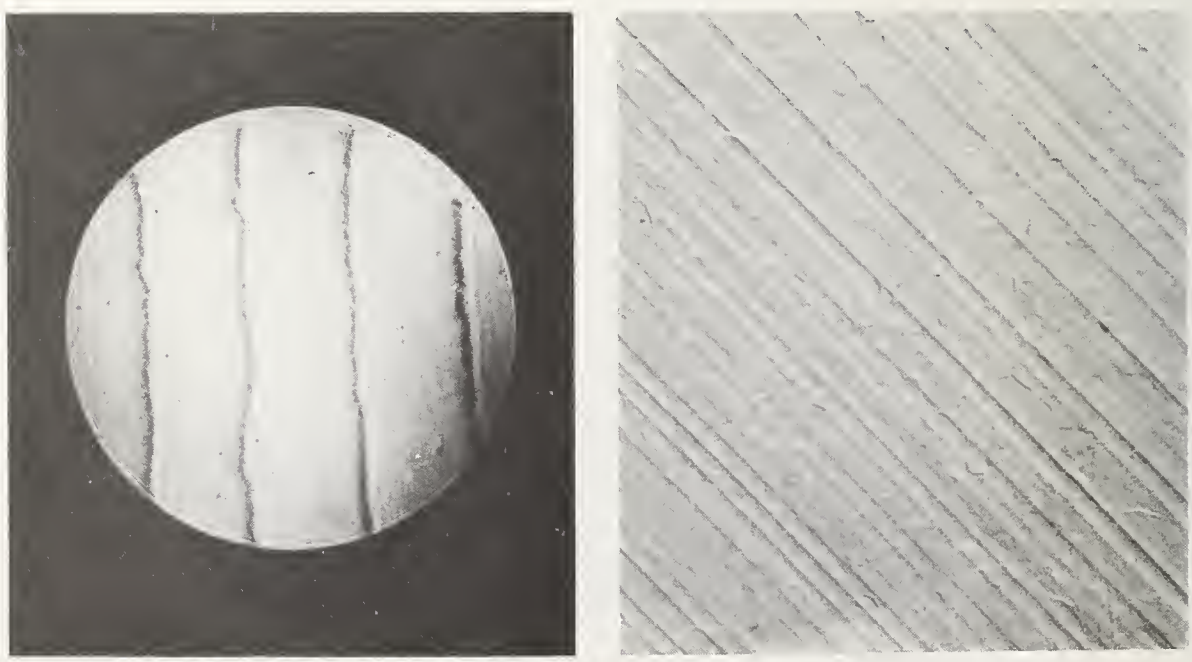

Figure 5. Interferogram and Nomarski micrograph of 3.86-cm diameter diamond-turned, solid copper mirror.

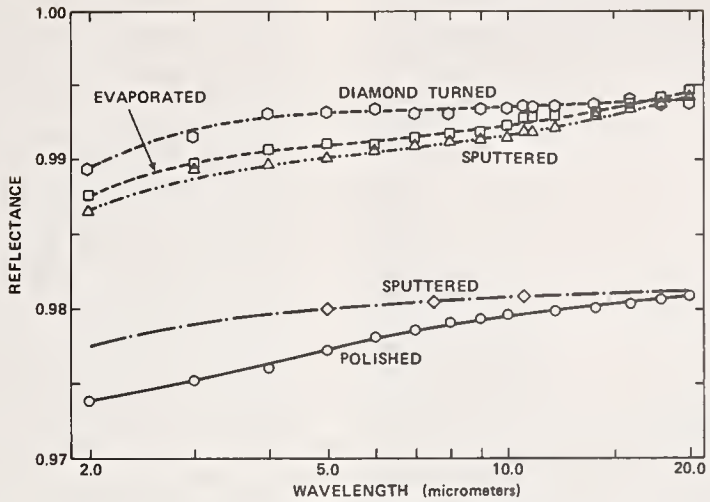

Figure 6. Infrared reflectance of diamond-turned, solid copper mirror compared with reflectance of copper mirrors prepared by other means. The other curves shown are for a polished bulk sample, an evaporated film, and two sputtered films.

Figure 7. Nomarski micrograph of diamond-turned silver mirror.

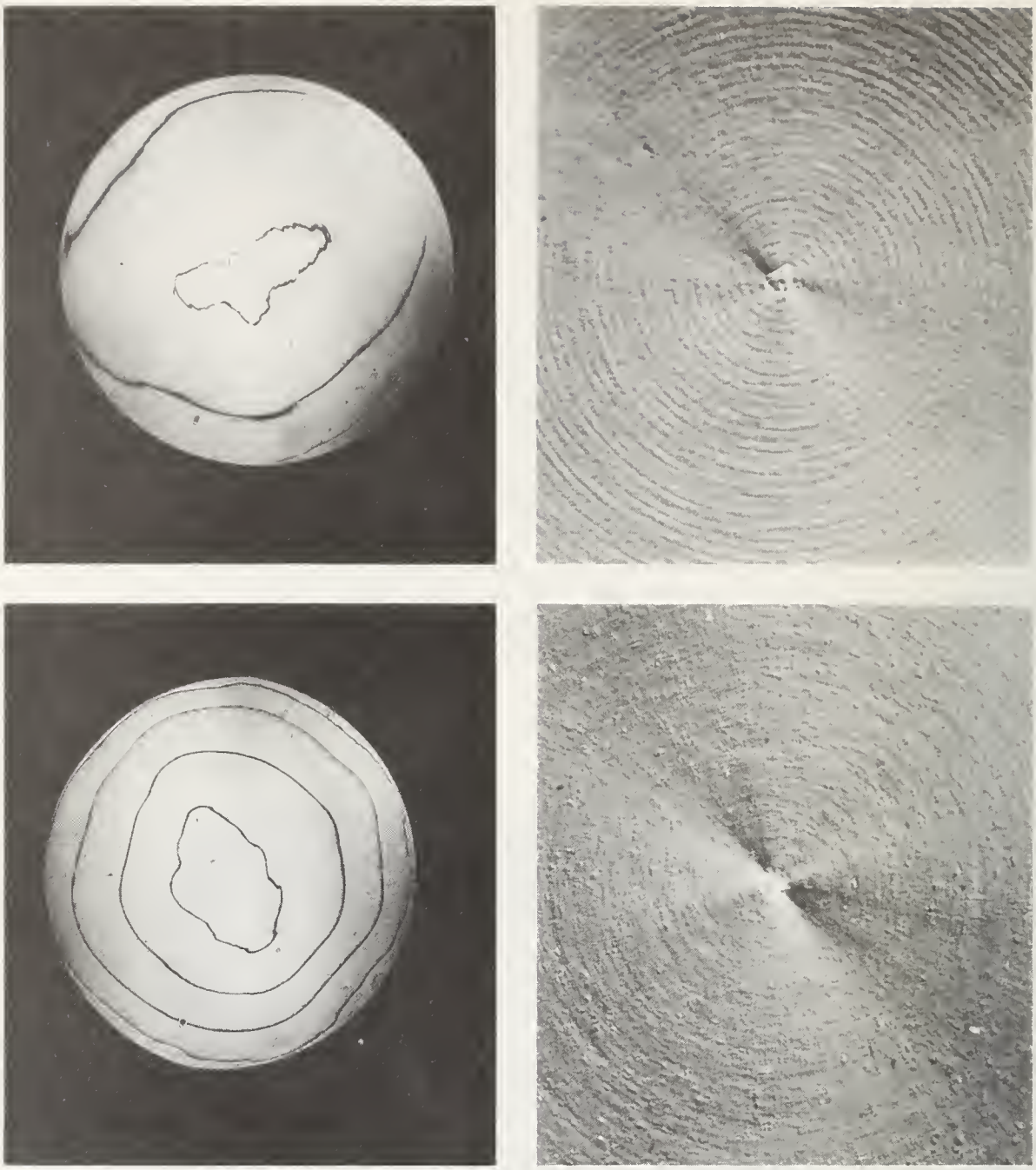

Figure 8. Interferograms and Nomarski micrographs of two 10.2-cm diameter, diamond-turned, solid aluminum mirrors.

COMMENTS ON PAPER BY BENNETT, et al

(See comments on paper by Sladky, et al which follows)

2.4 RESULTS OF OPTICAL MEASUREMENTS OF SURFACE QUALITY AND FIGURE OF DIAMOND-TURNED MIRRORS

R. E. Sladky

Fabrication Systems Development Department
Y-12 Development Division

R. H. Dean

Materials Testing Department
Production Certification Division

Oak Ridge Y-12 Plant
Oak Ridge, Tennessee 37830

Abstract

During the past year, the Oak Ridge Y-12 Plant[a] has diamond turned mirrors for the LASL High-Energy Laser and for other projects. The largest of these mirrors are flat, elliptical in shape, and 654 mm (25.5 in) on the major axis and 394 mm (15.5 in) on the minor axis. The concave mirrors are 394 mm OD. These mirrors were inspected for surface finish and figure. Results of this work will be summarized. In addition, blur circle was measured. Measurements of scattered light have also been made. In some cases, the diffraction pattern was related to the waves formed in the surface by the machining process. This information has been useful to the engineers doing research on the diamond turning of laser materials.

Key words: Blur circle; circular diffraction grating; diamond-turned mirrors; diffraction pattern; machine cusp; scattered light; surface figure.

1. Introduction

Development efforts in diamond turning at the Oak Ridge Y-12 Plant, which date back to 1962, were initiated to study the engineering principles related to precision machine tools. Diamond turning can be described as "superfinishing a metal surface by single-point tooling". However, a diamond tool alone, used in a high-quality machine, cannot produce the surface characteristics that are required for some applications such as the optical surfaces of mirrors needed for high-energy lasers. There are five requirements for successful diamond turning: (1) precise machine movements, (2) a vibration analysis, both static and dynamic, (3) dynamic balancing, (4) temperature control, and (5) sharp diamond tools.

The final test of how well these requirements have been met, or whether they are adequate for the desired results, depends on the performance of the part in its particular application. These results are usually not available for a long time after the part has been completed. Optical inspection in the laboratory provides immediate diagnostic information to the machine-tool engineer; and, the test data which are accumulated over a period of time will show long-range performance characteristics of the machines, individual deviations, and areas where improvements are needed. For these reasons, we have been working to make our optical testing program more comprehensive.

This paper will describe, first, the data that were accumulated in testing a series of mirrors that were made for a laser, and then describe additional tests that reveal the effects of machine parameters on mirror performance by their effects on the diffraction pattern.

2. Discussion

Surface Finish and Surface Figure

These data were obtained from a set of mirrors that were diamond turned for the LASL High-Energy Laser Project. The mirrors consist of an aluminum substrate electroplated with copper. A flat mirror of this set is shown in figure 1. It was made elliptical to fit into a tube. The dimensions are 394 by 654 mm (15.5 by 25.75 in). The surface finish of all the large mirrors was measured using a Leitz interference microscope, as shown in figure 2, at five positions across the surface. The flatness of the surface was measured with a 12-inch-diameter Davidson plano interferometer. The results of these measurements are shown in table 1. The average surface finish of these mirrors is 2.5 microinches peak to valley, and the data show that in some cases the surface finish is better in the center where the cut was continuous than at the ends where the cut was interrupted. The average deviation from flatness of these mirrors was 77 microinches.

The figure of the mirrors as revealed by the plano interferometer was saddle shaped. The ends of the major axis were lower than the center of the mirror and the ends of the minor axis were higher. The axis of the saddle was rotated somewhat clockwise (usually about 30 degrees with respect to the axis of the mirror). The reason for this saddle-shaped figure is believed to be due to the

(a) Operated by the Union Carbide Corporation's Nuclear Division for the US Energy Research and Development Administration.

Table 1. Surface Finish and Flatness of Large Diamond-Turned Mirrors
[Elliptical Shape, 394 x 654 mm (15.5 x 25.75 in)]

Mirror Number	Date	Left End (μin)	Left Midpoint (μin)	Center (μin)	Right Midpoint (μin)	Right End (μin)	Average (μin)	Flatness (μin)
538*	02-18-75	3.7	3.4	3.6	3.3	3.7	3.5	80
539	10-18-74	4.1	2.7	1.3	2.7	3.2	2.8	72
540	12-02-74	2.1	2.5	2.5	2.4	2.2	2.3	90
541	12-16-74	2.3	2.1	1.8	2.0	2.6	2.2	75
542	12-02-74	2.4	2.8	2.2	2.2	2.9	2.5	60
543	12-02-74	2.9	2.5	2.6	2.3	3.2	2.7	50
544	10-23-74	2.4	2.7	1.7	3.1	2.5	2.5	87
545	11-18-74	2.0	1.9	1.0	1.5	2.7	1.8	100
AVERAGE		2.6	2.5	1.9	2.3	2.8	2.5	77

*This mirror was turned after a new and larger spindle was installed.

elliptical shape of the mirror and the recess cut in the back of the mirror for the holding fixture. These characteristics provided a situation in which the body of the mirror would flex when it was rotated on the machine.

The spherical mirrors were fabricated with radii of curvature of 133 and 418 inches. The surface finish was measured in the same manner as it was for the flat mirrors. The figure was obtained from the classic Foucault knife-edge test. The knife edge was mounted on a compound slide at the center of curvature. The radius of curvature was not uniform from the edge to the center of the mirror, generally being longer at the center. Masks were placed in front of the mirror so that it could be studied one zone at a time, and the knife edge was moved back and forth on the compound slide to position it at the center of curvature of the zone. These data for a mirror with a radius of curvature of 133 inches are shown in figure 3, which illustrates that from the edge to the center of the mirror the radius of curvature varies about one-and one-half inch. A computer program was developed to relate the variations in radius of curvature to the contour accuracy of the mirror and the results of this analysis are shown in table 2. The computer program placed a perfectly spherical surface at such a position that the error in the actual surface is a minimum and then calculated the error for each zone. Thus, the maximum contour error for this mirror was 31 microinches, or 1/13 wavelength for CO_2 lasers.

Table 2. Contour Error of Mirror 0548

Distance from Center (in)	Contour Error (μin)
0.50	0
1.50	- 5
2.25	- 11
2.75	- 12
3.50	- 13
4.25	- 19
4.75	- 27
5.25	- 31
5.75	- 27
6.25	- 18
7.00	- 11
7.63	- 1

A summary of the data for the six mirrors is given in table 3. The surface finish of the spherical mirrors is about the same as it was for the flat mirrors, but the surface finish is not as good toward the edge of the mirrors with the short radius of curvature. The contour error is given both in microinches and in fractions of a wavelength for the CO_2 laser.

Blur Circle

The blur circle was the last item that was measured, and the time frame was such that it was measured on only one pair of mirrors. When a lens or mirror is illuminated with collimated light, this light will be focused to a spot which is called the blur circle. In the practical sense, the diameter of the blur circle depends upon the optical perfection of the indivual components in the system and the design of the system to eliminate or minimize those conditions that cause aberrations such as astigmatism, coma, and spherical aberration. The experimental arrangement is shown in figure 4. It consisted of a 6 mW He/Ne laser and a spatial filter/beam expander which expanded the beam to a 2.5-cm diameter. This beam advanced to the convex mirror which further expanded the beam, reflecting it to the 10.64-m radius-of-curvature mirror with a diameter of 394 mm, filling its aperture. The light coming from the latter mirror was collimated. This collimation was accomplished by adjusting the distance between these two mirrors to be equal to

Table 3. Surface Finish and Figure of Large Diamond-Turned Mirrors
[Concave, 394 mm (15.5 in) in Diameter)]

Mirror Number	Date	1" (μin)	3" (μin)	5" (μin)	Center (μin)	Average (μin)	Contour Error (μin)	Contour Error λ, CO_2
			Radius of Curvature: 10.6 m (418.86 in)					
535	10-28-74	2.9	3.0	2.4	2.1	2.8	- 76	1/5
536	11-18-74	2.7	2.8	2.3	2.4	2.6	+ 50	1/8
537	11-25-74	2.3	2.5	1.9	2.4	2.3	+ 10	1/42
AVERAGE		2.6	2.8	2.2	2.3	-	-	-
			Radius of Curvature: 3.4 m (133.8 in)					
546	10-26-74	3.5	3.2	2.9	2.1	2.9	+ 13	1/32
547	11-18-74	2.6	3.4	2.9	2.4	2.8	- 24	1/17
548	12-03-74	3.3	3.1	2.4	2.5	2.8	- 31	1/13
AVERAGE		3.1	3.2	2.7	2.3	-	-	-

the difference in their focal lengths. The collimated light proceeded to the 3.4-m radius-of-curvature mirror which focused the light to a small spot. The diameter of this spot was measured. All mirrors in the system were placed as close together as the width of the beams would allow to reduce astigmatism. The diameter of the blur spot was measured with the use of small apertures. The device holding the apertures was mounted on a compound slide so that the minimum diameter of the spot could be located. The aperture was then moved across the spot in steps of 0.001 inch and the power read from a Spectra-Physics power meter. The data obtained with a 0.6-mm aperture is shown in figure 5. The power transmitted through this pinhole is 76% of the power measured at this point if the pinhole is absent. When the 0.8-mm aperture is used (figure 6) the top of the peak is flat and 82% of the power is transmitted through the aperture.

Scattering and Diffraction

Let us begin the subject of scattering by saying that a diamond-turned surface is similar to a circular diffraction grating. As the disk turns on the spindle, the slide moves the diamond tool and a small spiral cusp remains on the surface. The spacings that remain on the surface may cause it to act as a grating. For example (figure 7), in one case the spindle speed was 112 rpm and the slide speed was 0.122 ipm. Dividing 0.122 by 112 and the cusp is 0.001 inch. This cusp spacing can be seen very easily with a surface-finish microscope at 50X. The theoretical surface finish (if the bit has a 1/8-inch nose radius) is equal to the square of the cusp spacing or tool advance, and for this example is 1.2 microinches. The surface of this specimen is shown in figure 8. When the beam of a He/Ne laser falls normally upon this surface a diffraction pattern is produced. The equipment for recording this diffraction pattern shown in figure 9, consists simply of an uncollimated laser with a one-millimeter aperture in the beam, the specimen, and the detector. The detector is at the end of a 45-cm arm attached to a rotary table, and the specimen is mounted over the center of the rotary table and aligned so that the angle of incidence is known, usually zero degree. The rotary table is motor driven and a scan can be made through ± 70 degrees. The first scan (figure 10) to demonstrate the results obtained from this system is from a 14,500-groove/inch diffraction grating from the spectrographic laboratory. Observe that there are two orders of diffraction on both sides of the zero-order peak and that the lines are tall and slim with almost no hash around the base. The diffraction pattern can be calculated from the grating equation:

$$n\lambda = d \sin\gamma,$$

since in this work the angle of incidence was kept at zero degree. Where there is a diffraction pattern and monochromatic light is used, it is interesting to calculate the order numbers to see if they can be obtained from the turning parameters. For the example mentioned (figure 11) the order number was:

$$n = \frac{d}{\lambda}\sin\gamma = \frac{2767 \times 10^{-6}\ \text{cm}}{63.28 \times 10^{-6}\ \text{cm}}\sin\gamma, \text{ or}$$

$$n = 43.72 \sin\gamma.$$

If the value for the tool advance that was obtained by counting fringes in the photograph shown before (figure 8) is used:

$$n = 45.15 \sin\gamma.$$

The diffraction pattern that was obtained from this copper mirror is shown in figure 12 with the order of diffraction marked above each peak. Although the peaks are very small, the orders were calculated up to the 16th order for this specimen. The value of n from the surface finish photograph was used to obtain whole numbers for the orders, rather than the value from the machine parameters. The latter are not accurate enough because the spindle speed is not calibrated accurately for each setting of the speed control.

Admittedly, these are not very good surfaces. A much better surface was investigated (figure 13) and no diffracted light was found that could be correlated with the machine parameters of a 0.210-ipm slide speed and an 800-rpm spindle speed where the cusp spacing is 263 microinches. It is clear, however, that there are some peaks near the zero-order peak, shown in figure 14. How can they be accounted for? Among the surface-finish pictures that were made, some were taken with the Reichert metallurgical microscope using the Nomarski attachment. This picture showed a series of waves (figure 15) at a magnification of 236X. The number of waves over a length of the picture was counted, and from this the wave spacing was determined to be 912 microinches—nearly four times the spacing calculated from the machine parameters. The large peaks on both sides of the zero-order peak were calculated to be exactly the first order, based on this wave spacing.

What about the actual cusp spacing? Can it be seen? At 240X, the cusps should be 1.6 mm apart on the Nomarski photographs, but the faint lines that are visible are spaced almost exactly 1.0 mm apart. The theoretical surface finish is 0.06 microinch or 15 Å, which would be visible on the Nomarski, but which could not be observed with the Leitz microscope which has a height resolution of one microinch. What then is the "grass" that is observed on the photograph (figure 16) from the Leitz surface-finish microscope which we have been reading as surface finish? Again, the spikes were counted in a length of picture and the spacing was the same as for the waves in the Nomarski picture at 240X. In other words, what we were calling "surface finish" and what we had thought were "tool cusps" are actually waves in the surface, and the surface finish is the height of the waves.

Unfortunately, most turned surfaces do not show the even waves displayed here; in fact, these are not even waves. If the width of each wave is measured, there is a fairly large distribution about the average which probably accounts for the additional small peaks shown around the large diffraction peaks. As a final comment, the machine engineers say that the spacing does not correspond to anything in the machine such as gear ratios, ratio of spindle rpm to motor rpm, and drive-belt speeds. So the cause of this pattern has not yet been determined.

A final important question is: Do these diffraction patterns made with a He/Ne laser relate to the performance of these mirrors in the infrared at 10.6 micrometres? We are starting to study that problem, and perhaps others can provide more information than we can at the present time. Dr. Bennett has point out that dust on the surface is an extremely important factor, and in his work he is evaluating all the factors that affect scattering and diffraction. We have a CO_2 laser with an output of 45 watts. When this was directed normally to the surface of several specimens we could not detect any light at the angles calculated for the first and second-order diffraction peaks using the grating equation discussed before. We are working to improve the sensitivity of the detector, and we think we know where to put it.

3. Conclusions

We have examined many more diamond-turned surfaces than we could summarize in this report. Some of them displayed superior surfaces in terms of flatness and finish. Possibly you will hear about them in other talks at this meeting. All the work we do will hopefully show what is necessary for turning better surfaces. It has also shown what we have to do to evaluate them better. We look forward to discussing this with you next year.

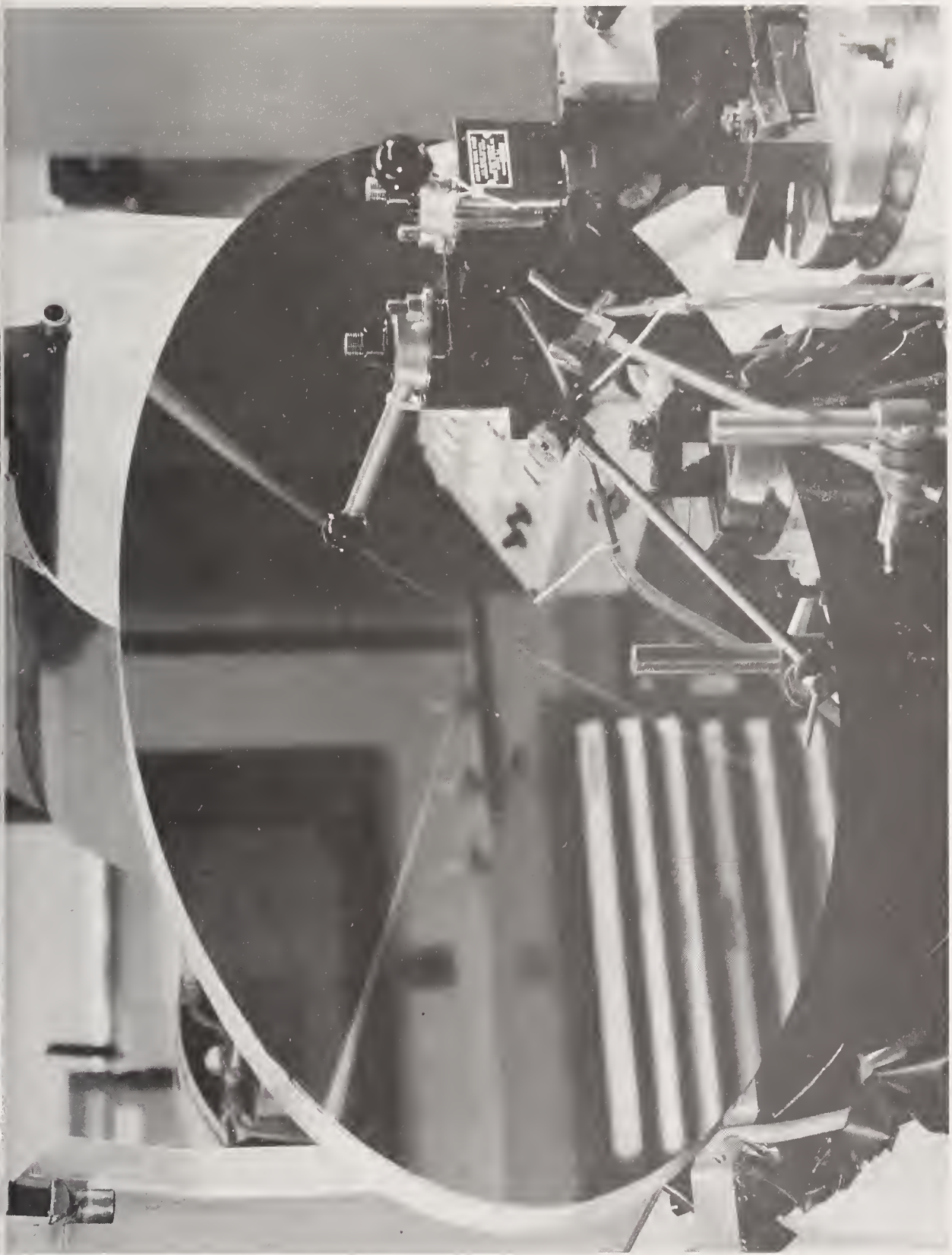

Figure 1. Finished elliptical mirror.

Figure 2. Measuring the surface finish of a large elliptical mirror with a Leitz surface finish interference microscope.

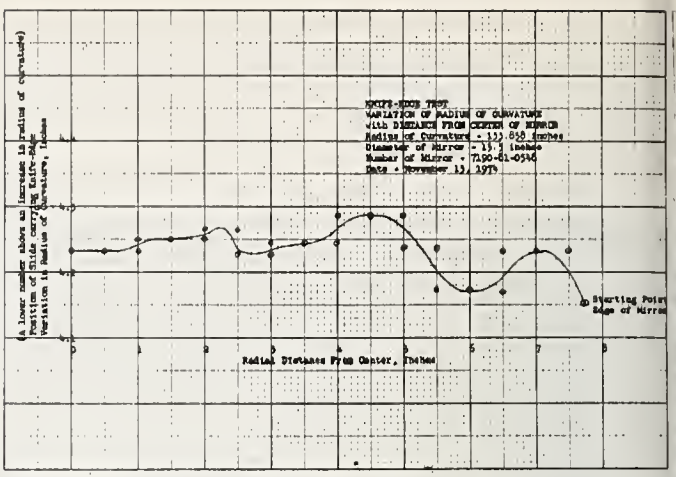

Figure 3. Knife-edge test variation of radius of curvature with distance from center of mirror. (Radius of curvature-133.858", diameter of mirror-15.5", number of mirror-7190-81-0548, date-November 13, 1974.)

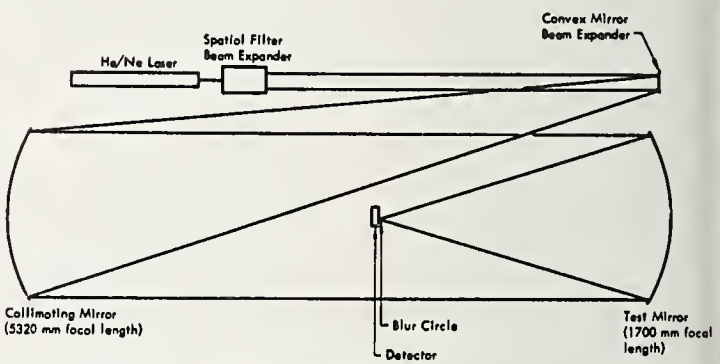

Slide 7. EXPERIMENTAL ARRANGEMENT FOR THE BLUR-CIRCLE MEASUREMENTS.

Figure 4. Experimental arrangement for the blur-circle measurements.

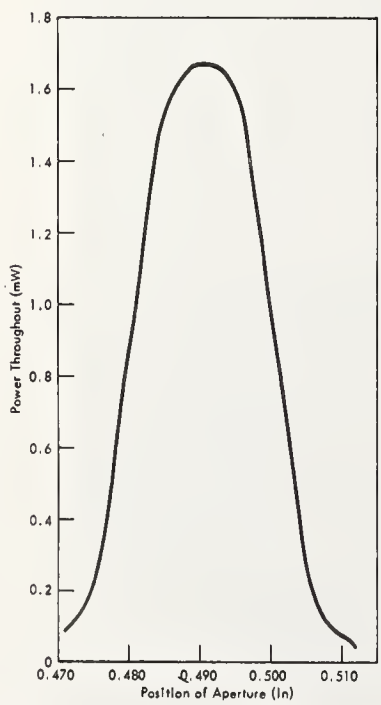

Figure 5. Scan of the blur-circle with a 0.6-mm aperture (76% of the power passes through).

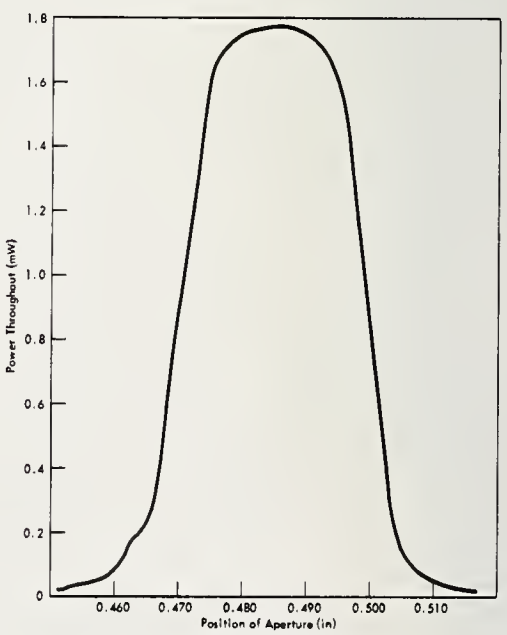

Figure 6. Scan of the blur-circle with a 0.8-mm aperture (82% of the power is transmitted).

Slide 10. Calculation of Cusp Spacing

Machine Parameters

Slide Speed: 0.122 inch/minute

Spindle Speed: 112 rpm

$$\text{Cusp Spacing or Tool Advance (TA)} = \frac{0.122 \text{ ipm}}{200 \text{ rpm}} = 0.001\,089 \text{ in} = 0.002\,767 \text{ cm}$$

When the surface is examined with a 50X microscope:

$0.001\,089 \times 50 = 0.054$ inch

The Theoretical Surface Finish is (for an 1/8" R tool):

Surface Finish = $(TA)^2 = 0.001\,089)^2 = 0.000\,001\,2\,\mu$ in, p to v

Figure 7. Calculation of cusp spacing.

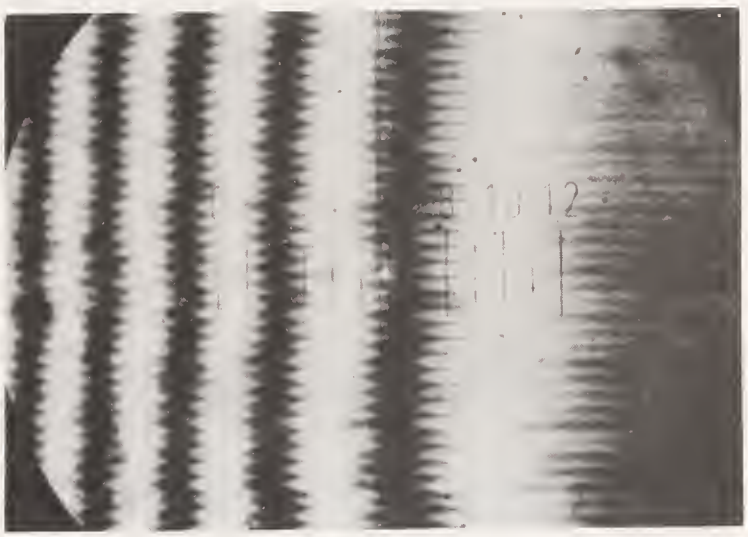

Figure 8. Surface finish of a copper diamond-turned surface with grating-like characteristics. (The cusp spacing on the surface is 0.001". On this picture, taken at 50X, the cusps are plainly visible.)

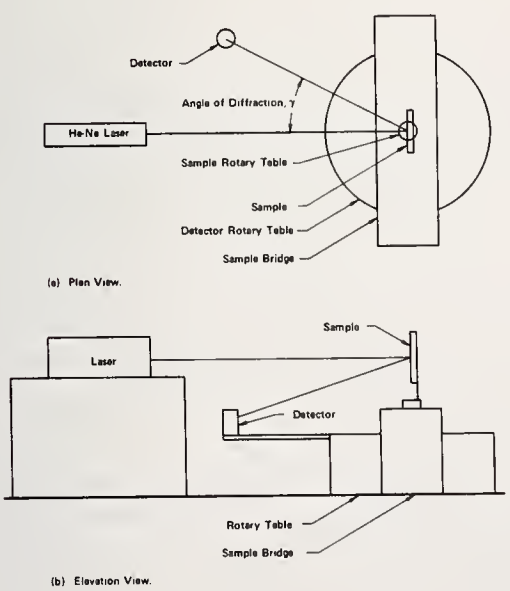

Figure 9. Plan and elevation views of apparatus for measuring scattered light.

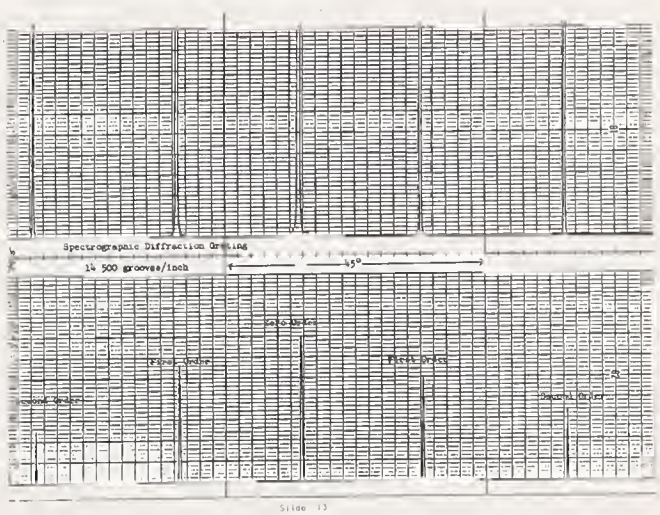

Figure 10. Scan from a 14,500-groove/inch diffraction grating.

Slide 14. Calculations with Grating Equation

$$n\lambda = d \sin \gamma \quad \text{(Normal incidence)}$$

$$n = \frac{d}{\lambda} \sin \gamma$$

When $d = TA = 2767 \times 10^{-6}$ cm:

$$n = \frac{2767 \times 10^{-6} \text{ cm}}{63.28 \times 10^{-6} \text{ cm}} \sin \gamma$$

$$n = 43.72 \sin \gamma$$

From Surface Finish Photograph:

There were 21 grooves in 3 cm at 50X

$$d = \frac{3 \text{ cm}}{21 \times 50} = 2857 \times 10^{-6} \text{ cm}$$

$$n = 45.15 \sin \gamma$$

Figure 11. Calculations with grating equation.

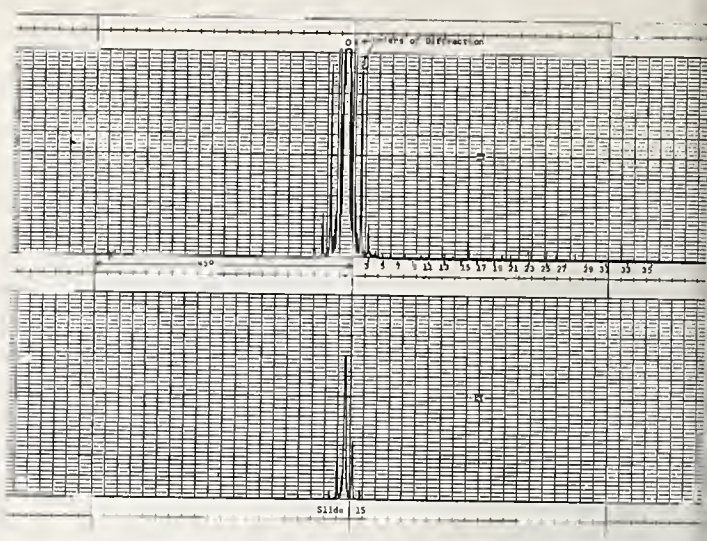

Figure 12. Diffraction pattern from the copper mirror.

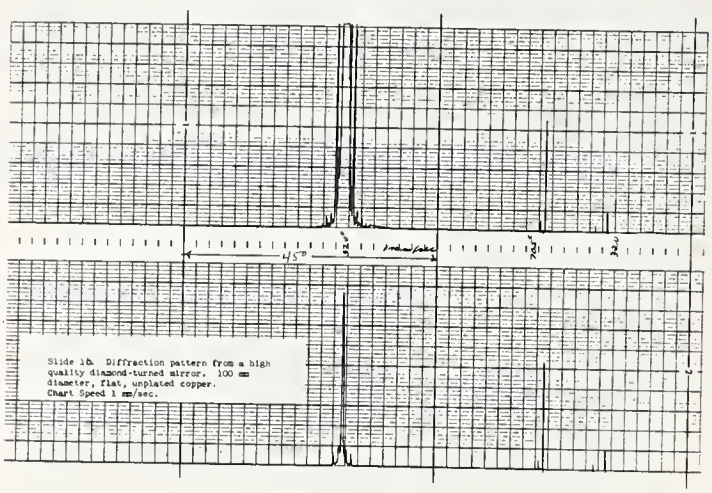

Figure 13. Diffraction pattern from a high-quality diamond-turned mirror. (100-mm-diameter, flat, unplated copper, chart speed-1 mm/sec.)

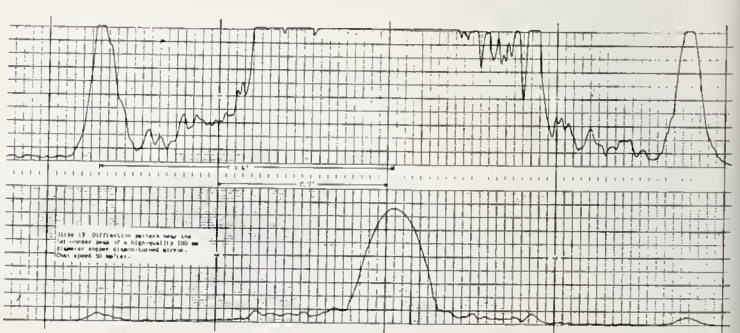

Figure 14. Diffraction pattern near the zero-order peak of a high-quality 100-mm-diameter copper diamond-turned mirror. (Chart speed, 50 mm/sec.)

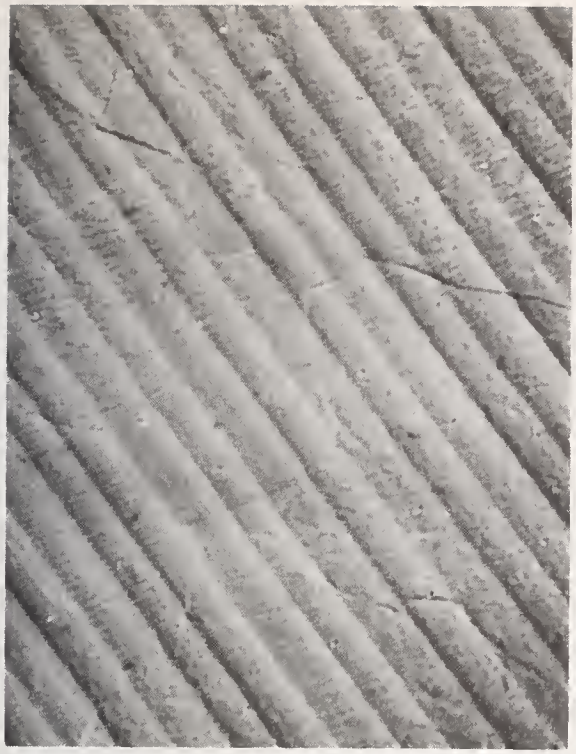

Figure 15. Nomarski polarization contrast. (This is a 100-mm-diameter diamond-turned copper disc, 236X.)

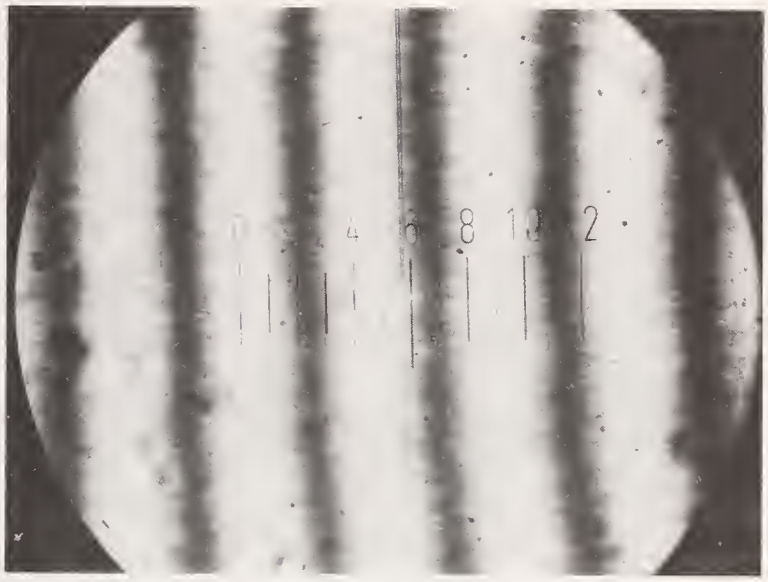

Figure 16. Leitz surface finish microscope. (This is the same 100-mm-diameter copper-turned mirror as in the previous slide. The structure in these fringes are waves in the surface, and not tool cusps, 50X.)

COMMENT ON PAPERS BY BENNETT, *et al* and SLADKY, *et al*

Several points were raised in the discussion concerning the factors which control the surface absorption reflectivity and damage threshold of diamond turned mirrors. The principle contribution to the damage is thought to be from subsurface structural defects induced by the diamond turning process. The residual damage level is thought to extend to a depth about five times the depth of the tool-cut. It was pointed out that annealing may help reduce the damage threshold by reducing the extent of that damage later. However, annealing may also generally degrade the optical figure of the surface. The characterization of the surface includes both the determination of the widely distributed microirregularities on the surface as characterized by an rms roughness and the occasional digs and scratches. Both contribute to scattering, but the net effect is different in the infrared from the visible. Surface characterization requires both a specification of the microirregularities and the macroirregularities. Scratch and dig characterization alone is too simple a description to be generally useful in determining the damage threshold. It has been observed in polished copper mirrors that improved the smoothness or reduced rms roughness yields a lower reflectivity and probably a lower damage threshold, evidence of an increase of surface absorption due to continued polishing of the surface. This was put forward as an example of the complexity of surface characterization required to determine the performance of metal mirrors for high power laser use.

2.5 Dielectric Coated Diamond Turned Mirrors

James R. Buckmelter, Theodore T. Saito, Richard Esposito

Air Force Weapons Laboratory
Kirtland AFB, NM 87117

and

Leonard P. Mott, R. Strandlund

Optical Coating Laboratory Inc.
Santa Rosa, CA 95403

Adherence of multilayer dielectric enhanced mirror coatings to diamond turned metallic surfaces was discovered to be a problem. Initial coating results demonstrated peeling and erratic optical properties for a variety of coating designs deposited on ERDA diamond turned copper, silver, and gold. The same coating designs deposited on polished molybdenum had excellent adherence and consistent optical properties. The adherence problem was determined to derive from two factors intimately connected with the diamond turning process, namely, oil adsorption and stress in the electroplated metal surface. These factors can be eliminated by stress relief in a heated oil bath followed by thorough cleaning in freon or trichloroethylene prior to coating. Procedures used to investigate dielectric coated diamond turned mirrors included absorption calorimetry, damage measurements with a 10 kW laser and Auger Spectroscopy.

Key words: Adherence; diamond machining; dielectric mirror; electroplating; laser damage resistance; stress relief.

1. Introduction

Diamond turning of optics can be defined as the use of a diamond tool on a precision lathe under very precisely controlled machine and environmental conditions to produce a finished optical component [1,2][1]. Diamond turning has two distinct advantages when compared to conventional optical fabrication. Because of machine accuracies many figures of revolution can be easily fabricated. For example, a very fast parabola [3], ellipses and compound axicons have been diamond turned. The second advantage is in the area of economy of fabricating large (greater than six inch) diameter flats. Diamond turning is also more economical when fabricating parts with unusual cross sections or parts which have holes in them. The optical properties of diamond turned surfaces are outstanding. Reflectivity at 1 and 10 microns compares favorably with ultra-high vacuum evaporated coatings of gold and silver and is better than most super-polished samples of copper and silver. Laser damage properties have also proven to be very competitive with conventionally fabricated optics [4].

To date, diamond turning has been useful only on soft metals such as gold, silver, or copper, and such metal mirrors are limited to experimental reflectivities at 10.6 microns of about 99.3 percent; whereas, multilayer dielectric enhanced mirrors have achieved 99.9 percent reflectivity [5]. It would be advantageous to combine the economies of diamond turning with the improved performance of multilayer dielectric enhanced mirrors. Accordingly a total of 32 diamond turned metal mirrors were coated at the Optical Coating Laboratory, Inc., in an initial attempt to produce superior multilayer dielectric enhanced mirrors for use at 10.6 microns. The results were unexpected and disappointing.

1. Figures in brackets indicate the literature references at the end of the paper.

NOTE: Micron(s) as used in this paper expresses micrometer(s).

2. Experimental

2.1. Sample Description

A total of 32 diamond turned mirrors, including 18 copper, 12 silver, and two gold, were coated with seven slightly different multilayer dielectric enhanced mirror designs. Fifteen of these mirrors exhibited complete peeling of the multilayer coating and were not tested at all. The remaining 17 mirrors were subjected to a variety of evaluation procedures in spite of very uneven quality. The 17 "good" mirrors included several that had only partially adherent coatings and many that had cosmetic defects that apparently were caused by inadequate cleaning of the metal surface prior to coating, but these were evaluated anyway due to the limited number of samples. For comparison, 12 polished molybdenum and six glass witness samples were also coated at the same time with the multilayer designs and all of these samples demonstrated good adherence and cosmetic quality. These samples were evaluated in parallel with the coated diamond turned mirrors. The substrates and coating designs are described in table 1 where the glass and molybdenum substrates are polished, and the copper, silver, and gold are diamond turned by either the Lawrence Livermore Laboratories (LLL) or by Union Carbide Y-12 at Oak Ridge, Tennessee.

2.2. Optical Evaluation

The multilayer dielectric coated samples were evaluated with a variety of techniques and the results are given in table 1. The 10.6 microns reflectivity was measured with a multiple bounce reflectometer which basically compares a reference signal to a sample signal which is varied by adjusting the number of times a 10.6 micron laser beam reflects between a known mirror and the sample mirror [6]. The reflectance of the pair of mirrors is then derived from the slope of the log of the signal ratio versus the number of reflections. This reflectometer is accurate to ± .2 percent, but typically gives lower reflectances on dielectric mirrors than absorption calorimetry (1-A) because the reflectometer sees only specular reflectance after several bounces; whereas, an absorption calorimeter can also include most of the scattered radiation.

R-6328 is the reflectivity at .6328 microns (HeNe) as compared to a good silver coating. The silver standard had a measured reflectance at 10.6 micron of 99.2 percent, so based on standard plots of reflectance versus wavelength, this standard would have an absolute reflectance at .6328 microns of 98.5 percent. This standard silver sample was arbitrarily set at 100 percent in a Cary 14 Spectrophotometer with a reflectance attachment and then all the dielectric mirrors were simply compared to the baseline set by the standard. This is not a particularly accurate measurement, perhaps ± 1.0 percent, but the values obtained are useful as an indication of how easily such optics might be aligned in a real system. Although no effort was made to design coatings which would have high reflectance at .6328 microns, as well as at 10.6 microns, several coating designs did have appreciable reflectance at the HeNe wavelength.

TIS is the total integrated scatter at .6328 microns as collected in an integrating sphere and compared to the total reflectance from a dielectric mirror [7]. A 100 percent reflecting dielectric mirror for .6328 microns is used to reflect a HeNe beam at the inside of an integrating sphere combined with a photomultiplier tube. The signal produced by the dielectric mirror is arbitrarily set at 100 percent and the sample mirrors are then introduced into the system, except that the reflected beam is aimed through a hole in the integrating sphere so that only the scattered light from the sample is collected. A typical polished metal surface might have a TIS near .5 percent and some diamond turned metal surfaces have had TIS values nearly indistinguishable from the background level (blue velvet) of about .04 percent. The TIS values are useful mostly as a qualitative tool since it is extremely sensitive to the ambient environment or to sample position. Different spots on the same sample can easily vary by factors of 2-5. Furthermore, there is no convenient method to relate a sample's performance at .6328 microns to that at 10.6 microns, except that 10.6 micron scatter is much lower [8]. The TIS values are useful for distinguishing coatings or surfaces that contain numerous imperfections that are not always apparent to the eye. It should be noted that dielectric coatings will never improve the scatter from the base substrate, due to the tendency of the coating to reproduce or even magnify original substrate defects as well as introduce new flaws.

The design wavelength for all samples was 10.6 microns, but due to the experimental difficulties involved in depositing an exact quarterwave optical thickness many of the coating designs had a design bandwidth that was not centered at 10.6 microns. However, since the maximum reflectance band is usually about 2 microns wide for the number of coating pairs involved in this study, the maximum reflectance of any sample was not seriously affected by the detuning of the multilayer stack. The effects of coating thickness variations or detuning were negligible compared to absorption effects or gross film imperfections such as pinholes or inclusions; but, the extent of detuning is an excellent indication of the control that the manufacturer has over his process. The tuning control of the manufacturing process is indicated in table 1 by λ-Scan. This was determined with a Digilab FTS-20 infrared spectrophotometer used in a reflectance mode. The λ-Scan value is the center of the reflectance band taken at half-maximum value.

An absorption calorimeter was used to measure the 1-Absorptance (1-A) values presented in table 1 [9]. This equipment employs a Coherent Radiation Model 42L CO_2 laser as a light source, and temperature monitors and heat capacities of the mirrors are calibrated in situ. The energy of the reflected beam is measured calorimetrically within 4 percent accuracy. The absolute accuracy of the measurement is ± 10 percent of the absorption measured and the precision is 0.0005.

The laser damage measurements were done with the AFWL 15kW, CW, CO_2, coaxial, electrical discharge laser (EDCL) [10]. This laser was operated at approximately 10 kW for all damage shots in order to get reasonably stable operation for the time periods involved. Most shots were run for 5 seconds, except that the 12 kW/cm^2 shots were run for 10 seconds and others, as noted in table 1. Laser intensity was varied by focusing the output beam with a one meter focal length copper mirror, but for the highest intensity, 46 kw/cm^2, a 25 cm focal length salt lens was used in conjunction with the one meter mirror to produce a beam area of 24 cm^2. Beam area was measured simply and directly by the use of plexiglass burn patterns taken at the same position as the mirror samples. The worst case accuracy for the intensity measurements was ± 30 percent, due mostly to variations in the laser output from run to run and to errors in beam area measurement. The variations in laser output were known, but were averaged for the sake of convenience in reporting the data. Nominal intensities used were 5, 12, 19, and 46 kW/cm^2; however, a few samples were run in a different test series with the same laser and the intensities were slightly different. These are noted in table 1. Also, the intensities given are all corrected for reflection losses at the various optical interfaces, such as the output beam splitter, focusing mirror, or lens. The laser power was measured with a Coherent Radiation model 213 power meter to better than ± 5 percent; and, since the EDCL lases with a uniform flat top intensity output, no corrections were necessary to account for a Gaussian distribution. This is to be contrasted to most other laser damage measurements where extensive calibration is required to define a highly focused Gaussian beam [11,12].
Laser damage in this study is simply defined as catastrophic or microscopic. Catastrophic damage involves a damaged area at least as large as the incident laser beam area; whereas, microscopic damage consisted of burn spots that were much smaller than the irradiated area. Samples that survived catastrophic damage are noted in table 1 with a greater than (>) sign, otherwise the intensity listed implies that the sample survived catastrophic damage at the preceeding intensity. Only four samples survived catastrophic damage and only one of these was a dielectric coated diamond turned mirror. Microscopic damage was extensive on these four samples and also on other samples in areas outside the catastrophic damage spot.

2.3. Microscopic and Metalurgical Evaluation

Several of the dielectric coated diamond turned mirrors with especially poor coating adherence were examined with a Nomarski phase contrast microscope. This revealed that an extensive orange-peel effect had developed in the metal surface during the coating process. This observation led to an experiment in which diamond turned gold and copper samples were heat treated in vacuum to 200°C for one hour. The gold sample developed an extensive orange-peel and the copper sample developed a pitted appearance. Other diamond turned substrates that were annealed in an oil bath at 150°C for one hour did not develop any surface changes. Since the dielectric coatings were deposited on unannealed substrates in vacuum at 150°C over

a period of several hours, the coating adherence was almost surely affected by the changes in the substrates brought about by the coating chamber environment. The vacuum heat treatment also made some metal surfaces noticeably dirtier. Evidently a prior cleaning in trichloroethylene and alcohol was not sufficient to remove all of the cutting fluid associated with the diamond turning process. Again the conditions necessary for depositing dielectric coatings probably caused the cutting fluid or other contaminant to migrate to the surface being coated and this resulted in poor cosmetic quality and also poor coating adherence.

Additional work was done on single crystal copper, one piece of which was diamond turned, and an adjacent piece from the same single crystal which was polished in a conventional manner [13]. Nomarski microscopy revealed numerous flaws, scratches, pits, etc., on the mechanically polished sample, while the diamond turned sample was of excellent cosmetic and optical quality. Laue back reflection x-ray patterns, however, demonstrated considerably more smearing for the diamond turned sample as compared to the conventionally polished sample indicating that the diamond turning process introduces more work-hardening than conventional polishing. X-ray reflection topography was also attempted with the result that the diamond turned surface produced a very weak broad peak extending over a degree or more. Only small random areas of the surface with very little detail were shown in the resulting topograph. In contrast, x-ray topographs of the mechanically polished surface showed an image for the entire surface which again indicates that diamond turning introduces considerably more damage into the metal surface. Finally, knoop micro-hardness measurements were made on both surfaces using a 15 gram test load. An average of five measurements on each surface resulted in a knoop hardness of 82 for the mechanically polished surface and 126 for the diamond turned sample; thus Laue patterns, hardness measurements, and x-ray topography all indicate that there is significantly more "cold work" in the diamond turned mirror than in the mechanically polished mirror regardless of the cosmetic or optical quality. The 10.6 micron reflectivity of the diamond turned copper was greater than 99.1 percent.

3. Discussion

The application of multilayer dielectric enhanced coatings to diamond turned surfaces has been unexpectedly difficult for reasons that are inherent in the diamond turning process. Most important, the diamond turned surfaces are severely cold worked and this results in extensive atomic mobility during the coating operation, which in turn adversely affects the adherence of the coating. Secondly, the diamond turning process only works so far on the soft metals such as gold, copper, silver, or aluminum. These materials cannot be mechanically scrubbed and so must be cleaned with a non-contact process which has not been sufficient. In addition, the best surfaces for the diamond turning process are electroplated since this gives a very fine grained structure amenable to diamond turning. Such electroplated layers can be highly stressed and must be annealed prior to coating.

The samples in this study which were successfully coated had erratic optical properties. Several dielectric coated diamond turned mirrors had very large 10.6 micron absorption and these mirrors also had lower laser damage thresholds as would be expected. Other mirrors with absorption comparable to the coated polished molybdenum samples also had roughly comparable laser damage thresholds. This indicates that the defect structure of the coating dominated the defects introduced by the diamond turning process for laser damage resistance of samples with comparable absorption.

Based on the information accumulated with the first group of samples, a second set of six polished molybdenum, four diamond turned gold, and four diamond turned copper substrates were coated. The diamond turned substrates in this set were all fabricated by LLL using electroplated layers of gold or copper; however, these samples were annealed at 150°C in an oil bath for one hour prior to cleaning and coating. The cleaning procedure consisted of an ultrasonic bath in trichloroethylene and a soaking in alcohol. Two multilayer coating designs were used and all substrates were coated with adherent dielectric coatings, but the cosmetic quality of the coated diamond turned mirrors was still unsatisfactory. These samples are described

in table 2. The cosmetic quality of these samples was not particularly good, but the most recent cleaning procedures were not used. There are two techniques that will produce suitably clean oil free surfaces. One consists of ordinary rinsing in trichloroethylene and alcohol followed by heating in vacuum to about 100°C followed by another rinse in clean trichloroethylene and alcohol. Observation under blue light indicates that this produces a clean surface. The second procedure involves cleaning for about 30 seconds with clean TF freon at 50°C in a vapor degreaser.

4. Conclusion

Dielectric coatings can be applied to diamond turned metal surfaces to form adherent multilayer dielectric enhanced mirrors that will be cosmetically and optically good. Such mirrors should be limited in laser damage thresholds by the same defects that limit conventionally polished surfaces. These limiting coating defects include the usual pinholes, inclusions, scratches, coating absorption, etc., that cause presently available coatings to damage at CW 10.6 micron irradiation levels of about 30 kW/cm^2.

The recommended substrates for diamond turning are oxygen free high conductivity (OFHC) copper, or electroplated gold, or silver, all of which should be annealed and thoroughly cleaned. A recommended multilayer dielectric coating would be $(ThF_4/ZnS)^n$ or $(ThF_4/ZnSe)^n$ with a metallic binder undercoating of perhaps gold, chromium, or titanium, but not silver. If such coatings can be deposited without defects, laser damage thresholds can be expected to increase substantially.

5. Acknowledgments

Several people contributed to this effort, but special mention should be made of Auger Analysis and hardness measurements by Dr. W. Ewing and Ms. J. Bruce of the Air Force Cambridge Research Lab; the optical measurements by Mr. R. Lester, Mr. M. Guadagnoli, and Mr. W. Kunzler of AFWL; the damage testing with Mr. R. Carlson of AFWL, and conversations with Mr. R. Austin of Perkin-Elmer.

6. References

[1] Saito, T.T., "An Introduction to the Machining of Optics," to be published in August issue of Applied Optics 14, 1975.

[2] Saito, T.T. and Simmons, L.B., "Performance Characteristics of Single Point Diamond Machined Metal Mirrors for Infrared Laser Applications," Ap. Opt. 13, 2647, 1974.

[3] Bryan, J.B., Donaldson, R.R., McClure E.R., Wayland, H.A., Clouser, R.W., "Diamond Turning of Parabolic Mirrors," Presented at Society of Parabolic Instrumentation Engineers, August 1973 Available as UCRL-51213 from Lawrence Livermore Laboratory.

[4] Saito, T.T., Milan, D., Baker, P., Murphy, G., "10.6μ 15 psec Laser Damage Study of Diamond Turned, Diamond Turned/ Polished and Polished Metal Mirrors," to be presented to the 1975 Laser Damage Symposium at Boulder, Colorado, July 1975.

[5] Braunstein, M., "Multilayer Enhanced Dielectric Mirrors," AFWL-TR-75-196, Air Force Weapons Laboratory, 1975.

[6] Wetzel, M.G., Saito, T.T. and Patterson, S.R., "Improvement of Absolute Accuracy for a Multiple Bounce Reflectometer Through a Detailed Effort to Reduce Systematic Errors," App. Opt. 12: 1558, 1973.

[7] Kurdock, J.R., "Low Absorptance Metallic Coatings for Metallic Substrates," AFWL-TR-74-28, Air Force Weapons Laboratory, 1974.

[8] Scheeley, S., "Scattering Characteristics of Mirrors and the Associated Inverse Scattering Problem," Ph.D. Thesis, USC, 1973.

[9] Saito, T.T., Callender, A.B. and Simmons L.B., "Calorimeter to Measure the 10.6 Micron Absorption of Metal Substrate Mirrors," Appl. Opt. 14: 721, 1975.

[10] Carlson, R. "A 15 Kilowatt CW, CO_2 Coaxial, Electrical Discharge Laser," to be published as Air Force Weapons Laboratory Technical Report.

[11] Huguley, C. and Loomis, J., "Optical Material Damage From 10.6 Micron CW Radiation," to be presented at NTSS Symposium on Damage in Laser Materials, Boulder Colorado 1975.

[12] Saito, T.T., Charlton, G and Loomis, J. "10.6 Micron Cw Laser Damage Studies of Metal Substrate Mirrors," Laser Induced Damage in Optical Materials, ed. Geunther A. NBS Special Publication 414, 1974.

[13] Bruce, J., Private communication

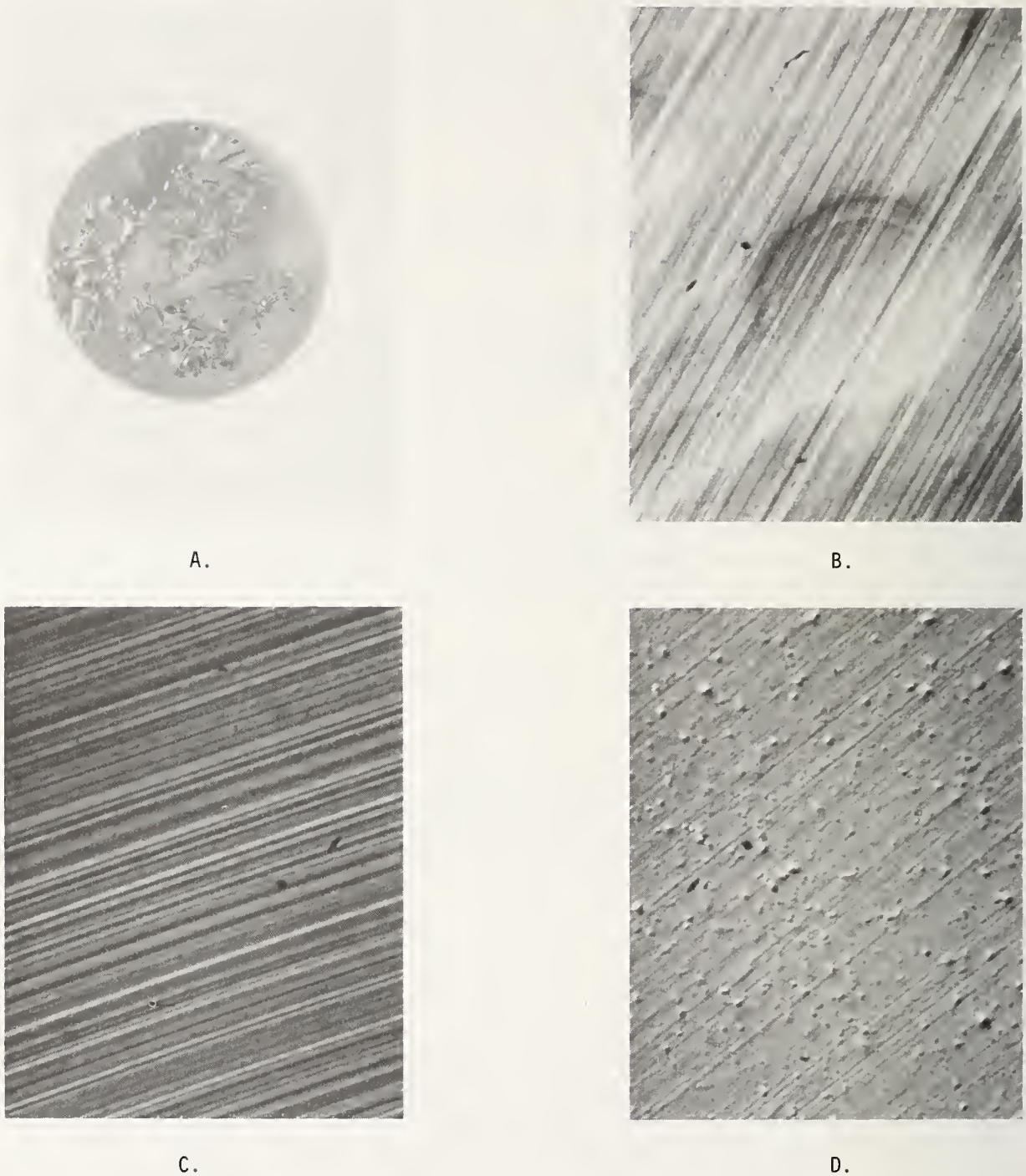

Figure 1. Nomarski photomicrographs of various diamond turned surfaces all at 100X.

A. Dielectric coated diamond turned LLL-Cu-54.

B. Diamond turned electroplated LLL-Au-3, vacuum baked 200°C one hour.

C. Diamond turned electroplated LLL-Au-28 oil bath annealed 50°C, vacuum baked 200°C one hour.

D. Diamond turned electroplated LLL-Cu-85 oil bath annealed 50°C, vacuum baked 200°C one hour.

Table 1. Sample Description and Optical Properties

Source	Substrate	Dielectric Design	R-10.6	R-.6328	TIS	λScan	1-A	Damage kw/cm^2
OCLI	Glass	$(ZnS/Ge)^5$	99.9			10.2		5.1
AFWL	Mo-156		99.2	25.	.4	10.3	99.81	46
AFWL	Mo-134		99.5	25.	.4	10.3	99.62	46
LLL	Cu-62		99.2	25.	.3	10.3	99.73	46
LLL	Cu-66		99.4	26.	.3	10.3	99.70	46
OCLI	Glass	$Au+(ZnS/Ge)^5$	99.9			10.3		5.1
AFWL	Mo-150		99.6	36.	.7	10.3	99.54	46
AFWL	Mo-147		99.7	37.	.9	10.3	99.87	46
LLL	Ag-13		93.3	26.	6.3	10.3	93.72	5
LLL	Cu-58		99.6	37.	.5	10.3	99.84	46
LLL	Cu-60		99.7	37.	.3	10.3	99.82	19
Y-12	Au-C6		93.6		.3	9.8	93.90	19
OCLI	Glass	$(ThF_4/ZnSe)^4$	99.6			10.6		10.8
AFWL	Mo-137		99.4	78.	1.3	10.6	99.78	>46, 5 secs
AFWL	Mo-157		99.6	79.	4.5	10.6	99.68	46
LLL	Ag-14		99.5	63.	5.6	10.6	99.70	46
LLL	Ag-15		99.6	62.	4.0	10.6	99.71	46
OCLI	Glass	$Au+(ThF_4/ZnS)^5$	99.4			10.5		10.8
AFWL	Mo-135		99.3	75.	1.7	10.5	98.90	>46, 5 secs
AFWL	Mo-155		99.4	75.	4.6	10.5	99.59	>40, 10 secs; >46, 5 secs
Y-12	An-M122/12		99.3	72.	3.0	10.5	99.60	46
LLL	Ag-3		99.2	56.	2.5	10.5	99.60	>46, 5 secs
OCLI	Glass	$Ag+(ZnS/Ge)^5$	99.8			10.3		10.8
AFWL	Mo-132		99.7	27.	.7	10.4	99.82	46
AFWL	Mo-136		99.8	27.	.6	10.4	99.78	46
LLL	Ag-10		94.0	24.	10.7	10.4	96.86	19
Y-12	Ag-M123/7		92.5	26.	4.9	10.4	96.28	12
LLL	Cu-50		98.6	28.	.6	10.4	99.85	46

Table 1. Sample Description and Optical Properties (Continued)

Source	Substrate	Dielectric Design	R-10.6	R-.6328	TIS	λ Scan	1-A	Damage kw/cm^2
OCLI	Glass	$Ag+(ThF_4/ZnS)^5$	99.3			10.4		10.8
AFWL	Mo-149		99.2	88.	6.2	10.4	99.81	46
AFWL	Mo-133		99.5	90.	1.7	10.4	99.62	>40, 10 secs; 46
LLL	Ag-11		99.5	52.	5.5	10.4	99.59	46
LLL	Ag-10		99.3	52.	5.2	10.4	99.56	46
LLL	Cu-49	$Ti+(ZnS/Ge)^4+ZnS$	99.7		.5	10.6	99.89	46
LLL	Cu-51		99.5		.5	10.5	99.87	46

Table 2. Sample Description and Optical Properties Group 2

AFWL	Mo-189	(ThF_4/ZnS)	99.3	92.	2.7	10.2	99.68
AFWL	Mo-192		99.4	80.	1.8	10.3	99.74
AFWL	Mo-193		99.4	77.	1.7	10.3	99.66
LLL	Au-20		99.5	96.	1.5	10.3	99.74
LLL	Au-24		99.4	85.	1.6	10.3	99.64
LLL	Cu-71		99.2	84.	2.0	10.3	99.57
LLL	Cu-72		99.2	48.	1.8	10.3	99.71
AFWL	Mo-178	(ZnS/Ge)	99.3	32.	.9	9.7	99.64
AFWL	Mo-182		99.5	34.	2.8	9.7	99.67
AFWL	Mo-185		99.6	29.	.5	9.6	99.63
LLL	Au-21		99.6	38.	.4	9.7	99.62
LLL	Au-25		99.4	23.	.4	9.7	99.62
LLL	Cu-69		99.4	37.	.5	9.9	99.58
LLL	Au-73		99.2	23.	3.6	9.8	99.45

COMMENT ON PAPER BY BUCKMELTER, *et al*

A comment was made regarding the cleaning of surfaces after preparation and it was emphasized that the cleaning must be performed before the surface dries out. Any contaminate which is on the surface in the form of a solution which subsequently dries out will be extremely difficult to remove. It was also pointed out that hydrocarbon contamination can be measured very readily in the wavelength region from 3.4 to 3.5 micrometers due to the strong absorption of hydrocarbons at that wavelength and that probing on 3.8 micrometers may still provide a sensitive test of hydrocarbon contamination. A further comment which was made offers the intriguing possibility that the reduced corrosion of diamond-turned mirrors may actually be due to the effect of the residual oil layer which remains on the mirror after the turning process.

2.6 SLIDE-POSITION ERRORS DEGRADE MACHINED OPTICAL COMPONENT QUALITY

J. B. Arnold
P. J. Steger

Fabrication Systems Development Department
Y-12 Development Division

R. R. Burleson

Laboratory Development Department
Y-12 Development Division

Oak Ridge Y-12 Plant
Oak Ridge, Tennessee 37830

An ultraprecision lathe is being developed at the Oak Ridge Y-12 Plant[a] to fabricate optical components for use in high-energy laser systems. The lathe has the capability to produce virtually any shape mirror which is symmetrical about an axis of revolution. Two basic types of mirrors are fabricated on the lathe; namely, (1) the mirrors which are machined using a single slide motion (such as flats and cylinders), and (2) the mirrors which are produced by two-coordinated slide motions (such as hyperbolic reflectors; large, true-radius reflectors, and other contoured-surface reflectors). The surface-finish quality of typical mirrors machined by a single axis of motion is better than 13 nm, peak to valley, which is an order of magnitude better than the surface finishes of mirrors produced by two axes of motion. Surface finish refers to short-wavelength-figure errors that are visibly detectable. The primary cause of the inability to produce significantly better surface finishes on contoured mirrors has been determined as positional errors which exist in the slide positioning systems. The correction of these errors must be accomplished before contoured surface finishes comparable to the flat and cylinder can be machined on the lathe.

Key words: Controlled environment; diamond machining; machined optics; nondistortion part support; position errors; quality and compatible part material; quality diamond tools.

1. Introduction

Exceptional-quality mirrors are required for high-energy laser-optics systems. This need has motivated research and development to improve existing production methods and to study and evaluate new techniques that may be applicable. Until recently, because of the intimate relationship between quality of the surface and the performance of the optics, experience has dictated that state-of-the-art polishing techniques will be needed to produce the desired surfaces. New developments in precision machining now indicate that surfaces of competitive quality can be generated using single-crystal diamond tools and specially constructed turning machines.

The Oak Ridge Y-12 Plant, since it is a sophisticated production facility, has the responsibility to develop and utilize precision machining technology. As a result of this obligation, the Plant has maintained a continuing program in the study of machine tools, their theory and operation, with particular attention to analyzing the behavior of machine-tool elements in relation to their overall performance. Part of this program was to study engineering principles as they apply to ultraprecise machining processes where maximum deviation from an idealized shape and size is not to exceed a few microinches. These studies, which involved basic diamond-machining experience using high-quality-edge, single-crystal diamond tools, helped to determine basic requirements for precision machining and led to the development of improved machine components. Significant advances have been made in precision-part machining technology. The data acquired served to establish engineering guidelines for building computer and numerically controlled machine tools that are capable of diamond turning shapes of revolution to a high quality.

Refinements of these machines and development of a total process for machining metal mirrors to the final quality required for laser optics is the motivation for the present development efforts.

2. Basic Criteria for Machining Optics

The basic criteria required for machining optics have been established for several years. Researchers have had reports published that discuss these criteria and define the relative importance of each criterion to the machining process. [1,2][1] Most researchers agree that at least five basic requirements must be met to achieve the capability to produce high-quality machined optics, namely: (1) use of a quality tool, (2) use of a quality and compatible part material, (3) use of a nondistortion part support technique, (4) prevent detrimental influence of the environment on the machining process, and (5) use of a quality machine.

(a) Operated by the Union Carbide Corporation's Nuclear Division for the US Energy Research and Development Administration.

1. Figures in brackets indicate the literature references at the end of the paper.

Quality Diamond Tools

Development of fabrication techniques to produce angstrom-quality edges on diamond tools was a significant milestone in the chain of events leading to optic fabrication by machining. Only with the single-crystal natural diamond has the necessary edge sharpness been produced and maintained to generate high-quality machined surfaces. Even when all the other machining requirements are met, it is not possible to produce quality optics using other known tool materials. The forerunner to the diamond tools used at Y-12 was the biological diamond knife. This knife was employed on a microtome machine which was used to slice very thin layers of suscepted cancer tissue in preparation for evaluation.

The first diamond tools were very similar to the biological diamond knives, with straight cutting edges and small, included edge angles. The use of these tools led to improved revisions; and, in 1967, the first curved tool was used at Y-12. The success obtained with the curved tools encouraged the design and development of various shapes and styles.

A view of two basic styles of diamond tools used at the Y-12 Plant is given in figure 1. The 45° shank tool has been commonly referred to as a "diamond knife" because of its close similarity to the biological diamond knife. The shank is orientated 45° with respect to the part when performing a machining operation. It is generally fabricated with an included edge angle of 78°, a 6° clearance angle, and a 6° positive back rake. Both straight and curved-edge tools are used. The curved-edge tools have radii of 1/16, 1/8, and 3/16 inch and arc lengths of 0.060 and 0.100 inch.

The horizontal-shank diamond tools have edge angles ranging from 77 to 85°, clearance angles ranging from 6 to 16°, and a 3° negative back rake. These tools are obtained with nose radii ranging from 0.001 to 0.032 inch, over 110° of arc, and to infinity for arc lengths of 0.060 to 0.100 inch. If particular needs dictate, special tool geometries and sizes other than the ones described are ordered.

Figure 2 provides a comparison of the edge quality of several items which are known for edge sharpness. It can be seen from the figure that the natural diamond edge is significantly better than the edges on the other items. The answer to the question: "How good are the natural diamond tools?", has been sought for many years. Various microscopes using different magnifications have been employed with limited success until the scanning electron microscope was used. Coating the opaque edge of the diamond with 150 Å of carbon and then 150 Å of gold made it possible to evaluate the edge of the tool at magnifications as high as 30,000X. Figure 3 is a compilation of several electron microscope photographs of a typical natural diamond tool. It can be seen from the figure that the diamond edge has flaws approximately 1/3 microinch (8 nm) in amplitude and 1 microinch (25 nm) in length. These silhouette electron microscope photographs are among the first made of a diamond edge and are believed to be true representations of the edge.

Quality and Compatible Material

Several materials have been machined at Y-12 to determine if they are compatible to the diamond turning process. High-purity, soft, face-center-cubic metals such as gold, silver, copper, lead, and aluminum have been found to be very compatible. Other metals such as high-purity iron, platinum, and nickel were diamond turned but failed to produce the desired optical properties.

Nondistortion Part Support

As the requirements for mirror-figure quality increased, so does the need for the use of nondistortion-part-support techniques. If a mirror is held in a strain during the machining operation, a near-perfect geometry could be machined on the mirror surface which would only distort once the mirror is removed from its machining fixture. To prevent such an incident from happening, several nondistortion support techniques have been investigated and utilized. Of these techniques, the use of a refined conventional vacuum system and the potting of the mirrors into a fixture using two-part castable rubber to hold the mirror in place have been found to have significant advantages over other evaluated techniques.

Vacuum fixtures have been used very successfully to hold mirrors which have a flat back. The face of the fixture must be machined with a network of narrow vacuum grooves which will allow adequate vacuum support with an acceptable amount of mirror distortion. The contact surface of the vacuum fixture is machined flat in order not to distort the back of the mirrors. The back of the mirrors are hand lapped to assure the highest degree of flatness. The vacuum-fixturing technique provides a significant advantage in the fact that it is relatively easy to remove the mirrors from the fixture after machining is completed.

Two-part castable rubber, such as Rubberjel[b] and DPR 336[c], has been used to hold mirrors in place during machining. Rubber in a liquid form is placed in a cavity in either the back of the mirror or in the fixture face prior to forcing these surfaces together. The rubber is allowed to cure at room temperature before the mirror and fixture are mounted on the machine. Metal safety catches are installed "finger tight" prior to machining. Once the machining process is complete, the mirror and fixture must be removed by forcing water into special part-removal grooves which have been provided in the face of the fixture. Figure 4 is an illustration of a nondistortion-part-support fixture.

(b) A product of the L. D. Caulk Company, Milford, Delaware 19963

(c) A product of Hardman Incorporated, Belleville, New Jersey 07109

Controlled Environment

Any influence of the environment must be controlled to prevent a detrimental effect on the diamond machining process. Effects of external vibration, temperature variation, humidity, and cleanliness are controlled on the diamond turning machines. External vibration is reduced by supporting the machines on pneumatic isolators (air bags), and the machines are housed in laboratories which are equipped with control systems that maintain a constant temperature, low humidity, and high cleanliness. Cutting fluids used in the machining process are closely controlled both for thermal stability and cleanliness. In areas where the environment cannot be satisfactorily controlled, partial to total flooding of critical components with thermally controlled fluids will successfully maintain machine stability [3].

Quality Machine

The machine on which diamond turning is performed must have the capability to rotate a part and position a tool accurately and vibration free.

The air-bearing spindle with an isolated motor and noninfluencing drive, has been used successfully to meet the part-rotating accuracy requirements. To eliminate vibration, which could be caused by an unbalanced rotary part, the parts are dynamically balanced at the speed at which they will be machined. A noncontact capacitance probe and storage oscilloscope are used in this dynamic balancing process. The radial motion of the lathe faceplate is measured at a low rpm and stored in the oscilloscope. The radial motion is then measured at the speed at which the part will be machined and again stored in the oscilloscope. If the recorded trace of the radial motions do not coincide, balance weights are added to the spindle. This process is repeated until the traces coincide within a couple of microinches [4].

Several machines have been used for machining optics which employ various tool positioning techniques. The Moore lathe, which is one of Y-12's most recently developed optical machining lathes, is seen in figures 5 and 6. The lathe consists primarily of a standard Model 3 Moore measuring machine base, modified for turning by the addition of an air-bearing spindle mounted horizontally on a cut-down vertical column. An ultraprecision Moore rotary table (C motion) has been installed on the bed of the lathe to allow the diamond tool to be rotated as it is moved in an X-Y plane, where the X motion is normal to and the Y motion is parallel to the spindle axis of rotation. A minicomputer is used in conjunction with positioning motors to control the X, Y, and C positional displacement of the tool when performing complex contouring operations; but, to perform simple facing and cylindrical operations, variable-speed (0 to 8.5 in/min) DC slewing motors are employed. The lathe has the capability to machine a 0.5-microinch (13-nm)-peak-to-valley (p-v) finish on a flat mirror, and a 2 to 4-microinch (50 to 100-nm)-p-v finish on a contoured mirror. Although this machine incorporates one of the most advanced and accurate positioning systems used at Y-12, errors in the system are believed to be the primary limiting factor in producing better-quality contoured surfaces.

An investigation was conducted to correctly define the X and Y positioning errors and to determine the cause of these errors. The first steps of the investigation consisted of the fabrication and evaluation of two large spherical radius mirrors. The mirrors were machined on the Moore lathe using stepping motors to drive the X and Y lead screws, and were first evaluated using the knife-edge inspection technique. A photograph of the inspection results of one mirror is presented in figure 7. The evaluation results indicated that periodic surface irregularities existed across the face of the mirrors. The knife-edge inspection technique is basically qualitative in nature; therefore, to define the amplitude of the wave, a precision-air-bearing LVDT with a sensitive amplifier and recorder was used.

Once the errors were defined, an additional large-radius mirror was machined on the lathe. The outer portion of the mirror surface was machined using the same parameters as for the first mirrors, while the inner portion was machined with the environmental control system turned off. It was first thought that the cycling of the temperature controller may have caused the geometry of the machine to fluctuate during the machining operation. Inspection results of the mirror revealed that the environmental control system had no effect on the surface irregularities in question. Efforts to correlate the irregularities with features of the Moore lathe were conducted by using a precision optical flat and the air-bearing LVDT. The air-bearing LVDT was fastened to the bed of the lathe in such a position that it would indicate Y movement of the bed as it moved along the face of the optical flat, which was fastened to the lathe column and parallel to the X travel. The LVDT indicated that the lathe bed had very little Y movement as it advanced in the X direction. A total indicator reading of less than 6 microinches (150 nm) was recorded over 14 inches (355.6 mm) of travel. The irregularities detected on the surfaces of the contoured mirrors could not be attributed to this straightness error.

Due to the fact that these contoured mirrors were produced by movements of both the X and Y axes, it was decided that the bed movement should be evaluated with both axes in motion. To aid in acquiring these data, a special control tape was fabricated that would drive the X axis 33 1/3 microinches (830 nm) while the Y axis advanced only 1/3 microinch (8.3 nm). This slope is representative of the range of slopes involved on the test mirrors. By positioning the optical flat at a 100-to-1 slope (with respect to the X axis) it was possible to measure and record incorrect positional movement of the bed in the Y direction as the LVDT moved along the optical flat. Figure 8 shows the results obtained from this measuring setup. It can be seen from the figure that the predominant errors, which repeat every 0.25 inch (6.35 mm) of the table travel in the X direction, have an amplitude of 4 microinches (100 nm), and errors which repeat every 1/12 inch (0.083 inch, 2.1 mm) have an amplitude of 2 microinches (50 nm). Much smaller errors of approximately 1 microinch (25 nm) in amplitude are very irregular and appear to repeat every 0.1 inch (0.25 mm). A careful evaluation of the figure will reveal that there is not one small wave which is repeating in every 0.1 inch (0.25 mm), but about 25 small waves which are repeating every 0.25 inch (6.35 mm).

To aid in determining the cause of the errors, a schematic diagram of the Moore lathe's X and Y positioning systems was drawn for evaluation (see figure 9). By labeling each component of the positioning systems with the proper number of revolutions made as

the bed advanced 1 inch (25.4 mm) in the X direction, it can be seen that the repeatable errors coincide identically with the revolutions and teeth engagement of the Y-axis drive train components. The Y primary worm makes four revolutions as the bed advances 1 inch (25.4 mm) in the X direction, and 12 teeth of the Y primary gear engage with the triple-thread worm over the same distance. The smaller waves correspond to each revolution of the Y secondary worm which makes 100 revolutions as the table travels 1 inch in the X direction.

Several revisions have been made to minimize the positioning errors. DC-encoded torque motors were installed on both X and Y axes, and an ultraprecision (200:1 reduction) primary worm and gear was installed on the Y axis. A series of slope tests were conducted to determine the value of each revision. These tests were first conducted before any revisions were made. Then, tests were rerun when the torque motors were installed and also when the new worm-and-gear system was installed. Results of these tests are reported in figures 10 through 13.

It can be seen from the figures that small-wavelength errors were eliminated when the DC torque motors were used. The reason that these errors were eliminated was because the secondary worm-and-gear system, which caused the errors, was bypassed, as shown in figure 14. It can also be seen from figures 10 through 13 that the new primary worm and gear did not reduce cyclic errors as had been anticipated. The amplitude of the errors produced by the new worm and gear is about the same as the amplitude of the errors produced by the original worm and gear, but have a shorter wavelength. The increased error frequency did cause the new worm and gear to be less desirable. It can be concluded from the test results that the most desirable surface finish could be produced when the DC torque motors and the original (40:1 reduction) worm and gear are used.

Two contoured mirrors, one with a 133-inch (3.38-m) radius and the other with a 418-inch (10.6-m) radius were machined and evaluated to determine if the surface finish of contoured mirrors would be improved, as had been indicated by later slope test results. Leitz-surface-finish photographs of the two mirrors were compared to surface-finish photographs of respective radius mirrors which had been machined using the original stepping motors to drive the lathe's positioning systems. A significant improvement in the longer-wavelength surface (figure 15) was observed. The data are reported in figures 15 and 16. The surface variations of the mirrors machined using the DC torque motors are estimated at 2 to 2.5 microinches (50 to 75 nm), peak to valley (p-v), whereas the surface finish of the mirrors machined using the stepping motors is estimated at 2.4 to 3.2 microinches (60 to 80 nm), p-v, with the difference due primarily to an absence of the longer-wavelength ripple. A higher degree of improvement was observed for the smaller-radius mirror than for the larger-radius or flatter-surface mirror due to the greater slope of the surface.

3. Future Work

The success obtained by using the DC-encoded torque motors to improve the surface finish of parts machined on the Moore lathe has been very encouraging. It appears likely that if continued short-wavelength contour improvement takes place, a better power transfer medium other than the existing worms and gears must be used. The possibility and practicality of using reduction rollers to drive the lead screws have been discussed with engineers from the Moore Special Tool Company. It appears practical at this time, but needs to be studied further. The possibility of incorporating a control system which will have laser interferometers as its positional sensing components will also be studied. Hardware required for the installation of laser interferometers on the Moore lathe has been designed and fabricated, and installation is under way. The basic layout of the installation is shown in figures 17 and 18. It can be seen in the figures that both X and Y table displacement will be monitored in horizontal planes which are relatively close to the respective slide levels. It was first felt that the laser interferometers should monitor slide displacement at tool height; but, after considerable study, such a setup was deemed to be impractical. Straightness tests of the slides indicate that pitch is very low and also repeatable; therefore, Abbe offset should not be a problem.

After installation, the laser interferometers will determine the X and Y tool displacement. The tool-displacement signals will be transmitted to a dynamic error-monitor system. The system will resolve an error signal by comparing the measured tool displacement to the commanded displacement. The error signal will be used to modify the command signal, thereby reducing the error in displacement. The electrical hardware for the system has been fabricated and set up temporarily on the Moore lathe to measure the slide-positioning errors. The temporary setup consisted of a laser interferometer, a fringes-to-inches converter, an error monitor, and a chart recorder. A block diagram of the setup, used to determine the errors in the Y-axis positioning system, is given in figure 19. This setup compares where the machine tool control system commanded the slide to go with where the slide actually went, as seen by the laser interferometer. This comparison is done on a continuous basis. The basic resolution of the system is one microinch when using a resolution extender on the laser interferometer. Inspection results obtained from the evaluation of both the X and Y axes are reported in figures 20 and 21. It can be seen from the figures that both axes have cyclic errors which correspond to each revolution of the lead screws. Short-wavelength errors are more apparent in the "b" figures where the horizontal scale is amplified. It can be seen in these figures that these short-wavelength errors correspond to each revolution of the triple-thread worms which drive the primary gears and the engagement of each thread on the worm. These errors, which have an amplitude of less than one microinch, will not be eliminated by this error-monitoring system. The small errors must be eliminated by the use of better power-transfer mediums such as reduction rollers.

4. Conclusions

Mirror manufacturing by the single-point diamond machining process is in an early stage of development, but success which has already been achieved proves that this process has a significant advantage in producing large, flat mirrors and contoured mirrors, such as hyperboles and parabolas, over conventional fabrication techniques.

5. References

[1] Bryan, J. B., Clouser, R. R., and Holland, E.; "Spindle Accuracy", *American Machinist,* pp 149 - 164; McGraw-Hill Inc, New York, Special Report Number 612; December 4, 1967.

[2] Warmbrod, W. M. and Williams, R. L.; *Laser Fusion Mirror Machining,* Y-DA-5130; Union Carbide Corporation-Nuclear Division, Oak Ridge Y-12 Plant, Oak Ridge, Tennessee; January 10, 1973.

[3] Bryan, J. B., Donaldson, R. R., McClure, E. R. and Clouser, R. R.; *A Practical Solution to the Thermal Stability Problem in Machine Tools,* MR72-138; Society of Manufacturing Engineers, 20501 Ford Road, Dearborn, Michigan 48128 (1972).

[4] Lewis, T. G.; *Ultra-Precision Machine Tool Elements and Machining Processes,* Y-1611; Union Carbide Corporation-Nuclear Division, Oak Ridge Y-12 Plant, Oak Ridge, Tennessee (1968).

6. Figures

(a) Typical diamond tools used for microinch machining.

(b) Photomicrograph of edge of diamond tool; 475X.

Figure 1. View of two typical diamond tools and a photomicrograph of the edge of a diamond tool.

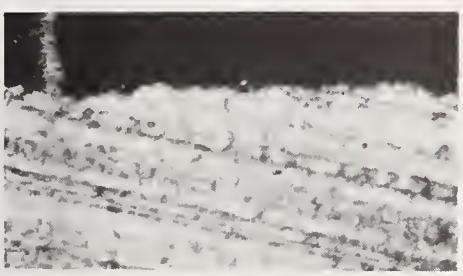

(a) Commercial carbide tool.

(b) Razor blade (stainless steel).

(c) Commercial diamond tool.

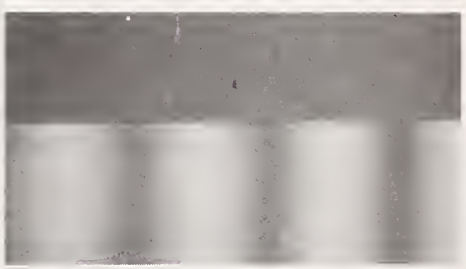

(d) Natural diamond tool.

Figure 2. Comparison of the edge quality of four items (425X).

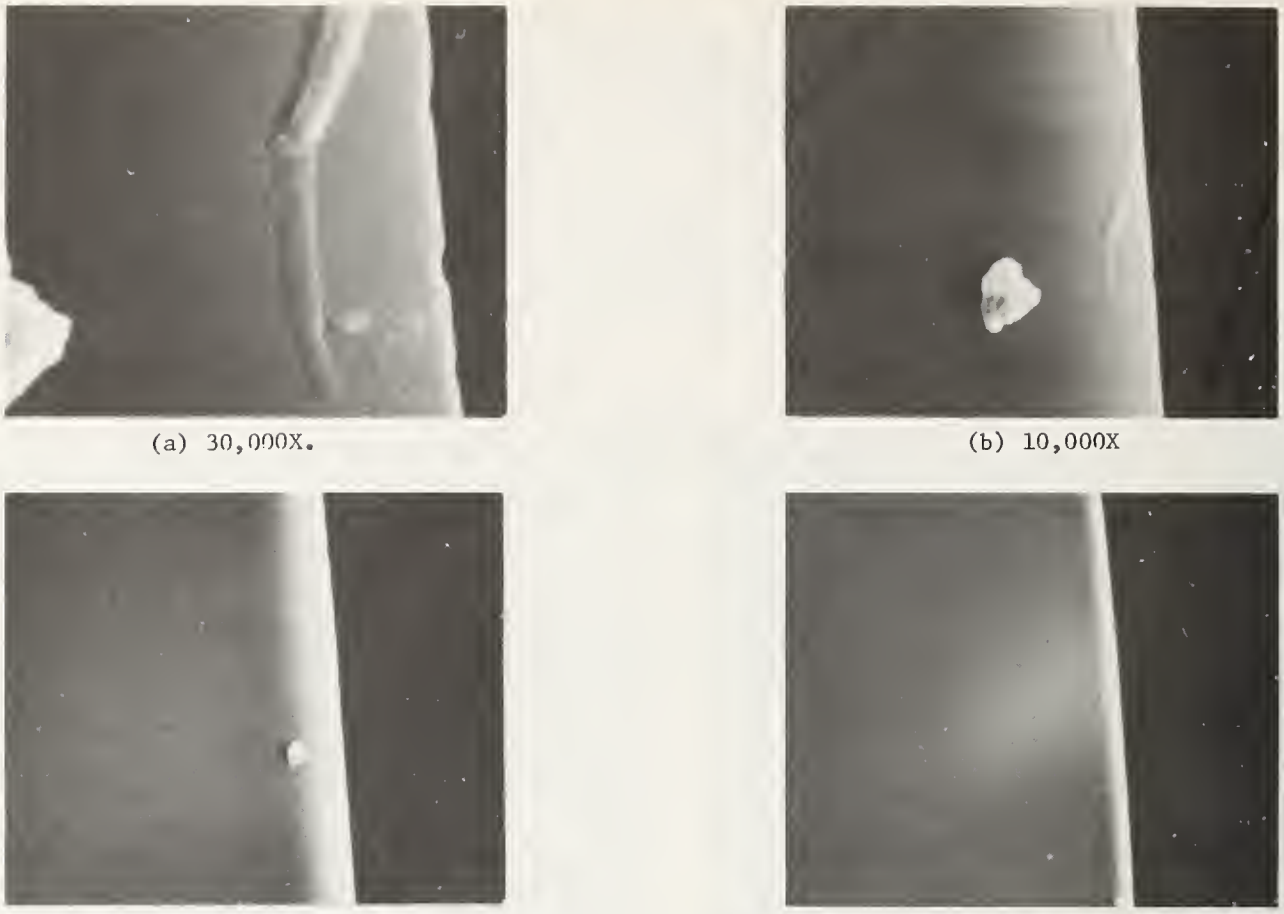

(a) 30,000X.

(b) 10,000X

(c) 3,000X.

(d) 1,000X.

Figure 3. Several electron microscope photographs of a typical natural diamond tool.

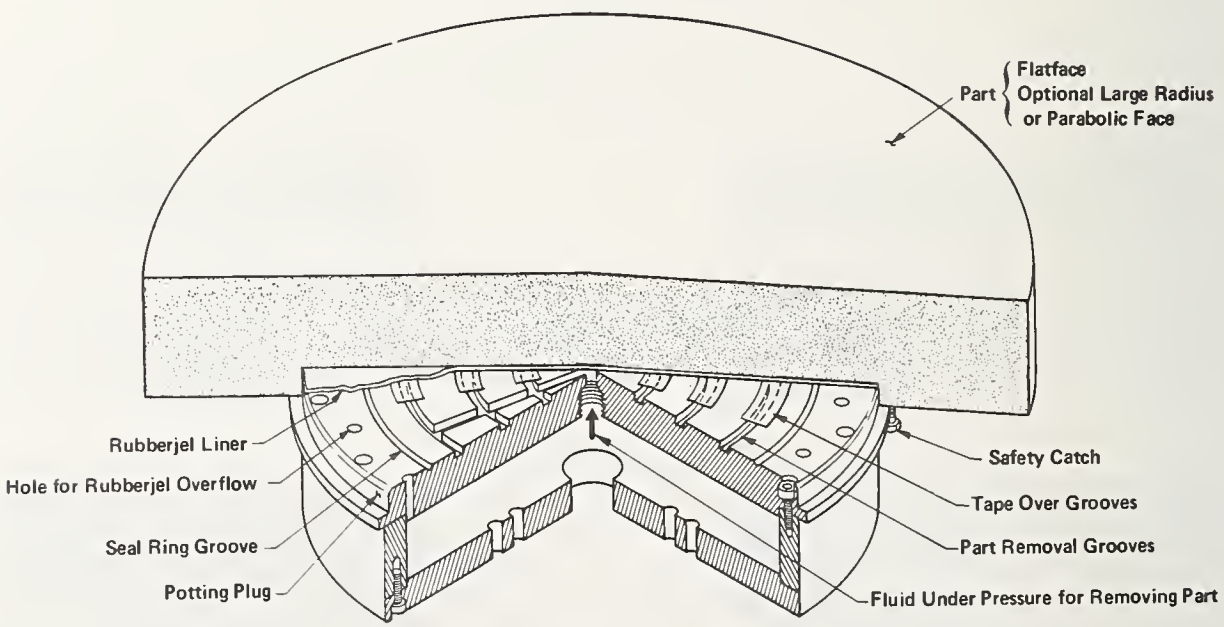

Figure 4. Part support for mirror machining.

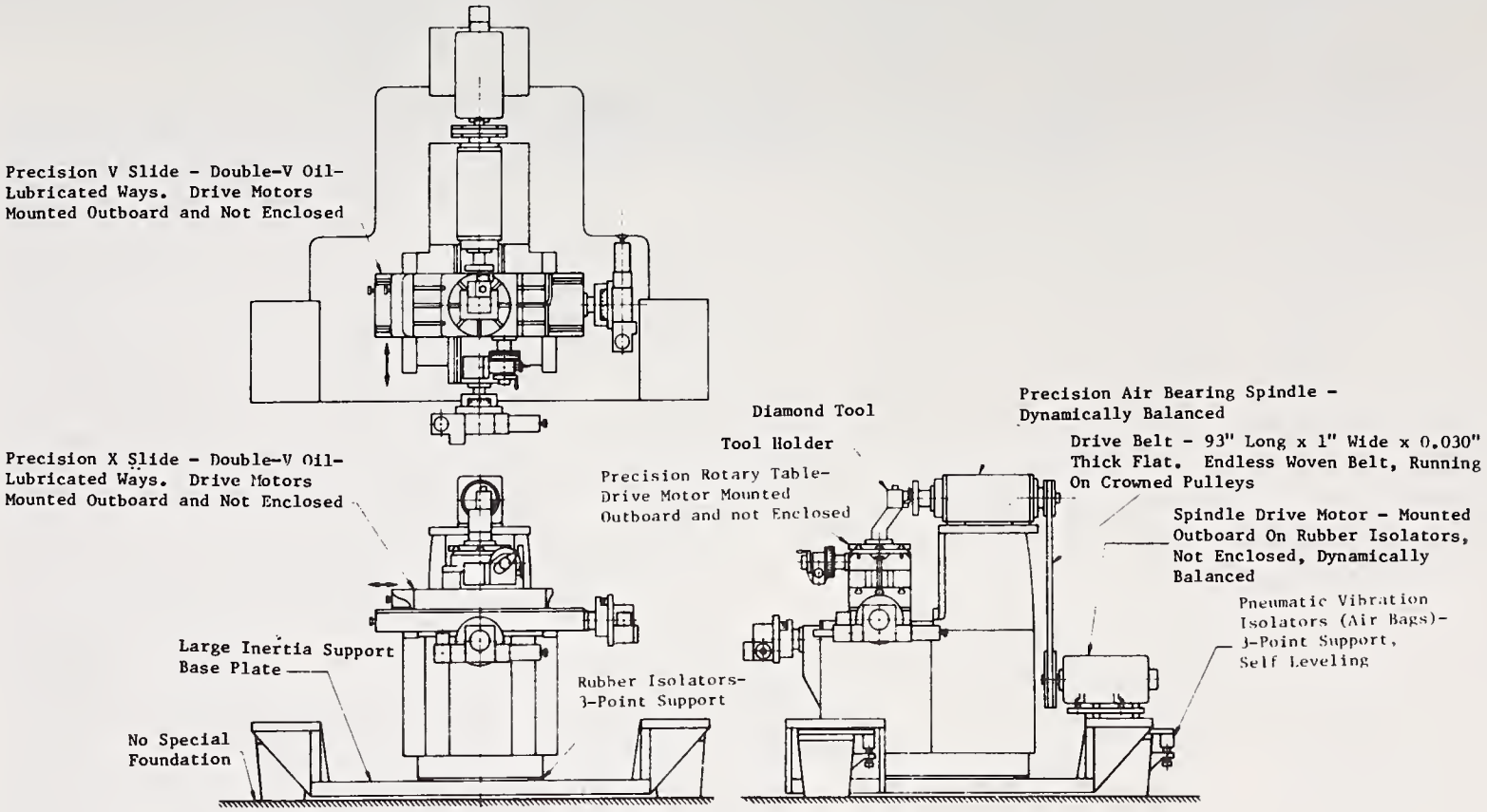

Figure 5. Principal components of the Moore machine lathe.

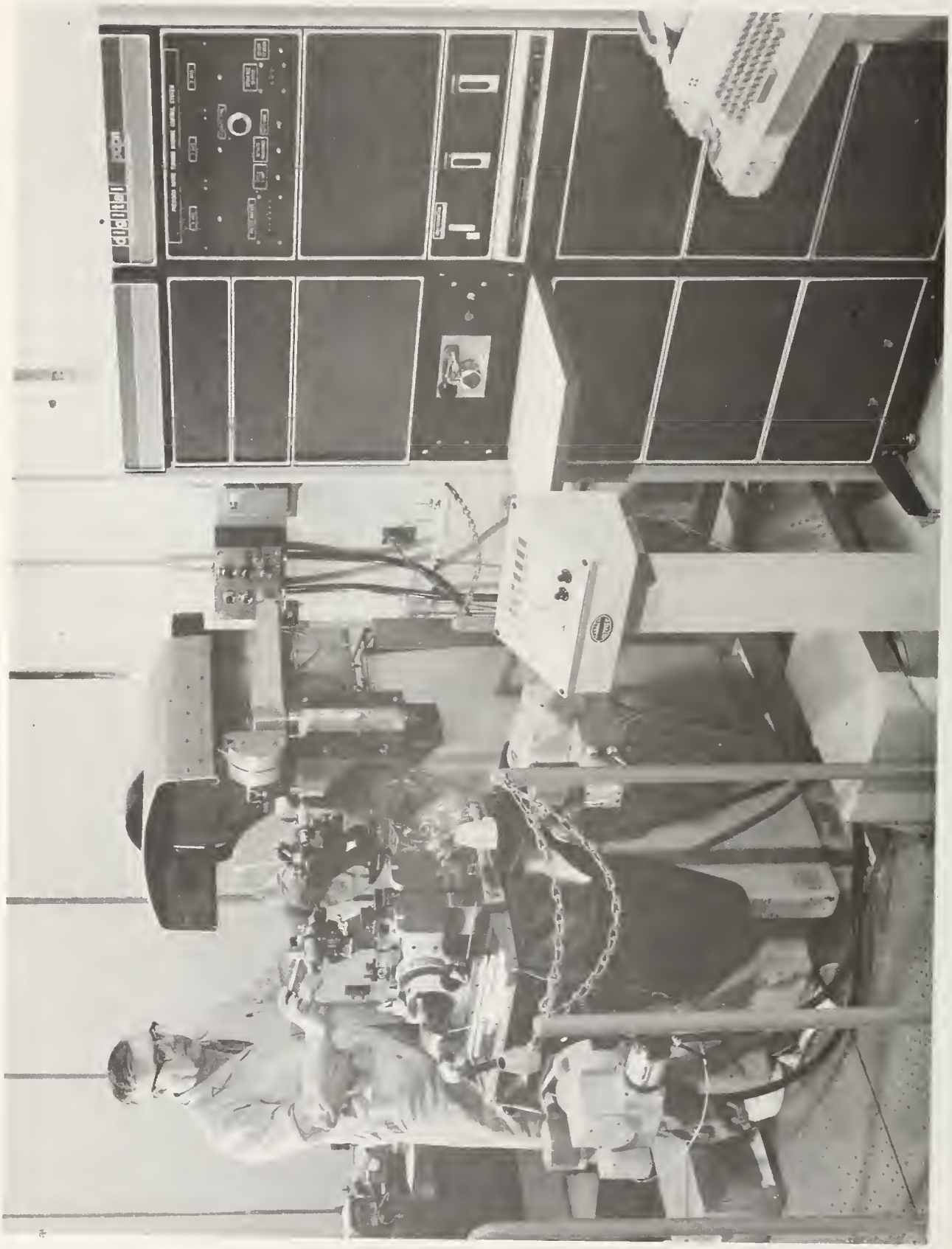

Figure 6. Overall view of the Moore machine lathe.

Figure 7. The knife-edge photograph indicates waves across the machined surface. [Radius of curvature 133.8 inch (3.398 m); diameter-15.5 inch (0.39 m)].

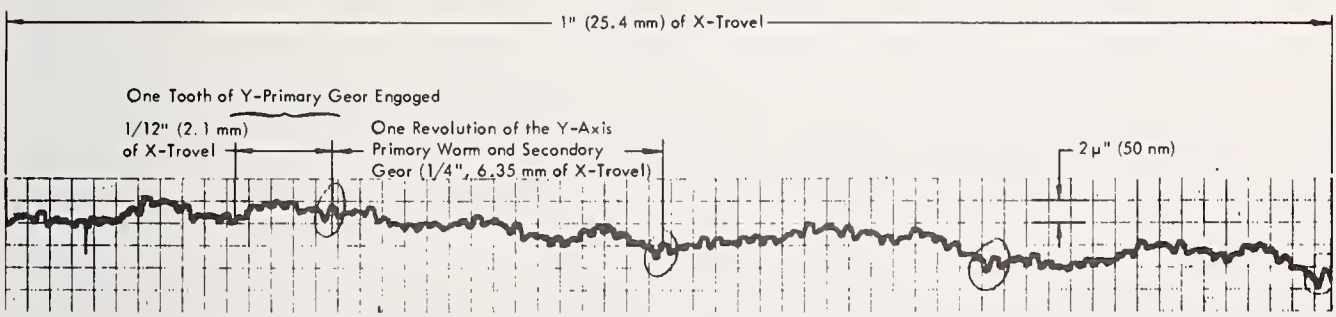

Figure 8. Error plot of the Y-axis positioning system.

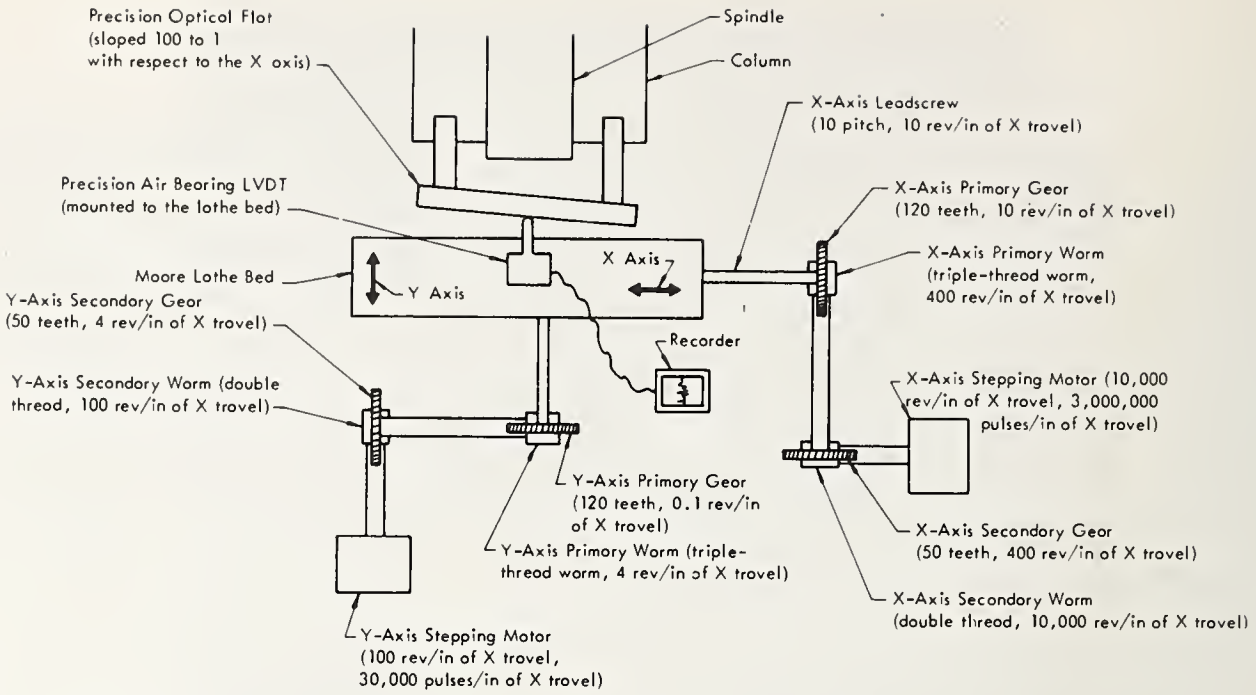

Figure 9. Moore lathe's X and Y drive systems and the measuring setup used to determine the positioning errors illustrated in figure 8.

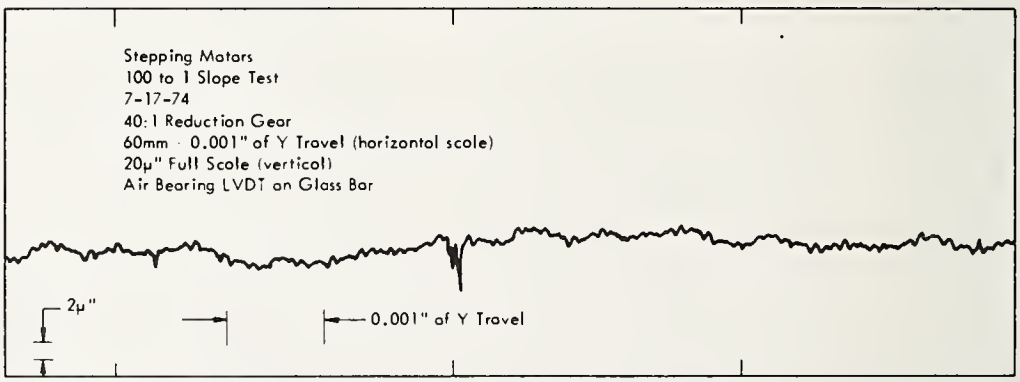

Figure 10. Slope test results. [The stepping motors and the original (40:1 reduction) worm and gear were used during this test.]

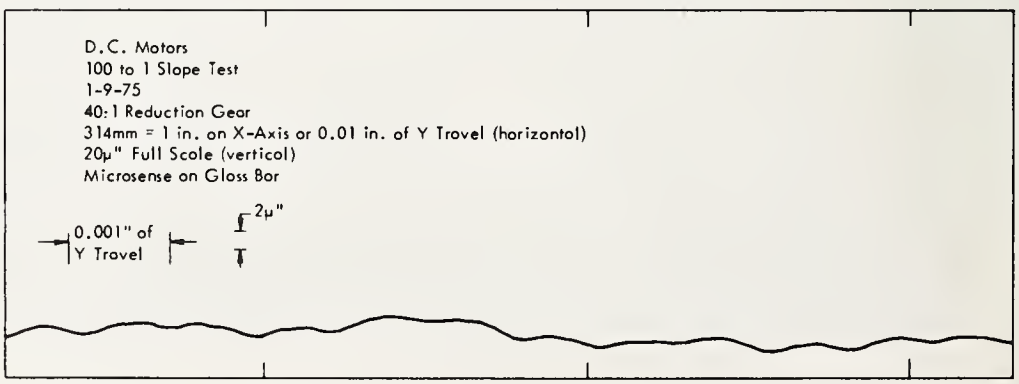

Figure 11. Slope test results. [The new dc encoded torque motors and the original (40:1 reduction) worm and gear were used during this test.]

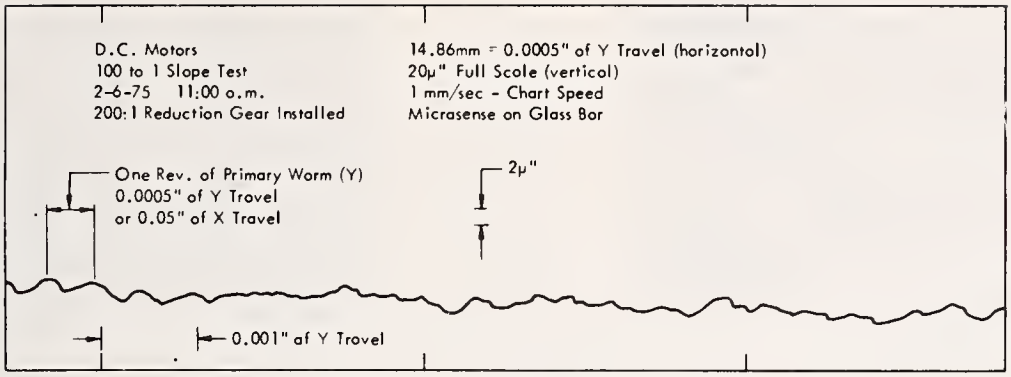

Figure 12. Slope test results. [The new encoded dc torque motors and the new (200:1 reduction) worm and gear were used during this test.]

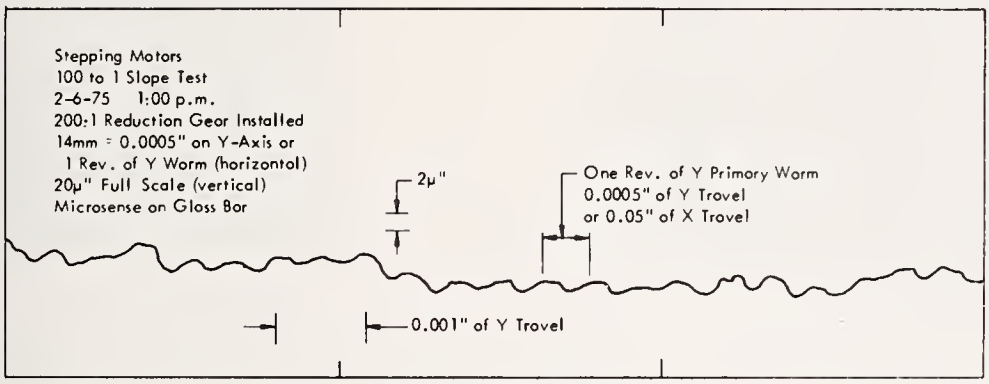

Figure 13. Slope test results. [The stepping motors and the new (200:1 reduction) worm and gear were used during this test.]

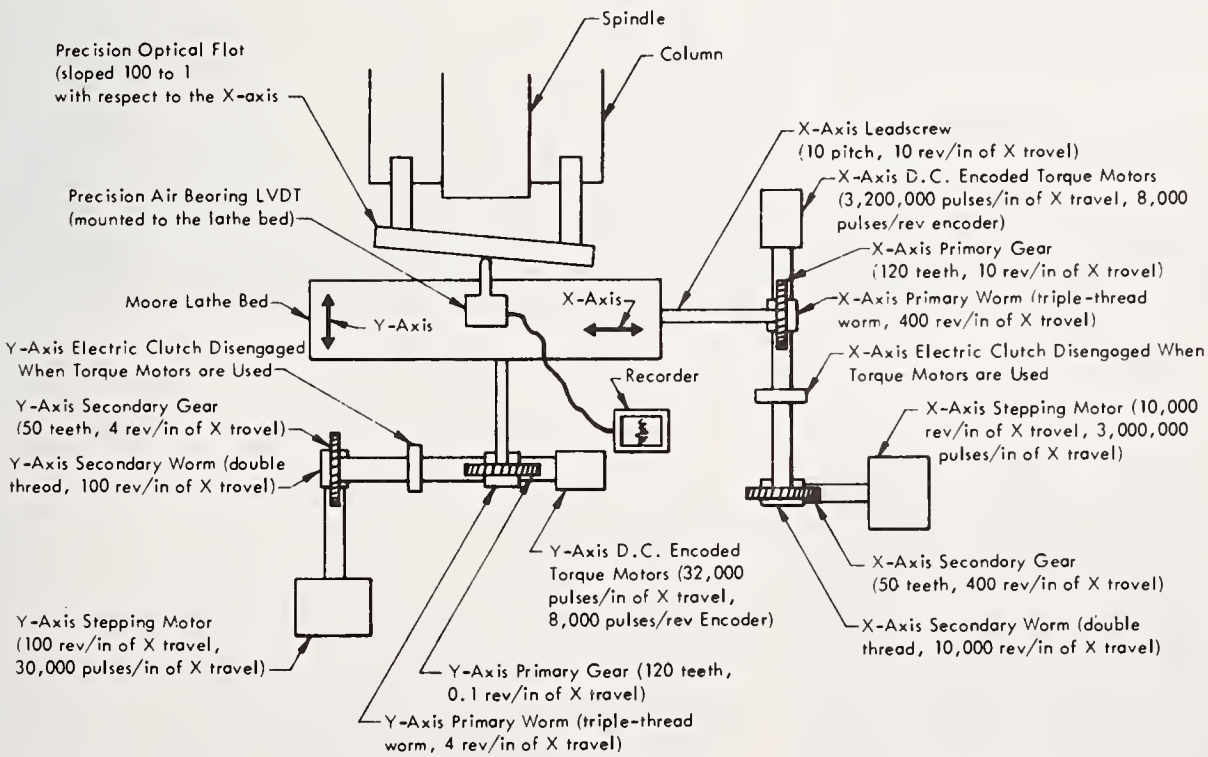

Figure 14. Schematic of equipment arrangement for slope tests.

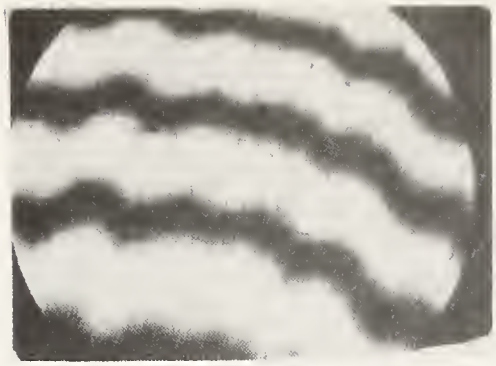

Near the center
3.0 microinches, P to V
Stepping motors (50X)

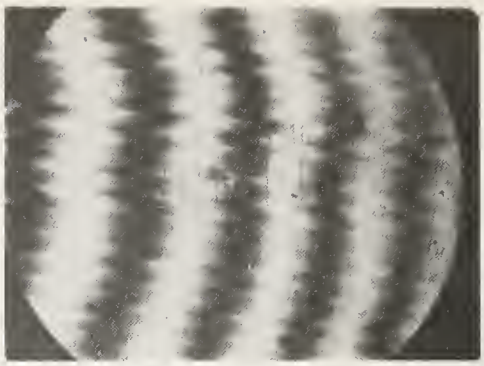

Four inches from the center
3.2 microinches, P to V
Stepping motors (50X)

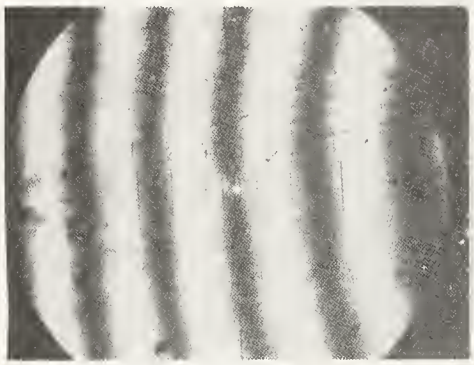

Near the center
2.5 microinches, P to V
dc torque motors (50X)

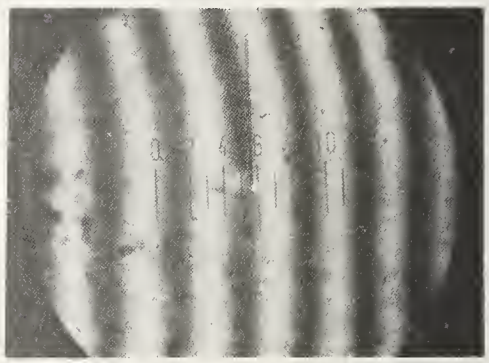

Four inches from the center
2.0 microinches, P to V
dc torque motors (50X)

Figure 15. The surface finish of a 133-inch-radius mirror machined using dc torque motors to drive the lathe slides is better than the surface finish of the mirror machined using stepping motors.

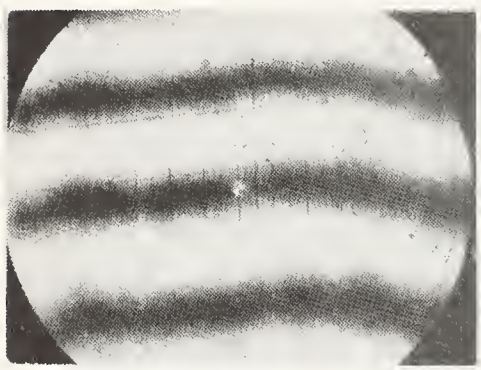

Near the center
2.4 microinches, P to V
Stepping motors (50X)

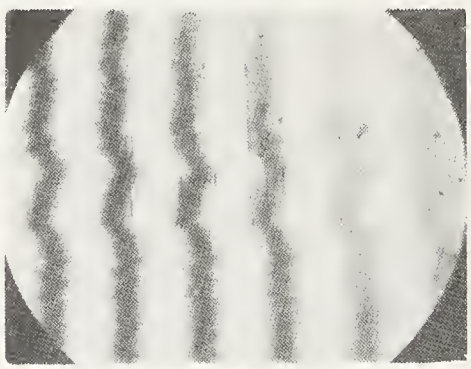

Four inches from the center
2.8 microinches, P to V
Stepping motors (50X)

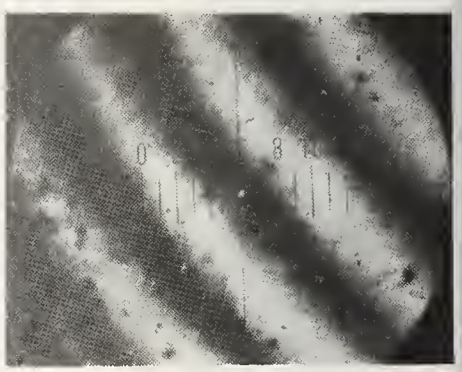

Near the center
2 microinches, P to V
dc troque motors (50X)

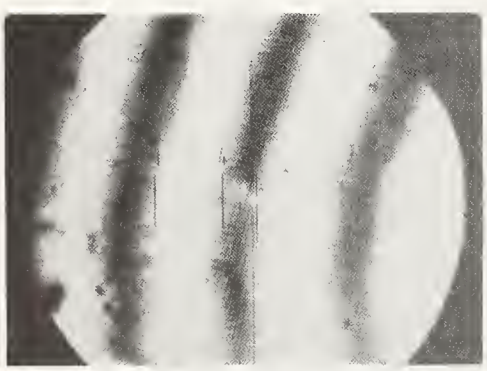

Four inches from the center
2.2 microinches, P to V
dc torque motors (50X)

Figure 16. The surface finish of the 418-inch-radius mirror machined using dc torque motors to drive the lathe slides is better than the surface finish of the mirror machined using stepping motors.

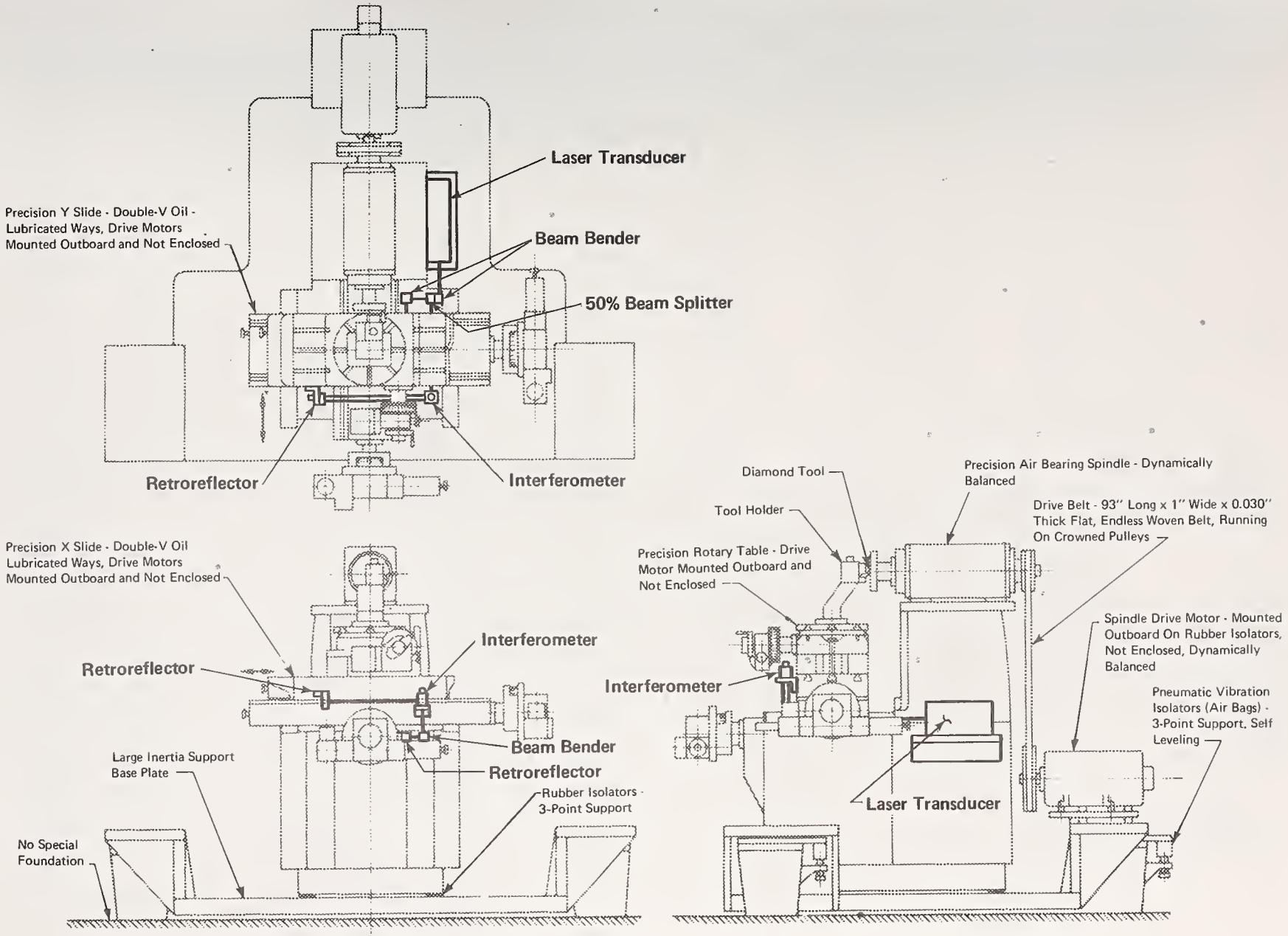

Figure 17. The laser interferometers monitor X and Y slide displacement in horizontal planes which are relatively close to respective side levels.

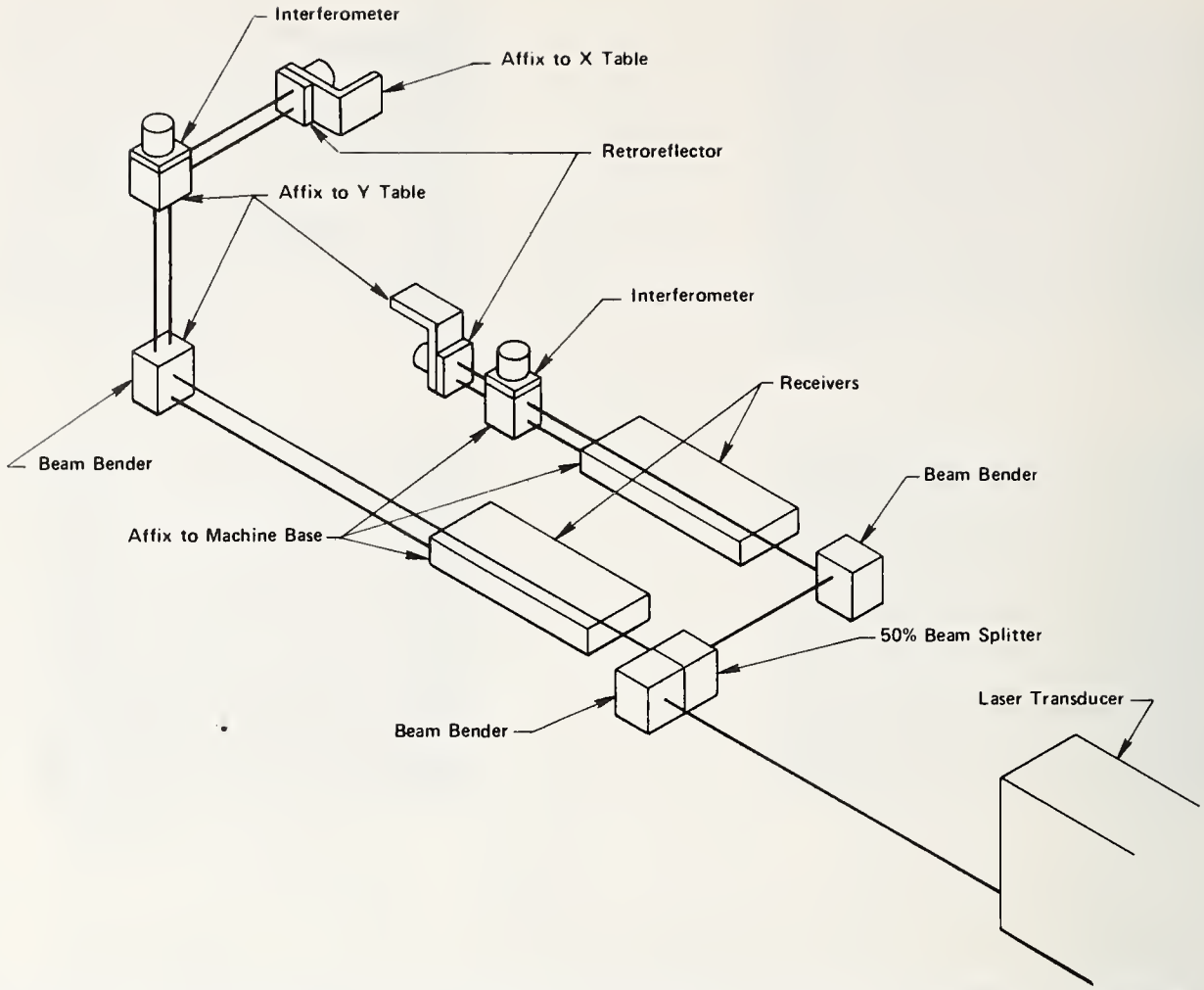

Figure 18. The components of the laser interferometer system are arranged to determine displacement of both the "X" and "Y" axes.

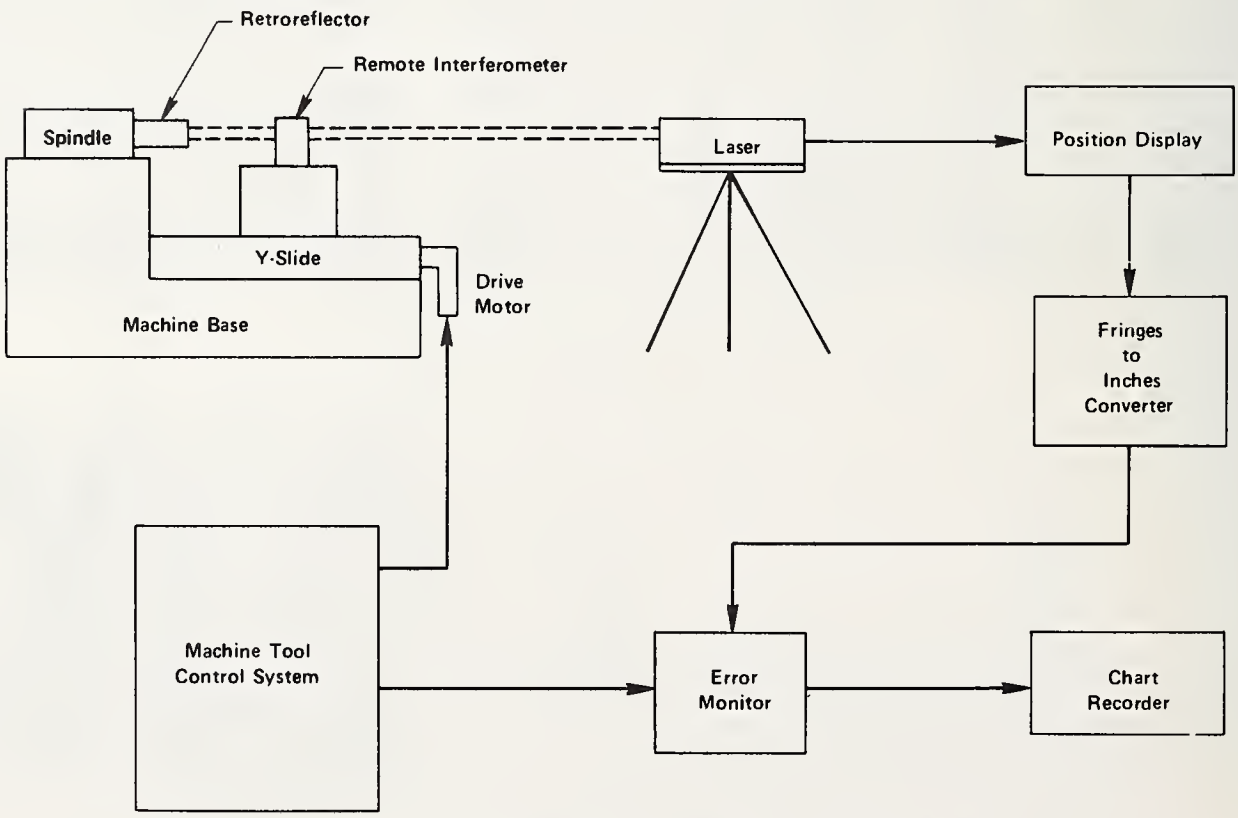

Figure 19. Dynamic error monitor block diagram.

a. Positioning error of X-axis lead screw.

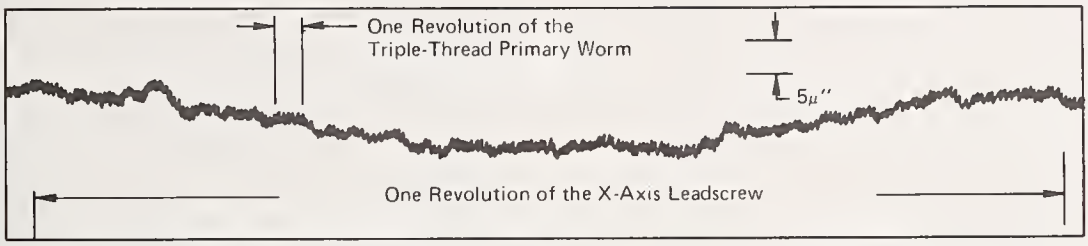

b. Positioning error of X-axis, primarily worm and gear.

Figure 20. Cyclic positional errors as detected by the dynamic error system correspond to revolutions of X-axis drive train components.

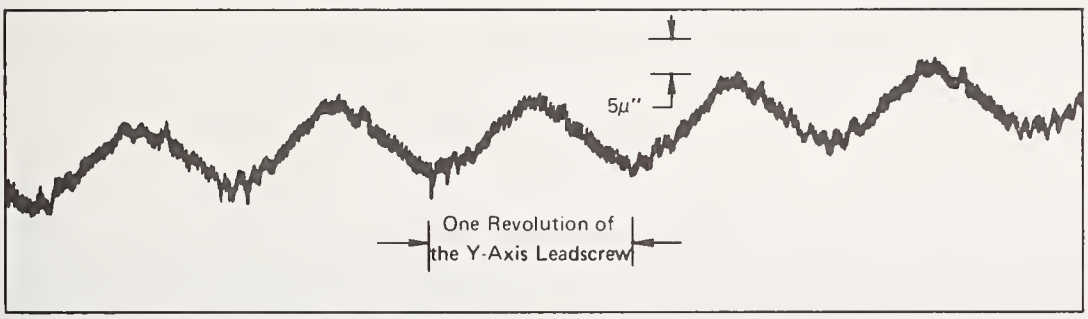

a. Positioning error of the Y-axis lead screw.

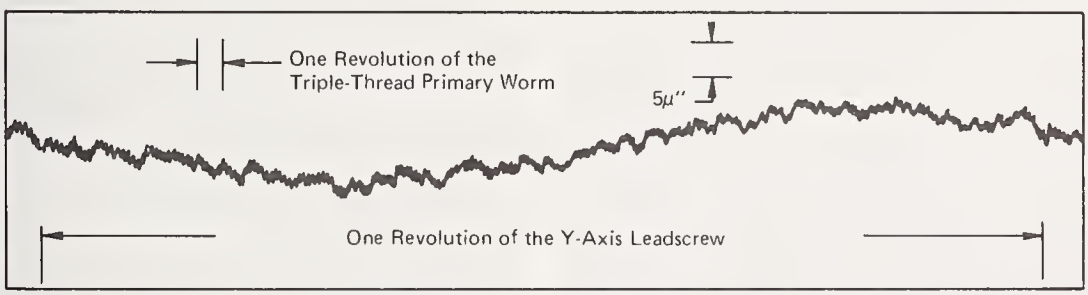

b. Positioning error of the Y-axis, primarily worm and gear.

Figure 21. Cyclic positional errors correspond to revolution of drive train components.

COMMENTS ON PAPER BY ARNOLD, et al

A number of the particulars of the diamond turning process and the machine parameters used in this study were discussed.

2.7 ULTRASONIC CLEANING OF OPTICAL SURFACES

W. E. K. Gibbs and A. D. McLachlan

Materials Research Laboratories
Department of Defense
Ascot Vale, Victoria, Australia

During the formal proceedings of the 1975 Symposium on Laser Induced Damage in Optical Materials, Dr. A. H. Guenther presented some recent results on the degradation of polished optical surfaces by ultrasonic cleaning procedures. This information was supplied to him by Dr's. W. E. K. Gibbs and A. D. McLachlan of the Materials Research Laboratories of the Department of Defense, Commonwealth of Australia. Materials studied included OFHC copper, beryllium copper, zirconium copper, stainless steel, kanigen and fused quartz. Results indicate that ultrasonic cleaning degrades polished surfaces, and if the cleaning process is vigorous enough for a sufficient duration of time, subsurface fracture introduced in the grinding process is made quite evident. At the conclusion of the transmission of this correspondence, a discussion on the subject of ultrasonic cleaning ensued.

Key words: Laser damage; metal mirrors; subsurface structure; ultrasonic cleaning.

1. Introduction

This ad hoc preliminary investigation was to determine the extent of ultrasonic cleaning damage on various materials. Damage had previously been observed on OFHC copper.

2. Samples

Samples tested were: OFHC copper, beryllium copper (Berylco 25-hardened), zirconium copper, stainless steel, "Kanigen" electroless nickel on copper, fused quartz (Vitreosil). The metal samples were 1" diameter x 1/2" thick, while the quartz was 1/2" x 1/2" x 1/8".

3. Polishing

Metal samples were polished on a "2 mm"-pitch lap using glycerol as the medium for "Linde A" alumina abrasive. Final polishing was with a "5 mm"-pitch lap using "Linde B" abrasive with glycerol as the medium. The quartz was polished on a "5 mm"-pitch lap with cerium oxide and water.

4. Microscopy and Cleaning

The metal samples were indexed to locate a given spot on the polished surface and photographs were taken on a Reichert MeF microscope by using the interference contrast technique (Nomarski). Two samples of fused quartz were polished, only one of which was ultrasonically cleaned. The quartz samples were coated with a thin coating of aluminum in order to enhance the reflectivity of the surface. Ultrasonic cleaning consisted of 3 intervals of cleaning of 15 minutes each in detergent, distilled water, and AR methanol. Samples were individually cleaned in a Branson Model D-100 ultrasonic cleaner.

5. Results

Micrographs clearly show the presence of pitting after ultrasonic cleaning, particularly in the softer materials, e.g., zirconium copper and OFHC copper. The beryllium copper showed little damage after 45 minutes of cleaning, and was thus cleaned for a further 45 minutes to give the results shown. The damage could be seen with the naked eye under glancing illumination on most of the samples (including fused quartz).

In interpreting the micrographs, it should be noted that the Nomarski technique renders some deep pits as bright spots for the contrast setting chosen.

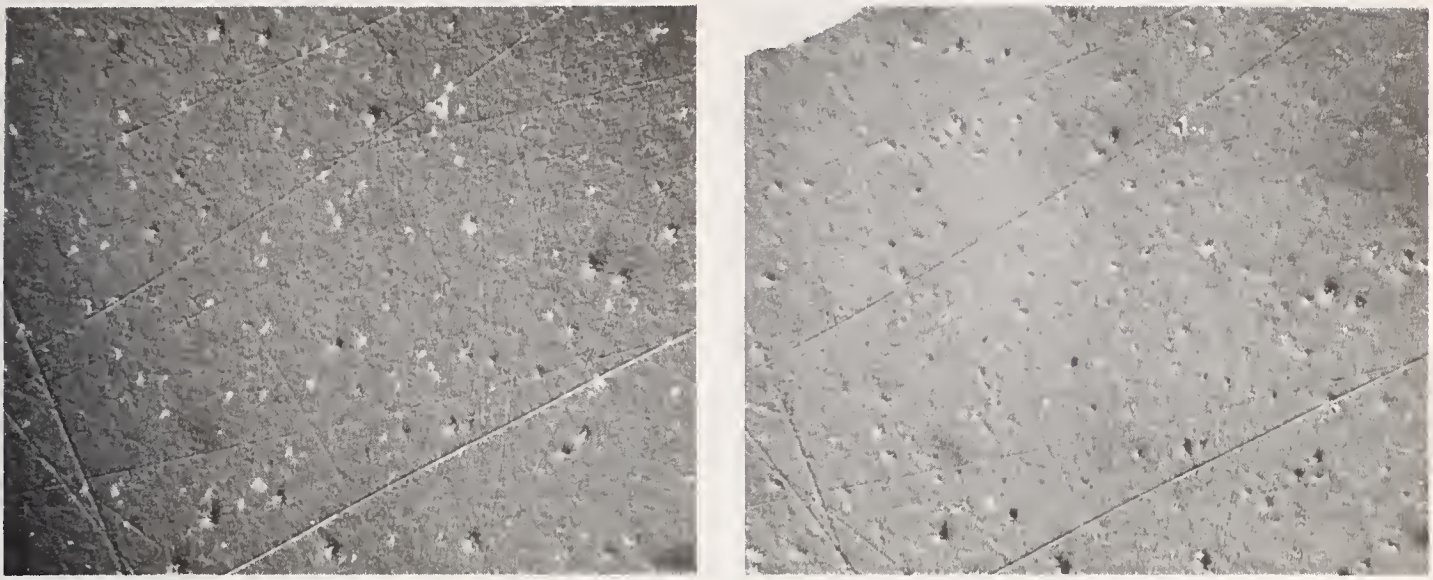

(a) (b)

Figure 1. OFHC copper. (a) As polished. Magnification 150X. (b) After 45 minutes of ultrasonic cleaning. Magnification 150X.

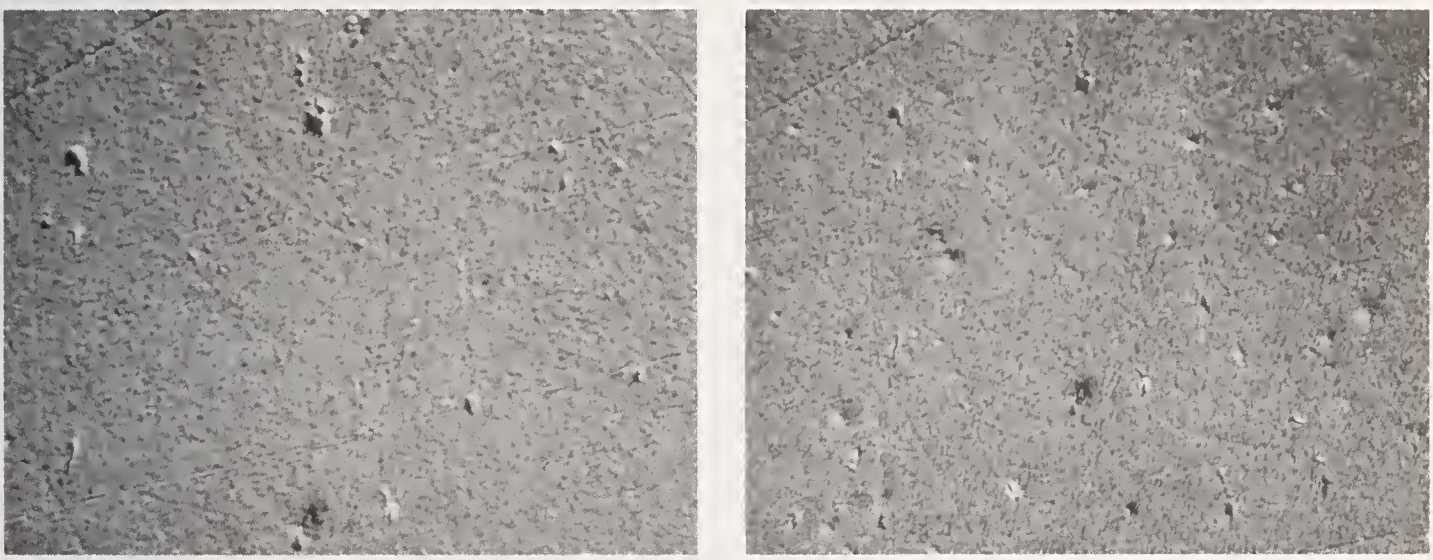

(a) (b)

Figure 2. Another sample of OFHC copper. (a) As polished. Magnification 500 X. (b) After 45 minutes of ultrasonic cleaning. Magnification 400X.

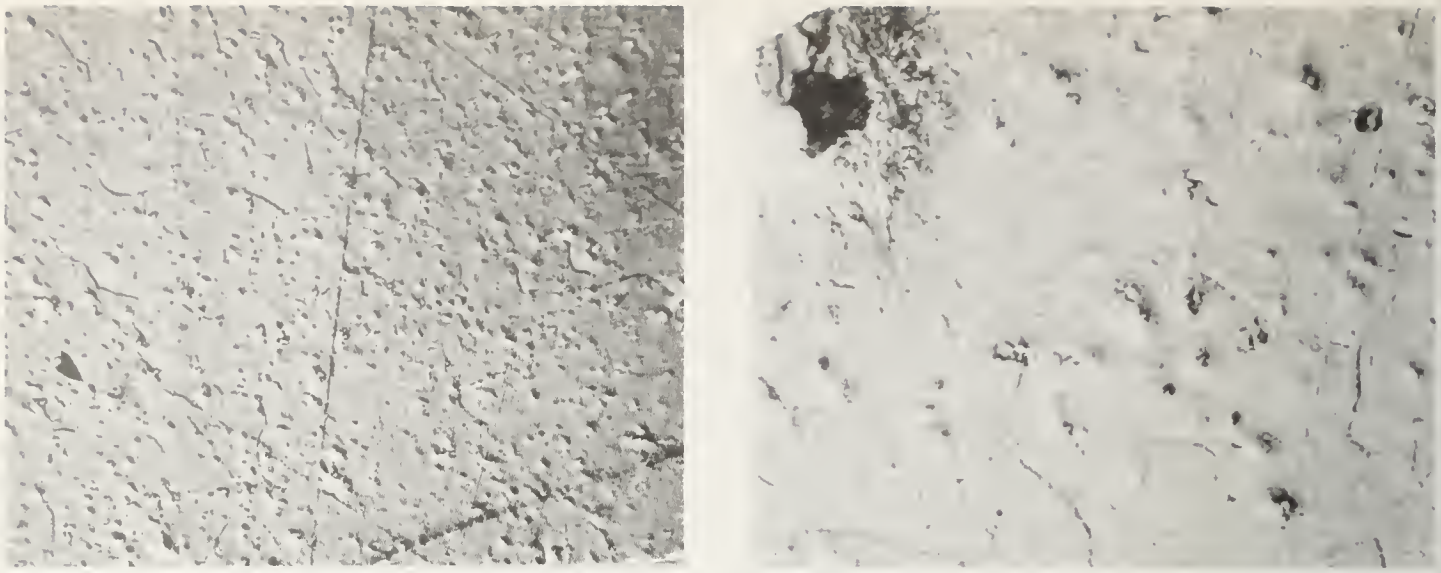

(a) (b)

Figure 3. OFHC copper. (a) After 45 minutes of ultrasonic cleaning exhibiting an area typical of a more severely damaged region. Magnification 150X. (b) Same area. Magnification 500X.

(a) (b)

Figure 4. Beryllium copper. (a) As polished. (b) After 90 minutes of ultrasonic cleaning of an area typical of the average damage to the sample. Magnification 150X.

(a) (b)

Figure 5. Beryllium copper (Berylco 25-hardened). (a) As polished. (b) After 90 minutes of ultrasonic cleaning. Magnification 500X.

(a) (b)

Figure 6. Zirconium copper. (a) As polished. (b) After 45 minutes of ultrasonic cleaning. Magnification 150X.

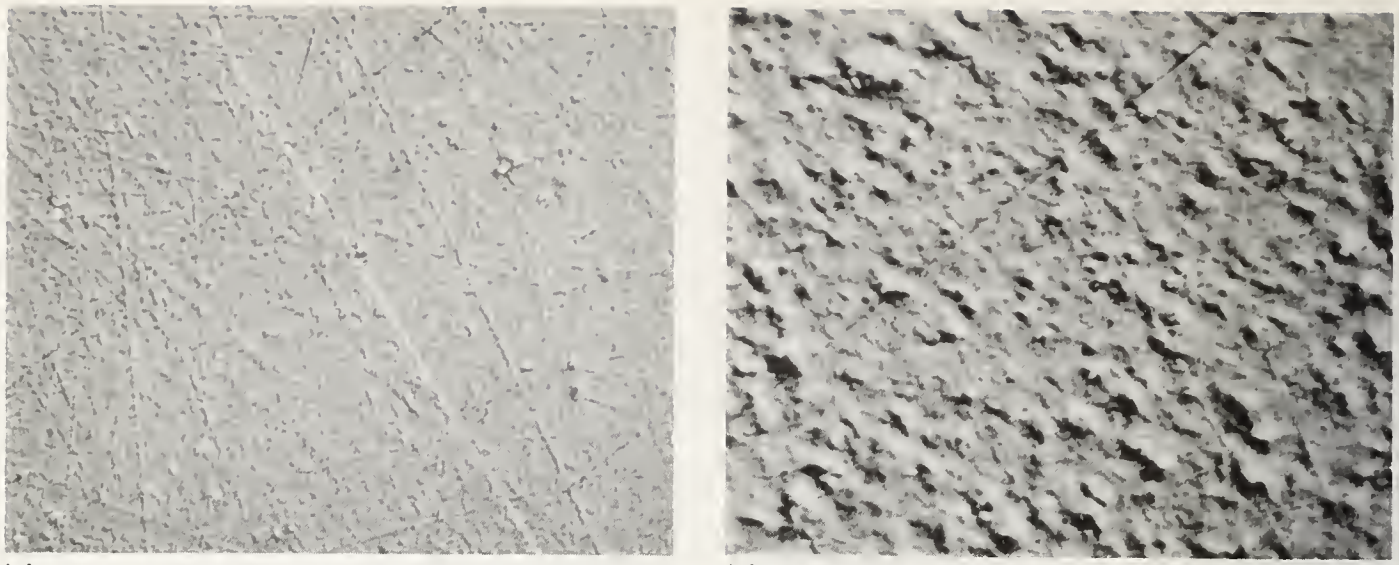

(a) (b)

Figure 7. Zirconium copper. (a) As polished. (b) After 45 minutes of ultrasonic cleaning. Magnification 500X.

(a) (b)

Figure 8. Stainless steel. (a) As polished. (b) After 45 minutes of ultrasonic cleaning. (Dark smudges are due to dust in the microscope; however, note the appearance of a new pit.) Magnification 150X.

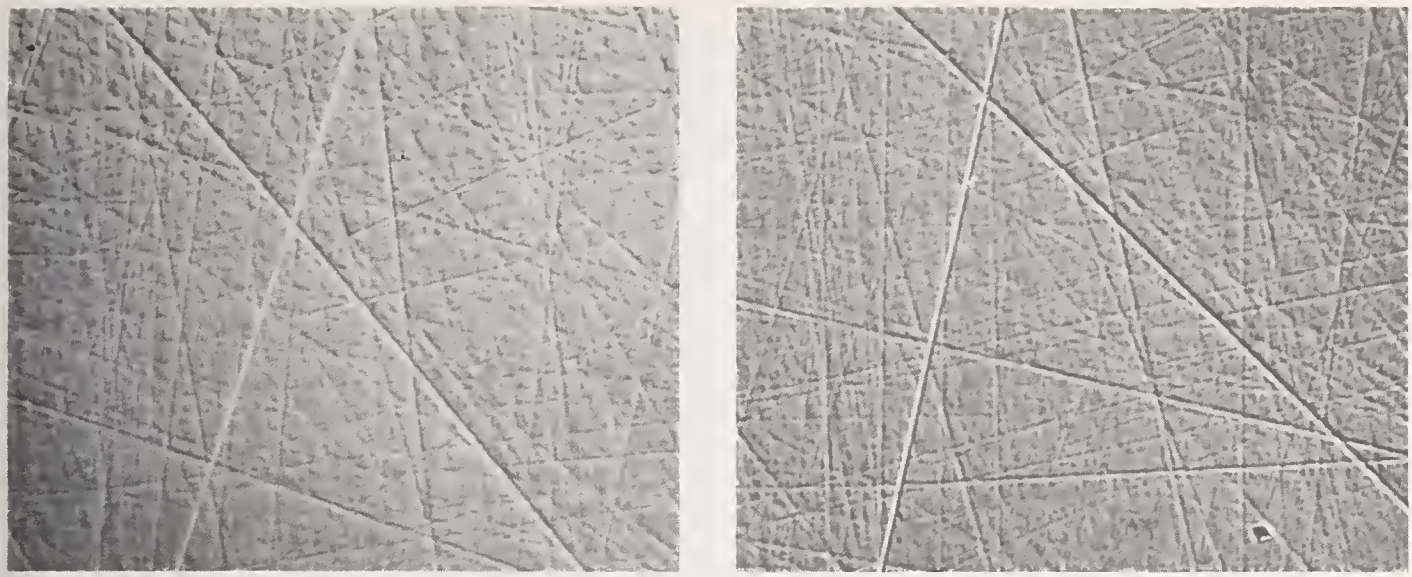

(a) (b)

Figure 9. Kanigen. (a) As polished. (b) After 45 minutes of ultrasonic cleaning. Note the appearance of a new pit and the increased apparent relief of the grinding marks. Magnification 500X.

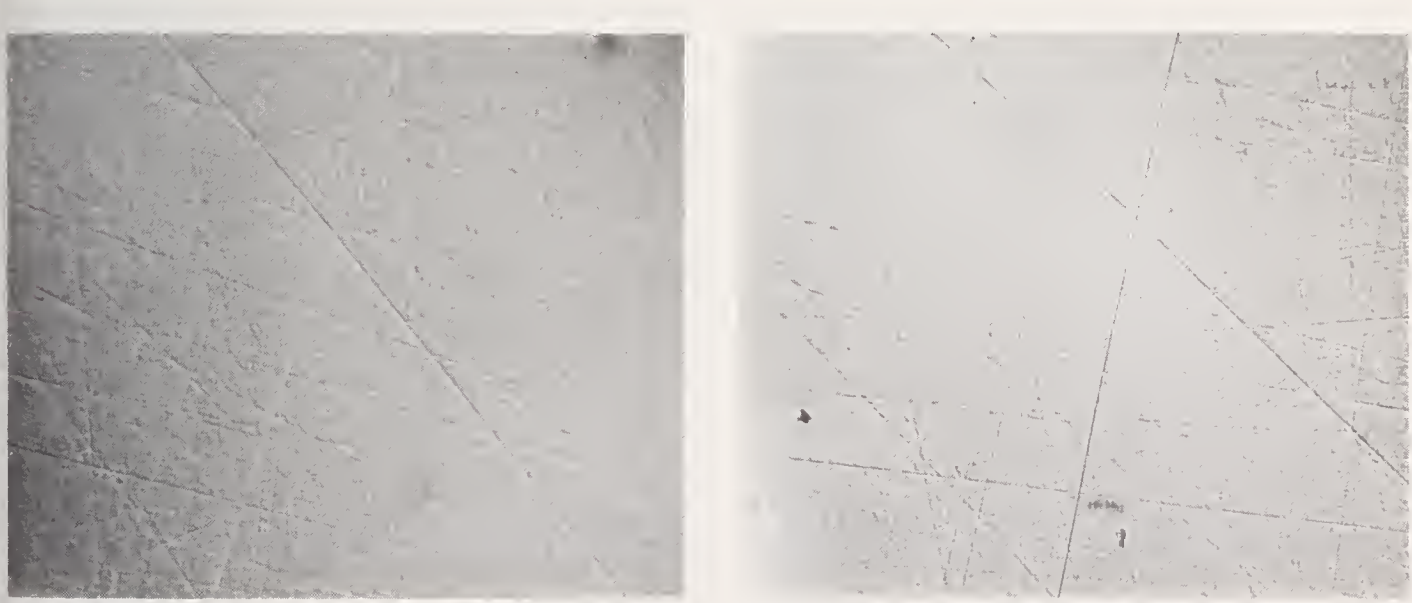

(a) (b)

Figure 10. Kanigen. (a) As polished. (b) After 45 minutes of ultrasonic cleaning. (Again dark smudges are due to dust in the microscope.) Note the appearance of two major pits uncovered during the ultrasonic cleaning. Magnification 150X.

(a) (b)

Figure 11. Fused quartz (Vitreosil). (a) A typical general area of the previous sample after 90 minutes of ultrasonic cleaning. (b) An area typical of the more severely damaged areas of the previous sample after the same minute ultrasonic cleaning. Magnification 500X.

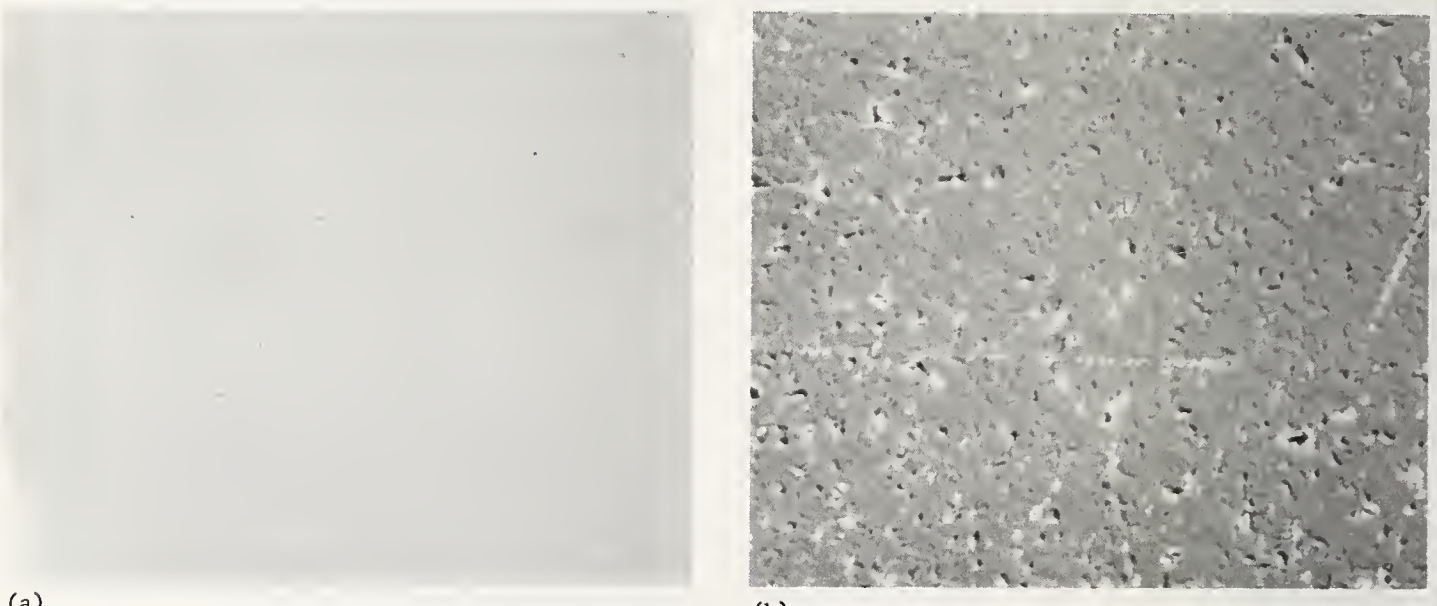

(a) (b)

Figure 12. Fused quartz (Vitreosil). (a) A typical general area of the previous sample after 90 minutes of ultrasonic cleaning. (b) An area typical of the more severely damaged areas of the previous sample after the same minute ultrasonic cleaning. Magnification 500X.

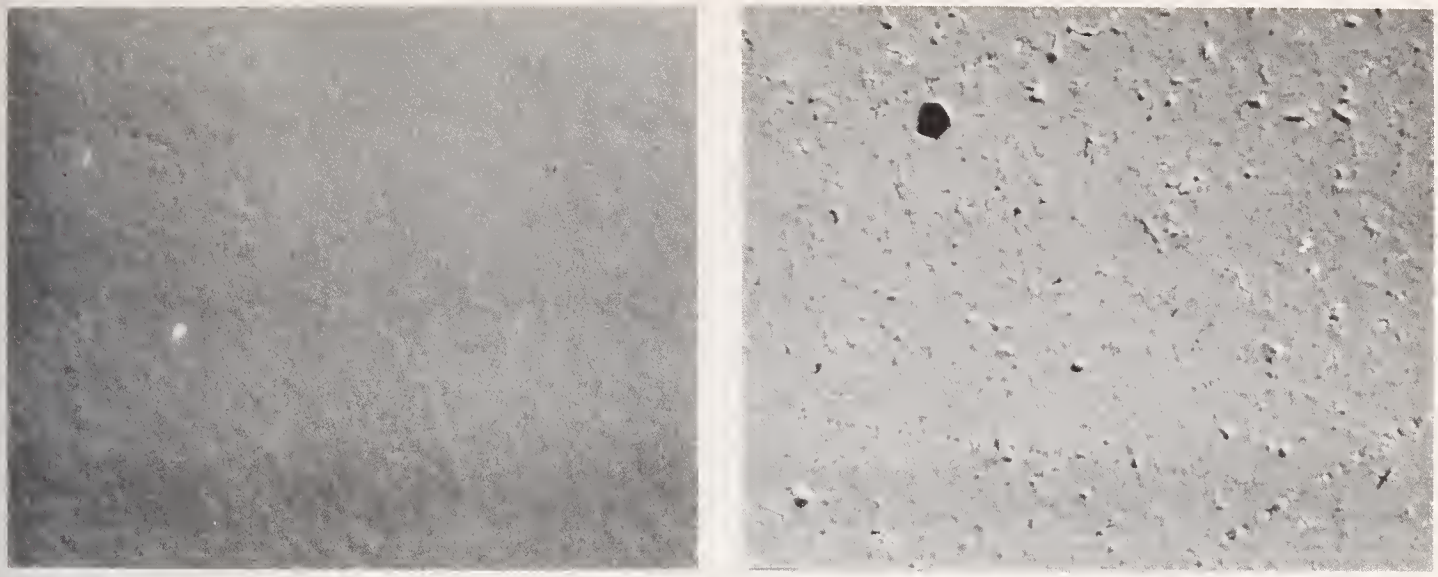

(a) (b)

Figure 13. Another sample of fused quartz. (a) As polished. (b) An area typical of the more severly damaged after 90 minutes of ultrasonic cleaning. Magnification 500X.

COMMENT ON PAPER BY GIBBS, *et al*

A number of people observed that prolonged ultrasonic cleaning can severely degrade optical surfaces. Exposures of tens of minutes in ultrasonic cleaning can lead to a total destruction of the optical surface and disruption of bonds between layers of material. Ultrasonically cleaned surfaces subjected to prolonged cleaning do not take dielectric coatings well. It was commented that a brief ultrasonic cleaning with a period of a minute or two can lead to an improvement in the optical surface by the removal of surface dirt, but that once a critical exposure has occurred the degradation of the surface occurs dramatically and sharply. Prolonged ultrasonic cleaning has even been observed to destroy the diamond tools used in the diamond-turning process.

3.1 THERMAL DIFFUSIVITY OF GERMANIUM, GALLIUM ARSENIDE AND CADMIUM TELLURIDE OVER THE TEMPERATURE RANGE 80 K - 900 K

Robert DOUSSAIN, Hubert P. LE BODO
Service des Essais Thermiques
LABORATOIRE NATIONAL D'ESSAIS
75015 PARIS - FRANCE

The laser flash technique was used to determine the thermal diffusivity of germanium, gallium arsenide and cadmium telluride over the temperature range 80 K- 1000 K. The main features of the experimental equipment are described. Values of thermal diffusivity (80-900 K) are reported.

Key words: Cadmium telluride; gallium arsenide; germanium; laser flash method; laser windows; thermal diffusivity.

1. INTRODUCTION

The extensive studies relative to laser induced damage in optical materials carried out by a number of laboratories have shown the importance of several physical parameters such as thermal diffusivity, thermal conductivity, optical absorption coefficient, thermal expansion coefficient, critical rupture stress and Young's modulus.

In application of a wide research program achieved under contract and involving 10 French laboratories, an experimental equipment was developed at the Laboratoire National d'Essais in order to measure the thermal diffusivity of semi-conducting compounds.

This property is defined as $\alpha = \frac{k}{c\rho}$, where

α is the thermal diffusivity, $cm^2\ s^{-1}$
k the thermal conductivity, $Wcm^{-1}\ K^{-1}$
c the specific heat, $J\ g^{-1}\ K^{-1}$
and ρ the density, $g\ cm^{-3}$,

Germanium, gallium arsenide, and cadmium telluride samples were studied and the results obtained were compared with available data from the Thermophysical Properties Research Center (TPRC) as well as with previously reported data.

2. THEORETICAL

In the flash method first reported by Parker, et al., [2][1] who used a xenon flash lamp as the source of radiant energy, the front face of a thin disk-shaped specimen is uniformly irradiated by a very short pulse and the resultant temperature history of the rear face is recorded by means of an adequate detector.

The front face is previously blackened in order to absorb the energy deposited by the beam. The thermal diffusivity of the sample is determined from the study of the temperature-versus-time curve, according to the boundary conditions.

The general mathematical formula used to determine thermal diffusivity is:

$$\alpha = \omega \frac{l^2}{\tau_{1/2}} \qquad \text{where}$$

l is the thickness of the specimen,

and $\tau_{1/2}$ the time required for the back face of the sample to reach one-half the maximum temperature rise.

In case of negligible heat losses at the front and rear faces and if we consider the laser pulse time as a Dirac function,the solution of the fundamental heat transfer equation may be written as follows [1]:

$$T(l,t) = \frac{Q}{c\rho l}\left[1+2\sum_{n=1}^{\infty}(-1)^n e^{-n^2\pi^2\alpha t/l^2}\right] \qquad \text{where}$$

$T(l,t)$ is the instantaneous back surface temperature rise at time t,

Q the surface density of deposited energy,

c the specific heat,

ρ the density,

α the thermal diffusivity

and n successive integers.

With the previously mentioned assumptions,the value for ω derived from this relation is 0.1388.

Since the shape of the temperature response curve being altered by heat losses, several mathematical models have been developed to take them into account.

The models from Cape and Lehman [3], Cowan [4,5], and Koyama and Larson [6] were applied to the studied materials,and a model including linear heat losses and the pulse duration corresponding to the neodynium glass laser used was developed. The resultant solutions were handled into a Hewlett-Packard HP 30 computer.

1. Figures in brackets indicate the literature references at the end of this paper.

3. EXPERIMENTAL

Thermal diffusivity measurements were achieved by means of the laser heat-pulse apparatus shown in figures 1 and 2.

The experimental assembly is constituted by the 3 following main parts: the laser source, the temperature regulated furnace, and the detection device.

- A neodynium glass laser operating in a conventional mode without Q-switching at 1.06 µm was used to heat the sample.

The size of the laser rod was: 23mm in diameter and 315mm in length. The duration of the laser pulses could be varied from 0.5 to 1.3 ms and the energy delivered by the beam from 5 to 180 Joules.

For some useful energetical levels, the beam uniformity was tested by means of a special paper.

The time distribution of the laser beam could be represented by the equation used by Koyama and Larson and the peak-time was estimated, in most cases, to be 190 µs.

The radiant energy delivered by the laser rod was monitored by means of a dual cone coated with a graphite layer and equipped with a thermopile.

- The main part of the regulated enclosure is a cylindrical inconel furnace(1430mm in length and 77/88 in inner/outer diameter). This furnace is thermally insulated with a refractory material.

For operation above 300 K, the tube furnace was electrically heated so as to obtain a uniform temperature in the central zone over 250 mm approximately. The furnace temperature profile was determined by means of 13 chromel-alumel thermocouples connected to an automatic potentiometer.
The ends of the enclosure, as well as the outer jacket, were cooled by a water flow. The measurements were made in vacuo up to 1000 K.

For operation below 300 K the apparatus was equipped with copper constantan (0.2 mm in diameter) thermocouples.
The cooling of the enclosure was obtained by a slow longitudinal liquid nitrogen flow, the rate of which could be adjusted by means of a valve lying between the diffusimeter and the liquid nitrogen container.
The temperature of the central zone was made uniform by an additional electrical heating. Nitrogen was drained out of the enclosure through an aperture located close to the window. In order to avoid freezing effect, the window was fitted with heating coils.

- The sample is located at the core of a stainless steel ring by use of 3 alumina tubular pins.

This ring lies on a cradle rigidly locked with a movable tube constituting a quite independant assembly.

Radiation shields made of nickel-chromium reflecting disks are located at the ends of the inner cylinder.

Before each laser shot, the front face of the sample was coated with a very thin colloïdal graphite layer absorbing the larger part of the laser radiant energy.

This coating was achieved by care of reproducibility on metallic samples considered as reference materials (Armco iron and OFHC Copper). For the studies performed on semiconductors, this thin layer was spread in order to avoid any transmission of the optical flux through the sample.

- Over the temperature range 300 K - 1000 K, where commercially available optical pyrometers lack sensitivity and time response requirements, chromel alumel thermocouples (0.2 mm in diameter) were used to measure the temperature rise of the back face of the sample as also the initial steady temperature.

The chamfered thermocouple wires were separated 1 to 2 millimeters in order to avoid temperature response errors and pressed against the rear face of the sample.

The output signal of the detector was connected to a high gain differential amplifier and then recorded on a 5103 N Tektronix storage oscilloscope equipped with a C-5 Polaroid camera.

4. RESULTS

Calibration of the system was carried out with Armco iron and OFHC copper samples.

The average values of the thermal diffusivity measurements results were compared with published and recommended values.

These materials are generally considered by most experimentalists as reference materials for thermophysical properties comparisons.

4.1. Armco iron

Measurements on Armco iron were achieved from 80 K to 840 K and the data obtained (table n°1) were compared with the values from Degiovanni, Morrison, et al., [7], Rawuka and Gaz [8], Shanks [9], as well as with TPRC data [10].

The overall estimated errors on the experimental results are less than $\pm$ 8% for all the tested materials.
A plot of the thermal diffusivity of Armco iron versus temperature is shown in figure n°3.
Micrographs of the studied samples were performed.

4.2. OFHC Copper

The thermal diffusivity of OFHC copper samples was determined over the temperature range 80 K to 750 K. Data obtained are reported in table n°2 and a plot of the thermal diffusivity versus temperature is presented in figure n°4. Comparisons were principally performed with the data reported by Butler and Inn [11], Adams and Wyman [12], as well as with the TPRC values.

4.3. Germanium

The tested samples were cut from an n-type germanium ingot exhibiting an electrical resistivity gradually decreasing from 33 Ωcm at one end to 15 Ωcm at the other end. The electrical resistivity of the monocrystalline samples was measured to be 20 Ωcm at 300 K. The crystalline plane was (1.0.0). The disks were machined with a precision of ± 100 µm and buffed on both surfaces.

A qualitative analysis of the impurities included in the various samples was performed by UV emission spectroscopy.

Arranging them in the decreasing intensity order, the detected elements were:

- Magnesium, silicon
- Aluminum, titanium
- Calcium, copper, iron (this latter element being hardly detectable)

It is to be mentioned that the detection intensity magnitudes may not coincide, in all cases, with concentration magnitudes.

The results of the thermal diffusivity measurements are shown in table n° 3 and a plot of these values versus temperature is given in figure n°5.

Comparison was achieved with the data from Abeles, et al., [13], Meddins and Parrott [14], and with TPRC recommended values.

4.4. Gallium arsenide

The electrical resistivity of the tested GaAs samples was above 10^7 Ωcm at 300 K and their crystalline plane was (1.1.1.). As for germanium, GaAs specimens were spectroscopically analyzed. The main impurities showed off were:

- Magnesium, palladium
- Gallium, silicon
- Calcium, copper, titanium
- Aluminum, silver, iron, and germanium (these 4 elements being hardly detectable)

The results obtained from 80 K to 850 K are shown on table n° 4 and plotted versus temperature in figure n°6.

Comparison was achieved with data from Timberlake and Davis [15] from 300 K to 850 K and our measured values closely agree with these later ones.

4.5. Cadmium telluride

Measurements were achieved on several polycrystalline undoped samples.

The studied samples contained the following impurities:

- Aluminum, silver, magnesium, silicon
- Germanium
- Calcium, copper, titanium
- Iron (in very low traces)

The data from our measurements are listed in table n° 5 and plotted versus temperature in figure n°7.

5. CONCLUSIONS

The laser flash method was used to determine the thermal diffusivity of germanium, gallium arsenide,and cadmium telluride over the temperature range 80 K-900 K. A device was designed and developed at the Laboratoire National d'Essais (France) in order to perform these measurements. Calibration of this system was carried out with Armco iron and OFHC copper specimens over the temperature range investigated and the measured values were compared with reported data. The estimated errors on the experimental results are less than $\pm$ 8% for the studied materials.

Improvements of the data acquisition system are expected which will induce a significant gain in sensitivity.

The investigation of the laser beam uniformity is planned in order to estimate errors in thermal diffusivity arising from a deviation from ideal spatial uniformity of the heating pulse.

6. ACKNOWLEDGMENTS

The authors wish to thank the Direction des Recherches et Moyens d'Essais du Ministère de la Défense which supported our work and gave its authorization for the presentation of this paper.

7. REFERENCES

[1] Carslaw, H. S. and J. C. Jaeger, "Conduction of heat in solids," 2nd Ed. (Clarendon Press, Oxford, 1959).

[2] Parker, W. J., R. J. Jenkins, C. P. Butler, and G. L. Abbott, J. Appl. Phys. 32, 1679-84 (1961).

[3] Cape, J. A. and G. W. Lehman, J. Appl. Phys. 34, 1909-13 (1963).

[4] Cowan, R. D., J. Appl. Phys. 32, 1363-70 (1961).

[5] Cowan, R. D., J. Appl. Phys. 34, 926-7 (1963).

[6] Koyama, K. and K. B. Larson, J. Appl. Phys. 38, 465-74 (1967).

[7] Morrison, B. H., D. J. Klein, and L. R. Cowder, (Proc. 6th Conf. on Thermal Conductivity, Oct. 19-21) 673-99 (1966).

[8] Rawuka, A. C. and R. A. Gaz, (Proc. 6th Conf. on Temp. Measurements Society) 55-67 (1969).

[9] Shanks, H. R., A. H. Klein, and G.C. Danielson, J. Appl. Phys. 38, no. 7, 2885-92 (1967).

[10] Touloukian, Y. S. ed., Handbook of the Thermophysical Properties of Matter, 10 (Plenum, New York 1973).

[11] Butler, C. P. and E. C. Y. Inn, USNRDL TR 177, 1-27 (1957).

[12] Adams, C. H. and M. E. Wyman, J. Appl. Phys. 40, no. 1, 344-50 (1969).

[13] Abeles, B. et al., Bi-monthly Prog. Rep., RCA Lab., Princeton, N. J., no's. 1 and 2, 1-36 (1959).

[14] Meddins, H. R. and J. E. Parrott, Brit. J. Appl. Phys. 2, no. 5, 691-97 (1969).

[15] Timberlake, A. B., P. W. Davis, and T. S. Shilliday, Advanced Energy Conversion 2, 45-51 (1962).

Table 1. Thermal diffusivity data for Armco iron.

T (K)	α (cm^2s^{-1})
100	0.550
150	0.339
200	0.255
250	0.219
300	0.195
350	0.177
400	0.162
450	0.149
500	0.136
550	0.122
600	0.110
650	0.100
700	0.091
750	0.083
800	0.076

Table 2. Thermal diffusivity data for OFHC copper.

T (K)	α (cm^2s^{-1})
100	2.02
150	1.48
200	1.29
250	1.20
300	1.14
350	1.10
400	1.07
450	1.05
500	1.02
550	1.00
600	0.99
650	0.98
700	0.96
750	0.95
800	0.94

Table 3. Thermal diffusivity data for germanium.

T (K)	α (cm^2s^{-1})
100	1.22
150	0.720
200	0.500
250	0.400
300	0.340
350	0.300
400	0.270
450	0.230
500	0.210
550	0.180
600	0.160
650	0.140
700	0.120
750	0.110
800	0.106
850	0.103
900	0.100
950	0.098
1000	0.093

Table 4. Thermal diffusivity data for gallium arsenide.

T (K)	α (cm^2s^{-1})
100	1.350
150	0.485
200	0.340
250	0.270
300	0.225
350	0.200
400	0.170
450	0.145
500	0.122
550	0.103
600	0.085
650	0.075
700	0.066
750	0.057
800	0.050

Table 5. Thermal diffusivity data for cadmium telluride.

T (K)	α (cm^2s^{-1})
100	0.240
150	0.160
200	0.110
250	0.074
300	0.046
350	0.033
400	0.025
450	0.022
500	0.020
550	0.018
600	0.016
650	0.015
700	0.014

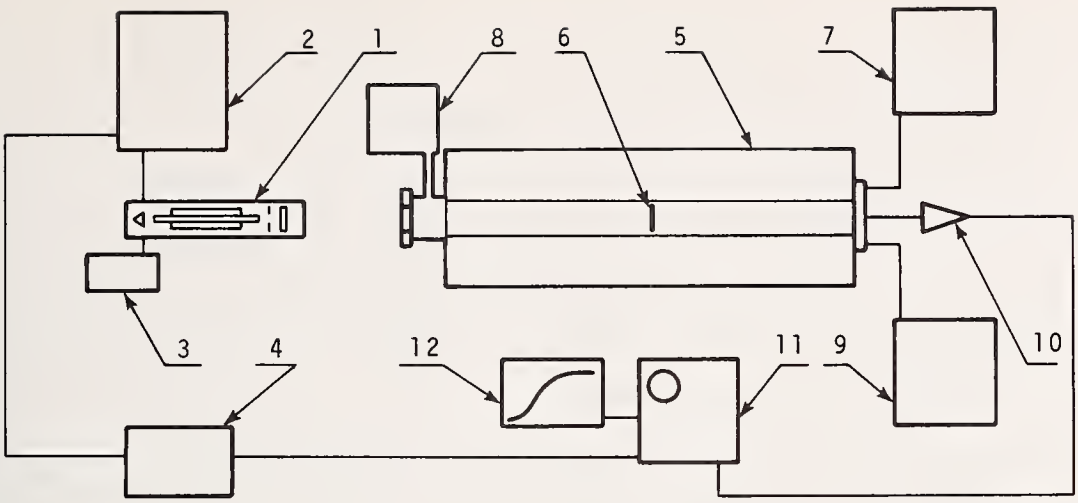

Figure 1. Schematic of the apparatus designed for thermal diffusivity measurements above room temperature.

1. Laser head
2. Laser power supply
3. Cooling unit
4. Laser trigger
5. Furnace
6. Specimen
7. Electrical power supply
8. Vacuum system
9. Temperature readout
10. High gain differential amplifier
11. Storage oscilloscope
12. Camera record

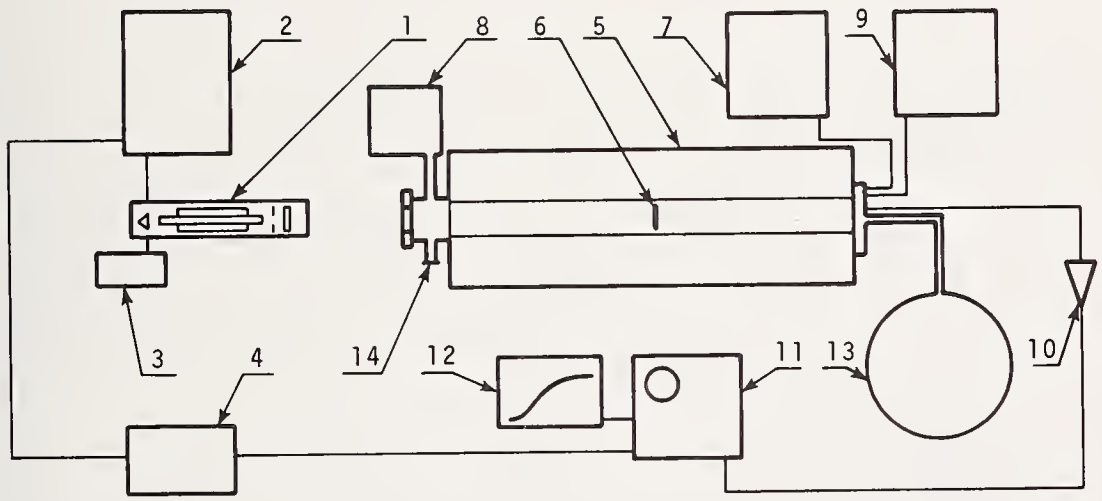

Figure 2. Schematic of the apparatus designed for thermal diffusivity measurements below room temperature.

From 1 to 12 (see captions of figure 1)
13. Liquid nitrogen container
14. Aperture for the exit of nitrogen

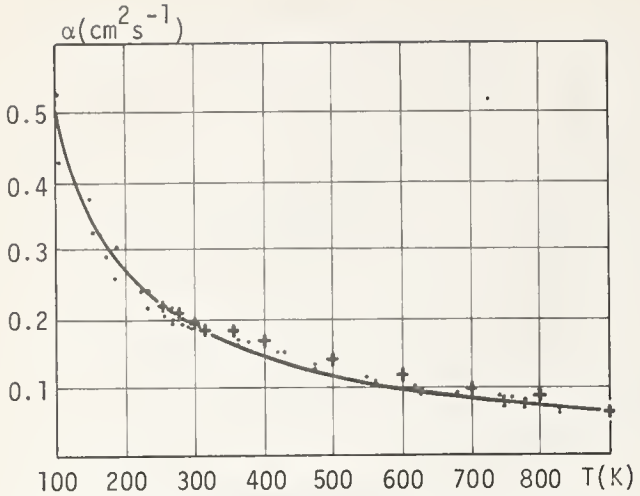

Figure 3. Thermal diffusivity of Armco iron. Crosses represent the TPRC data.

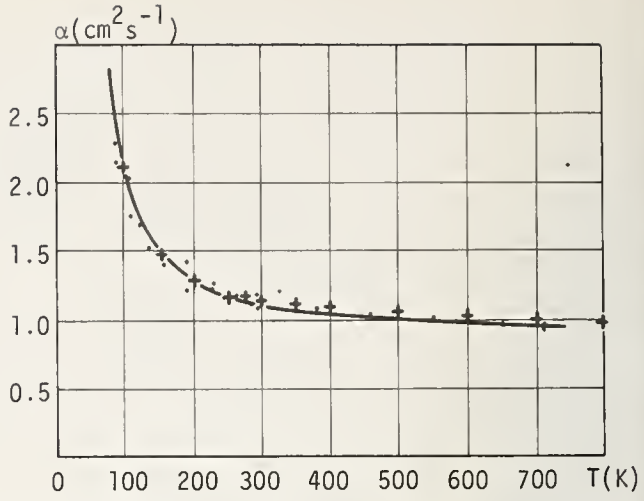

Figure 4. Thermal diffusivity of OFHC copper. Crosses represent the TPRC data.

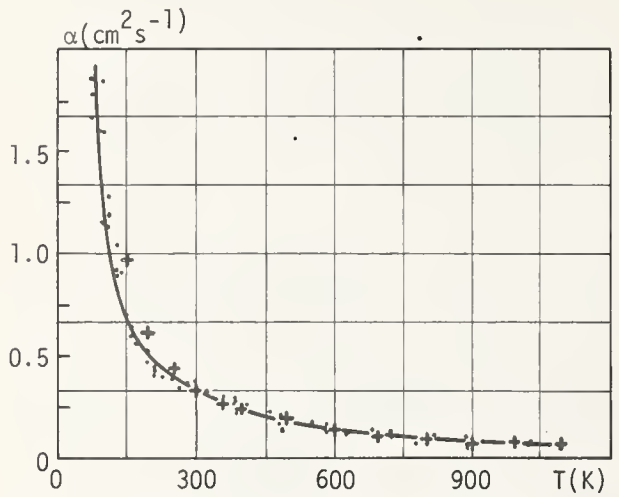

Figure 5. Thermal diffusivity of n-type germanium. Crosses represent the TPRC data.

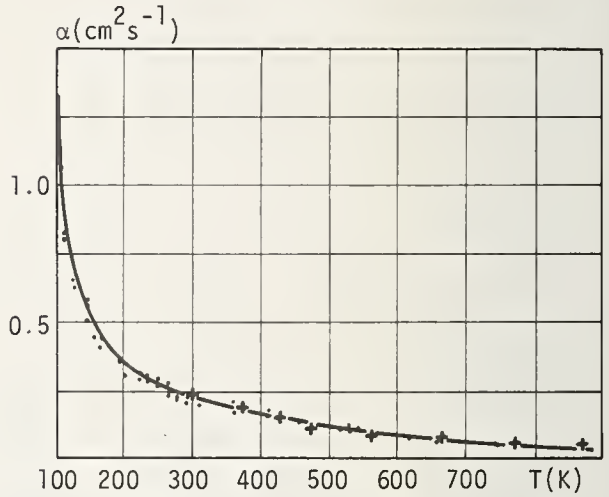

Figure 6. Thermal diffusivity of gallium arsenide. Comparisons were achieved with the results of Timberlake, et al.

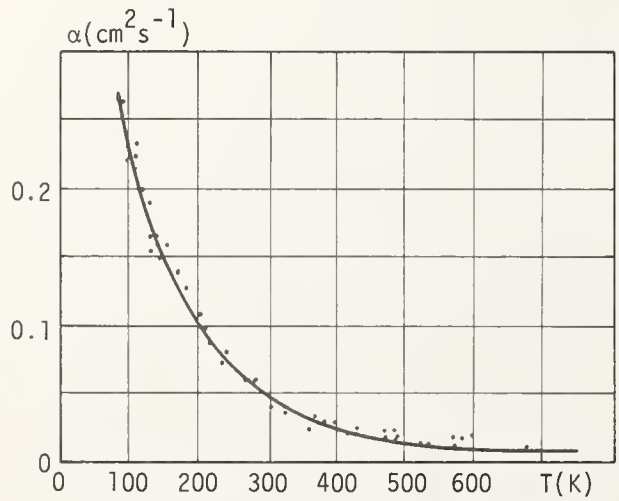

Figure 7. Thermal diffusivity of cadmium telluride.

NO COMMENT ON PAPER BY DOUSSAIN and LeBODO

3.2 Damage to 10.6 μm Window Materials Due to CO_2 TEA Laser Pulses*

K. M. Leung, M. Bass, and A. G. J. Balbin-Villaverde†

Center for Laser Studies
University of Southern California
Los Angeles, California 90007

Laser irradiation induced damage to several materials of interest for use as 10.6 μm laser system windows was studied. A pulsed CO_2 TEA laser, operating in the TEM_{00} mode was the irradiation source in these experiments. The light was focused onto the surfaces or into the bulk of the samples and the waveform of the transmitted pulse was monitored. Comparison of the incident and transmitted laser pulse waveforms shows the onset of laser induced damage as a distortion of the latter. Damage threshold data and a discussion of possible damage mechanisms for improved ZnSe, commercial and RAP grown KCl, and commercial NaCl are presented.

Key words: KCl; NaCl; pulsed CO_2 TEA laser damage; transmitted pulse; waveform distortion; ZnSe.

1. Introduction

One of the commonly used diagnostic techniques for monitoring laser-induced damage is to examine the temporal shapes of laser pulses that are transmitted through transparent dielectrics. When damage occurs on sample surfaces or in bulk materials, the transmitted pulse is attenuated in amplitude as well as distorted in waveform. In recent years Bass and Fradin [1][1] have demonstrated that when damage occurs, the transmitted ruby laser pulse is attenuated in a manner that is characteristic of the source of damage. They further showed that pulses which are attenuated very rapidly form damage regions in the bulk which are characteristic of the intrinsic mechanism such as an electron-avalanche breakdown. Other damaging pulses are attenuated in a very different manner and produce damage regions that appear to result from inclusion absorption. Last year at this symposium, Milam, et al., [2] described a new experimental technique for determining the cause of laser-induced damage. The new procedure was based upon this statistical nature of the times required to produce damage at many sites which were irradiated by equally-intense, square-waveform pulses. This permits identification of the damage mechanisms without requiring a threshold measurement. In the ir region Yablonovitch [3] observed similar statistical properties for damage due to CO_2 TEA laser pulses passing through alkali-halide crystals. However, the experimental observation was complicated by several longitudinal modes which contributed a time structure to the laser pulse.

At USC, a setup based on Milam's technique [2] to extract square-waveform pulses from the most intense portion of a CO_2 TEA laser pulse is under construction. This will make possible measurement of 10.6 μm survival curves in different ir materials. To date, however, we have employed the recent development of fast detection electronics to examine simultaneously both the transmitted and incident pulses of a CO_2 TEA laser. In this paper we describe the technique and discuss possible damage mechanisms for 10.6 μm window materials. The experimental results will be divided into

---

* This work was supported by Defense Advanced Research Projects Agency and was monitored by Air Force Cambridge Research Laboratories.

† Present address: Instituto de Fisica, Universidade Estadual de Campinas, Campinas, S. P., Brazil

[1] Figures in brackets indicate the literature references at the end of this paper.

two sections, one based on the transmitted pulse waveform analysis and the other on threshold measurements for surface and bulk damage on ten samples of three different ir window materials. Some damage morphology on typical samples will be discussed.

2. Experimental

The experimental setup for conducting pulsed CO_2 damage experiments is shown in figure 1. The basic apparatus consists of a pulsed CO_2 TEA laser, a beam attenuator, a test vacuum chamber, and an energy/waveform monitoring system. Three measurements are provided by using this setup: the incident energy at the sample, the spatial profile of the laser beam, and the waveforms of the incident and transmitted pulses. Details of individual components as well as test procedure are discussed below.

2.1. CO_2 TEA Laser Pulses

The performance and characteristics of the CO_2 TEA laser used in this work are described in table 1.

Table 1. CO_2 TEA laser parameters and performance data

Discharge length (double Rogowski electrodes)	41 cm
Energy storage capacitance	0.08 μf
Flow rate ratio ($He:N_2:CO_2$)	8.7:2.4:2.6 ℓ/min
Mirrors:	100%R - Flat/Si
	80%R - 10 meter/Ge
Brewster windows	KCl
Intracavity aperture diameter for TEM_{00} mode	6 to 9 mm
Cavity length	120 cm
Typical input energy	21 J
Typical output energy (9 mm aperture) for TEM_{00} mode	100 mJ
Typical width for gain-switched pulse (FWHM)	92 ns

The spatial profile of the laser beam was measured by a pinhole scan detector. Figure 2 shows that the beam profile was a Gaussian distribution. When a 9 mm intracavity aperture was placed 15 cm from the flat 100% reflecting mirror, the spot-size ($1/e^2$ radius of the intensity profile) at the focusing lens was measured to be 2.9 mm and 2.4 mm for a 6 mm intracavity aperture. The output pulse of the laser consisted of a 92 nsec gain-switched pulse followed by a long tail of ~1.6 μsec duration. Several longitudinal modes were able to oscillate and so the pulse waveform showed structure similar to that observed by Yablonovitch [3]. The self-locked output waveform was caused by the fact that the absorption of CO_2 molecules in the lasing medium can saturate [4]. The mode-locked waveform was composed of pulses having < 2.5 nsec duration and separated by 8 nsec, the cavity round-trip time. The fraction of the total energy in the gain-switched pulse was determined by measuring the areas under the gain-switched pulse and the long tail. These areas were equal, showing that half the total energy was in the gain-switched pulse. The total incident energy was measured with a thermopile (Hadron Model 100) calorimeter having an accuracy of ± 5%.

2.2. Experimental Procedures

The energy of the laser beam incident on the sample was selected by a beam attenuator consisting of Brewster angle ZnSe polarizers which provide extinction ratio of 1:16. A discussion of this device is given in Appendix A. Each laser shot was either focused onto the surface or into the bulk of a test specimen using a 3.8 cm focal length AR coated Ge lens. The focal position was determined by varying the lens to sample separation and observing burn spots on a piece of black photographic film (unexposed Poloroid Type 410) attached to the surface of the sample. The focal spot-size of the Gaussian mode beam w_0 was calculated by the following equation:

$$2w_0 = \frac{4\lambda}{\pi} \times \frac{f.l.}{2w}$$

where w is the measured laser spot size on the focusing lens. The calculated w_0 was in excellent agreement with the measured radius of many surface damage sites on ZnSe. All samples were studied in a plexiglas chamber evacuated by a mechanical pump to eliminate spurious breakdown due to dust or gas molecules near the surface of a sample. Onset of damage was monitored by (1) observing the visible plasma and changing appearance of the sample from the focal region, (2) examining the damaged region under the microscope, and (3) comparison of the incident and transmitted laser pulse waveforms. In this work, the waveform diagnostic technique was emphasized and found to be useful in understanding the damage process. A ZnSe beamsplitter located in front of the beam attenuator was used to direct a portion of the incident beam onto a photon drag detector (PD 1). The transmitted beam was re-collimated by a ZnSe lens and monitored by another photon drag detector (PD 2). Both detectors have similar response and rise time of 500 ps. Signals corresponding to incident and transmitted pulses were simultaneously displayed on upper and lower traces of a high-speed (400 MHz) dual-beam oscilloscope (Tektronix Model 7844), respectively. Typical traces are shown in upper corner of figure 3. For convenience, the transmitted pulse waveform was inverted and when no damage was produced the waveforms were registered with respect to each other in time. For this work, only single shot on single site testing is reported.[2]

3. Waveforms Analysis and Possible Damage Mechanisms

3.1. Comparison of Incident and Transmitted Pulses

Since the high-speed detector dual-beam scope combination can provide a time resolution of 2.5 nsec, it is possible to examine waveform distortion on this time scale and to measure the survival time of each damage site. For this reason, the analysis is based upon the comparison of incident and transmitted mode-locked pulses in the gain-switched pulse when no damage occurs during the experiment. There are typically 23 mode-locked pulses in a recorded signal. The transmission of individual mode-locked pulses is normalized to that at t = 0. The normalized transmission of the i^{th} pulse is defined as

$$T_i \equiv \frac{\mathscr{I}_i(t = t_i)}{\mathscr{I}_0} \quad \text{for } i = 0, 1, 2, \ldots$$

and

$$\mathscr{I}_i \equiv \frac{I_{out}(t_i)}{I_{in}(t_i)}$$

where I_{in} and I_{out} are the amplitudes of individual mode-locked pulses at time $t = t_i$. For illustration, the normalized transmission of a pulse which did not cause damage is plotted against time in figure 3. The solid line gives a good indication that no distortion of the transmitted waveform occurred (all T_i are very close to unity). The dashed curve shown on the same plot gives the normalized waveform of the gain-switched pulse. In general, waveform distortion was studied over a range of incident laser power from below threshold to 4 times threshold.

Since laser induced gas breakdown is thought to be caused by electron avalanche breakdown, we have examined the waveform distortion due to air breakdown pulses at 22 cm Hg pressure. The transmitted waveform distortion is depicted in figure 4. It is easy to see that air is completely broken down within one pulse at t_d = 72 nsec. We shall refer to the time when damage occurs, t_d, as the survival time.

3.2. Surface Damage on IR Window Materials

---

[2] For pulsed laser damage experiments, three types of threshold measurement have been practiced by different workers. They are single shot on single site (one to one), multiple shots with variable incident intensity on single site (n to 1), and multiple shots with constant incident intensity on single site ($\bar{n}$ on 1).

Seven surfaces of three ir window materials (ZnSe, KCl, and NaCl) were studied in these laser damage experiments. The waveform distortions for surface damage on NaCl, KCl, and ZnSe, as well as air breakdown, are shown in figure 5. To show the distortion more clearly three transmission curves are plotted in figure 6 for surface damage on three ir window materials at threshold. All samples survived until ~ 50 nsec and the complete attenuation took place within one to two pulses, except for KCl. If the incident power was raised above threshold, the survival time was reduced and transmission cut-off occurred in the second or third mode-locked pulse. A blue-white plasma was observed at or above threshold in all cases. The waveform distortion analysis for surface damage suggests that the damage mechanism is very similar to air breakdown.

3.3 Bulk Damage in IR Window Materials

Typical traces for bulk damage in NaCl, KCl, and ZnSe both at threshold and above threshold are shown in figure 7. For commercially fabricated NaCl, sharp cutoff at threshold, as well as above threshold, were characteristics of the transmitted pulse waveform distortion. In general, both ZnSe and KCl show very slow attenuation. For ZnSe, this slow cutoff was expected since inclusion absorption is the dominant cause of material failure. However, in the case of RAP grown KCl and commercial KCl, the observed slow cutoff suggests that very small inclusions in the bulk still play a dominant role in the damage process. In all cases, if no spark was observed for a particular site, waveform distortion could not be detected either. The spark in NaCl was yellow as expected for a sodium spark. Bulk damage in ZnSe was always accompanied by a yellow spark inside the medium. The observed color of this spark is due to the fact that it is surrounded by a medium which absorbs the blue and green parts of the spectrum.

For a more detailed view of damaging waveform distortion figures 8, 9, and 10 display transmission curves for NaCl, KCl, and ZnSe, respectively. The results of waveform distortion analysis for bulk damage in these materials is summarized in table 2. In addition, figure 11 gives the transmission versus gain-switched pulse energy for the case of bulk damage in commercial NaCl, RAP grown KCl, and old ZnSe as well as air breakdown. It implies that damage in these ir materials occurs when nearly half the energy contained in the gain-switched pulse has passed or just after the peak of the pulse.

Table 2. Bulk damage characteristics in ir window materials due to CO_2 TEA laser pulses

IR Materials	Color of Spark Formation	Condition of Site Fracture	Survival Time t_d at threshold	Time for Attenuation to Reach its Maximum	Possible Damage Mechanism
NaCl (commercial)	yellow	severe and large	56 nsec	50 nsec	intrinsic breakdown
KCl (commercial)	blue-pink	small	24 nsec	136 nsec	inclusion absorption
KCl (RAP)	"	"	80 nsec	>100 nsec	" "
ZnSe (Raytheon 1974)	yellow	small and in the bulk	56 nsec	30 nsec	inclusion absorption
ZnSe (Raytheon 1975)	"	"	40 nsec	>100 nsec	" "

4. Measured Damage Threshold in IR Window Materials

Table 3 summarizes our measurements of surface and bulk damage thresholds in three ir window materials, ZnSe, KCl, and NaCl. In this paper we report the axial peak power density P_0 (MW/cm^2) which is defined

$$P_0 = 2 \times P_{Ave} = 2 \left(\frac{4 \ell n 2}{\pi}\right)^{\frac{1}{2}} \frac{E_{total}}{\Delta\tau} .$$

Here $\Delta\tau$ is the FWHM for the gain-switched pulse of the CO_2 TEA laser. E_{total} is the net energy density in J/cm^2 deposited at the focal region of the sample during the gain-switched pulse. We emphasize again that the test results are reported for a single shot on a single site in contrast to other reports [5]. The damage threshold is defined as the lowest power density which damages 50% of the sites studied. The numbers in parenthesis in table 3 are the power densities which cause damage to 10% of the sites.

Table 3. Measured damage threshold on ir window materials due to CO_2 TEA laser pulses

Sample Material	Absorption[a] $\alpha_{total}(cm^{-1})$	Surface Finishing Method	Axial Peak Power Density P_0 (MW/cm^2)	
			On Surface	In Bulk
ZnSe (Raytheon 1974)	0.005	conventional	270	230
ZnSe (Raytheon 1975)	0.0005	diamond-polished	350 (270)	460 (350)
ZnSe (Raytheon 1975)	0.0005	super-polished	350 (270)	460 (350)
KCl (HRL-RAP)	0.00014	conventional	460 (350)	4600
KCl (HRL-RAP)	0.00026	- -	- -	1500 (760)
KCl (Harshaw Econoflat)	0.001	conventional	560 (165)	650 (150)
KCl (Harshaw)	0.0008	- -	- -	<190
KCl (Harshaw Comm.)	0.0023	- -	- -	<190
NaCl (Harshaw Econoflat)	0.004	conventional	1600 (1200)	6100 (5600)
NaCl (Harshaw Spectro.)	0.004	conventional	840	3900

[a] Values are provided by respective suppliers to be considered for reference only.

4.1. Damage in ZnSe

We have performed 10.6 μm damage experiments on three different surfaces of ZnSe crystals and in two different bulk materials. Raytheon Company furnished samples of its 1974 ZnSe material and its improved 1975 ZnSe. It should be noted that the improved ZnSe has much lower absorption than the 1974 material.

As seen in table 3, no significant difference was found in damage threshold for different surface finishing methods. Figure 12 shows the super-polished and diamond-polished surfaces obtained on improved ZnSe crystals for these experiments. The conventional surface on an old ZnSe crystal appeared to be very similar to the diamond-polished surface.

We have also investigated both visible and 10.6 μm scattering using the Optical Functional Tester at NWC described last year [6]. Bulk scattering was dominant in both old and improved ZnSe suggesting that inclusions in ZnSe may still be the major determinant of the 10.6 μm damage threshold. However, the improved ZnSe was the first sample of this material which could be damaged on the surface and not in the bulk. The morphology of the damage sites in ZnSe (see figure 13) further supports the fact that inclusions near the surface or inside the bulk play an important role in the damage mechanism.

4.2 Damage in KCl and NaCl

Since conventionally polished KCl surfaces are easily contaminated even under normal laboratory environments, only two surfaces were used for the experiment. Our interests in alkali halides are in understanding the damage mechanism,but not in the threshold comparison. Therefore, one should not be too serious about the comparison between KCl and NaCl listed in table 3. In general, conventionally grown NaCl crystals still have higher threshold values. The RAP grown KCl crystals are superior to conventionally grown KCl by an order of magnitude in damage threshold. Damage morphology on these crystal surfaces is quite similar and in general the damage site is larger than the laser beam cross section. Figures 14 and 15 show such morphology for KCl and NaCl surfaces. In bulk damage,

NaCl shows larger fracture along cleavage planes than KCl.

5. Summary and Conclusions

With a high-speed detector/dual-beam oscilloscope detection system we have begun to observe the dynamics of 10.6 μm laser induced damage in ir window materials. Comparison of the incident and transmitted laser pulse waveforms shows the onset of laser induced damage as a distortion of the latter. Survival time of surface and bulk damage for different materials can be accurately determined using this technique.

With the samples confined in an evacuated chamber, surface damage of NaCl, KCl, and ZnSe was similar to air breakdown, showing a sharp cutoff in the transmitted pulse waveform. Surface contaminants may cause early breakdown and generate a plasma similar to that in a gas breakdown. For bulk damage in old and improved ZnSe, the distortion of the transmitted pulse waveform suggests that two different kinds of inclusions are involved in the damage process. Measured threshold values of these ZnSe samples suggested that the improved material is indeed out-performing the old one. Damaging pulse waveform distortion for HRL RAP grown KCl is very slow and suggests that inclusions still play an important role in limiting the damage resistance of this material. The waveform distortion observed for Harshaw NaCl is fast and resembles that due to intrinsic breakdown. Measured threshold values of these alkali halides suggest that the breakdown field of NaCl may be greater than that of KCl in contrast to the result of "n on 1" experiments reported last year [7]. This conclusion, however, depends upon which samples are compared and so reports of relative breakdown fields must be cautiously evaluated.

In conclusion, we feel that the current results still do not provide a quantitative understanding of damage to 10.6 μm window materials due to CO_2 TEA laser pulses. A better statistical technique [2] will be applied at this wavelength in the coming year.

We further conclude that since different damage threshold values for a given material can be easily found in the literature, it is essential to exchange test specimens or work jointly on a particular experiment using different diagnostic techniques and equipment. To this end, USC and HRL have initiated a joint experiment to perform damage measurements on RAP grown KCl crystals and other samples.

6. Acknowledgments

The authors are grateful to Raytheon Company for providing the ZnSe samples, Hughes Research Lab. at Malibu, CA, for the RAP grown KCl samples, and Mr. Walter Spawr for his effort in polishing ZnSe for this work. The authors also thank many individuals at NWC, China Lake, CA, for their technical assistance in scattering experiments and Nomarski microscopy.

At the University of Southern California, we thank C. C. Tang and M. Chang for their assistance in data acquisition, and Professor J. Ward who has provided many fruitful discussions is especially acknowledged.

7. Appendix A. 10.6 μm Attenuator

For laser-induced damage experiments, it is desirable to have a variable attenuator which will control the incident laser energy continuously without affecting the duration, the polarization, and the spatial distribution of the laser pulse. In the visible and near ir region, the combination of one rotatable and one fixed Glan polarizer was used as a variable attenuator [8]. For 10.6 μm radiation, a pair of wire-grid polarizers on ZnSe substrates can provide two orders of magnitude attenuation [7]. However, these polarizers are very costly and are limited by low resistance to laser damage. In this work, we have prepared two relatively inexpensive ZnSe reflection polarizers as a beam attenuator. A detailed discussion of how this attenuator works is presented below.

It is well known that when a plane wave is incident upon a dielectric surface, the reflection coefficients can be described by Fresnel's equations. Let φ be the angle of incidence, r the angle of

refraction, and n the refractive index. Then the reflection coefficient for linearly polarized incident light with electric vibration perpendicular and parallel to the plane of incidence can be expressed as,

$$R_{\perp} = \frac{\sin^2(\varphi - r)}{\sin^2(\varphi + r)} \quad \text{and} \quad R_{\parallel} = \frac{\tan^2(\varphi - r)}{\tan^2(\varphi + r)},$$

respectively. If the angle of incidence is Brewster's angle, φ = arc tan(n) and $R_{\parallel}$ is zero. For ZnSe, φ_B = arc tan(2.40) at 10.6 μm and $R_{\perp} = \frac{1}{2}$.

A typical arrangement of reflection polarizers employs two oppositely sloping sets of plates mounted at Brewster's angle. Let the fixed polarizer be oriented to transmit the laser polarization and $\theta = 0^o$ be the angle of the rotating polarizer giving the maximum transmission through the combination attenuator. Then the transmitted laser intensity, I_{out}, at any rotation angle θ about the beam axis can be determined by means of Jones calculas as follows:

$$\begin{pmatrix} E_H \\ E_V \end{pmatrix} = \begin{pmatrix} 1 & 0 \\ 0 & p \end{pmatrix}^{\beta} \begin{pmatrix} \cos\theta & -\sin\theta \\ \sin\theta & \cos\theta \end{pmatrix} \begin{pmatrix} 1 & 0 \\ 0 & p \end{pmatrix}^{\alpha} \begin{pmatrix} \cos\theta & \sin\theta \\ -\sin\theta & \cos\theta \end{pmatrix} \begin{pmatrix} 1 \\ 0 \end{pmatrix} = \begin{pmatrix} \cos^2\theta + \sin^2\theta p^{\alpha} \\ \cos\theta \sin\theta (1 - p^{\alpha}) p^{\beta} \end{pmatrix}$$

and

$$I_{out} = I_{in} \left\{ (\cos^2\theta + \sin^2\theta p^{\alpha})^2 + [\cos\theta \sin\theta (1 - p^{\alpha}) p^{\beta}]^2 \right\}.$$

Here, p is related to the principal transmittance: $T_{\perp} = 1 - R_{\perp} = p^2$. α is the number of ZnSe surfaces in the rotatable polarizer and β the number in the fixed polarizer. For our case, $p^2 = \frac{1}{2}$, $\alpha = 4$, $\beta = 2$ and the normalized transmitted laser intensity is

$$\frac{I_{out}(\theta)}{I_{in}} = \left\{ \cos^4\theta + \frac{1}{16} \sin^4\theta + \frac{41}{64} \cos^2\theta \sin^2\theta \right\}.$$

This expression agrees with the measured calibration intensity as a function of rotation angle about the beam axis. The extinction ratio of our attenuator is 1:16.

One final remark on the design of this attenuator is to avoid the use of plates with parallel faces. A scheme proposed by Bird and Schurcliff [9] can be considered by readers for obtaining better performance polarizers. They employed two oppositely sloping groups of plates that were each slightly wedged by angle about 1^o. In addition, each group of plates was also "fanned" slightly. As a result, no reflected rays would follow the optical path of the main transmitted beam and produce unwanted interferences.

8. References

[1] Bass, M. and Fradin, D. W., IEEE J. Quantum Electron. QE-9, 890 (1973).

[2] Milam, D., Bradbury, R. A., Picard, R. H., and Bass, M., in Proc. 6th ONR/ASTM/NBS Symposium on Laser Induced Damage in Optical Materials: 1974, NBS Special Pub. 414, 169 (1974).

[3] Yablonovitch, E., Appl. Phys. Lett. 19, 495 (1971).

[4] Gilbert, J. and Lachambre, J. L., Appl. Phys. Lett. 17, 187 (1971).

[5] For example, see Wang, V. and Giuliano, C. R., "Measurements of Damage at 10.6 μm in Three Alkali Halides over a Range of Pulse Durations," this Proceedings.

[6] Soileau, M. J. and Bennett, H. E., in Proc. 6th ONR/ASTM/NBS Symposium on Laser Induced Damage in Optical Materials: 1974, NBS Special Pub. 414, 149 (1974).

[7] Allen, S. D., Braunstein, M., Giuliano, C., and Wang, V., in Proc. 6th ONR/ASTM/NBS Symposium on Laser Induced Damage in Optical Materials: 1974, NBS Special Pub. 414, 66 (1974).

[8] Bass, M. and Barrett, H. H., IEEE J. Quantum Electron. QE-8, 338 (1971).

[9] Bird, G. R. and Shurcliff, W. A., J. Opt. Soc. Am. 49, 235 (1959).

9. Figures

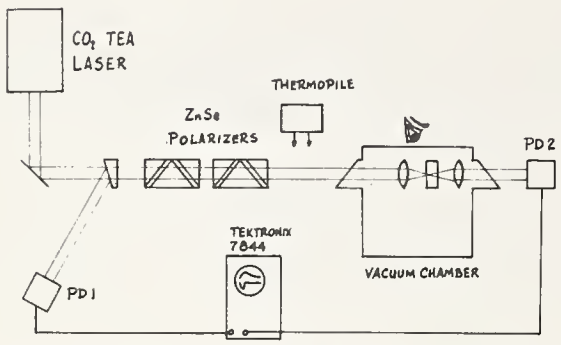

Figure 1. Schematic of the damage experiment. Both PD 1 and PD 2 are Ge photon drag detectors for monitoring the incident and transmitted pulses.

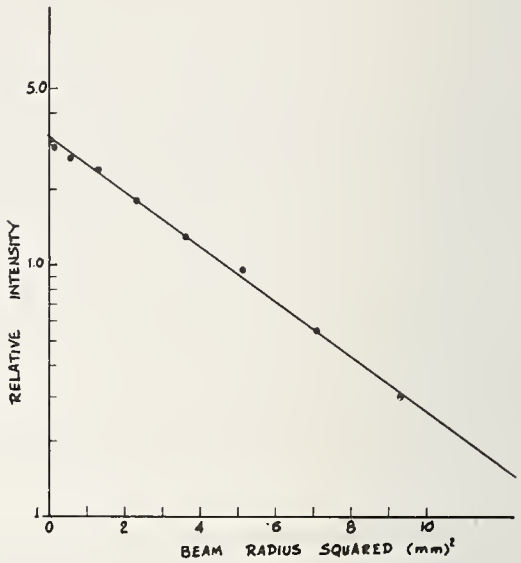

Figure 2. Pinhole scan of the CO_2 laser beam.

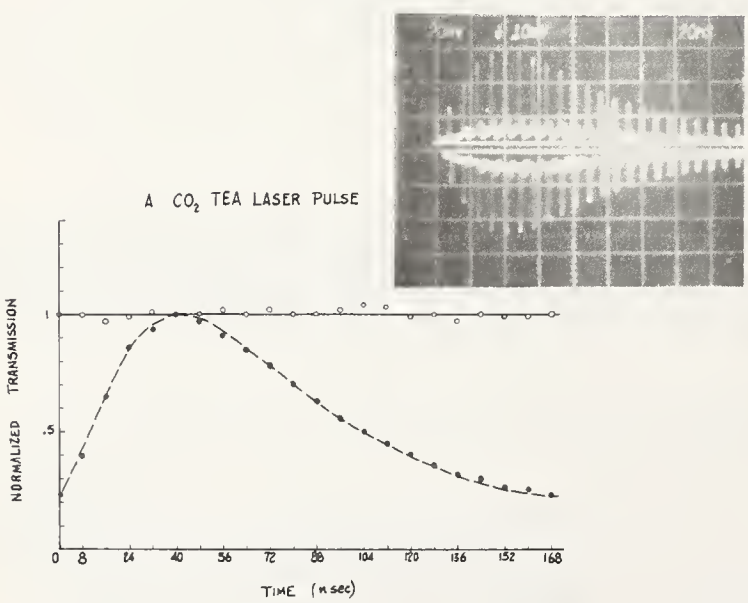

Figure 3. Transmission curve for a CO_2 TEA laser pulse. Dashed curve represents the laser pulse. $\Delta\tau$ is 92 nsec.

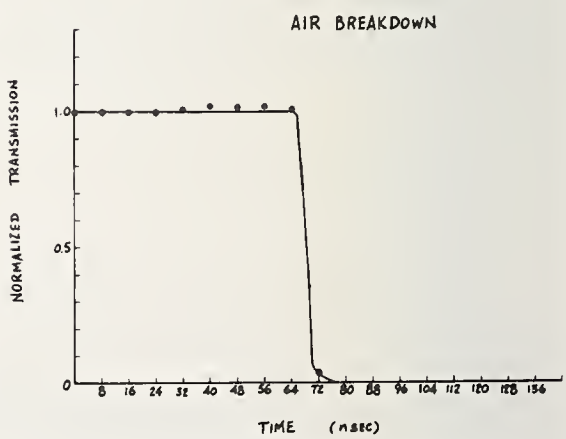

Figure 4. Transmission as a function of time for air breakdown.

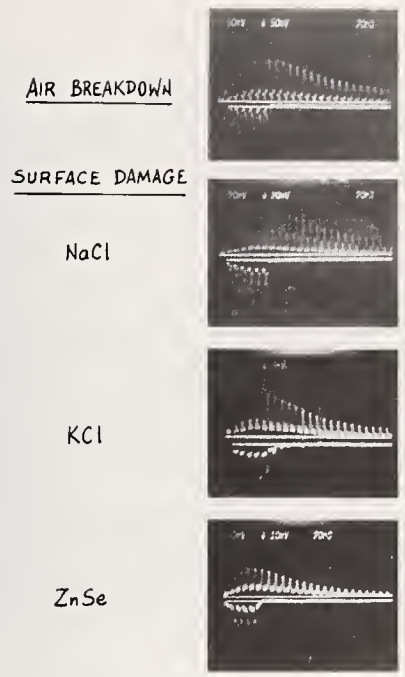

Figure 5. Typical oscilloscope traces for air breakdown and surface damage on NaCl, KCl, and ZnSe. The upper beam is the incident pulse and the lower beam is the transmitted pulse.

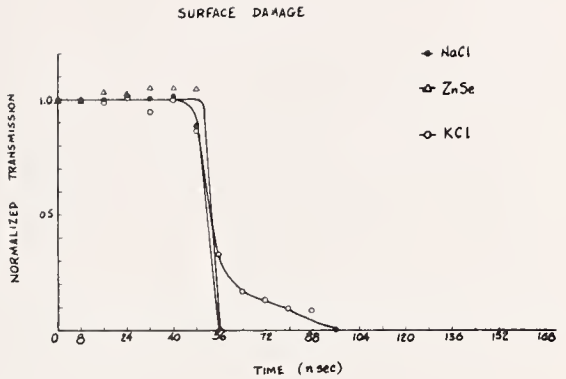

Figure 6. Transmission of mode-locked pulses as a function of time for surface damage on NaCl, KCl, and ZnSe.

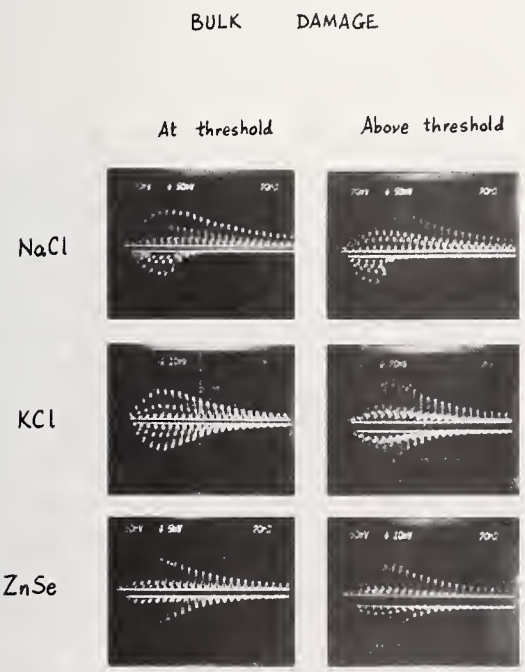

Figure 7. Typical waveforms for bulk damage in NaCl, KCl, and ZnSe at damage threshold and above threshold.

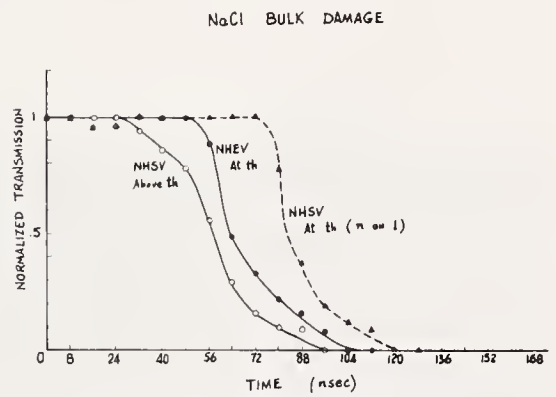

Figure 8. Normalized transmission of CO_2 TEA laser pulse as a function of survival time for NaCl bulk damage.

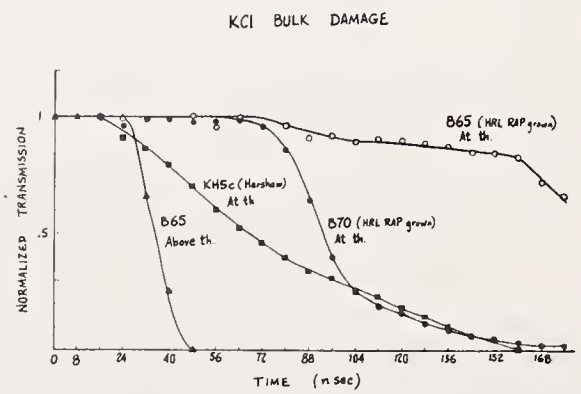

Figure 9. Normalized transmission of CO_2 TEA laser pulses as a function of survival time for KCl bulk damage.

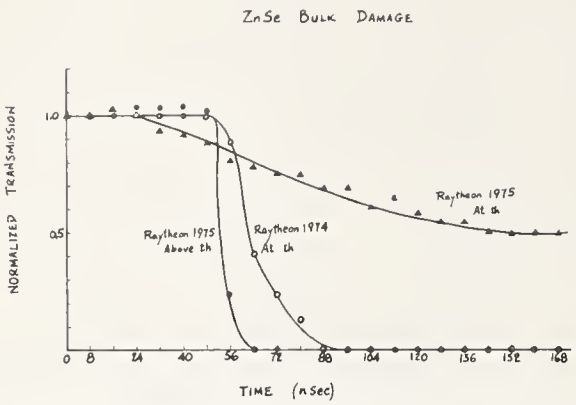

Figure 10. Normalized transmission of CO_2 TEA laser pulses as a function of survival time for ZnSe bulk damage.

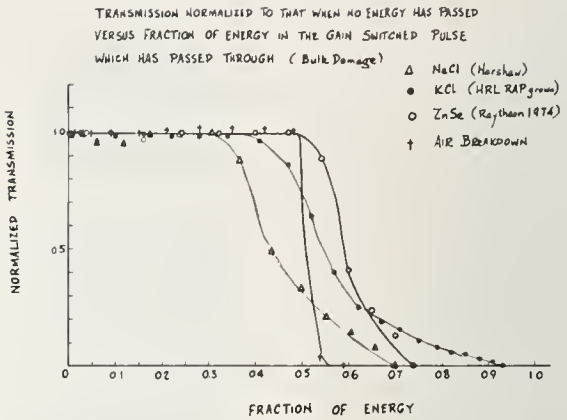

Figure 11. Normalized transmission versus fraction of energy contained in the gain-switched pulse for air breakdown, and bulk damage in NaCl, KCl, and ZnSe.

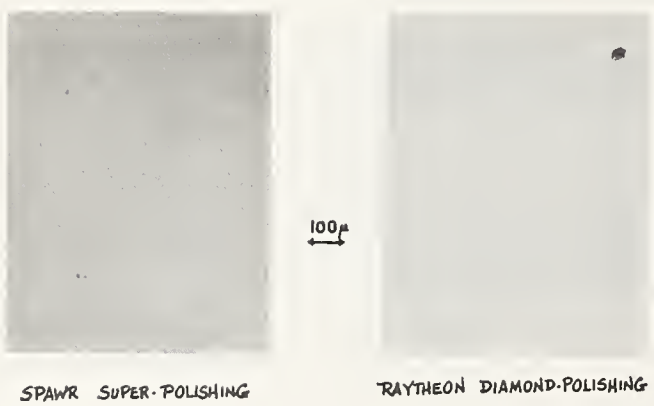

Figure 12. Nomarski micrograph of surfaces on improved ZnSe prepared by both super-polishing and diamond-polishing. The spots on the diamond-polished surface are probably due to inadequate cleaning of the protective Opticoat coating.

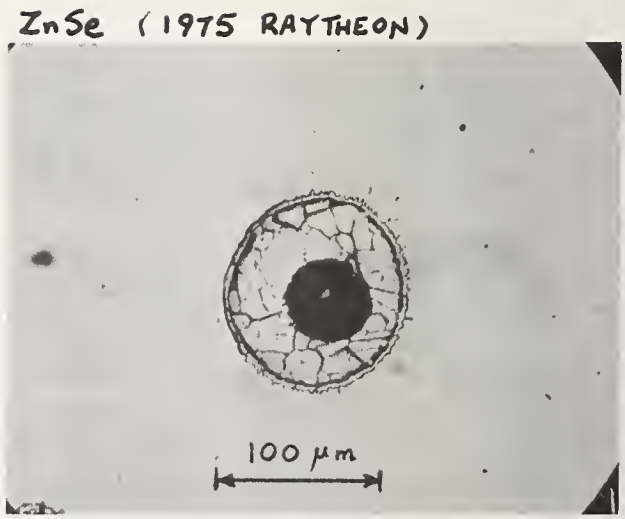

Figure 13. Damage site at threshold on a super-polishing surface of 1975 ZnSe observed with an optical microscope.

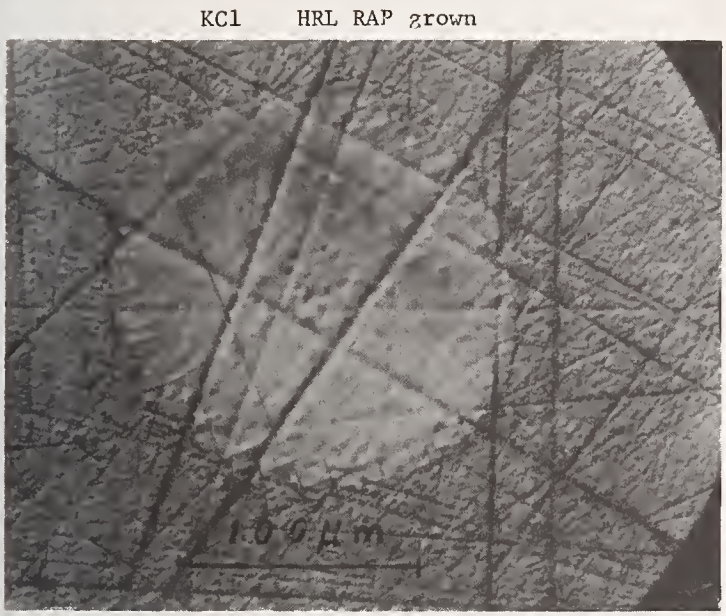

Figure 14. Nomarski micrograph showing a damage site on surface of RAP grown KCL (B70) at threshold.

Figure 15. Damage site at threshold on a conventional surface of Harshaw NaCl observed under an optical microscope.

COMMENT ON PAPER BY LEUNG, *et al*

There was a brief discussion of the details of sample preparation used in this work.

3.3 Improvements in the Breakdown Threshold in Alkali Halides at 10.6 μm*

V. Wang, C.R. Giuliano, S.D. Allen, and R.C. Pastor

Hughes Research Laboratories
3011 Malibu Canyon Road
Malibu, California 90265

Evidence has been found that the threshold for laser-induced breakdown in the bulk of single crystals is strongly dependent upon processing. Potassium bromide, KCl, and NaCl have been examined over a range of pulse widths (from 0.2 μs to 6 μs in selected cases and for a variety of pulse shapes using both single longitudinal mode and partially mode-locked multilongitudinal mode pulses. A breakdown threshold of over 12 GW/cm^2 (2.5 MV/cm) for KCl far exceeds the best values obtained in previously available commercial material at these pulse lengths. A comparison of breakdown threshold for conventional and reactive atmosphere processed (RAP) halides is made with comment upon the present ambiguities in breakdown mechanism. In addition to the measurement of damage thresholds of materials from different sources, the temporal profile of transmitted pulses at the time of damage was monitored.

Key words: Alkali halides; bulk damage; longitudinal mode control; pulsed 10.6 μm laser damage; RAP materials; transmitted pulse cutoff; variable pulse duration.

Introduction

Increasing evidence has linked laser-induced breakdown in pure materials such as the alkali halides to an avalanche process, which is thought to be similar to the process responsible for dc electrical breakdown. The breakdown threshold has been interpreted as an "intrinsic" property of the material, dependent primarily upon its band gap. The following evidence may suggest that laser-induced breakdown depends strongly upon material purity and that commercial materials available in the past are limited by localized effects. Previous evidence of unusually high thresholds has been found in ultrapure materials [1, 2][1].

The purified materials used in this study were prepared by a reactive atmospheric process (RAP) developed to lower 10.6 μm absorption in laser windows by removing water from the growth process [3, 4]. The commercial materials are standard low cost spectrophotometer materials that are commonly available. There is evidence from others [5], as well as our own experience, that low absorption laser quality crystals can and usually do tend to perform worse than the common spectrophotometer grades in laser breakdown measurements, apparently because of inclusions.

A significant improvement in the quality of the following measurements is gained by improved control of the CO_2 TEA laser output. By control of the pump duration and insertion of a longitudinal mode selector described elsewhere [6], pulses of different temporal shape and duration can be provided. Figure 1 illustrates the five pulse shapes chosen here. A typical, partially mode-locked multilongitudinal single transverse mode pulse consists of a gain switched spike of about 200 ns duration (FWHM) followed by a tail of several microseconds duration. The typical TEA laser pulse used in the experiments described contains a somewhat greater fraction of energy in its tail than usually seen in commercial TEA lasers because of details of the pump system, gas mix, and pressure. Figure 1(b) shows a single longitudinal mode pulse of the same overall envelope profile as figure 1(a), achieved by operating the low pressure intracavity longitudinal mode selector slightly below threshold. Operation of the discharge above the cw threshold results in the suppression of the gain-switched spike as seen in figure 1(c), and a more nearly square pulse of 1 μs followed by a tail of several μs [7]. Changes in the laser operating conditions allow selection of a longer 4 μs multilongitudinal mode pulse, as well as a 6 μs smooth single longitudinal mode pulse (figures 1(d), 1(e), respectively). All pulses used were single transverse mode, measured and monitored as described in [6]. The lens used was a 1 in. f.l. near-diffraction-limited f/1 germanium doublet from Laser Optics, Inc., with a spot size of 34 μm. Care was taken to properly calibrate the on-axis flux density of the system.

Preliminary evidence indicates that the laser may operate on more than one rotational line in the gain-switched mode. All measurements were made by irradiating a single site with progressively increasing flux levels until breakdown was reached. A new site is then chosen and irradiation is repeated starting with a flux well below breakdown.

*Work supported by the Defense Advanced Research Projects Agency through Air Force Cambridge Research Laboratories under Contract No. F19628-75-C-0135.

1. Figures in brackets indicate the literature references at the end of the paper.

Peak power quoted in the following section was determined by using the measurement of total pulse energy together with a monitor of pulse shape and duration using a photon drag detector and oscilloscope, system rise time is ~1 ns. By using a planimeter to determine the area under a typical recorded pulse, the peak power can be determined. An "equivalent" pulse length is also cited for a rectangular pulse of height and area equal to the original pulse. For the multilongitudinal pulse with rapid oscillations a slower detector which averages these rapid oscillations is used. Thus, for these pulses the instantaneous peak power is about eight times higher than that for the averaged pulse (figure 1(f)).

Test Results

An effort was made to test three alkali halides grown by two processes (RAP and Kyropoulos, unless otherwise stated) at several pulse lengths and using both single and multiple longitudinal mode pulses. A damage threshold in power flux dependent upon $\tau^{1/2}$ is suggestive of a localized thermal damage mechanism. Comparison of single and multiple longitudinal mode thresholds, or gain-switched TEA pulses versus smooth pulses gives large changes in the ratio of peak to average power. A comparison of these results gives a comparison of the effect on thresholds for 2 ns pulse trains, 150 ns, 1 μs,and 6 μs pulses, an appreciable range of pulse lengths.

A sampling of the type of results that are typical is shown in table 1 for KBr. Considerable scatter is typical of the data, but nevertheless the damage resistance of RAP KBr is clearly higher than that of the other materials. Although the data are incomplete, they suggest that the single longitudinal mode thresholds are far higher than the partially mode-locked multiple longitudinal mode results. This would suggest that the damage threshold is actually determined by the peak power in the 2 ns pulses that make up the mode-locked pulse trains, rather than by the average power. Remember that the power in the mode-locked pulse is measured by averaging over the high speed modulation. The commercial material does not show this strong time dependence, which might indicate that a slower mechanism is operative here, such as thermal inclusions precipitated failure. However, RAP KCl appeared to have the identical threshold for the first two types of pulses, which is compatible with both thermal and avalanche time constants. Breakdown was not reached for longer single mode pulses.

Table 1. Potassium Bromide Thresholds for Four Types of Pulses (GW/cm^2)

Pulse Shape	Mode Locked	Single Mode	1 μs	6 μs
Commercial	0.4 to 1.5	0.7 to 1.2	2.6	0.2 to 0.4
High Purity-RAP	1.35 to 2.5	>6.2	5 to 11+	>4

Table 2 compares the performance of these two sources of material for three materials at one pulse length, listed in order of increasing band gap. Again an improvement is indicated with the most noticeable case being KCl. (RAP NaCl has received relatively little development to date.) Of particular interest is the large and consistent difference seen for the two types of NaCl commercially available. One type is stated by the manufacturer to be grown by the Stockbarger method in vacuum for low absorption laser windows. The other type is air grown by the Kyropoulos method for spectrophotometers. The latter is three times more resistant in these multiple shot tests. Table 3 displays a similar set of data for a single-longitudinal mode gain-switched pulse. Again, measured values for the commercial materials are comparable with previous literature [8]. However, the breakdown field for RAP KCl exceeds 3.5 MV/cm compared with reported values of about 1.4 MV/cm. As a further elaboration of this trend, table 4 presents the damage thresholds of KCl for a variety of sources using one type of pulse. Most commercially available material we have tested suffers from inclusion-initiated damage in the bulk which is clearly visible under a microscope as a string of small damage sites. The maximum thresholds observed have been 0.5 GW/cm^2. In passing, we have noted that some of these same crystals can give the appearance of a reproducible bulk damage (by the criterion of [9]) when tested at 0.69 μm. RAP prepared KCl crystals possess breakdown thresholds comparable to the best NaCl samples available, with some evidence that the most reproducible samples result from recent improvements in processing.

Table 2. Mode-Locked Pulse Train (0.6 μs)

	Commercial Purity (GW/cm^2)	High Purity-RAP (GW/cm^2)
KBr	0.4 to 1.5	1.35 to 2.5
KCl	0.5 to 1.5	3 to 14
NaCl	5[a]	5 to 16
	12 to 16[b]	

[a]Stockbarger. [b]Kyropoulos.

Table 3. Single Longitudinal Mode Gain Switched Pulse

	Commercial Purity (GW/cm^2)	High Purity-RAP (GW/cm^2)
KBr	0.7 to 1.2	>6.2
KCl	1.6	>12
NaCl	—	>17

Table 4. KCl Damage Thresholds for 0.6 μs Mode-Locked Pulses

	Damage Threshold (GW/cm^2)
Commercial KCl (Inclusion type damage)	0.5
Commercial KCl	0.7 to 1.5
Commercial Europium Doped Polycrystalline	1.8
RAP B65-3	3
RAP B63-2	4 to 7
RAP B63-9	8 to 14
RAP B53-1	10 to 14
RAP B78-2 (CO_2 Carrier Gas)	10 to 14

As a further example of the type of pulse length dependence we have observed, table 5 summarizes the measurements made using two multilongitudinal mode pulses. Here, the large decrease in breakdown threshold for the longer pulse might suggest that some mechanism other than electron avalanche is responsible. Electron avalanche is expected to be a rapid process which would suggest little decrease in threshold for pulses of this length. Yet the increases do not follow the $\tau^{1/2}$ dependence expected for localized thermal mechanisms such as inclusions, nor do they follow the energy dependence of homogeneous absorption proportional to τ. However, the relatively complex temporal pulse shape of the pulses in this set of data may mask the true pulse length dependence of this mechamism.

Table 5. 10.6 μm Bulk Damage Thresholds for Three Alkali Halides at Two Pulse Lengths

Material		Damage Threshold (Power Density and Electric Field Strength)				Comments
		Pulse Length = 0.6 μs		Pulse Length = 4 μs		
KBr	Harshaw	1.03 0.73	GW/cm^2 MV/cm	0.36 0.43	GW/cm^2 MV/cm	
	RAP-HRL	1.25/1.7 0.8/0.94	GW/cm^2 MV/cm	0.34/0.37 0.42/0.44	GW/cm^2 MV/cm	
KCl	Harshaw	<0.52[a] <0.52[a]	GW/cm^2 MV/cm	<0.046[a] <0.15[a]	GW/cm^2 MV/cm	Damage by inclusions
		- -		0.095[b] 0.22[b]	GW/cm^2 MV/cm	Damage by inclusions
	RAP-HRL	6.08 to 14 1.8 to 2.7	GW/cm^2 MV/cm	2.05 1.03	GW/cm^2 MV/cm	
NaCl	Harshaw	4.6[a] 1.5[a]	GW/cm^2 MV/cm	>2.3[a] >1.08[a]	GW/cm^2 MV/cm	
		12 to 16.0[b] 2.5 to 2.9[b]	GW/cm^2 MV/cm	- -		
	RAP-HRL	4.9 to 16 1.6 to 2.9	GW/cm^2 MV/cm	- -		

[a]Stockbarger.
[b]Kyropoulos.

Temporal Characteristics of Transmitted Pulses

To provide insight into the avalanche process as well as to indicate whether the breakdown process was an inclusion mediated process or a homogeneous process, the transmitted light through the sample was monitored with a fast detector and preamplifier. It was found, as expected [10], that where inclusion damage was obvious from the morphology of the damaged sample (multiple damage sites from one shot), the transmitted light was not sharply cut off. Some samples with only one apparent damage site also exhibited the gradual cutoff characteristic of inclusion damage. Perhaps these samples contained more closely spaced defects of higher damage resistance resulting in the merger of these defect sites.

Figure 2 is a set of pulses transmitted through conventional KCl for three types of pulses. The upper photographs represent the last pulse before breakdown occurs and the lower row shows the sharp cutoff at breakdown. The multilongitudinal mode pulses on the left have two values for power density quoted. The numbers in parentheses represent direct measurements made on this photograph at the moment before damage. The other power density below is based upon the measured energy and the equivalent pulse length of 0.6 μs obtained from a typical pulse, with the rapid modulation averaged. Thus, the peak power from the train of partially mode-locked 2 ns pulses is much higher than the averaged power, as expected. A pulse with the same gain-switched envelope profile is shown in the center pair, but without modulation. Here the two power densities are more nearly equal. These smaller discrepancies are probably due to fluctuations in pulse shape and thus in equivalent pulse length. The third pulse is a 1 μs pulse followed by a small tail of several microseconds. The upper picture of the last pair also includes a blocked beam trace indicating that the residual modulation visible is caused by electrical noise. The important point illustrated here is in the comparison of breakdown values for the different pulses. For instance, the first two pulses, multimode and single mode, have a large difference in peak power, but essentially the same average power. This is consistent with a breakdown mechanism which responds to the averaged waveform and is consistent with both electrical avalanche mechanisms and thermal mechanisms. Since this material exhibited a similar peak power breakdown for the 1 μs pulse on the right, it is tempting to conclude that longer pulses in this range do not result in a decrease of breakdown threshold. This would be consistent only with a rapid process such as electrical avalanche with a nearly constant power flux threshold at these long μs pulse lengths, but inconsistent with a thermal model. This set of data points, taken by itself, would seem to provide strong support for an avalanche hypothesis. However, table 5 provides contradictory evidence.

A comparison of transmitted pulses for conventional KBr is shown in figure 3. Using 1 μs single longitudinal mode pulses, a pulse below threshold is shown in addition to four examples of pulses that cause breakdown. In the last case the pulse energy was purposely raised a factor of 2 above the threshold. For this sample breakdown occurred consistently between 1.6 and 1.8 kJ/cm^2, corresponding to a power of about 0.8 to 0.9 GW/cm^2 when calculated by dividing energy by an equivalent pulse length of 1.9 μs. The value for power obtained from the photon drag detector oscilloscope traces in these cases agrees only to within a factor of two with that obtained from dividing energy by pulse duration. The reason for this discrepancy has not been firmly established. Nevertheless, the point of special interest in this series of oscillographs is the large variation in breakdown times seen in the first three examples of figure 3. In the fourth instance, doubling the pulse energy did not result in simply halving the time to breakdown, at least in this instance, suggesting that the mechanism for breakdown is not likely to be energy dependent (such as simple absorption heating). Statistical fluctuations on this long time scale suggest further study of this aspect is warranted.

A direct comparison of modulated and smooth pulses of 0.6 μs duration was made on several samples. While the thresholds are often very close, the morphology of the damage site can be very different. A sample believed to fail by inclusion-mediated damage, RAP KCl B65-3 is shown in figure 4. Figure 4(a) shows the small microscopic site often obtained with a single longitudinal mode gain-switched pulse, as compared with the millimeter sized fracture typical of multilongitudinal pulses having the same envelope and energy (figure 4(b)). Longer single and multilongitudinal mode pulses were damage in a manner similar to figure 4(b). Larger fractures are expected with pulses of greater energy, as would arise from longer pulses or more damage resistant materials, but the strong morphological effect seen for the two pulses which differ only in their detailed temporal structure remains unexplained.

Summary

The scope of phenomena we have seen suggests that considerable work remains to be done before a damage mechanism and breakdown "threshold" can be meaningfully assigned to an alkali halide at 10.6 μm. Preliminary conclusions that may be drawn from this work include the following points.

- There is a large variation in threshold from samples grown by different methods. Some samples grown with special care can have consistent breakdown thresholds many times higher than conventional materials.
- There is a fairly large fluctuation in threshold for most materials. This might occur from spatial inhomogeneities or from purely statistical processes.
- The observation of a single damage site from a laser pulse has not always been accompanied by a sharp cutoff in the transmitted beam. While the appearance of a string of scattered damage sites from a laser pulse is always accompanied with an incomplete or undetectable cutoff, samples have been found to exhibit damage thresholds sufficiently high to be attributable to intrinsic mechanisms and to have a single damage site, and yet to occasionally have the incomplete cutoff characteristic of inclusions. It would seem that the morphology of the site and the behavior of the transmitted light cannot be used to unequivocally identify intrinsic processes.

The availability of relatively smooth, well-behaved pulse shapes at 10.6 μm suggests that detailed survival time studies of breakdown processes in these materials can now be carried out.

Acknowledgment

We gratefully acknowledge the contribution of A. Braunstein, M. Braunstein, and A. Pastor in the areas of technical management, materials growth, fabrication and preparation, technical discussion, and support measurements.

References

[1] Olness, D., "Laser-induced breakdown in transparent dielectrics," J. Appl. Phys. 39, 1 (1967).

[2] Allen, S. D., Braunstein, M., Giuliano, C., Wang, V., "Pulsed CO_2 laser damage studies of RAP grown KCl," NBS Spec. Pub. 414, Laser Induced Damage in Optical Materials: Dec. 1974.

[3] Pastor, R. C. and Pastor, A. C., "Crystal growth in a reactive atmosphere," Mat. Res. Bull. 10 (Pergamon Press, Inc., 1975) pp. 117-124.

[4] Pastor, R. C. and Pastor, A. C., "Crystal growth of KCl in a reactive atmosphere," Mat. Res. Bull. 10, (Pergamon Press Inc., 1975) pp. 251-256.

[5] Private correspondence, E. Yablonovitch (1974).

[6] Wang, V., Giuliano, C. R. and Gracia, B., "Single and multilongitudinal mode damage in multilayer reflector at 10.6 μm as a function of spot size and pulse duration," Proc. 1975 Laser Damage Symposium, Boulder, Colorado, July 1975.

[7] Gondhalekar, A., Heckenberg, N. R. and Holzhauer, E., "The mechanism of single-frequency operation of the hybrid-CO_2 laser," J. Quantum Electron. QE-11, 3 (1975).

[8] Yablonovitch, E., "Optical dielectric strength of alkali-halide crystals obtained by laser-induced breakdown," Appl. Phys. Lett. 19, No. 11, Dec. 1971.

[9] Fradin, D. W. and Bass, M., "Electron avalanche breakdown induced by ruby laser light," Appl. Phys. Lett. 22, No. 5, 1 March 1973.

[10] Bloembergen, N., "Laser-induced electric breakdown in solids," IEEE J. Quantum Electron. QE-10, No. 3, March 1974.

Figures

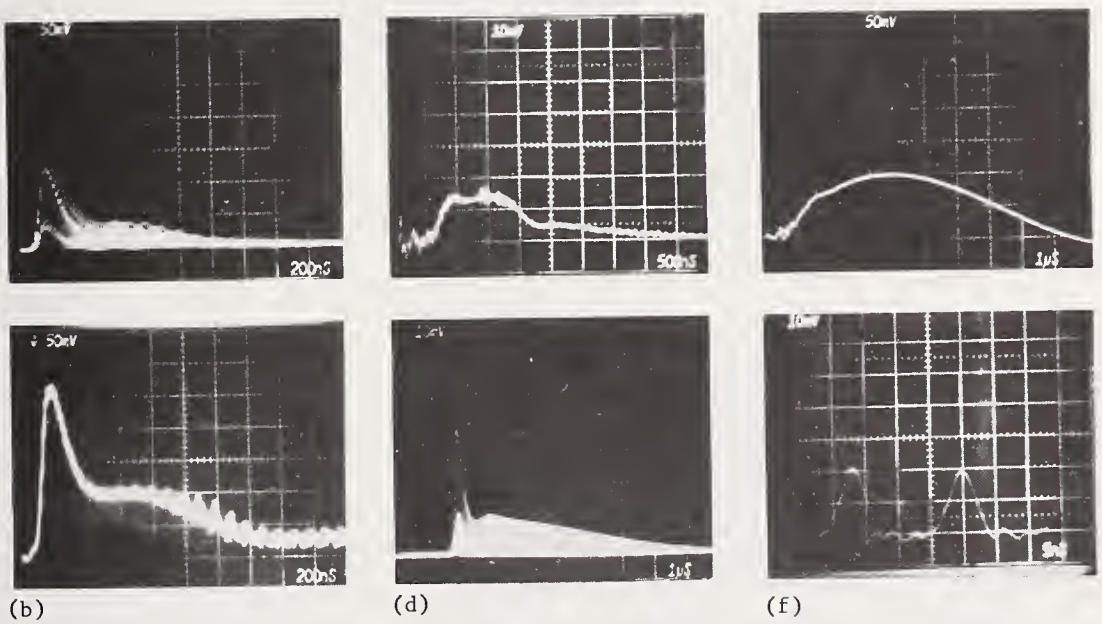

(b) (d) (f)

Figure 1. Oscilloscope traces of the five types of pulses used. (a) 0.6 μs multi-longitudinal gain switched pulse. (b) 0.6 μs single longitudinal mode gain switched pulse. (c) 1.9 μs single longitudinal mode pulse. (d) 4 μs multilongitudinal mode gain-switched pulse. (e) 6 μs single longitudinal mode pulse. (f) expanded view of typical multilongitudinal partially mode-locked pulse train of (a) and (d).

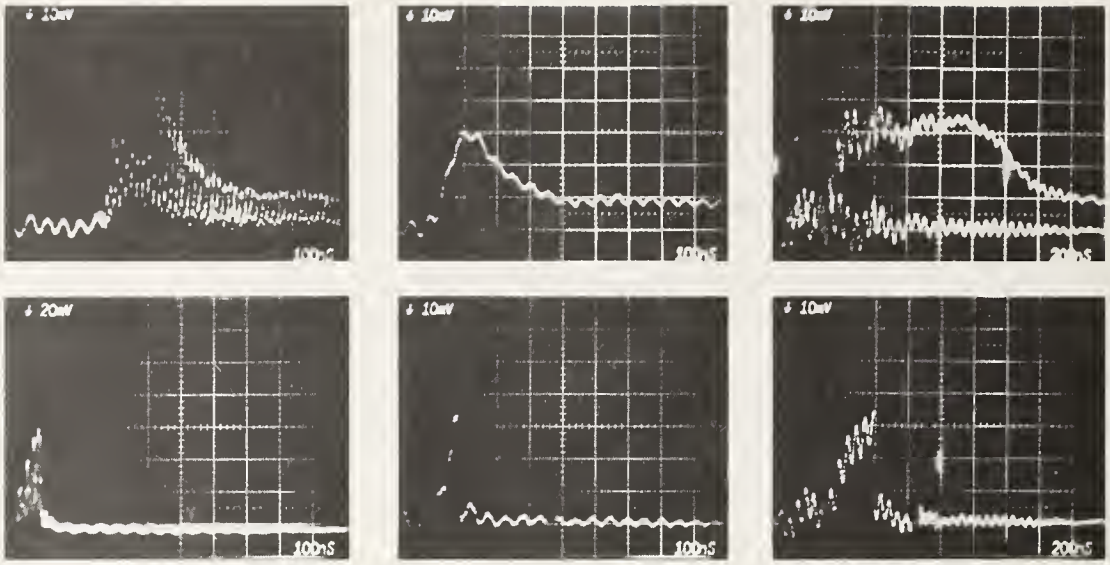

Figure 2. Transmitted pulses for three types of pulses through commercial KCl.

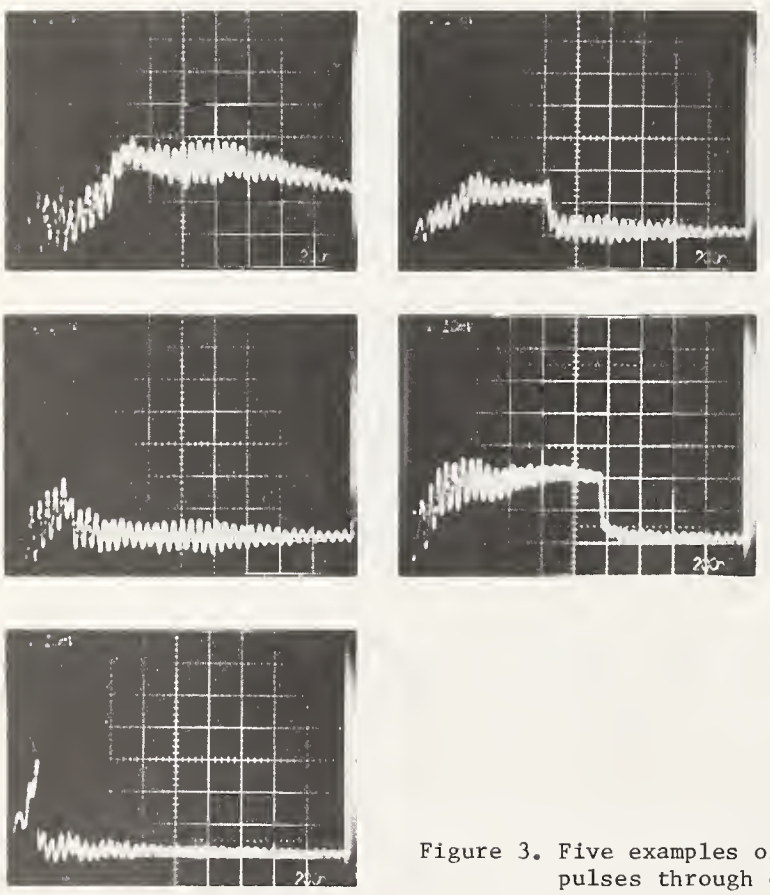

Figure 3. Five examples of 1.9 μm transmitted pulses through commercial KBr.

Figure 4. Breakdown sites in reactive atmosphere processed KCl B65-3.

COMMENTS ON PAPER BY WANG, et al

As has been mentioned in previous years the characterization of optical materials as polycrystaline or single crystaline must be used with some care where laser damage studies are involved. Unless the dimensions of the microcrystals in the polycrystalline material are small compared with the electron mean free path in the material there is no distinction between single and polycrystalline material. Thus in previous years it has been reported that the damage threshold for fused silica was significantly higher than that observed in crystalline quartz. However, in sodium chloride and other alkali-halides no distinction was seen between so-called polycrystalline material and single crystalline material. It was further brought out in the discussion that the morphology of the damage site is primarily sensitive to the total energy falling on the damage site during the pulse rather than the details of the damage process.

3.4 Optical Distortion by Laser Heated Windows

J. S. Loomis
Air Force Weapons Laboratory
Kirtland AFB, New Mexico 87117

E. Bernal G.†
Honeywell Corporate Research Center
10701 Lyndale Avenue South
Bloomington, Minnesota 55420

The optical distortion introduced in a collimated He-Ne beam by windows irradiated with a CO_2 laser has been measured interferometrically. Materials measured included ZnSe, KCl, NaCl, CaF_2, SrF_2, and BaF_2. Flux densities from the CO_2 laser were in the range 10-60 KW/cm^2 with total powers from 250 to 1000 watts for the ZnSe and the halides. The changes in the interferometric patterns observed can be attributed to a) isotropic phase shifts proportional to the local temperature, b) anistropic effects due to induced birefringence that affect both the symmetry of the interferometric pattern and the visibility of the fringes, c) localized phase shifts at the entrance and exit points due to surface absorption.

An analysis of the experimental observations is given using a scalar optics approach and temperature rise functions derived previously by the authors. Experimental comparisons of thermal sensitivity of various materials are given. Also, the relative value of the anisotropic changes in optical path as the window aperture is filled at constant flux density is calculated. This result allows the prediction of window behavior in large lasers from the results of interferometric tests with focused beams of the same flux density.

Key words: Infrared lasers; interferometry; stress birefringence; thermal distortion; windows.

I. INTRODUCTION

The optical aberration introduced by laser heated windows has been the subject of numerous recent theoretical and experimental studies [1-8][1]. The theoretical studies have fallen into two categories. The earlier treatments emphasized the development of figures of merit expressions for window materials based on simplified temperature profiles, and often, on estimated values of materials parameters. This approach yielded valuable broad guidelines on the relative potential of various materials [1,2]. More detailed treatments of thermally induced aberrations yielded more insight on the effects of the aberration on the far field power distribution, albeit at the loss of analytical expressions for figures of merit [3,4].

The bulk of the experimental results reported to date have emphasized the experimental verification of the predicted laser-induced window aberrations via either interferometric measurements [5,7,8] or measurements of the far-field intensity [5,6]. However, in order to produce measurable effects to verify theory with laboratoty-type lasers having single transverse mode beams and power outputs in the hundreds of watts, it has often been necessary to use samples with much higher absorption than are available from state-of-the-art materials or, to artificially raise the surface absorption by applying an absorbing layer on the surface of the sample. Thus, while the experimental results have largely confirmed the occurrence of various types of aberrations at high irradiances, the throughput capability of the materials tested has not been established for lack of good documentation on the power absorbed by the sample, the effect of coatings, and the absence of a scale-up model to predict the magnitude of the aberrations to be expected when the window aperture is filled by a beam having the same peak flux density as the tightly focused beam used to make the distortion measurements in the laboratory.

It is now clear that the CW power that can be trasnmitted through a solid window will be limited by laser-induced optical distortion. This is because the strength of candidate window materials has been increased to the point that laser-induced fracture would occur at powers above those that produce unacceptable beam aberrations. Therefore, in this paper we endeavor to present qualitative experimental results on the optical distortion produced by various window materials when irradiated by a laser beam focused to a spot size much smaller than the window diameter. The effects of thermally induced birefringence are shown to be dominant in the case of alkaline earth fluorides. We also give the results of a model that attempts to predict the increase in optical distortion to be expected when the diameter of the laser beam is increased from the focused case to an aribtrary value while keeping the flux density constant. If this model is correct, it should provide a method of predicting component performance in a high power laser from laboratory measurements. Finally, the interferometric observation of surface absorption is also reported.

†Work supported by Defense Advanced Research Projects Agency under Contract #DAHC-15-73-C-0464.

1. Figures in brackets indicate the literature references at the end of the paper.

II. ANALYSIS

The purpose of the analysis of the dynamic behavior of the interferogram during laser irradiation is to provide a common model for comparison of the response of various materials in terms of their physical properties.

Once the model is refined sufficiently to reproduce the results of interferometric measurements obtained during irradiation of windows with focused beams from laboratory type lasers (200-1000 watts), it can be used to predict the optical distortion and stress levels to be expected when the full aperture of the window is filled with the beam of a high power laser. This is a most important aspect of the analytical approach, because it reduces the amount of testing required in a high power laser facility.

The main task of the model is to produce expressions for the change in optical path produced by the absorption of laser radiation. This is because all the window aberrations produced by laser irradiation are caused by the non-uniform temperature rise resulting from absorption of energy from the beam. Thus, the total model for the window aberration requires the following components: a realistic calculation of the temperature rise of the window resulting from laser irradiation, calculation of the stresses resulting from the non-uniform temperature rise and, expressions for the change in refractive index resulting from the above. We deal with each of those questions below.

A. Temperature Rise of the Window

The interferometric measurements of laser-induced aberrations in solid windows are typically conducted with unclamped windows that have very small heat transfer to the mount. This is accomplished by having the window in a holder such as the ones used for calorimetric measurement of the absorption coefficient [9]. Assuming that the window is in the form of a disc of radius b and length 2ℓ, the heat flow problem associated with the calculation of the temperature rise resulting from absorption of energy from the beam is the same found in calorimetry. The boundary value problem to be solved is therefore [10]

$$\nabla^2 T + (Q/k) = (1/\kappa)\ (\partial T/\partial t) \qquad 0 \leq r \leq b,\ 0 \leq z \leq \ell \qquad (1a)$$

$$k(\partial T/\partial r) + hT = 0 \qquad r = b, \qquad (1b)$$

$$-k(\partial T/\partial z) = 0 \qquad z = 0, \qquad (1c)$$

$$k(\partial T/\partial z) + hT = 0 \qquad z = \ell \qquad (1d)$$

where h = heat transfer coefficient

k = thermal conductivity

$\kappa = k/\rho C$ = thermal diffusivity

ρ = density

C = specific heat capacity

Solutions for the temperature rise resulting from a gaussian heat input function with radius a used in equations (1a-1d) have been obtained before by the method of finite Fourier transforms [10] for beam radii smaller than, or equal, to half the window radius ($2a \leq b$) and by a finite element method for $2a \geq b$ [11]. The reason for using the two methods is due to optimal rate of convergence of the solutions in their respective regimes. The results obtained have been verified to agree in the overlapping region near $2a = b$ to within better than 5%.

B. Thermal Stresses

The thermal stresses are calculated here based on the isotropic thermoelastic model for plane stress given by Boley and Wiener [12] and used extensively by others. This approach is known to be inaccurate for several of the window materials of interest, which although possessing a cubic structure, exhibit strong elastic anisotropy. Thus, although isotropy is assumed in order to obtain analytic expressions for the thermal stresses, any experimental observations related to crystalline orientation cannot be expected to be describable by this model.

For the range of laser beam diameters $0<2a\leq b$, the stresses were obtained by term-by-term integration of the temperature distribution, eq. (10), [10], substituted into the thermal stress equations of [12].

C. Refractive Index

The changes in refractive index resulting from the inhomogeneous temperature rise and associated thermal stresses are calculated using expressions given by Jasperse and Gianino [2]. Because of the assumed elastic isotropy and the cylindrical symmetry of the temperature rise, the eigenvectors of the index ellipsoid correspond to radial and azimuthal polarizations and are given by [2]

$$\begin{pmatrix} \delta n_r(r,z,t) \\ \delta n_\theta(r,z,t) \end{pmatrix} = \left[\left(\frac{\partial n}{\partial T} \right)_\varepsilon - \frac{\alpha n_o^3}{2} (p_{11}+p_{12}) \right] T(r,z,t)\, \underline{I} - \frac{n_o^3}{2E} \begin{pmatrix} p_{11}-2\nu p_{12} & p_{12} - \nu(p_{11}+p_{12}) \\ p_{12}-\nu (p_{11}+p_{12}) & (p_{11}-2\nu p_{12}) \end{pmatrix} \begin{pmatrix} \sigma_r(r,z,t) \\ \sigma_\theta(r,z,t) \end{pmatrix} \tag{2}$$

where p_{ij}'s are stress-optic constants [13] and $\underline{I}$ is the 2x2 identity matrix; ν is Poisson's ratio, and E is the modulus of elasticity.

The equation above has a polarization-independent term proportional to the temperature rise and a polarization dependent term proportional to the thermal stresses. The relative magnitudes of the two terms will determine whether or not birefringence is important.

D. Transmitted Wave

The expressions above are based on a paraxial ray approximation. This is quite appropriate to the analysis of the interferometric measurements because the windows are illuminated with a well collimated beam in such experiments. Because of these experimental considerations, the spatial dependence of each electric polarization component of the electric field of the monochromatic wave from the HeNe laser source used in the interferometer can be written as

$$E(z) = E_o\, e^{ikz} \tag{3}$$

where

$$k = \frac{2\pi n(r,z)}{\lambda} \quad . \tag{4}$$

Thus, a change in refractive index δn in a window of thickness ℓ simply introduces a phase factor on the propagating wave such that

$$E(z) = E(z)\, e^{i\phi} \tag{5}$$

$$\phi = \frac{2\pi}{\lambda} \int_{-\ell}^{\ell} \delta n(r,z)\, dz \, . \tag{6}$$

Following Flannery and Marburger [4], we use the Jones matrix formalism in a cartesian coordinate system. Then the field

$$\begin{pmatrix} E'_x \\ E'_y \end{pmatrix}$$

resulting from propagation of the input field

$$\begin{pmatrix} E_x \\ E_y \end{pmatrix}$$

through the laser-heated window is given by

$$\begin{pmatrix} E'_x \\ E'_y \end{pmatrix} = A \begin{pmatrix} E_x \\ E_y \end{pmatrix} \tag{7}$$

where

$$A = e^{i\phi} \begin{pmatrix} \cos\delta + i \sin\delta \cos 2\theta & i \sin\delta \sin 2\theta \\ i \sin\delta \sin 2\theta & \cos\delta - i \sin\delta \cos 2\theta \end{pmatrix} \tag{8}$$

and

$$\phi = \tfrac{1}{2} (\phi_r + \phi_\theta) \tag{9}$$

$$\delta = \tfrac{1}{2} (\phi_r - \phi_\theta) \tag{10}$$

$$\phi_r(r,t) = \frac{2\pi}{\lambda} \int_{-\ell}^{\ell} \delta n_r(r,z,t)dz \tag{11}$$

$$\phi_\theta(r,t) = \frac{2\pi}{\lambda} \int_{-\ell}^{\ell} \delta n_\theta(r,z,t)dz \tag{12}$$

ϕ is therefore the average phase retardation and δ is the phase difference, which is proportional to the induced birefringence. We show below how these two quantities lead to polarization independent and polarization dependent effects, respectively.

E. Intensity Distribution in Interferogram

To calculate the intensity distribution in the observation plane of the interferometer, we assume that the input wave to the window and the reference wave are linearly polarized in the y-direction, i.e.,

$$E_{in} = E_{ref} = E(z) \begin{pmatrix} 0 \\ 1 \end{pmatrix}$$

where E(z) is given by eq. (3). Then the intensity is obtained by the interference of the wave propagating through the sample, eq. (7) above, and a reference wave of the form

$$E_1(r,z) = E_o \exp\left[i(kz+\Omega(r,\theta)\right] \begin{pmatrix} 0 \\ 1 \end{pmatrix} \tag{13}$$

where Ω (r,θ) is a function used to introduce bias fringes for reference purposes in the interferogram. These fringes are typically either equally spaced straight lines obtained by introducing a wedge in an arm of the interferometer, or circular fringes introduced by changing the curvature of the reference beam. For these two cases the form of Ω is

$$\Omega(r,\theta) = \frac{2\pi n_1 r \cos\theta}{d} + \frac{2\pi n_2 r^2}{d^2} \tag{14}$$

where n_1 and n_2 are the number of straight-line and circular fringe bias, respectively. In general the intensity resulting from the interference procedure is given by

$$I = K|E + E_1|^2$$

where K is a constant.

After some algebraic manipulation, it is found that the intensity for the fields of eqs. (7 and 13) is given by

$$I(r,z,t) = 2KE_o^2 \left[1+\cos(\phi+\Omega)\cos\delta+\sin(\phi+\Omega)\sin\delta\cos^2\theta\right] \quad (15)$$

with ϕ and δ as defined in eqs. (9 and 10).

An equivalent expression in terms of ϕ_r and ϕ_θ, as defined in eqs. (11 and 12) is

$$I(r,z,t) = 2KE_o^2 \left[1+\cos(\phi_r+\Omega)\sin^2\theta+\cos(\phi_\theta+\Omega)\cos^2\theta\right]. \quad (16)$$

Examination of eqs. (15 and 16) is very useful in terms of predicting qualitatively the effect of the laser irradiation on the intensity patterns observed interferometrically. Specifically, for the case of a circular fringe bias, when the first term of eq. (14) is zero, we see from eq. (15) that the fringe pattern remains circularly symmetric in the absence of birefringence. Thus, the effect of laser irradiation on the observed interferometric pattern will be that the circular bias fringes will move radially in a direction determined by whether the laser-induced lensing is positive or negative. The spacing between the reference fringes will measure the strength of the lens. Fringe motion is controlled strictly by the local temperature rise. From eq. (15) it is also clear that local fringe contrast becomes dependent on the angle θ as the birefringence increases, due to the rotation of the plane of polarization of the beam passing through the sample relative to the fixed polarization of the reference beam.

Similarly, examination of eq. (16) reveals that:

(i) As the phase retardation for r and θ polarizations become unequal (birefringence non-zero), the circular bias fringes will distort first into ellipses and then into more complicated shapes.

(ii) As the difference in phase retardation for the two polarizations becomes $\geq 1\lambda$, the fringe that started as a circle can divide into two distinct fringes as in biological cell division.

(iii) The interferometric pattern always retains a fourfold symmetry. Hence, only one quadrant needs to be analyzed.

(iv) The principal axes of the fringe patterns are parallel to the x and y axes, respectively. This results from the assumption of elastic isotropy and is not consistent with experimental results, as discussed below.

III. EXPERIMENTAL RESULTS

A. Procedures

The interferometric measurements were made by placing samples in one arm of either a holographic or a Twyman-Green interferometer. The arrangement in either case has been described before [14, 11]. The results obtained with either type of interferometer are equivalent. The holographic interferometer allows interferometric measurements on samples that are not perfectly polished and it permits more flexibility in the introduction of bias fringes, although at the expense of increased complexity.

Table I lists the properties of the samples used in the measurements and some parameters appropriate to the experiments. The potassium and sodium chloride samples were single crystals with (100) surfaces; the fluorides were also single crystals, but their crystallographic axes did not have any simple relationship to the surface; the zinc selenide was polycrystalline material prepared by the CVD process [15].

The lasers used to irradiate all samples to induce thermal distortion were CW CO_2 devices with power outputs up to 250 watts. Therefore, the laser power had to be considerably reduced when testing flourides since they are highly absorbing at the 10 μm wavelength and are not intended for use as windows in this region. The experimental results were all obtained by focusing the nearly TEM_{oo} beam from the laser to a spot .02cm^2 in area at the sample position using a 50cm focal length lens made of potassium chloride.

B. Results

The discussion in this section will be qualitative, dealing in comparisons of materials and symmetry effects related to birefringence. This is because the quantitative reduction of the interfero-

grams is not complete.

Figures 1-6 show a sequence of interferograms photographed at various times after the CO_2 laser was turned on. The laser power and spot size at the sample are given in table 1. The first photo in each figure shows the circular fringe bias introduced for reference purposes prior to turning on the CO_2 laser. The fringes in that first photo are numbered sequentially. In subsequent photos in each figure the fringes are numbered by keeping track of fringe motion on a video tape recorder playback from which the photos are obtained.

1. Alkali Halides and ZnSe

The first three materials in table 1, potassium chloride with a protective/AR coating of TlI-ThF_4, sodium chloride, and ZnSe are all window candidates for the CO_2 laser. Hence, we discuss the nature and magnitude of the optical distortion. The interferograms of optical distortion produced by the three materials under identical conditions of laser power and spot size, given in table 1, are shown in figures 1-3. Examination of the interferograms shows that the fringes retain their circular symmetry during irradiation which, as discussed in the previous section, indicates that birefringence effects are negligible for all three materials at the energy deposition rates of these experiments. Thus, one may expect to be able to correct for the window distortion using adaptive mirrors.

Comparison of figures 1-3 shows a very small change in optical path for sodium chloride; potassium chloride and zinc selenide show changes of the same magnitude, but the difference in sign of the fringes is indicative of the fact that the lensing is negative for the former and positive for the latter. However, a simple comparison of the photos is not sufficient to assign figures of merit to these materials.

Examination of table 1 reveals that the power absorbed in the three samples varies widely with a very substantial input into the coated KCl. The high absorption in the KCl case was totally dominated by the 0.5% loss in the ThF_4 layer which is process-dependent and in our experience can be lowered to 0.1%.

A better basis for material comparison is the number of fringes shifted for a given laser exposure per watt absorbed. This quantity, given in table 1, shows that sodium and potassium chloride are comparable (with a larger uncertainty in the value for sodium chloride due to the small change produced), while zinc selenide is about five times more sensitive to the dissipated power. This is consistent with previous experimental results on the optical distortion of uncoated halides and zinc selenide [8,16], as well as the theoretical predictions of relative sensitivity of semiconductors and ionic crystals to absorbed power [1]. The uncoated sodium chloride sample, due to its low absorption and excellent cancellation of the thermo-optic and thermal expansion contributions to the optical path change has the lowest distortion. It corresponds to less than 1/10 wave at 10.6μm.

The results for potassium chloride, figure 1, are particularly significant because they demonstrate the ability of the TlI-ThF_4 protective/AR coating to withstand exposure to the 12 KW/cm^2 flux density without damage in spite of the high absorption of the ThF_4 layer used. Comparison of figures 1 and 2 clearly shows that at the present time coating absorption is the limiting factor in halide performance. Furthermore, the low index ThF_4 coating contributes essentially all of the absorption, and is therefore the material that must be replaced to improve performance.

2. Alkaline Earth Fluorides

The interferometric results for fluorides are shown in figures 4-6. For these materials we will only discuss the birefringence effects, since as discussed above, their absorption at 10.6μm is very high and the absorbed power is high and not uniform along the thickness.

The most important observation in figures 4-6 is the verification of strong birefringence effects apparent for all fluorides as demonstrated by the evolution of birefringence which proceeds through the stage of fringe division as predicted for strongly birefringent materials in the last section. Hence, while the magnitude of the optical distortion in fluorides is small per watt of absorbed power, the polarization dependence will increase the difficulty involved in compensation.

A very significant feature that was observed in the optical distortion measurements on fluorides is that the principal axes of the elliptical fringes were not parallel to the polarization vector of the interferometer source (vertically polarized He-Ne laser). This observation is in disagreement with the prediction of the elastic isotropy model and is believed due to the elastic anisotropy of the fluorides, since the principal axes of the ellipses rotate as the samples are rotated in the holder. It clearly indicates the need to develop a model that handles the elastic anisotropy. We have not attempted any work along these lines because of the complexity involved, and because as pointed out before, the crystalline axes of the fluoride samples used did not have a simple relationship to the sample faces. The lack of a simple relation between crystal axes and sample geometry is also why all the photos in figures 4-6 were rotated to make their major axes vertical.

3. Surface Absorption

The interferometric observation of surface absorption is reported here because of the increasing need for measuring absorption of surfaces, coatings, and the potential value of interferometry for that purpose. The results reported here are not in the mainstream of this report and have not been analyzed in detail.

Figure 7 shows the relationship of the sample, viewing direction (interferometer axis) and CO_2 laser beam used to irradiate the sample inside the interferometer. The important point to notice is that the angle of incidence of the CO_2 laser beam is made large enough that the entrance and exit points at the two sample surfaces are separated in the field of view. For this arrangement, bulk absorption should produce optical distortion continuously over the area traversed by the beam. On the other hand, surface absorption would produce two non-overlapping centers of optical distortion, as observed in the photos of figure 8. The interferograms in the left side of the figure corresponds to the initial fringe bias before the CO_2 laser is turned on. The right side is the interferogram after irradiation for 25 seconds with a 300 watt beam focused to a diameter of 1mm. The sample used was a 1cm thick NaCl window with high surface absorption.

The interpretation of the optical distortion caused by surface absorption requires the calculation of the temperature distribution in the bulk. A more favorable arrangement for this type of measurement should be one where the interferometer probes the sample at right angles to the propagation direction of the CO_2 laser beam. Such a geometry would show how the temperature varies with depth.

IV. COMPUTATIONAL RESULTS

In this section we present the results of computations, based on the model of section I, concerning the spatial and polarization dependence of the optical distortion of window materials. We also present results on the magnitude of the optical distortion as the window aperture is filled at constant flux density.

For simplicity, we have chosen KCl and CaF_2 as characteristic of halides and fluorides. The numerical results presented represent the changes occurring 10 sec. after a $10KW/cm^2$ laser beam is turned on to a 2cm radius, 1cm thick sample. The absorption coefficient β is assumed to be $\beta=0.001cm^{-1}$. The heat transfer coefficient to the air was taken as $h=7.5x10^{-4}$ watts/cm^2, which is the measured value for KCl[4]. The other material parameters used are from [1, 2, 17, 18, and 19].

Figure 9 shows the spatial and polarization dependence of the optical distortion in KCl and CaF_2 when irradiated with a beam having a 1cm radius. The distortion is normalized to the peak distortion for each material. The difference in behavior of the two materials is clearly apparent. Potassium chloride behaves as a negative lens with a small amount of polarization dependence. Calcium fluoride behaves as a positive lens for θ-polarization and as a hybrid (positive in the center, negative for most of the aperture) for the r-polarization. Furthermore, the difference in phase retardation for the two polarizations is large, in agreement with the experimental results of the previous section.

Figure 10 is a plot of the difference in phase retardation between center and edge of the window versus the ratio of Gaussian beam diameter to window diameter at constant flux density. The phase retardation is given in units of the 6328Å wavelength of the interferometer source. This type of calculation, if proven valid, is what should allow the prediction of window performance in a large laser system from test results obtained using focused beams from laboratory sized lasers. The curves in the figure show that for equal thermal inputs the magnitude of the optical distortion is greater in KCl than in CaF_2, but that the birefringence is much more severe in the latter.

The difference in thermal stresses, normalized to the stress at the center, is shown in figure 11 as a function of the ratio of beam to window radius for potassium chloride. This difference determines the magnitude of the birefringence. The calculation in this case has been carried out to beam radii larger than the window radius in order to simulate the effect of more uniform illumination. The results show that the stress difference increases monotonically with beam radius. However, the slope clearly decreases for beam radii larger than the window radius as a result of the more uniform temperature rise produced by such a beam.

V. SUMMARY AND CONCLUSIONS

In this report we have presented experimental results of laser-induced thermal distortion by various candidate window materials. The results were used to compare the relative merits of the materials and to demonstrate the strong birefringence effects occurring in fluorides. We also presented a model that should be useful in predicting component behavior in large laser systems based on laboratory test results. Finally, we demonstrated the use of interferometry to observe surface absorption.

The results show conclusively the superiority of uncoated alkali halides for use at 10.6μm. However, absorption by the ThF_4 layer in coated halides seriously degrades their performance. Therefore, it is imperative that a low index coating material with lower loss than that of ThF_4 at 10.6μm be found since

ThF_4 is currently the low index material for zinc selenide as well as halide coatings.

The preliminary results presented here show clearly that polarization-dependent optical distortion due to induced birefringence is indeed likely to be significant in fluoride laser windows. Further work needs to be done to learn more about this problem and its relationship to the elastic anisotropy of those materials.

Finally, this report has emphasized the optical distortion effects produced by laser irradiation of various materials and how they are likely to scale-up. However, the relative merits of various materials in actual applications will be determined by many other factors as well, such as strength, fracture energy, environmental stability, and others. The need exists to perform nondestructive tests on fully coated components in large laser systems in order to reassess the areas in which further improvements in materials and processes is required.

VI. REFERENCES

[1] M. Sparks, J. Appl. Phys. 42, 5029 (1971).

[2] J. R. Jasperse and P. D. Gianino, J. Appl. Phys. 43, 1686 (1972).

[3] B. Bendow and P. D. Gianino, J. El. Matls. 2, 87 (1973).

[4] M. Flannery, J. H. Marburger, "Laser Induced Damage in Optical Materials: 1974", p. 31, NBS Special Publication 414, U.S. Government Printing Office, Washington, D.C. (1974). There are some phase factors missing in the aberration matrix given in this reference. The correct form is given above.

[5] A. Hordvik, Proc. First Conf. on High Power IR Laser Window Materials, p. 389, Hyannis, Mass. (1971), Air Force Cambridge Research Laboratories Report #AFCRL-71-0592.

[6] L. Skolnik, B. Bendow, P. D. Gianino, A. Hordvik, E. F. Cross, Proc. 2nd. Conf. on High Power IR Laser Window Materials, p. 15, Hyannis, Mass. (1972), Air Force Cambridge Research Laboratories Report #AFCRL-TR-73-0372(I).

[7] J. S. Loomis, C. A. Huguley, "Laser Induced Damage in Optical Materials: 1974", p. 94, NBS Special Publication 414, U.S. Government Printing Office, Washington, D.C. (1974).

[8] E. Bernal G., Proc. Fourth Conf. on High Power Infrared Laser Window Materials, p. 193, Tucson, Arizona (1974).

[9] E. Bernal G., B. G. Koepke, R. H. Anderson, R. J. Stokes, "Preparation and Characterization of Polycrystalline Halides", Quarterly Tech. Report #2, ARPA Contrach DAHC15-72-C-0227, Honeywell Corporate Research Center, Oct. 1972.

[10] E. Bernal G., Appl. Optics 14, 314, (1975).

[11] J. S. Loomis, C. A. Huguley, "Laser Induced Damage in Optical Materials: 1974", p. 94, NBS Special Publication 414, U.S. Govt. Printing Office, Washington (1974).

[12] B. A. Boley and J. H. Wiener, "Theory of Thermal Stresses", Wiley, New York, (1960).

[13] R. S. Krishnan, "Progress in Crystal Physics", Vol. 1, Viswanathan, Madras, India (1958).

[14] E. Bernal G., B. G. Koepke, R. J. Stokes, R. H. Anderson, Proc. Second Conf. on High Power IR Laser Window Materials, p. 413, Hyannis, Mass. (1972). Air Force Cambridge Research Laboratories Report #AFCRL-TR-73-0372 (II).

[15] The authors are indebted to Mr. John Fenter, Air Force Materials Laboratory, Dayton, Ohio, for kindly supplying this material.

[16] E. Bernal G., J. H. Chaffin, B. G. Koepke, R. B. Maciolek, R. J. Stokes, Honeywell Semi-annual Technical Report #2 on ARPA Contract #DAHC-73-C-0464, Jan. 1975.

[17] M. Sparks, H. C. Chow, J. Appl. Phys. 45, 1510 (1974).

[18] O. V. Shakin, M. F. Bryzhina, V. V. Lemanov, Sov. Phys. - Solid State 13, 3141 (1972).

[19] C. S. Sahagian, C. A. Pitha, "Compendium on High Power Infrared Laser Window Materials, Air Force Cambridge Research Laboratories Report #AFCRL-72-0170 (1972).

Table I. Experimental Results

Window Material	Coating	Thickness (cm)	Diameter (cm)	Total Absorption ($\beta\ell$)	Laser* Power (Watts)	Absorbed Power (Watts)	Fringe Shift** Power Absorbed (fringes/watt)
KCl	$TlI-ThF_4$	0.50	2.48	6.0×10^{-3}	250	1.5	2.7
NaCl-36	None	0.97	3.80	1.3×10^{-3}	250	.33	$\sim$ 3
ZnSe	None	0.62	5.1†	9.2×10^{-4}	250	.23	17
CaF_2-6	None	0.95	3.83	.95	10	9.5	
SrF_2-8	None	0.95	3.80	.45	10	4.5	
BaF_2-4	None	0.94	3.81	.20	25	5.0	

†Square sample - dimension is side of square

*Focused to .02cm^2 spot at sample

**Measured after 3 minutes of irradiation

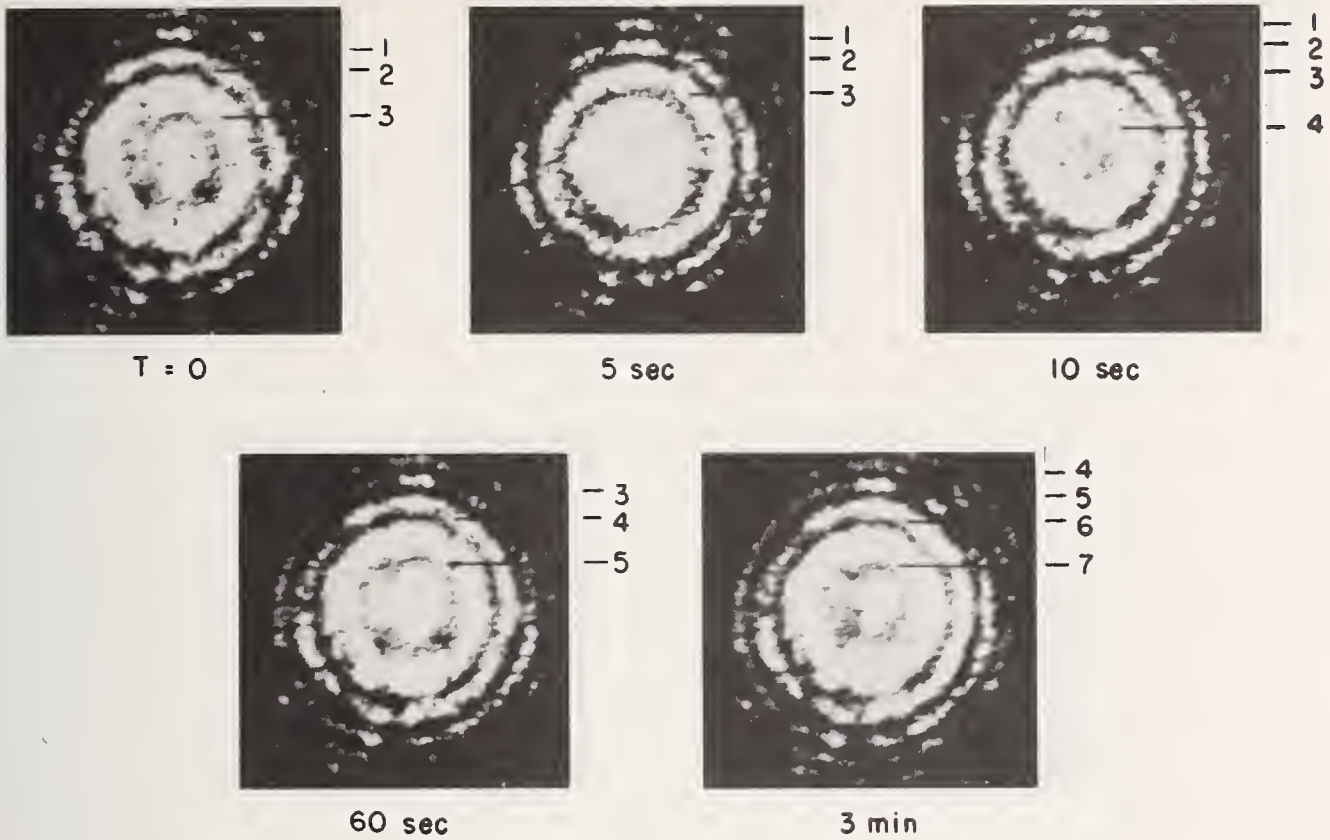

TLI6-4

Figure 1. Interferograms of laser-induced optical distortion introduced by single crystal potassium chloride coated with protective/AR coating of Tll-ThF_4. Upper left photo shows the fringe bias introduced for reference prior to irradiation.

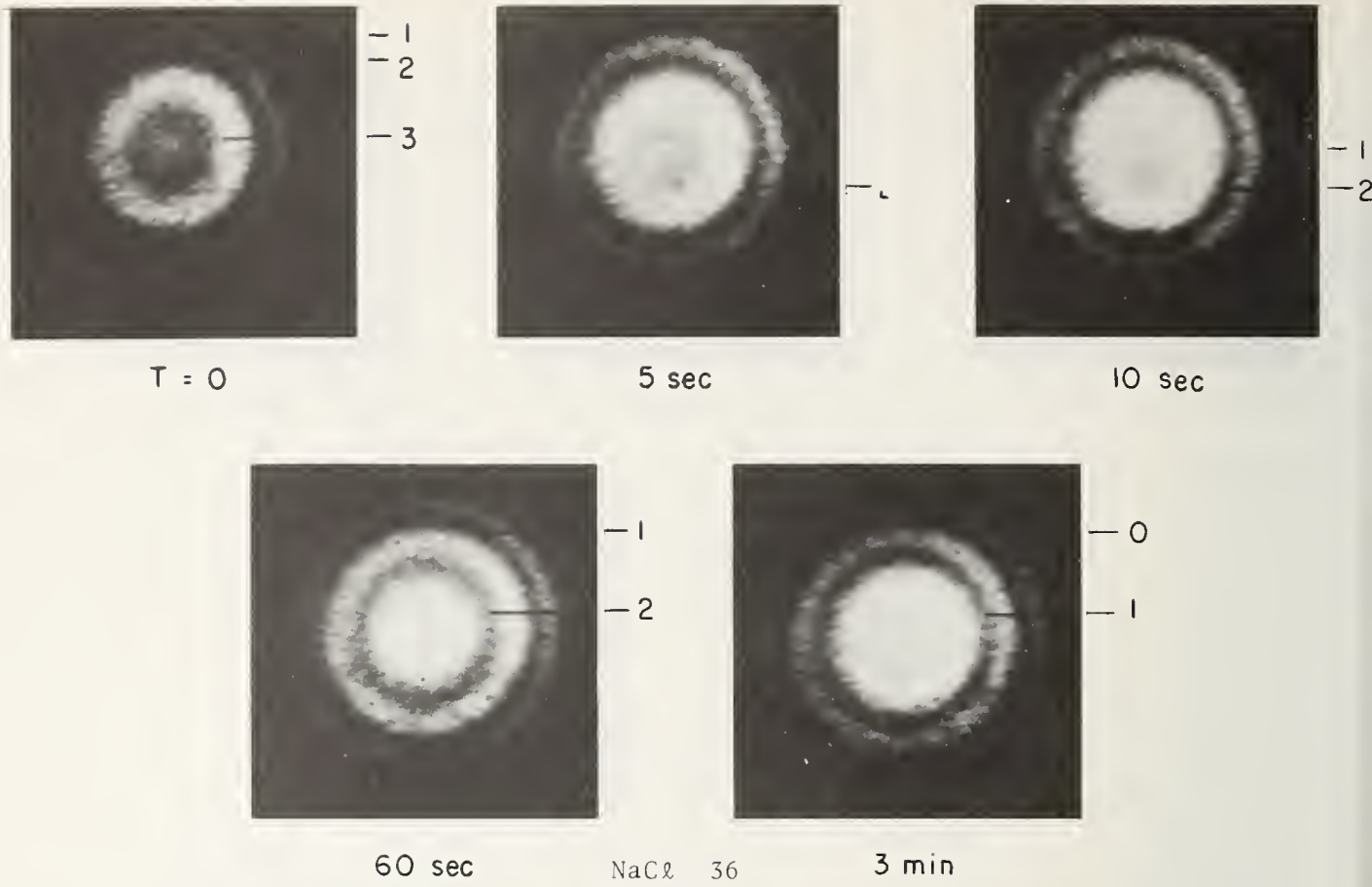

Figure 2. Interferograms of laser-induced optical distortion introduced by uncoated single crystal sodium chloride. Upper left photo shows the fringe bias introduced for reference prior to irradiation.

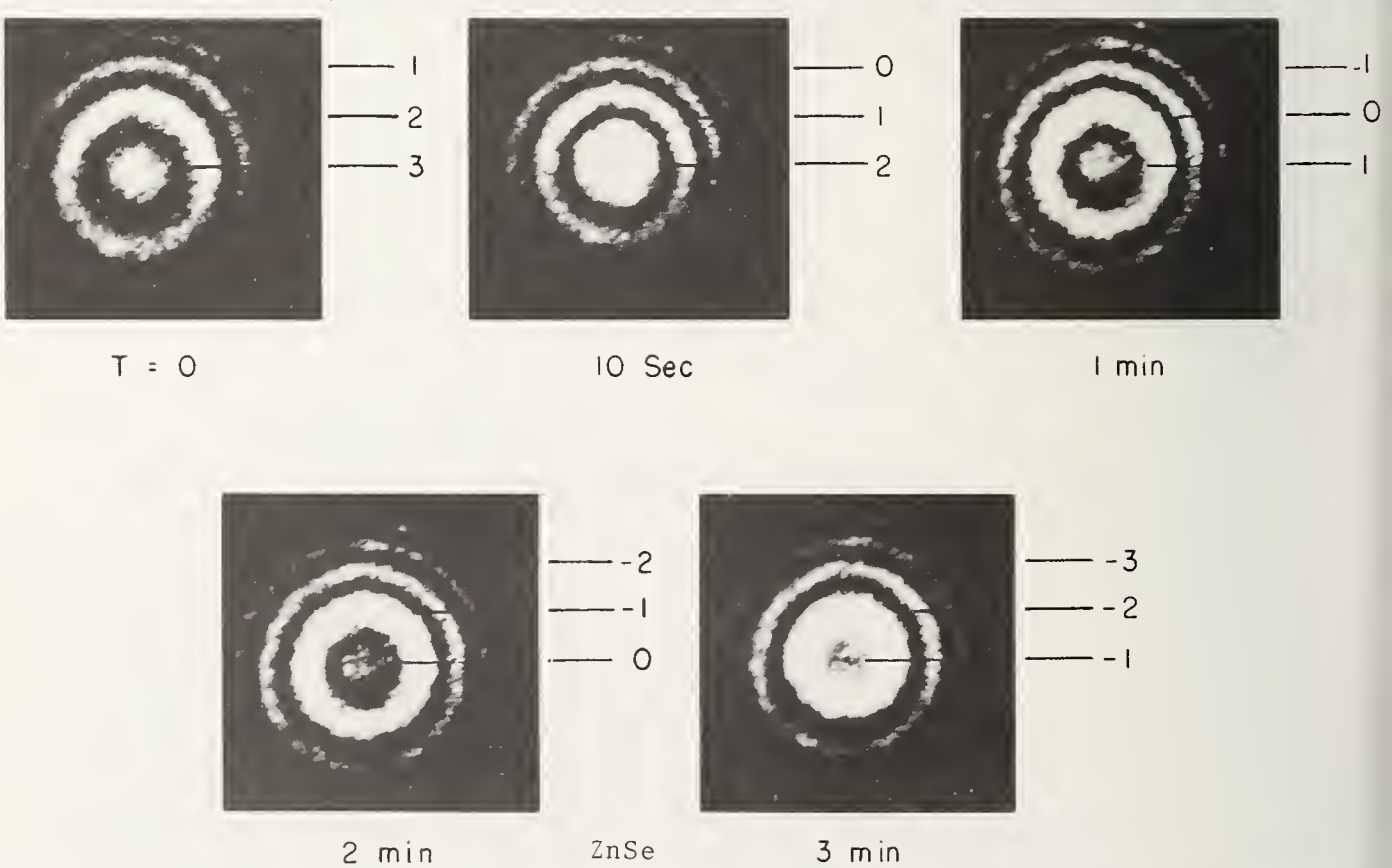

Figure 3. Interferograms of laser-induced optical distortion introduced by uncoated polycrystalline ZnSe prepared by CVD. Upper left photo shows the fringe bias introduced for reference prior to irradiation.

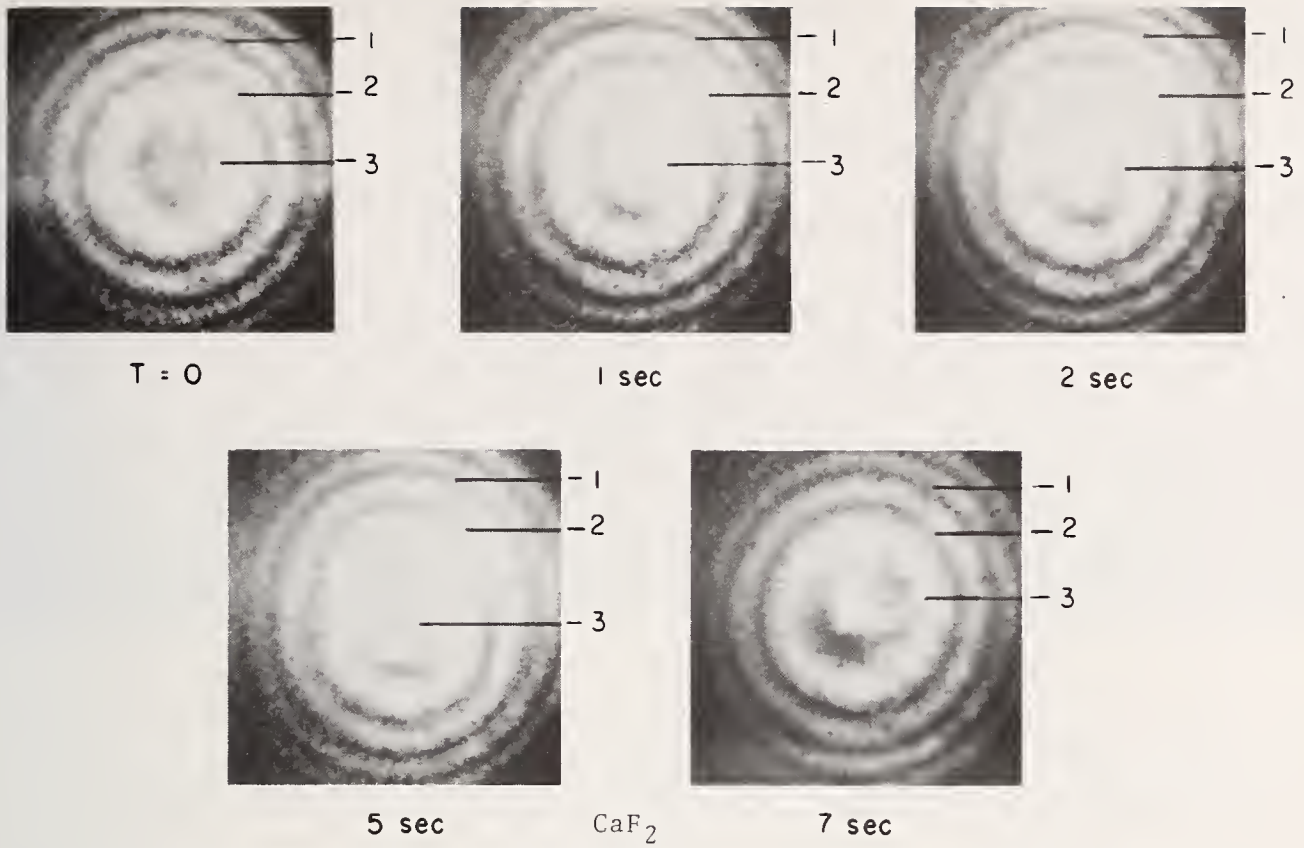

Figure 4. Interferograms of laser-induced optical distortion introduced by uncoated single crystal calcium flouride. Upper left photo shows the fringe bias introduced for reference prior to irradiation.

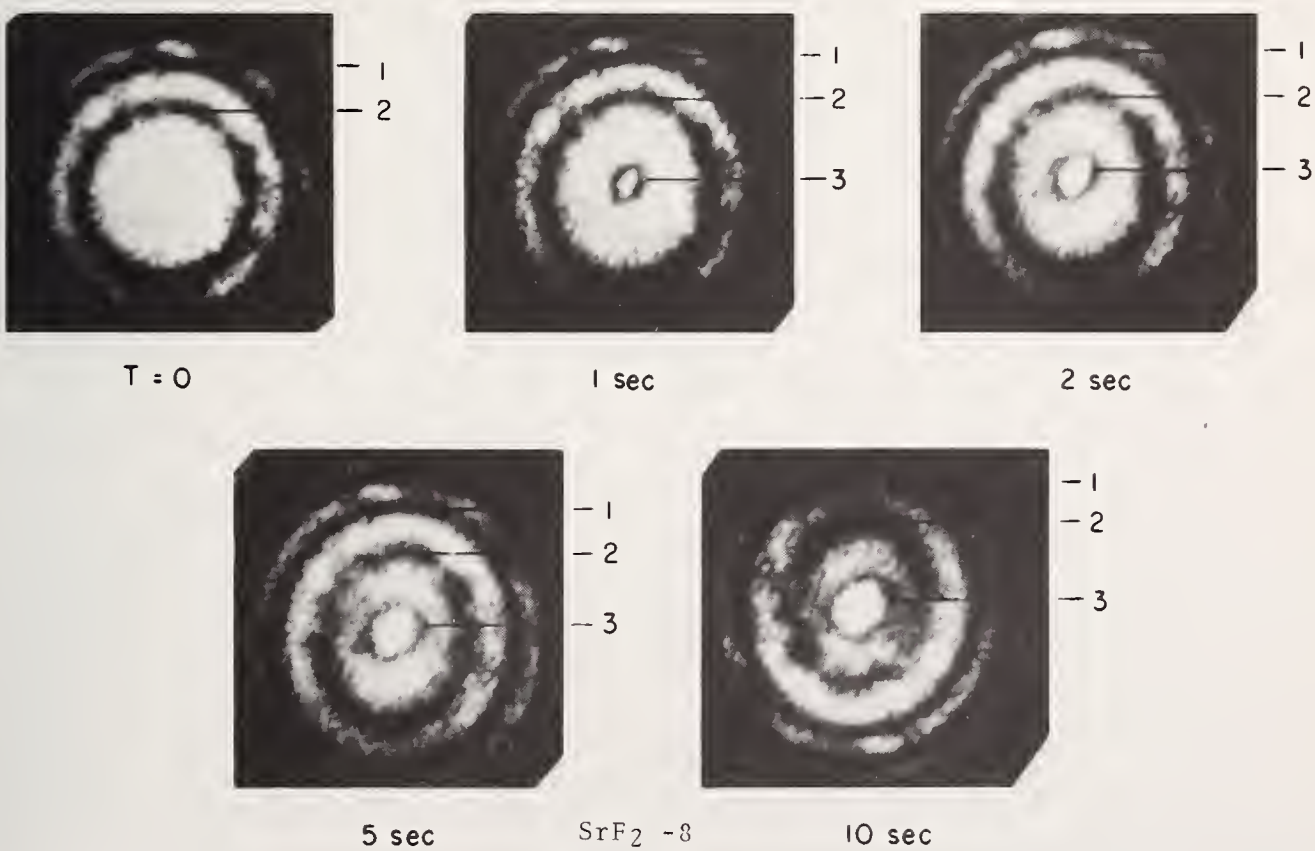

Figure 5. Interferograms of laser-induced optical distortion introduced by uncoated single crystal strontium flouride. Upper left photo shows the fringe bias introduced for reference prior to irradiation.

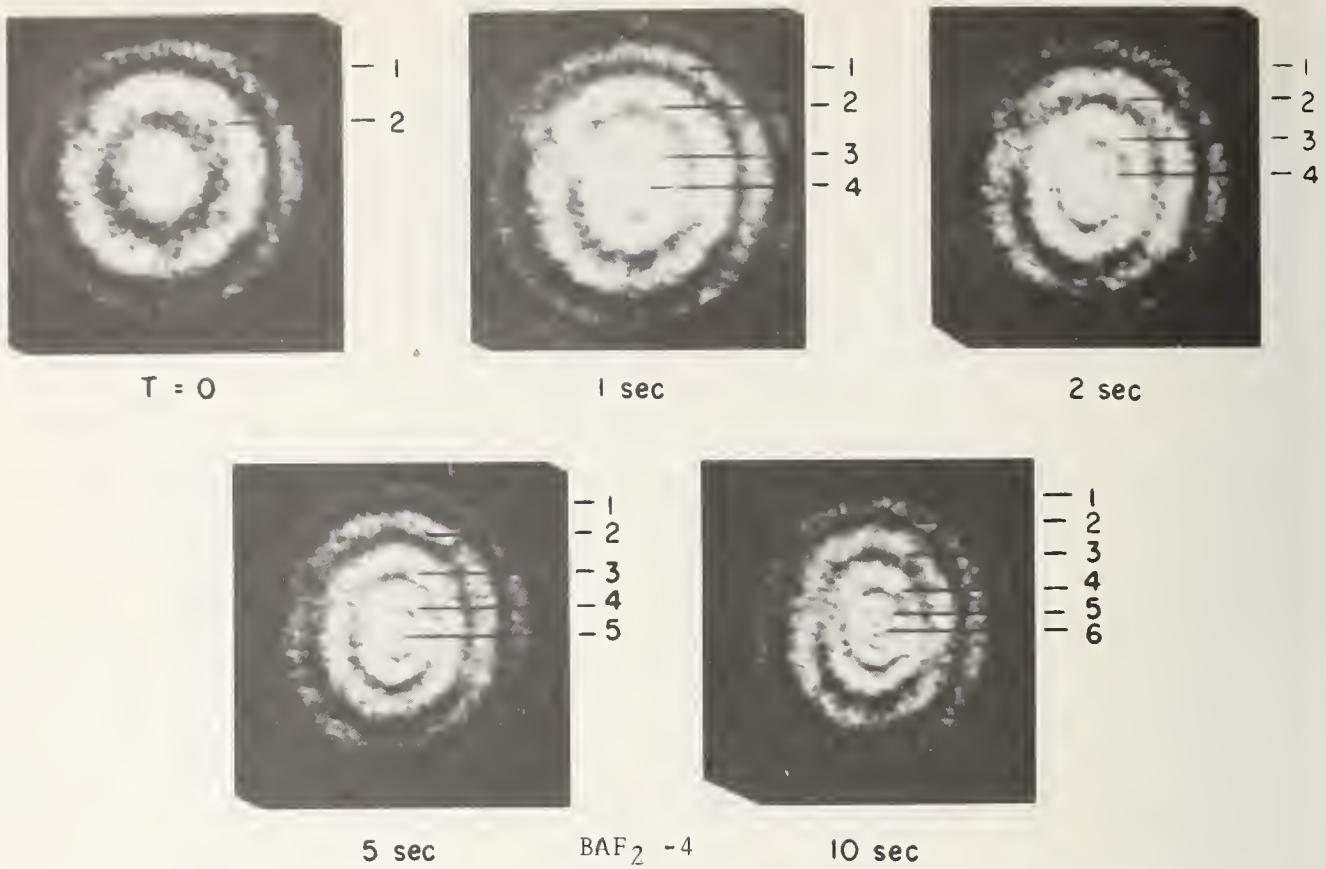

Figure 6. Interferograms of laser-induced optical distortion introduced by uncoated single crystal barium flouride. Upper left photo shows the fringe bias introduced for reference prior to irradiation.

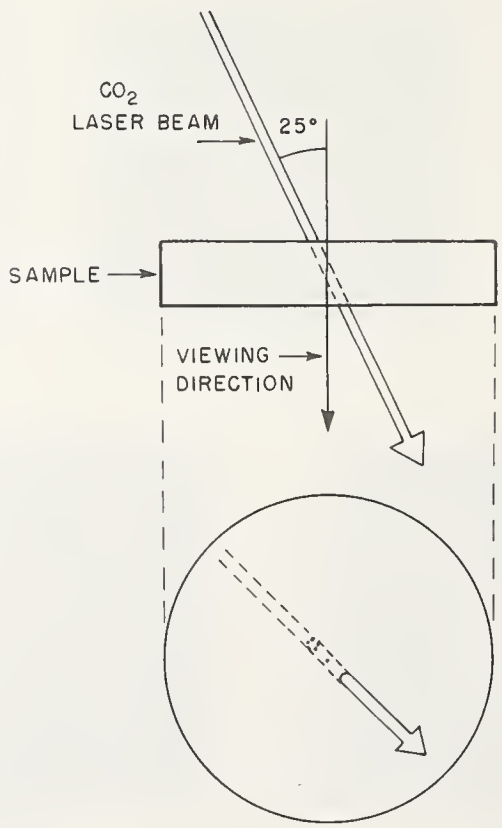

Figure 7. Diagram showing relative orientations of sample, CO_2 laser beam and interferometer axis (viewing direction) for observation of surface absorption.

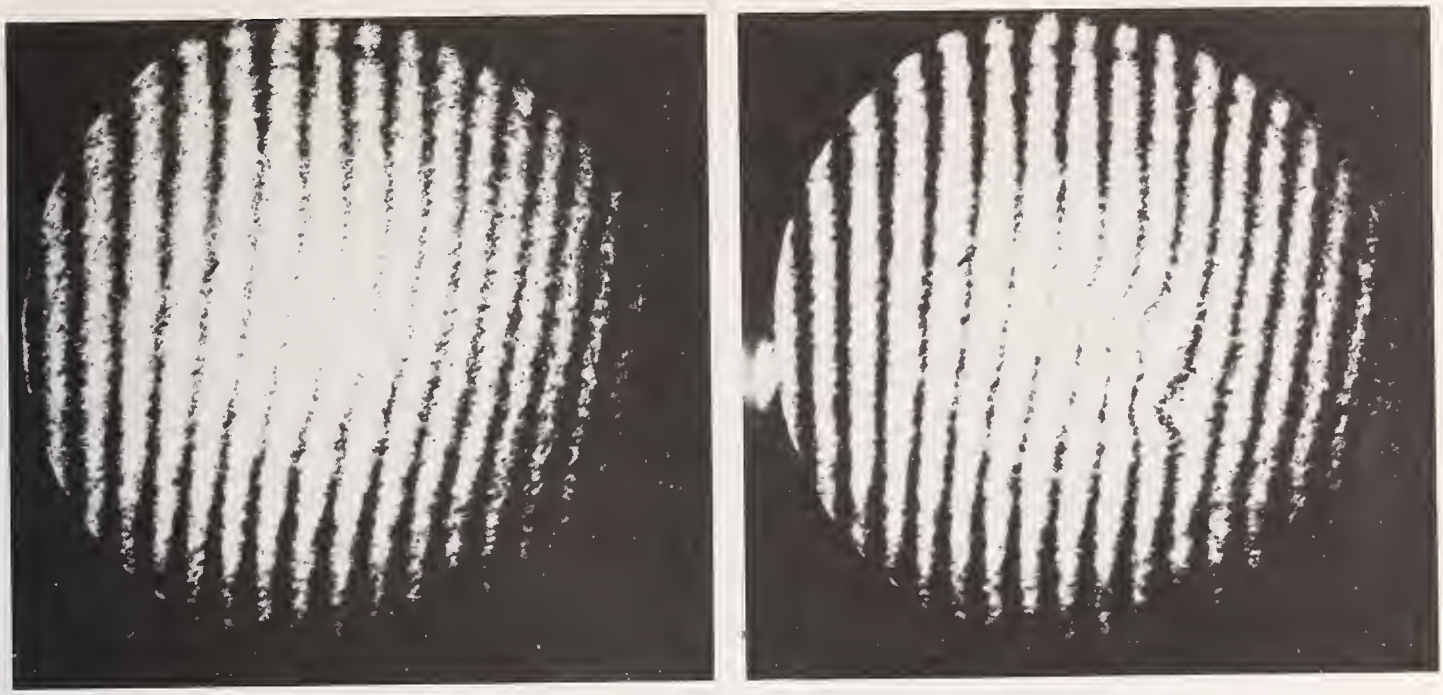

Figure 8. Interferograms showing surface absorption of CO_2 laser radiation by sodium chloride window. Left photo shows the bias fringe pattern introduced prior to irradiation. Right photo shows two localized centers of fringe distortion corresponding to entrance and exit points of beam.

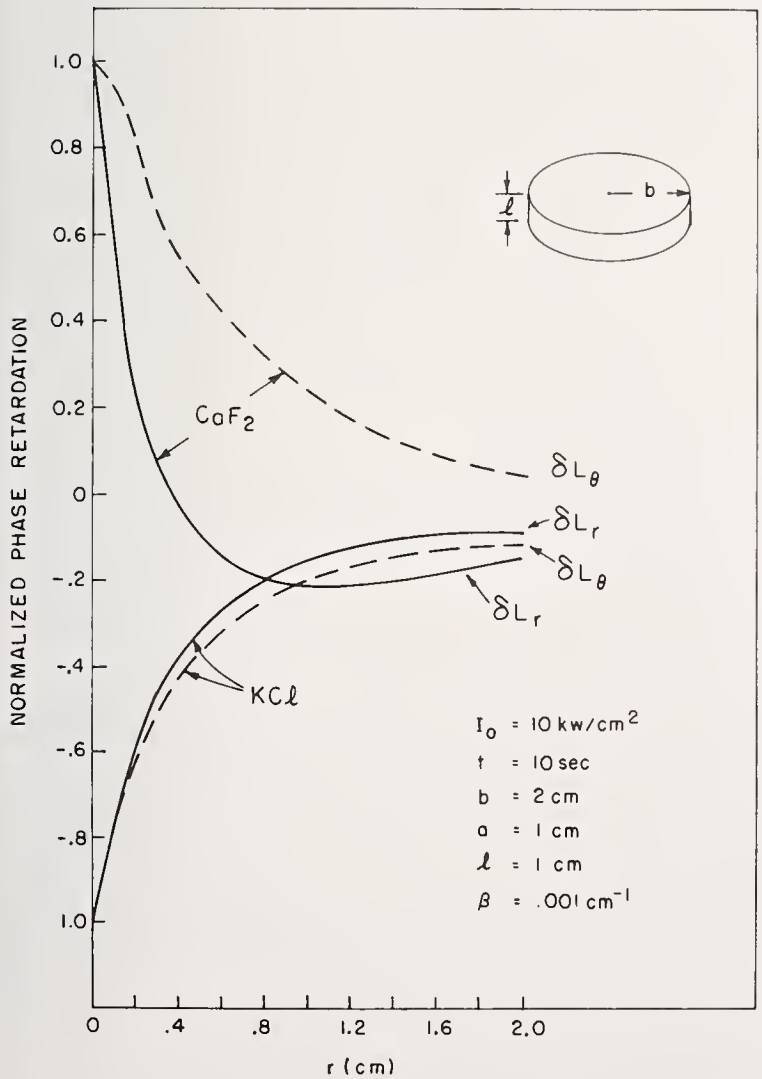

Figure 9. Spatial and polarization dependence of normalized optical path change in potassium chloride and calcium floride.

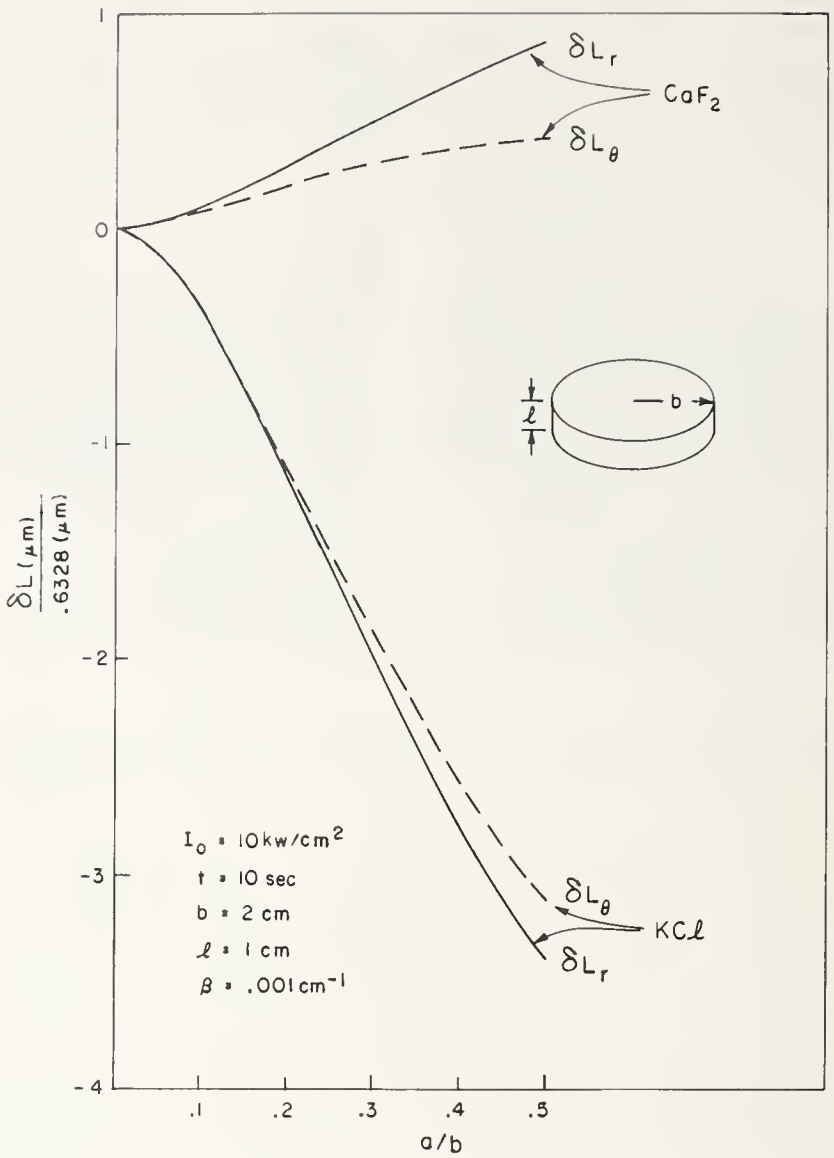

Figure 10. Difference in center-to-edge change in path retardation versus ratio of beam to window radius. (Constant flux density.)

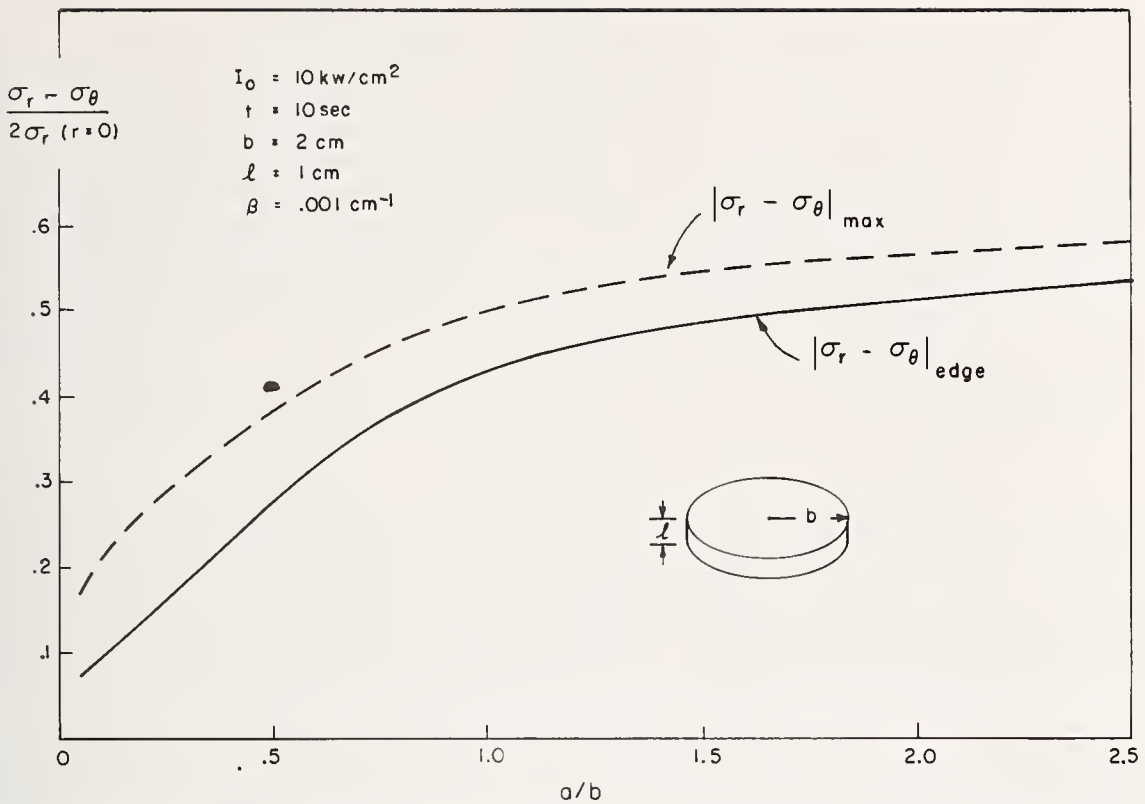

Figure 11. Normalized difference in principal stresses versus ratio of beam to window radius. (Constant flux density.)

NO COMMENT ON PAPER BY LOOMIS, et al

3.5 Thermal Distortion Studies of ZnSe Windows by Far Field Irradiance Measurements*

John A. Detrio and Roger D. Petty

University of Dayton Research Institute
Dayton, Ohio 45469

We have experimentally measured the effect of thermal lensing in ZnSe windows on the far field irradiance (at 10.6 μm) as a function of input power and absorption coefficient. These preliminary measurements are compared to the theoretical predictions of the figures of merit analysis. The undesirable effect produced by interference between reflections from the sample faces is successfully minimized by the use of wedged samples and ratiometric detection techniques. Beam slewing, which may also mask the desired data, is minimized by the use of a scanning slit at a primary mirror focus and a detector preceded by a diffuser and integrating sphere.

Key words: Far field intensity; laser windows; thermal distortion; thermal lensing; ZnSe.

1. Introduction

The objective of the work reported here is to experimentally test the predictions of the figure of merit analysis [1, 2][1] and thus determine its validity or limitations in its use as a tool for selecting one laser window material over another. In particular, we wished to test the comparison between samples of the same material which have different absorption coefficients. Additional experiments are planned to test the predicted variations between different materials, the scaling of the theory with respect to sample diameter, thickness, and the effect of surface absorption.

Two modes of failure are treated by the FOM analysis. These are the mechanical failures due to the thermally induced stresses fracturing the window or a failure due to optical distortions reducing the target intensity to the extent that the system fails to perform its desired function. The mechanical failures are being examined in a companion experimental study and will not be discussed here.

In [1], Sparks suggests that the theory should apply quite accurately (about 20%) to the covalently bonded materials such as ZnSe, but that the ionic materials' performance would be predicted with less accuracy (100%). The present work conforms so loosely to the theory that no estimate of the error can be made at this time. The experimental approach employed in this work was also suggested by Sparks [1] and it represents an extension of thermal lensing measurements previously made in our laboratories.

2. Summary of the FOM Analysis

The details of the figure of merit (FOM) analysis are contained in the references, but the salient features and assumptions of [1] will be summarized here to facilitate comparisons between the theory and the experimental attempts to quantitatively verify the FOM analysis.

The parameters employed in calculating the figure of merit include optical properties such as the refractive index, n, thermooptic coefficient, dn/dT, absorption coefficient, β, and mechanical and thermal properties such as the yield strength, σ, Young's modulas, E, linear expansion coefficient, α, specific heat, C_p, and thermal conductivity. In [2], six separate cases are considered: Pulsed and CW operation as determined by the laser pulse length compared to the thermal time constant of the window, two cases of sample cooling, either the edge or face being exposed to the cooling medium, and the two modes of failures discussed above--optical or mechanical fracture. The result of performing the FOM calculation for a given material is the maximum power (watts) that the sample can transmit under specific conditions of beam size and profile and with specific cooling conditions and pulse lengths for an "optimum" thickness of the material. The theoretical results are summarized in table 1 which is taken from [2].

---

* This work is supported by the Air Force Materials Laboratory.

[1] Figures in brackets indicate the literature references at the end of this paper.

Table 1. Summary of the FOM analysis [2].

Laser Operation Mode	Failure Mode (ΔT_{less})	Fracture ΔT_f	Optical ΔT_o
P_{pulse}		$\frac{\pi D^2 C\sigma}{2\beta t_{pulse} \alpha E(SF)}$	$\frac{\pi D^2 C\lambda}{32\beta t_{pulse} \lvert\partial_{nT}\rvert \ell_{gr}}$
P_{cw}	Cooling Mode		
	Edge $t_{less} = t_E$	$\frac{8\pi K\sigma}{\beta\alpha E(SF)}$	$\frac{\pi K\lambda}{2\beta \lvert\partial_{nT}\rvert \ell_{gr}}$
	Face $t_{less} = t_F$	$\frac{\pi D^2 h\sigma}{2\beta \alpha E(SF) \ell_{gr}}$	$\frac{\pi D^2 h\lambda}{32\beta \lvert\partial_{nT}\rvert \ell_{gr}^2}$

ℓ_{gr} is the greater of ℓ_f and ℓ_o where:

$$\ell_f = 0.433\, D\left(\frac{P(SF)}{\sigma}\right)^{1/2}$$

$$\ell_o = 0.842\, D\left[(n-1)(P/E)^2 (D/\lambda)\right]^{1/5}$$

$$t_E = \frac{C(D/2)^2}{4K}$$

$$t_F = \frac{C\ell_{gr}}{h}\left(1 + \frac{h\ell_{gr}}{3K}\right)$$

$$\partial_{nT} = (dn/dT) + \alpha(1+\nu)(n-1) + S$$

$$\Delta T_f = \frac{2\sigma}{\alpha E(SF)} \qquad \Delta T_o = \frac{\lambda}{8\ell_{gr}\lvert\partial_{nT}\rvert}$$

The assumptions used in formulating the FOM analysis are summarized in table 2. The problem is graphically depicted in figure 1. The radially symmetric laser beam profile incident on the absorbing window will give rise to a radially symmetric thermal profile. The sketch shows a calculated thermal profile using the FOM assumptions and the material parameters for ZnSe listed in tables 2 and 3, respectively.

Table 2. Assumptions of FOM analysis.

1. A diffraction limited, untruncated Gaussian beam incident on the window.
2. Intensity and temperature distributions across the window are radially symmetric and parabolic.
3. The intensity of the beam at the window edge (D/2) is 1/3rd of the central intensity.
4. The window is elastically and optically isotropic.
5. The window is thin $\ell << D$.
6. The window is clamped at the edge with a 1/2 atmosphere pressure applied.
7. A safety factor (SF) of four is assumed in the mechanical design.
8. The system optics are focused on a distant target through the window.
9. The power at which the window distortion reduces the far field intensity to one-half is defined as the FOM.

Table 3. Parameters of Interest for ZnSe. These values are taken from measurements in our laboratories.

$n = 2.406$	$\partial_{nT} = 9.32 \times 10^{-5}$/K	$C_p = 0.347$ J/g K
$\alpha = 7.2 \times 10^{-6}$/K	$K = 0.17$ w/cm K	$E = 1 \times 10^{7}$ psi
$\rho = 5.267$ g cm^{-3}	$\sigma = 6.1 \times 10^{3}$ psi	$\nu = 0.3$

The thermal profile is approximately parabolic and gives rise to a change in optical path difference which is parabolic in the radial coordinate. If one neglects the role of stress optic effects, this parabolic variation will produce a focusing effect. The window focal length is F_w. The system then possesses an overall focal length F_t given by:

$$F_t^{-1} = F_{tel}^{-1} + F_w^{-1} \tag{1}$$

where F_{tel} is the telescope focal length.

For thermally induced lensing with a long focal length, the intensity ratio at the target will be given by:

$$I/Io = \left[\left(\frac{8A\ell}{\pi\lambda\Delta T}\right)^2 + 1\right]^{-1} \tag{2}$$

where

$A = dn/dT + \alpha(1 + \nu)(n - 1)$
ℓ = thickness
λ = wavelength (10.6 μm)
ΔT = temperature difference between the center and edge of the sample.

The temperature difference is proportional to the incident power, P_{in}. The predicted variation of eq. (2) is plotted in figure 2. The nearly linear variation of I/Io vs. power from 0.85 to 0.5 has been useful in extrapolating the data to determine the experimental value of the FOM.

3. Experimental Approach

The experimental details are outlined in figures 3 and 4 which show, in the form of block diagrams, the optical layout and electronic circuitry, respectively. It is very helpful to have samples that are slightly wedged to minimize interference effects and to use ratiometric techniques to further reduce these effects. A variable delay gate and scanning slit at the primary mirror focus allow the peak far field intensity to be monitored. Variations in beam position on the detector would tend to produce intensity variations if it were not for the use of integrating sphere collecting optics and a ZnSe diffuser.

Our initial experiments were done with Pyrex substrate mirrors and thermally induced distortion in the mirrors was readily observed. The use of good metal substrate mirrors greatly reduced the influence of this type of lensing on our results. The mirrors tend to produce a negative focal length distortion while the ZnSe (and CdTe) undergo a positive lensing effect. The net result is a partial cancellation of the window lensing by the mirrors. Figure 5 shows the effect of mirror and laser output coupler lensing which is the system baseline when no window is present.

The distance to the target is about one meter. Longer focal length systems were less convenient and not as sensitive, while shorter focal length systems tended to be "noisy" with a great deal of signal jitter. The more intense focus also tended to cause difficulties at the scanning slit.

4. Results and Discussions

The results of the far field irradiance measurements (FFIM) are shown in figure 6. The theoretical curve is that predicted for samples 38 mm in diameter under CW irradiation in accordance with the other conditions specified by the FOM analysis. The data shown in figure 6 were obtained from FFIM made on samples of various values of absorption and which were plotted as shown in

figure 7. These curves were extrapolated (by a least squares technique) assuming a linear dependence of I/Io on the incident power. The value of P_{in} for the extrapolated curve for I/Io equal to unity was substracted from the value of P_{in} corresponding to I/Io equal to one half. This difference was then plotted as a function of $1/\beta$ in figure 6.

The most dramatic example of optical distortion yet observed occurred in a sample of low quality CdTe which also underwent thermal runaway. Due to the hazard posed by CdO vapor, which may result from destroying a CdTe sample, no further studies of this material were undertaken.

For reasons of economy and experimental simplicity, we have not precisely matched any of the theoretical assumptions in these initial efforts. The effect of not conforming to the theoretically assumed conditions may be examined by scaling the theory and by computational analysis. By using a system baseline scan with no window present, the effect of non-diffraction limited optics are partially mitigated. Using a beam size that is less than that specified in the theory produces a pair of offsetting effects. The smaller beam will tend to produce a shorter focal length distortion for a given total power, but the effect of the thermal conductivity tends to make the radial thermal profile more gradual with respect to the beam power profile and thus tends to increase the focal length for a given total power.

For windows which fail optically, such as ZnSe, the mechanical assumptions are not critical. Placing the focusing mirror after the window did not seem to have significant effects since both configurations (beam focused through window and focusing optics following the mirror) were employed with little difference. The latter configuration greatly simplified our experimental set-up.

5. Acknowledgments

The authors wish to thank John Loomis, formerly of the Air Force Weapons Laboratory, for a very stimulating discussion of the problem and Mary Wendeln for performing the computations.

6. References

[1] Sparks, M., J. Appl. Phys. 42, 5029 [1971].

[2] Sparks, M. and H. C. Chow, Proc. 3rd Conf. on High Power Infrared Laser Window Materials, III, 1083 (1973).

7. Figures

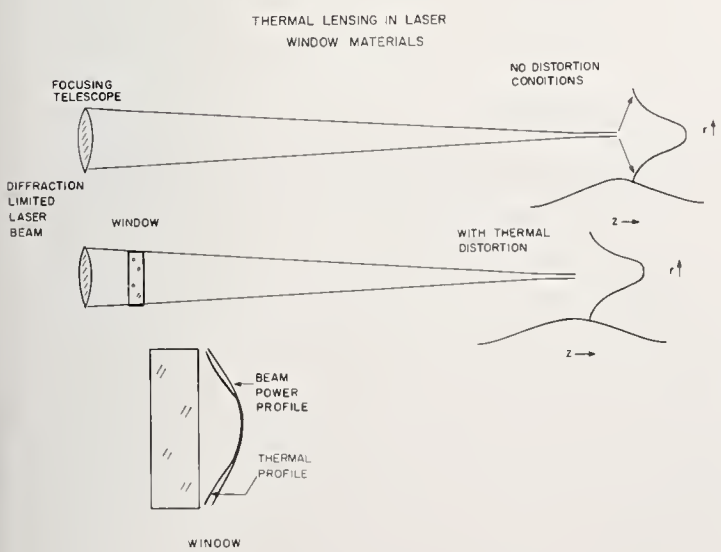

Figure 1. A schematic presentation of thermal lensing in a laser window. The far field intensities are only artistic interpretations of the intensity distributions. The beam power and thermal profile shown are taken from calculations made for ZnSe.

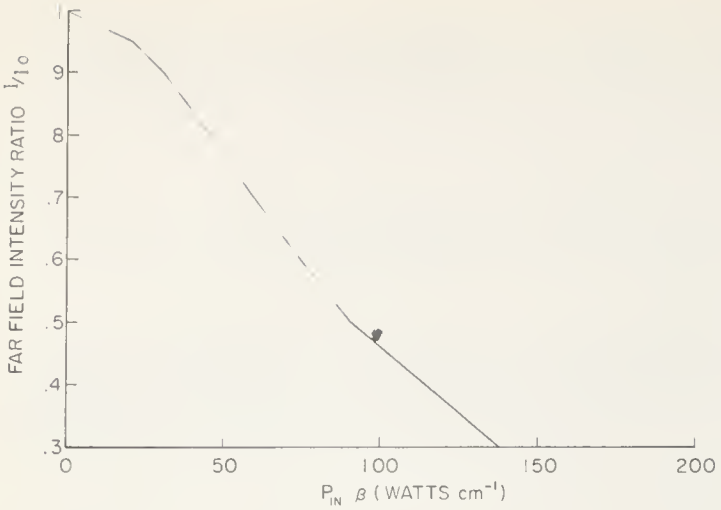

Figure 2. A normalized plot of far field intensity ratio predicted by eq. (2). The region of interest is from I/Io equal to unity to I/Io equal to 0.5.

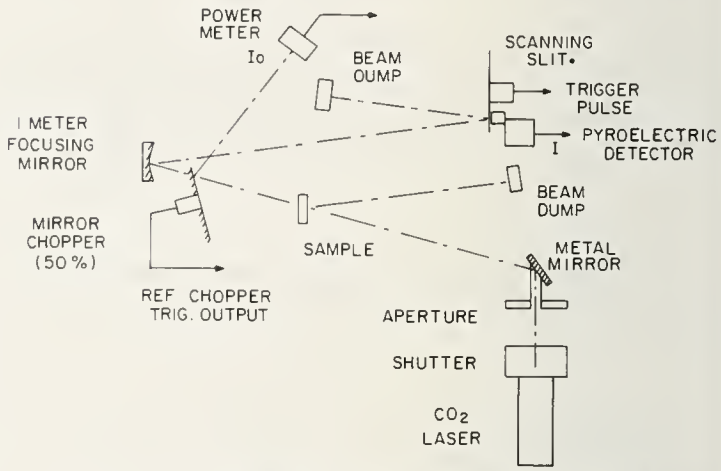

Figure 3. Schematic view of the optical layout employed in the far field intensity measurements.

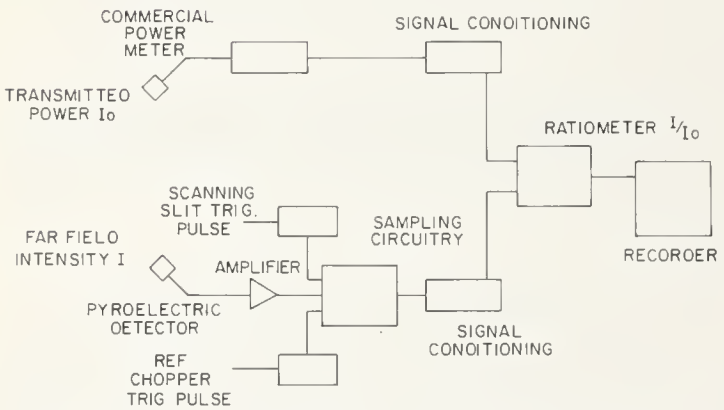

Figure 4. Block diagram of the electronics used to obtain the far field intensity ratio. The ratio-meter, power meter, and recorder are the only items not custom fabricated for this experiment.

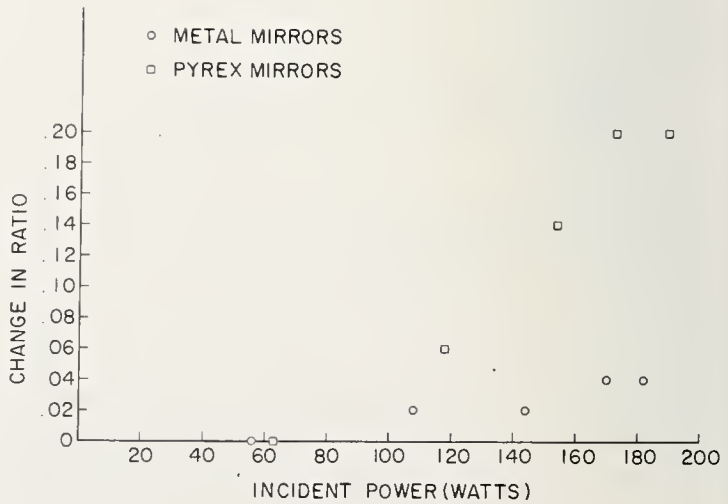

Figure 5. The effect of mirror substrates on the system's baseline lensing when no win-

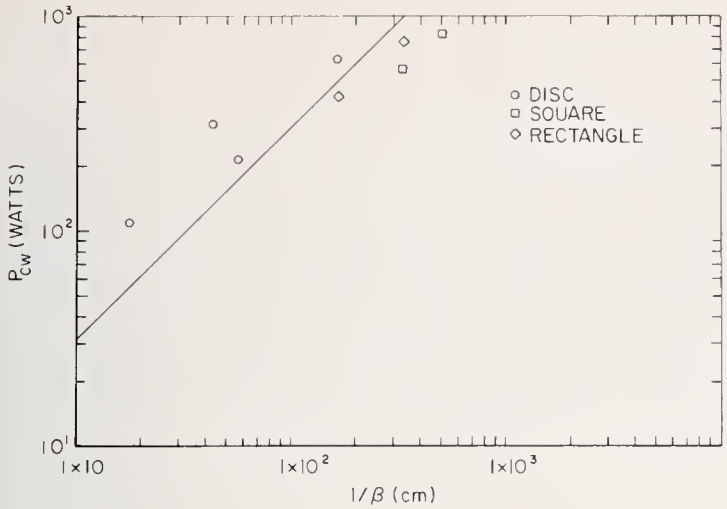

Figure 6. The measured and predicted variation of the power at which the far field intensity is reduced to 0.5 of the no-distortion value as a function of the absorption coefficient β.

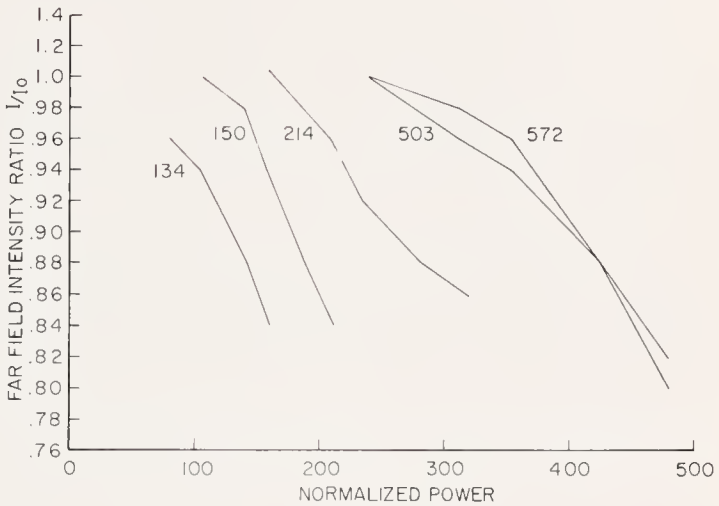

Figure 7. The far field intensity ratio measured as a function of input power. The data are normalized to samples of equal length in order to clarify the display. This plot should be compared to figure 2.

COMMENTS ON PAPER BY DETRIO, et al

It was pointed out by E. Bernal of Honeywell that the speaker had assumed stress effects are negligible in zinc selenide. The thermal distortion induced in that material is large, but is generally isotropic.

3.6 Spectral Emittance Measurements With a Cryogenically Cooled Instrument

D. L. Stierwalt
Naval Electronics Laboratory Center
San Diego, California 92129

We have been measuring spectral emittance of laser window materials for several years. The sensitivity of our apparatus was limited not by detector noise, but by background fluctuations caused by minute fluctuations in the temperature of the instrument. Because of this limitation a new instrument has been built which operates at 77°K. This greatly reduces the background radiation and allows us to take advantage of the higher sensitivity of a cooled detector. This instrument covers the spectral region from 2.5 to 14.0 microns with a spectral resolution of about 1-1/2%. The noise equivalent absorption coefficient appears to be about 10^{-6} cm^{-1} at 10.6 microns and about 10^{-5} cm^{-1} at 5.0 microns.

Several samples of NaF, NaCℓ, and KBr have been measured at temperatures from 200°K to 373°K. A number of bands were observed in these samples, some of which have been previously reported and some have not. These spectra will be presented as well as a description of the instrument.

Key words: Cryogenically cooled; spectral emittance.

Previously reported spectral emittance measurements were made using an infrared spectrophotometer operated at room temperature. The lowest value of emittance which could be measured with this apparatus was limited not by detector noise, but by noise caused by temperature fluctuations in the instrument. To eliminate this source of noise, an instrument was designed and constructed to operate at liquid nitrogen temperature. At this temperature the background radiation from the instrument is so low that temperature fluctuations do not contribute significantly to the noise. Cryogenic operation also allows us to use a photoconductive detector operating at 4.2°K and take advantage of the increased sensitivity under low background conditions.

The monochromator for the new instrument is a narrow bandpass circular variable filter (CVF) covering the 2.5 to 14.5 micron spectral region. The spectral bandwidth is about one percent of the wavelength over the entire range. The filter is made in three sections, each covering about one octave. The three sections can be seen mounted on the large gear in figure 1. The sample mirror is mounted on the optical bench. The tuning fork chopper is shown unmounted. In the lower left of figure 1 is the slit plate.

In figure 2 the slit plate and chopper are in place. The detector mirror can be seen in this figure.

Figure 3 shows the optical bench in place in the liquid nitrogen vessel. The sample holder and detector are not shown in these figures since they are mounted on the end plates of the cold chamber. All parts of the cold chamber are aluminum except for the mirrors which are copper. The cold chamber is suspended inside a stainless steel vacuum vessel.

Some preliminary data taken with the instrument are presented here. Figure 4 shows the absorption coefficient of a sodium fluoride crystal grown at NRL, identified as number 87. When this sample was run previously in the room temperature apparatus a shoulder was noted at about 6.5 microns, suggesting the presence of an unresolved band. The higher resolution of the new instrument shows a sharp band at 6.4 microns and an additional small band at 7 microns.

The results of several measurements indicate that the signal from 4.5 to 5.5 microns is too high because of long wavelength energy leaking through the CVF. Sodium fluoride has an emittance of nearly unity from about 12 to 20 microns. This is near the peak of the Plankian distribution so that the out-of-band energy from the sample is several orders of magnitude higher than the in-band energy. The out-of-band transmittance of the CVF has been measured and found to be less than 10^{-5} at the long wavelengths, but still more rejection is needed. Steps are being taken to install additional filtering.

The same is true of the 2.5 to 4.5 micron segment of the CVF. For this reason only the sharp bands at 3.4 and 3.5 microns are shown in figure 4. In figure 5 these two bands are shown on an expanded wavelength scale along with data for two other sodium fluoride crystals also grown at NRL. These three curves were all taken at 294°K. The large variation in absorption coefficient indicates that the bands are not intrinsic properties of the sodium fluoride.

Figure 6 shows the absorption coefficient at three temperatures for a freshly cleaved sample of sodium chloride of unknown origin. Again the absolute level is somewhat uncertain because of

insufficient filter rejection. Sharp bands can be observed at 4.7, 6.3, and 6.5 microns. The bands at 3.4 and 3.5 microns were also observed in this sample, although much weaker than in the sodium fluoride samples.

In figure 7 we see data on commercially grown potassium bromide. These curves cover a wider temperature range than those in the previous figures. This data demonstrates dramatically the effect of long wavelength leakage through the CVF. The apparent absorption coefficient at 4.5 microns is nearly proportional to the ratio of in-band to out-of-band energy for the three temperatures. This suggests that the signal is due almost entirely to long wavelength energy and the actual absorption coefficient at this wavelength is undetermined, but probably less than 10^{-3}. The only reliable data, then, is the band at 7.2 microns. No trace of bands at 3.4 and 3.5 microns was seen in this sample.

In summary, the preliminary data show that the new instrument has much higher resolution than the earlier instrument, and greater sensitivity at the longer wavelengths. Sensitivity at the shorter wavelengths is limited at present by long wavelength energy leaking through the CVF. Steps are being taken to add additional filtering to the instrument. This is expected to improve the short wavelength sensitivity by at least two orders of magnitude.

NOTE: Micron(s) as used in this paper expresses micrometer(s).

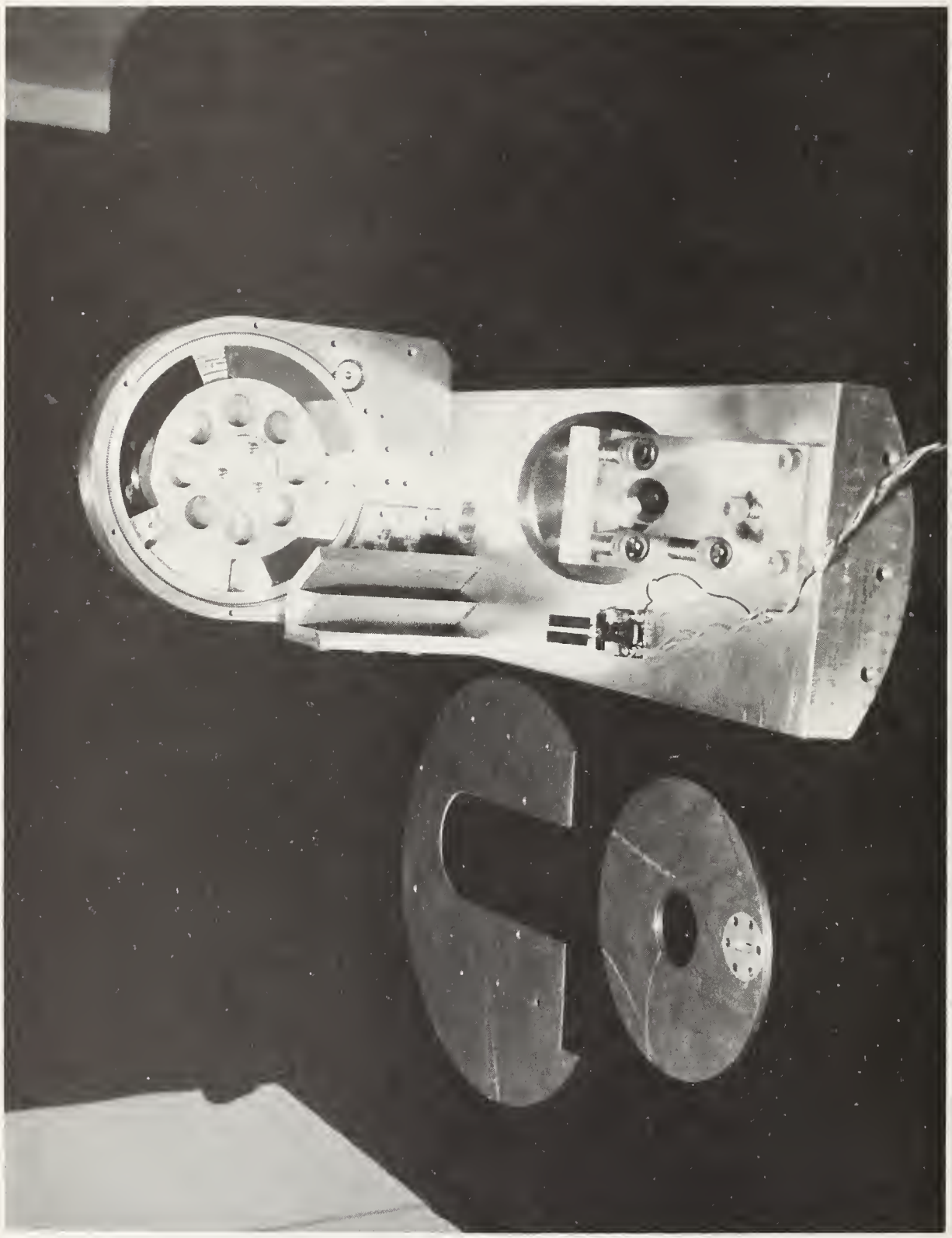

Figure 1. Photo of filter housing and optical bench.

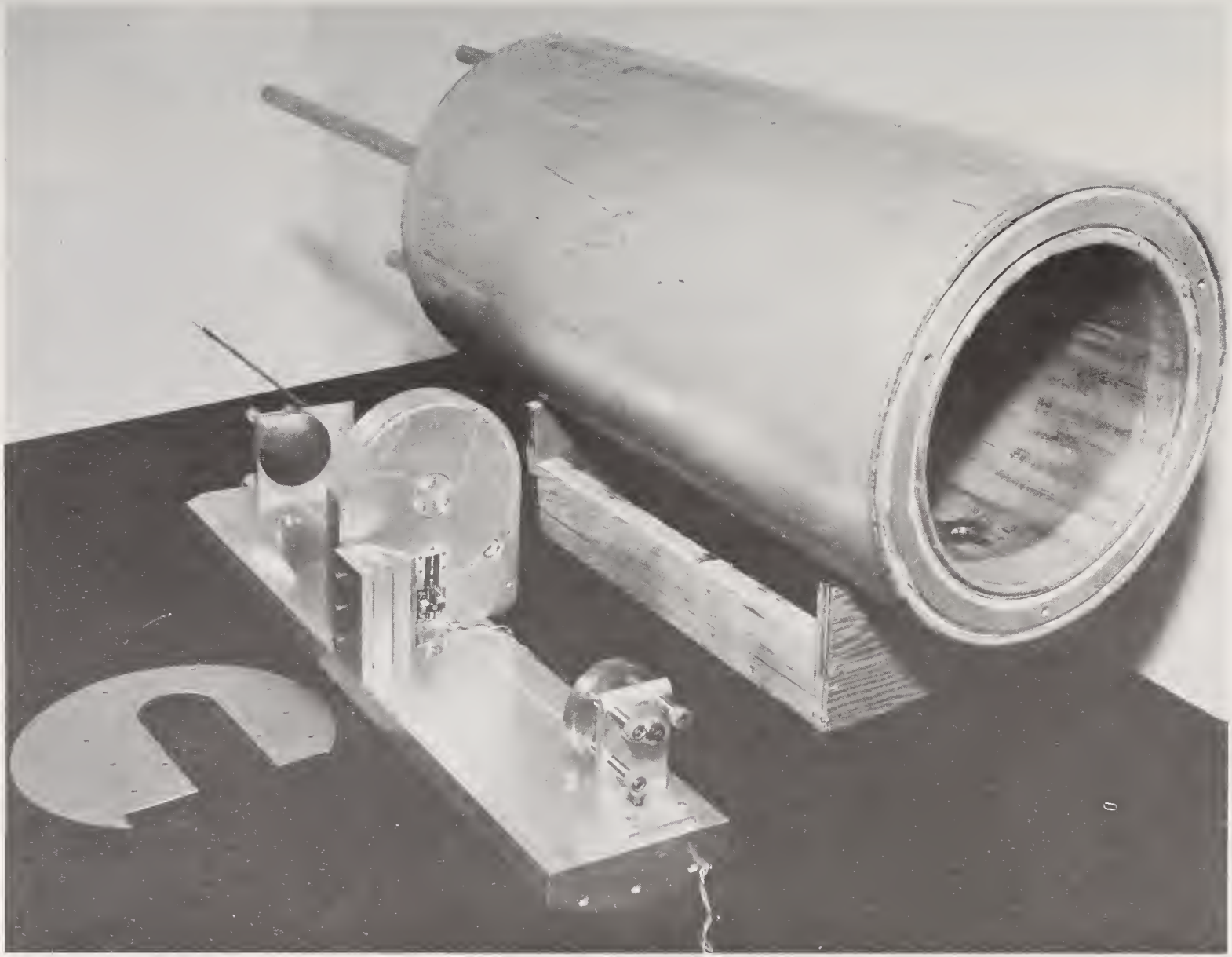

Figure 2. Optical system and liquid nitrogen tank.

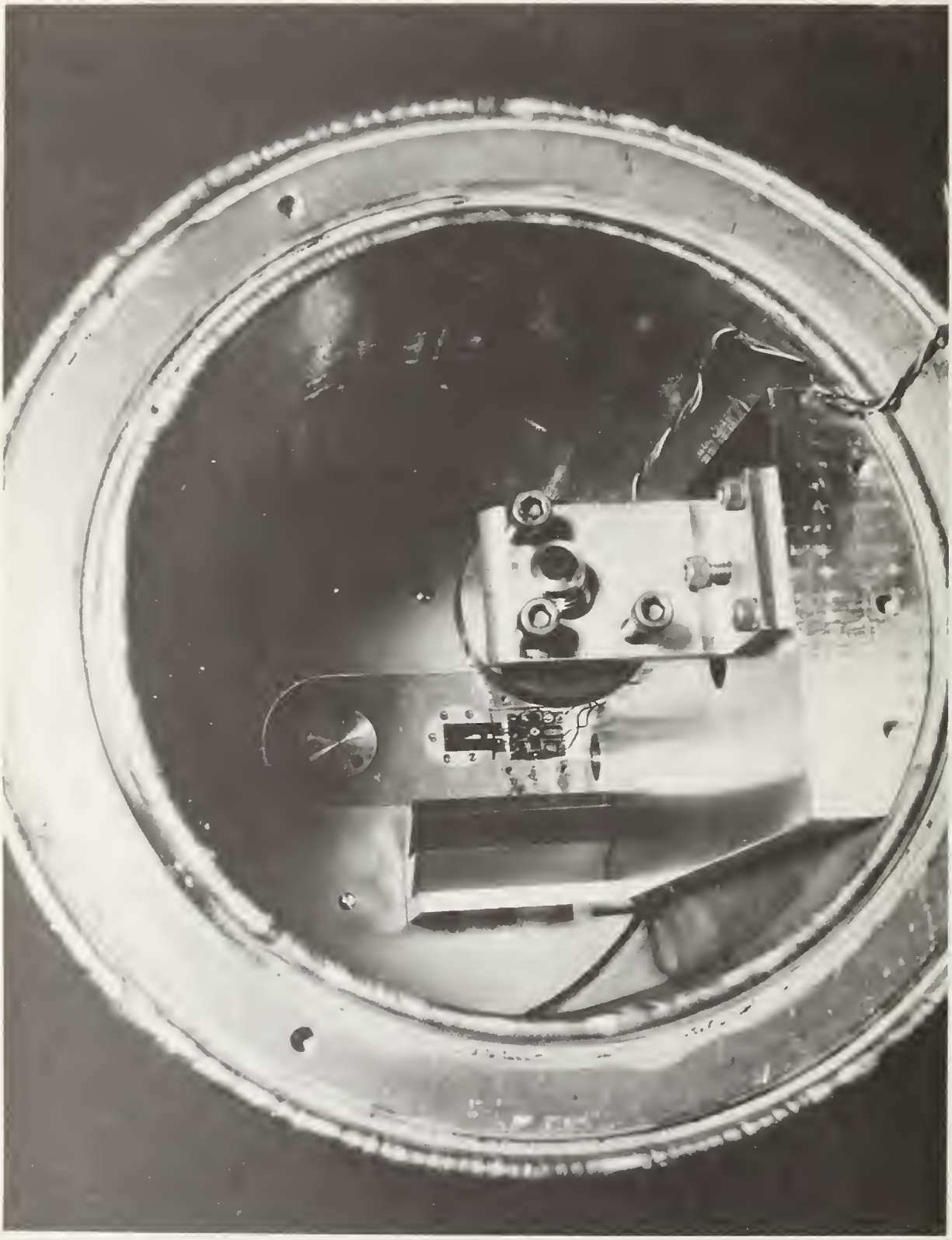

Figure 3. Optical system in place.

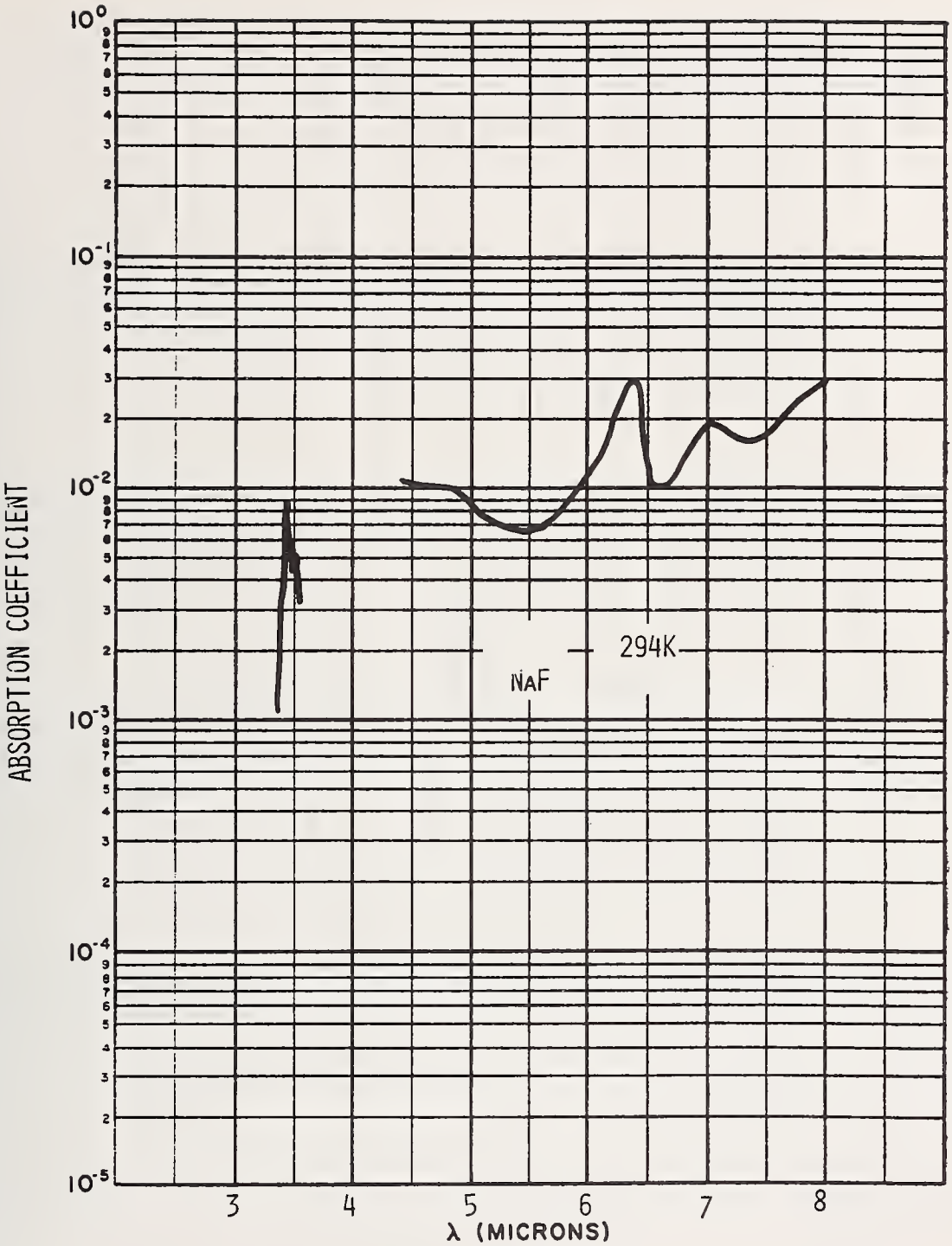

Figure 4. Absorptance coefficient of sodium fluoride at 294 Kelvin.

NOTE: Microns as used on figures 4-7 expresses micrometers.

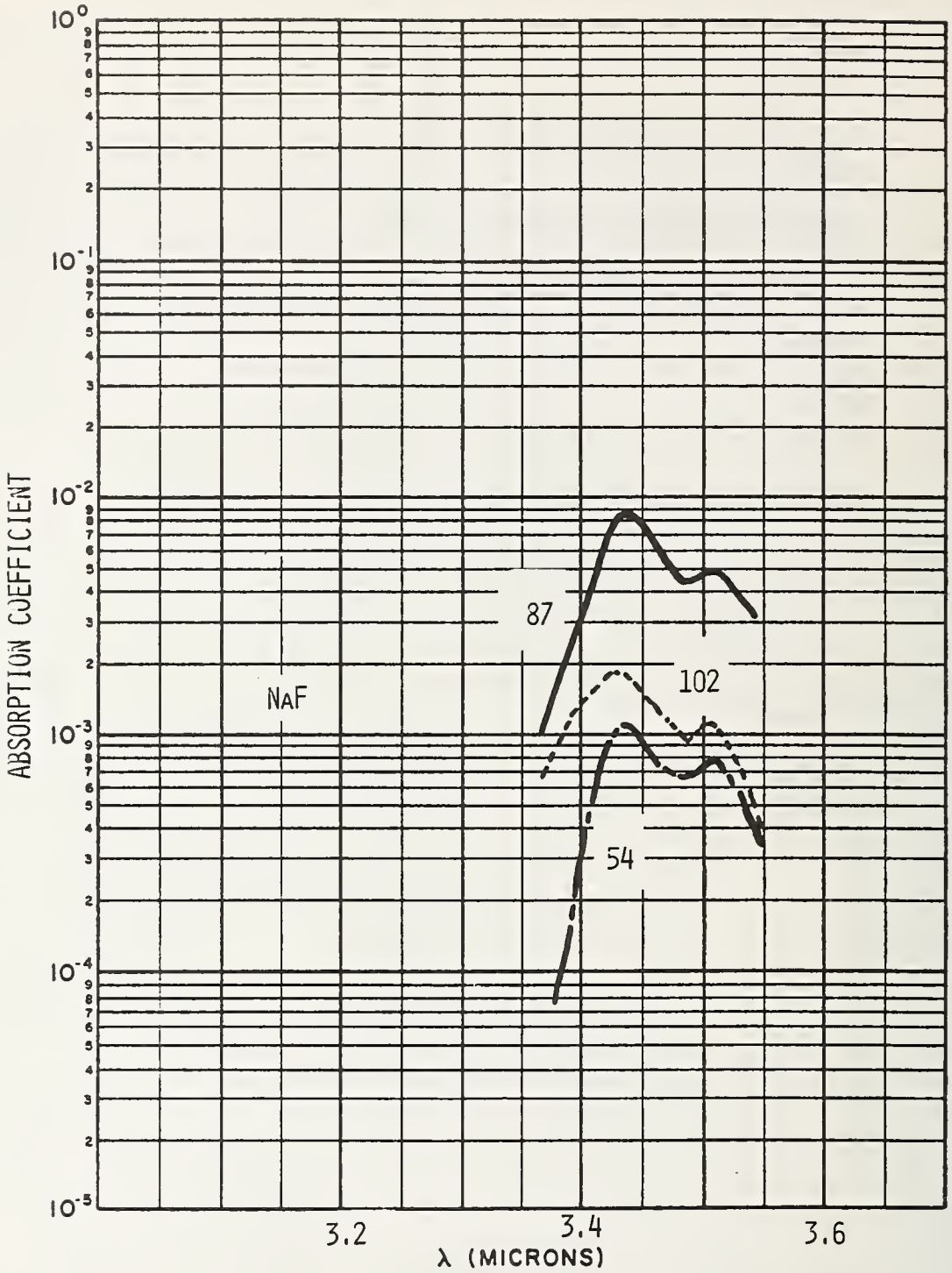

Figure 5. Absorptance coefficient of three samples of sodium fluoride in the 3.5 micron region.

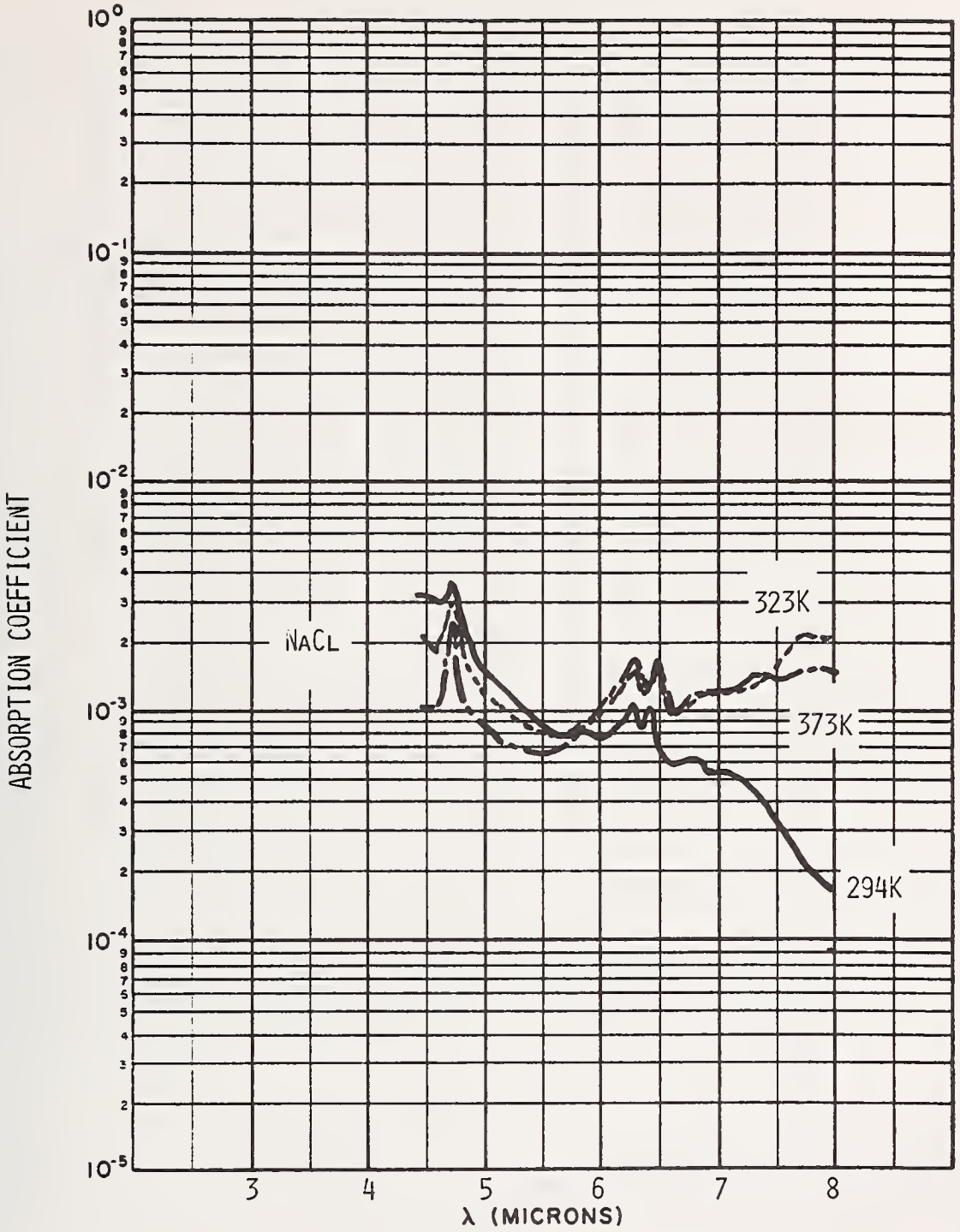

Figure 6. Absorptance coefficient of sodium chloride at 323, 373, and 294 Kelvin.

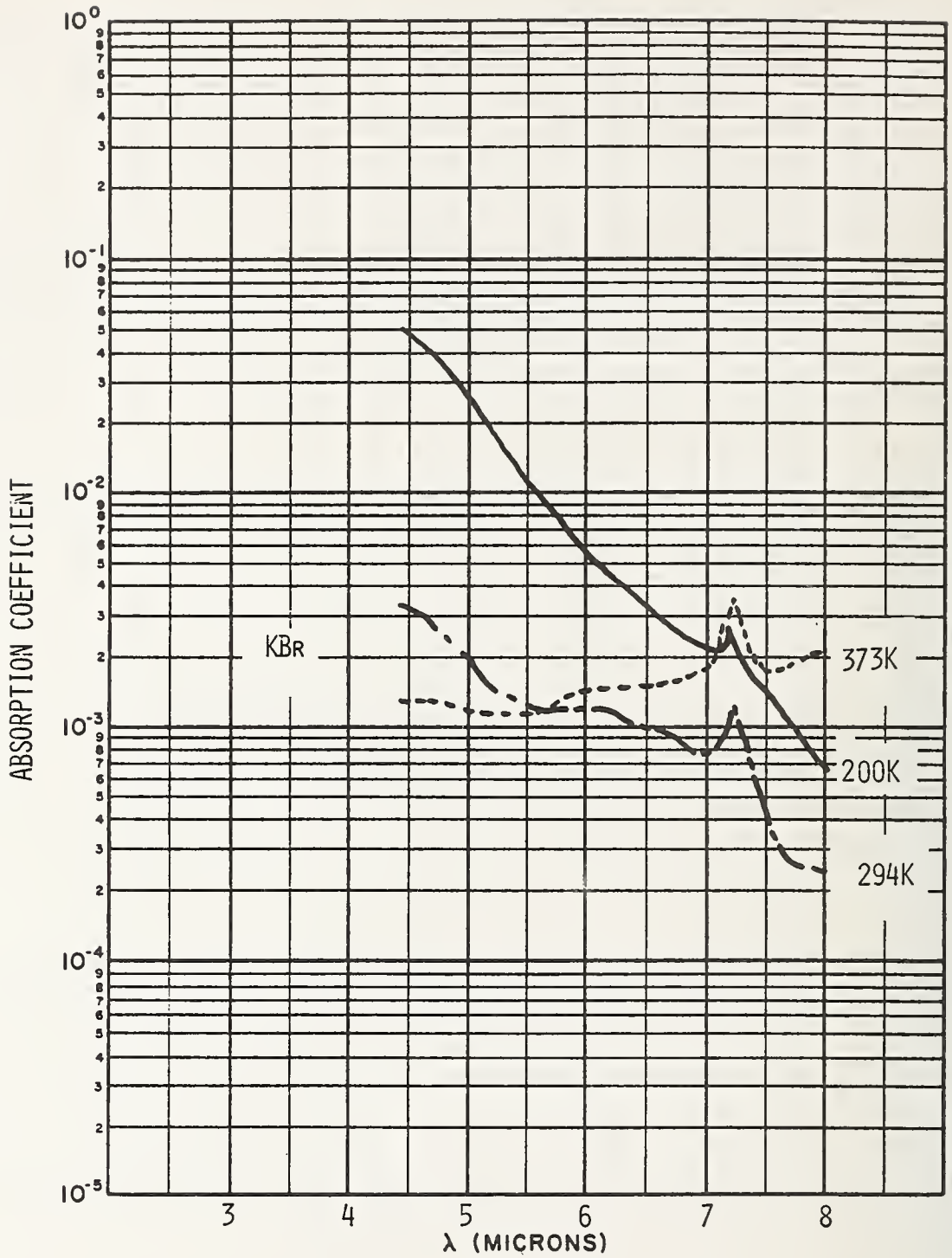

Figure 7. Absorptance coefficient of potassium bromide at 200, 294, and 373 Kelvin.

COMMENTS ON PAPER BY STIERWALT

In response to a question from the audience the speaker indicated that no special treatment of sample surfaces aside from normal cleaning procedures was used. The presence of absorption bands at 3.4 and 3.5 micrometers might be due to contamination of the surface by hydrocarbons.

3.7 Surface Studies with Acoustic Probe Techniques*

J. H. Parks and D. A. Rockwell

Departments of Physics and Electrical Engineering
University of Southern California
Los Angeles, California 90007

A new measurement technique will be discussed which utilizes acoustic surface waves to detect the surface depth dependence of radiative absorption. This will include a theoretical analysis of the detection process which relates these measurements to a quantitative model of surface absorption phenomena. This technique is generally applicable to study weak surface absorption at wavelengths for which a material is essentially transparent. Surface wave phase variations induced by the absorption of 10.6 μm radiation have been measured on KCl surfaces with a laser pulse energy of only $\sim$50 mJ. The surface absorption σ of these samples were measured by calorimetry to be $\sigma \sim 2 \times 10^{-4}$, and acoustic probe measurements on the same samples yielded $\sigma \sim 1 \times 10^{-4}$. Initial results of recent studies on both polished and etched alkali halide surfaces are discussed.

Key words: Acoustic probe techniques; infrared window laser absorption; KCl absorption; laser induced damage; surface absorption.

1. Introduction

Infrared absorption measurement techniques have been developed [1][1] which avoid the effects of the surface contribution. However, the surface absorption represents a practical limitation of high power laser optical materials and an understanding of the details is needed. The principle effort of our research program has been to develop a new measurement process [2,3] which utilizes acoustic surface waves to detect the surface depth dependence of radiative absorption. In addition, a detailed theoretical analysis of this detection process was derived to relate these measurements to a quantitative model of surface absorption phenomena.

These new experimental techniques and the related theoretical analysis involved advances beyond the current state of acoustic surface wave technology. In particular, it was necessary to develop techniques to propagate surface waves on non-piezoelectric solids which did not alter the surface characteristics under study nor require any special surface treatment.

Initial results of recent studies are presented which measure radiative absorption on KCl surfaces. Surface absorption of 10.6μm radiation was measured for both mechanically polished and chemically etched surfaces.

2. Surface Wave Detection of Radiative Absorption

A fundamental understanding of the physics involved in the surface wave detection of radiation was obtained in quantitative studies [2,4] on well known acoustic materials (α-quartz, lithium niobate). It was shown that surface wave propagation in a region heated by radiative absorption could be accurately described by a laser induced transient phase change given by

$$\Delta\phi(t) = \frac{4\pi\nu}{v_{so}} f_B \int_o^L [\varepsilon_r(t) - \alpha_v \Delta T(t)]dr. \qquad (1)$$

Equation (1) is valid when the temperature distribution is essentially uniform over the surface wave penetration depth, or $\partial T/\partial z \ll T/\lambda_s$. Here λ_s is the acoustic wavelength and z is a distance normal to the surface. The phase change arises from a change in propagation path length via thermoelastic strains, $\varepsilon_r(t)$, and also a change in wave velocity through the temperature variation of the elastic coefficients represented by $\alpha_v \Delta T(t)$. In eq. (1) ν is the frequency and v_{so} is the velocity of the surface wave, 2L is the acoustic path length, and r is the distance along the propagation path. The laser induced temperature change $\Delta T(t)$ is found by solving the heat equation, and has the spatial dependence of the Gaussian laser profile. The factor f_B accounts for the incomplete overlap of the acoustic beamwidth and the temperature profile.

* Research supported by Advanced Research Projects Agency.

1. Figures in brackets indicate the literature references at the end of this paper.

Experimental measurements of $\Delta\phi$ on α-quartz and lithium niobate were compared with theoretical calculations of eq. (1) using no adjustable parameters. The quantitative agreement between theory and experiment was within 15%. In these experiments the radiative pulse widths were long enough for heat diffusion to produce a uniform temperature within the surface wave penetration depth. In this way the need to account for propagation in the presence of an axial temperature gradient was avoided, and the resulting analysis provided a clear picture of the fundamental surface wave thermal interaction leading to the induced phase changes.

2.1. The Effect of a Temperature Gradient

Depending on the surface wave frequency and the extent of thermal diffusion, it may not be valid to assume that the temperature is uniform over the surface wave penetration depth. In the presence of such a spatial inhomogeneity, surface wave propagation becomes dispersive. In this case, measurement of the frequency dependence of the induced phase change yields information about the temperature distribution, and consequently, the surface absorption properties.

The contribution of the velocity variation to the phase change in eq. (1) cannot be represented by $\alpha_v \Delta T$ for propagation in the presence of an arbitrary temperature gradient. In this case the phase change is given by

$$\Delta\phi = -\frac{4\pi\nu}{v_{so}} f_B \int_0^L \left[\frac{\Delta v_s}{v_{so}}\right]_{\lambda_s} dr, \qquad (2)$$

when the strain contribution is negligible. The wavelength dependent velocity variation $[\Delta v_s/v_{so}]_{\lambda_s}$ follows from a perturbative treatment [5] of the wave equation in which the elastic coefficients exhibit spatial variation through their known temperature dependence. The perturbation approach allows a precise model of radiative absorption to be easily incorporated into the analysis.

Experimental measurements of the dispersive phase change have been made on Y-cut α-quartz [4]. In this case the exceptionally high bulk absorption coefficient of 241 cm^{-1} at 10.6 μm in quartz is responsible for a significant temperature gradient over the acoustic penetration depth. In the following section it will be shown that a surface absorption layer extending only several microns into a relatively transparent solid will also induce a temperature gradient and dispersive wave propagation.

3. Infrared Surface Absorption

In weakly absorbing materials the radiative absorption coefficient within 1-10μm of the surface can be significantly different than values for bulk absorption. The extent of this surface absorption depends on surface preparation including mechanical polishing and chemical etching procedures, immediate environmental impurity adsorption, and perhaps on the effects of surface dislocations induced during sample preparation. The resulting effect of these surface perturbations can be described by taking the radiative absorption coefficient to be a function of depth below the surface $\beta(z)$. A simple absorption model for weakly absorbing materials is shown in figure 1. The highly absorbing surface region, $\beta_s\ cm^{-1}$, extends a characteristic distance d into the material at which a transition to the bulk value $\beta_B cm^{-1}$ occurs. This model adequately represents the material absorption properties in the region probed by the surface wave. Although the sharp transition region from β_s to β_B may be somewhat unphysical, thermal diffusion during the laser puslewidth causes the acoustic probe measurement to be relatively insensitive to the finer details of the model.

Applying this model to express the intensity absorbed, we solve a one-dimensional heat equation to find the resulting temperature increase in terms of the parameters $\Delta T(\beta_s, d, \beta_B)$. The peak dispersive velocity variation is then derived using this temperature evaluated at the time $t=\tau_p$ which yields

$$\left[\frac{\Delta v_s}{v_{so}}\right]_{\lambda_s,\tau_p} \propto \sum_n \Delta T_n(\beta_s, d, \beta_B) \cdot A_n(\lambda_s/Z_T) \ . \qquad (3)$$

Here the sum is extended over the fourier temperature coefficients ΔT_n which characterize the absorption depth distribution. The factor A_n contains the dispersive behavior as a function of the variable λ_s/Z_T, where $Z_T(\tau_p)$ is the characteristic depth of the temperature distribution at $t=\tau_p$. This depth is determined primarily by thermal diffusion and thus dependent on the pulsewidth τ_p. The variable becomes $\lambda_s/Z_T \ll 1$ for long times during which the temperature becomes uniform over the surface wave penetration depth, or for high frequency surface waves. In this case A_n approaches a constant independent of wavelength indicating the ordinary regime of dispersionless surface wave propagation.

When the pulsewidth τ_p is short enough so that $d \lesssim Z_T \ll \lambda_s$, the measured phase changes will be sensitive to each of the parameters β_s, d, and β_B independently, and the complete distribution of the absorption coefficient may be determined. However, if the pulsewidth is long enough so that $d \ll Z_T \lesssim \lambda_s$,

dispersive propagation may be observed but the phase change will essentially be sensitive only to the product $\sigma=\beta_s d$. This parameter σ, usually referred to as the surface absorption, is included in calorimetric measurements of the percentage power absorbed by a sample of length L in the form

$$\frac{\Delta P}{P} = 2\sigma + \beta_B L. \qquad (4)$$

When the surface absorption, 2σ, from both surfaces is comparable to the bulk absorption $\beta_B L$, the surface contribution is not separable by calorimetric techniques. However, the acoustic probe technique will yield σ independently even in this case, since $\beta_B d << \beta_s d$ is usually satisfied in weakly absorbing materials.

3.1. Application of the Absorption Model to KCl

In KCl the bulk absorption of good samples is known [6] to be as low as $7\times10^{-5}cm^{-1}$. However, radiative absorption occurring in a thin surface layer is significantly greater, and leads to appreciable temperature gradients within the acoustic penetration depth. As an example the absorption model shown in figure 1 is applied to radiative absorption at 10.6μm in KCl using the parameters $\beta_s=10cm^{-1}$, $d=2\mu m$, and $\beta_B=2\times10^{-3}cm^{-1}$. The resulting temperature depth profiles are shown in figure 2 for radiative pulsewidths of 10 msec and 100 msec. In the absence of a highly absorbing surface layer, the presence of such temperature gradients at 10 msec would require a bulk absorption coefficient of ~200 cm^{-1}. The measurement of dispersive surface wave propagation resulting from these temperature gradients is then a direct indication of the existence of highly absorbing surface layers on weakly absorbing materials. The depth profiles of the acoustic energy are also shown in figure 2 for surface waves of frequency 28 MHz and 124 MHz. For $\tau_p=10$ msec we note that $d<<Z_T\simeq\lambda_s$ resulting in the conditions for dispersive propagation. However, for $\tau_p=100$ msec, dispersion would not be observed for these frequencies since $Z_T>>\lambda_s$. In both these cases $Z_T>>d$, which implies the acoustic probe phase changes would measure the magnitude of σ and not the complete set of distribution parameters.

The phase changes $\Delta\phi$ induced by the temperature gradient are shown in figure 3. The phase change per input laser power is plotted versus radiative pulsewidth. The curviture in these graphs is a measure of the effect of thermal diffusion. The acoustic probe at 28 MHz, with a penetration depth of ∿150μm, is much less sensitive to the redistribution of thermal energy than the 124 MHz probe having a penetration depth of ∿35μm.

In the limit of long pulsewidths, we note that $(\Delta\phi 28MHz/\Delta\phi 124MHz)\simeq 0.23$ which is simply the frequency ratio as predicted by eq. (2) for the phase change in this non-dispersive limit. However, for $\tau_p=10$ msec, we find $(\Delta\phi 28MHz/\Delta\phi 124MHz)\simeq 0.19$ which indicates the dispersion effects the order of 20%. To emphasize the effect of dispersion, figure 4 shows a log-log plot of the reduced phase change ($\Delta\phi$ per unit input power and per unit frequency), which eliminates the explicit frequency dependence given in eq.(2). These curves should coincide as dispersion vanishes for long τ_p. The increasing effect of dispersion for short τ_p reaches ∿43% at $\tau_p=0.1$ msec.

4. KCl Surface Studies

4.1. Coupling Surface Waves to KCl

The application of the surface wave measurement technique to KCl requires the ability to propagate waves on the surface of a non-piezoelectric material. This wave propagation must be generated by a technique which does not affect the surface properties under analysis. The technique should also be easily applicable to samples without additional preparation. A fluid coupling technique has been developed which satisfies both these requirements. As shown in figure 5, the surface wave is initially excited on a piezoelectric material (α-quartz), and subsequently coupled through a fluid layer onto the KCl surface. The inverse coupling returns the wave to the detection transducer. Although this method has previously received relatively little development, it is of a particular advantage for our purpose.

Our research has included an experimental study [7] of a fluid coupling technique which has resulted in successfully coupling surface waves to KCl. Phase changes on piezoelectric samples using the fluid coupling technique were compared with the results using direct surface wave excitation by interdigital transducers. This comparison verified that the laser induced phase change was reliably and reproducibly coupled through the fluid regions. Ortho-dichlorobenzene was used as the coupling fluid in these experiments. An experimental transducer configuration has been designed which accepts arbitrary samples sized and provides ample access to the sample surface for the infrared laser sources.

4.2. KCl Experimental Results

Experimental measurements of induced phase changes on KCl were obtained as shown in figure 6. The fluid layer used to couple waves to the KCl surface has been deleted for clarity. The RF reference signal and the transmitted RF signal are combined in a double balanced mixer which provides an output proportional to the sine of the phase change. The amplitude V_o was typically ~200 mV. The peak phase change signal was detected by a digital peak voltmeter and averaged by a PAR Boxcar. Surface wave frequencies of 124 MHz, 62MHz, and 28MHz were used in these studies.

A CO_2 laser pulse of ~65 watts was incident on the KCl samples with pulsewidths ranging from 2 msec to 100 msec. The pulse repetition rate was varied to maintain a constant duty cycle, D=.05, and the average power for each pulsewidth value was $\langle P \rangle \simeq 3$ watts. The signal/noise improvement ratio provided by the Boxcar (during 80 sec exposures and a time constant of 1 sec) was 15-30 for the shortest pulsewidths. Typical KCl phase change signals detected after amplification by the peak detector are shown in figure 7. Note that the signal detected for a pulsewidth of τ_p=0.5 msec required a CO_2 laser pulse energy of only ~35 mJ. The RMS phase noise at 124 MHz observed in the absence of incident radiation was $\delta(\Delta\phi)_N \simeq 0.2$ mrad.

Induced phase change data on KCl are shown in figure 8. Polished and etched samples of Harshaw KCl were measured and are referred to as Chemical Polish. These samples were then repolished mechanically at USC using standard techniques and measurements taken are referred to as Mechanical Polish. Although 3-frequency data were obtained for the Chemical Polish sample, mechanical repolishing introduced enough surface roughness to cause excessive scattering at 124 MHz. Previous measurements on expertly polished Hughes samples have been obtained routinely at 124 MHz. The absolute experimental uncertainty in the phase change measurements was typically 15%.

The data indicate that chemically etched surfaces provide a reduction of the surface absorption σ by at least a factor of 3-4. Similar results have been observed [8] in calorimetric measurements of KCl absorption. Figure 9 shows evidence of dispersive phase changes measured on the chemically etched sample. This is interesting since it indicates the presence of a surface absorption layer even after several microns of material have been removed during a 60 sec etch in concentrated HCl. An initial analysis of this data yields a surface absorption value, $\sigma \simeq 1\times10^{-4}$, for the chemically polished Harshaw sample. Calorimetric measurements on the same sample yield consistent results, $\sigma \simeq 2\times10^{-4}$, assuming a value of $\beta_B = 10^{-3}$ cm^{-1} used in eq. (4).

5. Acoustic Probe Sensitivity

The present results indicate the sensitivity of these surface wave techniques. If it is only required to obtain a relative measurement of surface absorption for different samples, the measurement can be taken at a single frequency and a single pulsewidth. We have found a phase change $\Delta\phi$=60 mrad at 124 MHz for a 100 msec, 70 watt pulse on a surface with $\sigma \sim 1\times10^{-4}$. A surface absorption of $\sigma \sim 2\times10^{-6}$ could be detected, $\Delta\phi \sim 1$ mrad, with the same laser pulse. This limit could be reduced further by operating at higher laser power. It is also important to point out that a laser pulse energy of only $\lesssim$25 mJ at τ_p=1 msec would be required to measure $\sigma \sim 1\times10^{-4}$ with a phase change $\Delta\phi \sim 1$ mrad.

However, dispersive phase change measurements require data at lower frequencies and shorter pulsewidths. Since the phase change is directly proportional to the frequency, the sensitivity will be reduced if depth dependence of the absorptive properties is of interest. For example, the smallest phase change at 28 MHz was measured for a 2 msec, 70 watt pulse on a surface with $\sigma \sim 1\times10^{-4}$. Since this was a factor of 2-3 above the noise, a surface absorption of $\sigma \sim 5\times10^{-5}$ represents a lower limit at this power for measuring an accurate, absolute value for σ from dispersive phase changes. This limit is comparable to the lowest surface absorption obtained on etched samples [6]. If it is desirable to determine the surface absorption parameters β_s and d independently, it is necessary to use radiative pulsewidths on the order of $\tau_p \lesssim 10$ μsec. Present TEA lasers (CO_2, HF, and DF) can provide sufficiently short pulses of high enough energy for such measurements.

6. Concluding Remarks and Planned Applications

The principle accomplishment of this research program has been the successful development of the surface wave measurement process and its associated theoretical description as a reliable research tool to detect and measure the details of weak surface absorption. This technique has been applied to studies of KCl after a method was developed to couple surface waves to non-piezoelectric samples. Results on KCl indicate a high sensitivity to the details of low level surface absorption. Current research plans include:

- measurement of $\beta(z)$ distribution on KCl surfaces
- measurement of σ on ZnSe
- absorption in thin films
- impurity diffusion into alkali-halide surfaces.

7. Acknowledgments

The authors wish to thank S. Allen, and A. Timber, Hughes Research Laboratories, for the KCl samples and their preparation. They also thank D. White and R. King, China Lake, NWC, for transducer fabrication.

8. References

1. M. Haas, J. W. Davisson, H. B. Rosenstock, and J. Babiskin, Proc. Int. Conf. Opt. Prop. Highly Transparent Sol., paper VI-B (Waterville, N.H. 1975).

2. J. H. Parks, D. A. Rockwell, T. S. Colbert, K. M. Lakin, and D. Mih, Appl. Phys. Lett. 25, 537 (1974).

3. D. A. Rockwell, T. S. Colbert, and J. H. Parks, in Proceedings of the International Conference on Optical Properties of Highly Transparent Solids, edited by S. S. Mitra and B. Bendow (Plenum, New York, 1975).

4. D. A. Rockwell and J. H. Parks, "Theory of Acoustic Surface Wave Detection of Radiative Absorption" (submitted for publication in J. Appl. Phys.).

5. B. A. Auld, Acoustic Fields and Waves in Solids, (Wiley, New York, 1973) Vol.II,p.294.

6. T. F. Deutsch, Appl. Phys. Lett. 25,109(1974).

7. D. A. Rockwell, and J. H. Parks, "A Technique for Acoustic Surface Studies of Non-Piezoelectric Materials" (to be published in J. Appl. Phys.).

8. H. G. Lipson, private communication.

8. Figures

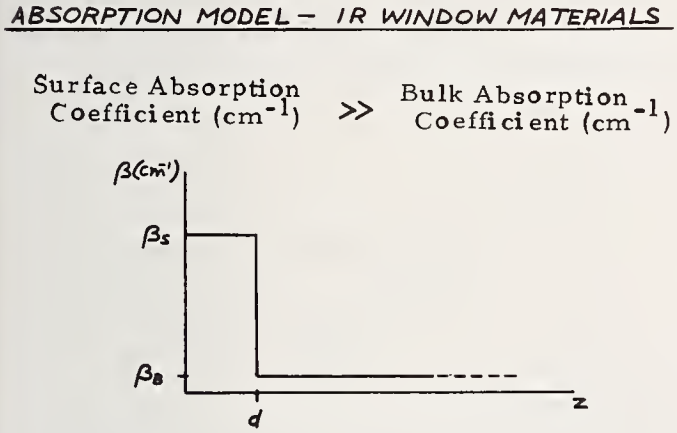

Figure 1. Absorption model for infrared window materials. The distribution $\beta(z)$ is used to calculate the temperature distribution and the induced phase changes measured on KCl surfaces.

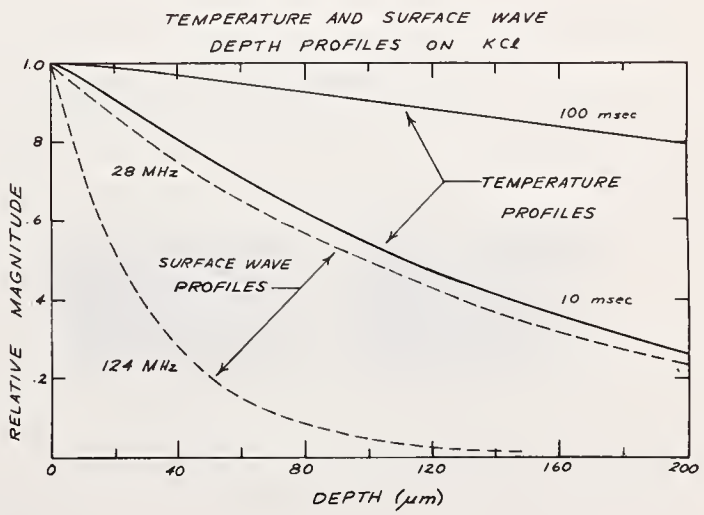

Figure 2. Temperature depth profiles for 10 and 100 msec laser pulsewidths calculated using the absorption model parameters $\beta_S = 10\ cm^{-1}$, $d = 2\ \mu m$ and $\beta_B = 2 \times 10^{-3} cm^{-1}$. The surface wave energy profiles at frequencies of 28 MHz are shown for comparison.

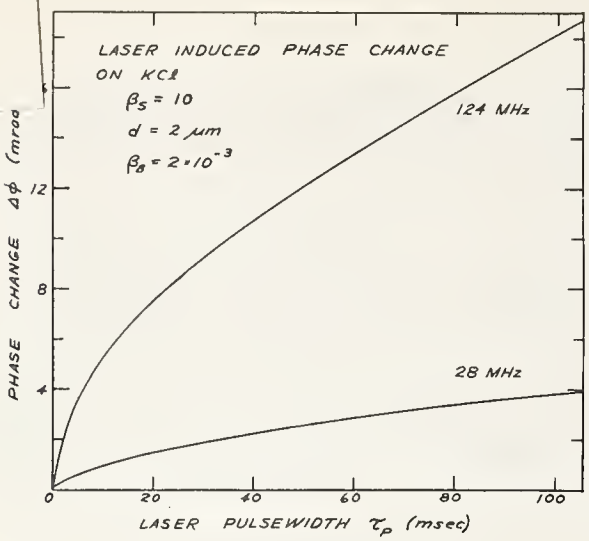

Figure 3. Laser induced peak phase change $\Delta\phi$ (mrad per incident laser power) versus laser pulsewidth is shown for surface wave frequencies of 28 MHz and 124 MHz.

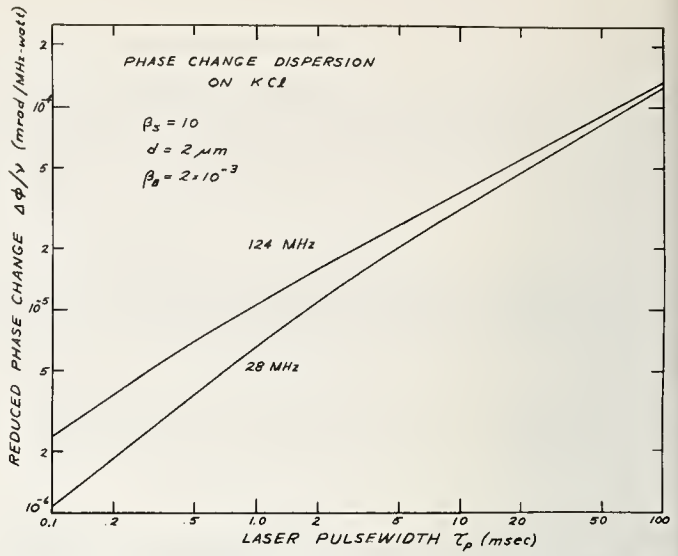

Figure 4. Log-log plot of peak reduced phase change ($\Delta\phi$ per frequency and per incident laser power) versus laser pulsewidth. Dispersive propagation is indicated by divergence of graphs for different surface wave frequencies.

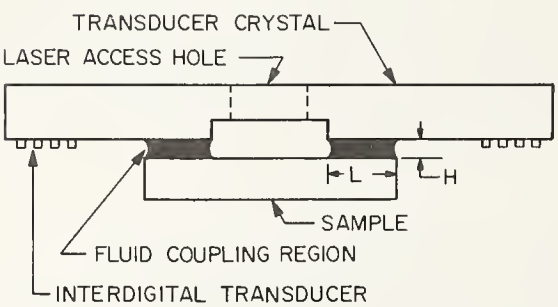

Figure 5. Schematic of the fluid coupling technique. Fluid interfaces couple the surface wave from (to) the piezoelectric transducer crystal to (from) the KCl sample.

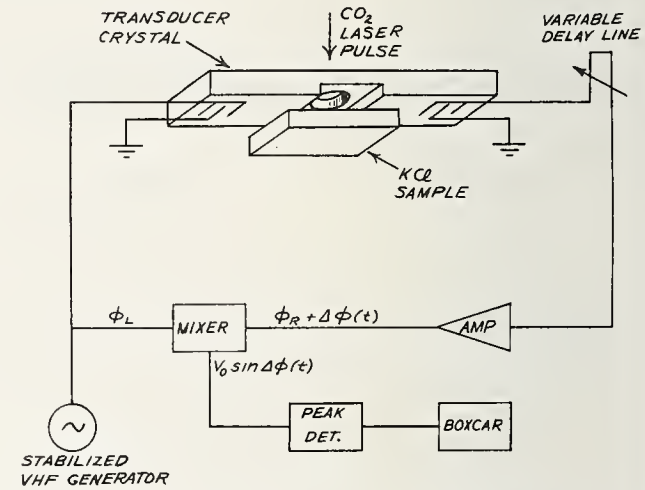

Figure 6. Experimental apparatus for measuring laser induced phase changes on KCl surfaces.

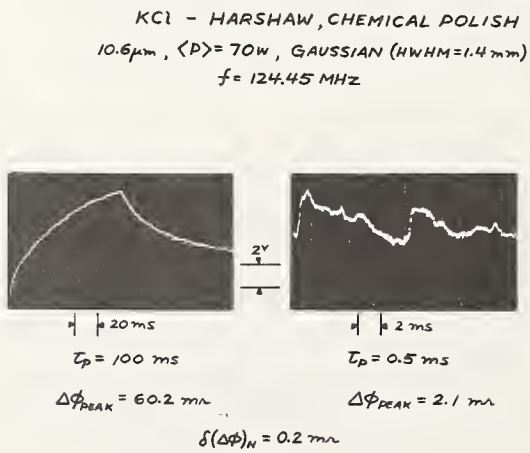

Figure 7. Typical oscilloscope data traces of the transient phase change induced on KCl by laser pulses of 0.5 and 100 msec pulsewidths. Scales are indicated for each trace as well as other pertinent data. $\delta(\Delta\phi)_N$ is the RMS noise value of the phase change measured in the absence of radiation.

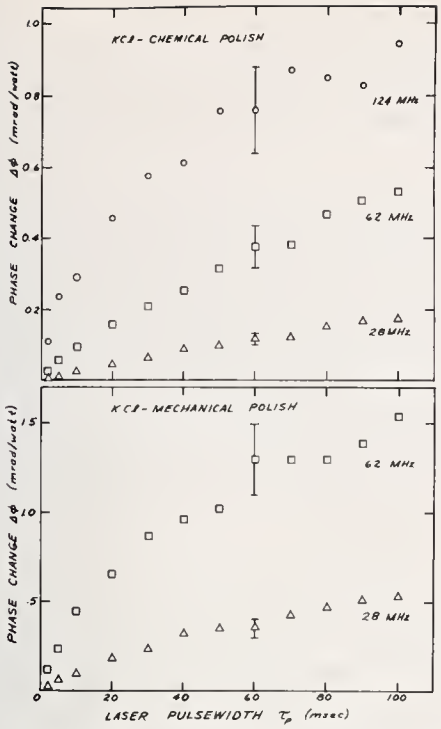

Figure 8. Phase change data versus pulsewidth at various frequencies for chemically polished and mechanically polished KCl surfaces. Bars indicate ± 15% experimental uncertainty.

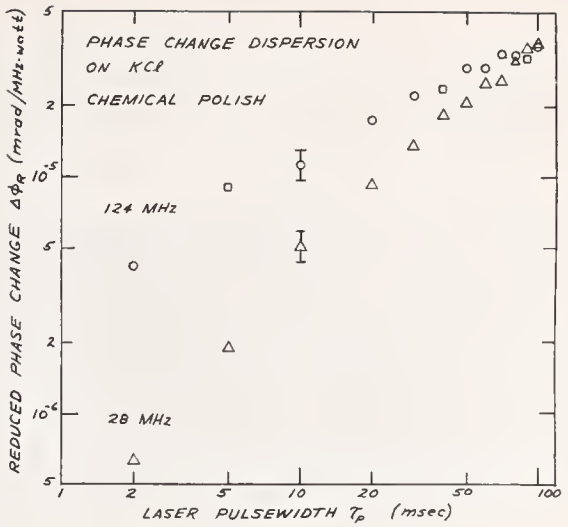

Figure 9. Phase change dispersion versus laser pulsewidth is indicated by the increasing divergence of $\Delta\phi$ as τ_p decreases. This data was taken on a chemically polished surface and experimental uncertainty is ± 15%.

COMMENT ON PAPER BY PARKS, *et al*

In work carried out at the Air Force Cambridge Research Laboratories it was observed that absorption dropped by significant factors when surface cleaning was applied to the sample giving further evidence of the dominant effect of surface absorption in determining the residual loss in these materials.

3.8 Photoelastic Constants of Infrared Materials*

Albert Feldman, Deane Horowitz, and Roy M. Waxler

National Bureau of Standards
Washington, D.C. 20234

Optical distortion occurs in infrared laser windows due to thermal gradients established by the absorption of high power radiation. Principal sources of distortion are the stresses produced by the thermal gradients. Because of the photoelastic effect, these stresses, which vary from point-to-point in the material, produce changes in the refractive index. We are measuring the photoelastic constants of infrared window materials. The measurements employ null techniques which have several advantages over other techniques that have been employed in the past. We present data obtained on Ge, reactive atmosphere processed (RAP) KCl, and KCl doped with KI.

Key words: Birefringence; germanium; KCl; refractive index; single crystal; stress optic constants.

1. Introduction

Stress can produce inhomogeneous refractive index changes that may be highly deleterious in optical components intended for diffraction limited operation. In high power laser windows, stresses may result from thermal gradients caused by the absorption of intense laser radiation [1][1]. The stress-optical constants are important parameters needed by laser system designers for calculating the effects of stress on the optical properties of these windows. In this paper we present the methods we employ for measuring stress-optical constants of important infrared window materials. These methods employ null techniques, which have the advantage of being relatively independent of intensity fluctuations in the radiation sources used [2]. Most of the techniques have been discussed previously [3], but are included for completeness. We present data obtained at 10.6 μm on specimens of single crystal Ge, single crystal KCl grown by the reactive atmosphere process (RAP), and single crystal KCl doped with KI. Data are also given for both types of KCl at 0.633 μm and 0.644 μm. Measurements will be continued on these materials so as to improve the precision of the data.

2. The Stress-Optical Constants

The stress-optical effect arises from the dependence on stress, σ_{kl}, of the optical dielectric tensor K_{ij}. By convention this relationship is expressed in terms of the change of the reciprocal of the dielectric tensor, K_{ij}^{-1} (or dielectric impermeability), thus

$$\delta K_{ij}^{-1} = q_{ijkl}\, \sigma_{kl} \tag{1}$$

where the stress optical constants q_{ijkl} are the components of a fourth rank tensor and the indices ijkl each take on values 1, 2, 3. This relationship is frequently expressed in a system of contracted indices (also called the Voigt notation), thus

$$\delta K_{m}^{-1} = q_{mn}\sigma_{n} \tag{2}$$

where m and n each take on values 1-6. Nye [4] discusses in detail the relationships between the tensors in the full notation and in the contracted notation. For the purposes of this discussion, we use the contracted notation.

In general, there exist 36 independent stress-optical constants, but for our crystals, which are of the cubic class m3m, there are only three independent constants, q_{11}, q_{12}, and q_{44}. To obtain all these coefficients requires three independent measurements of the change of refractive index with stress, but at least one experiment must measure an absolute change of refractive index.

* This work is supported in part by the Advanced Research Projects Agency of the Department of Defense.

1. Figures in brackets indicate the literature references at the end of this paper.

3. Stress-Induced Birefringence

In the present context, stress-induced birefringence is the measure of the relative refractive index change caused by a uniaxial stress. The change is relative because it measures the difference between the changes in refractive index of the two normal polarization modes of radiation propagating through a stressed crystal.

In this experiment, stress is applied along the axis of a specimen in the form of a rectangular prism that has a square cross-section perpendicular to the long axis. The ratio of height to width of a prism is approximately 3:1. For a cubic material two specimens are used with the axis of one specimen along the [100] direction and the axis of the other specimen along the [111] direction. These axes are chosen because the refractive indices are independent of the direction of radiation propagation in the plane perpendicular to the stress axis. The radiation that propagates into the specimen is polarized at 45° with respect to the stress axis. The state of polarization of the emerging radiation, which is determined by the stress-induced birefringence, is analyzed by any of several methods, depending upon the size of the birefringence, and wavelength of the radiation. In the case of Ge, where the stress-optical effect is large and the specimen can support a large stress, one need only to place an analyzer at 90° with respect to the incident polarization angle and photometrically detect nulls or fringes as a function of applied stress. The fringe count, N_B, per unit applied stress is

$$\frac{dN_B}{d\sigma} = \frac{m}{2}\frac{n^3}{\lambda} qt \begin{cases} q = q_{11} - q_{12} \text{ for [100] stress} \\ -q = q_{44} \text{ for [111] stress} \end{cases} \quad (3)$$

where n is the zero stress refractive index, λ is the wavelength, t is the specimen thickness, and m, which is the number of passes the radiation makes through the specimen, equals one. Increased sensitivity is obtained by allowing multiple passes.

In the case of KCl, it is impossible to obtain a minimum of one fringe, even for multiple passes of the radiation, because the material cannot support large stresses. We, therefore, employ a birefringent compensator technique for measuring the induced birefringence. For measurements at 10.6 μm we place a specimen of Ge in a stress frame between the KCl specimen and the analyzer. With zero load on the KCl, we stress the Ge to the first null position. After applying a stress to the specimen which removes the null, we adjust the stress of the Ge until the null is restored. Because the Ge has been previously calibrated, we can compute the stress-optical constants of the KCl. For measurements using the above technique in the visible, we employ either a stressed plate of fused silica or a Soleil-Babinet compensator.

Even greater accuracy and precision is possible in the visible if we employ another technique which makes use of a de Senarmont compensator. However, the apparatus for this technique is unavailable for the infrared.

In all cases, multiple passes of the specimen increases the sensitivity of measurement. In figure 1 we show an 8 pass arrangement of the birefringent compensator technique. Multiple passes, however, do not always help if internal strains occur in the specimens. These internal strains can be a major source of error [5].

4. Absolute Change of Refractive Index

In order to calculate the individual values of q_{11} and q_{12}, we require a measurement of the absolute change of the refractive of index. For this purpose we use Twyman-Green and/or Fizeau interferometers.

The Twyman-Green interferometer is assembled from components with a laser as the radiation source. The specimen, which must have sufficient optical quality so that fringes are observed at the interferometer output, is mounted in one arm of the interferometer. The shift of fringes as a function of stress is either detected photometrically or viewed on an imaging device. Pyroelectric detectors are used in the infrared at 10.6 μm and photomultipliers are used in the visible and near infrared. Fringes at 10.6 μm are viewed with a thermal image plate or a liquid crystal sheet, while in the visible and near infrared, fringes are viewed with a Si matrix tube and TV-monitor.

The fringe shifts per unit applied [100] stress for stresses parallel and perpendicular to the polarization of the radiation are, respectively,

$$\frac{\Delta N_1}{\Delta\sigma} = \frac{2t}{\lambda}\left[\frac{n^3}{2} q_{11} - (n-1)\, s_{12}\right] \tag{4}$$

$$\frac{\Delta N_2}{\Delta\sigma} = \frac{2t}{\lambda}\left[\frac{n^3}{2} q_{12} - (n-1)\, s_{12}\right], \tag{5}$$

where s_{12} is a component of the elastic compliance tensor. If s_{12} is not known, then it may be determined with Fizeau interferometry. The sample itself functions as a Fizeau interferometer if the faces are polished sufficiently parallel. Fringes are then obtained from the interference between reflections from the front and back surfaces, and the shift of these fringes as a function of stress is measured in the same manner as the shift of the Twyman-Green fringes. The fringe shifts per unit applied [100] stress for stresses parallel and perpendicular to the polarization of the radiation are, respectively,

$$\frac{\Delta N_1'}{\Delta\sigma} = \frac{2t}{\lambda}\left[\frac{n^3}{2} q_{11} - n\, s_{12}\right] \tag{6}$$

$$\frac{\Delta N_2'}{\Delta\sigma} = \frac{2t}{\lambda}\left[\frac{n^3}{2} q_{12} - n\, s_{12}\right]. \tag{7}$$

With eqs. (4-7) we can obtain q_{11}, q_{12}, and s_{12}.

In certain instances, such as in the case of KCl, we are unable to produce a minimum shift of one fringe using standard Twyman-Green or Fizeau interferometers. For this case we have constructed a modified Twyman-Green interferometer that is capable of detecting a 0.01 fringe shift at 10.6 μm. A schematic diagram of the interferometer for use with a CO_2 laser is shown in figure 2. The two arms of the interferometer are in close proximity in order to minimize instabilities due to air currents and vibrations. The effects of vibrations are also minimized by mounting the diagonal mirror onto the same base as the beam splitter and by mounting the two end mirrors on a common base. The specimen arm end mirror, which is mounted on a piezoelectric translator, undergoes a sinusoidal translation thus modulating the output intensity of the interferometer. The reference specimen at 10.6 μm is a crystal of a Ge in a compression apparatus. In the visible the reference specimen is fused SiO_2. We calibrate the reference specimen by measuring the force necessary to produce an integral number fringe shift. Fractional fringes are then obtained by linear interpolation. In operation, the reference specimen is stressed until the interferometer is at a null, which occurs when the fundamental harmonic of the output intensity is zero. A given stress applied to the unknown specimen will shift the interferometer away from null, whereupon we compensate for this shift by applying an incremental stress to the Ge which brings the interferometer back to null. From these data we then calculate the stress-optical constant using eqs. (4) or (5) provided s_{12} is known.

5. Results

In table I we show the results we have obtained for Ge compared with earlier reported results [6,7]. We have studied Ge primarily because it is the reference material used in our measurements of the photoelastic constants of other materials in the infrared. Ge is important also as an infrared window material and an infrared acousto-optical material.

Our measurements of the relative stress-optical constants at 10.6 μm are compared with earlier measurements [6] at 2.5 μm. From that earlier work, it can be shown that q_{11}-q_{12} has a large dispersion, whereas q_{44} has a small dispersion. This is verified in our results, where the values of q_{44} at 10.6 μm and 2.5 μm agree to within the experimental error, while the value of q_{11}-q_{12} at 10.6 μm continues the trend of the dispersion of shorter wavelength values.

From our measurements of stress-optical constants, q_{11}, q_{12}, and q_{44}, we have calculated the elasto-optic constants [4], p_{11}, p_{12} and p_{44}, and find a significant difference with the corresponding values obtained by Abrams and Pinnow [7]. Our results indicate that Ge has a smaller figure of merit as an acousto-optic modulator than they calculate from their data.

In table II are presented the values we have obtained for the stress-optical constants of RAP KCl and KCl doped with KI together with earlier reported values [5,8-15]. From our results we cannot infer any difference in the coefficients of these two types of materials. The values for $q_{11} - q_{12}$ are experimentally determined.

Table I. Photoelastic Constants of Ge in Units of $10^{-12} m^3/N$.

Coefficients	10.6 μm	2.5 μm
q_{11}	-.84 ± .04	
q_{12}	-.48 ± .03	
$q_{11}-q_{12}$	-.36 ± .02	-.20[a]
q_{44}	-1.09 ± .05	-1.12[a]
p_{11}	-.126	.27[b]
p_{12}	-.154	.235[b]
p_{44}	-.073	.125[b]

[a] [6].

[b] Absolute Values - [7].

Table II. Stress-Optical Constants of KCl in Units of $10^{-12} m^2/N$.

q_{11}	q_{12}	$q_{11} - q_{12}$	q_{44}	λ(μm)	Ref.
		1.70	-4.31	0.589	8
4.63	2.92	1.71	-3.62	0.589	9
		1.66	-4.42	0.589	10
		1.47	-4.94	0.589	11
		1.42		0.480	12
5.23	3.58	1.65/1.57	-4.49/-4.74	0.589	13
		1.81		0.633	5
4.6 ±.2	2.7 ±.8	1.7 ±.4	-3.9 ±.8	0.633	This work
		1.9 ±.1	-4.4 ±.2	0.644	This work
4.6 ±.2*	2.8 ±.2*	1.9 ±.2*	-4.6 ±.2*	0.633*	This work
		1.9 ±.1*	-4.7 ±.2*	0.644*	This work
		2.0	-	10.6	14
			-2.62	10.6	15
		2.5 ±1.0	-4.3 ±.9	10.6	This work
		1.5 ±0.6*	-	10.6*	This work

*Doped with KI.

There have been only two reported measurements of the absolute stress-optical constants q_{11} and q_{12} but the values of these respective coefficients in the two reports differ [9,13]. Our results agree most closely with values calculated from the results of Iyengar [9] who actually measured the elasto-optical constants.

Our values for $q_{11}-q_{12}$ in the visible tend to be slightly higher than earlier reported values. At 10.6 μm we at present cannot attribute any significance to the different values we obtain and the difference of our values from an earlier measurement [14].

Our values for q_{44} in the visible appear to fall within the range of earlier reported values. At 10.6 μm, however, our values suggest a small dispersion when compared to the visible. This latter result is in disagreement with an earlier measurement [15].

6. Acknowledgments

We thank Phillip Klein of the Naval Research Laboratory for supplying the RAP grown KCl and E. Berna of Honeywell for supplying the KCl doped with KI.

7. References

[1] Bendow, B., P. D. Gianino, A. Hordvik and L. H. Sholnik, Optics Comm. 7, 219 (1973); Bendow, B., and P. D. Gianino, Applied Physics 2, 1 (1973).

[2] Birnbaum, G., E. Cory and K. Gow, Appl. Optics 13, 1660 (1974).

[3] Feldman, A., I. Malitson, D. Horowitz, R. M. Waxler, and M. Dodge, Laser Induced Damage in Optical Materials:1974, NBS Spec. Publ. 414 (1974).

[4] Nye, J. F., Physical Properties of Crystals (Oxford University Press, London 1957) pp. 243-254.

[5] Wilkening, W. W., J. Friedman, and C. A. Pitha, "Measurement of Stress-Induced Birefringence in Alkali Halides," Third Conf. on High Power Infrared Laser Window Materials, 1973, AFCEL-TR-74-0085-I.

[6] Feldman, A., Phys. Rev. 150, 748 (1966).

[7] Abrams, R. L. and D. A. Pinnow, J. Appl. Phys. 41, 2765 (1970).

[8] Pockels, F., Lehrbuch der Kristalloptik, Leipzig: Teubner (1906).

[9] Iyenger, K. S., Nature 176, 1119 (1955).

[10] Bhagavantam, S. and Y. Krishna Murty, Proc. Indian Acad. Sci. A 46, 399 (1957).

[11] Bansigir, K. G. and K. S. Iyengar, Proc. Phys. Soc. London 71B, 225 (1958).

[12] Srinivasan, R., Zeit, f. Physik 155, 281-289 (1959).

[13] Rao, K. V. Krishna and V. G. Krishna Murty, Proc. Indian Acad. Sci., Sci. 64, 24 (1966).

[14] Chen, C. S., J. P. Czcznesniak, and J. C. Corelli, J. Appl. Phys. 46, 303 (1975).

[15] Pitha, C. A. and J. D. Friedman, "Stress-Optical Coefficients of KCl, BaF_2, CaF_2, CdTe, TI-1120 and TI-1173," Proc. of the Fourth Annual Conf. on Infrared Laser Window Materials, Nov. 18-20, 1974. Compiled by C. R. Andrews and C. L. Strecker (1975).

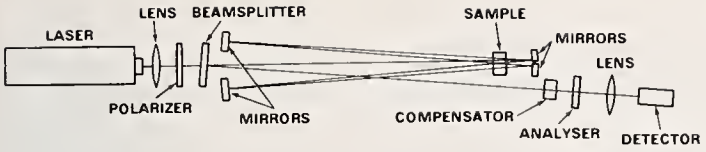

Figure 1. Eight pass measurement of stress birefringence.

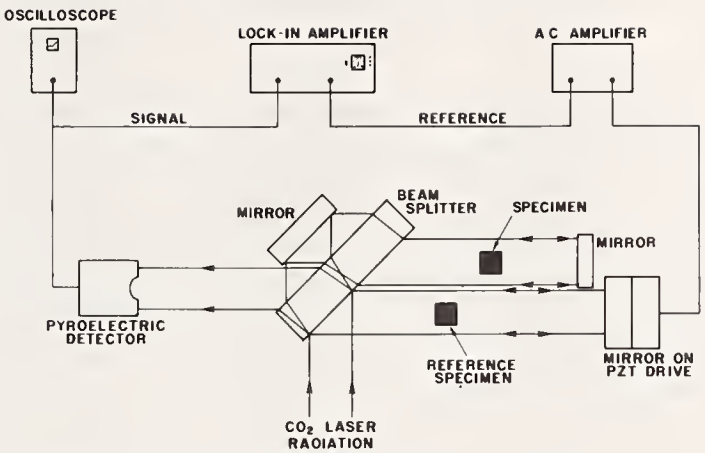

Figure 2. Modified Twyman-Green interferometer for measuring fractional wavelength changes of optic path at 10.6 micrometers.

NO COMMENT ON PAPER BY FELDMAN, et al

3.9 Refractive Index and Temperature Coefficient of Index of CVD Zinc Selenide*

Marilyn J. Dodge and Irving H. Malitson

National Bureau of Standards
Optical Physics Division
Washington, D.C. 20234

The refractive index of each of two prismatic samples of CVD ZnSe was measured from 0.5086 to 18.2 μm by means of the minimum-deviation method on a precision spectrometer. Data were obtained at temperatures near 20°C and 34°C and each set of data was fitted to a three-term Sellmeier-type dispersion equation, which permits refractive index interpolation within several parts in 10^{-5}. Using the data obtained at the two temperatures, dn/dT was calculated for both samples. A comparison of refractive index and dn/dT is made with other types of ZnSe.

Key words: Refractive index; temperature coefficient of refractive index; zinc solenide.

1. Introduction

The performance of a high-power laser system could be limited because of optical distortion of the window material. It has been reported [1][1] that the effect of a heated window can distort the beam and thus degrade the system at powers less than those required to fracture or melt the window. To predict the amount of distortion which can occur, it is necessary to know the refractive index, n, temperature coefficient of index, dn/dT, and the thermal-expansion and stress-optical coefficients of the material under consideration. An optical materials characterization program [2] is currently in progress at NBS to determine these pertinent optical properties. Although much work has been done to predict the oretically the dn/dT of candidate laser window materials, there is a lack of experimental data on refractive index and dn/dT to back up the theoretical calculations [3]. The refractometry laboratory at NBS is determining the index of refraction and dn/dT of selected window materials over a limited temperature range.

Chemical vapor deposited (CVD) zinc selenide is an important candidate window material. This polycrystalline material has a practical transmission range from 0.5 to 20.0 μm. A literature search has revealed that a comprehensive study of the refractive index and dn/dT of this material over its entire useful transmission range has not been reported. In addition to predicting distortion effects, this data is needed for designing lenses, prisms, and other transmitting components for use in laser systems operating in the 2 - 14 μm range. This paper will present a study on the refractive index and dn/dT for two samples of CVD ZnSe. Both samples were made by Raytheon Company[2] and are arbitrarily designated as sample A and sample B. Sample A was manufactured about 1971 and sample B in 1974. Sample B appeared to be optically better material than sample A and is considered by the manufacturer to be representative of what is now commercially available.

2. Experimental Technique

Both specimens were in prismatic form and were measured by means of the minimum-deviation method using a precision spectrometer shown schematically in figure 1 [4]. In the visible and near infrared regions of the spectrum, the index was measured at known emission wavelengths of mercury, cadmium,and helium. Beyond 2 μm, a glo-bar was used for the radiant-energy source, and measurements were made at known absorption bands of water, carbon dioxide, polystyrene,and 1,2-4 trichlorobenzene. A series of narrow-band interference filters was also used between 3.5 and 10.6 μm. A thermocouple with a cesium iodide window was used for the detector. This instrument has a scale that is accurate to within one second of arc. Therefore, the refractive index of good optical material can be measured within 1 to 2 x 10^{-5} over a wide wavelength range.

The index was determined for both samples at selected wavelengths from 0.5086 μm to 18.2 μm and at controlled room temperatures near 20°C and 34°C. Each set of experimental data was fitted by a least square solution to a three-term Sellmeier-type dispersion equation [5] of the form

---

*This project is sponsored in part by the Defense Advanced Research Projects Agency.

1. Figures in brackets indicate the literature references at the end of this paper.

2. The use of company and brand names in this paper are for identification purposes only and in no case does it imply recommendation or endorsement by the National Bureau of Standards, and it does not imply that the materials used in this study are necessarily the best available.

$$n^2 - 1 = \sum_{j=1}^{N} \frac{A_j \lambda^2}{\lambda^2 - \lambda_j^2} .$$

The index of refraction is represented by n, λ is the wavelength of interest in micrometers, the λ_j's are the calculated wavelengths of maximum absorption and the A_j's are the calculated oscillator strengths corresponding to the absorption bands. The λ_j's and the A_j's are not intended to have any physical significance and are influenced by the wavelength range covered by the experimental data. Primary emphasis is given to procuring a mathematical fit of the measured data useful for interpolation. This equation will fail when an attempt is made to fit data too close to an absorption edge. Because ZnSe is almost totally absorbing below 0.5 μm, it was not possible to fit the data below 0.5461 μm for either sample.

3. Index Data

The constants calculated for each dispersion equation, the specified wavelength range, the number of wavelengths, and the overall average absolute residual (the average difference between the experimental values and the calculated values) are given in table I.

Table 1: Constants for Dispersion Equations

Constant	Sample A		Sample B	
	20.3°C	30.8°C	20.8°C	33.5°C
A_1	4.2980149	4.2466487	4.4639521	4.2366336
A_2	0.62776557	0.68520488	0.46132463	0.69295365
A_3	2.8955633	3.3114671	2.8828867	2.7641692
λ_1	0.19206300	0.18807700	0.20107634	0.19283319
λ_2	0.37878260	0.37665162	0.39210520	0.36954401
λ_3	46.994595	49.694957	47.047590	46.148359
No. of Wavelengths	33	19	38	34
Wavelength Range (μm)	0.54-18.2	0.54-18.2	0.54-18.2	1.0-18.2
Average Absolute Residual of index X 10^5	6.2	15.6	4.1	7.4

It should be emphasized that these constants refer specifically to these two samples of CVD ZnSe under the stated experimental conditions. The average residual is indicative of the accuracy of the experimental data.

The refractive index was calculated at regular wavelength intervals using each set of fitted parameters. Figure 2 shows the refractive index plotted as a function of wavelength for sample B near 21°C. The index values range from 2.67544 at 0.54 μm to 2.32781 at 18.2 μm and is 2.40278 at 10.6 μm.

In figure 3, the refractive index of sample B is compared with that of sample A and results obtained by other experimenters. The values for sample B are represented by the zero line. All of the data were reduced to a common temperature of 20°C, using the dn/dT values determined for sample B which will be discussed below. Both single crystals studied by Marple [6] were in the form of prisms and the index was measured at selected wavelengths from the visible to the near IR with a stated accuracy of 4×10^{-3}. From about 1.2 to 2.5 μm the indices of the two samples are about the same, differing from the NBS sample by approximately -8 to -4 $\times 10^{-3}$. A prism of Irtran 4, which is hot-pressed polycrystalline ZnSe, was measured by Hilton [7] at selected wavelengths with an estimated uncertainty of 3×10^{-4}. Hilton's data were published in graphical form and the data shown were extracted from the smooth curve. The indices are generally higher than the NBS values by about 4×10^{-3} and agree with the data published on Irtran 4 by Kodak [8] which isn't shown here. The older CVD specimen of

ZnSe, sample A, is generally higher than the newer material, sample B, by 30 x 10^{-5} from the visible to 1 μm, then levels off to within ± 8 x 10^{-5} between 1.6 and 10.8 μm, rising to 65 x 10^{-5} at 18.2 μm. At 10.6 μm, sample A is higher than B by 9 x 10^{-5}.

4. Temperature Coefficient of Index

Sample B was measured at 38 wavelengths at an average room temperature of 33.5°C. An attempt was made to fit the data over the same wavelength range as at 20.8°C, but an acceptable fit could not be obtained. Dropping all wavelengths below 1.0 μm and fitting only the longer IR data a fit was attained with 34 wavelengths with an average absolute residual of 7.4 x 10^{-5}. The calculated index values at regular wavelength intervals for both temperatures were used to determine dn/dT as a function of wavelength from 1.0 to 18.2 μm. This data is shown graphically in figure 4. The solid portion of the curve represents the data calculated from the fitted values and the dashed portion represents values calculated from the raw data. For a mean temperature of 27°C, dn/dT steadily decreases from about 15 x 10^{-5}/°C at 0.5461 μm to a value of 7.4 x 10^{-5}/°C at 1.6 μm, remains fairly constant to 12.2 μm then decreases to 4.3 x 10^{-5}/°C at 18.2 μm. These values are considered accurate within 1.5 x 10^{-5}. However the change in wavelength of the absorption bands used for wavelength calibration as a result of the increase in temperature is not known. The positive dn/dT is typical of covalent crystals and is indicative of a shift of the strong absorption edges to longer wavelengths. This could explain the inability to fit the data in the visible region of the spectrum.

The dn/dT values obtained for the two CVD specimens in this study are compared with those of other researchers [9,10] at 10.6 μm in table II.

Table II: Temperature Coefficient of Refractive Index of CVD Zinc Selenide at 10.6 μm

Reference	Method	Temperature Range (°C)	dn/dT x 10^5
Dodge and Malitson			
(Sample B)	Minimum-Deviation	20.8-33.5	7.4
(Sample A)	Minimum-Deviation	20.8-30.8	6.8
Feldman, Waxler & Horowitz	Fizeau Interferometry	20-200	6.2
Skolnik & Clark	Laser-Doppler Interferometry	23-62	10.0
Kurdock	Off-Normal Interference	24-69	8.0-9.1

The values range from a low of 6.2 x 10^{-5}/°C to a high of 10.0 x 10^{-5}/°C. The average of all the values given is 7.8 x 10^{-5}/°C which is close to the 7.4 x 10^{-5}/°C obtained for sample B and the 8.0 x 10^{-5}/°C determined by Kurdock. The same method of measurement was not used in any two laboratories, which could account for the discrepancies.

Skolnik and Clark [10] have also determined dn/dT for Irtran IV and found the value to be 5.4 x 10^{-5}/°C at 10.6 μm. This is in fairly good agreement with a value of approximately 5 x 10^{-5}/°C determined by Hilton and Jones.

5. Conclusions

The results of this study indicate that the two samples of CVD ZnSe generally agree within 1 to 3 x 10^{-4} from 0.9 to 15 μm, the spectral region of current interest for use in high-power IR laser systems. The discrepancies in the values of dn/dT determined by different observers could be due to differences in the material; however, the different methods of measurement should not be ruled out as the cause. These data for the refractive index and dn/dT are only valid within the stated accuracies for the specimens reported in this study.

6. References

[1] Sparks, M., J. Appl. Phys. 42, 5029 (1971).

[2] Feldman, A., I. Malitson, D. Horowitz, R. M. Waxler, and M. Dodge, Laser Induced Damage in Optical Materials: 1974, NBS Special Pub. 414, 141, (1974).

[3] Tsay, Y., B. Bendow, and S. S. Mitra, Phys. Rev. B, 8, 2688 (1972).

[4] Rodney, William S. and Robert J. Spindler, J. Res. Nat'l. Bur. Stds. (U.S.), 51, 123, (1953).

[5] Sutton, Loyd E. and Orestes N. Stavroudis, J. Opt. Soc. Am. 51, 901 (1961).

[6] Marple, D.T.F., J. Appl. Phys., 35, (3), Pt.1, (1964).

[7] Hilton, A. Ray, and Charlie E. Jones, Appl. Opt., 6, 1513 (1967).

[8] Kodak Irtran Infrared Optical Materials, Kodak Publication U-72 (1971).

[9] Feldman, A., I. H. Malitson, D. Horowitz, R. M. Waxler, and M. J. Dodge, Proc. 4th Ann. Conf. on IR Laser Window Materials, ARPA, 117 (1974).

[10] Skolnik, L.H. and O. M. Clark, Appl. Opt., 13, 1999L (1974).

7. Figures

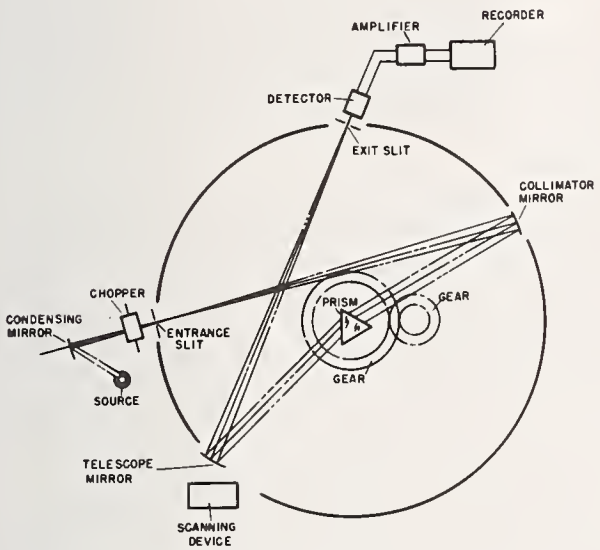

Figure 1. Schematic diagram of the modified Gaertner precision spectometer showing optical path. The prism is rotated at one-half the rotation rate of the telescope assembly by gear system, thus maintaining the condition of minimum deviation for any wavelength. The scanning device drives the assembly which scans the spectrum to identify lines or bands and determine their approximate scale positions.

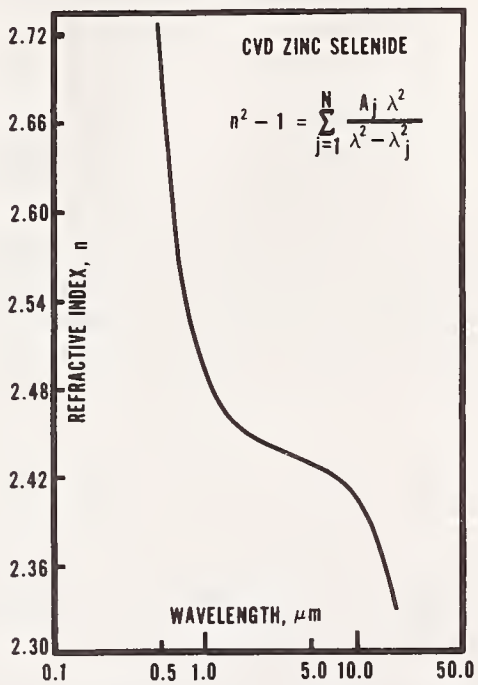

Figure 2. Refractive index of CVD ZnSe (sample B) as a function of wavelength (logarithmic scale). Data at 21°C were calculated from the dispersion equation.

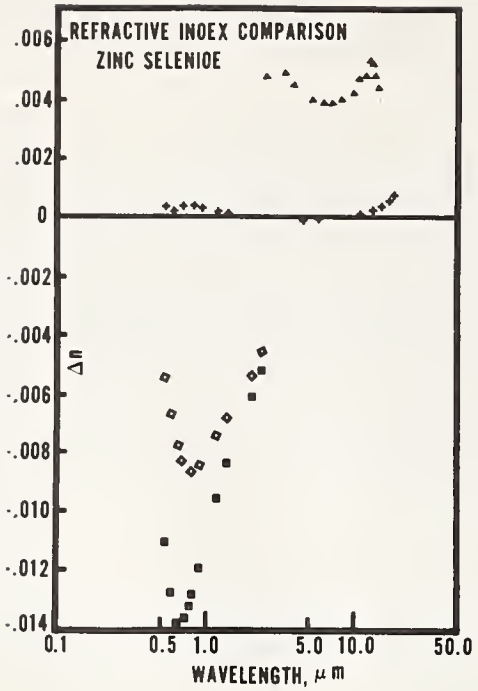

Figure 3. Comparison of NBS index values for CVD ZnSe (sample B) with NBS sample A and values reported by other observers. All data were reduced to 20°C. Refractive index of sample B is represented by the zero line. +NBS sample A, CVD ZnSe; ◻ Marple, single crystal; ● Marple, single crystal; ▲Hilton, Irtran 4.

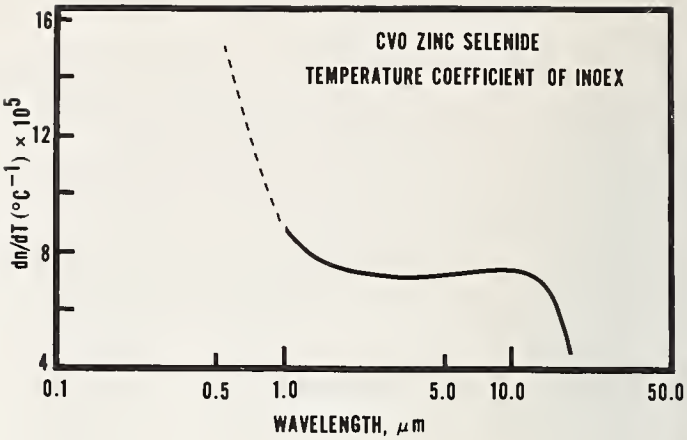

Figure 4. Temperature coefficient of refractive index of CVD ZnSe (sample B) at a mean temperature of 27°C. The solid portion of the curve represents data calculated from index values at two temperatures determined from dispersion equations, and the dashed portion indicates values calculated from raw data.

COMMENTS ON PAPER BY DODGE and MALITSON

There were two questions relating to the fitting of the refractive index data using the Sellmeier equation. In response to a question concerning the number of terms used in the fit the speaker responded that it was found by trial and error that a three-term Sellmeier equation provided the best fit consistent with the accuracy of the data. The second question arose concerning the use of the Sellmeier equation without correcting for the local field effects. The speaker indicated that this point had not been explored fully, but that a satisfactory fit was obtained using the Sellmeier equation without local field corrections. Another question arose concerning the possible temperature range over which minimum deviation measurements could be made in the speaker's laboratory. The response was that although to date only room temperature measurements had been made, it was possible to carry out these measurements over a temperature range from 15°C to 34°C.

3.10 Laser Window Test Facility[†]

Jacob L. Zar

Avco Everett Research Laboratory, Inc.
2385 Revere Beach Parkway
Everett, Massachusetts 02149

A test facility has been constructed for testing laser window material. This utilizes the focused beam from a 15 kW CW laser at 10.6 μm or other available lasers. Provision for cooling the window is included and also instrumentation for measuring optical and mechanical effects.

The irradiated area may be varied by positioning the specimen. The beam profile is very close to Gaussian. The intensity and beam profile is given as a function of diameter and distance from the focus.

Forty-seven natural diamonds have been tested to find the correlation between the UV absorption spectrum, the IR absorption spectrum and the absorption coefficient β at 10.6 μm. Transparency at 0.253 μm is roughly correlated with low values of β. A water cooled diamond window holder is also described.

Key words: Diamond absorption coefficient; laser window heating; laser window testing; Type II diamond windows.

1. Introduction

The development of high power lasers has simultaneously generated a requirement for the development of windows capable of transmitting the laser beam from one environment to another without significant distortion of the wave front. At one time, the best available windows were aerodynamic windows. However, they are not suited to all interfaces. Therefore, an extensive program of material development was funded by the U. S. Government to develop solid-state windows capable of transmitting high energy and high intensity laser beams for all useful wavelengths. These programs have born fruit in that there are now available improved window materials and coatings. There has arisen the need for a facility where windows may be tested for suitability for both pulsed and CW lasers.

This test facility should have the capability to measure changes in optical and mechanical properties of the window while transmitting the laser beam. For this, one needs access to high power pulsed and CW lasers, such as those available at the Avco Everett Research Laboratory, Inc. Therefore, an integrated research program has been authorized which calls for modification of an existing 10.6 μm high power laser test facility to test windows of various types. It will also be available under the authorization of our contract monitor to other laboratories who wish to test and evaluate their own materials.

One of the available lasers at Avco is the HPL* industrial laser. This can deliver a continuous beam of radiation at 10.6 μm with a power of about 15 kilowatts. A separate test station has been constructed for window testing. This is described in the next section. The experiment is mounted on a special moveable optical stand so that it can be transferred to other lasers for testing at other wavelengths or with pulsed beams. One of the available pulsed lasers is the 10.6 μm "breakdown" laser which can produce 80 J pulses of about 100 microseconds duration. When focused, it yields intensities approaching 10^9 W/cm^2. Other lasers with even shorter pulse lengths, higher power, or other wavelengths are available when scheduled.

[†]This program is supported by the Advanced Research Projects Agency and monitored by AFCRL under contract No. F19628-75-C-0066.

*Trademark of AERL, Inc.

2. Description of HPL Industrial Laser Test Facility

The laser is a closed cycle CO_2 machine producing a 10.6 μm beam of approximately 15 kW [1][1]. The output beam is collimated with a diameter of 3.8 cm and is transferred by mirrors and actuators to several work stations. Each work station may command the laser and has its own safety interlock system. When one is in use, the other stations may safely be entered for test preparation. The laser power control has closed loop feedback. The power, its rate of rise and fall and the exposure time may all be varied by controls at each test station.

The window test station is the third to be added to this laser. It is housed in a room about 6 ft. sq. with lucite panel walls. The experimentor may view the experiment and operate the laser from outside the room with complete safety.

The laser beam is brought to a sharp focus with an f/21 telescope. Diamonds and other small specimens may be put at the focus. For larger beams, the test specimen can be located off-focus. The laser mirrors and the holder for the test specimen are cooled by circulating water through a closed cycle heat exchanger. After passing through the test specimen, the beam is received in a calorimeter and the power measured. Alternatively, it may be absorbed in a beam dump. An exhaust is provided for removal of fumes generated either from the test specimen or from the beam dump. Compressed gases are available for flushing the surface of test samples.

For instrumentation of the test, a second laser beam from a visible laser such as helium neon, is passed through the window at an angle to the heating beam. The window is included in one leg of a Mach-Zehnder interferometer. Changes in the window are observed by interference and may be photographed. There is also available one or more thermocouples and a strip chart recorder for recording temperatures. Other types of instrumentation may be added as required by the experiment.

Figure 1 is a photograph of the facility used for testing small windows at the focus of the laser beam. A small diamond plate is mounted in the center of a holder and is edge cooled. The laser beam is focused through the window by two copper mirrors seen at the right above the sample holder. The interferometer and probe laser are positioned around the specimen holder.

A test was made of the power and distribution of the beam at several distances from the focus. This was done by allowing the laser beam to pass through apertures in polished copper plates and received on a flat plate calorimeter. The calorimeter has an anoidized aluminum surface and absorbs .995 of the instant laser energy at 10.6 μm [2]. The temperature rise of the plate is compared with that of a reference plate in the laser shadow by twelve differential thermocouples in series. Correction is made for the cooling of the calorimeter during the exposure time by extrapolating the cooling curve measured after the laser beam has been extinguished back to the midpoint of the beam duration.

The power transmitted through the aperture, P_h was measured at a power setting P, of 2000 watts for exposure of 2.0 seconds. The ratio of P_h/P is shown as a function of the hole radius r_h in figure 2. Observations were taken at 12.2 cm, 28 cm and 53 cm from the focus.

Assume that the intensity profile is a Gaussian intensity distribution

$$I \sim = \frac{P_o}{\pi r_o^2} \quad e^{-r^2/r_o^2} \tag{1}$$

where r_o determines the spreading of the beam and P_o is the peak central power. The power through a hole is then

$$P_h = \int_o^{r_h} 2\pi I_r \, dr = P_o \left[1 - \exp\left(-r_h^2/r_o^2\right) \right] \tag{2}$$

The data was then fitted by a least squares calculation and the constants P_o and r_o were determined from the data. The curves so obtained are shown plotted as the solid lines in figure 2. In particular, the calculated value of P_o could be independently compared to the value measured with a full beam. The difference between these quantities is a sensitive measure of whether the beam profile is correctly described by the laser function. In two cases the difference was unmeasurable and in the third case was about 6% and is believed to be due to experimental misalignments rather than to any inherent property of the laser beam. Figure 3 shows the beam profiles obtained from the fitted Gaussian profiles.

[1]Figures in brackets indicate the literature references at the end of the paper.

Figure 4 is a plot of r_o vs. the distance from the focus. The data points are shown as well as a straight line fitted by least squares. The linearity of this data shows that diffraction effect are negligible at these distances. It is difficult to measure the beam profile close to the focus because of the high intensity and small size. However, burn patterns were made on blackened steel with the beam at the focus of the f/21 telescope. These showed a diameter of 1 mm which is consistent with the size of a diffraction limited beam of 10.6 μm and the type of laser cavity employed in the HPL industrial laser. At 15 kW, the intensity at the focus for a 1 mm beam diameter is 2×10^6 W/cm^2. The peak intensity is somewhat higher and it may be further increased, if desired, by using optics of shorter focal length.

3. Diamond Spectra

We have examined 47 natural diamonds to determine the infrared, the ultraviolet spectra and have measured the absorption coefficient for 10.6 μm radiation. The diamonds (clear natural stones)* were in the shape of discs from 2 to 2.5 mm diameter by approximately 0.5 mm thick. The UV spectra were obtained with a Cary Model 1756 spectrometer and the infrared spectra with a Perkin Elmer Model 457 spectrometer. Because the diamonds were small, it was difficult to concentrate sufficient light intensity through them. Therefore, a Perkin Elmer 4X, All Reflecting Beam Condenser was used with the spectrometers and the instruments adjusted to give at least half scale deflection of the recorder by reducing the intensity of the reference light beam.

Figure 5 shows the ultraviolet spectra obtained with representative diamonds. These are shifted by an arbitrary amount along the vertical (intensity) scale so that they do not overlap. The number on the right is the identifying serial number of the diamond. It will become apparent from the measurement of β, the absorption coefficient at 10.6 μm described in the next section, that diamonds #13 and 28 have the lowest values of β. Diamonds #43 and 38 have much higher β's and the others fall in between. Figure 5 shows that diamonds with a high β (#43 and 38) also have a high absorption coefficient at .25 μm, whereas diamonds with low β (#13 and 28) also have a low absorption at this wavelength. This figure further shows that the precise shape of the ultraviolet absorption edge is variable. For instance, diamonds 46 and 23 have very similar shaped absorption edges,whereas we shall find a factor 3 difference in the values of β.

It would be very useful if the transparency at .25 μm could be used as a basis for selection of the uncut stones. In order to characterize the spectrum by a single number, the following definition was used. The transmission at .25 μm, $I_{.25}$, was compared to the transmission at .40 μm, $I_{.40}$, measured with the spectrometer. The relative absorption at .25 μm was defined as

$$A_{.25} = 1 - (I_{.25}/I_{.40}) \tag{3}$$

Table I lists all of the data obtained for the 47 diamonds. The values of $A_{.25}$ are given in column 3.

In a similar way, the infrared absorption spectrum was obtained from 2.5 μm to 15 μm. These spectra are shown in figure 6 for the same diamonds. Again, the curves are displaced along the intensity scale to prevent overlapping. (The discontinuity in the spectra at 5.0 μm is due to automatic switching of the spectrometer optics.)

Some diamonds, notably #'s 13, 28, 42, and 39 show no significant absorption in the region from 7.5 to 8.5 μm. Others, notably #'s 38 and 43 show a very well developed absorption band and still others show intermediate amounts of absorption. This band has been attributed to interstitial nitrogen atoms lying in the (100) planes in concentrations up to several times 10^{20} atoms/cm^3 [3]. The nitrogen impurity in natural diamonds reduces the thermal conductivity at low temperatures by about an order of magnitude, presumably by scattering of phonons. It also increases the indent hardness and reduces the plastic flow by interfering with the migration of dislocations. A pronounced absorption band at 8 μm may also have a significant tail extending to 10.6 μm and thus increase β for the window at this wavelength.

All of the diamonds were transparent at 12.5 μm. The spectra have been characterized by a relative absorption $A_{7.9}$ which compares the transmission at 7.9 μm to the transmission at 12.5 μm as read from the spectrogram.

$$A_{7.9} = 1 - (I_{7.9}/I_{12.5}) \tag{4}$$

The values of $A_{7.9}$ are given in table I, column 4.

* These were kindly lent to us by Lazare Kaplan & Sons, Inc.

The correlation between the absorption at .25 μm and at 7.9 μm is presented in figure 7. Here, the circles represent the individual diamond numbers and the relative absorption values are cross plotted. One sees that those diamonds with low values of $A_{.25}$, namely diamond #'s 13, 28, 39, and 42, also have low values of $A_{7.9}$. Presumably these are Type II diamonds and should also have low values of β. There is a group of diamonds with values of $A_{7.9}$ only slightly higher which have higher values of $A_{.25}$. Finally, there is a very large group of diamonds with high values of absorption at both wavelengths. These latter are very likely to be Type I diamonds.

4. Direct Absorption Measurements

The diamonds that were chosen for a direct determination of β at 10.6 μm were all of those with low and intermediate values of $A_{.25}$ and some of those with a high absorption. Thus, the distribution of β's could reveal whether the transparency to the .25 μm mercury line is correlated with β.

The experiment consisted in passing a focused 10.6 μm laser beam through the diamond, measuring the incident and transmitted intensity and the heating resulting from absorption. The diamonds were sufficiently parallel across the small irradiated spot diameter so that internal reflection would interfere to an unknown degree with the transmitted beam. A correction was therefore applied to the measurements to give corrected values of β. The correction was calculated by the procedure for multiple internal reflection except that allowance was made for absorption within the plate [4].

The laser beam was approximately 20 watts, obtained from a Perkin Elmer Model 6200 CO_2 laser. A collimated beam, 1.3 cm diameter was sharply focused through the diamond with a copper mirror of 10 cm focal length. Approximately 12% of the laser power was transmitted through a hole in the mirror into a differential thermocouple calorimeter so that the laser power could be monitored. After passing through the diamond, the energy was received on a calibrated absorber and integrated. The temperature rise of the absorber was recorded and converted to the transmitted beam intensity. The specimens were clamped between two thin copper discs having a hole for transmission of the laser beam. A copper-constantan thermocouple was attached to the holder. Absorption of energy by the diamond was transmitted to the holder and the temperature recorded. The weight of the copper diamond holder was .59g. Its heat capacity was .23J/°C. The heat capacity of an average size diamond was .0036J/°C. For the incident beam intensity, the diamond was removed from the sample holder and the transmitted beam measured directly.

A correction is needed for the amount of energy that was intercepted by the diamond holder from fringes of the laser beam. Therefore, a calibration run was made in which the heating of the holder alone was measured as a function of the exposure time. The power absorbed by the holder alone was about .08 watts. This was substracted from the power absorbed by the diamond plus holder to give the absorption of the diamond alone.

The results of the direct absorption experiment are also shown in table 1, columns 5 thru 11. Column 5 is the exposure time, 6 gives the incident laser power; column 7 is the transmitted power; column 8 is the temperature rise of the diamond and holder; column 9 is the power absorbed in the diamond alone. Column 10 is the value of β obtained without correction for interference between the transmitted and internally reflected beam. Column 11 is the value of β obtained after correction for this effect. The values of β are plotted against the relative absorption in the infrared, $A_{7.9}$ in figure 8 and against the relative absorption in the ultraviolet $A_{.25}$ in figure 5. Note that the scattering in the data is amplified by the use of a logarithmic plot. The lowest value of β that has been observed is .021 for diamond # 28.

The data shows that $A_{.25}$ is a rough guide to the value of β, but it is not quantitatively reliable. For example, diamonds # 28 and 13 have similar values of $A_{.25}$ but a factor 3 difference in β.

Approximately 20% of the diamonds have values of β less than .5; however, if a selection had been made of those diamonds with values of $A_{.25} \leq .75$, only half of the low β diamonds would have been found. The conclusion of this spectroscopic study is that if diamonds show a high absorption in the ultraviolet, they also have a high absorption at 10.6 μm. If they show a high transparency in the ultraviolet, they also have a low absorption at 10.6 μm. However, there are a number of diamonds for which the ultraviolet spectrum is an unreliable guide to the 10.6 μm absorption.

5. Design of Diamond Holder

Figures 8 and 9 show that we can expect to find diamonds for windows with $\beta \leq .3\ cm^{-1}$. The diamond cutters say that they may have difficulty in cutting plates thinner than 2 mm because of the danger of cracking. We may therefore expect an absorption by the window of 6% or less of the transmitted power. The diamond temperature may not exceed 800 °C, the temperature at which transition to diamond becomes accelerated. The transmitted power therefore depends on the efficiency of cooling of the window that can be provided.

Table 1. Data for Diamond Spectra and Absorption

Specimen No.	Thickness cm	$A_{.25}$	$A_{7.9}$	Exposure Time sec.	Incident Power watts	Transmitted Power watts	ΔT °C	Absorbed Power watts	Uncorrected β cm^{-1}	β cm^{-1}
1		.974	.321	*						
2		.914	.262	*						
3		.989	.384	*						
4	..048	.876	.408	10.3	33.1	17.4	62.6	1.37	.62	.81
5	.053	.885	.209	10.2	25.6	18.6	47.8	1.01	.76	.72
6		.980	.421	*						
7		.996	.458	*						
8		.996	.340	*						
9		1.000	.583	*						
10		1.000	.576	*						
11		.920	.277	*						
12	.060	.747	.102	15.1	32.2	19.9	37.2	0.58	.30	.34
13	.042	.480	.006	43.9	34.9	16.6	25.4	0.068	.045	.067
14		.925	.277	*						
15		.986	.310	*						
16		1.000	.900	Diamond turned black in a few seconds.						
17		.985	.407	*						
18		.998	.440	*						
19		.977	.326	*						
20	.036	.914	.259	15.1	29.8	18.0	49.3	.75	.71	.80
21	-	.961	.263	*						
22		1.000	.586	*						
23	.079	.830	.196	15.4	26.9	18.6	24.1	.32	.15	.16
24	.051	.938	.207	15.3	27.9	18.9	31.4	.46	.33	.35
25		1.000	.973	*						
26		.976	.336	*						
27		.986	.327	*						
28	.052	.446	.048	39.5	36.2	16.8	23.5	.028	.015	.021
29	.070	1.000	.624	15.2	24.1	16.5	123.0	2.07	1.28	1.23
30		.943	.273	*						
31	.053	.847	.113	24.9	32.3	17.9	47.3	.46	.27	.34
32		.988	.406	*						
33	.048	.863	.130	15.3	33.3	20.2	25.4	.35	.22	.27
34		1.000	.330	*						
35	.051	.857	.123	15.2	27.1	19.2	40.9	.63	.46	.45
36		.989	.406	*						
37		1.000	.442	*						
38	.039	1.000	.481	13.8	29.1	18.1	65.8	.1.08	.97	1.07
39	.056	.636	.026	9.5	34.9	18.8	25.3	.46	.24	.30
40		.841	.154	*						
41		.990	.371	*						
42	.047	.526	.083	13.7	37.2	18.5	21.9	.26	.15	.21
43	.056	1.000	.633	8.0	25.0	15.9	99.5	2.56	1.92	1.95
44		.982	.391	*						
45		.979	.297	*						
46	.060	.813	.210	15.2	25.5	18.3	66.4	1.08	.72	.81
47		.846	.277	*						

* Not tested for β

A water-cooled window holder has been designed in which the diamond is clamped at the edges of its parallel faces between two water-cooled copper discs. This is shown in figure 10. Thin annular gold washers distribute the clamping force uniformly to the window surface. Water flowing at high velocity is brought into contact with the edge of the diamond by constructing the holder in the shape of a nozzle with the window located at the smallest cross section. It is estimated that a Reynolds Number of about 40,000 will be reached by the water flowing over the diamond surface. The expected heat transfer coefficient will be about 6.7 watts/cm^2 deg. If we allow the diamond temperature rise to be 600 °C, the heat transfer to water will be 1500 watts. For an absorption of .06, the transmitted laser power may be 25 kW. In addition to the heat transfer to the water, there is also conduction heat transfer to the cooled metal surfaces that clamp the edge of the diamond. However, in this case, the heat must be transferred through metal interfaces. According to McAdams [5] the contact coefficient for heat transfer between machined surfaces under moderate pressure is h_c = 1.7. In our diamond holder, there are two such surfaces in series and two in parallel giving 1.7 as an estimate of the resultant conduction heat transfer coefficient. The clamped surface will have about the same area as the water-cooled surface; therefore, it is estimated that the conduction heat removal will only be about 25% of the heat transferred directly to water at the edge of the window. This 25% additional margin is more than sufficient to compensate for another source of temperature to be discussed next.

In addition to the ΔT at the surface, there is also a radial temperature distribution $\Delta T(r)$ due to the heat conduction within the diamond. The maximum value of $\Delta T(r)$ depends on the distribution of laser flux. It is clear that the smaller the spot diameter, the larger will be the conduction ΔT. For a focal spot of .2 cm radius, the central temperature rise is about 35 ^{o}C or about 7% of that at the surface. The conclusions of these estimates is that it should be easy to transmit the laser beam from our 15 kW HPL industrial laser through a diamond window.

Figure 11 shows a photograph of two of the diamond plates that have been obtained for testing as laser windows. Information on the test results of these and of some zinc selenide windows will be made available as soon as the tests can be done.

6. References

[1] Hoag, E., H. Pease, S. Staal, and J. Zar, Performance characteristics of a 10 kW industrial CO_2 laser system, Applied Optics 13, (1959), (1974).

[2] Jacob, J., E. Pugh, J. Daugherty, and D. Northam, R.S.I. 44, 471 (1973).

[3] Strong, H. M. and R. M. Chrenko, Further studies on diamond growth rates and physical properties of laboratory-made diamonds, J. Phys. Chem. 75, 1838 (1971).

[4] Zar, Jacob L., Investigations into the feasibility of high power laser window materials, AFCRL-23-75-0264 (1975).

[5] McAdams, W. H., Heat transmission, (McGraw-Hill, New York 1954).

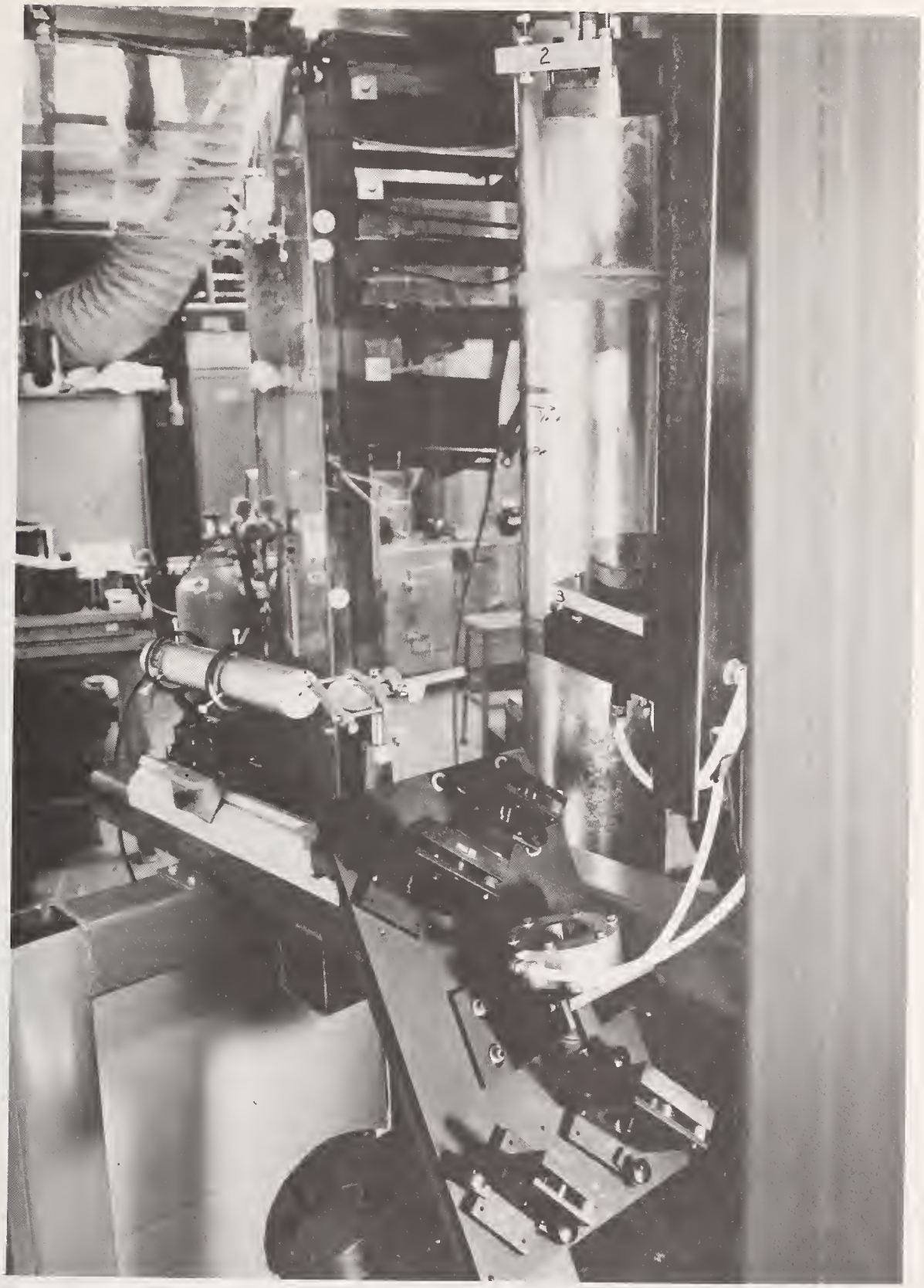

Figure 1. Window test facility with edge cooled diamond window holder.

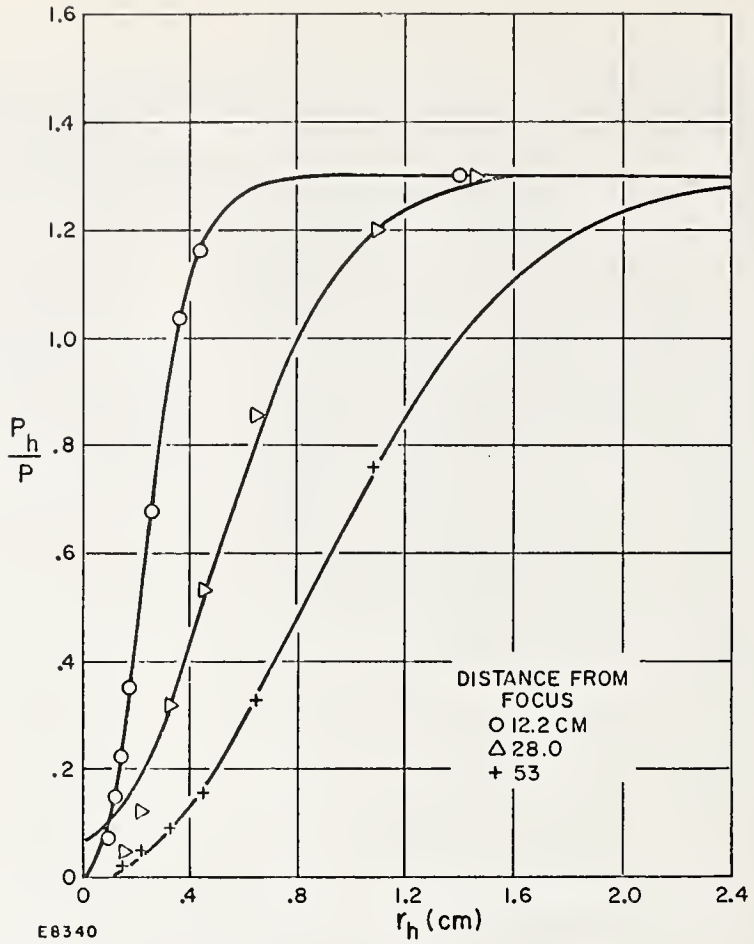

Figure 2. Intensity of laser beam transmitted through aperatures of radius r_h.

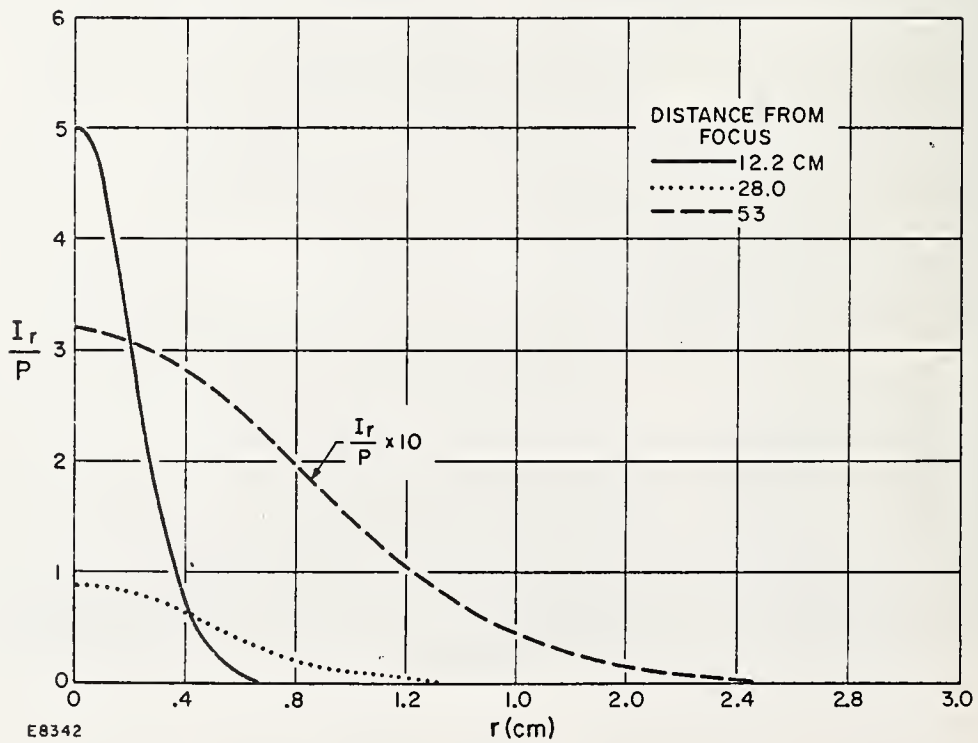

Figure 3. Gaussian beam profile at various distances from focus.

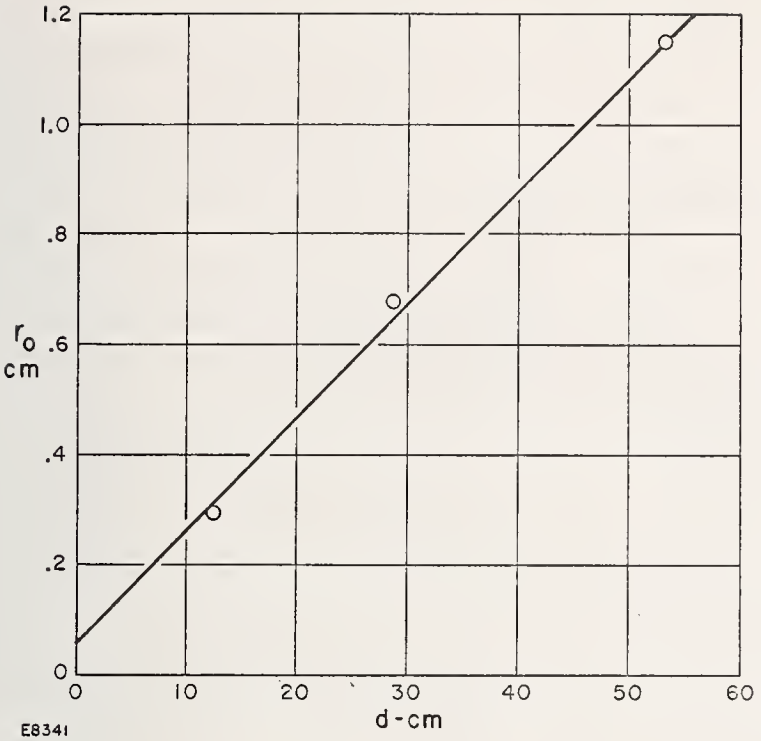

Figure 4. Mean widths of laser beam at various distances from focus.

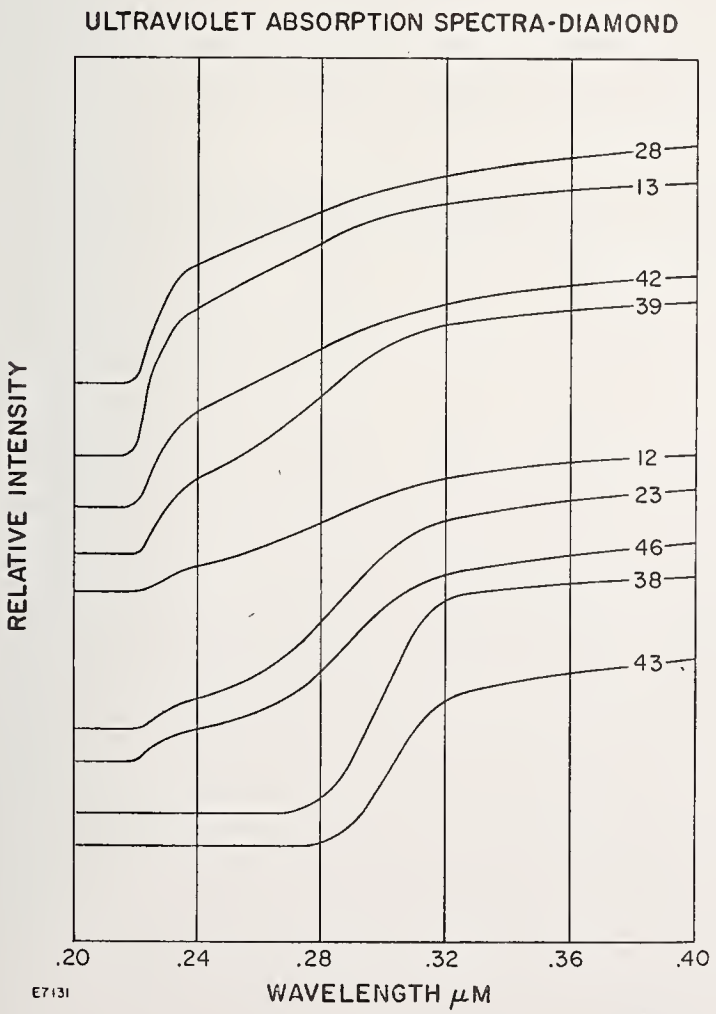

Figure 5. UV absorption spectrum of representative sample diamond discs.

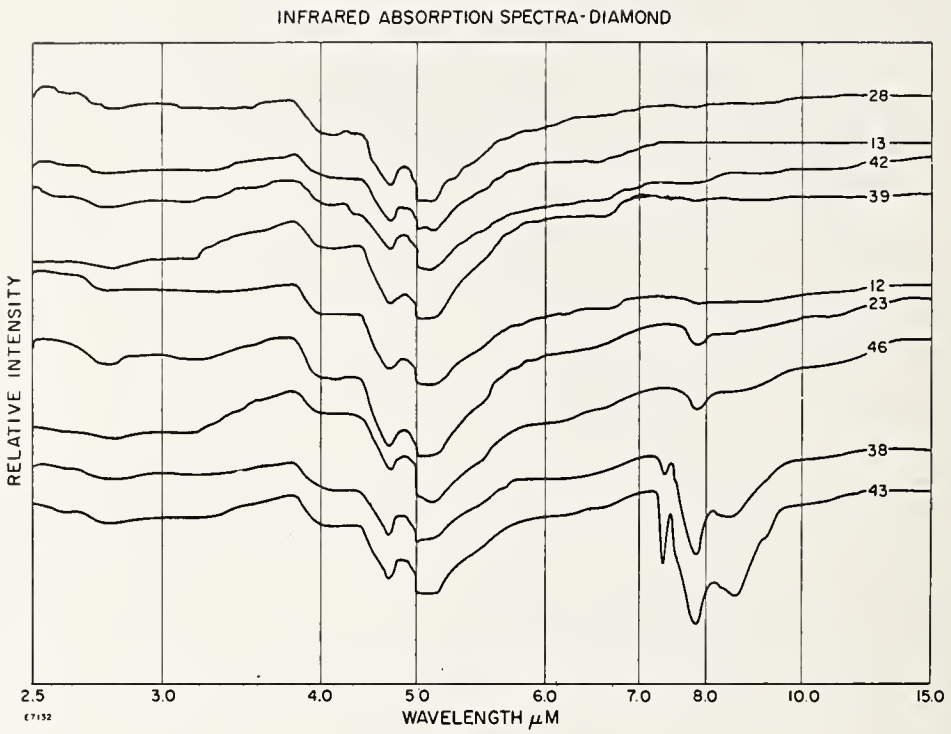

Figure 6. IR absorption spectrum of representative diamond discs.

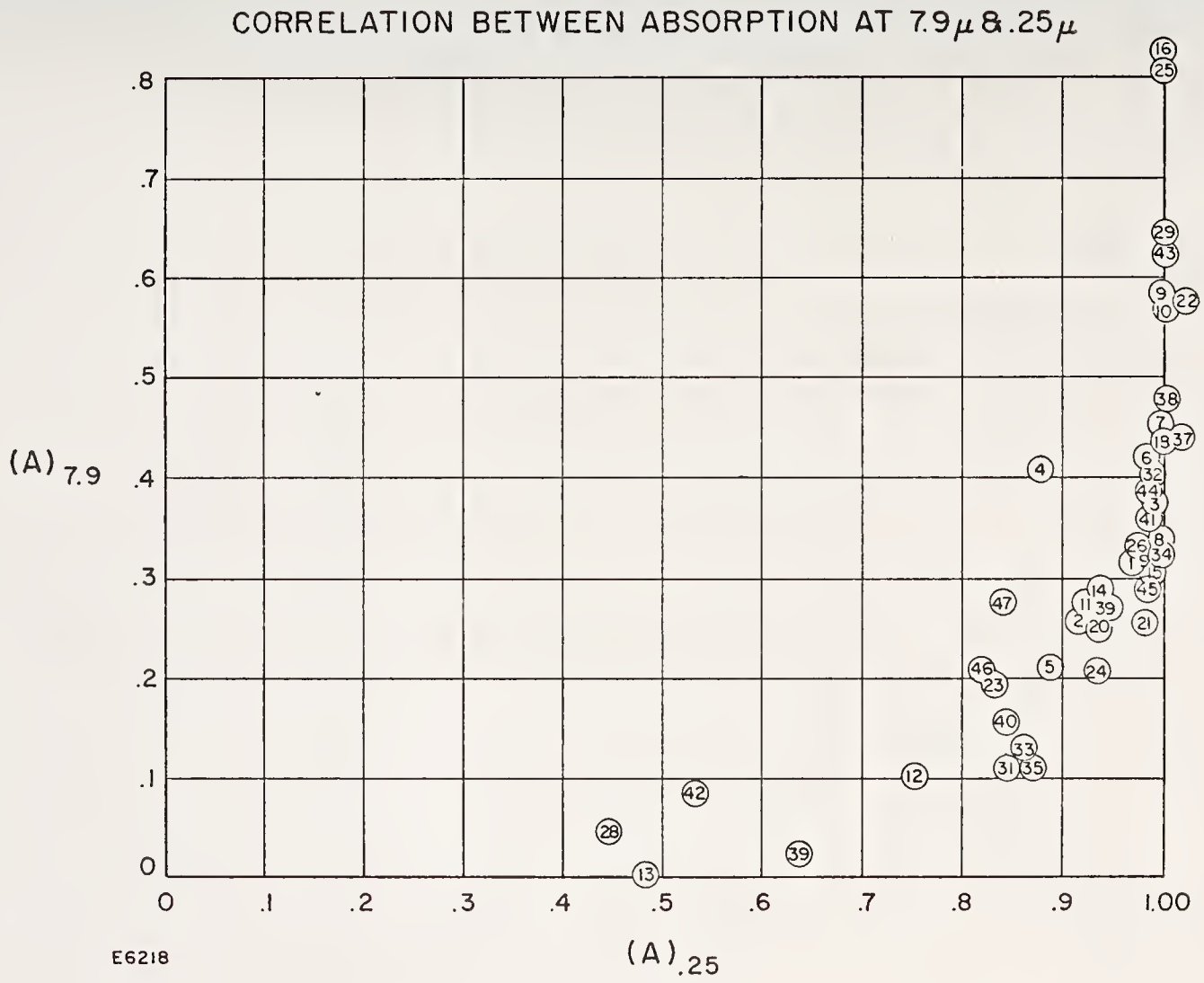

Figure 7. Correlation between absorption at 7.9 μm and .25 μm for 47 natural diamonds.

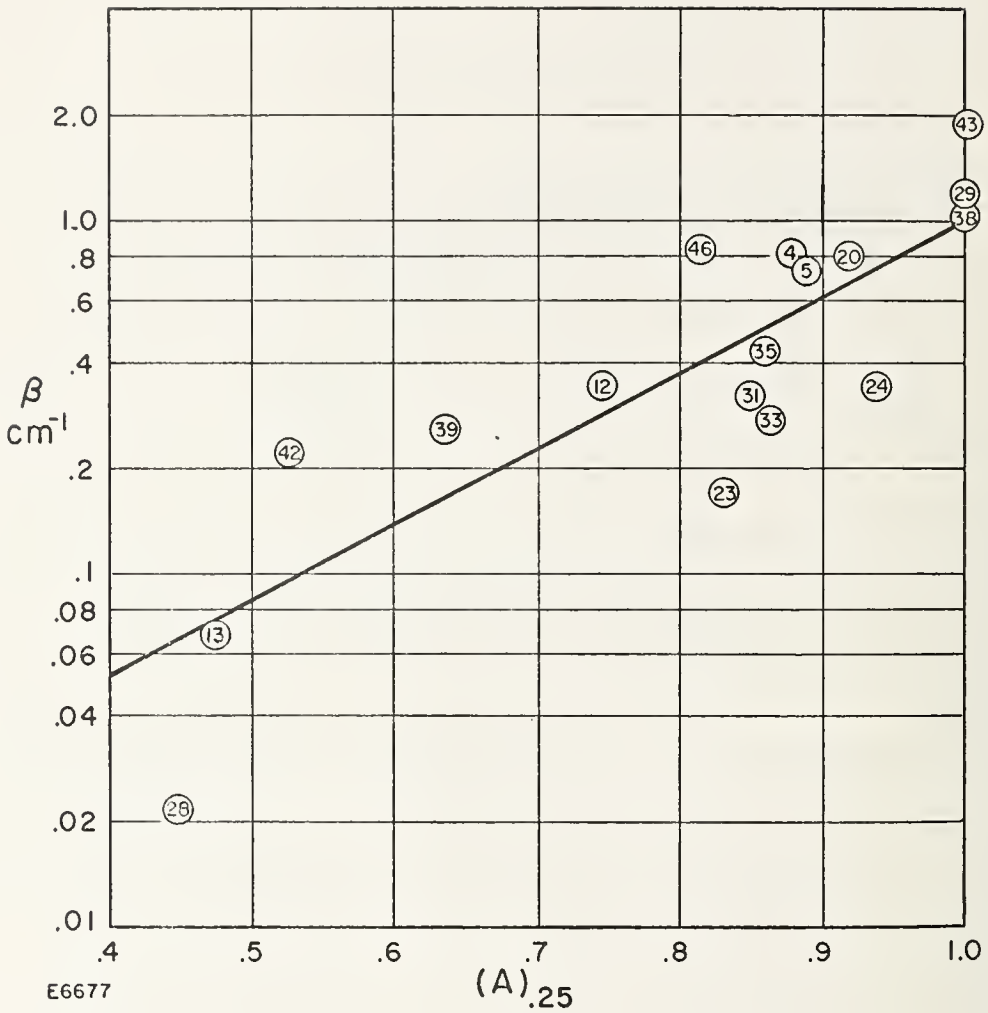

Figure 8. Distribution of absorption coefficient, β versus absorption at .25 μm for Type I and Type II diamonds.

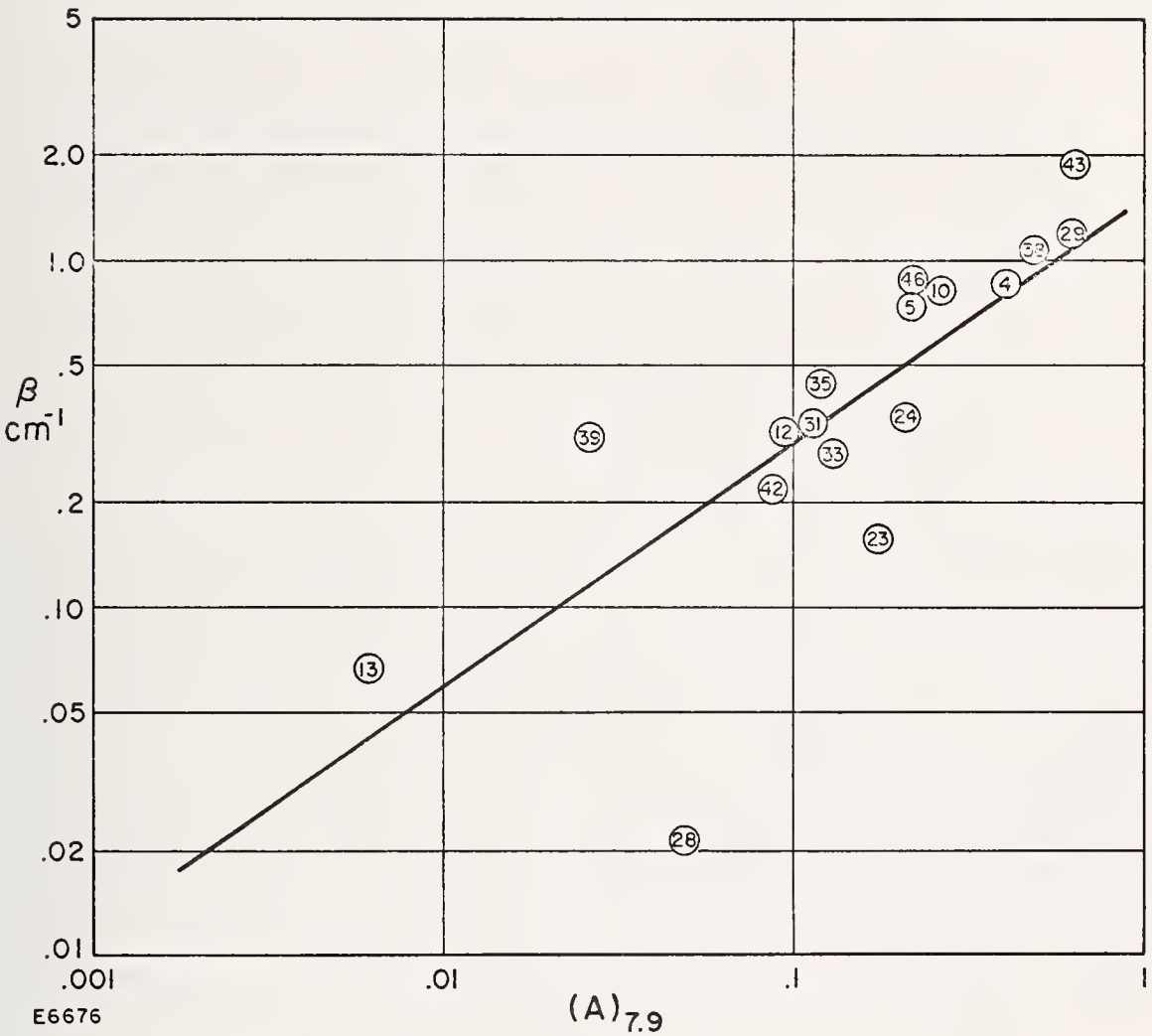

Figure 9. Distribution of absorption coefficient, β versus absorption at 7.9 μm for Type I and Type II diamonds.

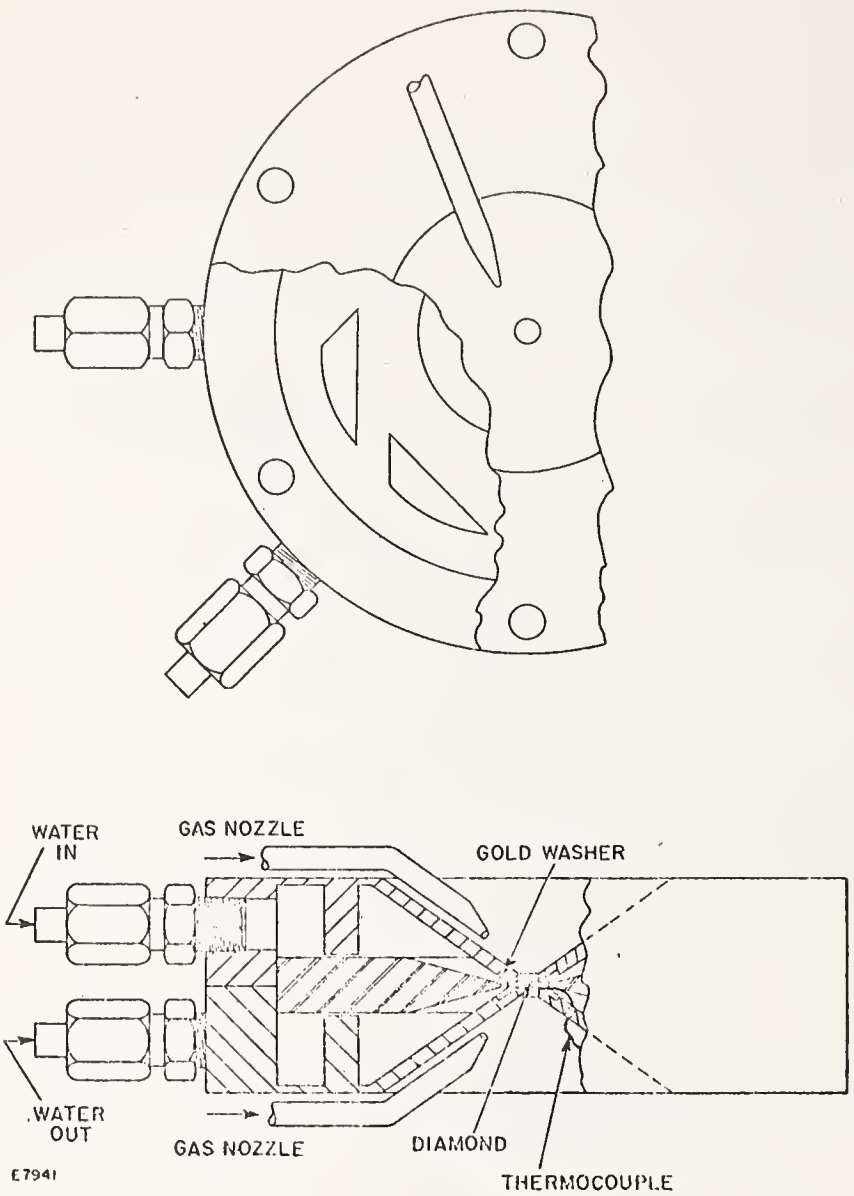

Figure 10. Water cooled diamond window and window holder.

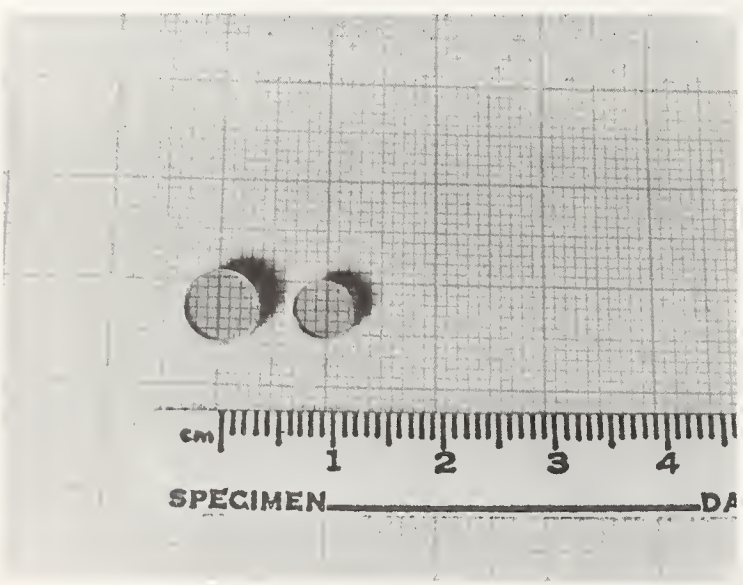

Figure 11. Type II diamond discs to be tested as windows.

4.1 Optical Material Damage From 10.6μm CW Radiation

Carl A. Huguley and John S. Loomis

Air Force Weapons Laboratory
Kirtland Air Force Base, New Mexico 87117

Damage studies of a variety of optical materials including KCL, ZnSe, NaCl, Mo, and Cu substrates were conducted. Most of the samples were substrates with optical coatings, and several were gratings. Typically, a rectangular grid of thirty irradiation sites was used. An analysis of damage thresholds was accomplished.

Key words: CO_2 laser radiation; Cu; CW laser damage; grating; infrared windows; KCl; mirror; Mo; NaCl; window; ZnSe.

1. Introduction

During the past few years, an effort was made to explore the problem of damage to optical components, such as windows and mirrors, that results from continuous irradiation at 10.6μm [1, 2, 3][1]. During the current series of measurements, the goal was to examine the effects of irradiating each sample at a number of locations with various incident powers, rather than to irradiate the center of the sample several times with increasing power levels. In this manner, it was hoped to learn something about the statistical nature of CW damage--and to look for microscopic damage as a precursor of catastrophic damage.

In subsequent portions of this paper, the experimental apparatus is described first followed by a discussion of measurements of power and spot size--the maximum power achieved after the focusing optics was 600 watts, with a spot size of 1-mm diameter. Next, the criteria for defining damage and the sequence of measurements is explained, and calculations of the temperature rise at the center of an irradiated spot is presented. Finally, the results of measurements on a variety of windows, mirrors, and gratings are given.

2. Apparatus

The test apparatus described herein, shown in figure 1, is very similar to that used earlier [1, 2, 3]. A Sylvania, Model 971, Gas Transport Laser (GTL) was used as the radiation source to produce a continuous power of 1000 watts at 10.6 microns. The laser's beampower was continuously monitored throughout the test by using a mirror chopper (in lieu of a beam splitter)to deflect a portion of the beam into a Coherent Radiation, Model 201, Power Meter.

Control of the beam's access to the sample was effected by a solenoid-actuated, mirrored-surface shutter, which could be switched within 10 msec. After the shutter, the beam passed through a 1.27-cm diameter graphite aperture and onto a 25-cm focal length, NaCl, plano-convex, uncoated lens, which was used to focus the CO_2 beam 1.7 cm in front of the sample. The sample was so mounted that the beam impinged upon it at an angle of incidence of approximately 8°, which allowed the reflected portion of the beam to be directed into a graphite dump. The sample was supported in an x-y positioning device that was used to move the sample into different irradiating locations.

1. Figures in brackets indicate the literature references at the end of the paper.

NOTE: Micron(s) as used in this paper expresses micrometer(s).

3. Power Measurements

The power meters used during these tests required periodic calibration because the calibration constant had earlier been observed to change with age and usage. To combat this drift, these meters were intercompared every few months or at the beginning of a test series. A mirrored chopper with a one-percent duty cycle reflected a uniform portion of the beam into these power meters for continuous measurements during the test series. The power after the lens (see figure 1) was measured to be a factor of 60 ($\pm$ 3) times the power reflected from the mirror chopper.

4. Measurement of Beam Radius

A scanning edge technique [1, 4] was used to measure the diameter of the CO_2 laser beam at the location of the damage tests. A massive aluminum block with a 45° milled edge was mounted on a translation stage, and a power meter behind this edge was used to measure the laser power transmitted past the edge. Total power was monitored by the previously mentioned chopper/power meter technique, while the ratio of transmitted power to total power and the position of the edge were recorded as the edge was moved in discrete steps into the beam.

The focused intensity distribution was assumed to be Gaussian

$$I = I_o \exp\left[-2\,(x^2 + y^2)\,/b^2\right] \tag{1}$$

where x and y are the coordinates from the center of the beam, and b is the radius ($1/e^2$). The power transmitted past the aperture is given by

$$P = \int_{-\infty}^{\infty}\int_{-\infty}^{x} I\,(x,y)\,dxdy \tag{2}$$

$$P = \frac{P_o}{2}\ \mathrm{erfc}\ \left(\frac{\sqrt{2}\,x}{b}\right)$$

where

$$P_o = \frac{1}{2}\pi b^2\, I_o\ .$$

The solid line in figure 2 is a graph of eq. (2), near the midpoint of the curve (optic axis). For power ratios of $0.3 < P/P_o < 0.7$, the curve can be approximated by a straight line given by

$$\frac{P}{P_o} = 0.5 + 0.8\,\frac{x}{b}\ , \tag{3}$$

and beam radius is then calculated from the slope of this line. The result of this measurement was a beam radius of 0.50, $\pm$ 0.05 mm, which correlates with the previously measured value [1].

5. Test Procedures

Each test specimen was first examined for defects in the coating or substrate and then for optical quality.

Next, an irradiation conditioning run was made with the lens moved upstream (from the sample) to a point where the diverging beam was the same size as the specimen. The specimen was then irradiated--with power levels beginning at 120 watts, then raised to 600 watts over a 30-second period, and then maintained at 600 watts for an additional 30 seconds. Throughout the conditioning phase, the peak intensity was below 130 watts/cm^2, and no damage or scintillations were observed. Specimen conditioning had earlier been observed [1] to increase the damage threshold.

The damage test itself was a series of 30 shots (each shot is a 2 second or 30 second pulse of laser power on the sample), with the test piece being moved after each shot to produce a five-by-six matrix shot array as shown in figure 3. Each row (beginning at top left) received a successively higher power unless substantial damage was observed, at which time subsequent shots were made at lower power levels. After the damage test, each specimen was examined with a Nomarski microscope.

6. Damage Criteria

Specimen damage was first correlated to the 5 X 6 shot array--defects not lying at matrix locations were not identified as damage sites. Damage to the specimen was then categorized by the size and the nature of the damaged area. Damage that was large enough to be seen with the naked eye (i.e., of the same size as the beam) was classified as "macro" damage, while damage that required magnification to be visible was called "micro" damage. At the majority of damage locations, characteristic ash marks were in evidence; but with the halide samples, many damage spots indicated a local fracturing or cratering of the substrate.

The determination of a damage threshold was often a value judgment, since the sample might be damaged twice at one power and not at all at the next higher power. Such inconsistency was ascribed to inhomogeneity of the sample. Thus, whenever possible, the following criteria was applied in determining "damage threshold."

(a) If only one damage spot (resulting from the three, equally-timed pulses) at a given power was found, it was categorized as <u>below</u> the average threshold.

(b) If two damage spots at a given power were found, such power/time combination was categorized as being <u>at</u> the average damage threshold.

(c) If three damage spots at a given power/time combination were found, such level was considered to be <u>above</u> the damage threshold.

7. Heat Conduction Effects

The temperature rise at the center of an irradiated spot on a window or mirror depends upon the difference between the heat flow into the material (from absorbed laser radiation) and the conduction of heat away from the irradiated spot (into the cooler surrounding material) a steady-state thermal profile develops within a few seconds [2]. When the heat flow reaches the outer edges of the specimen (see figure 4), the temperature at all points rises uniformly with time until the heat loss to the external world becomes significant. The rate of dT/dt rise is given by

$$\frac{dT}{dt} = \frac{P_A}{C} \qquad (4)$$

where P_A is the power absorbed (watts) and C is the heat capacity of the specimen (Joules/°C).

The initial temperature rise (or temperature offset between different points on the specimen) depends upon the laser beam geometry, on the thermal conductivity of the specimen, and on the beam radius. Figure 5 is an example of this dependence on beam radius, where the calculation assumed a KCl specimen irradiated for 10 seconds. The ratio of temperature to absorbed power is plotted because the temperature is proportional to the total absorbed power. For spot radius (B) larger than the specimen radius (A), the temperature rise at the center (or at any spot) is given approximately by eq. (4); but, for laser spot sizes much smaller than the specimen radius, the temperature at constant power becomes very large--increasing rapidly as the spot size decreases. At constant intensity, however, the temperature rise decreases with a decrease of spot size because of heat conduction. For the beam size used in these tests (and assuming a sample in which the absorbed power is distributed evenly throughout the thickness of the specimen) the temperature at the center during steady-state rise is given by

$$T = 0.556 \frac{P_A}{kd} + \frac{P_A t}{C} \qquad (5)$$

where k is the thermal conductivity, and d is the specimen thickness. Equation (5) accurately represents the thermal situation of test windows after 30 seconds and prior to 300 seconds (the external time constant). For metal mirrors, heat conduction is much more effective in reducing temperature gradients because the metallic thermal conductivity is so much higher than are the materials in the window. On the other hand, absorption occurs on the surface, which has the effect of increasing the temperature near the surface.

Table 1 presents the calculated temperature rise (per watt absorbed power) in three different materials after a 2-second and 30-second irradiation. An external heat transfer coefficient of 0.001 watt/cm^2 - °C and a specimen radius of 1.9 cm was assumed for all three materials. An eigenfunction series solution to the heat conduction equation (expressed in cylindrical geometry with axial symmetry) was used [5, 6]. The front surface temperature rise was calculated for molybdenum, but this temperature rise was not very different from the three materials (in table 1). In each case, the temperature rise after 30 seconds was only half again as much as the temperature rise during the first 2 seconds.

8. General Results

The results of the damage tests on different kinds of specimens are presented in a series of tables. Each table gives the total absorption (when available) of the specimen and the peak intensity at which damage was observed As discussed in section 6, isolated spots at lower intensity were not assumed to be the actual damage threshold, but an asterisk in the table denotes those samples where such damage was observed. For several specimens, although damage from lower intensities at multiple locations was clearly evident, isolated undamaged higher-intensity sites could be observed. This phenomenon is denoted in the tables by a "plus" sign.

High-power optical components that have sustained isolated damage sites (much smaller than the actual beam size) have been observed in use, yet they have shown no deterioration in optical quality or absorption. Thus, the first appearance of damage--especially microscopic damage--need not indicate the end of a component's usefulness, and such damage should not be used as the definition of damage threshold.

As with past studies, the type of damage observed has almost always involved burning or melting of the substrate and coating. At lower intensities (and sometimes independent of any microscopic damage), occasional sparkles (from the specimen) were observed [2] with durations much less than the irradiation time. With most specimens, however, microscopic damage was accompanied by sparkling of almost continuous duration. Of course, macroscopic damage was generally marked by a highly visible plume and the production of smoke.

9. Window Results

Table 2 presents the results of damage tests to four ZnSe windows, two of which were uncoated and two were ThF_4/ZnS anti-reflection coated. Only one of these samples sustained damage--a coated window that reached melt temperatures (1100°C) in less than 2 seconds at 120 kW/cm^2. Such temperatures are far in excess of the nominal 20°C temperature rise that was calculated for this sample's measured absorption rate (a local absorption value in excess of 10 percent would have been required to generate enough heat to reach the melting temperature of ZnSe). No blemishes or microscopic defects were observed at that site prior to irradiation. Furthermore, blemishes on other ZnSe samples have been irradiated without catastrophic damage, although local melting has been observed on a few other coated ZnSe windows [2, 3]. Interferometric techniques that measure local absorption as a function of position on the sample are currently being developed to determine those inhomogeneities in absorption that could be used to predict potential damage sites.

Also presented in table 2 are results of tests on thirteen coated KCl windows. Multilayer anti-reflection coatings, each of a different design, were applied to seven of these samples; while the other six had single-layer coatings of various materials applied to them. Two of the specimens (KCl 298 and KCl 300) had AFWL-designed $As_2S_3/KCl/As_2S_3$ coatings [7]. These coatings had a very hazy appearance, but their total absorption was unchanged (or even slightly lower) from the measured value for the uncoated substrates. Another specimen, which had a ZnSe/Ge coating design specified, failed at a very low intensity as had other specimens with coatings that used Ge. The remaining four anti-reflection coated specimens were coated with proprietary commercial materials.

Figure 6A, a photograph of the full KCl #292 window (3.8-cm daimeter), shows one of the more ideal damage patterns. Note that this picture shows an isolated damage spot at 90 kW/cm^2 (top row), no damage at 120 kW/cm^2 for 2 seconds, but macroscopic damage for all of the 30-second shots, and damage over the entire row at 150 kW/cm^2. These damage sites were areas of burned and melted material, approximately 0.08 cm in diameter (about the size of the incident beam), as shown in figure 6B.

The results of this survey of anti-reflection coated materials indicate that the damage threshold is lower for these specimens that have higher absorption levels. Materials with opaque coatings of Ge or CdTe do not have a high resistance to laser-induced damage. Opaque semiconductors all have a relatively low band-gap, which suggests that the damage mechanism may be that of thermal runaway. The single-layer KCl samples all showed low, on the order of 10 kW/cm^2, damage thresholds.

10. Abraded KCl Window Results

To assess the possible effects of surface absorption on the damage process, a series of samples were prepared by lapping one surface of each sample on a polishing wheel charged with various grades of alumina grit. The resulting surfaces had the appearance of ground glass, with greatly increased scatter and absorption over that of the untreated material (nominally 0.15-percent absorption). The damage test was conducted as described in paragraph 5, and table 3 lists the resulting absorption and damage intensity. As expected, samples with larger grit sizes demonstrated higher absorption (except for those charged with the smallest grit size).

The circles in figure 7 show the damage intensity for each specimen as a function of its absorption. Although these data would appear to be fitted by a smooth curve, as illustrated, they do not correlate with the hyperbolic dependence expected if peak temperature rise was the sole factor in producing damage. The damage mechanism in all of the abraded samples was thermal-induced fracture, with some pitting of the abraded surface. The x-marked data points in figure 7 are taken from some of the data for coated KCl windows in table 2. These points

can be construed to lie along the same general curve as do these abraded specimens, albeit with much higher scatter about the curve. This behavior suggests that the damage to coated KCl windows may be due to the higher absorption of the substrate because of the presence of the coating--rather than by the coating failing first and producing subsequent failure in the substrate. This hypothesis is substantiated by earlier observations [2] of As_2S_3-coated KCl windows that failed with little or no damage to the coating itself.

11. Mirror Results

The mirrors tested in this study were composed of $(ThF_4/ZnSe)^n$ and $(ThF_4/ZnS)^2$ multi-layer dielectric stacks deposited on molybdenum or TZM substrates. Some of these substrates had been Ag and ThF_4 coated, prior to the deposition of the multi-layer dielectric stack.

The mirror testing was conducted as outlined in paragraph 5, and these results are summarized in table 4. Some of the mirrors had previously been tested at 46 kW/cm^2 (uniform illumination) without damage [9], but these results showed failures from about 60 kW/cm^2 to greater than 150 kW/cm^2. There seems to be (from table 4) more of a correlation between the grouping by identification number (i.e., manufacturer or batch group) and damage level than with any other characteristic of the mirror. One can conclude that, under continuous radiation [1], the dielectric-coated mirrors can survive intensity levels as high as can bare metal mirrors, but that extrinsic effects are more likely to be present (with the coated mirrors).

12. Grating Results

For these tests, gratings of the RMG series were furnished by PTR Optics, and the others were made by Perkin-Elmer [8]. Table 5 summarizes the results of damage tests (conducted as previously described) on these gratings.

In general, the damage characteristics of gratings were very similar to those of metal mirrors, but the damage levels were generally at or above 150 kW/cm^2. The RMG gratings were not intended for high-power applications so it was not surprising that some of these samples did not endure well. It should be noted that with metal substrates, the resistance to CW radiation can persist even for high-absorption surfaces (like GBC-26), which have an estimated surface temperature rise of 650°C after a 30-second focused irradiation of 600 watts. For example, this particular (GBC-26) grating began to glow after 10 seconds at a 600-watt power level. More nearly typical damage morphology is shown in figures 8 and 9.

Figure 8 shows a conventionally-ruled grating that has a spacing of 118.2 lines/mm and a groove depth of 0.11μm (GT-6). It also shows that the ThF_4 coating has started to melt near the damage site. Figure 9 shows the damage to an ion-polished grating having rectangular-shaped grooves with a spacing of 127 lines/mm and a depth of 0.12μm. The damage spots in both cases are burn pits about 0.008 cm in diameter, which is about one-tenth the size of the incident beam.

13. Conclusions

It has been shown that, for many types of optical components--including windows, mirrors, and gratings--damage resistance to focused continuous radiation beyond 150 kW/cm^2 can be achieved. For windows, damage resistance deteriorated at absorptions higher than about 0.5 percent. However, bare-metal surfaces on mirrors and gratings would survive temperature rises resulting from much-higher (6 to 10 percent) absorption. The coatings on all types of optical materials were shown to survive to the limits of the substrate, but overall damage was much more likely to result earlier (at lower intensities). Damage to KCl windows was shown to be highly correlated with the total absorption of the window.

14. Acknowledgments

The authors gratefully acknowledge the assistance of L.A. Marrero, Z.M. Green, J.P. Buehler, R.S. Lester, and G.B. Charlton in collecting and reducing the data for this paper.

15. References

[1] Saito, T.T., Charlton, G.B., and Loomis, J.S., Proc. 6th ASTM Symp. Damage in Laser Mat's., NBS Spec. Pub. 414 (1974).

[2] Loomis, J.S. and C.A. Huguley, Proc. 6th ASTM Symp. Damage in Laser Mat's., NBS Spec. Pub. 414 (1974)

[3] Loomis, J.S. and T.T., Saito, "Third Conference on High Power Infrared Window Materials," vol. 3, Air Force Cambridge Research Labs, AFCRL-TR-0084 (III) (1973).

[4] Skinner, D.R. and R.E. Wictcher, "Measurement of the Radius of a High-Power Laser Beam Near the Focus of a Lens", J. Phys. E: Sci. Instrum. 5, 237 (1972).

[5] Bernal, G., Enrique, "Heat Flow Analysis of Laser Absorption Calorimetry", Appl. Optics 14, 314 (1975).

[6] Laughlin, W.T. and R.C. Vrem, "Unsteady-state Heating of a Finite Disc by Continuous and Repeatively Pulsed Laser Radiation," Air Force Weapons Laboratory, AFWL-TR-72-236 (1973)

[7] Loomis, J.S., "Anti-reflection Coatings for Potassium Chloride Infrared Windows," Laser Digest, Air Force Weapons Laboratory, to be published.

[8] Harris, J.S., Slomba, A.F., et al., "Diffraction Grating Development," AFWL-TR-74-218 (1975).

[9] Buckmelter, J.R., et al., "Dielectric Coated Diamond Turned Mirrors", to be published elsewhere in this volume.

16. Tables and Figures

Table 1. Temperature Rise per Watt Absorbed Power for Some Typical Materials.

Material	Thermal Conductivity (watt/cm-°C)	Heat Capacity ($joule/cm^3$-°C)	Thickness (cm)	Temperature Rise/ Watt Absorbed	
				2 sec (°C/watt)	30 sec (°C/watt)
ZnSe	0.12	1.90	0.8	4.97	7.53
KCl	0.07	1.35	1.0	6.59	9.90
Mo	1.44	2.57	0.6	5.45	7.01

Table 2. Damage Results for Windows

Sample Identification	Absorption (percent)	Damage Intensity (KW/cm^2)	Remarks
ZnSe 58C-WL-8A	-	>150	Uncoated
ZnSe 58C-WL-7A	0.13	>150	Uncoated
ZnSe 82A-1G	1.30	>150	AR Coated
ZnSe 76A-3B	0.86	120*	AR Coated
KCl 300	0.21	150*	AR (1) (As_2S_3/KCl/As_2S_3)
KCl 298	0.29	>150*	AR (2) (As_2S_3/KCl/As_2S_3)
KCl 297	0.46	90+*	AR (3) (As_2S_3/KCl/As_2S_3)
KCl 292	0.66	120*	AR (4) (As_2S_3/KCl/As_2S_3)
KCl - SS	0.41	>150*	AR Coated (5)
KCl 41	2.1	23	AR Coated (6) Opaque
KCl 33	1.2	10*	AnS/Ge AR Coated (7) Opaque
KCl 299	0.16	90+*	As_2S_3 /2
KCl 34	3.4	10+*	/2 Coated Opaque
KCl 50	1.8	14*	/2 Coated Opaque
KCl 35	3.0	10+*	/2 Coated Opaque
KCl 51	2.3	10*	CdTe Coated
KCl 49	3.0	7.5	Ge /2

* Isolated Damage spots at lower intensity

\+ Isolated undamaged spots at higher intensity

Table 3. Damage Results for Abraded KCl Windows

Sample Identification	Absorption (percent)	Damage Intensity (KW/cm^2)	Remarks
KCl 202	1.53	11 *	25 m grit
KCl 203	1.34	8 + *	25 m grit
KCl 204	1.14	20 +	25 m grit
KCl 205	0.58	60 +	10 m grit
KCl 206	0.53	70 *	10 m grit
KCl 207	0.60	70 + *	10 m grit
KCl 208	0.54	60 *	1 m grit
KCl 209	0.47	90 *	1 m grit
KCl 210	0.47	80 *	1 m grit
KCl 211	0.88	30 *	0.1 m grit
KCl 212	0.61	>15 *	0.1 m grit

* Isolated damage spots at lower intensity

\+ Isolated undamaged spots at higher intensity

Table 4. Damage Results for Mirrors

Sample Identification	Absorption (percent)	Damage Intensity (KW/cm^2)	Remarks
M 130	0.85	150	$Au(ThF_4/ZnS)^2$
OCLI 4A	1.10	90 +	$Au(ThF_4/SnS)^2$
OCLI 3A	0.22	150 *	$Mo(ThF_4/ZnSe)^4$
AM 51	0.14	>150	$Mo(ThF_4/ZnSe)^3$
AM 18	0.13	>150 *	$Ag+ThF_4(ThF_4/ZnSe)^3$
AM 23	0.13	>150 *	$Ag+ThF_4(ThF_4/ZnSe)^3$
AM 40	0.13	>150	$Mo(ThF_4/ZnSe)^3$
AM 53	0.25	140 *	$Mo(ThF_4/ZnSe)^4$
T 86	0.14	90 * +	$Ag+ThF_4(ThF_4/ZnSe)^3$
T 85	0.15	60 +	TZM $(ThF_4/ZnSe)^3$
T 80	0.29	120 * +	TZM $(ThF_4/ZnSe)^3$
T 78	0.07	150 *	$Ag+ThF_4(ThF_4/ZnSe)^3$

* Isolated damage spots at lower intensity

\+ Isolated undamaged spots at higher intensity

Table 5. Damage Results for Gratings

Sample Identification	Absorption (percent)	Damage Intensity (KW/cm^2)	Remarks
RMG 1		>150	Solid Al ruled grating
RMG 2		>150	OFHC-Kanigen-Al ruled grating
RMG 3		60	Al-Kanigen-Al ruled grating
RMG 4		<15	Si-Al ruled grating
RMG 5		<1.5	Glass-Epoxy-Al Replica grating
GT-6	0.97	>150 *	TZM/Au ruled grating ThF_4 over coat
GM-7	0.88	>150 *	moly/Al ruled then Au over coat
GT-7	1.15	>150	TZM/Au ruled grating
GM-8	1.07	150	ion-polished moly/Au over coat
GBC-26	13.4	150	BeCu ruled/Au over coat
GM-18	1.0	>150	ion polished moly/UHV Au over coat

* Isolated damage spots at lower intensity

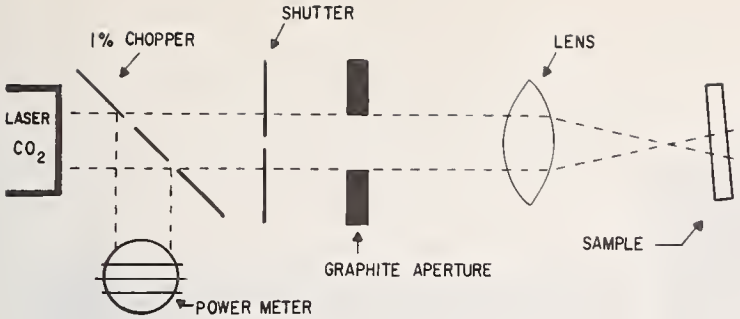

Figure 1. Diagram of damage-testing apparatus.

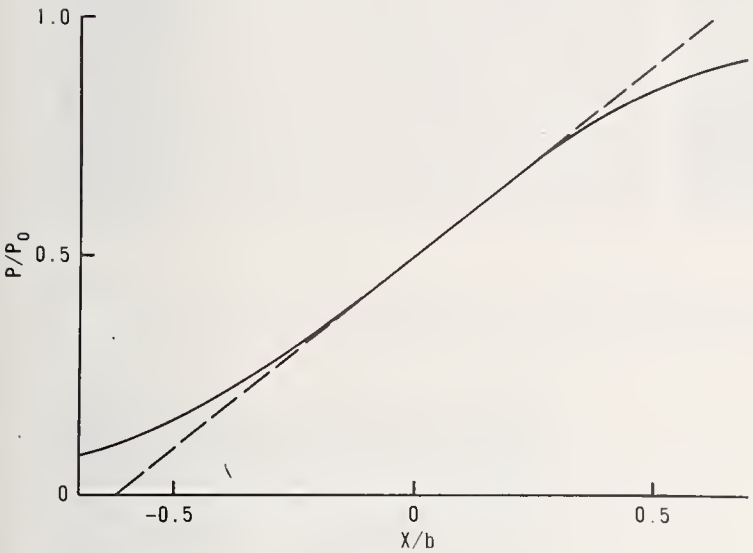

Figure 2. Power transmitted past an edge when the edge is near the center of the laser beam (x = 0).

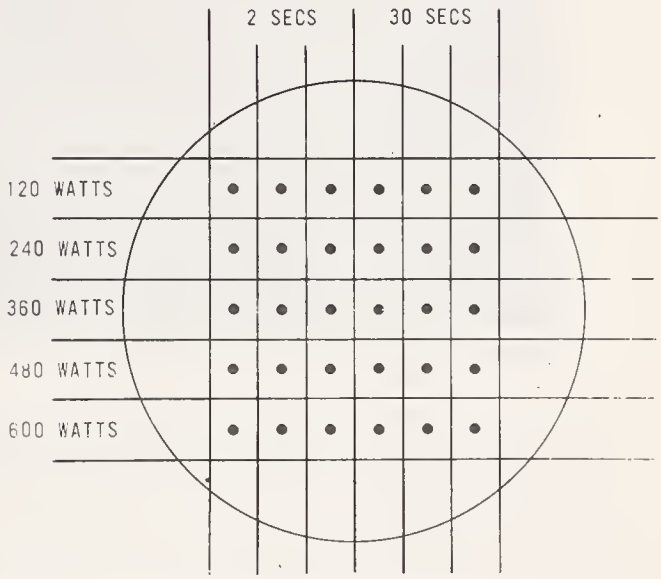

Figure 3. Irradiation matrix for damage study. Sequence began at top left corner.

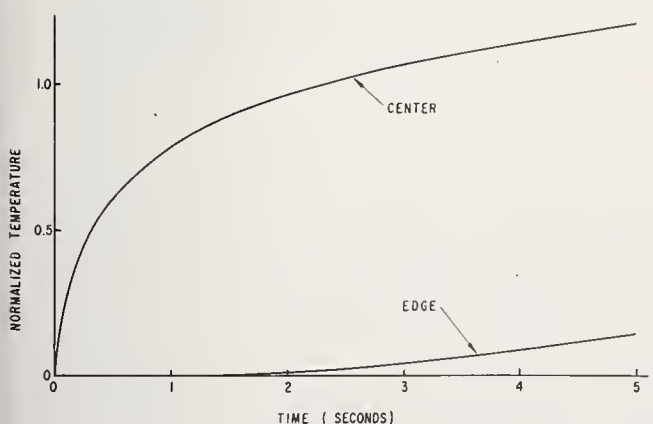

Figure 4. Average temperature at the center and edge of a potassium chloride window as a function of time.

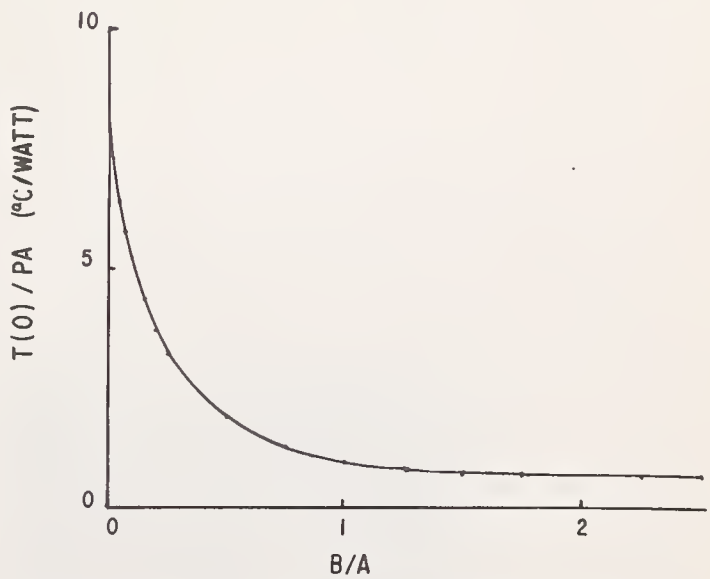

Figure 5. The ratio of peak temperature rise to absorbed power as a function of beam radius ratio to specimen radius after ten seconds of irradiation. The specimen was assumed to be potassium chloride.

(a)

(b)

Figure 6. Damage pattern produced on KCl #292. Picture A shows the entire specimen (3.8-cm diameter). Picture B shows close-up of a damage site.

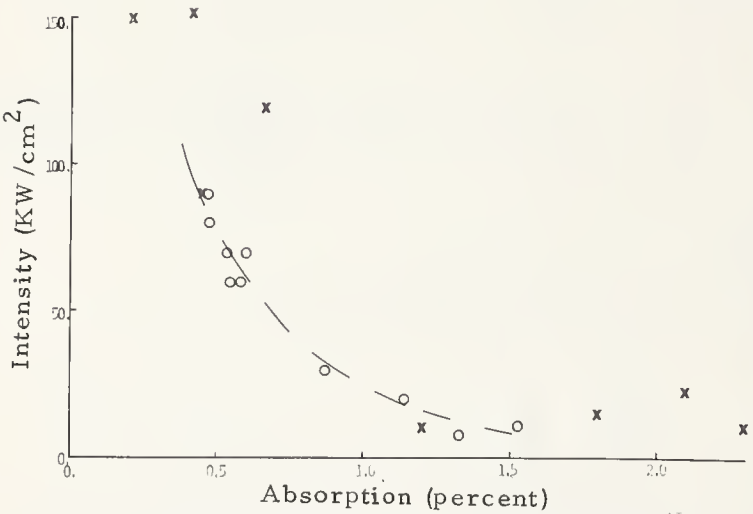

Figure 7. Damage intensity versus absorption for abraded KCl specimens (circles) and coated KCl windows (crosses).

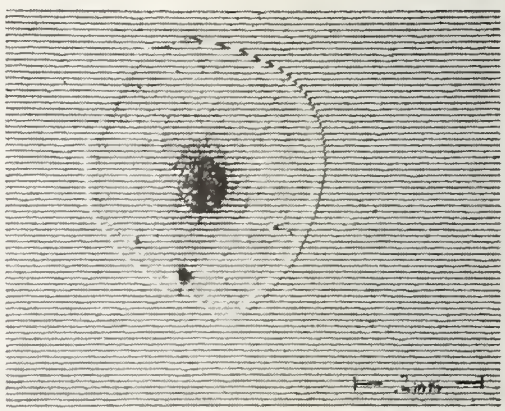

Figure 8. Damage spot on a conventionally ruled grating (line spacing 118.11/mm). The damage spot is about 0.08 mm in diameter.

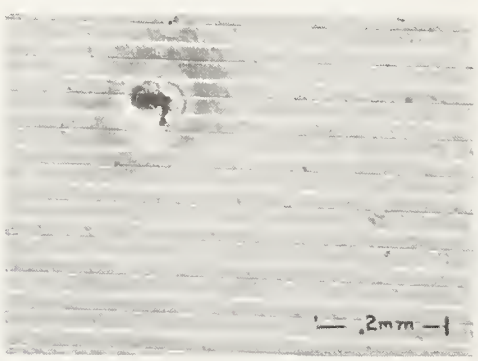

Figure 9. Damage spot on an ion-polished grating (line spacing 127/mm). The damage spot is about 0.08 mm in diameter.

COMMENTS ON PAPER BY HUGULEY, *et al*

The physical basis of the pre-conditioning effect noted at the observed level of irradiation is not clear. The level of irradiation at which this effect is observed seems anomalously low in terms of creating microplasmas at the surface. Another observation concerned damage levels on gratings. Traditionally it has been held that due to the rulings gratings should exhibit a lower damage threshold than the corresponding substrate material. In this work evidence was seen exactly to the contrary. No explanation of this discrepancy was forthcoming.

4.2 10.6μm COMPONENT DAMAGE FROM A 20 μsec RAPIDLY PULSED LASER

Dr. Alan B. Callender

Air Force Weapons Laboratory
Kirtland AFB, New Mexico 87117

Extrinsic lower bound thresholds have been found for some window materials and coated and uncoated metal mirrors. The results differ from single shot data in that formation of breakdown plasmas in the vicinity of the components appear to be more likely after several high repetition rate shots have been made. No major conditioning effects have been observed.

Key words: Pulsed lasers; mirror damage; window damage.

1. Introduction

Rapidly pulsed electric discharge lasers (RPEDLs) provide an intermediate regime for laser damage study mechanisms between very high peak power single pulse lasers and high average power CW lasers. Although the peak power densities are much less than those encountered with single pulse systems, pulse damage still does occur. Also, the average power densities are very much less than those of interest for past CW damage studies; but it appears that the average power density can, in fact, couple possibly through either of two mechanisms to reduce the damage threshold drastically after the first few pulses in a high-rate burst.

A new parameter, the laser's duty cycle, must be considered in explanation of damage mechanisms and thresholds. Air flow flush time is also a factor for one candidate mechanism. A third factor, which will strongly influence the importance of the duty cycle, is the thermal time constant of the component.

The experimental work reported here was performed on the AFWL EDL which has been described previously [1][1]. At the time of this work this device delivered 60J pulses of 20 μsec duration at rates up to 150 pps.

Most AFWL interest has been associated with mirror surface damage rather than (surface or bulk) window damage. Some tests have been made on candidate window material, but this work has been limited by the lack of acceptable cleaning equipment on site.

2. Models

The power density regime at which single pulse damage to metal mirrors has been observed is approximately 1-15MW/cm^2 for 20μsec pulses. Some CO damage tests on mirrors [2] and on unfinished metal targets [3] with the Northrop 100μsec pulse length EDL show that a damaging plasma is struck at less than 4 MW/cm^2. Other CO_2 work has shown much higher (power density) thresholds at 0.6μsec [4] . Here the bare metal failure point was estimated at about 60 MW/cm^2 with later results showing somewhat higher levels [5]. All of these power densities are low for air breakdown, but surface temperature rises may be high enough to yield substantial metal vapor near the surface which could aid in plasma formation [6].

To check this possibility surface temperature rises were calculated for the pulse lengths involved for polished copper. The values are all surprisingly low (∿100°C), but they show only 20% deviations from the mean. By contrast, the power densities vary by more than an order of magnitude. The inadequacy of temporal data make closer comparison difficult. New instrumentation is needed to discriminate between power-dependent damage mechanisms and surface temperature rise mechanisms. Pre-heated and pre-chilled mirror damage experiments will be conducted at AFWL later this year to test the temperature rise mechanism further. Care will, of course, be taken to ensure that the surfaces are free of condensed water.

If the mechanism is surface heating the temperature rises (∿100°C for copper) are rather low for metal vapor formation unless evaporation is occurring at surface proturberances. As at least some of the tests have been made on surfaces which had RMS roughness less than 5nm with no significant difference in results, one should not expect large defects to be essential, though they are known to help. Unfortunately, thermal transport parameters become somewhat nebulous, like electron transport parameters, near the metal surface; but one should expect that features on the surface which show poor electron transport, and thus higher optical absorption, will also show poor heat transfer with consequent runaway.

The dependence of surface temperature on duty cycle and cooling place the RPEDL in a mixed category. A calculation procedure is presented in section 4. If the duty cycle exceeds 1 x 10^{-3} for an uncooled mirror, for example, the temperature at the end of the 26th pulse will be about 14% greater than for an equivalent single shot. Since the AFWL EDL can exceed a duty cycle of 2.5 x 10^{-3} this effect was studied by varying the repetition rate. Cooling works to reduce the effect of pulse pile up in surface

1. Figures in brackets indicate the literature references at the end of the paper.

temperature by allowing a rapid approach to a steady state in which the average surface temperature is set by the average flux and cooling characteristics and the peak temperature is limited to the single shot rise plus the average temperature rise associated with the average power level.

Unfortunately, even though the uncooled mirror will reach a higher final temperature after a short burst than the well cooled mirror, the presence of vapor build-up in front of the mirror may make either mirror fail early. This would be shown by the presence of a smaller plasma followed by thorough breakdown on each pulse for the remainder of the burst if no flushing is used. This was observed in the experiments reported here.

Future experiments should include fast power detectors and either data collection equipment which can sample at rates of ten samples per cavity round-trip time (to account for the presence of mode-locked trains) or real-time high bandwidth analog analyzers to derive the surface temperature from optical power with only a minor time lag. Comparisons of data on different lasers or on the same laser with slight random variations in its gas mixture are otherwise very difficult to make.

3. 10.6μm EDL Damage to Components

The preliminary experiments which have been made at AFWL were primarily made to determine safe limits for system design. These experiments have been conducted on window and mirror material candidates which were thus selected on the basis of contractor experience and with special emphasis on component survivability under occasional (possibly dust induced) surface plasmas. For this reason only a few coated samples were tried.

In the experiments an RdF large cone calorimeter was used to measure the net energy in a pulse or series of pulses. For mirror tests the calorimeter was located about 60 cm along the beam path after reflection from the mirror. In window tests a mask of brightly finished tungsten foil (0.25 mm thick x 2 x 5 cm) was constructed to aperture the beam to a square cross-section with edge of 2.0 cm, about 1 cm before the window, and the calorimeter measured the energy transmitted 30 cm behind the window.

The RdF calorimeter was calibrated by comparison with absorbed energy measurements on a 5 cm diameter plane molybdenum mirror whose absorption had previously been measured.

Window tests were made about 2.0 m before the focal plane of a 10 m focal length spherical mirror which received the (relayed) output of the AFWL EDL. At that time the output was a near-field annulus, about 7 cm outside diameter and 6 cm inside diameter, and definitely somewhat more intense near the inner edge. Single-shot burn patterns in front of and behind the tungsten mask showed substantial uniformity over a 2 cm diameter circle with a single hot spot about 1 mm diameter located 5 mm off-pattern center. Unfortunately, the relative intensity cannot be estimated.

Mirror tests were made in the focal plane of the 10 m spherical mirror. Some diagnostics had been made on the machine output using transmission grating and wedged window beamsplitters. The results were that 20% or more of the integrated output over a single pulse or over up to ten at high rate (> 50 pps) was within the central peak of the pattern which would be expected from an annular plane wave [7]. This should be compared with the expected value of ~ 0.40 for the central peak energy to total energy ratio. In this sense the laser output was "50% of diffraction limited" performance. Thus, although the shape was not measured within this spot size, it is still somewhat reasonable to assume that the peak on axis intensity is about half of the value to be expected from an annular plane wave with the given total energy. This spot is calculated and measured, in the split-off beam, to be about 1.3 mm radius which agrees reasonably with the observed burn pattern radius of 1.4 mm. The peak energy density is then, per joule incident on the focusing mirror or seen in the calorimeter, about $9.6 \times 0.5 = 4.8$ J/cm^2. The first factor, 9.6, is the calculated on-axis intensity gain due to the mirror and the second factor, 0.5, is to account for the observation that only 50% of the calculated fraction of the total energy was within the first dark ring.

The temporal output of the AFWL EDL consisted of a leading power peak of about 100 nsec duration followed by a 20 μsec pulse with a fairly flat top and fast falling edge. The leading peak was at least twice and sometimes as much as four times the average power. Some pulses had a rapid oscillation (100 nsec to 1 μsec period) during the main pulse which had a peak-to-peak amplitude which was about equal to the average.

The results were encouraging for mirrors and somewhat discouraging for windows. A summary is presented in tables I and II.

Mirror tests began with the bare polished molybdenum sample, which had been used just before the damage test to calibrate the RdF calorimeter. For the calibration series this mirror was thermally isolated, instrumented, and used about 3 m before focus at energies up to 60 J/pulse. The energy density may be guessed to be of the order of 3 J/cm^2 maximum. Absorbed energy was observed during the damage tests on this mirror and compared with the previous EDL sustainer voltage-energy curve. The first surface flash created a melt pit about 2 mm diameter x 0.5 mm deep and the temperature rise was eight times the expected value.

The bare copper samples showed surface plasmas for low repetition rate loading above 200 J/cm^2 (average beam axis power density 10 MW/cm^2 during pulse), but no visible damage was created up to the available limit of ∿ 290 J/cm^2.

These samples might well have had rather less input from the last pulses in a sequence due to breakdown of the disturbed air in front of the sample. They showed also that the calorimeter was too close to the sample in that the calorimeter would break down at about 180 J/cm^2, and during a burst of pulses, the breakdowns would occur outside of the calorimeter but, after the test mirror. This might well have been caused by neutral copper vapor from the calorimeter's previous breakdowns. Energy estimates were based on the single pulse values (without breakdowns) for the same laser operating conditions.

The silver-plated mirror test was accompanied by many breakdowns between the calorimeter and mirror but none on the mirror. At the end of the test (∿ 60 breakdown pulses in all) a 2 cm diameter circular area of the mirror appeared to have been plated with copper and copper oxides.

Dielectric coated mirrors showed much lower thresholds. In both cases the first surface plasma not only evaporated the coating over a 3 mm diameter circle, but also evaporated some of the substrate material as well. It appears that thermal coupling from the plasma to the metal was much enhanced by the presence of the coating. Unfortunately, lack of sufficient energy output for large area loading at realistic fluence did not allow further testing of these damaged samples to determine whether the damage would spread.

A mistake in planning of geometry for the window tests was discovered [8] after the tests in that the strongly converging beam used will greatly reduce self-focusing damage levels in comparison to the collimated or expanding beam cases. This was nonetheless fortunate in that self-focusing damage was observed for nearly all impurity doped (for strength enhancement) samples, but not for the NaCl or KCl undoped samples, or for ZnSe (undoped). A power density dependent effect, like self-focusing, may have been the cause of the anti-reflection coating failure on the ZnSe sample, as the actual failure area was about 1 mm diameter and in the same location as the bubble tracks. The hot spot in the burn pattern mentioned earlier did not correspond to the bubble tracks. It might be that a very short output spike has a quite different divergence from the rest of the pulse. Further tests will be made with spatially filtered diverging or collimated beams.

The preliminary tests reported here will be followed by further tests with better beam quality. Tests and development on mirrors will concentrate on means of combining massive polished or machined copper or gold coatings on molybdenum substrates. Window efforts will continue with ZnSe and various halides.

Table 1. Mirror damage performance.

Mirror	Failed	Survived	Remarks
1. Bare polished Mo. (Source in parentheses)	(S) 240 J/cm^2	(S) 190 J/cm^2	Observed 8X enhanced absorption on damaging pulse, which was the first pulse to strike a surface plasma.
2. Bare polished Cu (Spawr)	Could not damage	rep. 10 @ 10 pps 290 J/cm^2	Struck plasmas but could not find damage with 400X Nomarski microscope.
3. Bare diamond-turned Cu (Y12)	"	"	"
4. Diamond turned Ag electroplated onto Cu blank (LLL)		rep 10 @ 10 pps 290 J/cm^2	Many plasmas struck in calorimeter bombarded sample and plated Cu.
5. Polished Cu coated with ThF_4 (Spawr)	rep. 10 @ 10 pps 38 J/cm^2	(S) 42 J/cm^2	Surface flashed and coating blistered.
6. OCLI design #2 on diamond-turned Au electro dep. on Cu	(S) 22 J/cm^2		Surface flash, coating completely destroyed on first shot.

Test Modes: S = single pulse

rep. = repetitively pulsed N pulses @ M pulses/second.

Table II. Window damage performance.

1.	KCl uncoated single crystal, old sample with some haze.	~ 3 J/cm^2 single shot	Hazed surface ablated uniformly over 2 cm diameter irradiated area.
2.	Uncoated single Crystal NaCl	rep. 7 @ 150 pps 5 J/cm^2	Surface impurities visibly burned away at this level. Could not cause gross cracking or ablation.
3.	Uncoated single crystal KCl	rep. 10 @ 150 pps 5 J/cm^2	Surface burn pits. Could not damage bulk at maximum available fluence = 10 J/cm^2.
4.	Uncoated single crystal rubidium doped KCl	rep. 4 @ 150 pps 8 J/cm^2	Small burn pit.
5.	Uncoated polycrystalline rubidium doped KCl	rep 10 @ 150 pps ~ 6 J/cm^2	1 mm diameter interior bubble track.
6.	Uncoated Sr doped KCl (very clean surface)	(S) ~ 3 J/cm^2	1 mm diameter interior bubble track.
7.	Uncoated ZnSe	(S) ~ 8 J/cm^2	Small surface burn pits where flashes occurred.
8.	Anti-reflection coated ZnSe	rep. 100 @ 150 pps passed > 3 J/cm^2 died ~ 5 J/cm^2	Catastrophic coating failure on rear surface with window breaking.

Test Modes: S = single pulse
rep. = repetitively pulsed N pulses @ M pulses/second.

4. Surface Temperature Rise

For times such that the characteristic length $\sqrt{4Kt}$ is much less than either the laser spot size or the thickness of the plate one can use the solution given by Ready [9] when the incident beam is uniform in the plane of the surface and a rectangular pulse in time. This is, for surface temperature $Z(0,t)$

$$Z(0,t) = \frac{2aF}{k}\left(\frac{Kt}{\pi}\right)^{1/2}. \tag{1}$$

Substitution of the heat capacity per unit volume ρC_p into the diffusivity K then leads to

$$Z(0,t) = 2aF\left(\frac{t}{\pi\rho C_p k}\right)^{1/2}, \tag{2}$$

a is the optical absorption coefficient.

After the pulse is over the appropriate solution includes a cut-off:

$$Z(0,t) = [2aF/(\pi\rho C_p k)^{1/2}]\ \{t^{1/2} - (t-b)^{1/2}\ \Theta(t-b)\}. \tag{3}$$

Extending this result in the usual way for periodic problems, the periodic input surface temperature is

$$V(0,t) = \sum_{M\neq 0}^{\infty} Z(0,t-MT)\,\Theta(t-MT) \tag{4}$$

where T is the period of the repetition.

One estimates surface temperature pulse pile-up using eq. (4) provided that t is not too large.

5. Conclusions

In all repetitive irradiation tests there was a breakdown on each pulse following the (relatively weak) initial breakdown pulse. This held even for repetition rates as low as 1 pps. At high repetition rates the later breakdowns would occur progressively further up the beam from the sample. This is probably indicative of the presence of target vapor moving up the beam in this unflushed system. Future tests will incorporate dry nitrogen flushing.

Thus, these experiments do not discriminate between the possibly gradual build-up of target vapor, followed by a series of breakdowns, and the cumulative temperature rise of the surface alone. Discrimination will be achieved in the future by flushing of vapor build-up and by the use of cooled targets.

6. Acknowledgments

The author gratefully acknowledges helpful discussions with Raymond V. Wick, Ralph R. Rudder, and Dennis Riley.

6. References

[1] Rudder, R. R., "The Interaction of Multiple Laser Pulses with Solid Matter," Laser Digest, Fall 1974,(Jan 75) AFWL-TR-74-344, Air Force Weapons Laboratory.

[2] Holmes, S. and P. Kraatz, Proc. 5th ASTM-ONR-NBS Symposium on Laser Induced Damage in Optical Materials, NBS Spec. Pub. 387 (1973).

[3] Rudder, R. R., "Initial experimental observations of the interaction of pulsed five micron radiation with solid targets," Laser Digest, Summer 1974, AFWL-TR-74-241, Air Force Weapons Laboratory, Kirtland Air Force Base, NM, September 1974.

[4] Wang, V., A. Braunstein, M. Braunstein, J. E. Rudisill, and J. Y. Wada, Proc. 5th ASTM-ONR-NBS Symposium on Laser Induced Damage in Optical Materials, NBS Spec. Pub. 387 (1973).

[5] Wang, V., J. E. Rudisill, C. R. Giuliano, M. Braunstein, and A. Braunstein, Proc. 6th ASTM-ONR-NBS Symposium on Laser Induced Damage in Optical Materials, NBS Spec. Pub. 414 (1974).

[6] Riley, Dennis, private communication, AVCO-Everett Research Laboratory, Everett, MA, February 1974.

[7] Hanlon, J. A., private communication, AFWL/ALO, Kirtland Air Force Base, NM, March 1975.

[8] Wick, R. V., private communication, AFWL/LRE, Kirtland Air Force Base, NM, November 1974.

[9] Ready, J. F., "Effects of high power laser radiation," (Academic Press, New York, 1971).

COMMENTS ON PAPER BY CALLENDAR

The question was asked concerning the comparison of the results obtained in this work with the results reported by Saito earlier in the conference for short pulse single shot damage. The speaker responded that due to the different sample characteristics it was not possible to make a comparison. However, he emphasized that a significant reduction in the damage threshold over the single shot value was observed in this work and this was attributed both to an increase in temperature which accumulated during the course of irradiation and the buildup of absorbing vapor near the surface due to repetitive pulsing.

4.3 Laser Damage Measurements at CO_2 and DF Wavelengths

J. O. Porteus, M. J. Soileau, and H. E. Bennett
Michelson Laboratories, Naval Weapons Center
China Lake, California 93555
and
M. Bass
Center for Laser Studies, University of Southern California
Los Angeles, California 90007

Preliminary results from laser damage tests conducted with CO_2 and DF lasers on samples mounted in a newly constructed ultrahigh vacuum sample chamber are reported. The lasers operate single mode and the pulse lengths are 100 nsec for CO_2 and about 500 nsec for DF. A precise method of focusing which permits accurate determination of power densities is described. Incorporated in the test chamber are a scanning electron imager, an optical microscope, a profiling Auger system, and a charged particle collector for *in situ* analysis. Analytical results are presented and implications for physical damage processes are discussed. Measurements in nitrogen on aluminum samples indicate that the threshold for N_2 breakdown is reduced some 20 times in the vicinity of the aluminum surface. Laser supported gas plasma waves are formed which shield the surface, and no physical damage occurs for single 100 nsec pulses even at power levels of 10 GW/cm^2. However, in vacuum damage does occur at about the expected power levels. No significant difference between the damage threshold for polished and machined aluminum surfaces was found.

Key words: Al mirrors; Auger spectroscopy; damage morphology; electron emission; electron imaging; ion emission; laser-induced damage; surface characterization; surface temperature.

1. Introduction

Improvement in the performance of laser-damage-resistant materials requires a better understanding of the damage process and how it relates to material characteristics. This requires the ability to critically examine various aspects of damage on well-characterized samples under well controlled conditions. In this paper we describe a newly completed facility based on this approach, and discuss early results that we have obtained on aluminum mirrors. Experiments are performed both in vacuum and in 1 atm of N_2 with pulsed laser sources operating at wavelengths of 10.6 and 3.8 μm. The arrangement of the various optical components is described in section 2. In section 3 we describe the temporal and spatial characteristics of the lasers and outline an accurate method of focusing the beam on the sample. In section 4 we describe the test chamber and its facilities for sample characterization and for monitoring damage phenomena. Conditions under which the various samples were prepared are described in section 5. In section 6 we present data on damage thresholds. Damage morphology and the related phenomena of electron and ion emission are discussed in section 7, together with implications regarding the damage process. Finally, section 8 is a summary of the work.

2. Optical Arrangement

The optical arrangement of our laser damage analysis facility is shown in figure 1. Either of two pulsed laser sources are used, one operating with CO_2 for 10.6 μm radiation, and the other operating either with HF or DF for radiation at 2.8 or 3.8 μm, respectively. A HeNe laser is also provided for convenience in aligning the optics. Temporal beam characteristics are measured by a photon drag detector. Beam intensity is controlled by a rotating polarizer and analyzer, following which the pulse energy is measured by a pyroelectric energy meter. The beam then enters the test chamber where it is focused on the sample by a ZnSe lens having a focal length of 12 cm.

3. Laser Characteristics and Focusing

The lasers operate single-mode with reproducible temporal and spatial characteristics. Figure 2 shows the measured dependence of intensity on time, together with functions which describe this dependence analytically. The latter provide a convenient basis for accurate heat flow calculations. Available power levels are more than adequate for damage testing with 1.5 J in 100 nsec from the CO_2 laser and 0.5 J in 200 to 800 nsec at the DF wavelength. Figure 3 shows the measured spatial profile of the CO_2 laser beam, which is represented by a Gaussian to within 4%. When focused by the 12 cm lens the profile at the sample surface is represented by $\exp[-(r/93\ \mu m)^2]$. The spatial profile of the DF laser beam is similar, but has not yet been characterized with comparable accuracy.

Proper focusing is accomplished by a method illustrated in figure 4. The beam from a CW CO_2 laser passes through the lens along its optic axis, is reflected from the tilted sample and returns off-axis through the lens to cross the incoming beam at a distance q in front of the lens. If q can be determined, the focal length f is calculable from the simple lens formula and the corresponding distance

p(>f) separating the lens and sample. The crossover distance is established by a thermocouple detector whose two junctions straddle the incoming beam. With p fixed, an oscillating signal is produced by the changing position of the return ray with respect to the detector as the sample is rocked about an axis perpendicular to the line connecting the detector junctions. As illustrated by the signals a and b, which were obtained with the crossover point on opposite sides of the detector, a phase reversal (and signal null) occurs at the position of coincidence. A focusing accuracy of better than 10 μm, which is well within the focal range of the lens, is easily achieved.

4. Test Chamber

The test chamber and the analytical instrumentation are indicated schematically in figure 5. The chamber is designed for ultrahigh vacuum, including bakeout. However, present measurements were made without baking, either at pressures below 1×10^{-7} Torr or in 1 atm of N_2. The sample is mounted on a precision manipulator and may be placed alternatively in positions S_1 or S_2. Position S_1 permits irradiation and simultaneous monitoring of laser-induced effects. Visible changes in the sample surface are monitored by scattered light observed with a 20X optical microscope. A biased Faraday cup with grounded entrance grid provides intensities and time-of-flight energies of charged particles emitted by the sample. Other features planned, but not available in time for the present measurements, are a mass analyzer, electronic scattered light detector, and an evaporator. Auger analysis and sputter profiling, if desired, are possible with the sample in position S_2.

Figure 6 is a photograph of the test chamber in its present form. The laser entrance port faces right. Surrounding this are four smaller ports containing a viewing window, microscope, particle collector, and scattered light source. The Auger analyzer and coaxial electron gun are in the large port to the left of the photograph. In smaller ports above this are the sputter gun for Auger profiling and a glancing electron gun used for Auger spectra of insulating samples. The sample manipulator is mounted in the top of the chamber.

An electron imager operating in conjunction with the Auger probe beam permits precise positioning for analysis of selected surface features. Ultimate spatial resolution is 5 μm. Figure 7 shows an electron image of the central portion of a large damage crater with an optical (Nomarski) micrograph of the entire crater for comparison. The electron imager also provides valuable information on the electron emission characteristics and its variation across the surface, which, as will be shown, is related to damage phenomena.

Surface contaminants, as revealed by Auger analysis, may enhance optical absorption and lower damage thresholds. Figures 8a and b show examples of Auger spectra from undamaged portions of polished and sputter-deposited Al surfaces, respectively. The absence of C, N, and Mg on the sputter-deposited surface is noteworthy. Since samples are exposed to air when they are transferred from the preparation facility to the test chamber, surface oxidation is unavoidable. Future work is planned on samples deposited, or sputter-cleaned in the test chamber to determine the effect of the oxide layer on damage phenomena.

5. Sample Preparation

The five different types of samples used are listed in table 1. Machined surfaces were cut on a lathe. Polished Al surfaces for testing and for substrates were prepared from the machined surfaces by loose grinding and polishing using bowl feed, pitch lap, and 0.3 μm Al_2O_3 compound. Care was taken to grind long enough with each grit to remove the subsurface damage left by the previous grinding operation. Quartz substrates were polished using bowl feed also, and had equivalent surface roughnesses under 20 Å rms. DC sputtered aluminum coatings were nominally 1500 Å thick, deposited in a previously baked system at a rate of 60 Å/min in a 3 μm Ar atmosphere. The RF sputtered aluminum coating was nominally 2000 Å thick and was deposited in an Ultek 2400 system at a rate of 1600 Å/min in a 20 μm Ar atmosphere. The UHV evaporated aluminum coating was 1400 Å thick and was deposited at a rate of 720 Å/min in a vacuum of 2×10^{-8} Torr.

Table 1. Damage Thresholds on Aluminum.

λ	Surface	Substrate	(1-R)	Threshold Energy Density (J/cm^2)	Peak Power (MW)
10.6 μm	Polished 2024	...	0.026	14	140
	Machined 2024	...	...	14	140
	DC Sputtered	Al	0.017	8	80
	DC Sputtered	Qtz.	0.015	7	70
	RF Sputtered	Qtz.	0.024	6	60
	UHV Evaporated	Qtz.	0.012	4	40
3.8 μm	Polished 2024	...	0.038	63	204

6. Damage Thresholds

Damage threshold results obtained in vacuum are summarized in table 1. The threshold energy density or peak power is defined as that required to produce visible pitting. Thresholds of machined and polished surfaces are about the same. In the case of coated surfaces the threshold is significantly lower in spite of the lower absorptivity (1-R) of the coating. Coating thicknesses are estimated to be less than 10% of the thermal diffusion depth $\sqrt{2\ a t_p}$, where a is the thermal diffusivity and t_p is the duration of the laser pulse [1][1]. Consequently, a thermal barrier at the substrate interface would cause a larger amount of energy to be deposited within the coatings than within an equivalent layer of the uncoated surfaces. In the case of the Al-coated Al substrates the oxide layer at the interface may introduce such a barrier. Comparison of results for the sputtered vs. UHV deposited coatings suggests that the thermal barrier is mitigated by sputtering leading to an increased threshold, again in spite of a higher absorptivity. The higher threshold at 3.8 μm is mainly a result of the longer pulse duration, which provides more time for the energy to dissipate.

Attempts to damage the polished sample at 10.6 μm in 1 atm of N_2 failed, even at power densities as high as 470 MW/cm^2. The reason for this is a drastic lowering of the N_2 breakdown threshold by the presence of the Al sample. Numerical results are given in table 2. The low level breakdown is triggered by electrons emitted by the sample. Results with the sample tilted 60° are consistent with thermionic emission, the N_2 breakdown threshold rising roughly as the secant of the angle, i.e., in accordance with the power increase required to maintain a given power density at the sample surface. Thermionic emission has been directly observed in experiments performed in vacuum, as discussed in section 7. We were able to damage the sample in N_2 at 3.8 μm. In this situation successive pulses at the same position on the surface produced damage at power levels lower than that of the initial pulse. This may be attributed to removal of the oxide layer, which has a lower work function and hence produces a higher electron emission than the bare Al. This interpretation is supported by electron imaging, in which damaged areas appear darker than the surrounding undamaged areas.

Table 2. Nitrogen Breakdown Threshold at 10.6 μm

Without Polished Aluminum Sample	272 J/cm^2	272 MW
With Sample	8 J/cm^2	8 MW
Sample Tilted 60°	13 J/cm^2	13 MW
Damage Threshold	>470 J/cm^2	>470 MW

7. Damage Morphology and Related Phenomena

Damage craters produced at 10.6 μm on the sputtered and polished Al surfaces are compared in figure 9. Generally, craters consist of a central depression surrounded by a raised rim. Craters on the polished Al surface, either with or without the sputtered coating, are less regular than on the quartz substrates, obviously a result of the poorer finish and uniformity.

An important bit of information for damage mechanisms is the relationship between pulse energy and crater size. This is presented in figure 10 for the polished Al surface at 10.6 μm. The large scatter in the data points is characteristic of polished Al and corresponds to the nonuniformity noted in figure 9. The solid line is the result of a one-dimensional heat flow calculation of the energy required to produce melting based on the beam spatial profile, the Drude temperature variation of absorptance, and the temporal characteristics of the laser pulse. Although the threshold region is fairly well represented, the larger craters extend well outside the predicted melt area. Possible explanations for this aside from possible shortcomings of the model, are expulsion of molten material beyond the melt zone and distortion of unmelted material. Attempts to resolve this discrepancy are in progress.

Perhaps the most important key to understanding damage mechanisms is the sample temperature. In principle, temperature can be inferred from the laser-induced electron emission if the surface is well characterized and the emission process is known. Figure 11 reproduces an oscilloscope trace of the laser output signal and the corresponding collected electron signal. Note that the electron signal follows the individual mode-locked laser pulses. If the emission is purely thermionic, the relationship between temperature and electron pulse height is as given in figure 12. Here we have plotted the Richardson-Dushman equation [2] using the known geometrical and electrical characteristics of the detector, and assuming that the emitting area is delimited by the 1/e radius of the beam profile. Unfortunately, the value of the work function, Φ, which parameterizes this relationship, is not known for the oxidized surface, but is indicated by electron imaging to be below the value for clean Al. The latter, fortunately, has been measured at room temperature, although no data is available on temperature dependence [2]. Multiphoton photoelectric and field-assisted emission (Schottky effect), which have been neglected, tend to lower the effective work function. Space charge effects, which have also been neglected, tend to limit the electron emission and thus appear to raise the work function. However, due to the pulsed emission and high fields present, the influence of space charge is probably small. In consideration of these uncertainties, the Al curve in figure 12 at best provides an upper limit on the temperature for a given pulse height. A maximum temperature of approximately 2350 K is obtained for a typical peak electron signal of 500 mV.

1. Figures in brackets indicate the literature references at the end of the paper.

Another revealing symptom is the crater profile. Figure 13 compares the profile of a crater produced by a 20 mJ CO_2 pulse with the profile of the laser beam and a model calculation. Integration of the observed profile over the crater volume indicates no net removal of material, i.e., the volume of material in the cusps essentially cancels that in the central hole. Calculation from simple kinetic theory of the amount of material evaporated within the times and temperatures available confirms this result. The conclusion is that the crater is formed by pressure applied to the molten metal, rather than by vaporization or ablation.

Models of laser damage due to the reaction pressure of vaporizing material have been proposed in the literature [3,4]. The calculated surface pressure from vaporization of Al amounts to 0.07 atm at 2350 K. Another source of pressure is the momentum of the radiation itself. This amounts to 0.25 atm at the center of the focused 20 mJ pulse if the radiation is fully absorbed, and up to 0.5 atm if partially reflected. These surprisingly large values are due to the combination of small focal area and short pulse duration. In comparing the relative importance of these two sources of pressure, one must consider the impulse, i.e., the relative times available for the respective pressures to act. A simple calculation indicates that the vapor pressure will fall by an order of magnitude within approximately 20 nsec of the termination of the laser pulse. Assuming that vaporization is suppressed by radiation pressure during the 100 nsec pulse, the time available for the radiation pressure to act dominates. We conclude that if our estimate of maximum temperature is correct, radiation pressure is the major cause of cratering at CO_2 wavelengths.

To demonstrate that the radiation pressure can produce a crater of the type observed, we have modeled the surface profile of a molten pool of Al responding statically to the combined effects of radiation pressure, surface tension, and confinement (figure 13). The boundary of the melt zone is taken as the outside edge of the large cusps in the observed profile. The case depicted corresponds to total absorption of the radiation, which produces a crater of minimum depth. Although it does not accurately represent the dynamical situation, the model strongly suggests that our basic interpretation of the damage morphology is correct.

Although no significant material removal can be detected from crater profiles, the particle collector detects the emission of a small number of ions. Figure 14 shows the collector signal due to positive ions from a sputtered coating at a pulse energy of 15 mJ. Such ion signals are commonly observed at power levels insufficient to produce a visible plasma, and occasionally, even when visible damage is not observed. The most remarkable feature is the high energies of the ions, as indicated by the time-of-flight corresponding to the peaks. Such energies cannot be accounted for by thermal vaporization and definitely indicate the involvement of an electric field. The laser field strengths are commonly in the range of 10^6 V/cm in these experiments, which may be adequate for thermally-assisted field-ion desorption. This is consistent with the magnitude of the ion signals observed near threshold, which commonly correspond to desorption of less than 1% of an atomic monolayer of Al. The possibility that fields developed across the oxide layer may play a significant role must not be overlooked, however, and will be investigated in future work.

8. Summary

A laser damage facility which can provide definitive information on failure modes of damage-resistant materials is now operational. Well-characterized pulsed laser sources combined with well-controlled and comprehensively monitored testing are key features. Damage studies of polished and coated Al surfaces have been made at 10.6 μm with some preliminary testing at 3.8 μm. Damage thresholds of coated surfaces are generally lower than those of polished or machined surfaces, in spite of greater surface purity and uniformity, and higher reflectance. This is attributed to the coating-substrate interface, which acts as a barrier to heat flow. Damage in 1 atm of N_2 is inhibited by gas-breakdown induced by thermionic emission from the sample surface. Dimensions of damage craters obtained in vacuum are in fair agreement with calculated dimensions of the melt zone near threshold, but exceed the calculated dimensions at higher pulse energies. A rough estimate of the maximum surface temperature has been obtained from the electron emission. Based on this estimate and the shape of the crater profiles, the dominant damage mechanism at 10.6 μm is found to be melting, accompanied by displacement of material due to radiation pressure. However, a small amount of material removal has been detected in the form of positive ions.

9. Acknowledgment

The authors are indebted to W. R. Compton for the heat flow calculations. The theoretical aspects of this work and the DF measurements were supported by the Office of Naval Research under Task Area No. RO220202 and the experimental measurements at CO_2 wavelengths by the Naval Air Systems Command under Task Area No. RO2201001.

10. References

[1] Ames, W. F., *Nonlinear Partial Differential Equations in Engineering* (Academic Press, New York, 1965), pp. 158-62.

[2] Riviere, J. C., "Work Function: Measurements and Results," in *Solid State Surface Science*, Vol. 1 (Dekker, New York, 1969), pp. 179-289.

[3] Ready, John F. *Effects of High-Power Laser Radiation* (Academic Press, New York, 1971), pp. 109-14.

[4] Batanov, V. A., F. V. Bunkin, A. M. Prokhorov, and V. B. Fedorov, Soviet Phys. JEPT 36, 311 (1973).

11. Figures

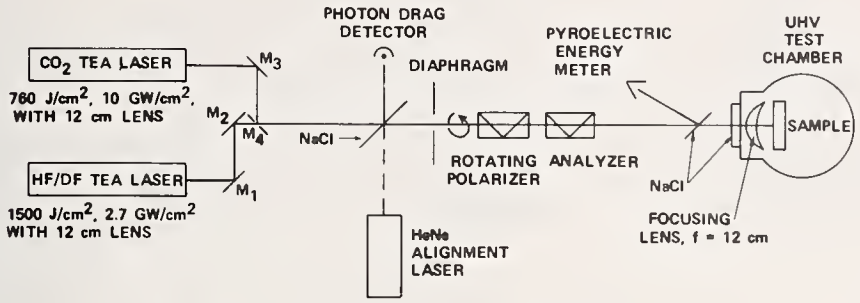

Figure 1. Optical arrangement of laser damage facility, showing TEA lasers, beam line, beam control, and monitoring instrumentation and the test chamber.

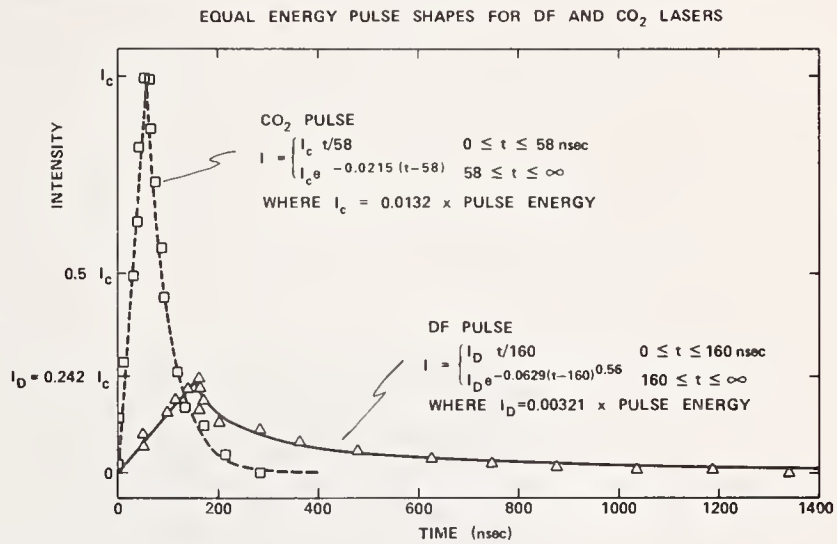

Figure 2. Temporal profiles of output from CO_2 and DF lasers, showing empirically derived functions used for analytical representation of the measured data points.

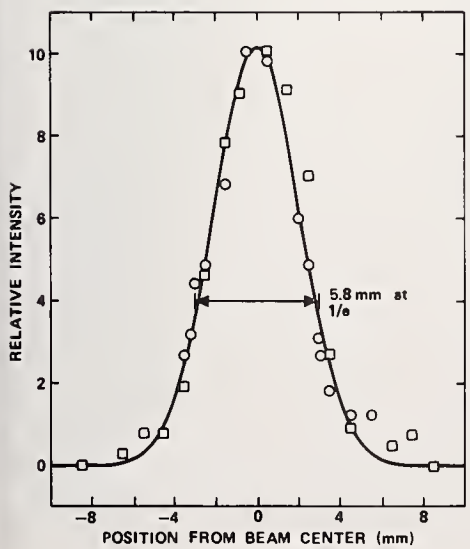

Figure 3. Spatial profile of output from CO_2 laser, showing Gaussian fit to measured data points. Circles and squares indicate profiles measured in two orthogonal planes.

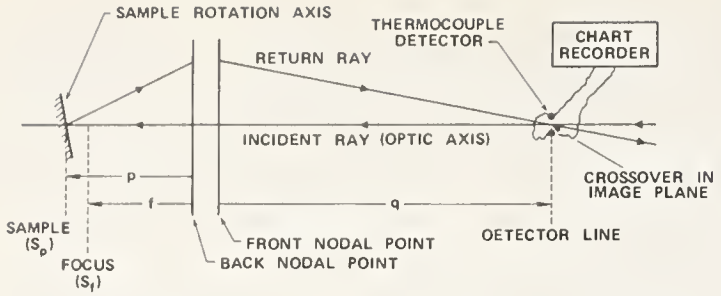

Figure 4. Procedure for focusing the beam on the sample. The detector remains fixed and p is varied until the crossover distance q coincides with the detector line as shown in the figure, using the method outlined in the text. The proper sample-to-lens distance f is then calculated using the lens formula.

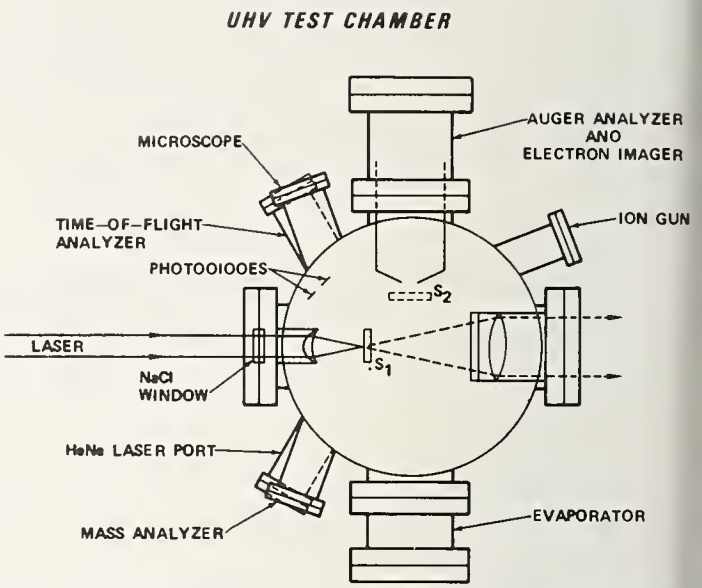

Figure 5. Schematic of the test chamber in its completed form.

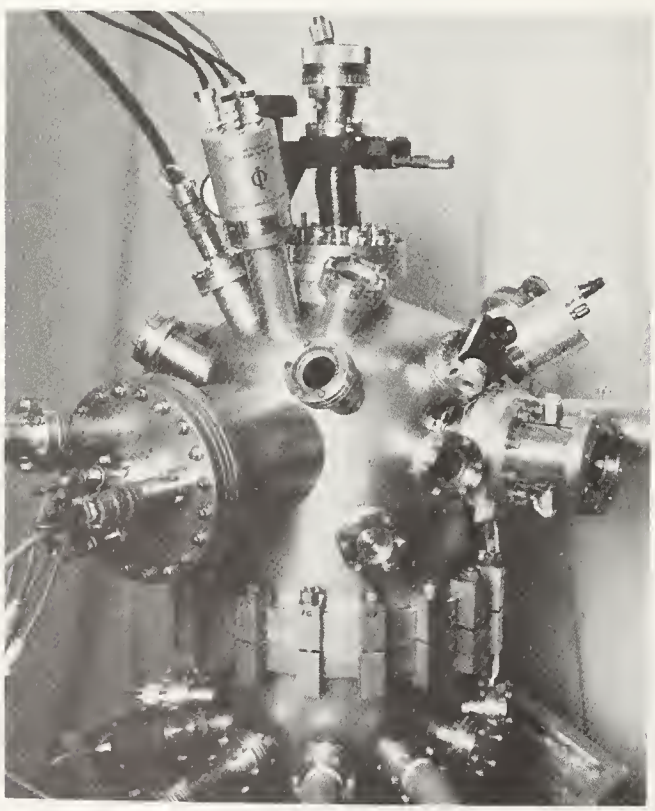

Figure 6. Laser-damage test chamber.

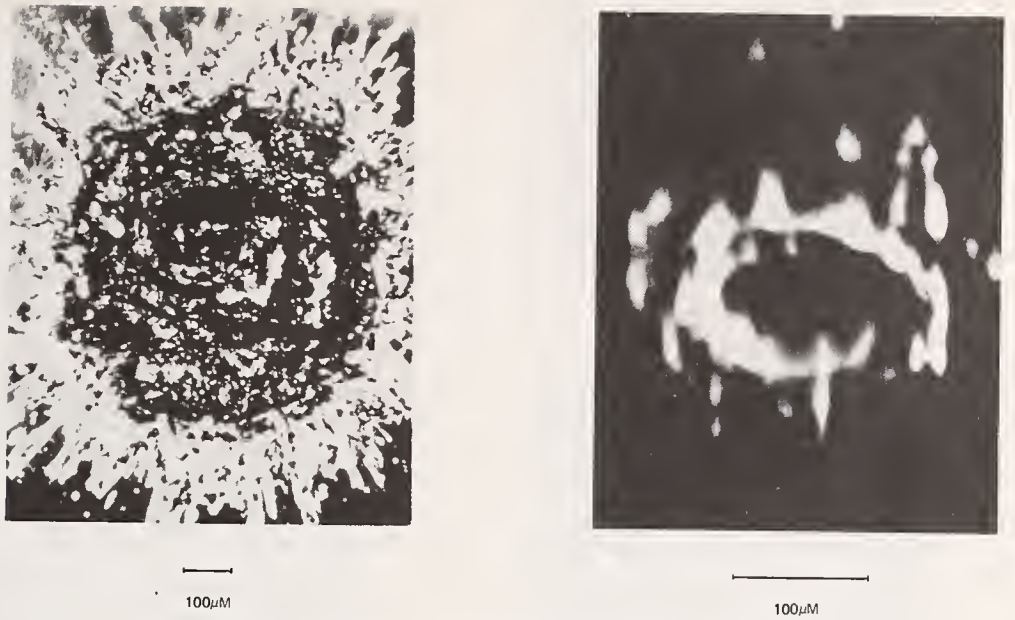

Figure 7. Comparison of Nomarski micrograph of large damage crater (left) with electron image of central portion of the same crater (right).

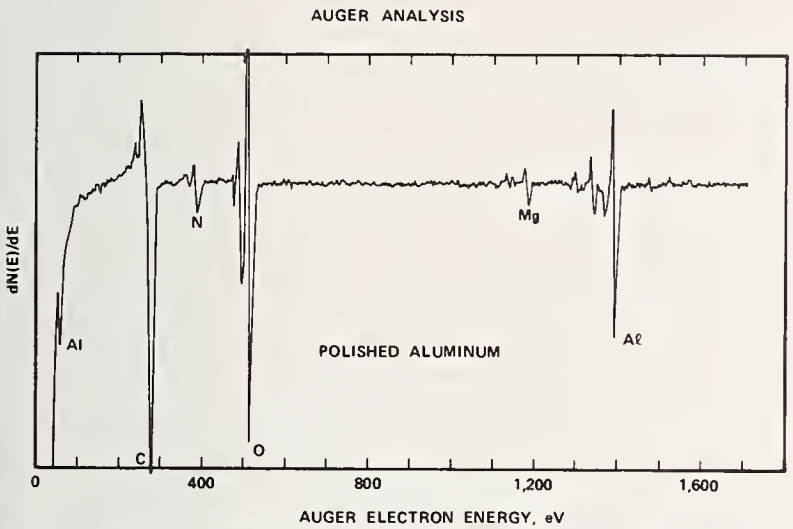

Figure 8(a). Auger spectrum of polished Al surface.

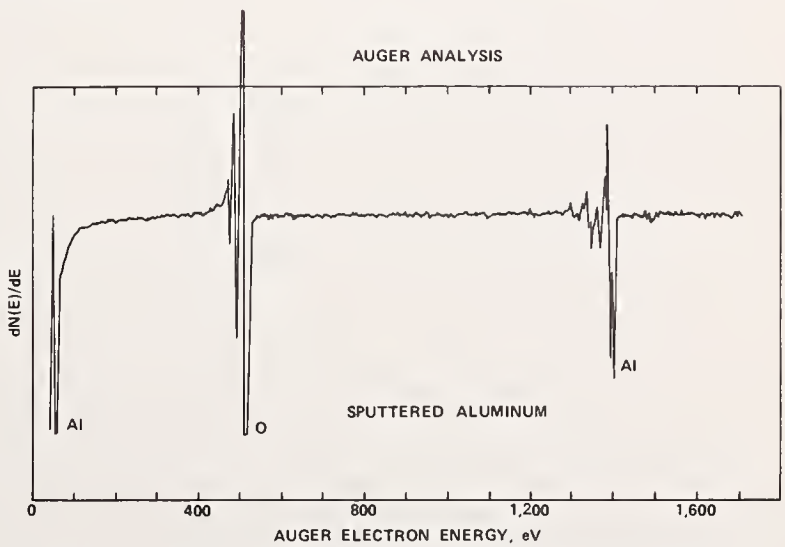

Figure 8(b). Auger spectrum of sputter-deposited Al surface. Note the absence of C, N_2, and M_g, as compared to figure 8(a).

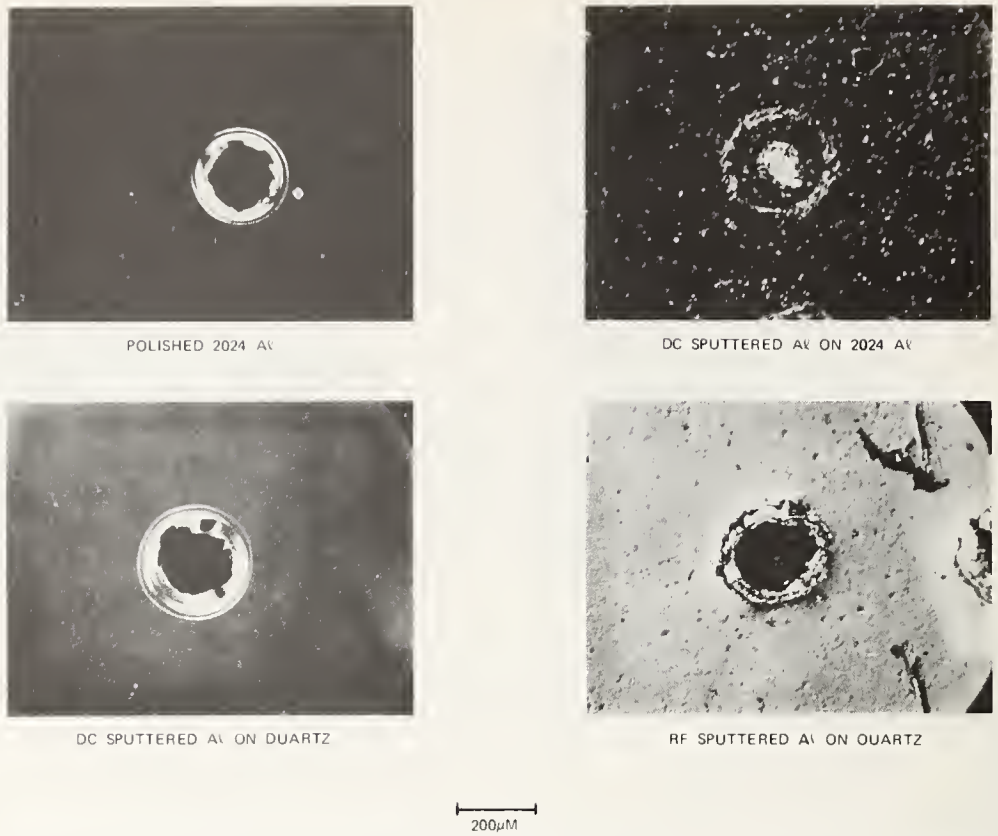

Figure 9. Comparison of damage craters produced on different Al sample types at 10.6 μm.

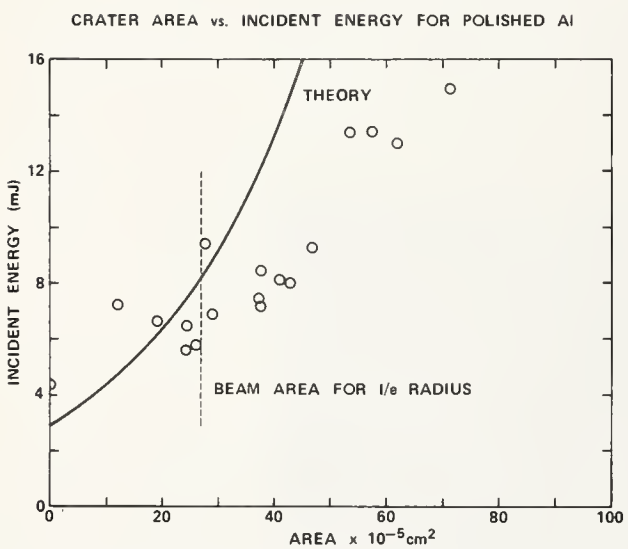

Figure 10. Pulse energy vs. crater area on polished Al at 10.6 μm.

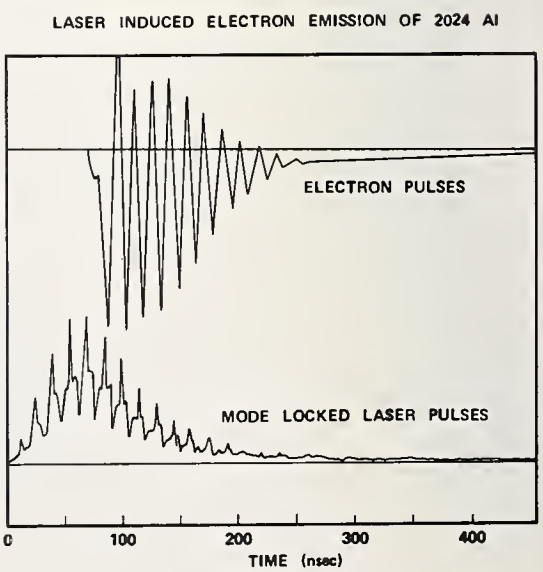

Figure 11. Simultaneous oscilloscope traces of laser-induced electron emission (upper trace) and laser intensity (lower trace). The synchronization of the two traces is not necessarily significant due to possible differences in cabling length from the two signal sources.

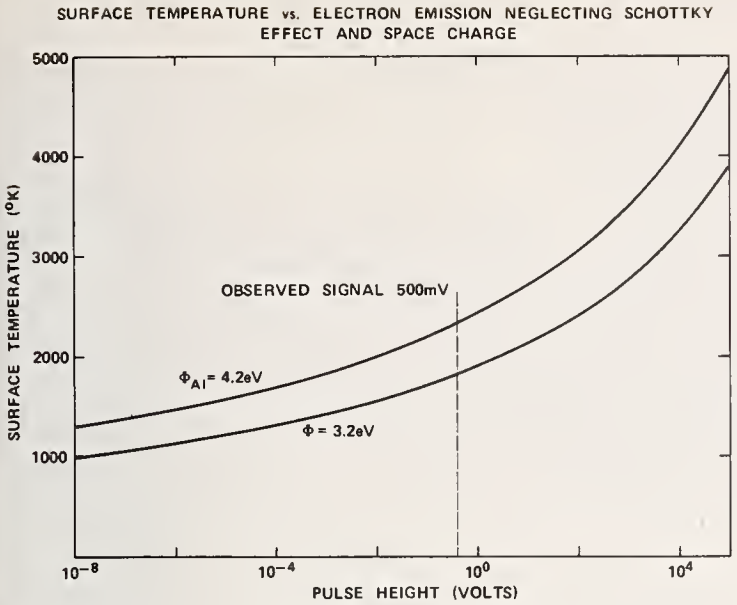

Figure 12. Surface temperature vs. height of laser-induced electron pulses based on thermionic emission and known experimental parameters. The upper curve represents the emission of an unoxidized Al surface (ϕ = 4.2 eV), while the lower curve represents an arbitrary surface with ϕ = 3.2 eV.

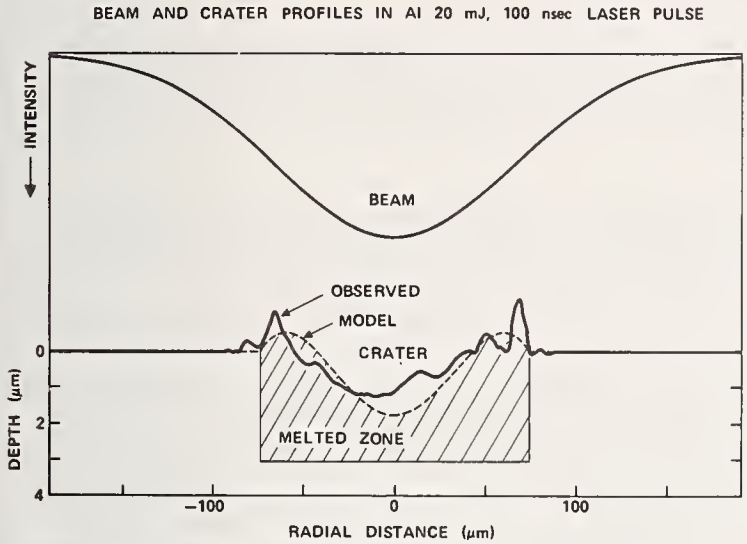

Figure 13. Comparison of beam profile with observed and model profiles of a crater produced in polished Al with a 20 mJ, 100 nsec laser pulse at 10.6 μm. The observed profile was obtained from a profilometer trace. The model profile indicates the combined effects of radiation pressure, surface tension and confinement of the molten metal (uniform pressure) in a static situation.

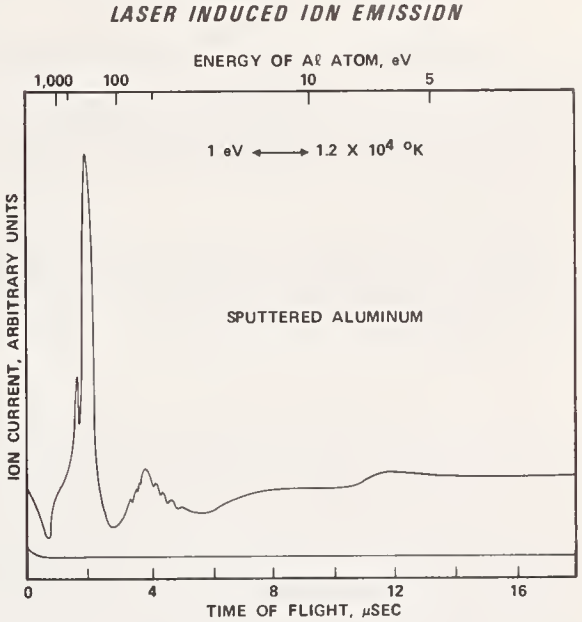

Figure 14. Laser-induced ion emission from a sputter-deposited surface. The energy scale at the top of the figure applies to Al ions having time-of-flight indicated by the scale at the bottom. The lower trace is the intensity of the laser pulse, which is essentially zero after 0.1 μsec.

COMMENTS ON PAPER BY PORTEUS, et al

It was pointed out by Peter Braunlich of the Bendix Research Laboratories that the observation reported in this paper that the work function of bare aluminum is higher than that of the oxide contradicts recent results of Baxter of General Motors Research Laboratories. In Baxter's work the opposite observation was made. No explanation of this discrepancy was available. It was also brought out in the discussion that metals can be expected to remain good reflectors well above the melting point. The theoretical basis for this is the Drude theory which is assumed to apply in the liquid state as well as below the melting point.

5.1 Single and Multilongitudinal Mode Damage in Multilayer Reflectors at 10.6 μm as a Function of Spot Size and Pulse Duration*

V. Wang, C.R. Giuliano, and B. Garcia

Hughes Research Laboratories
3011 Malibu Canyon Road
Malibu, California 90265

An extensive series of measurements was carried out upon several high reflectivity multilayer dielectric ($ZnSe/ThF_4$) enhanced reflectors (typically 99.8%) using a CO_2 TEA laser. Measurements were made using smooth single longitudinal mode pulses, partially modelocked multilongitudinal mode pulses, and a range of pulse lengths extending from 0.6 μs to 6 μs. Studies were conducted at spot size diameters ranging from 50 μm to 255 μm. It is observed that damage thresholds are independent of pulse duration or pulse temporal shape (energy dependent) and evidence is presented that the damage is caused by inclusions, and that the average separation of inclusions, their absorption, and the film absorption can be inferred. A defect-limited damage threshold (90 J/cm^2) and a lower limit to the defect-free threshold (4.4 kJ/cm^2) for the film is established.

Key words: Absorbing inclusions; damage statistics; laser damage; reflectors; 10.6 μm; thin film; ThF_4; ZnSe

Introduction

Previous papers [1-3][1] have reported on the development of enhanced multilayer dielectric mirrors. The goal was to develop multilayer dielectric coating materials and deposition techniques in order to reproducibly fabricate enhanced metallic reflectors with minimum absorptance at a wavelength of 10.6 μm and maximum resistance to damage from CO_2 laser irradiation. The measurement of damage threshold on these reflectors as a function of beam focal spot size, pulse length, and pulse shape are reported here.

Interpretation of the experimental data allows extrapolation of the damage properties of these reflectors to large-scale beams and longer pulses than those employed in the damage experiments described here.

Experimental Conditions

The experimental setup for the laser used in this experiment is shown in figure 1. The pulsed laser used to perform these damage threshold measurements has been refined for more than 2 years for this purpose. The uv preionized CO_2 TEA laser typically yields 200 mJ at a pressure of 550 Torr from a 50 cm x 5 cm x 2.5 cm transverse discharge. A 2.5 m approximately hemiconfocal cavity, an uncoated Ge resonant output reflector, and an adjustable aperture set at about 1.2 cm selects the TEM_{00} mode while providing an essentially untruncated output. An intracavity longitudinal mode selector consisting of a 1 m low pressure longitudinal discharge tube installed between the high pressure transverse discharge and the output coupler provides a single longitudinal mode smooth output of 175 mJ with no mode beating evident, and also serves to suppress the initial gain-switched spike characteristic of TEA lasers [4]. A beam attenuator consisting of two wire grid polarizers on ZnSe substrates allows attenuation without rotation of the output polarization [5]. Wedged NaCl beamsplitters allow monitoring of the energy in each pulse by a polyvinylfluoride (PVF) pyroelectric detector. Absolute calibration of the pyroelectric monitor is provided by a Hadron Model 100 cone thermopile with a 1 cm aperture.

Tests are conducted in an evacuated sample chamber (~20 mTorr) to eliminate extraneous effects from dust and air breakdown. The sample is mounted on a translator at the focal point of the Ge focusing lens and observed through an off-axis 50x microscope. The appearance of any microscopic visible lesion in the film is regarded as an indication of damage threshold.

By control of the transverse discharge, variation of the gas mixture and total pressure, and operation of the low pressure discharge for longitudinal mode control, four types of pulses could be selected. These are shown in figure 2. The basic pulse consists of a typical TEA laser gain-switched partially mode-locked pulse as used previously [1-3] with an equivalent pulse length of 0.6 μs. (The equivalent pulse length is defined by integrating the area under a pulse and defining a rectangular pulse of equal area and of height equal to the peak of the pulse. For rapidly modulated mode-locked pulses the modulation is averaged. Power density is obtained by dividing the energy density by the equivalent pulse length.) A pulse consisting of a 1 μs single longitudinal mode pulse followed by a

*Work supported by Air Force Weapons Laboratory, Kirtland Air Force Base, New Mexico under Contract No. F29601-74-C-0060.

1. Figures in brackets indicate the literature references at the end of the paper.

tail (equivalent pulse length of 1.9 μs), a 4 μs equivalent pulse length gain-switched pulse, and a 6 μs single longitudinal mode pulse are available by modifications to the laser parameters and operation of the low pressure CO_2 discharge section.

No provisions for rotational line control are included in the laser and preliminary measurements indicate the possibility of multiple rotational line operation during the gain-switched modes of operation.

A near diffraction-limited beam is available and the focal spot sizes are measured at the beam waist by the method discussed in [6]. These results are tabulated in table 1.

Table 1. Ratio of Measured-to-Calculated Spot Size

Lens f.l., cm	Maximum rms Wavefront Aberration, λ	Spot Size,[a] μm		Measured/Calculated Ratio
		Calculated Diffraction Limit	Measured Spot Size	
3.81	0.13	37	50	1.35
6.35	0.025	61	72	1.18
12.7	0.036	123	140	1.14
25.4	(nil)	246	255	1.04

[a] e^{-1} diameter for intensity, 2δ.

Summary of Laser Performance

Control of a large number of operating parameters of the laser has been necessary to achieve the present output, pulse length, and pulse shape. Some relevant changes which improved those desirable aspects of the laser output include electrical pump pulse shape and duration, electrode profile and spacing, gas mixture and pressure (especially CO_2 fraction and the addition of H_2), and a modest increase in mirror radius.

In its final form this system has allowed us for the first time

- To study the influence pulse length over a 10:1 range
- To compare the effect of pulse modulation and the high instantaneous power in a gain-switched mode-locked pulse with a smooth single longitudinal mode pulse of easily characterized instantaneous intensity
- To compare the effect of beam spot size upon damage threshold over a range of five to one.

To our knowledge, this is the first time a single transverse mode CO_2 TEA laser has been used to study laser damage with a variable pulse length and single longitudinal mode control. It also represents the first study of spot size on damage threshold at 10.6 μm.

Threshold Measurement Procedure

From time to time evidence arises suggesting that the damage resistance of a particular region of a material may be affected by its past history of laser irradiation. This type of effect which has been reported previously [2], but has not been studied in great detail can result in either positive or negative conditioning. Generally, the kinds of conditioning effects observed are positive; i.e., the level at which irreversible damage occurs is higher if the irradiated region is subjected to a number of pulses of relatively low intensity prior to the damaging pulse than it would be if the site had never been previously irradiated at some relatively low level that is believed to be insufficient to cause damage.

In an attempt to determine whether significant conditioning occurs a specific threshold measurement sequence was employed as follows. A sample site is irradiated in steps increasing by ~15% until damage is observed. The threshold value obtained in this manner is referred to as the multiple-shot threshold. Following the observation of damage at a given site the beam is relocated to a fresh region and the sample is irradiated again, this time with a pulse that is 15 to 30% less intense than the one that was previously seen to cause damage in the adjacent site. If damage then occurs at the new site, the sample is moved again to a new site and the power reduced still further. This procedure

continues until no damage is found at which time the power is then increased at the same site until damage occurs. This is referred to as the single-shot damage threshold.

Hence some sites are subjected to a number of nondamaging pulses prior to damage and others are damaged on a single shot. Figure 3 illustrates schematically an idealized sequence of measurements that might be taken for two kinds of samples, one which shows a well defined threshold and another which shows a marked positive conditioning effect.

Fabrication of Multilayer Reflector Samples

Because the goals of the program included the need to generate reflectors having the highest possible damage threshold, good environmental stability, and good adherence so that the resulting mirrors could be easily cleaned, materials meeting these rigid demands had to be found.

The materials presently available that are suitable for use in low absorptance coatings at 10.6 μm are very limited. Thorium tetrafluoride and ZnSe have proved to be some of the best candidates for this work. Therefore, the ThF_4/ZnSe system was selected for concentrated effort because of its potential for meeting all the goals. These dielectric materials were deposited directly on polished molybdenum mirror blanks. Earlier emphasis was placed on the ability to prepare reproducible ThF_4 films with minimal absorption. Film layers having lower absorption than previously realized had to be synthesized and applied in stable configurations involving a minimum of six to eight layers to achieve the goals of the program. Minimization of the number of layers was important since the physical thicknesses required at 10.6 μm (1 to 2 μm) are an order of magnitude larger than those used at visible wavelengths, and many films of this thickness tend to develop texture, surface roughness, and cracks because of strain and expansion coefficient differentials.

This minimization of layers is realized through maximization of the difference in refractive index between the dielectric materials employed in the alternate layers and also through maximization of the reflectivity of the surface of the metal substrate. During the course of this experimental effort, the reflectance of many Mo blanks were measured. The range observed was 97.8 to 98.8%.

Considerable effort was expended to control the starting materials used for coating. Deposition techniques were also found to be essential for the preparation of the high reflectance, low absorptance, damage resistant mirrors. All depositions were done in a Balzers 510 vacuum system.

Determination of Absorption Index of Dielectric Films

We feel the first consideration in the development of multilayer designs is to determine the absorption indices in single layer films of quarter-wave or half-wave optical thickness. This is done prior to the fabrication of enhanced metallic reflectors.

ThF_4

With the rapid development of damage-resistant high-index materials of low absorption, the absorption coefficient of ThF_4 became the limiting factor in achieving lower loss coatings and also the limiting factor in the damage resistance of low absorptance designs. Absorption index values of this material can be improved substantially by elimination of the effects of water vapor and other contaminants. The purity of the starting material is also essential for improved damage resistance. In past work experimental results with reflector systems were poor as a result of difficulty with the ThF_4 starting material. To meet the goals of the program the best starting material had to be found. Three different sources of ThF_4 were evaluated, and the results are summarized in table 2.

Table 2. ThF_4 Evaluation

Run Number	ThF_4 Source	ThF_4 Absorption Coefficient, cm^{-1}
4-4-74	Poly-Research Pressed Powder	16.6 to 20.7
4-18-74	Cerac Inc. TS-108	11.5
4-23-74	HRL Crystal Chunks	16.6

The ThF_4 absorption coefficient (cm^{-1}) values in the table above are a factor of 3 to 4 higher than needed to fabricate 99.9% reflectors routinely. Since the HRL crystal chunk material is known to be free of major impurities and has produced consistently good results in the past, the deposition conditions were suspect rather than the starting materials. The Poly-Research pressed powder had a dirty exterior appearance and black residue was left in the source after each deposition. The material was considered inferior and was eliminated from further consideration.

To lower the ThF_4 absorption index values, work was begun to find methods of eliminating residual water during deposition. Lower ultimate base pressures in the vacuum system became of prime importance for the elimination of suspected residual water. Long-term pumpdowns became a necessity. With these long-term pumpdowns, pressure ranges of 6 to 7 x 10^{-8} Torr were achieved. Typical system pressures after a run were 2 to 3 x 10^{-7} Torr. An extensive series of experiments showed that another important variable in controlling the water content, and thus the 10.6 μm absorption of deposited ThF_4 films, is substrate temperature. The optimum temperature is 150°C. With the lower base pressures and the optimum substrate temperatures the minimum absorption coefficients in the films were found to be near 1 cm^{-1}. With absorption coefficients in this range multilayer work could continue.

ZnSe

To determine the absorption in the ZnSe film material, a number of film deposition runs were made in which quarter wavelength films were deposited on KCl substrates. The ZnSe source material (Raytheon CVD) produced films that had too small an absorption to distinguish from the KCl substrate. The upper limit on the ZnSe film absorption index which this implies is 0.6 cm^{-1}. An absorption coefficient of this order is considered excellent, and no problem was foreseen with the use of this material.

Coating Techniques

During the course of this experimental effort, the objective was to prepare films which might be incorporated in low absorptance coatings, compatible with each other, and finally compatible with molybdenum mirror blanks. All of these requirements were met by ThF_4 and ZnSe.

ThF_4 Films

The deposition technique used for this material was evaporation by a resistance-heated tantalum box source. Typical deposition rates were 6300 Å/min.

ZnSe Films

The deposition technique used for this material was evaporation by a resistant-heated molybdenum source with an aluminum oxide crucible insert. There was no advantage in depositing this material onto an elevated temperature substrate. The absorption index would remain the same regardless of temperature. However, all films were deposited at elevated temperatures (150°C) because this parameter was needed for the ThF_4 films. Typical deposition rates were 7700 Å/min.

This experimental effort came to a successful completion with the fabrication of reflectors on the Mo mirrors with 99.92 and 99.93% reflectance. Reflectors with the same design have been shown previously to have pulsed CO_2 laser damage thresholds in localized areas more than twice as high as the best metal mirrors; with reduced absorption, particularly of the ThF_4 material, even higher damage thresholds might be expected. At the reflectance levels now attainable it is possible to consider the use of uncooled reflectors in many applications where water-cooled reflectors had previously been used.

Experimental Results

Damage Measurements for Different Pulse Durations

One of the means by which different types of damage mechanisms can be distinguished is by the performance of damage threshold measurements for pulses of different duration. A typical set of data is presented in table 3 for a single thorium fluoride-zinc selenide dielectric enhanced reflector on a silver overcoated molybdenum substrate surface. Although there is a wide range of values over which damage occurs,the ranges for this sample overlap substantially for the different pulse lengths employed, indicating essentially a constant energy density damage threshold. A constant energy density threshold was also observed for the other samples having the same coating design as that for which data are presented in table 3.

NOTE: 1 torr = $\frac{101\ 325}{760}$ Pa.

Table 3. Reflector Mo AM-56 Mo/Ag /$(ThF_4/ZnSe)^4$

Absorption = 0.30%
Spot Size = 140 μm diameter

4209-15

	DAMAGE THRESHOLD			
	0.6 μs MODE-LOCKED	1 μs SINGLE LONGITUDINAL MODE	4 μs MODE-LOCKED	6 μs SINGLE LONGITUDINAL MODE
MULTIPLE SHOT THRESHOLD	50-290 J/cm^2 80-480 MW/cm^2	110-460 J/cm^2 110-460 MW/cm^2	110-200 J/cm^2 17-70 MW/cm^2	70-290 J/cm^2 28-40 MW/cm^2
SINGLE SHOT THRESHOLD	15-75 J/cm^2 25-125 MW/cm^2	~70 J/cm^2 ~70 MW/cm^2	(70-110 J/cm^2) (17-275 MW/cm^2)	(50-90 J/cm^2) (8-15 MW/ cm^2)

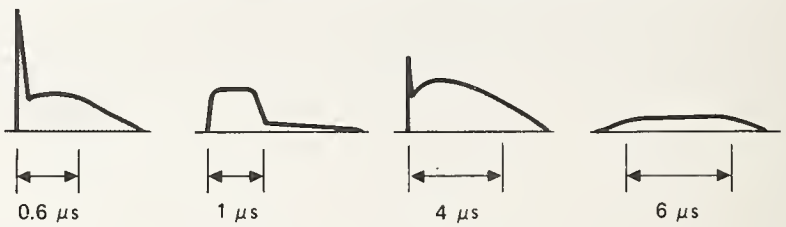

This observation of a constant energy density threshold over a range of different pulse durations is consistent with two different interpretations that involve a thermal damage mechanism.

1. The light is absorbed in a uniformly lossy film that is essentially being heated uniformly throughout during the time of the laser pulse. Damage then occurs when the film reaches some critical temperature (e.g., melting point). This case would also apply to a film that has local defects or inclusions that are small and so close together than the thermal diffusion length is comparable to the mean defect spacing.

2. The damage is caused by the heating of a local defect or inclusion that is essentially uniformly heated throughout its volume during the time of the irradiating pulse and during which time its rate of heat loss to the surrounding host material is negligibly small.

The constant energy density threshold, combined with the data for different spot sizes presented, next suggest that mechanism 2 is the more likely choice.

From the work of Duthler and Sparks [7] it is possible using a few simple assumptions to obtain limits on the sizes of defects or absorbing inclusions responsible for the damage in the mirrors studied.

The following expressions are taken from [7]. The approximate time required for heat to diffuse from the inclusion surface to the center is

$$\tau = 4\, C_I\, a^2/9\pi K_I \quad . \tag{1}$$

The approximate time required for heat to diffuse from the inclusion into the host is

$$\tau_H = C_H a^2/3K_H\eta \quad , \tag{2}$$

where a is the inclusion radius, C and K are heat capacity and thermal conductivity, respectively, and η represents a thermal coupling efficiency between the inclusion and the host.

The constant energy density threshold is equivalent to the expression

$$\tau_a \ll t_p \ll \tau_H \quad , \tag{3}$$

where t_p is the laser pulse duration. Statement (3) must be valid over the range of pulses employed in the damage experiments, 0.6 to 6 μs.

Using the above considerations one can derive an expression for the range of inclusion radii

$$\frac{3K_H \eta t_2}{C_H} \ll a^2 \ll \frac{9\pi K_I t_1}{4C_I} \quad , \tag{4}$$

where t_1 and t_2 are the lower and upper extremes of pulse durations over which the constant energy density threshold is observed, 0.6 and 6 μs, respectively.

Taking values of $K_H/C_H \sim 0.04$ cm^2/s and $K_I/C_I \sim 1$ cm^2/s, typical of dielectrics (ThF_4) and metals (Cu), respectively, and a value of $\eta \sim 0.1$, we obtain 2.7 μm $\ll a \ll$ 21 μm.

It should be pointed out that the limits obtained for the inclusion radii from (4) are only to be taken as approximations and are given as an indication of the kind of data available from pulse duration damage studies in these types of materials. In fact, the value taken for η which determines a lower limit for a is at best an order of magnitude estimate. A value for η of 0.01 would extend the low end and widen the range to 0.85 μm $\ll a \ll$ 21 μm. It should also be pointed out that the wide range of possible values for inclusion radii indicates only that particles within this range will behave with a constant energy density threshold over the pulse durations studied, and should not be interpreted to mean that the films actually contain inclusions having this wide a range of radii. In fact, because of the lack of obvious inclusions on microscopic inspection of these films, the low scattering, and thickness of the individual layers, it is likely that the defects are very small, of the order of 1 μm or less.

The value of the defect dominated damage threshold obtained next and the modeling of inclusion heating dynamics developed in [2] both support the thesis that the inclusion defects are limited to a relatively small range of sizes of the order of 1 μm. The presence of a large range of inclusion sizes should imply an observable pulse length dependence, rather than a constant energy density threshold. The damage morphology for these reflectors is shown in figures 4 and 5.

The Effect of Spot Size Upon Damage

It has been long recognized that the apparent damage threshold of many materials changes with the diameter of the illuminating beam [8]. The difficulty in obtaining a diffraction limited focus increases with more tightly focused beams, as well as the difficulty in finding the beam waist, measuring the spot size, and detecting damage threshold. However, beyond these effects there still can exist a marked increase in damage threshold for small beams when there is a random distribution of defects or localized absorption sites. For example, if a very tightly focused laser beam is used, and defects or inclusions are small and spaced far apart in comparison, then the preponderance of damage thresholds would register the intrinsic threshold. Conversely, a large beam of uniform illumination would be expected to cause damage at the weakest defect or inclusion. The damage threshold with large beams, whether due to some intrinsic property of the material, or due to localized weaknesses, is sharp and deterministic. Small tightly focused beams might tend to have large fluctuations in damage threshold, whether from inherent statistical mechanisms or from randomly scattered localized weaknesses. Since the present multilayer dielectric reflectors show statistical variation in damage threshold with the spot sizes we have used indicating an inclusion/defect spacing comparable to the beam size, a study of the spot size dependence has been made to better characterize the defect limited damage threshold and the damage threshold obtained in regions that are free of defects, referred to here as the "intrinsic" film threshold.

Seven similar 6- and 8-layer ThF_4/ZnSe reflectors have been tested at four focal lengths, of 3.81 cm, 6.35 cm, 12.7 cm, and 25.4 cm, which gave measured spot sizes of 50 μm, 72 μm, 140 μm, and 255 μm, respectively. These tests were performed using a smooth 6 μs single longitudinal mode pulse.

The results of several thousand test shots on these reflectors is presented in figure 6. The energy density for threshold is plotted versus the size of the illuminating spot. The spot size 2δ is the diameter at the e^{-1} intensity points of the illuminating beam and the energy density is the on-axis value obtained by dividing the total energy by $\pi\delta^2$. The data from these seven reflectors are combined in figure 7 where the standard deviation σ, the mean, and the extremes are shown.

Using the expressions developed in [8] (shown in figure 7) by DeShazer and coworkers, we can derive an average inclusion spacing d_o from the curve drawn through these data. Using 90 J/cm^2 as

the defect limited threshold and 4.4 kJ/cm^2, the highest threshold recorded for the "intrinsic" film threshold, we arrive at an average inclusion spacing of d_o = 25 μm.

Coincidentally, this value is similar to values found in thin films of ZnS, MgF_2, ZrO_2, and TiO_2/SiO_2 by DeShazer. However, the ratio of "intrinsic" to defect-limited damage threshold for these systems is about 50, as compared with the value of 3 assumed by DeShazer.

"Unconditioned" single shot damage data are summarized for the same seven reflectors in figure 8. These data give similar but lower results with

$$I_i = 1.35 \text{ kJ/cm}^2$$

$$I_d = 40 \text{ J/cm}^2$$

$$d_o = 28 \text{ μm} .$$

Several assumptions, which are only approximately true, are implicit in the expression in figure 7. First, a Poisson distribution of point defects is assumed by the expression, whereas other evidence seems to indicate particles with a size not very far removed from the mean spacing. Second, it is assumed that each defect possesses the same damage threshold. Third, a two-dimensional sheet of particles is assumed, whereas the actual sample is a three-dimensional stack of films. A situation could be encountered where the beam encounters no defects at the first maximum in field (at the outermost interface of high and low index films), but fails to damage a defect several layers below which happens to be below the inclusion damage threshold. A subsequent shot at a higher flux level damages this imbedded inclusion. This would give the effect of defects with a range of damage thresholds. Thus, the interpretation of the spot size statistics used here is only semiquantitatively correct; the inclusion spacing should be viewed as an approximation, but the two limiting thresholds should remain correct.

In the limiting case where the mean inclusion spacing is very large compared with the beam diameter (a situation that hopefully will be achieved as mirror technology advances for 10.6 μm reflectors), the distribution of measured thresholds would be expected to cluster about the two extreme values given by either the intrinsic or the inclusion-limited damage thresholds.

Summary

Variations of pulse length, pulse shape, and spot size have led to a model where these multilayer dielectric reflectors are limited in both absorption and damage threshold by the presence of localized absorbing defects. The damage threshold for pulses typical of e-beam TEA lasers is expected to be about 90 J/cm^2 for large beams. This threshold is apparently independent of pulse length and the usual variations in pulse temporal shape over the range 0.6 to 6 μs tested here.

The pulse length study, together with absorption measurements, suggests that the local defects are possibly metallic, highly absorbing particles of ~1 μm in radius. This is consistent with an observed threshold of ~90 J/cm^2. The measurements of damage threshold as a function of spot size indicate that the mean defect/inclusion spacing is 25 to 30 μm.

The intrinsic limitation of these films is expected to be as high as 4400 J/cm^2, and perhaps limited by only linear absorption in the ThF_4 or ZnSe.

Acknowledgments

The authors wish to acknowledge helpful technical discussions with A. Braunstein and M. Braunstein. The skilled technical assistance of T.E. Horne in construction of the apparatus and in taking damage threshold measurements is acknowledged as is the assistance of Donald Williams in fabrication of the multilayer samples.

References

[1] Wang, V., Braunstein, A.I., Braunstein, M. and Wada, J.Y., "Investigations of Pulsed CO_2 Laser Damage of Metal and Dielectric-Coated Mirrors," Proceedings Laser Induced Damage in Optical Materials: NBS Spec. Pub. 372 (1972).

[2] Braunstein, A.E., Wang, V., Braunstein, M., Rudisill, J.E., and Wada, J.Y., "Pulsed CO_2 Laser Damage Studies of Windows and Window Coatings," and Wang, V., Braunstein, A., Braunstein, M., Rudisill, J.E., and Wada, J.Y., "Pulsed CO_2 Laser Damage Studies of Metal and Dielectric Coated Mirrors," Proceedings Laser Induced Damage in Optical Materials: NBS Spec. Pub. 387 (1973).

[3] Wang, V., Rudisill, J.E., Giuliano, C.R., Braunstein, M., and Braunstein, A., "Pulsed CO_2 Laser Damage in Windows, Reflectors, and Coatings," proceedings Laser Induced Damage in Optical Materials: NBS Spec. Pub. 414 (1974).

[4] Gondhalekar, A., Heckenberg, N.R., and Holzhauer, E., "The Mechanism of Single-Frequency Operation of the Hybrid-CO_2 Laser," J. Quantum Electron. QE-11, 3 (1975).

[5] Garvin, H.L. and Kiefer, J.E., "Wire-Grid Polarizers for 10.6 μm Radiation," presented at IEEE/OSA CLEA Conference May 30 - June 1, 1973, Washington, D.C.

[6] C.R. Giuliano, and D.Y. Tseng, "Damage in Lithium Iodate With and Without Second Harmonic Generation," p. 84, proceedings from Symposium on Laser Damage, NBS Spec. Pub. 387 (1973).

[7] Duthler, C.J. and Sparks, J., "Theory of Material Failure in Crystals Containing Infrared Absorbing Inclusions," Proceedings of a Symposium Sponsored by Office of Naval Research, May 15-16, 1973, Boulder, Colorado, NBS Spec. Pub. 387.

[8] DeShazer, L.G., Newnam, B.E., and Leung, K.M., "The Role of Coating Defects in Laser-Induced Damage to Thin Films," Laser Induced Damage in Optical Materials: NBS Spec. Pub. 387 (1973).

Figures

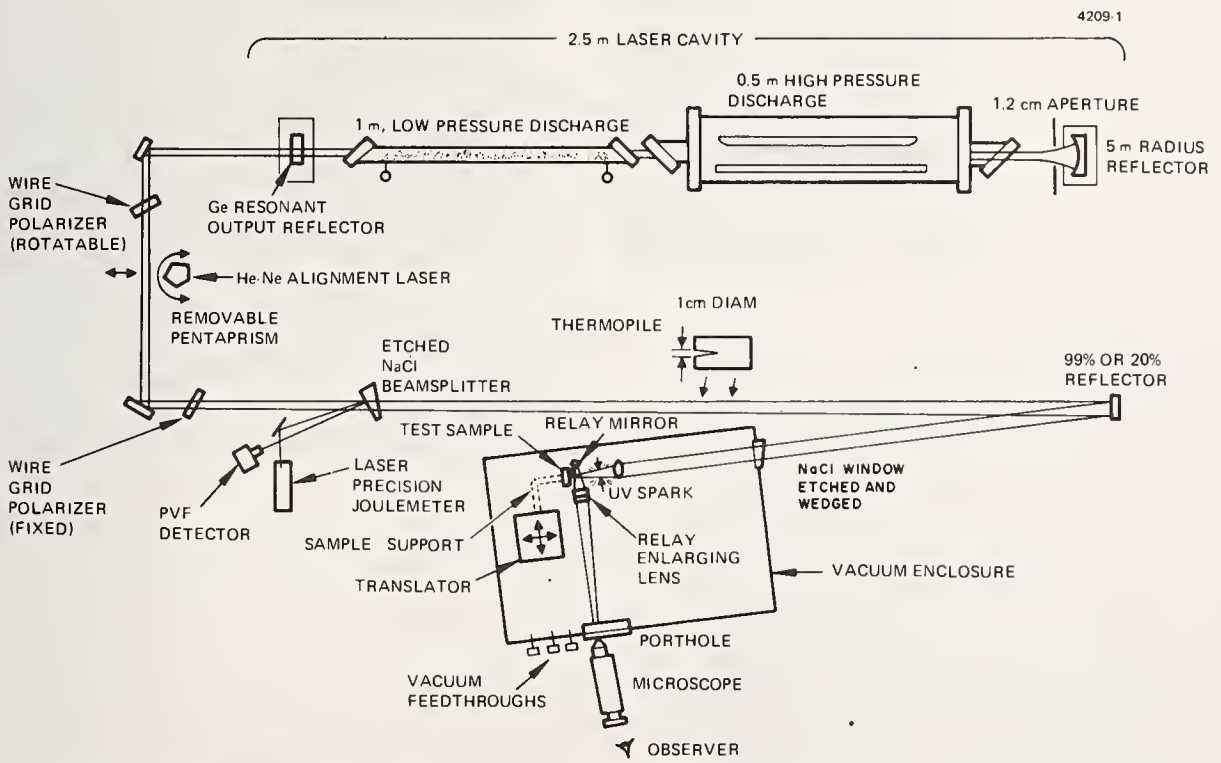

Figure 1. Schematic of laser, optical cavity, optical train, attenuators, detectors, alignment system, and sample chamber with microscope and focusing lens.

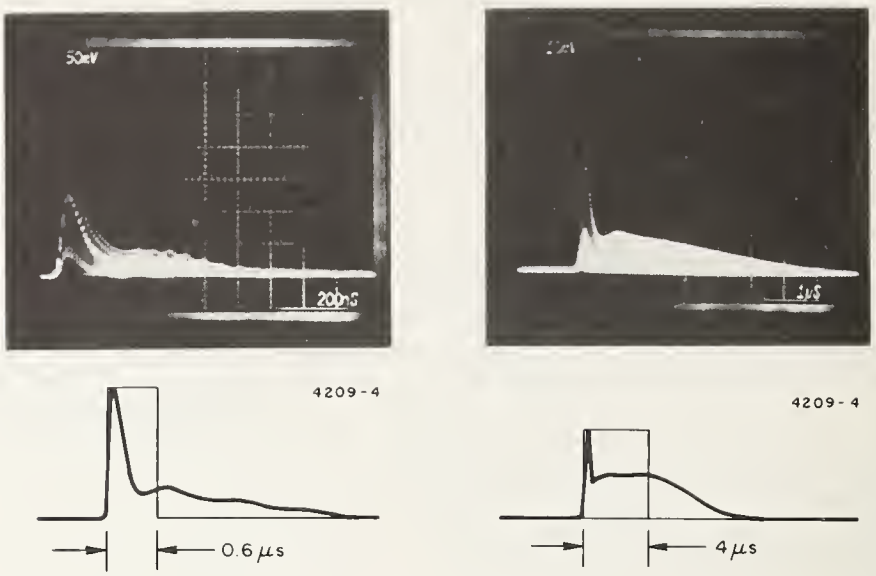

Multilongitudinal mode pulses

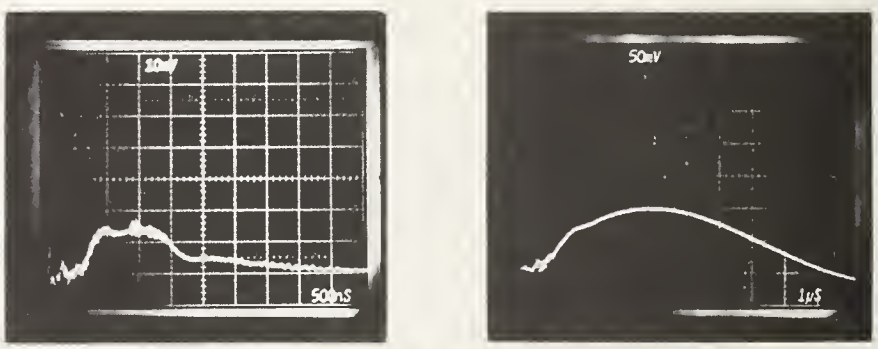

1.9 μs

6 μs

Single longitudinal mode pulses

Figure 2. Oscilloscope traces of the four types of pulses used.

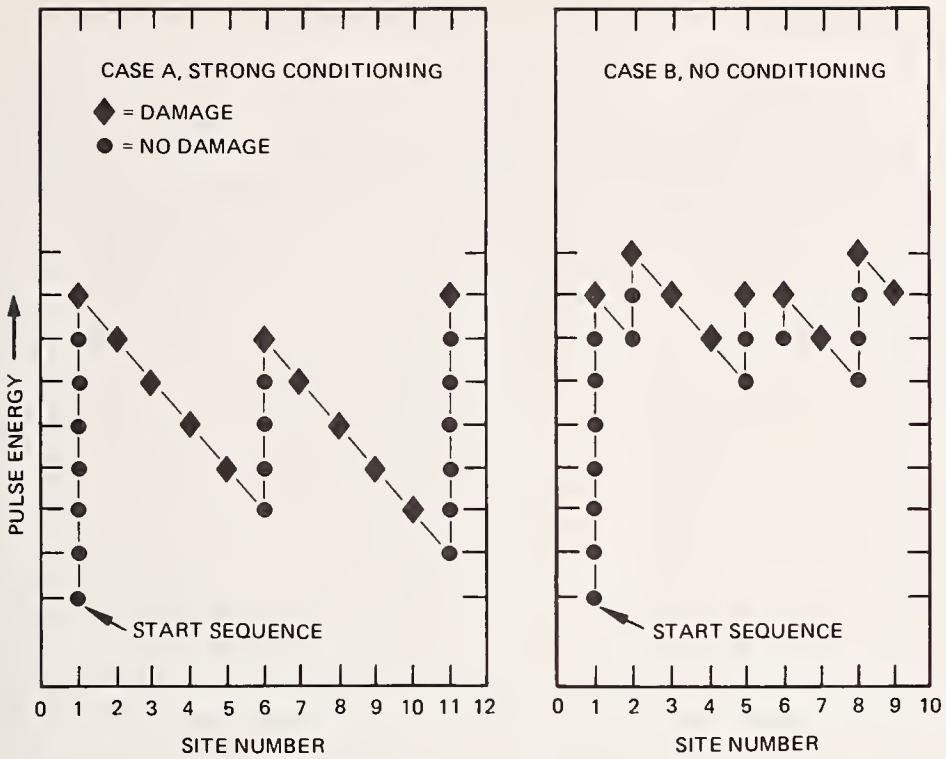

Figure 3. Sequence for irradiating sample sites. Case A, strong "conditioning." Case B, no "conditioning."

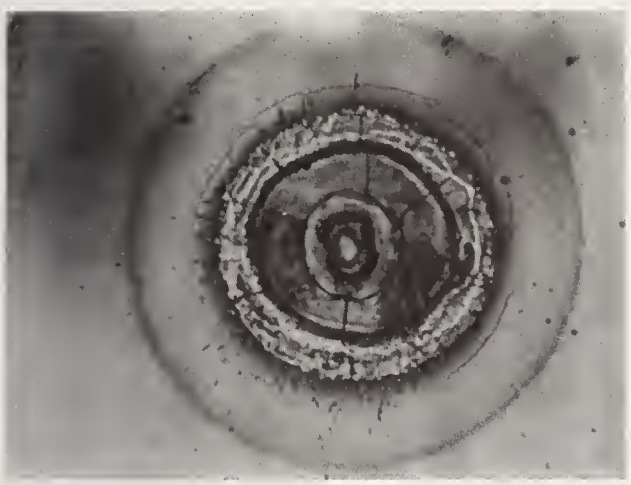

Figure 4. Damage in No. AM-57 Mo/Ag/$(ThF_4/ZnSe)^4$, 1300 J/cm^2, pulse length is 6 μs, single longitudinal mode, 50 μm beam diameter.

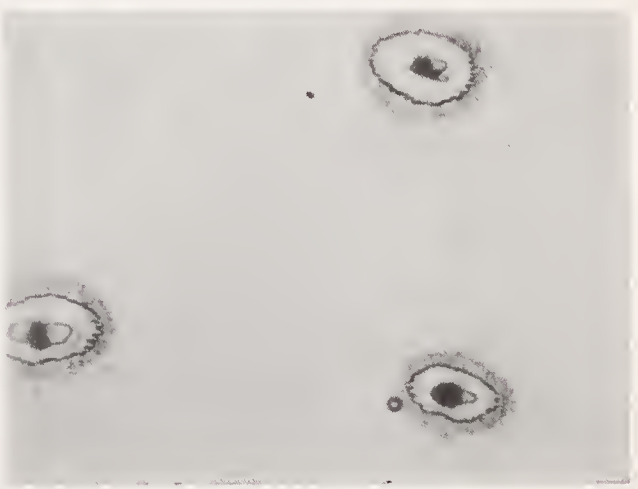

Figure 5. Damage in sample Mo AM-57, Mo/Ag/$(ThF_4/ZnSe)^4$, 70 J/cm^2, pulse length is 6 μs, single longitudinal mode, 255 μm beam diameter.

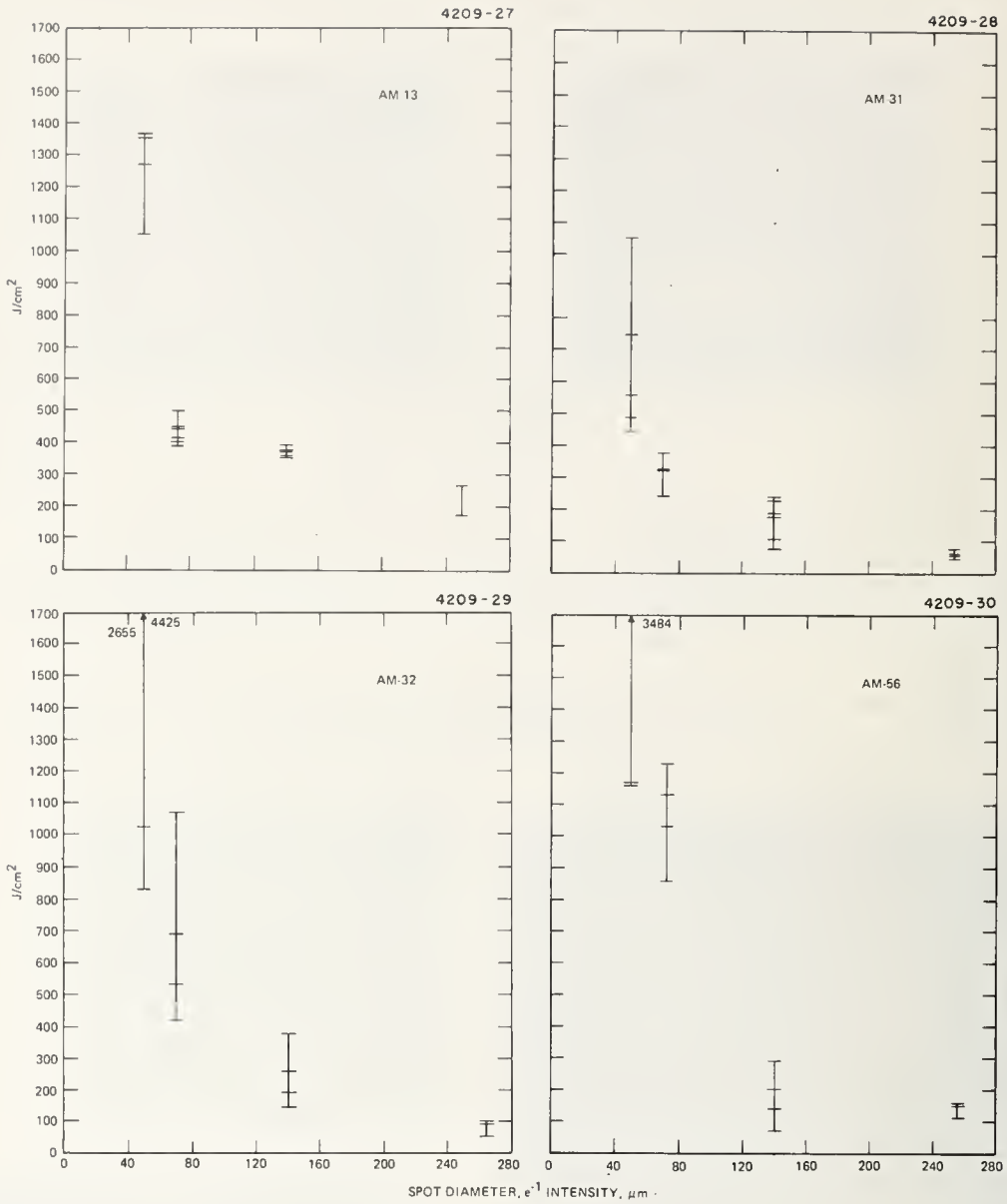

Figure 6 (continued on next page).

Figure 6 (continued)

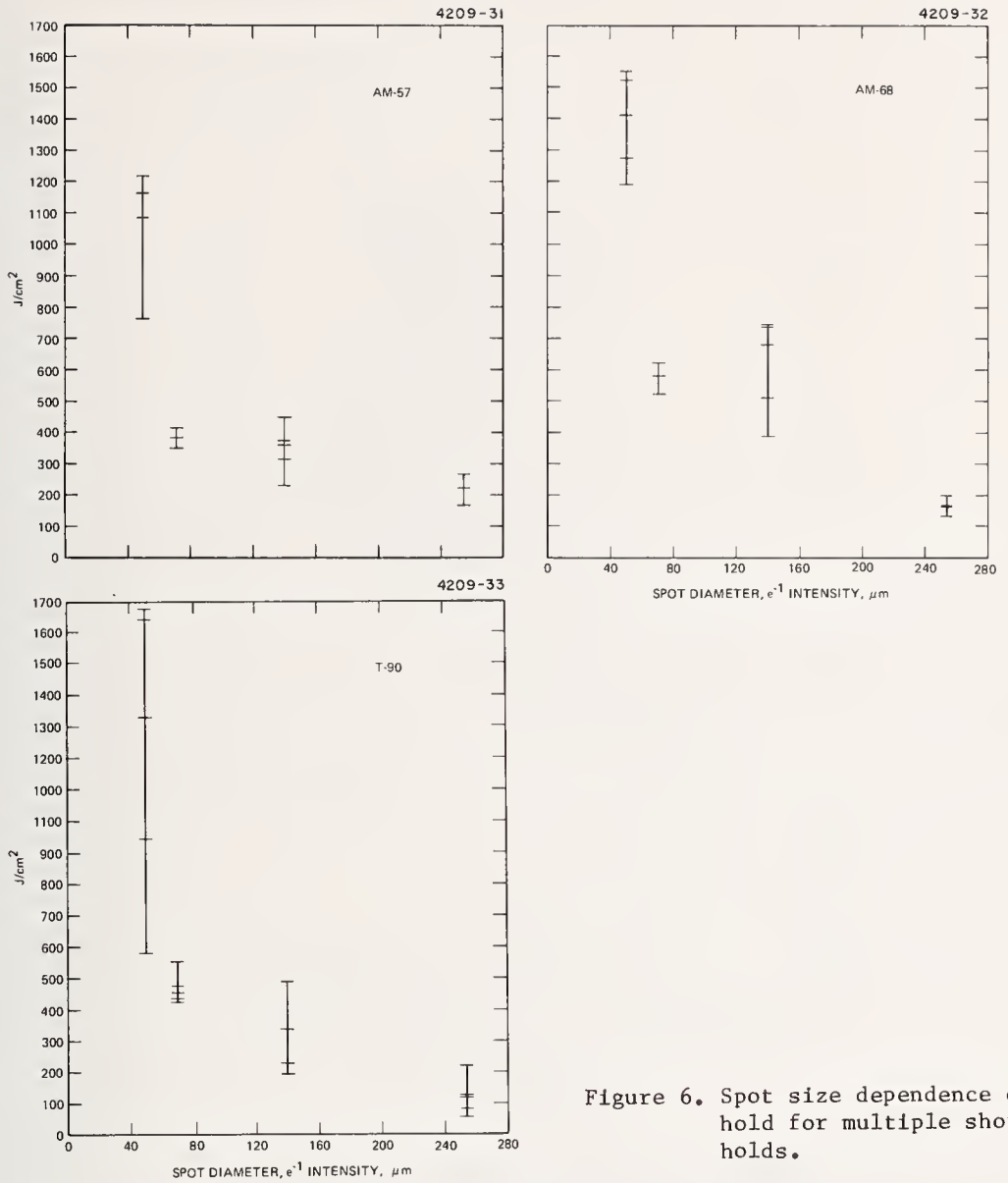

Figure 6. Spot size dependence of damage threshold for multiple shot damage thresholds.

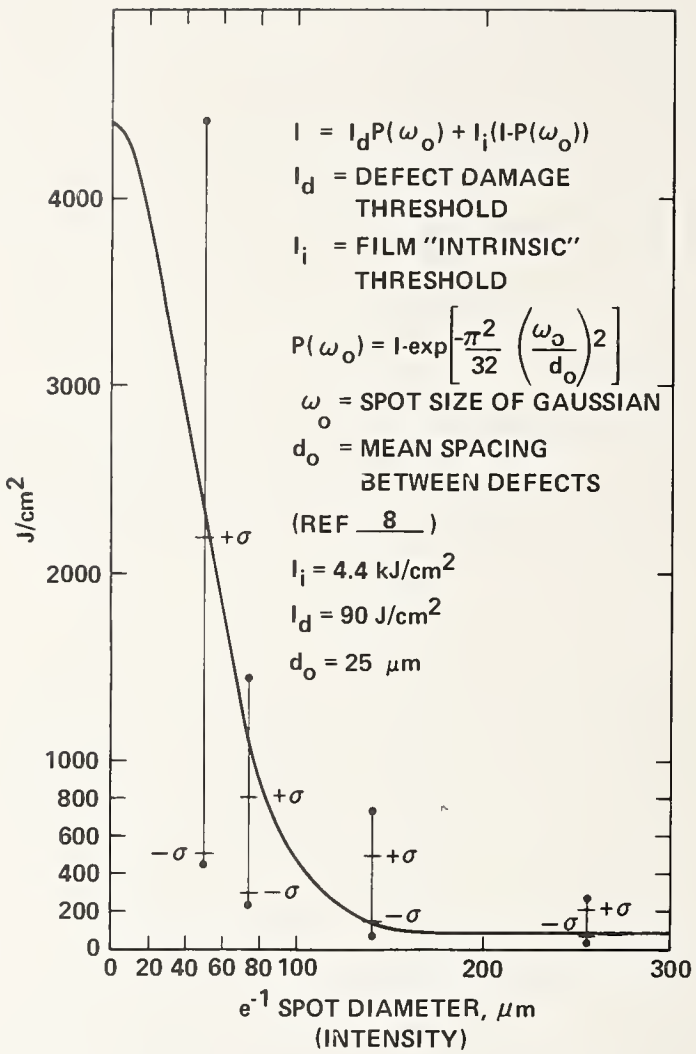

Figure 7. Summary of damage thresholds for seven reflectors obtained for multiple thresholds. Curve represents best fit of above expression for chosen values of I_1 and I_d.

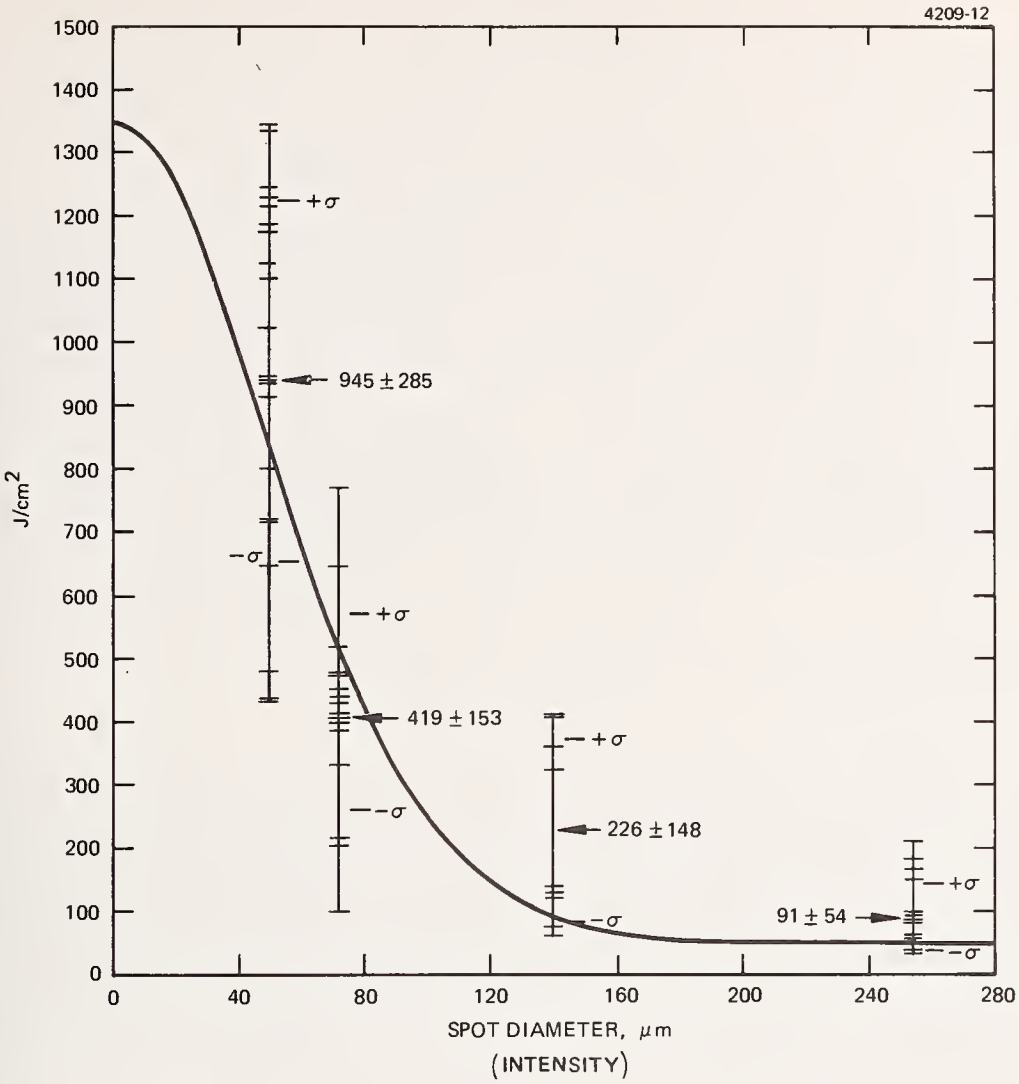

Figure 8. Single shot damage thresholds as a function of spot size.

COMMENTS ON PAPER BY WANG, et al

Although the identity of the damaging defects in this work is unclear the speaker observed that care in the choice of starting materials and careful control of the processing of the material did yield significant improvement in damage threshold. Surfaces of substrate materials were prepared with careful attention to minimizing the occurrences of scratches and digs and typical surface roughnesses were kept to the order of 20 Å rms. The question was raised as to why if the damage was attributed to the presence of metal rich defects that regions of high metal concentration were not seen in the vicinity of damage sites. In the ensuing discussion it was proposed that this might be attributable to the fact that it is not metal inclusions which are damaging, but instead pin holes and defects in the dielectric coating. A further question was raised expressing concern that the observed values of surface damage when extrapolated to zero spot size gave values higher than the observed bulk damage in zinc selenide. The answer was that the bulk damage in this material is limited by defects, and therefore would be expected to be lower than the extrapolated value of the surface damage.

5.2 Temperature and Wavelength Dependence of the Reflectance of Multilayer Dielectric Mirrors for Infrared Laser Applications

D. L. Decker

Michelson Laboratories, Naval Weapons Center
China Lake, California 93555

The absorptance of mirrors used in high energy laser applications is significant in determining the heat load which must be removed by cooling and the magnitude of the associated thermal figure distortion. For design purposes it is necessary to know the absorptance not only at room temperature, but also at temperatures up to and above the actual operating temperature of the mirror. The damage threshold is also related to the absorptance and to its variation with temperature, dA/dT. Since temperature and wavelength dependence is needed, it is most convenient to infer the absorptance from absolute reflectance and scattering measurements, rather than from direct measurement. The present paper describes instrumentation capable of making relative reflectance vs. temperature measurements with a precision and accuracy of 7×10^{-5}. Temperature dependence data over the range from 25°C to 125°C is presented and analyzed for several commercially obtained dielectric multilayer mirror designs intended for use at 3.8 μm. These mirrors have absolute reflectances above 0.997 and show a reflectance variation with temperature, $|dR/dT|$ of 5×10^{-5} or less.

Key words: Multilayer dielectric mirror; optical absorptance; reflectance; scattering; temperature dependence; wavelength dependence.

1. Introduction

Metal mirrors have in the past held near exclusive province in high energy laser applications as a consequence of high thermal conductivity and relatively low absorption. However, in the mid infrared increasing use of multilayer dielectric mirrors is being made as technology improves and old prejudices die. The usual multilayer dielectric mirror consists of many quarter-wave thick layers of alternate low and high index [1,2].[1] The response of the "stack" is, of course, defined by the superposition of constructively interfering waves transmitted through and reflected from the layers of the mirror. The design reflectance can, in principle, be increased to values as close to one as desired by increasing the number of layers in the stack, limited only by scattering from imperfections, residual absorption in the films, and practical limitations on the uniformity of the optical thicknesses of the films of the stack. Reflectances greater than 0.999 are possible with current technology. The viability of a multilayer dielectric mirror in high energy applications depends upon maintenance of its initial very low absorptance. Even very small changes in absorptance (representing large fractional changes) as occur, for example, as the temperature increases during operation are important. Since temperature and wavelength dependences are needed it is most convenient to infer the absorptance from absolute reflectance and scattering measurements rather than by direct measurement. Experimentally, the challenges presented here are nontrivial: for an initial absorptance of 10^{-3}, a 10% change is only 10^{-4} absorptance units. This paper provides results and analysis of three commercially produced multilayer dielectric mirrors intended for use at the DF laser wavelength (3.8 μm), together with some experimental detail.

2. Experimental Program

The designs are $ZnS/ThF_4/Ag$ (R1), $ZnSe/ThF_4/Ag$ (R3), and $Si/SiO_x/Ag$ (R4) deposited on ultralow expansion (ULE) glass. They were designed and produced by Optical Coating Laboratories, Inc. (OCLI), Santa Rosa, California. Figure 1 presents measured values of absolute reflectance for design R3 from 3.6 to 4.2 μm. Three sets of data are plotted. Original absolute reflectance measurements "Δ" were made in March 1974, measurements made one year later "□" after storage at room temperature in dry nitrogen, and the points "o" after cycling to 120+°C. Figure 2 presents similar data for design R1 and figure 3 for design R4. It is obvious that designs R3 and R4 are much more stable than R1 in both storage and upon temperature cycling.

Before proceeding further it is important to briefly describe the measurements performed to generate this data. The points denoted by "Δ" and "◇" are the results of near normal incidence absolute reflectance measurements performed in our laboratory at room temperature and have an uncertainty of ±0.0005 [3]. In addition, relative reflectance measurements have been made using a near normal incidence reflectometer recently designed and constructed specifically for temperature dependence measurements [4] (see figure 4). This instrument measures the ratio of the absolute reflectance R_s of the sample at temperature T, to the absolute reflectance R_r of the reference at temperature T_o, $R_s(T)/R_r(T_o)$. The uncertainty of the reflectance ratio measurement is $\pm 3 \times 10^{-5}$. If $R_r(T_o)$ is known, the absolute reflectance of the sample as a function of temperature can be computed:

1. Figures in brackets indicate the literature references at the end of the paper.

$$R_s(T) = \left[R_s(T)/R_r(T_o)\right]. \quad (1)$$

The values "o" in figures 1, 2, and 3 were computed from the changes in measured relative reflectance, and absolute reflectance measured before temperature cycling, using eq. (1). The uncertainty in the computed absolute reflectance (eq. 1) is completely dominated by the uncertainty in the measurement of $R_r(T_o)$ and is thus ± 0.0005. The temperature dependence of mirror performance is provided by evaluation of not only thermal cycling stability, but also the absorptance and scattering at elevated temperature. Figure 5 presents raw relative reflectance data as a function of temperature for design R1 at 4.2 μm. Sample and reference in each set of measurements reported here are nominally identical, having been sliced to dimension by a diamond wafering saw from an original 1.52-inch diameter sample. The initial departure from unity is thus a measure of the spatial uniformity of the original sample. Design R1 in fact displays a much larger initial departure from unity than either R3 or R4. This departure is strongly wavelength dependent, varying from a part in 10^4 at 3.6 μm to a part in 10^3 at 4.2 μm. The temperature coefficient of reflectance of R1 at 4.2 μm, $dR/dT \sim -5.3 \times 10^{-5}/°C$ is larger than for any other design and wavelength.

The reflectance and its temperature dependence are obviously both more or less strongly wavelength dependent. The temperature dependence of such a device can come from a number of sources: most simply, from the temperature dependence of the optical thickness of the various layers of the stack, with the resulting change in "tuning." It is clear that such an effect will be wavelength dependent, and in fact may result in the high reflectance band shifting in wavelength. From the linear coefficient of expansion (α) for a single layer, and the variation of index of refraction dn/dT, the variation of optical thickness (nd) of that layer can be computed

$$\frac{1}{(nd)}\frac{d(nd)}{dT} = \alpha + \frac{1}{n}\frac{dn}{dT}. \quad (2)$$

If the film design is known and a multilayer design program is available, then changes in response can be readily evaluated. Of course, if the reflectance is limited by absorption in the stack or by scattering, the behavior of the reflectance of the device with temperature is not described so simply. If significant absorption is present, regardless of the specific mechanisms, the temperature dependence of the stack reflectance will be relatively large. This is simply a consequence of all dispersive mechanisms being more or less strongly temperature dependent. On the other hand, if the reflectance is limited by scattering, the temperature dependence of the device reflectance would be expected to be much smaller. This can be seen from the following argument. Visible and near infrared scattering in high quality optics is nearly always the consequence of distributed microirregularities or dust; i.e., scratches and other macroscopic cosmetic blemishes are usually not important. In the case of distributed microirregularities, the ratio of the fractional intensity ΔR of light scattered to R_o, that reflected, is given by the expression [5]

$$\Delta R/R_o = (4\pi\delta/\lambda)^2, \quad (3)$$

where δ is the rms roughness of the surface microirregularities and λ is the wavelength. From this expression one can simply compute the temperature dependence:

$$d\Delta R/dT = (dR_o/dT)(\Delta R/R_o). \quad (4)$$

If we assume that all of the incoming beam which is not reflected is scattered, $\Delta R/R_o \lesssim 10^{-3}$ for the multilayer dielectric mirror designs considered here. A precise value for dR_o/dT for the present purposes is not necessary, and we can set $dR_o/dT \sim 10^{-4}/°C$ as a very conservative maximum estimate. The temperature dependence of the fractional intensity of the light scattered from distributed microirregularities, $d\Delta R/dT$ is then $10^{-4}/°C \times 10^{-3} \simeq 10^{-7}/°C$. A similar calculation can be made of the temperature dependence of the scattered light associated with localized microirregularities, yielding a temperature coefficient $\sim 10^{-8}/°C$, again assuming that all light which is not specularly reflected is scattered [6]. These values, especially the latter, are very much smaller than any value of dR/dT which could be reliably measured by the present experimental apparatus over even a 1000°C temperature increment. Any strong reversible temperature or wavelength dependence in the reflectance of a multilayer dielectric mirror must be due to absorption or changes in stack "tuning." There is one exception to this observation: If we are near a dipole resonance of the localized scattering particles the scattered light intensity will be strongly temperature and wavelength dependent [7].

All of the mechanisms considered up to this point apply to reversible temperature effects. Any changes in structure or composition as a consequence, for example, of intra- or inter-layer diffusion will likely result in index changes in the layers involved. Such effects will be temperature activated, and result in *irreversible* variation of mirror performance with temperature, as is very evident in the temperature cycling data for design R1 (figure 2). Figure 6 presents computed absolute reflectance vs. temperature for designs R1 and R3 obtained from relative reflectance measurements at two selected wavelengths. The difference in performance of R1 at wavelengths separated by only 0.4 μm is striking. Since many DF lasers have an output which extends from 3.6 to over 4.0 μm, the requirement for detailed examination of performance with wavelength is obvious. Figure 7 is a plot of similar information for

design R4. The variation of the reflectance with temperature is nearly wavelength independent, and has a value, $dR/dT \sim + 3 \times 10^{-5}/°C$, ignoring hysteresis.

It is instructive to compare the temperature dependence of the multilayer dielectric mirror designs considered here with the performance of a metal coated mirror. The absorption in a good metal (e.g., silver) in the infrared is a consequence of electron-phonon scattering, the same mechanism which limits the electrical conductivity to finite value. The variation of the absorptance (or reflectance) with temperature can be simply related to the variation of the dc conductivity with temperature. For silver in the near infrared, and at temperatures near room temperature the calculated variation of reflectance with temperature, dR/dT, is $-1.5 \times 10^{-5}/°C$ [7]. Figure 8 is a plot of the change in reflectance from an initial value as a function of temperature at 10.0 μm wavelength. The calculated slope falls between the slopes of the data taken with ascending temperature "•" and desending temperature "o". However, at 4.0 μm wavelength, results are obtained which do not agree even to sign with theoretical predictions (see figure 9). This data is particularly interesting since silver is the initial film in all three multilayer designs, and since there is evidence that the fields at the silver film are not negligible, i.e., the silver film is participating in the response of the mirror. In fact, the measured temperature dependence of the reflectance of silver films at 4.0 μm is identical with the temperature dependence of design R4 near 4.0 μm. This may be coincidental, but could also possibly be the origin of the effect. With the exception of the temperature dependence data on silver films, there are no measured values of the corresponding dependence available for the other materials in the dielectric mirror designs considered here, as thin films, and in some cases the information even for bulk is not available. This, combined with incomplete information concerning the stack design, has limited theoretical calculations to a few simple estimates.

Total hemispherical (integrated) scattering measurements (TIS) at a wavelength of 3.39 μm have also been made. Preliminary differential scattering measurements at the same wavelength indicate that most of the scattered light is contained in a narrow cone about the specular direction. Most of the scattered light is thus collected by the optics of the absolute reflectometer, and the quantity, 1-R, is to the first approximation equal to the absorptance, at least for designs R1 and R4. Table 1 contains a summary of several important characteristics of the three designs, dR/dT, where it provides a meaningful description of the reversible temperature dependence, ΔR, the irreversible change in reflectance upon temperature cycling to 120+°C, values of 1-R, and TIS measurements at 3.39 μm. Notice that the TIS level for R3 is more or less a half order of magnitude larger than the value of 1-R, and since a precise correction for the amount of scattered light falling outside the collection angle of the absolute reflectometer is not available, the actual absorptance of R3 may be significantly less than 1-R. In other words, the measured value of reflectance of R3 may be determined by scattering. This possibility is further reinforced by the observation of a very small temperature dependence of the reflectance dR/dT, and very high stability on temperature cycling. In the case of design R1, the computed "absolute absorptance" 1-R is a factor of two or three larger at all wavelengths than the TIS at 3.39 μm. It is interesting that the largest irreversible and reversible changes with temperature in this design occurred at wavelengths for which the initial reflectance was highest. This is in fact what would be expected from "detuning" effects--the stack would be most sensitive to "detuning" where its "Q" was greatest. Like R3, design R4 does not appear scatter limited, and the nearly constant and large values of dR/dT and relatively high stability on thermal cycling suggest that its performance is determined not by stack detuning but perhaps by absorption, possibly in the initial silver film.

Table 1. Summary of experimental results for OCLI dielectric mirror designs R1, R3 and R4 at various wavelengths near 3.8 μm.

MIRROR DESIGN		WAVELENGTH, μm 3.6	3.8	4.0	4.2	4.4	4.6	SCATTERED LIGHT AT 3.39 μm
R-1 $ZnS/ThF_4/Ag$	dR/dT	?	?	-0.2	-0.53	–	–	
	ΔR	-1.0	-5.9	-17.0	-15.3	–	–	
	1-R	25.9	20.7	29.8	35.1	–	–	8.5
R-3 $ZnSe/ThF_4/Ag$	dR/dT	0.00	0.06	0.03	0.00	–	–	
	ΔR	1.9	2.9	0.3	-4.7	–	–	
	1-R	0.9	-1.3	3.1	9.5	–	–	19.0
R-4 $Si/SiO_x/Ag$	dR/dT	0.25	0.27	0.29	0.40	0.24	0.25	
	ΔR	-1.4	0.7	-0.7	-3.1	-1.7	0.0	
	1-R	18.6	9.0	5.0	6.8	14.2	52.2	11.0
ALL ENTRIES X 10^{-4}								

3. Conclusions

In the evaluation performed here, design R3 emerges clearly superior in most respects, possessing the smallest reversible temperature dependence, lowest apparent absorption, and very small irreversible changes upon temperature cycling. The first two factors presumably also relate to a higher damage threshold. However, the total light scattered by R3 is a factor of two larger than from the other designs. The conjecture that R4 might be plagued with a thermal runaway problem is laid to rest with the discovery that the design possesses a nearly wavelength independent, large and *positive* temperature coefficient of reflectance. In a given application, scattered light, or perhaps stability upon temperature cycling may be the most important consideration, and thus determine which design would be optimum.

Since a quantitative predictive capability for the dielectric mirror parameters evaluated in this paper is not yet available, only by direct measurement can mirror performance be determined. This is especially true of the dependence of mirror characteristics with temperature. Of course, this latter comment is not restricted to dielectric mirrors, but applies to high energy laser optics in general. The small changes in absorption which occur, for example, when the temperature is changed, represent large fractional changes, and are very important from a design standpoint. Determination of performance at elevated or depressed temperature is consequently an essential complement to room temperature evaluation. It is hoped that this paper will encourage a greater effort to characterize materials and components at actual operating temperatures.

4. References

[1] Vasicek, A., *Optics of Thin Films* (North-Holland Publishing Co., Amsterdam, 1960), pp. 234-239.

[2] Costich, V. R., in *Handbook of Lasers*, R. J. Pressley, ed. (The Chemical Rubber Co., Cleveland, Ohio, 1971), pp. 155-170.

[3] Bennett, H. E. and W. F. Koehler, "Precision Measurement of Absolute Specular Reflectance with Minimized Systematic Errors," J. Opt. Soc. Am. 50, 1 (1960).

[4] Decker, D. L., in *High Energy Laser Mirrors and Windows* (Semi-Annual Report No. 2, ARPA Order 2175, Naval Weapons Center, April 1973), pp. 34-49.

[5] Bennett, H. E. and J. O. Porteus, "Relation Between Surface Roughness and Specular Reflectance at Normal Incidence," J. Opt. Soc. Am. 51, 123 (1961).

[6] Decker, D. L., in *High Energy Laser Mirrors and Windows* (Semi-Annual Report No. 6, ARPA Order 2175, Naval Weapons Center, May 1975), pp. 25-44.

[7] Decker, D. L., in *High Energy Laser Mirrors and Windows* (Semi-Annual Report No. 4, ARPA Order 2175, Naval Weapons Center, March 1974), pp. 66-83.

5. Figures

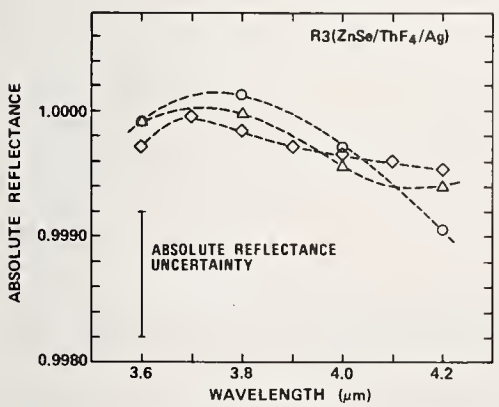

Figure 1. Absolute reflectance of OCLI mirror design R3 vs wavelength. Symbols are described in text.

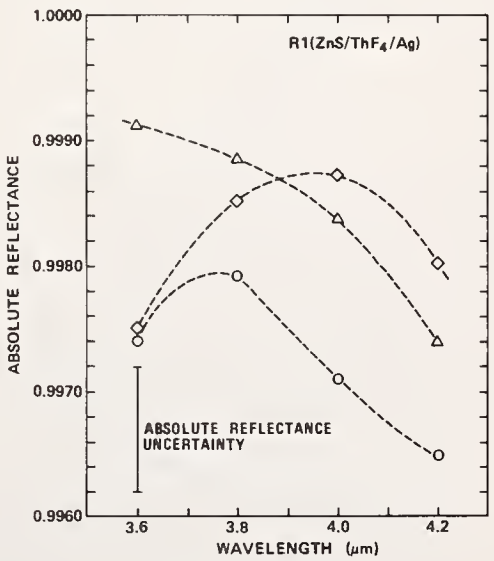

Figure 2. Absolute reflectance of OCLI mirror design R1 vs wavelength. Symbols are described in text.

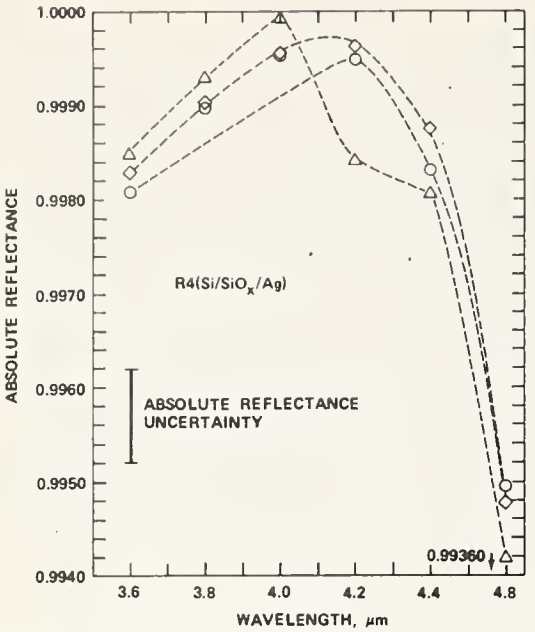

Figure 3. Absolute reflectance of OCLI mirror design R4 vs wavelength. Symbols are described in text.

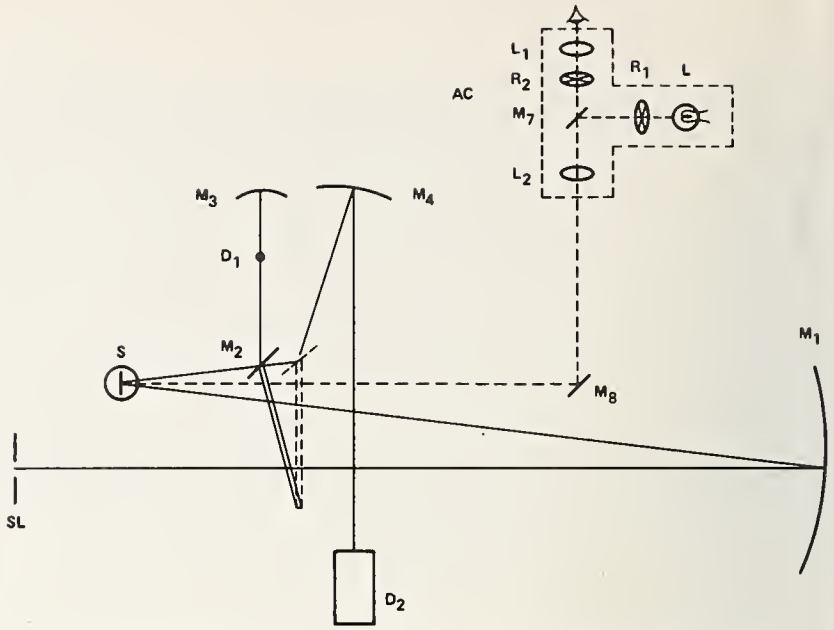

Figure 4. Schematic of the relative reflectometer used in temperature dependence studies. Light from the monochromator exit slit SL is focused by M_1 at S, where the sample and reference can be alternately positioned. The reflected light is then passed to either a thermocouple detector D_1 or a photomultiplier D_2. AC is an autocollimator used for the critical alignment of sample and reference.

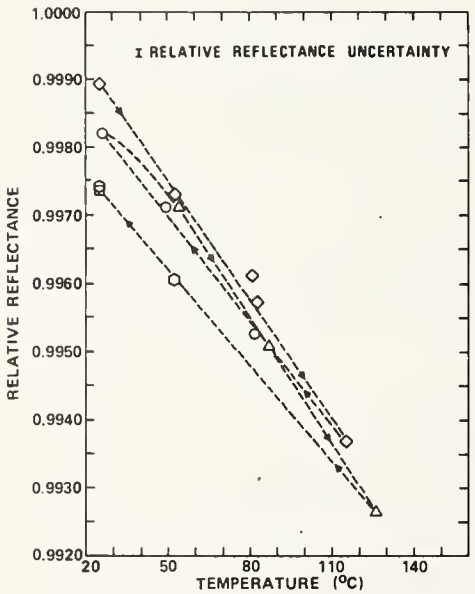

Figure 5. Experimental relative reflectance of OCLI dielectric mirror design R-1 vs. temperature at a wavelength of 4.2 μm. Sample and reference are nominally identical. Thermal/temporal history as follows: "○" ascending temperature, "o" decending temperature, "Δ" ascending temperature, "o" decending temperature, "□" 60 hours after return to room temperature.

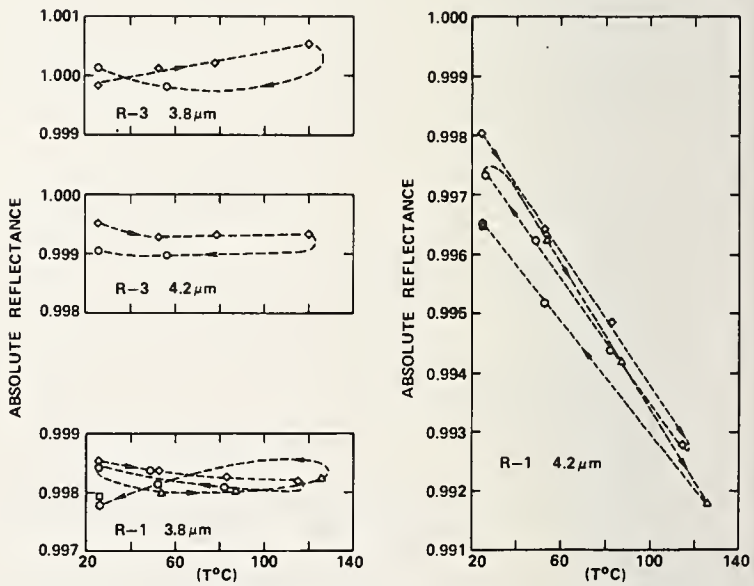

Figure 6. Computed absolute reflectance of OCLI mirror designs R3 and R1, at the wavelength 3.8 and 4.2 μm. Thermal/temporal history as indicated in figure 5. Uncertainty in computed absolute reflectance is ± 0.0005.

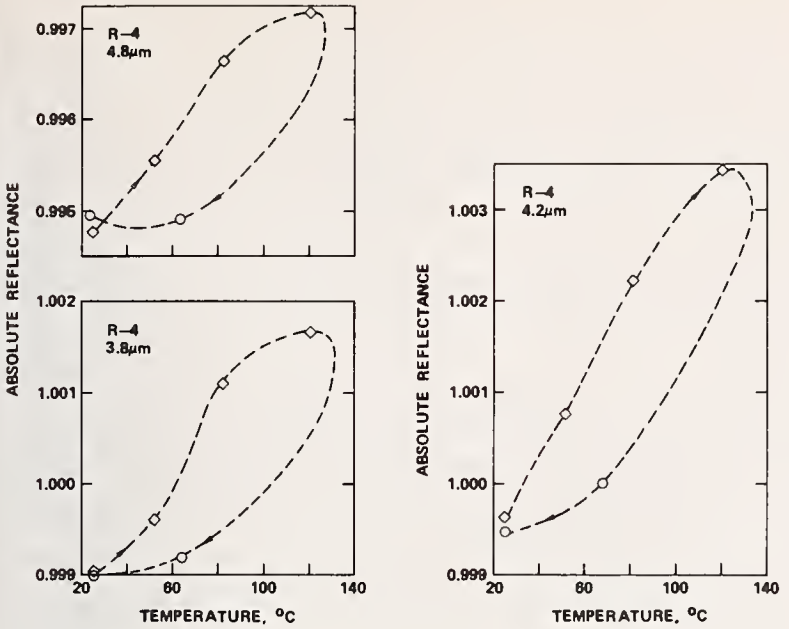

Figure 7. Computed absolute reflectances of OCLI mirror design R4 at the wavelengths 3.8, 4.2, and 4.6 μm. Thermal/temporal history is as indicated in figure 5. Uncertainty in computed absolute reflectance is ± 0.0005.

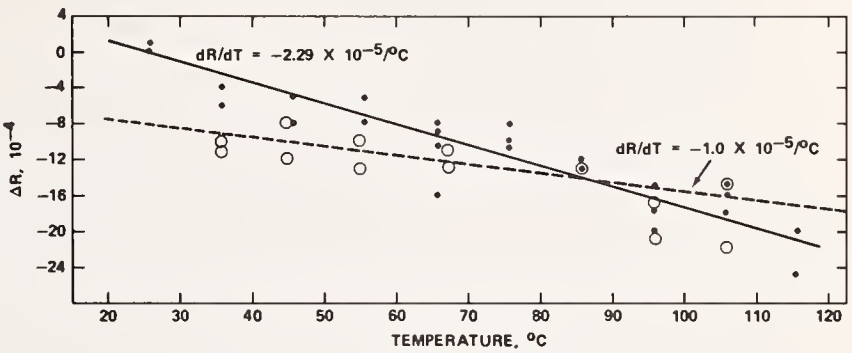

Figure 8. Change in normal incidence absolute reflectance of standard vacuum evaporated thin film silver deposited on supersmooth fused quartz as a function of temperature at 10.0 μm wavelength. The points marked (•) were taken with increasing temperature and the points marked (o) with temperature decreasing.

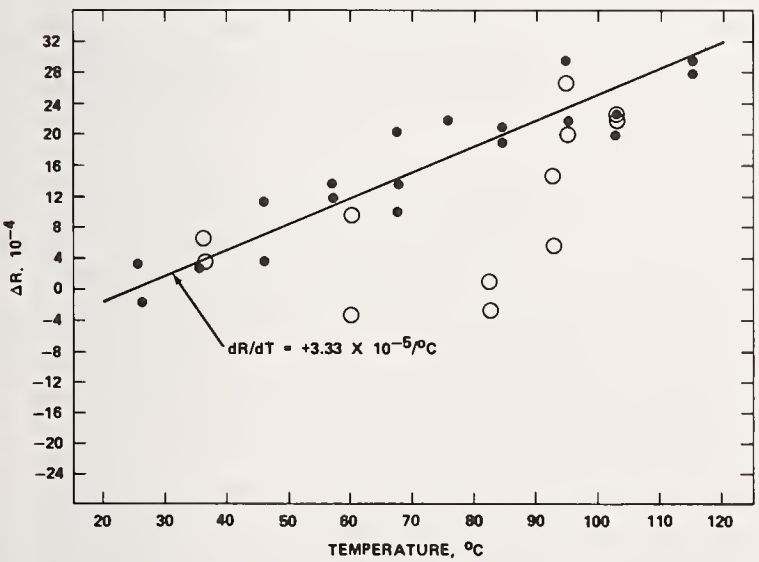

Figure 9. Change in the normal absolute reflectance of standard vacuum evaporated thin film silver deposited on supersmooth fused quartz as a function of temperature at 4.0 μm wavelength. The points marked (•) were taken with increasing temperature and the points marked (o) with temperature decreasing.

COMMENTS ON PAPER BY DECKER

It was pointed out that irreversible changes in the film observed over times like hours may be due to thermal strain accumulation. After heating the film over longer periods of time, such as days, strain relief occurs and the film reverts to its original state and original reflectivity. It was further pointed out that inter-layer diffusion led to permanent long term changes in film reflectivity upon thermal cycling. Thus for example, in some films a change in absorption up to a factor of 2 was observed if the film was heated to 120° for one-half hour. Further thermal cycling increased the absorption up to a factor of 3 over its initial value.

5.3 PREPARATION AND EVALUATION OF ZnS/CeF_3 AR COATINGS FOR 10.6 MICRON KCl LASER WINDOWS

A. Golubovic, W. Ewing, R. Bradbury, I. Berman, J. Bruce and J. J. Comer

Air Force Cambridge Research Laboratories
Hanscom AFB MA 01731

The possibility of using ZnS/CeF_3 as a 2-layer antireflection coating for 10.6 micron laser window materials was investigated. Both sputtered and sublimed layers of ZnS were deposited on well characterized Bridgman RAP grown KCl substrates. CeF_3 layers were thermally evaporated onto both bare and ZnS coated KCl substrates. The chemistry and structural quality of the coatings were examined by several characterization techniques including x-ray diffraction, electron microscopy and diffraction, scanning electron microscopy, Auger spectroscopy, Nomarski microscopy, and emittance spectroscopy. Pulsed laser damage studies at 10.6 microns were performed to evaluate the damage threshold of the coatings.

Key words: CeF_3; CO_2 pulsed laser damage; coating topography; KCl; laser window coatings; ZnS.

1. Introduction

Potassium chloride is a prime candidate for 10.6 μm laser window material due to its low optical absorption and high damage threshold at 10.6 μm. However, its application in high energy laser optics requires antireflection coatings which at the appropriate wavelength - 10.6 μm, must be non-absorbing as well as isotropic, homogeneous, and stable to environmental stress-intensive conditions. The simplest form of antireflection coating is a single layer quarter wave coating whose refractive index is equal to the square root of that of the substrate. Since KCl has a refractive index, n, of 1.454, single layer coating designs cannot be implemented because materials with the appropriate index are not available. With a 2-layer AR coating, a high index/low index combination of materials of suitable thicknesses can provide zero reflectance at a single wavelength. One such coating which has been investigated on KCl is $ZnSe/ThF_4$ [1][1]. Results have shown that there is significant absorption due to this coating. One of the contributing factors may be the dissociation of ThF_4 upon deposition.

The rare earth fluorides as a class, are low refractive index materials. As a possible alternative to $ZnSe/ThF_4$, an AR coating stack based on CeF_3 was investigated. Of the rare earth fluoride which we have studied, CeF_3 was chosen because it adhered well and did not dissociate on deposition. Although it is a hexagonal material, the difference between $n_{ordinary}$ and $n_{extrodinary}$ is approximately 4% and should not effect the performance of this material as a coating. For these studies, ZnS was selected as a first layer material. This paper evaluates the damage threshold of rare earth fluoride-based AR coating stacks, particularly ZnS/CeF_3 on KCl.

2. Deposition of Coatings

KCl substrates were prepared from boules of RAP Bridgman material grown at AFCRL. The substrates were polished and etched as described previously [2]. Typical sample substrates were single crystal disks $1\frac{1}{4}$" in diameter and $\frac{1}{4}$" thick, with various crystallographic orientations.

ZnS coatings were deposited by both evaporation and RF sputtering techniques. All sputtered depositions of ZnS were performed with a turbo-pumped system under an argon atmosphere. Depositions made at RF power levels from 50 to 200 watts yielded different deposition rates and substrate temperatures as given in table 1.

1. Figures in brackets indicate the literature references at the end of the paper.

Table 1. Deposition conditions for sputtering of ZnS.

RF Power	50 W	100 W	125 W	150 W	200 W
Deposition Rate (Å/sec)	1.0	2.75	3.53	4.50	6.17
Substrate temperature (^{o}C)	$< 100^{o}$	$\sim 120^{o}$	$120^{o} - 140^{o}$	$\sim 150^{o}$	$150^{o} - 170^{o}$

At power levels above 200 watts, the coatings did not adhere to the substrate. Prior to deposition, the substrates were sputter etched for 60 seconds by argon bombardment at 50 watts RF power.

Thermally evaporated ZnS coatings were produced in a 10^{-6} Torr coating chamber using an indirect pancake heater of tantalum over a vitreous carbon crucible. Deposition rate of 6 Å/sec was controlled to ± 1 Å/sec. Samples were cleaned in-situ by AC Ar^{+} bombardment prior to deposition. The substrate temperature was at room temperature to start, but rose to 100°C during the coating process due to radiant heating from the ZnS source.

Deposition of CeF_3 was performed at $1\text{-}2x10^{-7}$ Torr by evaporation of CeF_3 (CERAC/PURE 99.9%) from a tantulum tube source. Attempts at sputtering CeF_3 coatings produced dissociation of the CeF_3 and were abandoned. The thickness of the deposition layer was controlled by a quartz crystal thickness monitor and measured after each run by stylus (Dektak) and Tolansky microscope techniques. The sublimation temperature was 1200°C. The deposition rate was 2.25 Å/sec on KCl and 2.0 Å/sec on ZnS coated KCl. The KCl substrate was heated to 150° during deposition, but the ZnS coated KCl substrate was kept at 100°C.

3. Characterization of Coatings

The chemistry and structure of the CeF_3 and ZnS laser window coatings were investigated by several different techniques. X-ray and electron diffraction were used to determine composition, crystallinity and the presence of preferred orientation. X-ray techniques involved either x-ray diffractometry of the coated surface, or x-ray powder diffraction of just the coating after removal from the substrate. Reflection or glancing angle electron diffraction patterns were obtained from the coating before removal from the substrate. Identification was made by comparison of the diffraction data with the ASTM Powder Diffraction file. Also the preferred orientation of the film with respect to the substrate was determined from the diffraction data. Both the surface chemistry and a profile of the chemistry throughout the film thickness and interface were investigated with Auger spectroscopy. Transmission and scanning electron microscopy, as well as Nomarski interference contrast microscopy were used to reveal coating and substrate surface topography. Spectral scans were taken of each coated specimen, and some preliminary measurements of optical absorption at 10.6 microns were made. Finally pulsed laser damage at 10.6 microns was done to compare and evaluate the various coatings and coating parameters. The results of these various analyses are summarized below.

Sputtered ZnS coatings on KCl were identified as the cubic form of ZnS with a strong preferred orientation of {111} planes parallel to the substrate surface. This (111) preferred orientation was observed regardless of the substrate crystallographic orientation, and was also observed on glass substrates. Only those coatings sputtered at a low rate (1 Å/sec) deviated from this preferred orientation. The surface texture was rough, regardless of deposition rate. Transmission electron micrographs of figure 1, showing replicas of ZnS surfaces deposited at various rates, dramatically reveal the details of the coating topography. It can be seen that the surface roughness varies with deposition rate. There is a decrease in grain size with an increased rate of sputtering in the range of 2.5 Å/sec (100 W) to 6.5 Å/sec (200 W), resulting in a decrease in roughness. An image of the electron diffraction pattern, attached to the corner of each micrograph, shows the (111) orientation of each layer. However, a change in both orientation and texture is observed upon decreasing the deposition rate to 0.9 Å/sec (50 W). Scanning electron microscopy of a cross-section of a typical sputtered ZnS

film (150 W) revealed the growth structure of these films. Figure 2 shows the columnar growth of the ZnS crystals normal to the substrate along the [111] direction, and the surface roughness related to these individual crystals.

The presence of contaminants in sputtered ZnS films was examined both on the film surface and throughout its thickness including the interface by Auger spectroscopy. The spectrum of figure 3 shows the principle Auger structure of ZnS. The major contaminants are oxygen (probably present in the argon sputter gas during deposition), and argon from the sputter cleaning gun in the Auger system. The oxygen level shown was consistent throughout the ZnS layer thickness, reaching a peak at the ZnS/KCl interface. This can be seen in the Auger profile (figure 4) of the ZnS/KCl interface The interface appears to be potassium-rich, probably due to Cl desorption during the first stages of sputtering.

Some preliminary measurements of the 10.6 μm optical absorption coefficient of sputtered ZnS coatings on KCl were made. The average value for the three coatings measured was 28±4 cm^{-1}. No differences were observed on coatings sputtered at different rates.

Evaporated ZnS films were quite different in both texture and crystallographic orientation from those films prepared by sputtering. Many of the evaporated films exhibited a preferred orientation of {110} planes parallel to the plane of the substrate in contrast to the {111} structure of the sputtered films. The surface topography was less pronounced as seen in figure 5, in which electron micrographs of replicas of ZnS coatings prepared by both methods are shown. The evaporated films, although smoother, were often found to vary in crystallinity and orientation.

CeF_3 coatings were prepared on both bare and ZnS coated KCl substrates. On KCl, they were found to be crystalline, hexagonal structure CeF_3, with usually a preferred orientation of {10.0} planes approximately parallel to the substrate surface. The coating surface was fairly smooth and fine grained; average grain size was less than 300 Å. In the 2-layer coatings, CeF_3 deposited on ZnS is polycrystalline with no preferred orientation. Electron micrographs of surface replicas (figure 7) reveal that the smaller CeF_3 crystallites tended to fill in valleys between the sputtered ZnS peaks, smoothing out somewhat the roughness of the ZnS surface.

Spectral scans were made of each coated specimen as a first evaluation test. Figure 8 shows the spectral response of a ZnS/CeF_3 AR coated KCl which gives a peak transmission at approximately 10.6 μm.

Spectral emissivity measurements were made on three coated samples. To eliminate the effects of substrate and instrumental variations between measurements, one sample was half coated with CeF_3 allowing measurements to be made on both coated and uncoated KCl in one run. Spectral emittance scans of both coated and uncoated areas of this sample are shown in figure 6. The relatively high baseline of the spectrum for the uncoated area indicates that this substrate is of rather poor quality. By comparison, the emittance of the coated area in the 10.6 μm region shows an increase of about 50%. This implies a higher overall absorption for the coated sample in this region.

All of these coatings were stable and adhered well to the substrate during numerous experiments in our New England humidity. When failure occurred, it often did so along specific linear and parallel directions. The optical micrographs of figure 9 illustrate this failure in a ZnS coating; light gray areas are coating, dark gray areas are substrate. The first micrograph contains a series of linear and parallel faults visible on the surface of the coating - these are not scratches. The next two micrographs illustrate that failure of the coating has occurred along these faults which are visible in the substrate as well as the coating. By x-ray diffraction, these faults were found to be parallel to the trace of substrate {110} type planes, and may indicate slip along these {110} planes caused by stress associated with the coating.

4. Laser Damage of Coatings

Pulsed laser damage testing was used to evaluate the relative merits of the various coatings described above. The experimental arrangement used is shown in figure 10. A TEA laser, operated in the TEM_{oo} mode was used, combined with a 10 cm focal length lens to focus the beam on the sample surface. CaF_2 attenuator plates were used to select the amount of laser energy incident on the sample surface. Characteristics of the TEA laser are listed in table 2.

Table 2. Characteristics of TEA CO_2 Laser Pulses

Pulse Energy	~65 millijoules, reproducible to 5%
Repetition Rate	1 pps
Spatial Mode	TEM_{oo}, Gaussian to $I/I_o \leq 0.01$
Mode Diameter	5.5 mm
Longitudinal Modes	Many
Pulse Width	100 nsec, FWHM

The spot size in the focal plane of the lens was 180 μm, which was calculated both from cavity parameters and from a beam scan with good agreement. The sample was adjusted so as to be in the waist of the beam, which is 0.5 mm long for a 10% variation in the beam diameter. The sample and indexing head were adjusted so that the sample was normal and moved perpendicular to the beam. Energy was measured using a Scientech Model 362 calorimeter located on the sample side of the 10 cm lens.

Damage experiments were performed by irradiating selected sites with known combinations of attenuators in the beam. At least 10 sites were irradiated for each selected energy density. The presence of damage was determined by examination of the surface at a magnification of 100x. The resulting threshold values are summarized in table 3.

Table 3. 10.6 Micron Pulsed Laser Damage Thresholds for Coated KCl

COATING	THRESHOLD (J/cm^2)
CeF_3	35
ZnS, sputtered (50 W)	65
" (100 W)	40
" (150 W)	40
" (200 W)	40
ZnS, evaporated	35
CeF_3 & ZnS (50 W)	5-6
" (100 W)	6-7
" (125 W)	7-10
" (150 W)	13-15
" (200 W)	10-13
CeF_3 & ZnS, evaporated	< 6

The following observations can be made from the data of table 3:

(1) Both CeF_3 and ZnS single layer coatings on KCl have approximately the same damage threshold, 35-40 J/cm^2.

(2) The sputtered ZnS coatings all had similar threshold levels, 40 J/cm^2, independent of their deposition rate, except for the 50 W sample which had a higher threshold of 60 J/cm^2. The evaporated ZnS layers damaged at a slightly lower energy than the sputtered layers.

(3) When the CeF_3 and ZnS were combined to form a 2-layer AR coating, the damage threshold of 5-15 J/cm^2 was significantly lower than all values observed for single layers regardless of material or deposition method. However, threshold values increased with increasing ZnS sputter deposition rate. For these 2-layer coatings, damage usually occurred only in the top or CeF_3 layer and these are the energy values reported here. Figure 11 shows typical single and double layer damage sites, clearly differentiated by varying shades of gray.

The sensitivity of the damage threshold to the deposition rate of the ZnS first layer, and the damage occurring primarily in the CeF_3 second layer may both be explained by examination of the first layer surface topography. In figure 2 electron micrographs of replicas of ZnS surfaces sputtered at various deposition rates, showed that ZnS crystallite size decreased with increased deposition rates. These crystallites were crystallographically oriented with their {111} planes approximately parallel to the substrate surface, and had a surface morphology of {100} facets. Thus the surface of the coating is composed of these "pyramids", on the order of $\frac{1}{4}$ micron across with surface roughness decreasing with decreasing crystallite size or increasing deposition rate. The CeF_3 was deposited on this irregular surface. During laser damage testing the laser beam was scattered at this rough, CeF_3/ZnS interface, causing the low level damage observed in the CeF_3 layer. However, the reason for the low damage threshold in the 2-layer coatings composed of a much smoother evaporated ZnS is not understood. Even though they are smoother, several anomalies have been observed in these films such as amorphous material, unidentified phases, and foreign particles on the surface. Future experiments with stricter control of the vacuum and higher purity raw materials may result in improved damage threshold levels in these evaporated coatings.

5. Conclusions

This experiment points out two very important items to be concerned with in the development of coated laser optics.

(1) The mechanical properties of both the substrate and the individual coatings must be considered. Stress developed in the coatings can cause severe changes in the substrate, such as slip.

(2) Interface topography may contribute significantly to the total absorption of the coating stack. This points to the requirement that each layer in a coating be investigated individually as a coating stack is developed.

In summary, an antireflective coating stack based on CeF_3 may be a viable alternative to ThF_4. Most of the difficulties encountered in these experiments were with the ZnS first layer, where further studies are needed.

6. Acknowledgments

The authors thank H. Posen for many valuable suggestions and discussions, J. Larkin, who provided KCl substrate material, N. Pickering for the SEM picture, H. Lipson for the optical absorption data, R. Brown for the emittance spectroscopy data, and J. Fitzgerald and C. Bergeron for technical assistance.

7. References

[1] M. Braunstein and J. E. Rudisill, Proc. of 4th Annual Conf. on IR Window Materials, 1974.

[2] A. Golubovic et al, Proc. of Conf. on Laser Induced Damage in Optical Materials, 1974.

NOTE: Micron(s) as used in this paper expresses micrometer(s).

$$1 \text{ torr} = \frac{101\,325}{760} \text{ Pa}.$$

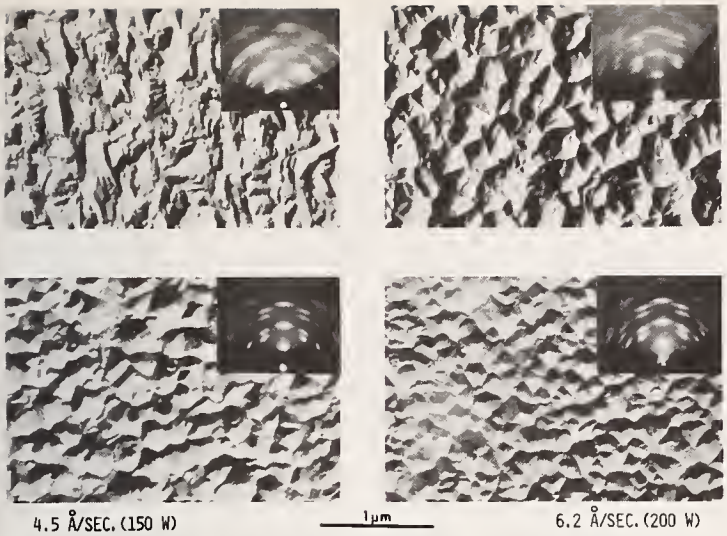

Figure 1. Electron micrographs illustrating orientation and texture of sputtered ZnS as a function of deposition rate.

Figure 2. Scanning electron micrograph of sputtered ZnS illustrating columnar growth perpendicular to the substrate surface.

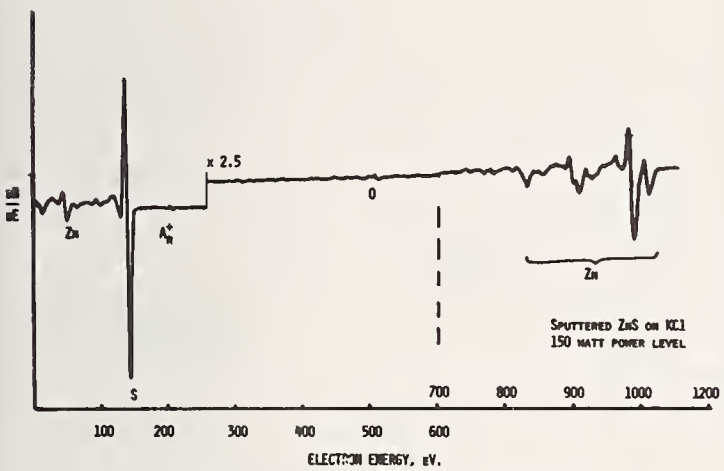

Figure 3. Auger spectrum of sputtered ZnS on KCl.

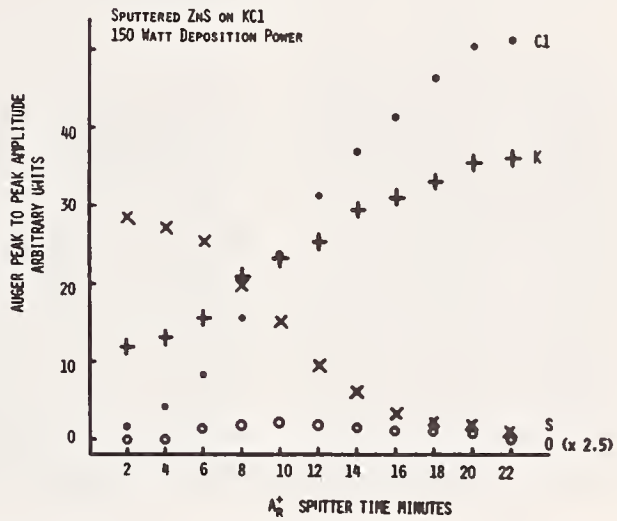

Figure 4. Auger profile of ZnS/KCl interface.

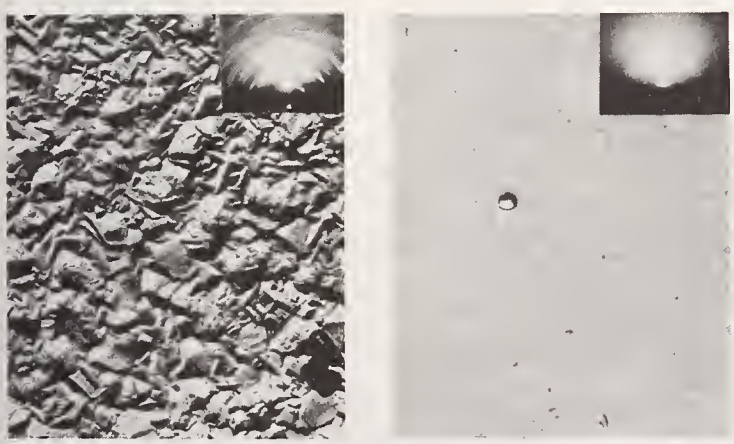

Figure 5. Electron micrograph comparing surface texture of sputtered and evaporated ZnS coatings on KCl.

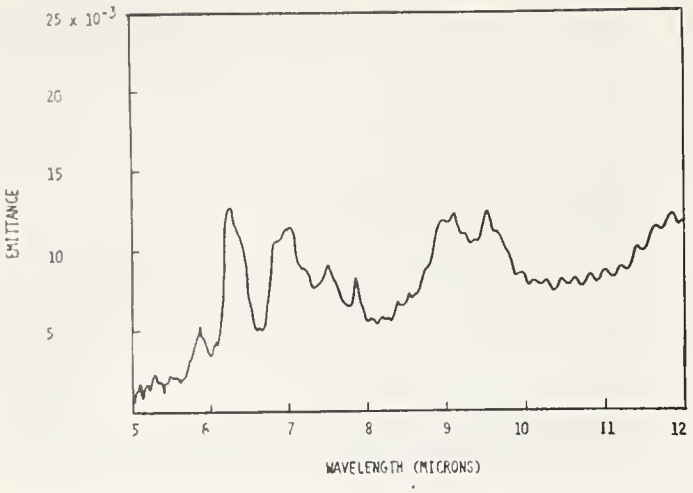

Figure 6(a). Spectral emittance scan of uncoated KCl.

NOTE: Microns as used in figures 6a and 6b expresses micrometers.

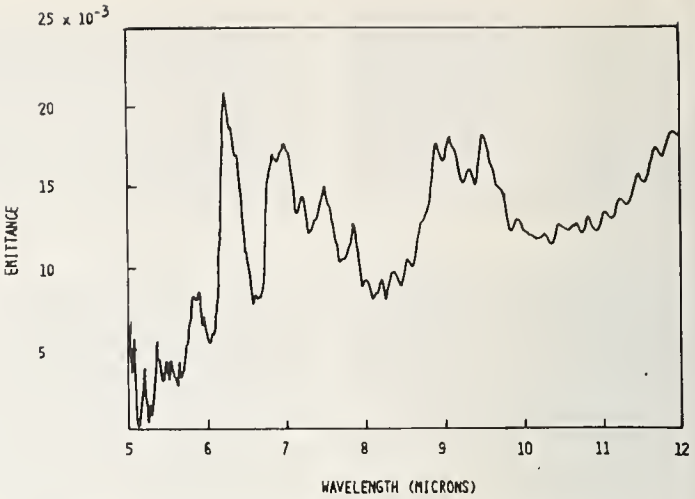

Figure 6(b). Spectral emittance scan of CeF_3 coated KCl; coating thickness is 1.3 microns.

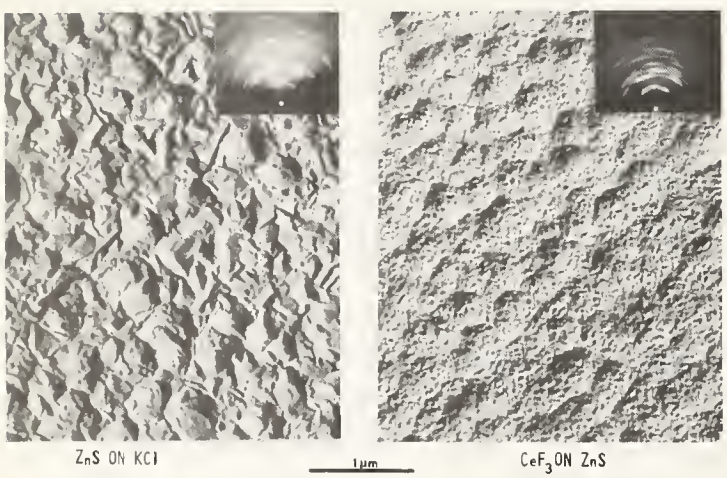

Figure 7. Electron micrographs of surface texture after first and second layer deposition on KCl.

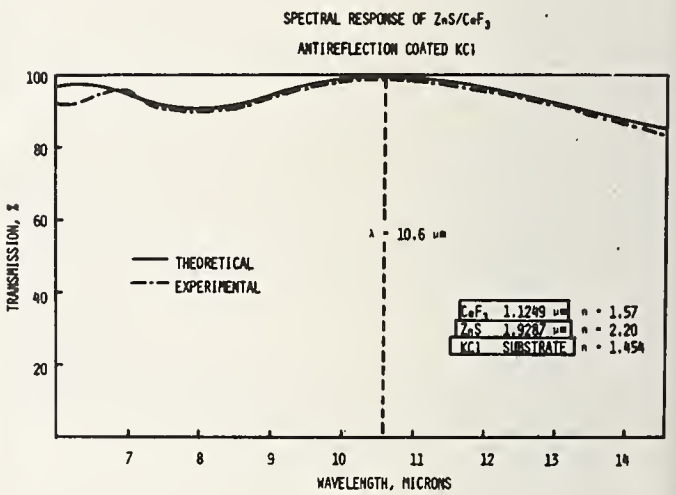

Figure 8. Spectral response of ZnS/CeF_3 anti-reflection coated KCl.

Figure 9. Nomarski micrographs of ZnS coating on KCl illustrating failure due to slip.

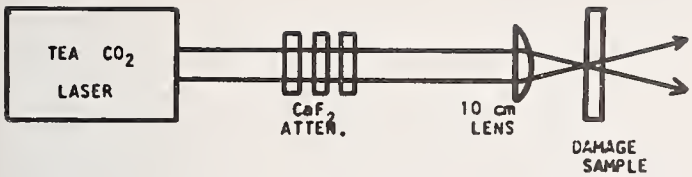

EXPERIMENTAL SET-UP FOR PULSED CO_2 LASER DAMAGE EXPERIMENTS

Figure 10. Experimental set-up for pulsed CO_2 laser damage experiment.

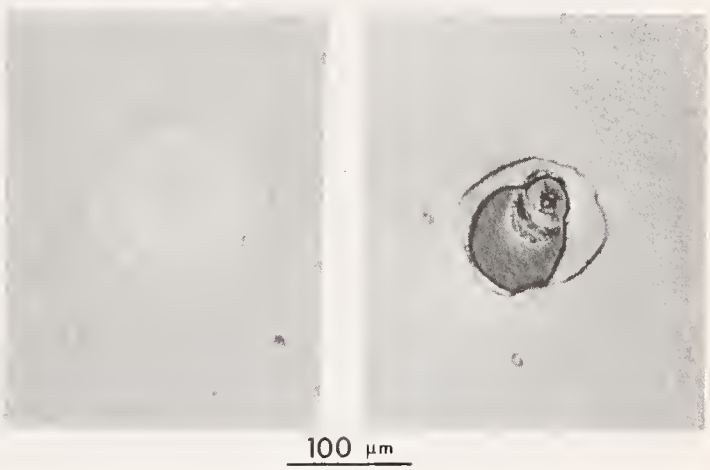

Figure 11. Micrographs illustrating damage sites on a 2-layer ZnS/CeF_3 AR coating on KCl: left one shows only top layer damage; right one show 2-layer damage, dark gray area is KCl substrate.

NO COMMENT ON PAPER BY GOLUBOVIC, et al

5.4 As_2S_3 Coatings on KCl

A. D. Baer, T. M. Donovan, and M. J. Soileau

Michelson Laboratories, Naval Weapons Center
China Lake, California 93555

Potassium chloride (KCl) and quartz windows were coated with As_2S_3 at deposition temperatures of 80°C and 22°C. The index of refraction of As_2S_3 coatings is a function of deposition temperature for KCl windows, but not for quartz windows. Coatings deposited on KCl at 80°C are more durable and less absorbing than those deposited at 22°C. It is suggested that deposition temperature affects the properties of coatings on KCl because the composition of the surface of polished KCl windows changes with temperature. As_2S_3 coatings were produced with an optical absorption of 1.7 cm^{-1} at a wavelength of 10.6 μm, as compared with 1.1 cm^{-1} reported for bulk As_2S_3.

Key words: As_2S_3; coating deposition; index of refraction; laser windows; 10.6 μm; surface composition.

1. Introduction

As_2S_3 coatings show promise for use with high-power lasers because they can tolerate high-intensity radiation, and protect alkali halide surfaces from water vapor [1][1]. Since the absorption of thin-film As_2S_3 is higher than that of bulk As_2S_3, the optical performance of As_2S_3 coatings does not appear to be limited by intrinsic properties of As_2S_3. Some feature of the thin films seems to be degrading their optical performance. For thin films on KCl windows, the composition of the window surface during deposition may be a critical feature. A KCl surface or interface is not necessarily stoichiometric. Palmberg and Rhodin found that when KCl is bombarded with electrons, the surface quickly reaches a composition characteristic of the temperature: potassium rich at room temperature, and stoichiometric at high temperatures [2]. The composition changes quickly because bombardment with electrons, even electrons with energy less than 50 eV, caused chlorine and potassium to be liberated [2]. Very mild bombardment produces a potassium-rich surface at room temperature. Consequently, it is not surprising that Golubovic and co-workers found a potassium-rich layer between KCl windows and germanium coatings deposited by sputtering and by electron beam evaporation [3]. Here we confirm that the surface of polished KCl is nearly stoichiometric at 80°C, and show that As_2S_3 coatings deposited on polished KCl at 80°C are more durable and less absorbing than coatings deposited at 22°C. Deposition temperature is shown to significantly affect the properties of coatings on KCl, but not the properties of similar coatings on quartz.

2. Measurements

The stability of As_2S_3 coatings on KCl was determined by raising the temperature of coated disks of KCl single crystals until the coatings re-evaporated. The disks were 7 mm in diameter and 2 mm thick. Coatings were deposited and maintained in a vacuum of less than 10^{-7} Pa (10^{-9} torr). The temperature of a coated disk was monitored with a thermocouple mounted at the edge of the disk. Voltage from the thermocouple electronically controlled a heater which warmed the disk. This feedback system held temperature constant within 1°C, until manually changed; response time of the system to manual temperature changes was 3 minutes. Using this system, the temperature of coated disks was adjusted upwards from 100°C in 10°C increments, waiting at least 2 hours at each temperature. The coatings re-evaporated during the wait at 150°C. Re-vaporization at 150°C compares with dissociation of bulk As_2S_3 at 340°C [4] and softening of bulk As_2S_3 at 200°C [5]. The instability of As_2S_3 coatings sets an upper limit of 150°C on deposition temperature.

Stoichiometry of uncoated KCl surfaces was studied by comparing the heights of potassium and chlorine peaks on Auger spectra. Single crystal disks of KCl were mounted in the vacuum system described above. Auger spectra were measured on a disk at various temperatures, both in increasing and decreasing sequence. After a temperature change, the temperature of the disk was allowed to equilibrate for at least an hour before an Auger spectrum was recorded. The Auger electron beam was 1 μA at an energy of 2 keV. Figure 1 shows Auger spectra recorded with the KCl cold and hot. Two changes occur in the surface composition as the temperature is increased: water, indicated by the O peak, vanishes; and the relative number of chlorine atoms on the surface increases. The relative number of chlorine atoms is proportional to the ratio of the chlorine to potassium Auger peak heights [6]. This ratio, obtained from measured Auger spectra, is plotted as a function of temperature on figure 2. As shown, the relative number of chlorine atoms increases until 90°C, after which it remains approximately constant. Previous workers found the stoichiometry of the surface to behave as shown by the dashed line on figure 2, and that the surface was stoichiometric at temperatures above 65°C [2]. Present work finds the stoichiometric edge to be at 90°C rather than 65°C. In either case, these data show that a KCl surface under light bombardment is stoichiometric above 90°C and potassium rich at room temperature.

1. Figures in brackets indicate the literature references at the end of the paper.

Interpretation of the Auger data is complicated because the electron beam was large enough to produce changes in the surface during measurement. Chlorine and potassium are removed from the surface by both thermal and electron-induced desorption, and with present instrumentation it is difficult to determine which is more important. At low temperatures the electron-induced desorption seems to be dominant, but at 90°C some other mechanism, perhaps thermal desorption, becomes dominant and causes the surface to be stoichiometric. In this case, it would be possible to make the KCl surface stoichiometric by heating it above 90°C.

In order to test the effect of deposition temperature on window coatings, KCl windows were coated at both low and high temperatures. As_2S_3 coatings 2 μm thick were deposited on window blanks, 39 mm in diameter and 5-8 mm thick, in the bell jar diagrammed in figure 3. The vacuum system includes a diffusion pump with liquid nitrogen trap and has a base pressure of 10^{-6} Pa (10^{-8} torr). Arsenic trisulfide, 99.999% pure, was evaporated at a rate of 1.4 nm/sec from a quartz bottle with a tantalum insert heater [7]. The windows were supported by a stainless steel plate and heated with an infrared lamp, while the temperature of the steel plate was monitored. Room temperature coatings were deposited with the lamp off. High-temperature coatings were deposited after the steel plate had been warmed to 80°C for at least 2 hours; after deposition, the window was allowed to cool for at least 2 hours before removal from the vacuum system. The same apparatus was used for coating all the windows discussed.

The transmission of the coated windows was measured using a Perkin-Elmer 180 spectrometer. The index of refraction, n, was calculated from the ratio of optical transmission measured at adjacent maxima and minima in a spectral region with low absorption and dispersion, and from known values of n for the windows; this method for calculating n was chosen because it does not require a knowledge of the thickness of the coating. All points plotted for KCl and the points plotted at 3.5 μm for quartz in figure 4 were determined from the position of a maximum or minimum, and the value of n at 3.5 μm. By using the ratio method, uncertainties due to error in the estimate of film thickness are eliminated. The film thickness and film uniformity were also measured in separate experiments. Over a distance of 0.5 inch, the coatings deposited at 22°C and 80°C were uniform to better than 1%.

The value of the indices of refraction shown on figure 4 could be in error for several reasons. First, the index of refraction may be significantly different at the two wavelengths of the adjacent maximum and minimum; however, in the present case at 3.5 and 8.5 μm, the index of refraction is essentially constant for As_2S_3 in both bulk and coating form [8]. Second, the formula relating a ratio to the index of refraction was derived assuming lossless media. In the present case, the fraction of light absorbed in the coatings was measured calorimetrically and found to be between 4×10^{-4} and 1.5×10^{-3}. Whether the losses are assumed to occur at the interface or to be spread throughout the film, the correction for absorption increases our estimate of n, but by no more than 0.2%. This source of error is small relative to the 2.5% difference in n for different deposition temperatures shown in figure 4. Third, the wavelength calibration of the Perkin-Elmer 180 could be in error, introducing an uncertainty in the index of refraction of the windows. This possible source of error is insignificant. However, uncertainties in transmission of ±0.2% may add as much as 0.3% uncertainty to n in our particular case. Finally, there may be systematic errors. For example, the value of the index of refraction of As_2S_3 on quartz at 3.5 μm found with the ratio method is 1.5% lower than that found using thickness measurements and the position of the transmission maxima, and 3.5% lower than the index of refraction reported in the literature [8]. However, the values plotted in figure 4 were obtained using the same method of analysis from data measured under identical conditions, so that systematic errors would be the same. For the purpose of comparison done here, the values of n in figure 4 are accurate to ±0.5%, sufficiently accurate to document the changes of 2.5% actually found.

As shown in figure 4, the deposition temperature significantly affects n for As_2S_3 on KCl, but not on quartz. Evidently the elevated temperature affects the coating because it alters the KCl, but not the quartz. The index of the coatings on KCl appears to be approaching that of coatings on quartz as the deposition temperature is increased; that is, when excess potassium is likely to be present on the KCl during deposition, the index of refraction of the coating deviates further from that of the quartz coatings.

Durability of high- and low-temperature coatings was estimated by comparing how long each would last when subjected to a standard buffing. Two 2.2-μm coatings were buffed off KCl windows using Linde A polishing compound with a triacetin slurry and a polishing wheel. Under identical conditions, it took four times as long to remove the high-temperature coating as it did the low-temperature coating.

Optical absorption at 10.6 μm was determined from calorimetric measurements [9,10]. The absorption of the 80°C window increased 0.04% when it was coated with a 2.2-μm As_2S_3 film. Assuming that all the increased absorption is in the film, the β of this film is 1.7 cm^{-1} [9]. Values of β for various coatings are compared with that for bulk As_2S_3 in table 1. The range of values shown for KCl with a 22°C deposition temperature represents a large number of coatings. The best coating produced at 22°C, using the most careful handling procedures, had an absorption of 2.9 cm^{-1}. The absorption of coatings produced at 80°C, 1.7 cm^{-1}, is significantly lower than the 2.9 cm^{-1} and close to the absorption reported for bulk As_2S_3.

Table 1. Absorption of As_2S_3 prepared in various ways. Coatings are approximately 2.2 μm thick.

Form	Window	Deposition temp (°C)	β (cm^{-1})
Coating	NaCl	22	8
Coating	KCl	22	2.9–11
Coating	KCl	80	1.7
Bulk	—	—	1.1*

*P. A. Young [1].

3. Discussion

The measurements presented above indicate three empirical relationships: (1) The stoichiometry of a KCl surface under electron bombardment is a function of temperature; room temperature surfaces have excess potassium. (2) Coatings deposited on windows held at 80°C are more durable and less absorbing than coatings deposited on windows held at 22°C. (3) The index of refraction of As_2S_3 coatings is a function of deposition temperature on KCl, but not on fused quartz. Deposition temperature affects the coating because it alters KCl; otherwise one would expect the index of refraction of coatings on quartz to depend as strongly on deposition temperature as does the index of refraction of coatings on KCl. Some critical property of the KCl surfaces must depend strongly on temperature between 22°C and 80°C. This property could be long-range order, or lattice parameter, or composition. Composition is a prime candidate because it can change so much between 22°C and 93°C (more than a factor of four in figure 1). We tentatively conclude that it is excess potassium on KCl surfaces during deposition that degrades the optical and mechanical properties of optical coatings.

This conclusion can be verified by probing the surface more delicately with electron and photon beams. The large electron beam, 1 μA, required for standard Auger spectroscopy interacts too strongly with As_2S_3 coatings and KCl surfaces; the surface changes significantly during the measurement. Consequently, Auger measurements will have to be done with more sensitive instrumentation so that measurements can be made with a beam current smaller than 1 μA. A photon beam is less damaging than an electron beam, but photoemission measurements require special high-energy light sources. Both kinds of measurement can be done, but they require the application of improved instrumentation.

4. Acknowledgments

The authors gratefully acknowledge the assistance of E. J. Ashley and J. M. Bethke.

5. References

[1] Young, P. A., Thin Solid Films 6, 423 (1970).

[2] Palmberg, P. W. and T. N. Rhodin, J. Phys. Chem. Solids 29, 1917 (1968).

[3] Golubovic, A., W. Ewing, J. Bruce, J. Comer and D. Milan, Proc. Symp. Laser Induced Damage in Optical Materials, NBS Spec. Pub. 414 (1974), p. 76.

[4] The stability of As_2S_3 used here was determined by differential thermal analysis.

[5] Savage, J. A. and S. Nielsen, Infrared Phys. 5, 195 (1965).

[6] Palmberg, P. W., G. E. Riach, R. E. Weber and N. C. MacNeal, "Handbook of Auger Electron Spectroscopy," (Physical Electronics Industries, Inc., Edina, Minn., 1972).

[7] The design of the As_2S_3 evaporator was based on information obtained from the Servo Corporation of America.

[8] Young, P. A., J. Phys. C: Solid State Phys. 4, 92 (1971).

[9] Loomis, J. S., Appl. Opt. 12, 877 (1973).

[10] Loomis, J. S., "Calorimetric Absorption Measurement of Infrared Optical Materials," Laser Division Digest, Air Force Special Weapons Center, Kirtland, AFB, N. M., TR LRD-72-1 (1972), p. 29.

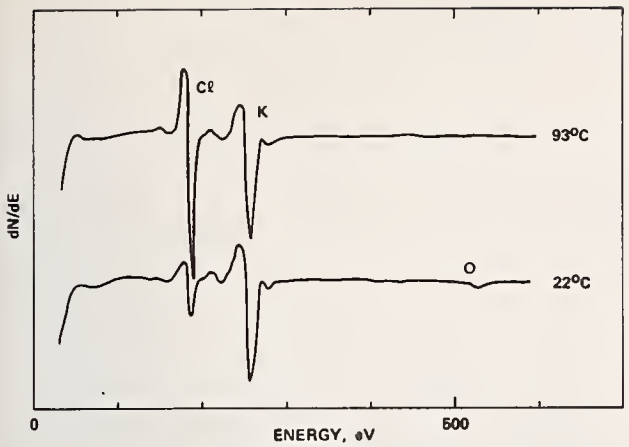

Figure 1. Auger spectra measured with 1-μA, 2-keV electron beam on single-crystal, KCl disks. The mix of atomic species on the surface changes with temperature.

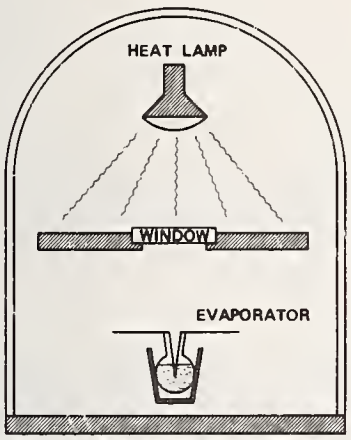

Figure 3. Diagram showing bell jar in which trial depositions of As_2S_3 on KCl and quartz windows were performed.

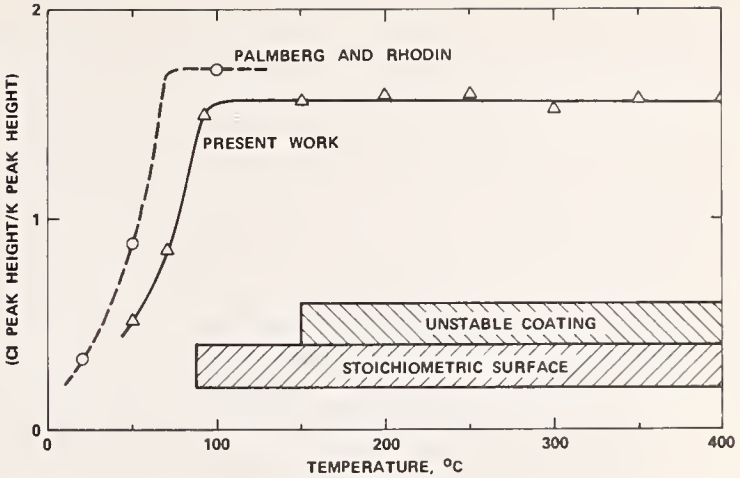

Figure 2. Ratio of Cl and K peak heights for Auger spectra recorded on KCl at various temperatures. Circular data points were taken from Auger spectra reported by Palmberg and Rhodin who found the surface to be stoichiometric at temperatures above 65°C [2].

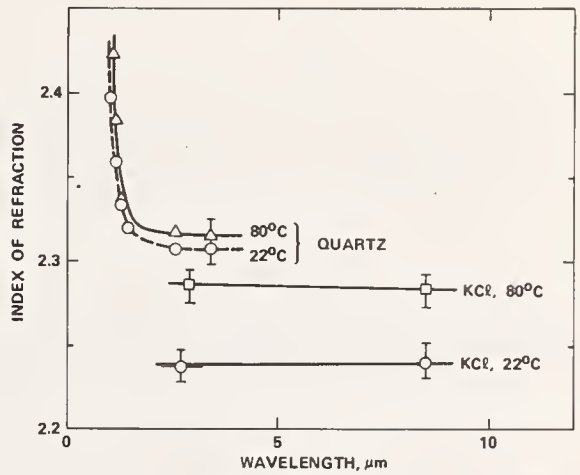

Figure 4. Index of refraction of As_2S_3 coatings deposited at different temperatures on KCl and quartz windows. Points with error bars were determined from the ratio of transmission maxima to minima as measured with a Perkin-Elmer 180 spectrometer. Other points were determined from the wavelength of a maximum or minimum.

NO COMMENT ON PAPER BY BAER, *et al*

5.5 DESIGN FOR HIGH POWER RESISTANCE

By

Arnold L. Bloom and

Verne R. Costich

Coherent Radiation, Palo Alto, Calif.

The influence of materials parameters such as thermal conductivity, intrinsic stress, thermal expansivity, and Young's modulus on coating performance is discussed. Metal, metal-dielectric, and dielectric multilayer films at both 1.06 μm and 10.6 μm are considered. Calculations are presented for various combinations of coatings and substrates.

Key words: Damage threshold; optical coatings; thin films.

Coatings develop intrinsic stresses during deposition in a vacuum chamber and are further stressed when they are cooled from their deposition temperature to ambient temperature due to mismatch between their expansion coefficient and that of the substrate. It is this prestressed multilayer which is exposed to a high power pulse for a short period of time. We will indicate the prestresses existing in common 1.06 μm and 10.6 μm coating designs and the additional stresses introduced during laser pulses.

Silver Reflector for 10.6 μm

The most commonly used 10.6 μm mirror is silver with a very thin dielectric overcoating of thorium fluoride. The absorption occurs in a very thin region near the surface of the silver called the skin depth (about 0.07 μm for silver exposed to 10.6 μm pulses). The temperature rise can be computed for a very short pulse of one joules/cm^2 by use of the equation:

$$\Delta T = \langle E \rangle^2 \frac{\pi n k}{C_p \rho \lambda},$$

where $\langle E \rangle^2$ is the square of the electric field in the film, with $\langle E \rangle^2 = 1$ in air, $n - ik$ is the complex index of the film, Cp is the specific heat, ρ is the density in grams/cm^3, and λ is the wavelength of the incident radiation.

Silver has such great thermal conductivity, that in a one microsecond pulse, the heat absorbed in the skin depth of 0.07 μm is conducted to a depth of 2.6 μm. The computed temperature profiles versus depth are illustrated in figure 1. Note that the surface temperature rises in proportion to the square root of the pulse duration as does the depth of penetration of the temperature distribution. A one microsecond pulse of energy density 10.0 joules/cm^2 will introduce 0.1 joules/cm^2 in a 2.6 μm deep region and thus cause the surface temperature to be raised by 220°C, at which temperature the film will start to degrade. Longer pulses will allow more energy to be conducted into the film. Therefore, the energy density damage threshold is proportional to the square root of the pulse length if the film is thick enough, i.e., of greater thickness than the penetration depth. Conclusion: use thicker films of silver for long pulses or check out the thermal conductivity of the substrate.

Coating Materials

For 1.06 μm coatings, TiO_2, and SiO_2 are commonly used, while at 10.6 μm, ZnS and ThF_4 are used, sometimes in conjunction with silver. The relevant parameters of these coatings are given in table 1. Note that some of the data has been estimated from known data on similar materials. Note that ZnS has negative intrinsic stress (compressive) which makes it damage easily at 1.06 μm as will be seen below.

Dielectric films of quarter wavelength optical thickness have physical thicknesses of 0.12 μm and 0.20 μm, respectively, for TiO_2 and SiO_2 tuned at 1.06 μm, 1.2 μm, and 2.0 μm, respectively, for ZnS and ThF_4 tuned at 10.6 μm. Figure 2 shows the temperature rise in a maximum reflectance stack of such layers at 1.06μm, Since the absorption in SiO_2 is much smaller than that in TiO_2, there is a discontinuity at the odd-numbered interfaces. The even-numbered interfaces, being at nodes of the electric field, have no immediate temperature rise. Note that the shape of the temperature rise in the first two layers is repeated many times down through the stack, but the amplitude is decreased by a factor of about $(n_H/n_L)^2$ in each succeeding repetition. In a short time conduction will smooth the temperature excursions versus depth. The time taken to smooth to $\frac{1}{e}$ of the original excursions was computed for this coating and all the coatings considered below. Table II gives these thermal diffusion time constants for the materials and designs considered here. Note that for ZnS/ThF_4, which could be used at both wavelengths, the time constant for 10.6 μm is two orders of magnitude larger than the time constant for 1.06μm. This is logical, since, if both distributions have 1°C excursions, the distribution caused by the 10x more gross wavelength can be smoothed only by the conduction of heat 10x as far, but it has temperature gradients only 1/10 as great. Note from the table that for picosecond pulses the heat always "stays in place", while for microsecond pulses one can assume a uniform temperature throughout the multilayer, but that time has not permitted any of the heat to be conducted away into the substrate.

Stresses in Coatings for 1.06 μm

There are three sources of stress in coatings exposed to 1.06 μm pulses:

1. Intrinsic stress due to the deposition process. Values for this component of the stress are given in table 1.

2. Thermally induced stress due to the mismatch of expansion (contraction) coefficient between the coating and the substrate. This component is given by the equation $\sigma = Y[(\alpha_1 - \alpha_s)\Delta T]$ where α_1 is the coating's expansion coefficient from table 1, α_s is the substrate's expansion coefficient, ΔT is the temperature of deposition minus that of ambient (before the pulse) in degrees centigrade, and Y is Young's modulus of the coating as given in Table I.

3. Stress induced by the pulse. This is given by $\sigma = -Y\alpha_1 \Delta T$ where α_1 is the the coating's expansion coefficient from table 1, Y is Young's modulus from table 1, and ΔT is the temperature rise, which in the short pulse domain is a non-uniform function within each layer. Note that since ΔT, α_1, and Y, are always positive, the induced stress must always be compressive.

The computed stresses in a TiO_2/SiO_2 maximum reflector deposited at 300°C on Bk-7 and used at 20°C are shown in figure 3. The dotted line indicates the intrinsic stress components. The solid line indicates the combination of intrinsic stresses and the stresses introduced by the cooling from the temperature of deposition to that of ambient, i.e. the stresses in the coating before the pulse. The dashed line indicates the stresses in the coating immediately after a five joule/cm^2 short pulse. Note that even though the SiO_2 layers were heated, their expansion coefficient is so low that the pulse-induced stress is negligible. The stress at each level in the multilayer is the integral of the plotted curves from the air surface down to that depth. The integral is tensile at all interfaces. If the pulse energy density were increased to 50 Joules/cm^2, the top layer becomes highly compressive and the stress on the first interface surpasses its strength (estimated at 10^5 dynes/cm). In fact, real coatings probably have areas with greater absorption and less strength, which will damage at lower energy densities. The damage will show the characteristics of compressive buckling. That is, it will look like a burst paint blister, and will be more likely to occur near the edge of a large beam than in the central region of the beam where there should be no asymmetrical shear forces.

Figure 4 shows the same stresses in the same coating deposited onto fused silica. Note that this coating is so tensile that it is about to craze (form hairline cracks of tensile rupture). The laser pulse again causes the high index layers to become less tensile (eventually more compressive). Note that the highly tensile prestress in this coating on fused silica causes it to be about twice as damage resistant as the same coating on Bk-7.

The temperature rise in a 1.06 antireflection coating of TiO_2 and SiO_2 deposited on fused silica is shown in figure 5. A non-quarter wave design is used because it has lower reflectance.

The intrinsic, ambient and pulse-induced stresses in this coating are shown in figure 6. Being highly tensible, this AR should be highly damage resistant. It damages, when the substrate/TiO_2 interface can no longer stand the stress. This interface is believed to be less strong than the more chemically pure interfaces between the layers (4×10^4 dynes/cm is our guess). Figure 7 shows the stresses in this AR coating on Bk-7. The stress integral is compressive, becomes more so during a pulse and is therefore not as damage resistant as it would be on fused silica.

Coatings for Use at 10.6 Microns

Since 10.6μm pulses are usually longer than 20 nsec, table II indicates that the long pulse domain is of interest. The intrinsic and ambient stresses computed per a ZnS/ThF_4 reflector, deposited at 150°C on ZnSe, are shown in figure 8. Note that the stress scale has been changed. ZnS is used at 10.6μm because it has a compressive intrinsic stress which will compensate the low index material's tensile intrinsic stress. This allows thick coatings to be deposited without buckling or crazing. If after a long laser pulse, the coating is heated to 100°C above ambient, the compressive pulse-induced stress will be -0.035×10^{10} dynes/cm^2 for the ZnS layers and -0.012×10^{10} dynes/cm^2 for the ThF_4 layers. Failure will take place at the substrate interface. Increasing the ThF_4 layer thicknesses will not improve matters because that would increase the absorption, and thus increase the temperature and the pulse-induced compressive stress.

The stresses in an enhanced metal reflector of ZnS/ThF_4 on silver are shown in figure 9. This is a poor design since it is so compressive even before the pulse, because of silver's large expansion coefficient. When deposited on molybdenum this coating is less compressive as shown in figure 10. In fact, use of a lower expansion coefficient would have produced a tensile design which would be more resistant to laser pulses of high energy density. In these last two figures, the effect of a 100°C temperature rise in the coating but not the substrate is the same as above, -0.035×10^{10} dynes/cm^2 for ZnS and -0.012×10^{10} dynes/cm^2 for ThF_4.

Conclusions and Recommendations

Of the metal films used to make reflectors for 10.6μm, silver has the best thermal conductivity and will therefore rise less in temperature. But, since silver starts to degrade at 200°C, copper or gold may be better and should be considered.

Of the dielectric materials used at 1.06μm, ZnS/ThF_4 shows too much compressive strain to be very resistant. TiO_2/SiO_2 used at 1.06 has a short (good) thermal diffusion time constant and is highly tensile on fused silica, yielding better damage resistance. To maintain surface figure with a highly tensile coating the substrate must be at least of 6:1 = diameter: thickness. ZrO_2 was not considered due to lack of basic data and because it is so non-reproducable that it is no longer commonly used in the production of high power resistant optics.

At 10.6μm, mirrors made of ZnS/ThF_4 maintain their integrity, but are slightly compressive. It would be better if they were produced with such high tensile stress as to be almost crazing. Twice as high a damage threshold would result from such a design. For very long pulses (1 millisecond or longer) or cw exposure, the thermal conductances of the substrate should be optimized, enhanced metal reflectors with no more than four dielectric layers on top of a metal that is stronger, less expansive and less temperature sensitive than silver should be used.

We have learned much in the course of this work and would like to thank C.E. Thomas and KMS Fusion for their timely testing of various coating experiments. Two references we have found useful are "The Mechanical Properties of Thin Condensed Films" by R.W. Hoffman in Physics of Thin Films, Volume 3, 1966, and "Stresses Developed in Optical Film Coatings" by A.E. Ennos, Applied Optics, 1966.

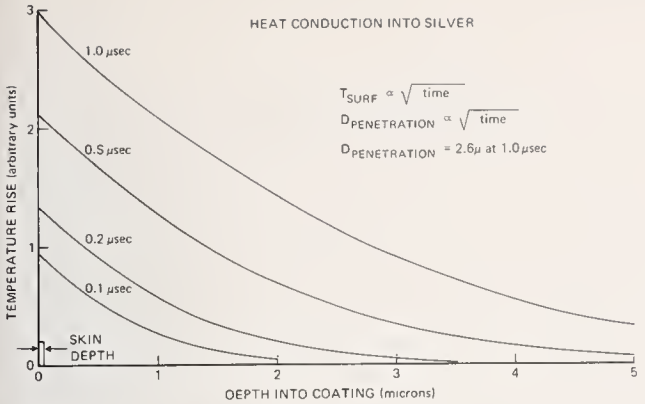

Figure 1. Computed temperature rise in silver versus depth and time.

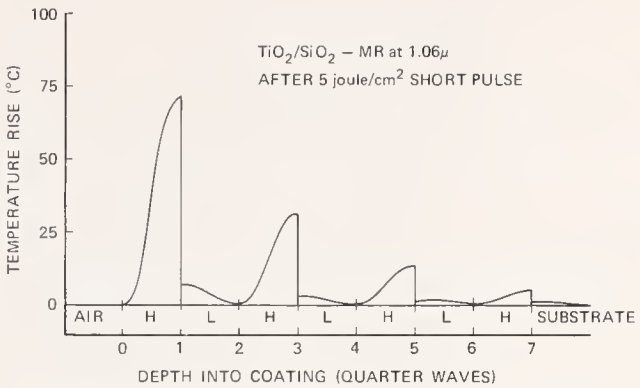

Figure 2. Computed temperature rise after a 5 joule/cm^2 pulse for TiO_2/SiO_2 maximum reflector at 1.06 μm.

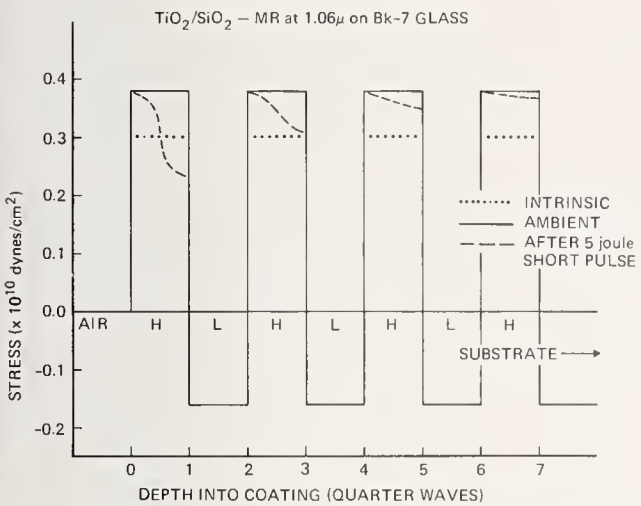

Figure 3. Computed stresses in the coating of figure 2, when deposited on BK-7, cooled to ambient, then exposed to a 5 joule/cm^2 pulse.

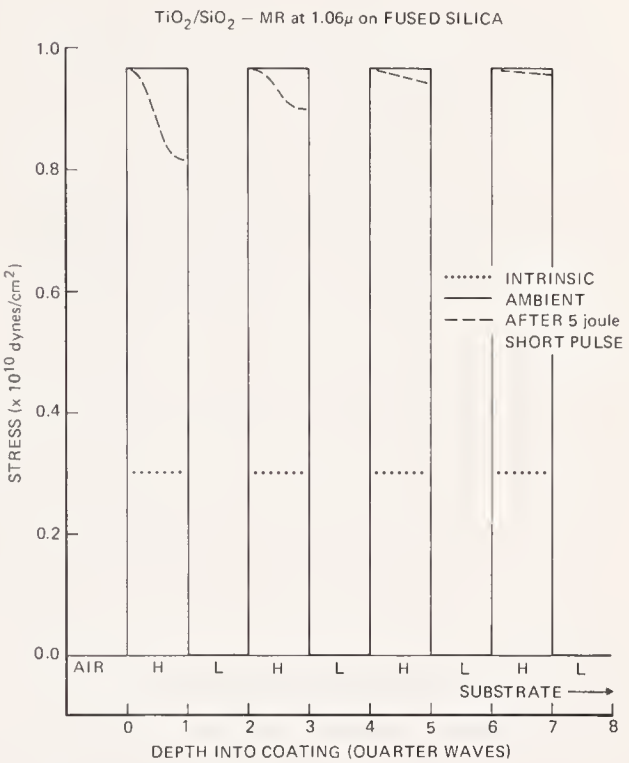

Figure 4. Computed stresses in the coating of figure 2, when deposited on fused silica, cooled to ambient, then exposed to a 5 joule/cm^2 pulse.

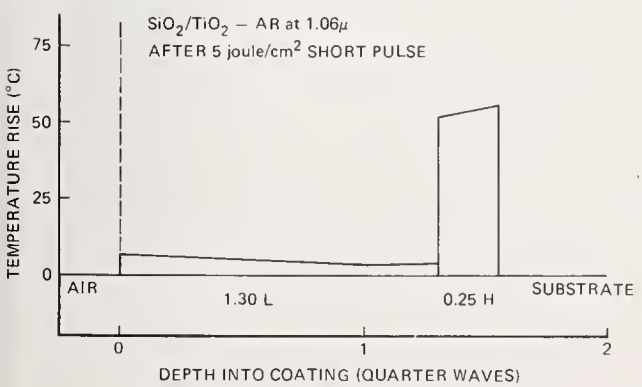

Figure 5. Computed temperature rise after a 5 joule/cm^2 pulse for a TiO_2/SiO_2 anti-reflection coating at 1.06 μm.

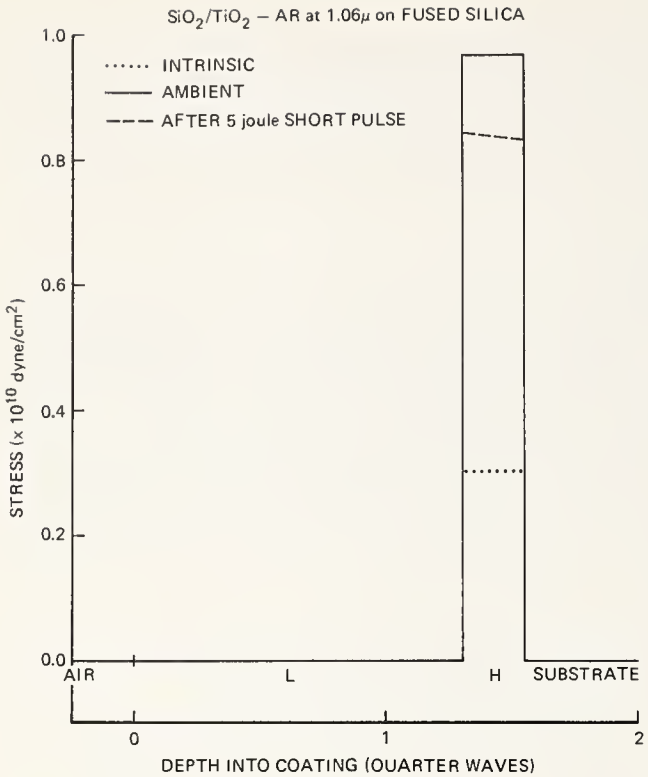

Figure 6. Computed stresses in the coating of figure 5, when deposited on fused silica, cooled to ambient, then exposed to a 5 joule/cm^2 pulse.

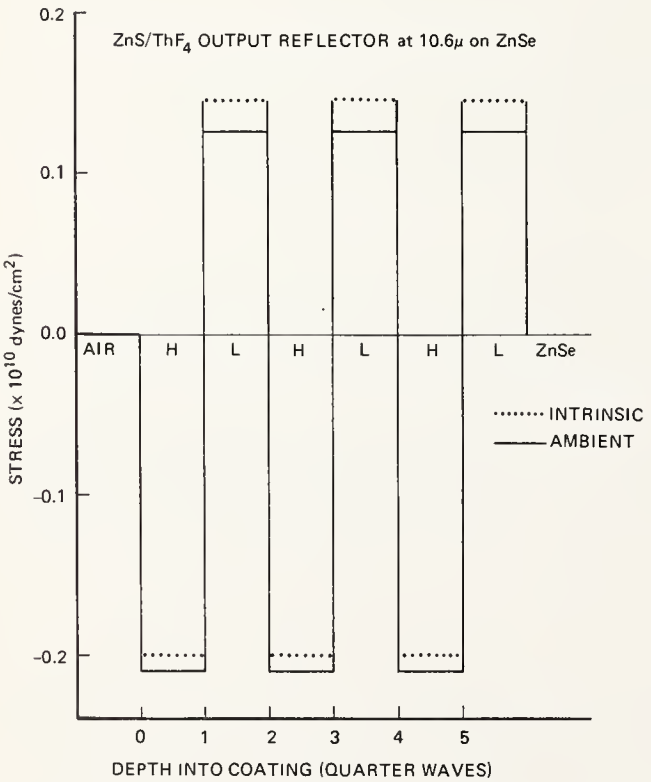

Figure 8. Computed stresses in a ZnS/ThF_4 output mirror coating in 10.6 μm deposited on ZnSe and cooled to ambient.

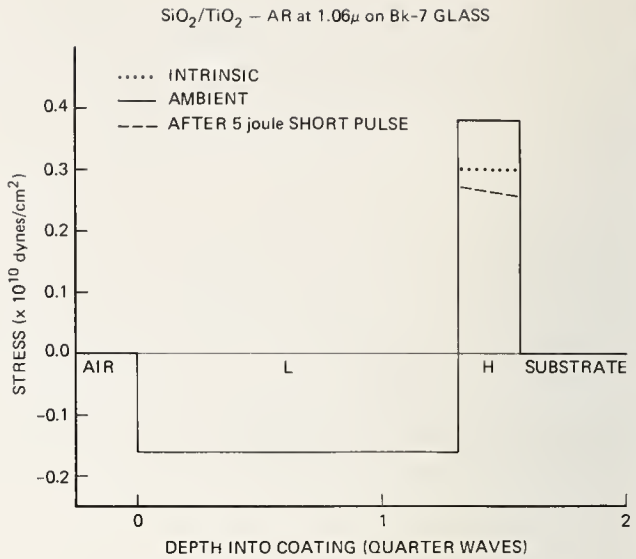

Figure 7. Computed stresses in the coating of figure 5, when deposited on BK-7, cooled to ambient, then exposed to a 5 joule/cm^2 pulse.

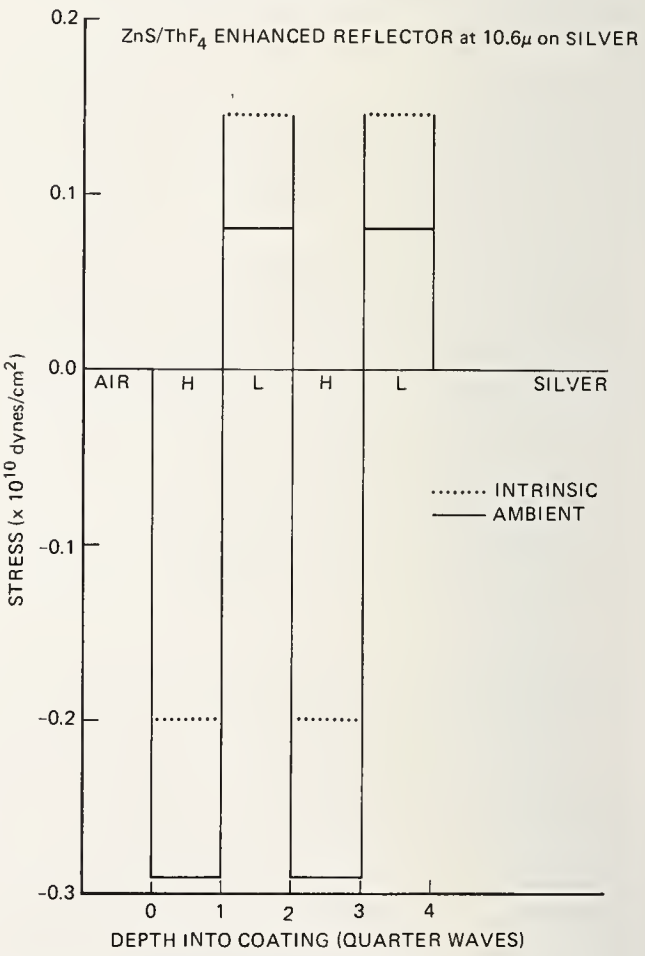

Figure 9. Computed stresses in a ZnS/ThF_4 enhanced metal reflector at 10.6 μm deposited in silver and cooled to ambient.

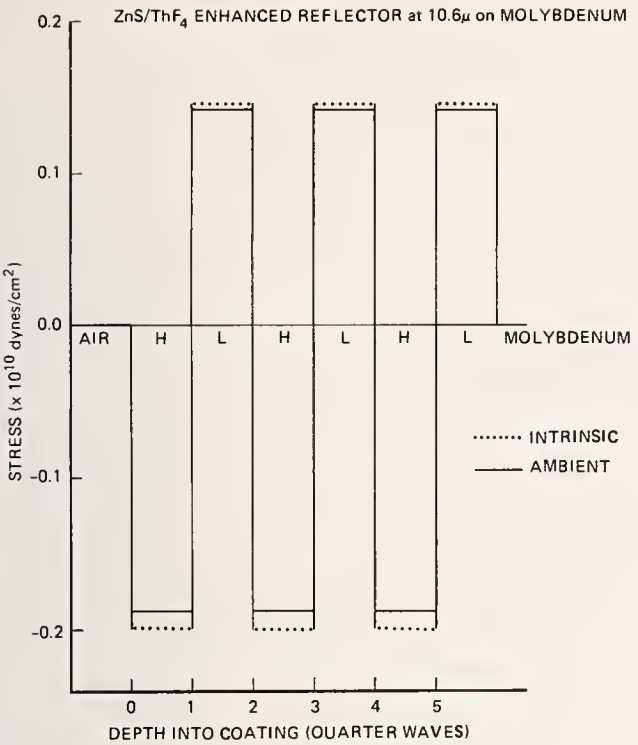

Figure 10. Computed stresses in the coating of figure 9, when deposited on molybdenum and cooled to ambient.

Table 1. Characteristics of coating materials.

CHARACTERISTICS OF COATING MATERIALS

	TiO_2	SiO_2	ZnS	ThF_4	Mo	Ag	ZnSe
Density	4.3	2.7	3.98	6.3	10.2	10.5	5.42
C_p	0.169	0.22	0.12	0.048*	0.059	0.056	0.08
Heat Conductivity	0.10	0.015	0.05*	0.05*	1.4	4.18	0.05
Expansion Coefficient ($\times 10^{-6}$/°C)	8.8	0.5	7.1	4*	5	20	8.5
Intrinsic Stress (10^{10} dyne/cm^2)	0.30	≈0	-0.2	0.145	0.55	0.085	-0.2**
Young's Modulus ($\times 10^{10}$ dyne/cm^2)	280	108	50	30*	340	75	50**

* estimated
** taken same as ZnS

Table II. Thermal diffusion time constants for some common coating designs.

THERMAL DIFFUSION TIME CONSTANTS

Coating Design	Tuned Wavelength	
	1.06μ	10.6μ
TiO_2/SiO_2 — MR	36 psec	—
ZnS/ThF_4 — MR	200 psec	20 nsec
SiO_2/TiO_2 — AR	6.5 psec	—
ThF_4/ZnS — AR	200 psec	20 nsec
Silver	500 psec	150 psec
Molybdenum	—	0.06 psec

COMMENTS ON PAPER BY BLOOM and COSTICH

The point was raised that stress and crystallography of a thin film are strongly dependent on the method of deposition. Under the circumstances it was asked how can one measure the stress accurately. The authors referred the questioner to an article by R. W. Hoffman in Vol. 3 of the Physics of Thin Films. This article is entitled "Mechanical Properties of Thin Films." The question was then raised as to how important the stress effect is in the damage process considering that other effects such as impurities and defects tend to mask the considerations presented in this paper. The authors emphasized the fact that synergistic effects are present in the damage process and that the various causes of damage interact, but that in general highly stressed films tend to fail more readily than films without residual stress whatever the principal cause of the damage. A further point was raised concerning the application of bulk properties to the thin film. Here the authors indicated that they only could make general inferences with regard to the applicability of bulk properties in design of thin films, but they felt that in general they provided a useful guide to the design of multilayer coatings. The method put forward in this paper has been used to achieve improved coatings in practical cases.

5.6 INFLUENCE OF STANDING-WAVE FIELDS ON THE LASER DAMAGE RESISTANCE OF DIELECTRIC FILMS*

Brian E. Newnam, Dennis H. Gill and George Faulkner

University of California
Los Alamos Scientific Laboratory
Los Alamos, NM 87545

The influence of standing-wave electric fields on the damage resistance of dielectric thin films was evaluated for the case of 30-ps laser pulses at 1.06 μm. Single-layer films of TiO_2, ZrO_2, SiO_2, and MgF_2 were deposited by state-of-the-art electron-gun evaporation on BK-7 glass substrates with uniform surface preparation. The film thicknesses ranged from one to five quarter-wave increments.

The thresholds for TiO_2 films of odd quarter-wave thickness were greater than for even multiples which correlated well with the calculated internal maximum electric fields. Threshold variations for ZrO_2 films were apparent,but not as distinctly periodic with film thickness. Negligible variations were obtained for SiO_2 films, again correlating with electric-field calculations.

Additional tests allowed comparisons of thresholds for 1) back- and front-surface films for normal incidence; 2) S- and P-polarized radiation at an incidence angle of 60°; and 3) circular and linear polarizations for normal incidence. The thresholds were compared with calculated standing-wave field patterns at various locations in the films. A definite correlation was generally found between the internal field maxima and the thresholds, but in a few coatings defects apparently decreased or prevented any correlation.

Key words: Damage thesholds; dielectric thin films; electric fields; electron-gun evaporation; picosecond pulses; rf sputtering; standing-wave patterns.

1. Introduction

The purpose of this experimental study was to determine whether or not there is a direct correlation of the standing-wave (SW) electric field distributions in optical coatings with their laser-induced damage thresholds. Standing-wave field distributions are quasi steady-state interference patterns produced by superposition of traveling waves interreflected at various parallel impedance discontinuities, e.g., air-film and film-substrate interfaces.

As early as 1971, Turner [1][1] reported that half-wave (HW) optical films had lower damage thresholds than quarter-wave (QW) films, from which he suggested a possible correlation with the internal SW field patterns. In 1972 Newnam and DeShazer [2] observed that <u>both</u> QW and 3QW films of TiO_2 had higher thresholds than

*This work was performed under the auspices of the Energy Research and Development Administration.

[1]Figures in brackets indicate the literature references at the end of this paper.

the HW films for 13-ns duration ruby laser pulses. Further damage experiments were conducted at 0.6943 μm by Newnam [3] with various front- and back-surface films, and the thresholds were found to be in qualitative agreement with calculated SW field patterns.

Notwithstanding, these correlations of damage thresholds and SW field distributions, Milam, et al., [4], suggested that state-of-the-art coatings (1973) of TiO_2, ZrO_2, and SiO_2 contained absorbing inclusions of such number and size as to preclude the build-up of standing-wave fields. The absorbing inclusions were deduced to be the sites of early damage to the films. Furthermore, they demonstrated a scaling law in thin films between the laser pulsewidth τ and the size of a film defect most likely to be damaged first. This relationship, originally formulated by Hopper and Uhlmann [5] for bulk materials, predicts that large defects are damaged most easily by long pulses, and vice versa, in proportion to $\tau^{\frac{1}{2}}$. Further research by DeShazer, et al.,[6], produced a correlation of the defect density with the measured damage threshold dependence on laser spot-size radius.

At present, the general agreement on laser-induced damage in thin film coatings is that the thresholds are limited by absorbing inclusions. However, it is difficult to ignore the aforementioned threshold correlations with the standing-wave electric field patterns. Now, the state-of-the-art of thin film deposition techniques yield optical coatings with fewer defects and with increased damage resistance compared to that of a few years ago. It is important to determine whether SW field distributions affect the thresholds of these coatings or if their effect is inoperative in the presence of film defects.

Since small film defects are more numerous than large ones and are more susceptible to damage by short laser pulses, damage experiments were conducted with 30-ps pulses at 1.06 μm. It was considered that damage measurements at this pulsewidth would be a severe test of the presence of SW field effects. In addition, thermal diffusion of absorbed heat from the locations of maximum fields is minimal during this pulse duration.

The test samples were single-layer films of TiO_2, ZrO_2, SiO_2, and MgF_2 deposited by state-of-the-art electron-gun evaporation by CVI Laser, Inc., on BK-7 glass substrates with uniform surface preparation by bowl-feed polishing. In addition, a few TiO_2 coatings prepared by rf sputtering on BK-7 glass and Optocil I fused silica substrates were included. All coating substrates had a 2° wedge to prevent SW interference effects with the second uncoated substrate surface.

Damage thresholds were measured as a function of film thickness (from one to five quarter-waves), direction of laser incidence (back- and front-surface films for normal incidence), and for S- and P-polarized radiation incident at 60°. Additionally, tests with circular versus linear polarizations for normal incidence were performed to determine if multiphoton absorption was an important physical process leading to damage. Such a process would further emphasize the electric-field distributions in the films.

The measured thresholds were compared with the corresponding calculated SW field distributions. A definite correlation was generally found between the internal field maxima and the thresholds, but in a few coatings defects apparently decreased or prevented any correlation.

In section 2, the experimental parameters of the laser and damage detection scheme are described. The experimental results are given in section 3 and compared with the SW field calculations. Section 4 includes an analysis of the results in terms of single-pass flux density versus SW fields, and a summary of our findings appears in section 5. The equations derived for the standing-wave fields are included in an appendix, section 7.

2. Experimental Parameters

2.1. Laser Apparatus

The laser consisted of a mode-locked, Nd:YAG oscillator from which a single pulse was extracted by a Pockels cell/electronic trigger arrangement and augmented by three YAG amplifiers. The net output was approximately 75 mJ in a 30-ps pulse with a TEM_{00} spatial distribution. The energy was measured with an accuracy of ± 5% with a calorimeter of LASL design [7], and a two-photon fluorescence camera measured the pulsewidth. A fast Si photodiode and a Tektronix 519 oscilloscope monitored the mode-locked pulse train.

The output of the laser was focused with a 2-m lens to a spot-size radius of 0.5 mm at the sample plane, located in front of the lens focal plane (figure 1). The beam profile was measured at the sample plane by directing a small portion of the beam onto a Reticon RL 256EC linear diode array (resolution of 0.05 mm) centered on the beam with an X-Y translation device. The signal was recorded on a Tektronix 7633 storage oscilloscope and the resultant photograph allowed a measure of the beam spot-size and shape as shown in figure 2. We found it necessary to measure the beam profile on every shot since the beamwidth was not constant. Beamwidth variations were directly related to shot-to-shot variations in the switched-out oscillator pulse energy and the resultant degree of gain saturation in the third YAG amplifier.

The damage test facility was housed in three adjacent rooms. One room contained the laser apparatus, the second was darkened and contained the damage experiment including energy and spark detectors, and the third contained the monitoring electronics. In this way, laser flashlamp emission and room lights did not interfere with visual and photoelectronic monitoring of damage, thereby enabling accurate detection of damage thresholds.

2.2. Detection of Damage

Damage was detected by two methods simultaneously (figure 1). Optical breakdown, accompanied by a high-temperature spark, was detected with a photomultiplier (RCA6655A) with a purple-transmitting filter (peaked at 4180 Å, 160 Å bandwidth) to discriminate against scattered flashlamp radiation and the laser pulse. The photoelectric signal, proportional to the energy in the laser-induced spark emission, was measured with a Tektronix 556 oscilloscope (figure 3). The sensitivity of the spark detection system was such as to detect a single spark 1 μm in diameter with black-body temperature equal to the melting point of ZrO_2 (2983°K).

Evidence of laser-induced disruption of the surface of a coating was manifested by increased scattering of a probe beam from a low-power (2 mW) He-Ne laser aligned collinearly with the pulsed laser beam. By comparing the level of scattering before, during (with N.D 9 safety goggles), and after pulse irradiation, changes in the coating structure could be detected. This method has been called laser-induced scatter (LIS) detection [2].

We found that for films with high damage resistance and low initial scatter, the sensitivity of these two methods of damage detection were comparable. For films with low damage resistance, the LIS method was more sensitive, which indicated that film damage occurred before very high spark temperatures were reached.

2.3. Test Procedure

Each sample was first wiped once with lens tissue moistened with reagent grade acetone and gently blown with a jet of Freon gas to remove any adhering dust particles. For laser irradiation experiments at normal incidence, the samples were oriented at an actual angle of 1° to prevent retroreflection into the laser system. Great care was taken to absorb the reflected and transmitted laser beams with Schott glass filters located far from the view of the spark-detecting photomultiplier system. In determining the damage thresholds, a given area of a sample was irradiated by one shot only. Sites of irradiation were spaced several millimeters apart. The energy of the incident laser beam was controlled by Schott neutral density filters to lie as close to the threshold as possible. Thus, easily visible damage rarely occurred. This care was necessary to prevent damage products from one area from influencing the thresholds of adjacent areas. An adequate sampling of the damage resistance was obtained with an average of 40 shots.

3. Experimental Results

The damage resistance of each thin film coating is reported here as a range of threshold energy densities rather than a single value. This provides a more realistic description of this film property which was found to vary over the surface area. The top end of the threshold range was defined as the maximum energy density for which neither visible damage nor spark radiation of a minimum magnitude were detected. The bottom end of the threshold range was defined as the minimum energy density for which damage was detected either by the LIS method or by the occurrence of a spark with at least the prescribed radiant energy. Since the laser spot-size was large (0.5 mm), no statistical nature of damage should be inferred [8]. The range of threshold values is believed to be a measure of the variable damage resistance of the coatings from one area to another.

For purposes of immediate comparison, each series of test results is accompanied by illustrations of the corresponding calculated SW electric-field distributions in the films and in the surrounding media. The field distributions are all normalized to the incident electric field-squared in air, $|E_0^+|^2$. The mathematical expressions for these fields are given in the appendix.

3.1. Damage Threshold Versus Film Thickness

The results for TiO_2 films are shown in figure 4, and it is apparent that films with odd quarter-wave thicknesses have greater damage resistance than those with even multiples. The corresponding SW field distributions calculated for 1-, 2-, and 3-QW thicknesses are illustrated in figure 5. (The distributions for 4- and 5-QW films are just sinusoidal extensions of the fields in the 2- and 3-QW films, respectively.) It is evident that the SW field pattern in the half-wave film is relatively larger than those in the odd quarter-wave films. For a refractive index of 2.32 measured at 1.06 μm for these films, the ratio of the maximum values of $|E/E_0^+|^2$ for half- and quarter-wave films is 1.4. (The selection of the field maxima for comparison rather than values at particular locations, such as the air-film interface, will be discussed in section 4). As justified in the next section, for linear absorption it is appropriate to compare the inverse of this ratio with the damage thresholds using the quarter-wave thresholds (upper and lower) as the references. The dashed lines in figure 4 are the damage thresholds predicted by a linear dependence on the SW electric fields. Good qualitative agreement is seen, but a higher order dependence could fit better.

It is not reasonable to expect absolute quantitative agreement in these tests because we are comparing the damage thresholds of coatings deposited on consecutive coating runs. Slight variations in the coating deposition parameters can produce films with some variability.

The results for ZrO_2 films are shown in figure 6, and though an oscillation of the damage thresholds is apparent with increasing thickness, it is not as definite as seen for TiO_2 films. This is consistent with the lower refractive index for ZrO_2 of 1.90. One of the 3QW films is seen to have a notably low threshold. This might indicate higher film absorption or absorbing inclusions. The 5QW films had much lower initial scatter than the other samples which could explain their higher damage threshold ranges. The corresponding SW field distributions for QW and HW films of ZrO_2 are shown in figures 7 and 8 along with other film materials for comparison. The dashed lines in figure 6 are the predicted thresholds due to linear absorption at the locations of the maximum electric fields in the films. Qualitative agreement is seen.

The results for SiO_2 films are shown in figure 9. The high end of the thresholds is nearly constant with film thickness. This is in good quantitative agreement with the dashed line calculated from the SW field maxima in figures 7 and 8. The film index, 1.45, is very close to that of the substrate, 1.506. The low end of the thresholds shows no recognizable thickness dependence. The randomness is likely due to variable film quality. This is not unexpected since the bottom end of the threshold range is a measure of film imperfections, e.g., absorbing inclusions and sites of enhanced electric fields. The high ends of the threshold ranges would be more likely to show a consistent dependence such as that predicted by the SW field distributions.

Figures 10 and 11 are plots of previous results reported in 1972 [2] for irradiation of TiO_2 and ZrO_2 coatings at the ruby laser wavelength of 0.694 μm with 13-ns pulses. Though the number of thresholds plotted is small, the same general dependence with film thickness reported herein for 30-ps pulses of 1.06 μm radiation is obvious. For 13-ns pulses, however, any temperature patterns replicating the absorbed SW fields in the films would be largely smeared out by thermal diffusion since $(Dt)^{\frac{1}{2}} = 2.1X$ and 1.2X the physical thicknesses of QW films of TiO_2 and ZrO_2, respectively, at the ruby wavelength. The ratio of the average fields in HW and QW thick films would remain nearly constant during this longer pulse, however. This ratio, 1.4, is identical to that for the SW field maxima (observe the sinusoidal dependence of the SW field expressions in the appendix). Therefore, the measured cyclic variation of the damage thresholds with film thickness observed in figure 10 is not unexpected.

The observed thickness dependence of the damage thresholds allows us to state that the <u>total</u> laser energy absorbed in thin dielectric films is <u>not</u> the important quantity for predicting damage resistance. If total absorption was important in the damage process, then a 5QW-thick film, which absorbs 5X more energy than a 1QW-thick film (both have the same SW-field pattern), would have a much lower damage threshold. This is contrary to the experimental results presented in figures 4, 6, and 9 in which

the thresholds for QW, 3QW, and 5QW films of each respective material are nearly the same.

3.2. Damage Resistance of Back- Versus Front-Surface Coatings

When radiation is incident upon a coating from the substrate side, the SW field distributions set up in the coating differ greatly in magnitude from those for front-surface films. The fields calculated for QW back-surface coatings shown in figure 12 may be compared with those in figure 7 for front-surface QW films. The SW maxima in figure 12 are from 20 to 40% greater, so that reduced damage thresholds are predicted. The damage thresholds for both front- and back-surface irradiation at normal incidence are listed in table 1 for QW films. In each case, the upper threshold value for front-surface films exceeded that for back-surface films. The values were corrected for the 4% reflection loss at the bare glass surface in the case of the back-surface films. The correction for enhanced axial intensity by large-scale self-focusing in the substrate was determined to be only 2 to 3%. Except for the sputtered coating, B-32, the lower threshold values were nearly the same for both orientations, however, suggesting limitations due to film defects. The meaning of the values in the last column will be discussed in section 4.

Table 1. Damage thresholds for front- and back-surface coatings.

Sample[†]	Coating	Peak Energy Density (J/cm^2)		Ratio of Thresholds Front/Back	Ratio of Max. E-Fields Squared Back/Front	Ratio of t^2 Back/Front
		Front	Back			
B-32	TiO_2, $\lambda/4$	5.5-9.2	2.5-3.4	2.2-2.7	1.4	1.1
C-1a	TiO_2, $\lambda/4$	3.3-6.8	3.9-5.2	.85-1.3	1.4	1.1
C-6	ZrO_2, $\lambda/4$	3.5-7.9	3.4-5.6	1.0-1.4	1.4	1.2
C-2	MgF_2, $\lambda/4$	2.6-7.3	2.5-6.9	1.05	1.2	1.0

[†]Sample B-32 was rf sputtered onto Optocil I; others were E-gun deposited onto BK-7.

3.3. Damage Threshold Versus Polarization State for Non-Normal Incidence

A second way to generate different SW field distributions in a given coating sample is to irradiate with S- and P-polarized light at a large angle of incidence. The SW field patterns for both polarizations and an angle of incidence of 60° are shown in figures 13 to 16. Except for the case of the QW TiO_2 film, the magnitudes of the fields are not very different. If SW fields dominate over other considerations in determining the damage threshold, then the films illustrated in figures 14 to 16 would be expected to have equal thresholds for S- and P-light.

However, an additional phenomena, the vectorial field effect, must be considered when using P-polarized light, which has an electric field component normal to the film surface. According to the vectorial field effect [9], the component of the electric field normal to the surface is much more efficient in producing photoemission of electrons than the tangential component. If photoemission were important in initiating laser-induced damage in the films being considered, then the damage thresholds for P-polarized light would be less than for S-polarization. For 60° incidence, the incident normal electric field component E_{oz}^+ equals 0.867 of the magnitude of the total incident field, or $|E_{oz}^+/E_o^+|^2 = 0.75$, a large fraction.

The experimental results for this test series are listed in table 2. For the last three samples, the P-thresholds were equal to, or slightly greater than the corresponding S-thresholds. This result suggests that photoemission is not important in initiating damage in TiO_2, ZrO_2, and MgF_2 thin films. Rather the ratios of the P- and S-thresholds are in agreement with the ratios of the SW electric fields within 20%.

Table 2. Damage thresholds vs linear polarization state for an incidence angle of 60°.

Sample	Coating	Peak Energy Density (J/cm^2)		Ratio of Thresholds $\mathcal{E}_s/\mathcal{E}_p$	Ratio of Max. E-Fields Squared $\lvert E_p/E_s \rvert^2$	Ratio of t_p^2/t_s^2
		S-Pol	P-Pol			
C-1a	TiO_2, $\lambda/4$	2.1-6.9	1.5- 5	1.4	1.7	1.6
C-1b	TiO_2, $\lambda/2$	1.1-4.0	1.6-5.0	0.7-0.8	1.0	1.6
C-2b	ZrO_2, $\lambda/2$	2.2-4.4	2.3-5.5	1.0-0.8	1.1	1.4
C-3a	MgF_2, $\lambda/2$	3.0-7.7	2.9-7.7	1.0	1.05	1.15

3.4. Damage by Circularly and Linearly Polarized Light

If multiphoton absorption processes lead to damage in dielectric films, then maxima in the internal SW electric field distributions would be even more important than for linear absorption. For example, the absorption coefficient for two-photon absorption is proportional to $|E|^2$. For one-electron atoms, Parzynski [10] has predicted that the ionization probability (from the ground state) for N photons is different for circularly and linearly polarized light. His theoretical ratios of the probabilities for these two irradiation conditions are given in table 3 along with experimental data for cesium [11,12]. The data agree well with Parzynski's ratios. Note that no difference was predicted or observed for linear (N=1) absorption.

Table 3. Multiphoton ionization by circularly and linearly polarized light.

N	Theoretical Ionization Probability Ratio† [10] P_{circ}/P_{lin}	Data Reported for Cesium [11,12]
1	1	1
2	1.14	1.28
3	2.18	2.15
≥ 4	<< 1	-

†For one-electron atom in ground state.

The theory and results for one-electron atoms suggested a comparison of the damage thresholds for linearly and circularly polarized laser radiation for the optical thin film materials being considered. These tests were performed with the recognition that the theory was not developed for these materials, but that if any differences were measured for the two polarization conditions, an applicable theory should be sought.

The damage thresholds for three QW film materials are listed in table 4. If Parzynski's theory were applicable, the threshold ratios should be 0.88, 0.46, and >> 1 for 2-, 3-,and ≥ 4-photon ionization, respectively. The ratio of the thresholds, $\mathcal{E}_C/\mathcal{E}_L$, for MgF_2 and TiO_2 are equal to or slightly greater than 1.0. For ZrO_2 the ratio of the upper thresholds, 0.76, is very close to that predicted for two-photon ionization.

We conclude that either linear absorption leads to damage first for MgF_2 and TiO_2, or the theory does not apply. However, two-photon absorption may possibly be present prior to damage in ZrO_2 films. (Evidence for two-photon absorption at 0.694 μm in ZrO_2 is presented elsewhere in these proceedings by Picard, et.al.) A firm conclusion based on the present results will require modification of Parzynski's theory for the materials tested.

Table 4. Damage thresholds for circularly and linearly polarized light.

Sample	Coating Description	Peak Energy Density (J/cm^2)		Ratio of Thresholds $\mathcal{E}_C/\mathcal{E}_L$
		Linear	Circular	
C-6	ZrO_2, $\lambda/4$	3.5-7.9	4.8-6.0	1.4-0.76
C-2'	MgF_2, $\lambda/4$	2.6-5.7	2.6-5.7	1.0
B-32	TiO_2, $\lambda/4$	5.5-9.2	6.1-9.1	1.1-1.0
B-33	TiO_2, $\lambda/4$	6.3-10.1	7.6-12.2	1.2

4. Analysis

In this section, theoretical expressions for the damage threshold are alternately derived in terms of the SW fields and the field of the first-pass traveling wave (TW) in the film medium. Both predictions are then compared with the measured damage thresholds in each of the preceding experiments. We assume absorption to be the mechanism leading to damage, but a similar analysis could be attempted in terms of elastic properties of the film materials.

The power absorbed per unit volume from an electromagnetic wave of intensity I traveling in a medium having a complex refractive index $\underline{n}$ is $P_a = -dI/dz = \alpha I$. The quantity α is the absorption coefficient (cm^{-1}), which can be a function of the intensity as I^{N-1} for N-photon absorption. For linear absorption, α is related to the imaginary part of $\underline{n}$ (= n-ik) by the relation $\alpha = 4\pi k/\lambda$. For a plane wave, $I = \bar{E}^2/\eta$ where $\bar{E}^2$ is the mean square of the electric field averaged over several cycles ($\frac{1}{2}|E|^2$), and $\eta = (\mu/\varepsilon)^{\frac{1}{2}}$ is the wave impedance. In terms of the incident intensity I_o (= $|E_o^+|^2/2\eta_o$), the power absorbed (watts/cm^3) at a distance z in a weakly absorbing medium is

$$P_a(z) = \alpha n \left|\frac{E(z)}{E_o^+}\right|^2 I_o \quad . \tag{1}$$

A similar expression for the energy absorbed per unit volume (joules/cm^3) from a light pulse with incident energy density $\mathcal{E}_o$ is

$$\mathcal{E}_a(z) = \alpha n \left|\frac{E(z)}{E_o^+}\right|^2 \mathcal{E}_o \quad . \tag{2}$$

By rearranging, we obtain the incident energy density at the threshold of damage, $\mathcal{E}_o^*$,

$$\mathcal{E}_o^* = (\mathcal{E}_a^*(z)/\alpha n) \left|\frac{E(z)}{E_o^+}\right|^{-2} \quad . \tag{3}$$

In analyzing the measured damage thresholds for a possible correlation with the SW field distributions, it was first necessary to determine what location in the films was most susceptible to early damage. Therefore, we made a preliminary comparison of the thresholds with the SW field values at several film planes. The comparisons were made with the SW fields at the: 1) air-film interface; 2) film-substrate interface; 3) planes of field maxima; and 4) average field-squared. In almost all cases, the best correlation was obtained with the field maxima. Thus, only the maximum value of $|E/E_o^+|^2$ for each film material and sample orientation is used in the ensuing analysis.

Now, damage may occur either during the first pass of the laser beam through the film as a traveling wave or as the field evolves to a standing-wave distribution. The value of $|E/E_o^+|^2$ of the first-pass TW immediately inside the film is equal to t^2, where t is the Fresnel transmission coefficient. (Expressions for t are listed in the appendix.) Then by eq. (3), the damage threshold for a traveling wave is reached when

$$\mathcal{E}_o^* = \mathcal{E}_a^*/\alpha n t^2 \quad . \tag{4}$$

If the film is weakly absorbing and inclusion free, the traveling wave has nearly constant intensity across the film thickness. For such films, however, it is possible to show that the maximum value of the corresponding SW field-squared is always larger than t^2. Examples of this fact are given in table 5 in which the computed ratios of $|E/E_o^+|^2_{max}/t^2$ for each film material and sample orientation used in this experimental program are tabulated. The ratios for the low-index films, SiO_2 and MgF_2, are generally only a little larger than 1.0, so that SW-field effects on their damage thresholds might be hard to distinguish. The ratios for the high-index films, ZrO_2 and TiO_2, are considerably greater than 1.0, so that SW-field effects should be obvious in the damage thresholds of such ideal films.

Table 5. Comparison of standing-wave and traveling-wave fields in thin films.

Coating Description†	Angle of Incidence	Direction of Incidence	Square of Maximum E-Field $\lvert E/E_o^+\rvert^2$	Fresnel Factor t^2	Ratio $\lvert E/E_o^+\rvert^2/t^2$
$TiO_2(\lambda/4, 3\lambda/4, 5\lambda/4)$	0°	Front	.46	.36	1.28
$TiO_2(\lambda/2, \lambda)$	0°	Front	.64	.36	1.78
$TiO_2(\lambda/4)$	0°	Rear	.65	.40	1.63
$TiO_2(\lambda/2)$	0°	Rear	.92	.40	2.30
$TiO_2(\lambda/4)$	60°, S-pol.	Front	.17	.14	1.21
$TiO_2(\lambda/4)$	60°, P-pol.	Front	.30	.23	1.30
$TiO_2(\lambda/2)$	60°, S-pol.	Front	.32	.14	2.29
$TiO_2(\lambda/2)$	60°, P-pol.	Front	.32	.23	1.39
$ZrO_2(\lambda/4, 3\lambda/4, 5\lambda/4)$	0°	Front	.55	.48	1.15
$ZrO_2(\lambda/2, \lambda)$	0°	Front	.64	.48	1.33
$ZrO_2(\lambda/4)$	0°	Rear	.80	.56	1.43
$ZrO_2(\lambda/2)$	0°	Rear	.92	.56	1.64
$ZrO_2(\lambda/2)$	60°, S-pol.	Front	.32	.21	1.52
$ZrO_2(\lambda/2)$	60°, P-pol.	Front	.34	.30	1.13
$SiO_2(\lambda/4, 3\lambda/4)$	0°	Front	.69	.67	1.03
$SiO_2(\lambda/2, \lambda)$	0°	Front	.68	.67	1.01
$MgF_2(\lambda/4)$	0°	Front	.78	.71	1.10
$MgF_2(\lambda/2)$	0°	Front	.76	.71	1.07
$MgF_2(\lambda/4)$	0°	Rear	.94	.69	1.36
$MgF_2(\lambda/2)$	60°, S-pol.	Front	.46	.40	1.15
$MgF_2(\lambda/2)$	60°, P-pol.	Front	.48	.46	1.04

†Substrate is BK-7 glass, refractive index n = 1.506.

In state-of-the-art optical thin films in which absorbing inclusions are known to be present, it is possible that the first-pass TW may be sufficiently absorbed by an inclusion to prevent a SW field from evolving at that location. If the absorptance of the inclusion is sufficiently great and its diameter appropriately scaled to the laser pulsewidth, the temperature of the inclusion can increase sufficiently to damage the surrounding film material [4,5]. However, it is also conceivable that damage could first occur to defect-free regions of film material adjacent to an absorbing inclusion

if 1) the pulsewidth-to-inclusion-diameter scaling is not optimum and 2) the SW field in the adjacent material is sufficiently greater than the traveling wave striking the inclusion.

Whether or not SW field effects are important in the films tested in this study can be evaluated by comparing the threshold ratios shown in figures 4, 6, and 9, and in tables 1 and 2 with the corresponding ratios of maximum SW electric fields and t^2 ratios.

4.1. Evaluation of TiO_2 Films

In figure 4, the evidence of SW field effects in TiO_2 films is pronounced. The calculated SW field maxima in even-QW films are 40% greater than those in odd-QW films, whereas for the first-pass TW fields t^2 is a constant value (0.36) with thickness. The observed ratios (odd to even QW) for the upper thresholds ranged from 1.4 to 1.8; the ratios for the lower thresholds ranged from 1.5 to 2.0. These values compare very well with the 1.4 value predicted by SW field theory.

In table 1, the ratio of front- and back-surface coating thresholds for the sputtered TiO_2 film greatly exceed both the values predicted for the ratios of the SW field maxima and the traveling waves, 1.4 and 1.1, respectively. This is not fully understood. The coating had very low scatter and presumably fewer defects than E-gun produced coatings. Possibly nonlinear absorption could be emphasized at the SW field maxima, or the air-film interface absorbed abnormally to result in the 2.2-2.7 threshold ratio obtained.

The results for the E-gun deposited TiO_2 film (C-1a) were reasonable. The upper threshold ratio, 1.3, compares well with the 1.4 value predicted by SW fields, but the lower ratio of 0.85 is closer to the 1.1 TW prediction. It is understandable that the lower end of the threshold range could be a measure of the limitations posed by absorbing defects.

In table 2 the threshold ratio, 1.4, for the QW TiO_2 coating is somewhat lower than that predicted for both SW and TW fields, 1.7 and 1.6, respectively. A definite correlation is not possible here. However, threshold ratios for the HW film, 0.7-0.8, match the SW ratio of 1.0 much better than the TW ratio of 1.6.

In summary, the measured thresholds for TiO_2 coatings consistently correlated well with SW field maxima.

4.2. Evaluation of ZrO_2 Films

In figure 6 the threshold variations with thickness are generally in accord with those predicted by SW theory, but are not as uniformly distinct as for TiO_2 coatings. This is expected since the values of $|E/E_o^+|^2_{max}/t^2$ are smaller, which means the possible influences of SW fields compared to the first-pass TW field cannot be as great. The calculated SW field maxima in even-QW films are 16% greater than those in odd-QW films, whereas for the first-pass TW fields t^2 is a constant value (0.48) with thickness. The observed ratios for the upper thresholds ranged from 1.15 to 1.5; the ratios for the lower thresholds ranged from 1.0 to 1.8. These ratios have a wide range, but they generally were greater than 1.0 with one notable exception, which indicates the influence of SW fields.

In table 1 the upper threshold ratio for the QW ZrO_2 coating is 1.4 in agreement with the SW ratio. The lower threshold ratio of 1.0 is closer to 1.2, the ratio of TW field t^2 values. This implies that the lower threshold is controlled by absorbing defects.

In table 2 the HW ZrO_2 coating has a threshold ratio of 1.0-0.8 which is in near accord with the ratio of SW fields, 1.1.

In summary, the measured upper thresholds for ZrO_2 coatings generally correlated well with SW field maxima, but there was some evidence that the lower thresholds were restricted by defects.

4.3. Evaluation of MgF_2 Films

The difference between the influence of SW and TW fields in MgF_2 films cannot be very great since the values of $|E/E_o^+|^2_{max}/t^2$ are not very much greater than 1.0 (table 5). In table 1 the threshold ratio for the QW MgF_2 coating, 1.05, is very close to the 1.0 ratio of t^2 values for the first-pass TW fields. The ratio for the SW fields, 1.2, is also not too different. In table 3, the HW MgF_2 coating has the same damage threshold for both P- and S-polarizations. This ratio of unity compares well with the ratio of SW fields, 1.05, but the ratio of t^2 values is also not too distant at 1.15.

In summary, the measured thresholds for MgF_2 coatings showed minor SW field influence. This was predictable, with or without film defects, because of the small refractive index, 1.38, of this material relative to air and glass.

4.4. Evaluation of SiO_2 Films

The only threshold measurements performed on SiO_2 coatings are shown in figure 9 as a function of thickness. Due to this material's index of refraction being close to that of the glass substrate, not much variation was expected or observed at the upper threshold end. The random variation of the lower thresholds was presumably due to film defects.

5. Summary

The specific findings of this experimental study using 30-ps, 1.06-μm laser pulses were:

a. A definite correlation was generally found between the internal standing-wave electric field maxima and the damage thresholds, but in a few coatings defects apparently decreased or prevented any correlation. Designers of coatings for intense laser beams cannot afford to neglect standing-wave field considerations.

b. Damage thresholds of TiO_2 films showed a strong dependence on the internal standing-wave electric field maxima.

c. The higher end of the damage threshold range for a given coating of ZrO_2 correlated well with the internal SW field maxima, but there was some evidence that the lower end of the threshold range was restricted by film defects.

d. Damage thresholds of MgF_2 coatings were influenced by SW field maxima to a minor degree. This was due to either or both the low refractive index and film defects.

e. Damage thresholds of SiO_2 coatings on glass were not influenced by SW fields due to the refractive index being nearly equal to that of the substrate. Random variations of the lower thresholds were presumably due to film defects.

f. Damage thresholds for circularly polarized light directed at normal incidence on TiO_2 and MgF_2 coatings did not differ from their respective thresholds for linearly polarized light. By Parzynski's theory, linear absorption only is prominent in these films. A lower threshold for circularly polarized light incident on a ZrO_2 coating may indicate the presence of two-photon absorption.

g. Photoemission via the vectorial photoeffect was not important in initiating damage in TiO_2, ZrO_2, and MgF_2 thin films.

6. Acknowledgments

The authors are indebted to Y. H. Hahn of CVI Laser, Inc., for supplying optical coatings deposited by the electron-gun method and to W. J. Coleman and J. S. Hartman of Battelle Pacific Northwest Laboratories for TiO_2 coatings deposited by rf sputtering. The skillful preparation of the typed manuscript by Jo Ann Painter is also gratefully acknowledged.

7. Appendix

Calculation of Electric-Field Distributions

The standing-wave electric-field intensity distributions were calculated using the equations below as derived in reference 3. Subscript o refers to the medium from which the beam is incident (air for a front surface coating), subscript 1 refers to the dielectric film, and subscript 2 refers to the following medium (substrate for a front surface coating).

A. Normal Incidence

The field expressions are

$$\left|\frac{E_o}{E_o^+}\right|^2 = \frac{A^2 + B^2}{|D|^2} ,$$

$$\left|\frac{E_1}{E_o^+}\right|^2 = \frac{t_1^2 \, [1 + r_2^2 + 2r_2 \cos 2(\delta_1 - k_1 z)]}{|D|^2} ,$$

and

$$\left|\frac{E_2}{E_o^+}\right|^2 = \frac{t_1^2 \, t_2^2}{|D|^2} ,$$

where

$$A = (1 + r_2) \, [\cos (\delta_1 - k_o z) + r_1 \cos (\delta_1 + k_o z)] ,$$

$$B = (1 - r_2) \, [\sin (\delta_1 - k_o z) + r_1 \sin (\delta_1 + k_o z)] ,$$

$$|D|^2 = 1 + r_1^2 r_2^2 + 2 r_1 r_2 \cos 2\delta_1 ,$$

$$r_m = \frac{n_{m-1} - n_m}{n_{m-1} + n_m} ,$$

$$t_m = \frac{2n_{m-1}}{n_{m-1} + n_m} ,$$

$$\delta_m = k_m d_m , \quad \delta_o = 0 ,$$

$$k_m = \frac{2\pi}{\lambda_o} n_m ,$$

and

$$d_m = \text{layer thickness} .$$

Parameters r_m and t_m are the Fresnel reflection and transmission coefficients, respectively.

B. Non-Normal Incidence, S-Polarization

The field expressions are the same as for normal incidence, but the Fresnel coefficients are redefined as

$$r_m = \frac{n_{m-1} \cos \phi_{m-1} - n_m \cos \phi_m}{n_{m-1} \cos \phi_{m-1} + n_m \cos \phi_m} ,$$

$$t_m = \frac{2n_{m-1} \cos \phi_{m-1}}{n_{m-1} \cos \phi_{m-1} + n_m \cos \phi_m} ,$$

and

$$\delta_m = k_{z,m} d_m \quad , \quad \delta_o = 0 \quad ,$$

$$k_{z,m} = \frac{2\pi}{\lambda_o} n_m \cos \phi_m \quad ,$$

$$\cos \phi_m = \frac{(n_m^2 - n_o^2 \sin^2 \phi_o)^{1/2}}{n_m} \quad .$$

C. Non-Normal Incidence, P-Polarization

The field expressions are

$$\left|\frac{E_o}{E_o^+}\right|^2 = \frac{A^2 + B^2}{|D|^2} \quad ,$$

$$\left|\frac{E_1}{E_o^+}\right|^2 = \frac{t_1^2 [1 + r_2^2 + 2r_2 \cos(2k_1 z - 2\delta_1 + \pi)]}{n_1^2 |D|^2} \quad ,$$

and

$$\left|\frac{E_2}{E_o^+}\right|^2 = \frac{t_1^2 t_2^2}{n_2^2 |D|^2} \quad ,$$

where

$$A = (1 + r_2) [\cos(\delta_1 - k_o z - \pi) + r_1 \cos(\delta_1 + k_o z + \pi)] \quad ,$$

$$B = (1 - r_2) [\sin(\delta_1 - k_o z - \pi) + r_1 \sin(\delta_1 + k_o z + \pi)] \quad ,$$

$$|D|^2 = 1 + r_1^2 r_2^2 + 2r_1 r_2 \cos 2\delta_1 \quad ,$$

and

$$r_m = \frac{n_m \cos \phi_{m-1} - n_{m-1} \cos \phi_m}{n_m \cos \phi_{m-1} + n_{m-1} \cos \phi_m} \quad ,$$

$$t_m = \frac{2n_m \cos \phi_{m-1}}{n_m \cos \phi_{m-1} + n_{m-1} \cos \phi_m} \quad .$$

D. Fresnel Transmission Coefficients

When calculating the Fresnel transmission coefficient, t_m, for comparison with the maximum relative electric field squared, $|E/E_o^+|^2$, as explained in the text, the above formulas can be used except in case C, non-normal incidence, P-polarization. For case C, the equation above is actually for the H field, t_{m_H}. The correct value to be used (for this direct comparison) is

$$t_{m_E} = \frac{n_o}{n_m} t_{m_H} \quad .$$

E. Exit-Surface Calculations

For exit-surface coating calculations, the equations as presented give electric fields normalized to the incident field in the substrate, $E^+_{o,s}$. For normalization to the incident field in air, $E^+_{o,a}$, the correct relation is

$$E^+_{o,s} = t_{a,s} E^+_{o,a} \quad ,$$

where for normal incidence

$$t_{a,s} = \frac{2}{1 + n_s} \quad .$$

All calculations reported in the text are referenced to air. This same normalization factor must be used for the Fresnel transmission coefficients when calculated for direct comparison with E-field ratios, thus

$$t_{a,f} = t_{a,s} t_{s,f} \quad .$$

8. References

[1] Turner, A. F., Damage in Laser Materials: 1971, NBS Spec. Pub. No. 356, 119 (1971).

[2] Newnam, B. E. and DeShazer, L. G., Laser Induced Damage in Optical Materials: 1972, NBS Spec. Pub. No. 372, 123 (1972).

[3] Newnam, B. E., "Laser Induced Damage Phenomena in Dielectric Films, Solids and Inorganic Liquids," dissertation, University Microfilm, Ann Arbor, MI.

[4] Milam, D., Bradbury, R. A., and Bass, M., Appl. Phys. Lett. 23, 654 (1973).

[5] Hopper, R. W., and Uhlmann, D. R., J. Appl. Phys. 41, 4023 (1970).

[6] DeShazer, L. G., Newnam, B. E., and Leung, K. M., Appl. Phys. Lett. 23, 607 (1973).

[7] Watt, B. E., Appl. Opt. 12, 2372 (1973).

[8] Bass, M., and Barrett, H. H., Laser Induced Damage in Optical Materials: 1972, NBS Spec. Pub. 372, 58 (1972).

[9] Fischer, T. E., J. Vacuum Sci. and Tech. 9, 860 (1972).

[10] Parzynski, R., Opt. Commun. 8, 79 (1973).

[11] Fox, R. A., Kogan, R. M. and Robinson, E. J., Phys. Rev. Lett. 26, 1416 (1971).

[12] Kogan, R. M., Fox, R. A., Burnham, G. T., and Robinson, E. J., Bull. Am. Phys. Soc. 16, 1411 (1971).

9. Figures

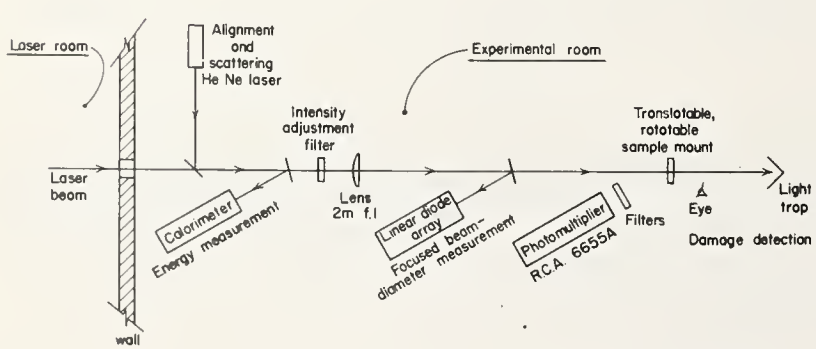

Figure 1. Schematic diagram of laser-induced damage system showing laser beam diagnostics and damage detection methods.

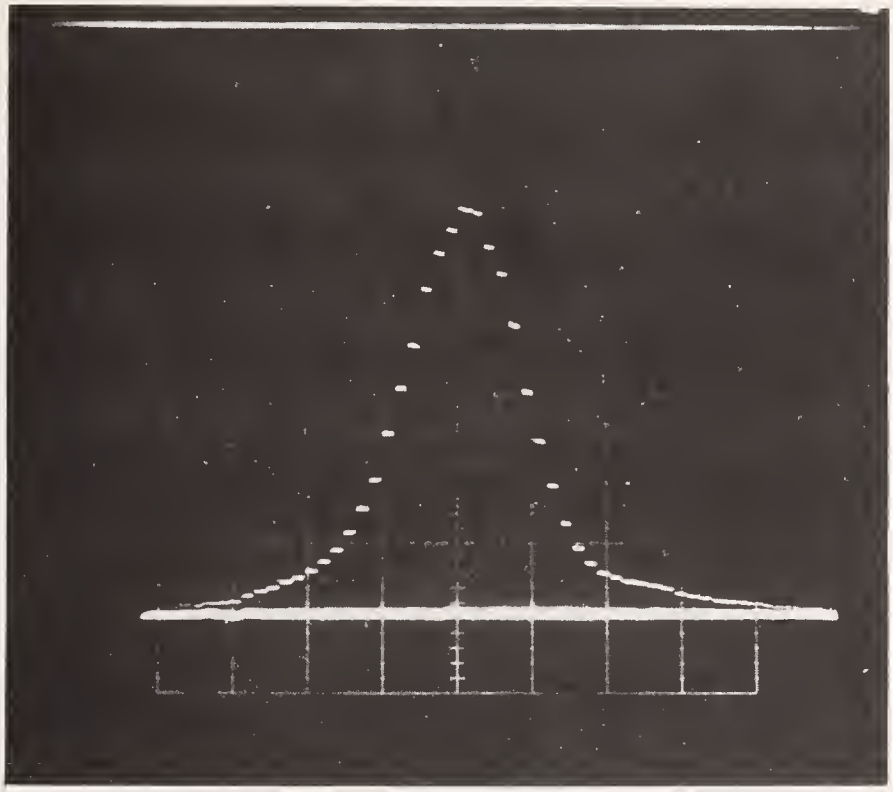

Figure 2. Laser beam profile as measured by linear diode array located at equivalent sample position. Diodes are spaced .05 mm center-to-center, thus this pulse had a diameter of 0.70 mm at the 1/e height.

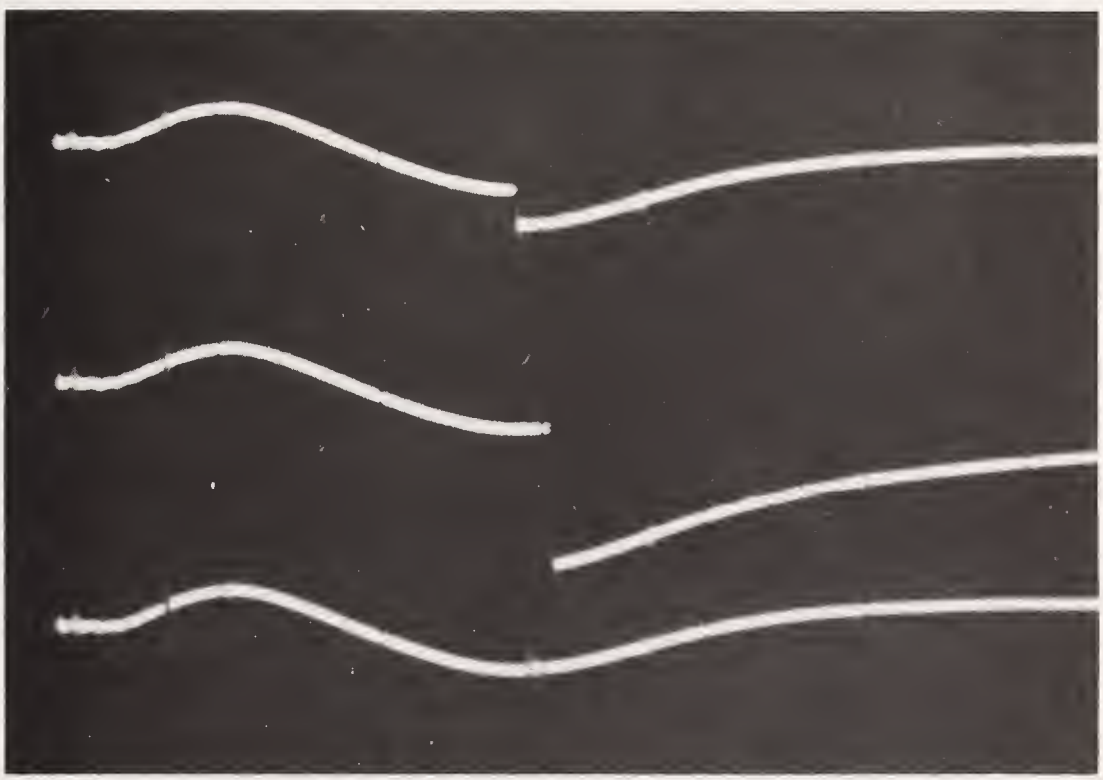

Figure 3. Oscilloscope traces from photomultiplier spark detector for three shots: a) threshold, b) above threshold, c) no damage.

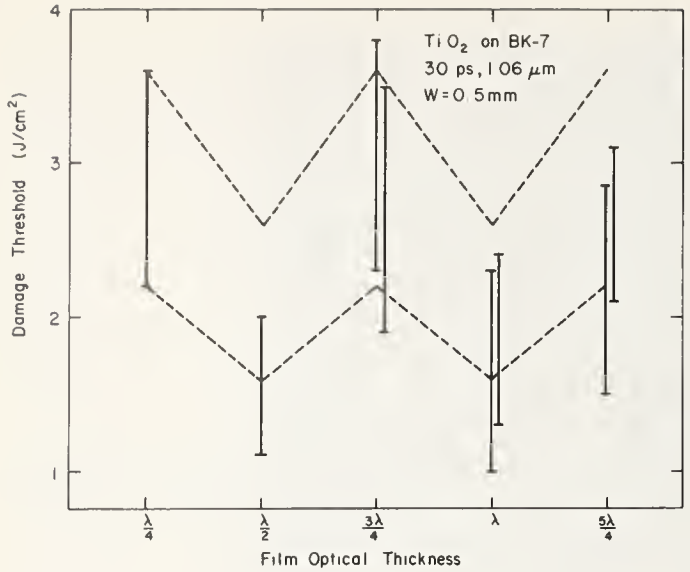

Figure 4. Damage threshold versus film optical thickness for TiO_2; 1.06-μm, 30-ps pulses.

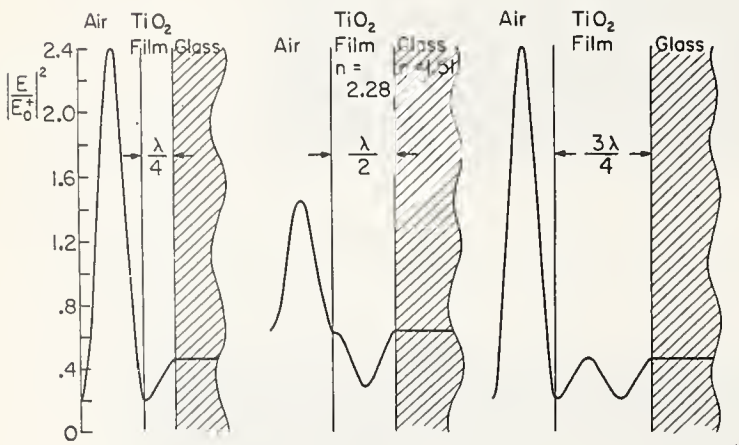

Figure 5. Standing-wave electric field intensity distributions for λ/4, λ/2, and 3λ/4 films of TiO_2. The distributions are normalized to the incident electric field-squared in air, $|E_o^+|^2$.

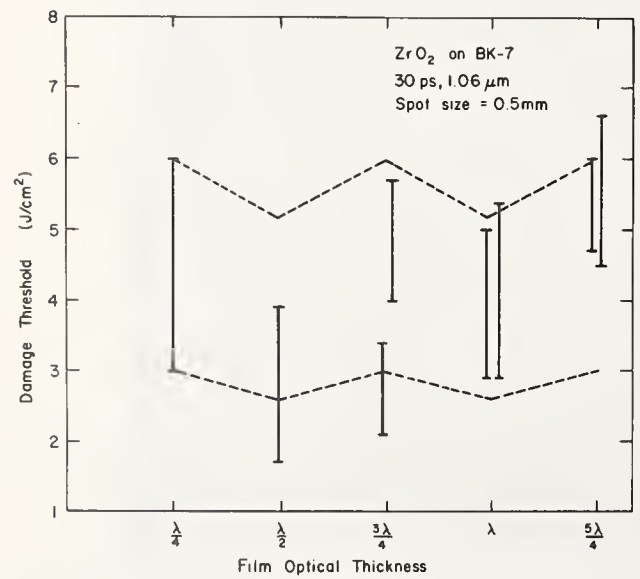

Figure 6. Damage threshold versus film optical thickness for ZrO_2; 1.06-μm, 30-ps pulses.

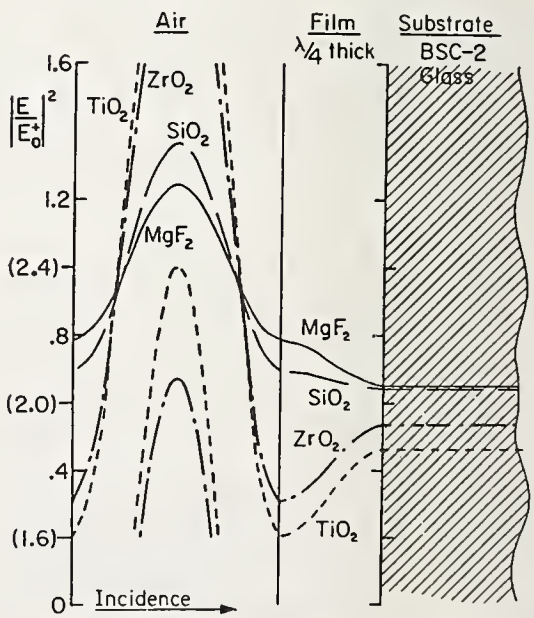

Figure 7. Standing-wave electric field intensity distributions for λ/4 films of TiO_2, ZrO_2, SiO_2, and MgF_2. For the distributions in air, the intensity scale is broken at 1.6 and the peaks have been displaced downward and plotted on the scale in parenthesis.

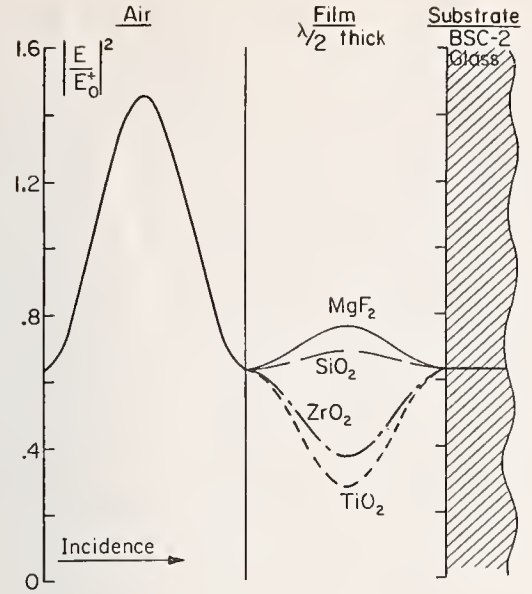

Figure 8. Standing-wave electric field intensity distributions for λ/2 films of TiO_2, ZrO_2, SiO_2, and MgF_2.

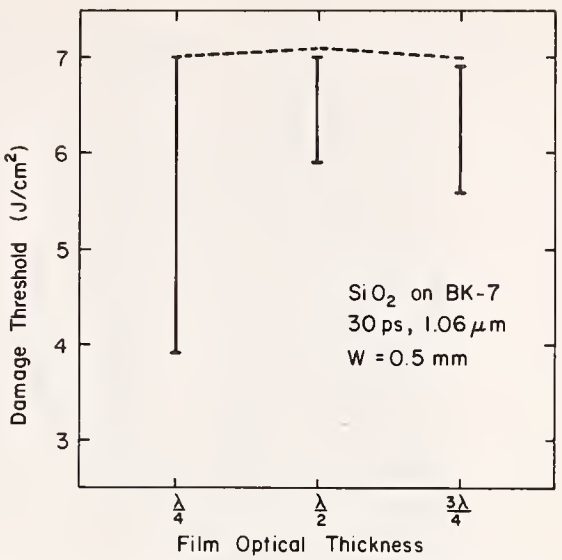

Figure 9. Damage threshold versus film optical thickness for SiO_2; 1.06-μm, 30-ps pulses.

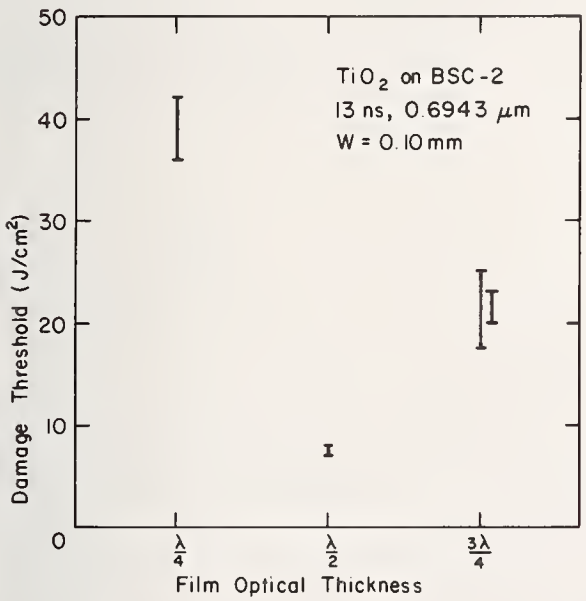

Figure 10. Damage threshold versus film optical thickness for TiO_2; 0.6943-μm, 13-ns pulses.

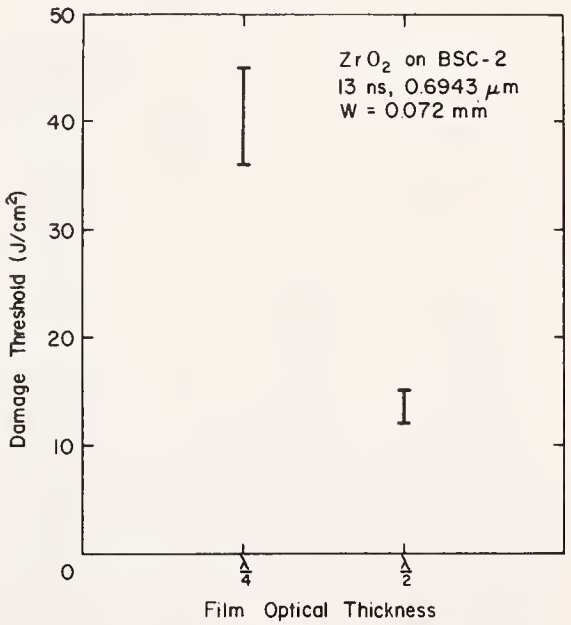

Figure 11. Damage threshold versus film optical thickness for ZrO_2; 0.6943-μm, 13-ns pulses.

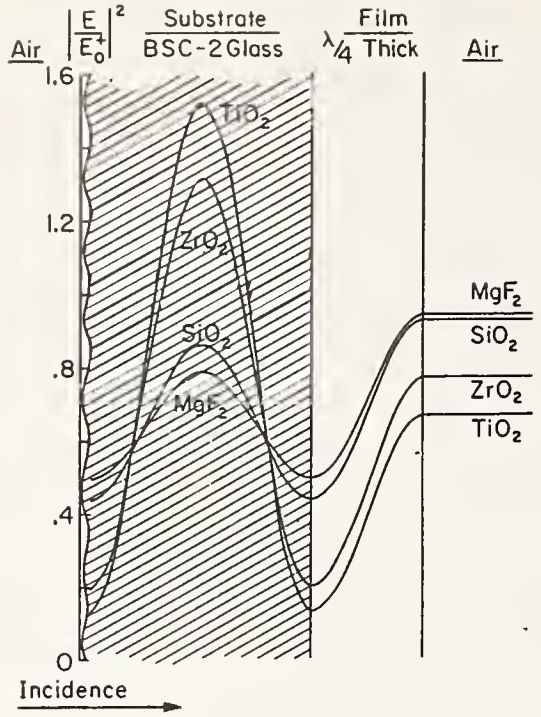

Figure 12. Standing-wave electric field intensity distributions for $\lambda/4$ back-surface coatings of TiO_2, ZrO_2, SiO_2, and MgF_2.

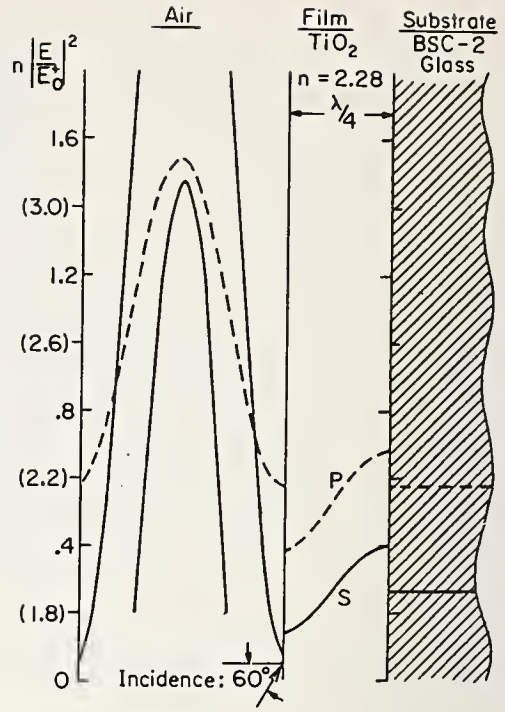

Figure 13. Standing-wave electric field intensity distributions for $\lambda/4$ front-surface coating of TiO_2, for an angle of incidence of 60°. Both S- and P-polarizations are shown. For the distribution in air, the scale is broken at 1.8 and the peaks have been displaced downward and plotted on the scale in parenthesis.

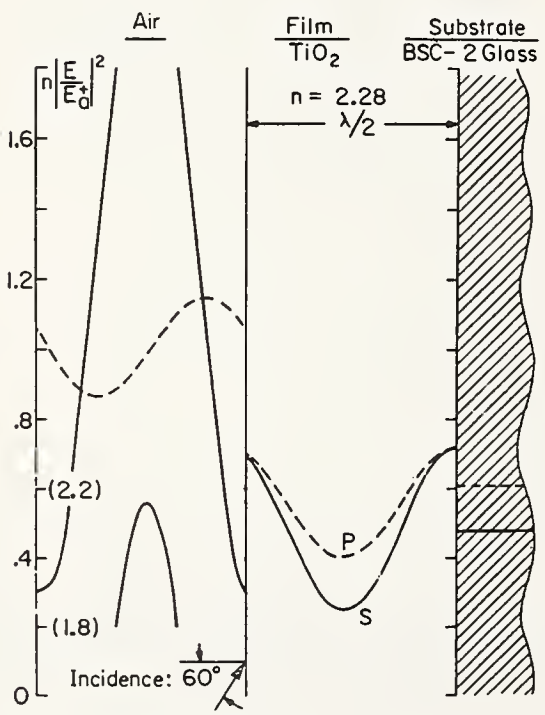

Figure 14. Standing-wave electric field intensity distributions for $\lambda/2$ front-surface coating of TiO_2, for an angle of incidence of 60°. Both S- and P- polarizations are shown. The scale is broken at 1.8 in figure 13.

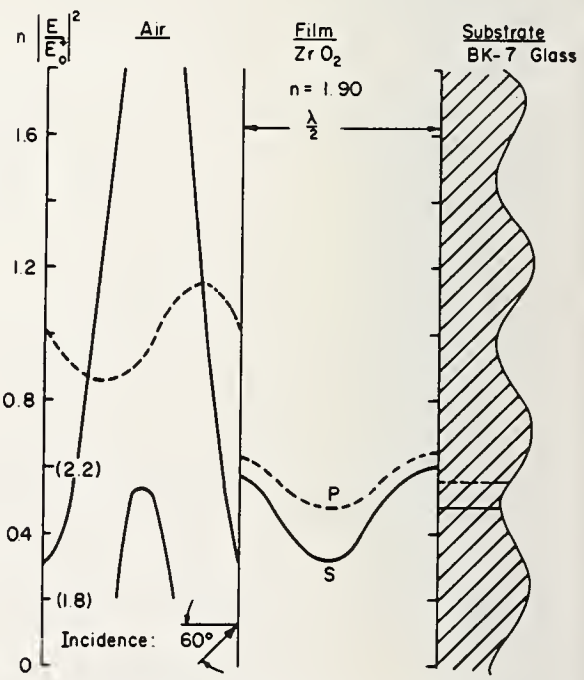

Figure 15. Standing-wave electric field intensity distributions for $\lambda/2$ front-surface coating of ZrO_2, for an angle of incidence of 60°. Both S- and P- polarizations are shown. The scale is broken at 1.8 as in figure 13.

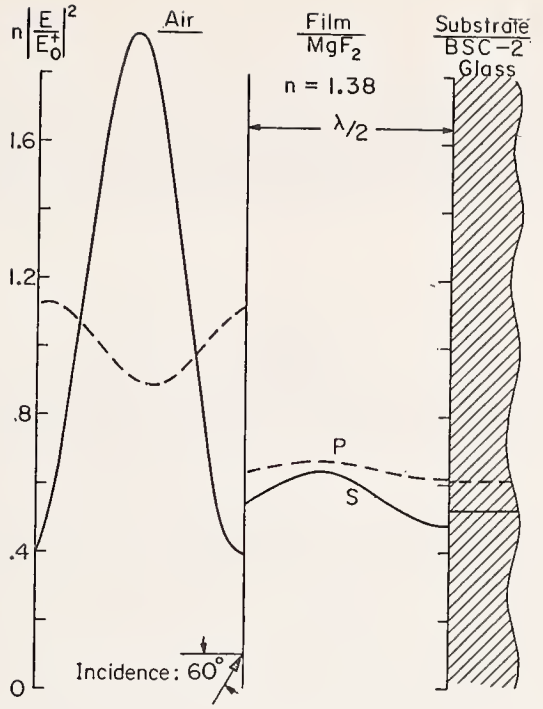

Figure 16. Standing-wave electric field intensity distributions for $\lambda/2$ front-surface coating of MgF_2, for an angle of incidence of 60°. Both S- and P- polarizations are shown.

COMMENTS ON PAPER BY NEWNAM, *et al*

There was extensive discussion of the question of whether or not one would expect a different morphology to be observed if the damage occurred by avalanche ionization sensitive only to the electric field intensity or if the damage occurred at the site of a defect or an inclusion. The point was raised that in the short pulses used in this experiment the electric field induced effect would always dominate and that there would not be sufficient energy in the pulse to cause defect mediated damage. Furthermore, even in longer pulses since the damage was occurring at threshold it might be possible to tell for small defects which was the dominant effect. The reason is as follows: the standing wave pattern is responsive to the average properties of the thin film structure, and the field is most intense at the peak of the standing wave. The damage occurs at a weak point in the thin film whether it is an inclusion, a defect, or a region of impurity. Thus, whatever the cause of the damage on a local scale it is responsive to the average properties of the electric field distribution. For these reasons it would seem to be extremely difficult to obtain morphological evidence of the initial cause of the damage process.

5.7 Threshold Ambiguities in Absorptive Laser Damage to Dielectric Films†

R.H. Picard, D. Milam*, and R.A. Bradbury

Air Force Cambridge Research Laboratories
Hanscom AFB, Massachusetts 01731

and

John C.C. Fan

Lincoln Laboratory, Massachusetts Institute of Technology
Lexington, Massachusetts 02173

The threshold energy density for laser-induced damage arising from homogeneous absorption in thin dielectric films is dependent upon the laser irradiance. This is illustrated by measurements of the time to breakdown of rf sputtered films irradiated by tightly focussed square-waveform ruby laser pulses. We are able to show that the increase of threshold with decreasing irradiance is due to two mechanisms: (1) cooling of the film by conduction of heat to the substrate and (2) two-photon absorption in the film itself.

Key words: Damage threshold; dielectric films; heat conduction; laser damage; multiphoton absorption; rf sputtering.

1. Introduction

It has been shown previously by a number of investigators that the breakdown of dielectrics due to irradiation in the small focal spot of a tightly focussed laser beam is a statistical process. This was shown first for the case of intrinsic electron-avalanche breakdown [1][1] and then for the cases of damage due to absorbing inclusions and dielectric structural defects [2, 3, 4]. In all these cases the damage threshold can only be defined statistically, and hence the concept of a threshold is of limited utility. When irradiating apparently equivalent sites with equivalent laser waveforms, damage may occur at any time during the pulse or pulse train.

On the other hand, breakdown due to homogeneous absorption in the irradiated material is non-statistical, and materials which damage due to homogeneous absorption should exhibit a sharp damage threshold, even in small focal spots [4]. Nevertheless, one must still exercise caution in quoting threshold energy densities for damage in this case since the threshold depends on the laser irradiance, or equivalently on the laser pulse duration. We wish to illustrate this point by describing the results of damage experiments on a series of rf-sputtered single-layer dielectric films which we subjected to irradiation by a constant laser field.

In [4] it was shown that in such an experiment one could determine whether the mechanism responsible for breakdown was homogeneous absorption, or one of the other mechanisms mentioned above by analyzing the statistical variation of the time until damage, or survival time, for different sites on the sample. Hence, we were able to select those sputtered films in our study which damaged due to homogeneous absorption. Concentrating on the homogeneous absorbers, we varied the survival time by varying the irradiance and determined the dependence of the energy density threshold on the survival time. This is equivalent to a measurement of the dependence of the threshold energy density on pulse duration.

---

* Present address: Lawrence Livermore Laboratory, Livermore, California 94550.

† The Lincoln Laboratory portion of the work was sponsored by the Department of the Air Force.

1. Figures in brackets indicate the literature references at the end of the paper.

Although the pulse-duration dependence of the damage threshold has been discussed [5] and measured (for example, [6, 7, 3]) many times before, these authors were invariably concerned either with damage to bulk dielectrics or with situations where the cause of damage was unknown or known not to be homogeneous absorption. Moreover, in our measurements we have been able to identify the reasons for the irradiance or pulse-duration dependence of the damage threshold by comparison with model calculations.

2. Experimental Procedure

The apparatus and the experimental technique are the same as described in [4]. The samples are irradiated by 20 - 30 nsec, square-waveform ruby laser pulses. A typical pulse waveform is shown in figure 1. This pulse is obtained by switching out the central portion of the output from a single-longitudinal-mode, single-transverse-mode Q-switched laser by means of a Pockels cell shutter. As shown in figure 2 the pulse is focussed onto the sample and recollimated by a pair of lenses, then detected and displayed. A portion of the light is picked off by a beam splitter prior to focussing and displayed on the same oscilloscope trace to serve as a reference.

An idealized scope trace is shown in figure 3. The time delay before damage occurs, or survival time, t_d is measured from the width of the transmitted pulse shown on the right, and the beam power is determined from the height of the reference pulse shown on the left by using a radiometer to calibrate the detector. Since the beam is known to have a Gaussian spatial profile, the irradiance I at the center of the focal spot may be determined from the beam power and the spot size. A 6 μm focal spot (FWHM) was used in this series of experiments.

After irradiating a large number of sites on the same sample, each with one pulse, we are able to select those samples in which damage is due to homogeneous absorption. In figure 4 we show data from a sample in which breakdown is not due to homogeneous absorption. Even though all five sites shown are subject to the same irradiance, damage occurs at random times during the pulse. (In figures 4 and 6 the positions of the transmitted and reference pulses are interchanged, relative to their positions in figure 3.) We show a typical plot of t_d versus I in figure 5 for a sample which is damaging due to some process other than uniform absorption.

Figures 4 and 5 are to be contrasted with figures 6 and 7 which show data characteristic of damage due to homogeneous absorption. In the latter case, breakdown is quite deterministic, a given irradiance leading to a well-defined time delay before damage. We shall refer to a line drawn through the data points of figure 7 as the heating curve for the sample; assuming that damage occurs when the material reaches a given temperature T_d, the heating curve determines how long it takes to heat the sample to T_d as a function of the level of irradiation. An alternate way to represent the data in figures 5 and 7 is in the form of a survival curve, or plot of the fractional number of sites surviving as a function of time [4].

In figure 8 we show survival curves for the sample of figure 7 at three different irradiances. The absorptive nature of the breakdown process is also apparent from the survival curve; however, we will show only heating curves for samples in the rest of this paper.

3. Sample Preparation

The samples used in our experiments were single-layer dielectric films prepared by rf sputtering in a Class 100 clean room at Lincoln Laboratory. Some conditions of the deposition process and properties of the samples produced are listed in table 1.

Table 1. Conditions of Preparation of Sputtered Films

Substrate material	CG 0211 or CG 7059 fire-polished glass.
Substrate preparation	Ultrasonic cleaning in hot detergent solution for less than 5 min. Ultrasonic rinse in distilled deionized water. Dry in N_2 gas boiled off from liquid. Sputter etch in Ar/O_2 mixture.
Target diameter	5 in.
Target (film) material	SiO_2, ZrO_2, or Al_2O_3
Sputtering power	100-200 W
Sputter bias	0-30% of sputtering power
Sputtering pressure	10^{-2} Torr
Sputtering gas	Ar or Ar/10 vol% O_2
Deposition rate	15-50 Å/min
Film thickness	440-1500 Å

The bare substrates were tested and found to be very resistant to damage. A prime motivation of the study was to determine the influence of preparation conditions, in particular the presence of a bias and the sputtering gas, on damage characteristics; this subject will be treated in a future publication. In this paper we confine ourselves to analyzing the heating curves of those samples which damaged due to uniform absorption.

4. Results and Analysis

We have already shown the heating curve for one of the Al_2O_3 samples in our study in figure 7. Since the laser pulses have a square temporal waveform, we need only multiply the ordinates in figure 7 by the corresponding abscissae to obtain the threshold energy density as a function of irradiation time (or, alternately, as a function of irradiance). The result is shown in curve (f) of figure 9. We also show the time dependence of threshold for five other samples in this figure (curves (a) - (e)). In all cases the threshold energy density increases by a factor of two or three as the survival time increases from the shortest to the largest values observed in the experiment. Of the two ZrO_2 samples shown, sample (a) has a threshold twice as high as sample (b) for 20 nsec pulses, but the thresholds are comparable for pulses shorter than 4 - 5 nsec. Moreover, SiO_2 sample (c) appears to have a higher threshold than SiO_2 sample (d) for the longer pulses, while the reverse appears to be true for the shorter pulses.

In an attempt to understand the time dependence of threshold, we assume that damage occurs when some part of the sample reaches a damaging temperature T_d. Then the heat Q deposited per unit volume in the material by the laser pulse is given by

$$Q \equiv c_v \rho \Delta T_d = \alpha I t_d, \qquad (1)$$

where c_v is the specific heat, ρ the mass density, α the linear absorption coefficient of the sample, and ΔT_d is the temperature rise needed to reach temperature T_d. This simple model predicts a hyperbolic heating curve. In figure 10 we show a least-squares fit to the data points for SiO_2 sample (d) of figure 9. The absorption coefficient obtained if one assumes that T_d is the melting point of the material ($\alpha = 38.9\ cm^{-1}$) is shown in the figure. It is clear that the theoretical curve does not fit the data. This should also have been clear from figure 9, since eq. (1) predicts that the threshold energy density is independent of time.

One of the most obvious possible mechanisms to explain the observed behavior is cooling of the sample by heat conduction. The characteristic length for heat diffusion in a time t is $\ell_D = (Dt)^{\frac{1}{2}}$, where $D \equiv \kappa/(c_v\rho)$ is the thermal diffusivity, κ being the thermal conductivity. Assuming $D \cong 5 \times 10^{-3}$ cm^2/sec and t = 30 nsec, we obtain $\ell_D \cong 0.1$ μm = 1000 Å. Since $\ell_D << 3$ μm, the radius of our focal spot, we can ignore radial heat loss; on the other hand, since $\ell_D \cong d$, the thickness of the film, we must consider longitudinal losses by thermal conduction into the non-absorbing substrate.

The one-dimensional diffusion equation for this slab geometry can be solved exactly by Laplace transformation [8], if we assume a uniform rate of heat deposition in the film by the laser beam. In general, the solution is in the form of an infinite series [9], but it takes on a particularly simple form it we make the following reasonable assumptions: (1) No heat loss at the front surface of the film (air); (2) infinite surface conductance at the rear surface (substrate); (3) thermal impedance matching at the film-substrate interface (that is, values of D and κ for film and substrate approximately equal). The equation for the heating curve is then

$$Q \equiv c_v \rho \Delta T_d = \alpha I t_d f(Z), \tag{2}$$

where [10]

$$f(Z) \equiv (1+2Z^2)\,\mathrm{erf}\,Z + \frac{2}{\pi^{\frac{1}{2}}} Z e^{-Z^2} - 2Z^2, \tag{3}$$

and

$$Z \equiv \frac{d}{2(Dt_d)^{\frac{1}{2}}}. \tag{4}$$

Comparing eqs. (2) and (1) and noting that $f(Z) \leq 1$, we see that cooling steepens the heating curve, as required to fit the data points in figure 10. In figure 11 we show the results of performing a least-squares fit of the data points in figure 10 to eq. (2) rather than eq. (1), still with the single adjustable parameter α. The improvement in the fit is dramatic, and we can conclude that the temporal dependence of threshold for this sample is due to thermal conduction to the substrate.

The next obvious question to ask is whether conductive cooling can account for the increase of energy threshold for damage with time for all of the samples shown in figure 9. To answer this we look at the data for sample (a), a ZrO_2 film with d = 600 Å. The data points are shown in figure 12 along with the best fit assuming cooling to the substrate, indicated by the solid line with triangles (Δ). Even though the film is thin and the effect of cooling is appreciable, we find that the predicted heating curve is not steep enough and that the fit is poor.

We are led to ask what other mechanisms might steepen the heating curves. One possible mechanism is nonlinear absorption which makes the curves steeper by lowering the threshold energy density for short times (high irradiances). If we stop at the lowest-order nonlinearity, that is two-photon absorption, the heating curve, eq. (2), is modified to the form

$$Q \equiv c_v \rho \Delta T_d = (\alpha I + \beta I^2)\, t_d\, f(Z), \tag{5}$$

where β is the two-photon absorption coefficient. The best least-square fit with adjustable α and β is indicated by the solid line without symbols in figure 12. This curve fits the data well. The one- and two-photon absorption coefficients

required for the best fit (α = 9.1 cm^{-1}, β = 2.4 cm/GW) and indicated on the figure.

To determine what fraction of the threshold variation is due to two-photon absorption and what fraction due to cooling, we also show in figure 12 a fit with $\alpha = 0$, indicated by a solid line with x's (x). We see that this fit with β = 2.8 cm/GW is nearly indistinguishable from that in which we had allowed $\alpha \neq 0$. We are led to conclude that this sample is a two-photon absorber with little or no linear absorption. By contrast, with sample (d) we had found no need to invoke any two-photon absorption ($\beta \cong 0$).

In general, the situation is not so simple, and we find that a given sample exhibits both linear and two-photon absorption. In figure 13 we show the data points for sample (e), figure 9 (SiO_2, d = 550 Å), with the same three fits. The best fit for this sample is midway between the fit with $\beta = 0$ and the one with $\alpha = 0$.

5. Summary and Conclusions

Letting $W \equiv It_d$ be the threshold energy density, we may rewrite eq. (5) to show explicitly how the threshold energy density changes,

$$W = \frac{Q}{f(Z)(\alpha+\beta I)} \quad . \tag{6}$$

Hence, there are two factors which change the value of W, cooling by heat losses to the substrate, represented by f (Z), and nonlinear absorption, represented by $\alpha+\beta I$. We may write the ratio R of the maximum and minimum thresholds observed as a product of two factors, the first representing the effect of cooling and the second the effect of nonlinear absorption, that is

$$R \equiv W_{max}/W_{min} = R_c \cdot R_{nl}, \tag{7}$$

where

$$R_c = f_{max}/f_{min}, \qquad R_{nl} = (\alpha+\beta I_{max})/(\alpha+\beta I_{min}). \tag{8}$$

In table 2 we summarize the fractional increase of threshold energy density for the six samples of figure 9 and identify that part of the increase due to cooling and that part due to two-photon absorption. We take W_{max} = W for t_d = 20 nsec and W_{min} = W for t_d = 4 nsec, even though in some cases our data extends over a greater range.

The variation R in threshold energy density ranges from a factor of 1.77 for sample (d) to a factor of 2.78 for sample (a). There is no simple correlation between film thickness and threshold change, although cooling is significant for all of the samples, giving rise to a 26% increase in threshold for the thickest sample and an 81% increase for the thinnest. To account for the complete time dependence of the threshold energy density, one must assume that nonlinear absorption occurs in the film. For three of our samples the increase of threshold due to nonlinear absorption exceeds 50%. On the other hand, only a 5.5% threshold variation could be attributed to two-photon absorption in the case of sample (d), a sample we have already identified as a linear absorber in section 4.

In a future publication we will attempt to identify correlations between the behavior of our samples under irradiation and the conditions under which they were prepared.

Table 2. Sources of Variation of Threshold Energy Density W

Sample	Material	Thickness (Å)	Percent increase in threshold between 4 and 20 nsec		
			Total[a] (R-1)	Due to cooling[b] (R_c-1)	Due to nonlinear absorption[b] (R_{nl}-1)
(a)	ZrO_2	600	178	64	66
(b)	ZrO_2	1150	92	30	52
(c)	SiO_2	440	131	81	29
(d)	SiO_2	600	77	66	5.5
(e)	SiO_2	550	135	72	35
(f)	Al_2O_3	1500	119	26	71

[a] Read from figure 9.

[b] Calculated from eqs. (7) and the values of α and β determined from least-squares fits.

6. References

[1] Bass, M., and H. H. Barrett, IEEE J. Quantum Electron., QE-8, 338 (1972).

[2] DeShazer, L.G., B.E. Newman, and K.M. Leung, Laser Induced Damage in Optical Materials: 1973, edited by A.J. Glass and A.H. Guenther (U.S. Govt. Printing Office, Washington, 1973), p. 114; Appl. Phys. Lett. 23, 607 (1973).

[3] Bliss, E.S., D. Milam, and R.A. Bradbury, Appl. Opt. 12, 677 (1973).

[4] Milam, D., R.A. Bradbury, R.H. Picard, and M. Bass, Third Conference on High Power Infrared Laser Window Materials, November 12-14, 1973, Vol. III, edited by C.A. Pitha, H. Posen, and A. Armington (Air Force Cambridge Research Laboratories, Bedford, Mass., 1974), p. 1011; Laser Induced Damage in Optical Materials: 1974, edited by A.J. Glass and A.H. Guenther (U.S. Govt. Printing Office, Washington, 1974), p. 169.

[5] Bliss, E.S., Damage in Laser Glass, edited by A.J. Glass, A.H. Guenther, C.M. Stickley, and J.D. Myers (American Society for Testing and Materials, Philadelphia, 1969), p. 9; Opto-Electronics 3, 99 (1971).

[6] Avizonis,P.V., and T. Farrington, Appl. Phys. Lett. 7, 205 (1965).

[7] Zverev, G.M., T.N. Mikhaĭlova, V.A. Pashkov, and N.M. Solov'eva, Zh. Eksp. Teor. Fiz. 53, 1849 (1967) [Sov. Phys.-JETP 26, 1053 (1968)].

[8] Carslaw, H.S., and J.C. Jaeger, Conduction of Heat in Solids, 2nd edition (Clarendon Press, Oxford, 1959), pp. 297-326.

[9] An analysis similar in some respects for the heating of metals has been carried out by M. Sparks and C.J. Duthler, Fourth Technical Report, Contract No. DAHC15-73-C-0127 (Xonics, Inc., Van Nuys, Calif., 1974).

[10] If Z <<1 (film very thin or time long or diffusivity large), then we have f (Z) ~ Z, and eqs. (2) through (4) give rise to $T_d \sim Q \sim t_d^{\frac{1}{2}}$, as is used in simple diffusion models of metal heating. (See, for example paper by T.T. Saito, D. Milam, P. Baker, and G. Murphy in these Proceedings.) However, this simplification is not available to us here.

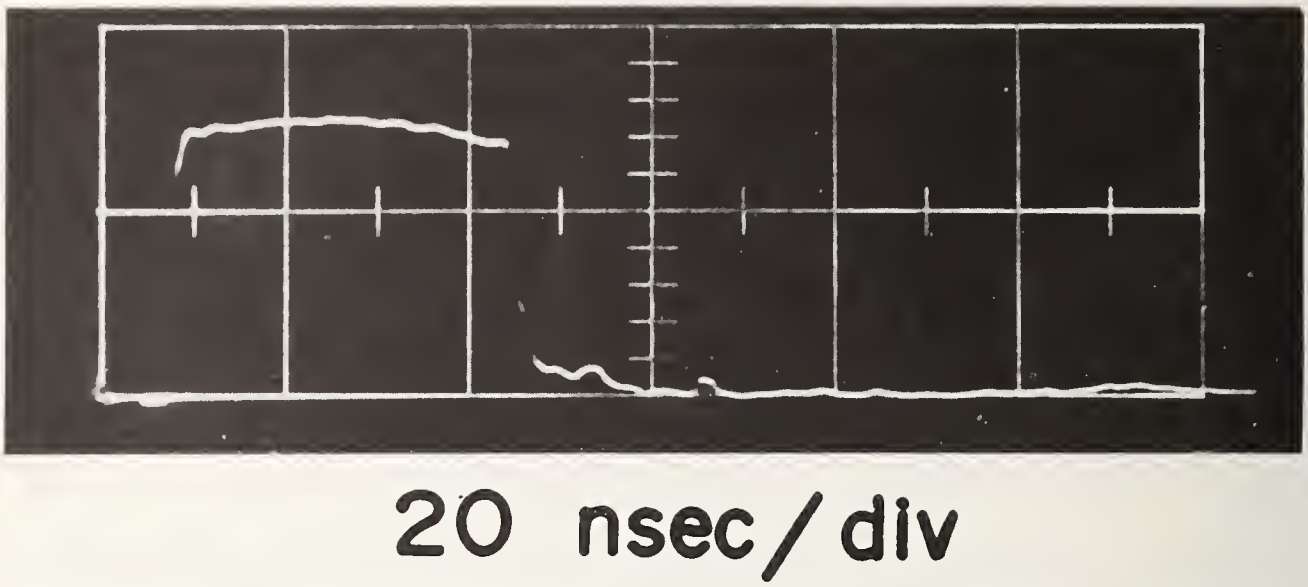

Figure 1. Square-waveform pulse selected by shutter from Q-switched ruby laser pulse.

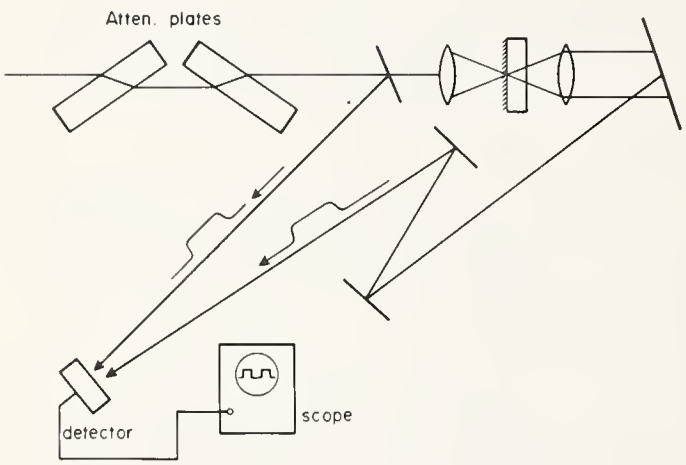

Figure 2. Set-up for damage experiment. The sample is placed at the common focus of the lens pair.

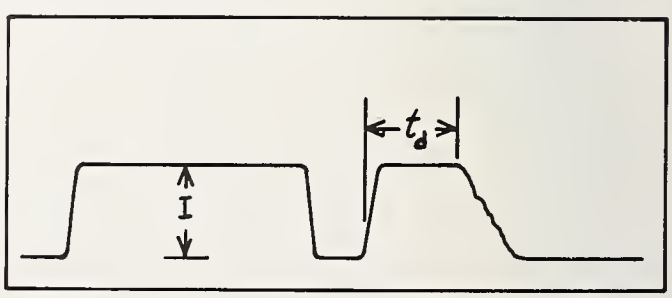

Figure 3. Idealized oscilloscope display recorded during damage experiment. Irradiance I is determined from reference pulse (on the left) and time delay until damage t_d from pulse which transversed sample (on the right).

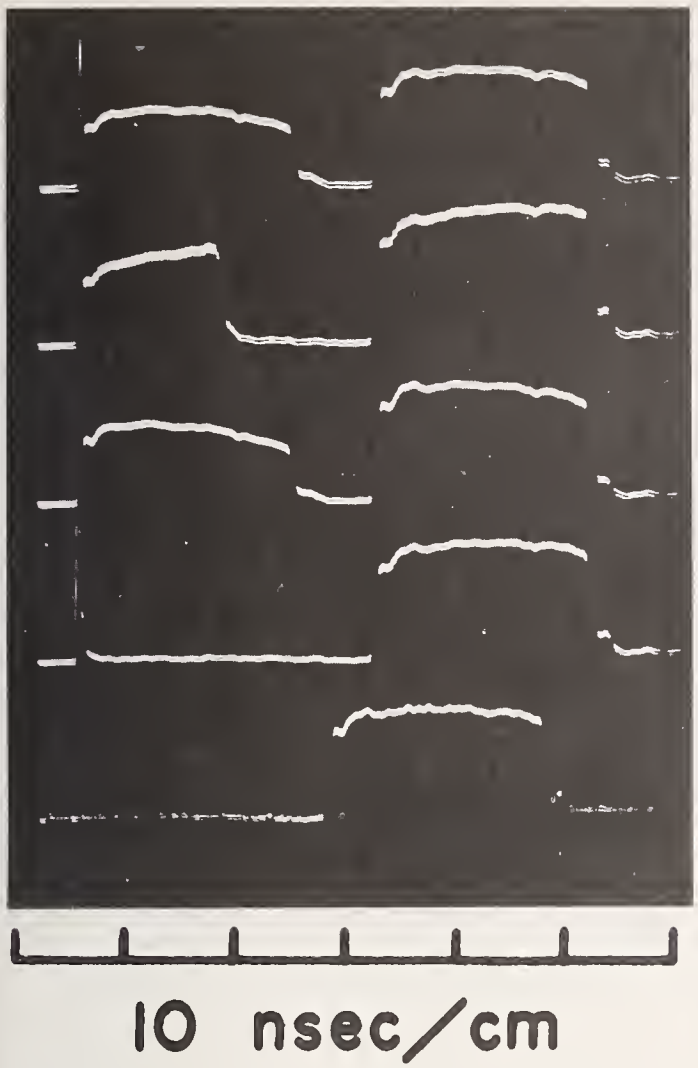

Figure 4. Typical data for a sample which is not damaging due to uniform absorption. The reference pulse is on the right, and the pulse passing through the sample is on the left.

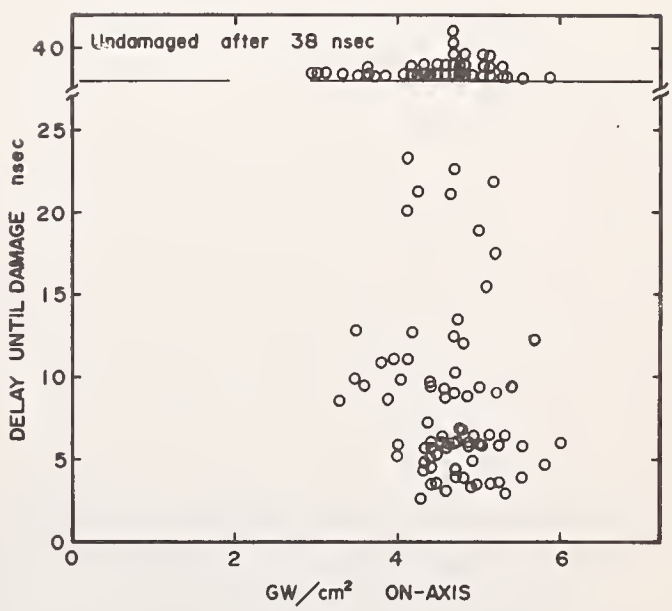

Figure 5. Typical plot of data points for time delay and on-axis irradiance for a sample damaging due to some process other than uniform absorption. It is not possible to draw a curve through the points, demonstrating the usual statistical character of small-spot damage.

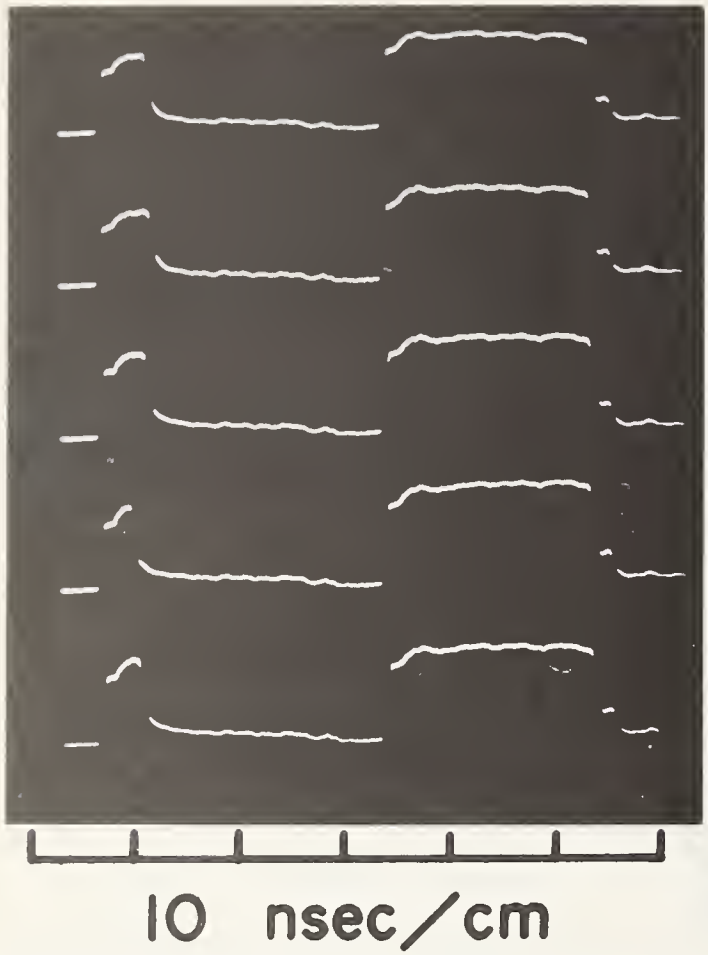

Figure 6. Typical data for a sample damaging due to uniform absorption. Positions of the two pulses are the same as shown in figure 4.

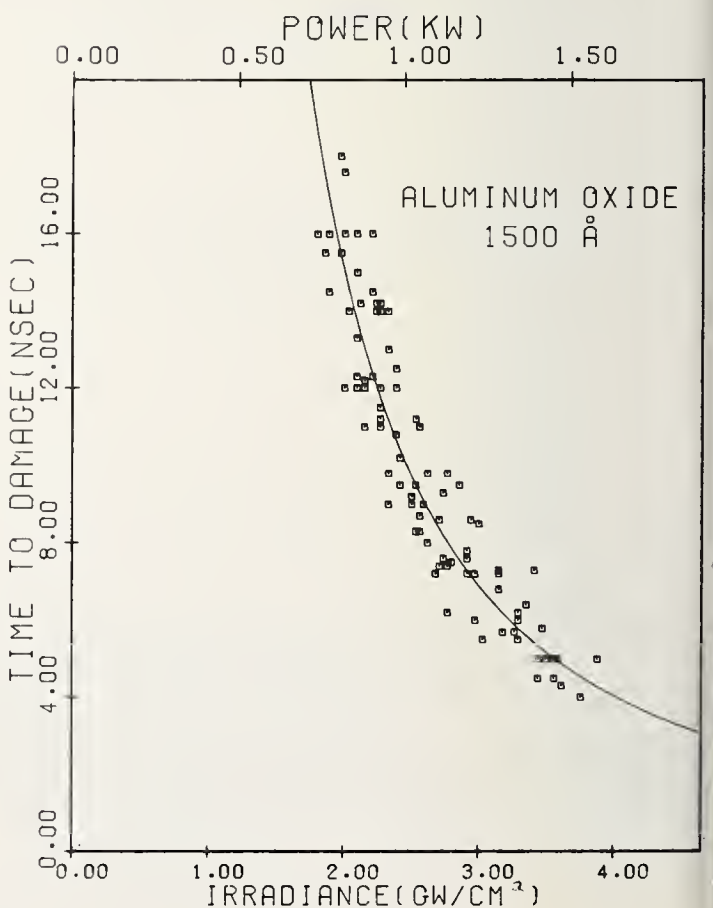

Figure 7. Plot of time delay versus irradiance for a sample which has damaged due to uniform absorption. Breakdown is non-statistical, and one can draw a smooth curve (the heating curve) through the data points. The laser power is indicated on the upper horizontal axis.

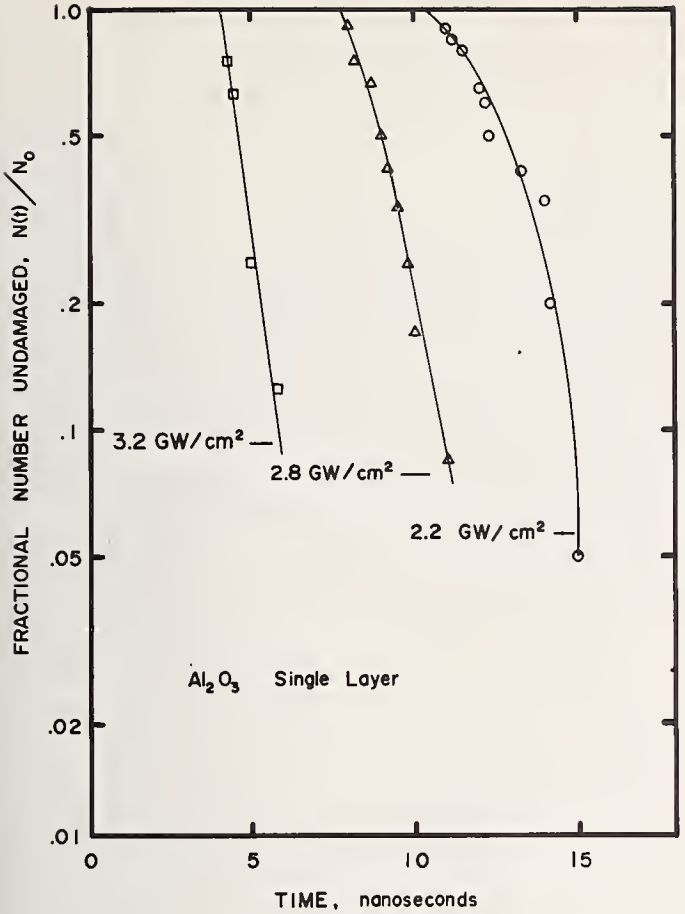

Figure 8. Survival curves, or plots of survival probability versus time, for the absorbing sample of figure 7.

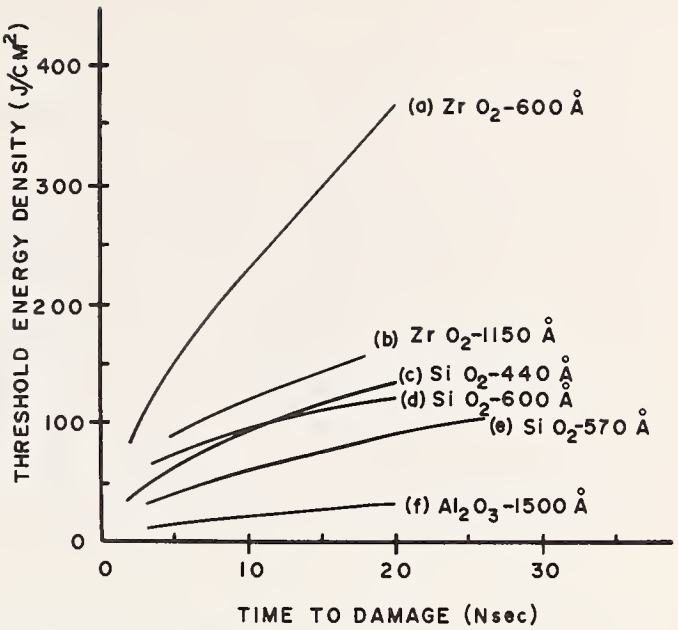

Figure 9. Threshold energy density versus time delay for six sputtered single-layer films, showing the dependence of threshold energy for damage on survival time. The sample shown in figures 7 and 8 is represented by curve (f).

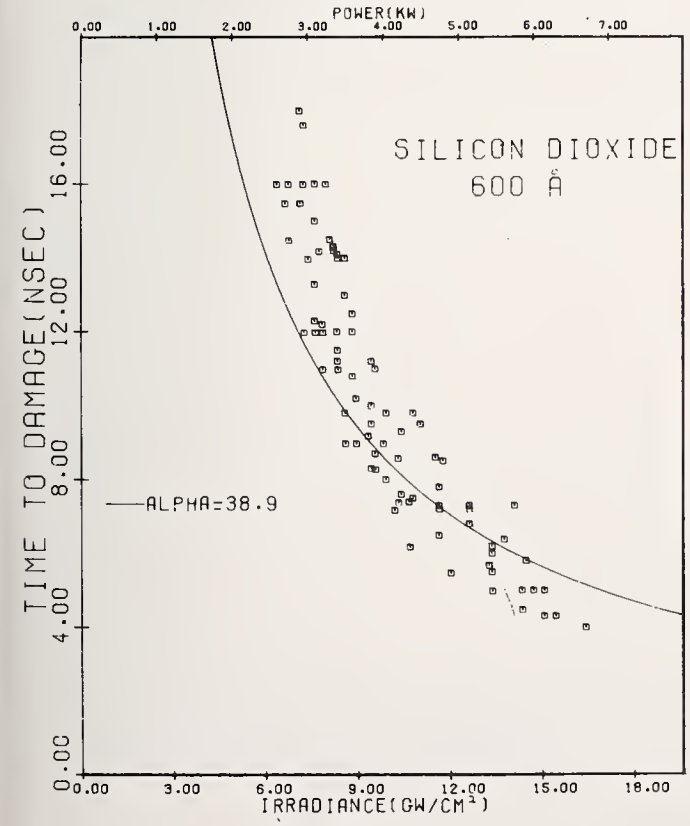

Figure 10. Data points for SiO_2 film (sample (d) of figure 9) with heating curve obtained by least-squares fit to data points, assuming heating rate proportional to irradiance and no heat losses. Best estimate for absorption coefficient α is listed on plot in cm^{-1}.

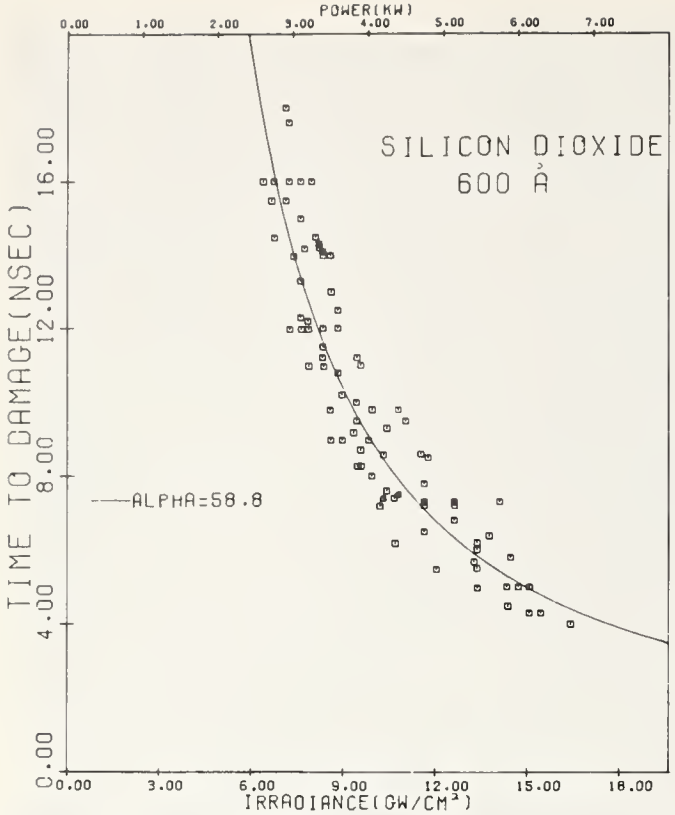

Figure 11. Data for sample of figure 10 fit to a heating curve which assumes cooling of the film by thermal conduction to the substrate.

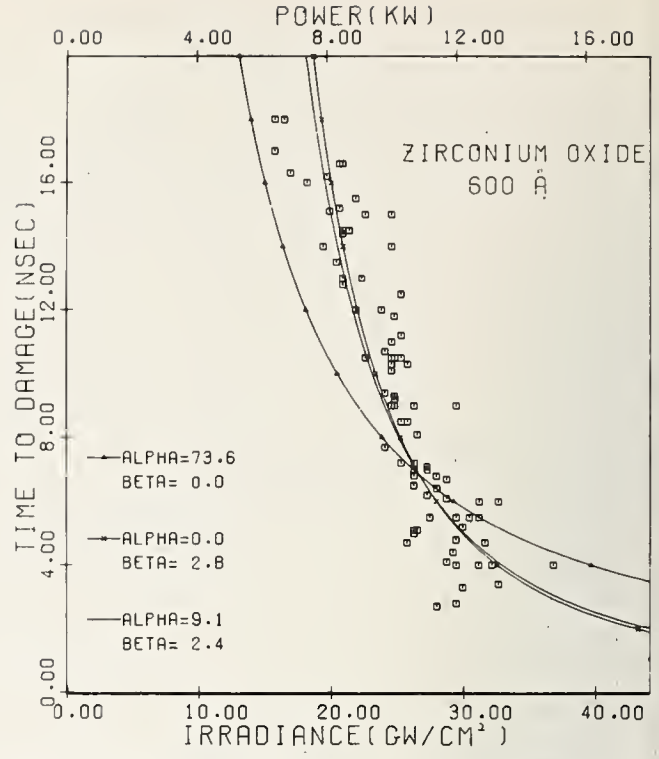

Figure 12. Data points for ZrO_2 film (sample (a) of figure 9) fit to three different heating curves assuming (1) linear absorption only (—Δ—), (2) two-photon absorption only (—X—), and (3) both one- and two-photon absorption (solid line without symbols). The linear and two-photon absorption coefficients α and β are listed for each of the plots, α in cm^{-1} and β in cm/GW. All three fits allow for conductive cooling to the substrate.

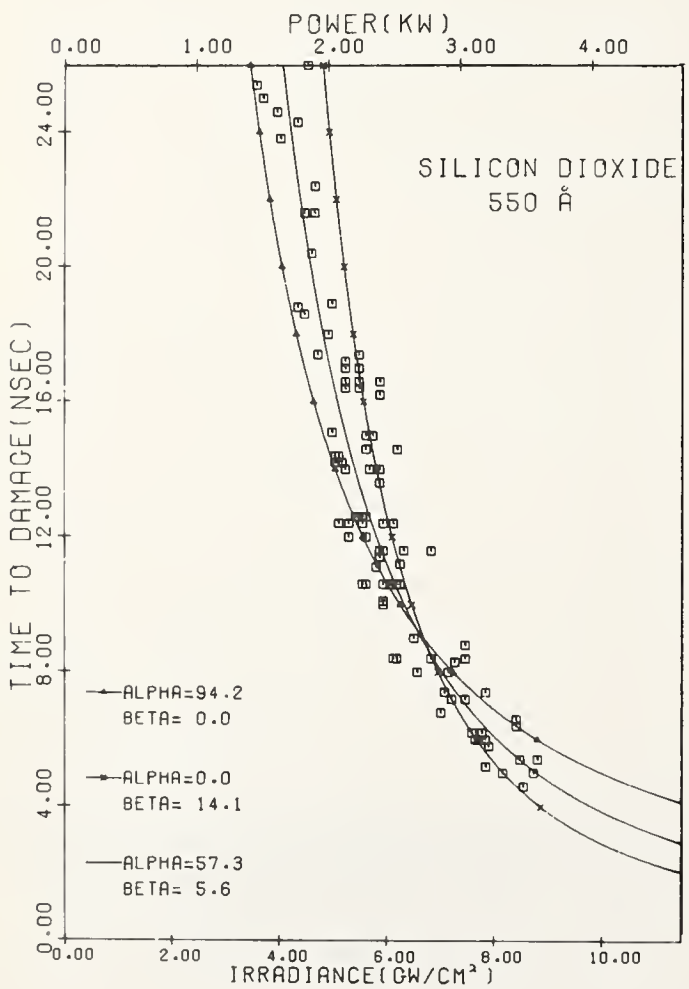

Figure 13. Data points for SiO_2 film (sample (e) of figure 9) fit to three different heating curves. The fits used are the same as in figure 12.

COMMENTS ON PAPER BY PICARD, *et al*

In this paper evidence was presented of two-photon absorption in materials in which two-photon absorption is energetically forbidden in the bulk material. The question was therefore raised as to whether one would expect to see a different band structure in the thin film material than is observed in the bulk material. The point was raised that variations of the energy level structure from the bulk properties might indeed be expected to occur in thin films. One possible cause of new levels was the phenomenon of band bending due to the abrupt termination of the lattice in the intermittent structure of the thin film. The authors of the paper felt that this was one possible cause of the multiphoton absorption, but that other mediating impurities or defects might also play a role. Whatever the cause or location of the intermediate states was there were observed to be homogeneously distributed throughout the materials on the scale of the experiment. The resolution of the experiment was determined by the full width half maximum spot size of the laser probe used in this work, which was 6 micrometers. The question was raised as to whether or not the electric field distribution in the thin film had been explicity taken into account in this work. The authors responded that it had not, but due to the thickness of the films they did not feel that it would be a significant effect.

5.8 Time Resolved Study of Laser-Induced Structural Damage in Thin Films*

Nabil Alyassini and Joel H. Parks

Departments of Physics and Electrical Engineering
University of Southern California
Los Angeles, California 90007

A time resolved optical probe technique reported previously was used to study laser induced structural damage in thin film dielectric coatings. Experimental data indicates that thin film damage frequently occurs without any detactable spark or distortion to the transmitted damaging ruby pulse and that structural damage to thin film can occur up to 40 nsec after passage of the damaging Q-switched ruby pulse through the site. In addition damage threshold of λ/4 ZnS single layer film indicates the presence of a film/substrate adhesion effect.

Key words: Adhesion effect; laser induced damage; optical probe technique; thin film; time resolved damage.

1. Introduction

This paper presents the results of time resolved damage studies of thin films using optical probe techniques [1-3][1]. These techniques allow the detailed temporal development of laser induced damage to be monitored. The time resolution can include effects occurring during the laser pulse and can also be extended to observe phenomena well after the damaging laser pulse has past, covering a range 0.5-50 nsec. In addition, these optical probe methods proved to be an extremely sensitive detector of small film damage occurring with site diameters ~1μm.

In section 2 the experimental technique is described and the film configurations studied are presented. The primary results discussed in section 3 include an indication of the sensitivity and utility of the probe technique. In the concluding section 4 we summarize the primary results of these studies.

2. Experimental Technique

Figure 1 shows the experimental arrangement used in this study[1-3]. In order to monitor structural changes in the film during and after irradiation with the single mode TEM_{oo} Gaussian ruby laser, a 3 mW unpolarized TEM_{oo} He-Ne laser was employed to probe the film internally at the critical angle for the film/air interface. The reflected probe beam was detected with a silicon PIN photodiode (HP 5082-4207) which was dc coupled to a 500 MHz Tek. 7904 oscilloscope. The optical probe detection system had a measured risetime of less than 1 nsec and was synchronized [3] in time to the damaging ruby pulse with a measured accuracy of better than ±0.25 nsec.

Internal probing of the film at its critical angle was chosen in order to:
- Eliminate any possible spark perturbation of the probe beam,
- Maximize sensitivity of probe to structural variations at film/air interface since the reflectivity angular gradient is maximum at the critical angle,
- Maximize resolution of probe detection system since detected signal is maximum at this angle.

The calculated spot size radius of the probe at the film/air interface was less than 4μm and the measured spot size radius of the ruby at the film was 35μm. Each site was irradiated only once. Tests were conducted on λ/4 ZnS, λ/4 MgF_2, bi-layer of λ/2 MgF_2 on top of λ/4 Zns, and a 17-layer film of ZnS/T F_4 $G(HL)^8HA$. All the coatings were tested as entrance and exit surface film, except the bi-layer coating which was tested only as an entrance surface film. All the films were thermally deposited on BSC-2 dove prisms as shown in figure 1. More detailed description of the experimental arrangement can be found in [3].

3. Experimental Results and Discussion

Figure 2 shows a typical data set for an entrance surface λ/4 MgF_2 film damage of ≃30μm diameter. The traces shown are exact replicas copied from original photographs of the oscilloscope traces and

* Partially supported by Advanced Research Projects Agency and Joint Services Electronics Program at U.S.C.

1. Figures in brackets indicate the literature references at the end of this paper.

arranged to emphasize the important times in the evolution of damage. Such a data set is typical of the thin films coatings studies when the damage site is relatively large. In such a case distortion of the transmitted damaging ruby pulse was always present as shown in trace (a) (output pulse).

Figure 3 shows typical data set for a smaller damage site, which in this case was 10 μm diameter entrance surface λ/4 ZnS damage. Note that the transmitted damaging ruby pulse shows no detectable distortion even though a spark was detected with this damage. The fall time of the probe trace for this site is much slower than the site shown in figure 2.

It should also be pointed out that no major detectable difference between the probe traces for entrance and exit sites was found in the collected data for all the films studied.

3.1. Sensitivity of Optical Probe Technique

The dip in the transmitted damaging ruby pulse could not be due to absorption by the visible spark that sometimes was detected with thin film damage since a spark was also detected at many sites without any detectable dip in transmitted damaging ruby pulse. It is also not due to absorption by the film or absorbing inclusions since the energy needed to thermally damage a film site is negligible relative to energy of the damaging ruby pulse, and in addition, the extraction of such energy would be occurring continuously during the pulse. Even when thin film damage is due to an avalanche type process, the energy needed to create $10^{18} - 10^{19}/\text{cm}^3$ free electrons by ionization, and the subsequent energy absorbed by such a density of free electrons in the irradiated film site is too small to be detectable in our set-up.

Hence we conclude that the dip in transmitted damaging ruby pulse for the thin film case is due to scattering by the deforming site. It appears from our results though, that the damaging ruby pulse is not very sensitive to relatively slow deformation in the film on which it was normally incident. Only when the deformation was relatively violent, reaching a peak in less than 10 nsec, did it cause detectable scattering of the damaging ruby pulse.

The probe beam is insensitive to changes in the film index since it was incident at the critical angle for the film/air interface. Linear absorption by the film or an absorbing inclusion should be going on continuously and would not explain the sudden dip in the reflected probe intensity. However, laser induced deformation in the film could cause excessive scattering of the reflected probe intensity and a sudden dip in probe trace. This deformation could result from melting, vaporization, or cracking in the film due to thermal stresses. It can be assumed that the probe beam was scattered by these deformations as they were taking place. When the resulting damaged site was relatively free of debris or bubbles, and larger than the probe cross section at the film, the probe trace recovered almost completely. When the site appeared with considerable debris or bubbles or was smaller than the probe cross section at the film, the probe trace showed only slight or negligible recovery (see figure 2 and 3). The start of the dip in the probe trace indicates the instant at which the laser induced deformation in the film effected the probe. The fall time of the probe gives a measure of how long a time this deformation of the irradiated site takes to reach a peak or plateau as far as the effect in scattering the probe is concerned. The recovery time of the probe indicates the time needed for such deformation effects to subside.

Distortion to the transmitted damaging laser pulse has been used as an indicator of laser induced damage to dielectric thin films [4]. Our dielectric thin film data indicates that this is not a positive indication of small damage near threshold. In general, the spark that sometimes accompanies thin film damage is a better indicator, even though it is well known that the spark itself is a less sensitive detector of damage than the LIS method [5]. We have also employed the LIS method as a damage indicator throughout this study [6]. In the few cases when the LIS method failed to detect damage, the site induced scattering was clearly revealed by a drop in the probe trace. Such sites which occurred in the λ/4 ZnS and the 17-layer film had a diameter of less than 2-3 μm and relatively smooth edges. Figure 4 shows the morphology and data set of such a site which was revealed only by the probe method. The calculated minimum detectable damage size was 1.5μm in diameter [3].

We have also found that the lack of distortion of the transmitted damaging ruby pulse, or the lack of an accompanying spark, does not necessarily occur only at lower power intensities or energy densities. We have detected damage in λ/4 ZnS film without a spark or distortion to the transmitted damaging ruby pulse at slightly higher energy densities than other sites in the same film at which a spark and/or distortion was detected.

3.2. Time Evolution of Structural Damage

Another interesting result is that the structural damage of the irradiated site as revealed by the dip in the probe trace, always occurs during the time of interaction of the damaging ruby pulse and the film. The data set for such a site in λ/4 MgF_2 film is shown in figure 5. Note that the structural damage which is indicated by the drop in the probe trace starts ≃25 nsec after the passage of the damaging ruby pulse. The site temperature probably induced thermal stresses which reached a critical value about 25 nsec after passage of ruby pulse causing the crack shown in the

SEM photo of the site. On the average a lower incident field intensity implied a longer time delay between the start of the dip in the probe trace and the peak of the ruby pulse.

3.3. Possible Film/Substrate Adhesion Effect

Figure 6 shows the standing wave field in an entrance and exit $\lambda/4$ ZnS film. The measured peak threshold intensity at points of maximum field inside the film are also shown. The exit surface film exhibit a higher threshold density than the same film used on the entrance surface. This difference in the measured threshold could be due to an adhesion effect at the film/substrate interface. This could decrease the entrance surface film threshold since the standing wave field is maximum at the film/substrate interface in that case. The other films tested did not reveal any difference in their threshold data.

The importance of the standing wave field on the morphology of the film damage is shown in figure 7. The standing wave field in this case is maximum in the layer nearer the laser source and drops off progressively in successive layers. In the entrance film case the top few layers seem to have fused together, while in the exit film case the inner few layers changed phase and the resulting stresses ruptured the film.

4. Conclusions

Damage to thin dielectric films can occur without any detectable distortion in transmitted damaging laser pulse and/or an accompanying spark. Thus both are questionable indicators of weak damage.

For damage that is the order of 2-3 um in diameter or greater, the optical probe technique prove to be as sensitive as the LIS method. In cases when the damaged site was of smaller size, the damage was revealed by the probe trace behavior and undetected by the LIS method.

Damage does not necessarily occur during the time of interaction between the laser pulse and the film. The development of laser induced thermal stresses can cause damage well after passage of the laser pulse through the site.

A possible adhesion effect in the film/substrate interface of $\lambda/4$ ZnS film was detected causing a lower threshold intensity when film was used as an entrance surface relative to its value when used as exit surface film. The effect of the field standing wave on morphology of film damage was also pointed out.

5. Acknowledgments

We would like to acknowledge discussions with Prof. J. Marburger and Prof. R. W. Hellwarth. The film depositions were prepared by Mr. H. R. Owen and SEM photographs were taken by Mr. Jack Worrall, both of U.S.C.

6. References

[1] J. H. Parks and N. Alyassini, 4th. ASTM Symp., Damage in Laser Mat'ls., NBS Spec. Pub. 372, 104 (1972).

[2] N. Alyassini, J. H. Parks and L. G. DeShazer, 5th. ASTM Symp. Damage in Laser Mat'ls., NBS Spec. Pub. 387, 133 (1973).

[3] N. Alyassini, Ph.D. Thesis, University of Southern California, 1975 (University Microfilm, Ann Arbor, Mich).

[4] D. Milam, R. A. Bradbury, R. H. Picard and M. Bass, 6th. ASTM Symp. Damage in Laser Mat'ls., NBS Spec. Pub. 414, 169 (1974).

[5] B. E. Newnam and L. G. DeShazer, Op. Cit., 123 (1972).

[6] We found experimentally that using a fixed 40X telescope to examine the LIS level before and after irradiation is easier and more sensitive to changes in the scattering level than using the unaided eye.

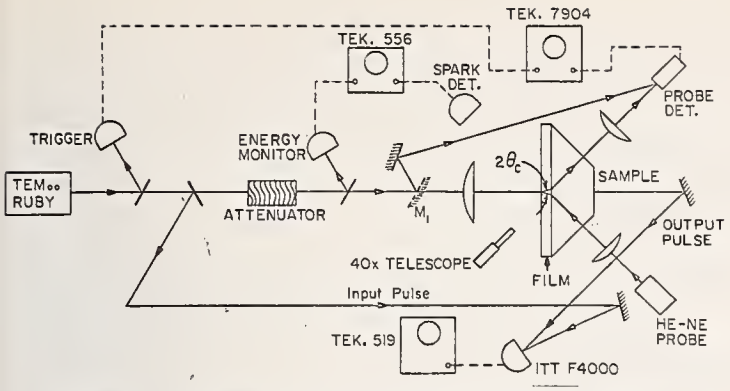

Figure 1. Schematic of experimental arrangement and optical probe technique for study of thin film damage.

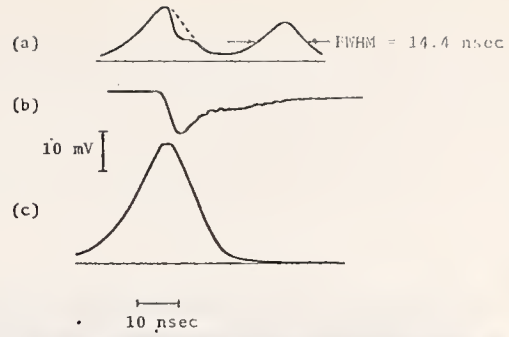

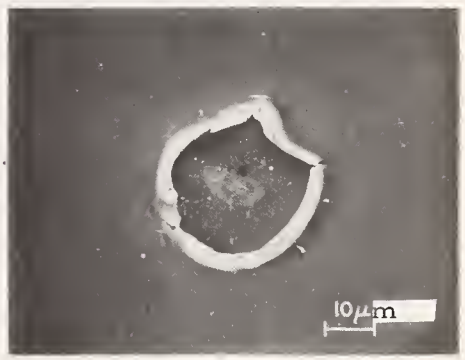

Figure 2. Typical entrance site damage in λ/y MgF_2 film; site C3,9. (a) output (left) and input pulses of damaging ruby pulse, (b) optical probe trace, (c) damaging ruby pulse, (d) SEM photograph. A spark was detected with this site. The incident peak field measured 0.624 mW/cm.

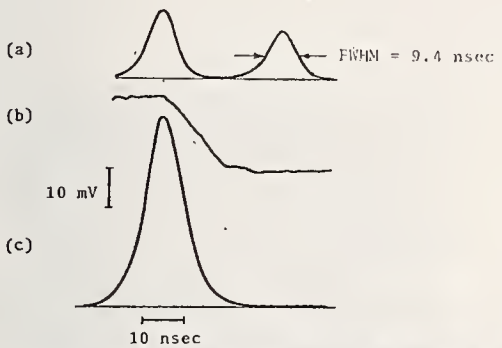

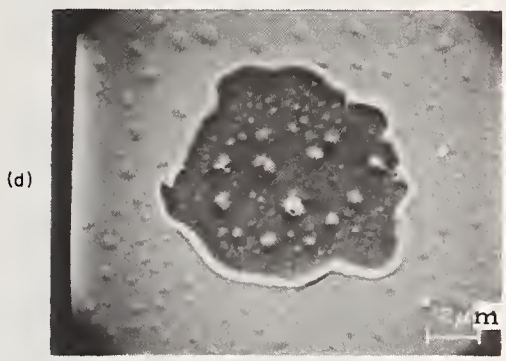

Figure 3. Typical entrance site damage data in λ/4 ZnS film; site F_5, 5. (a) output (left) and input pulses of the damaging ruby pulse, (b) optical probe trace, (c) damaging ruby pulse, (d) SEM photograph. Note that no distortion is detectable in the output pulse although a spark was detected with this site. The incident peak field measured 0.615 mV/cm.

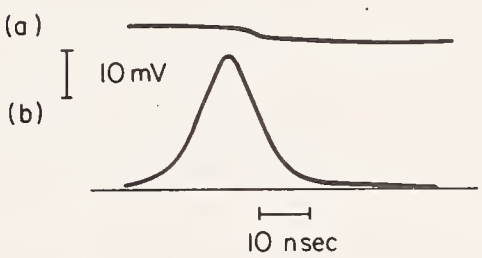

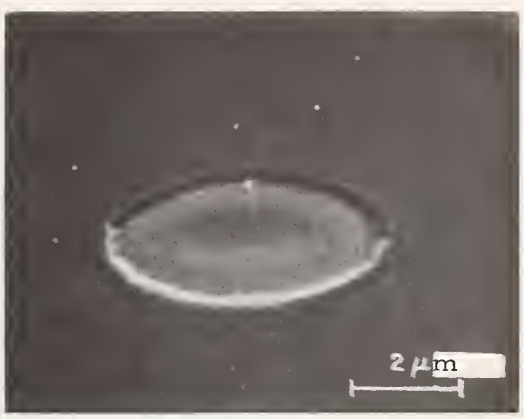

Figure 4. Data set of an entrance site damage in a 17-layer film, site H6,5. (a) optical probe trace, (b) damaging ruby pulse, (c) SEM photograph. This damage site was not detected by the LIS method although the probe trace indicates the occurrence of damage. The incident peak field measured 0.59 mV/cm.

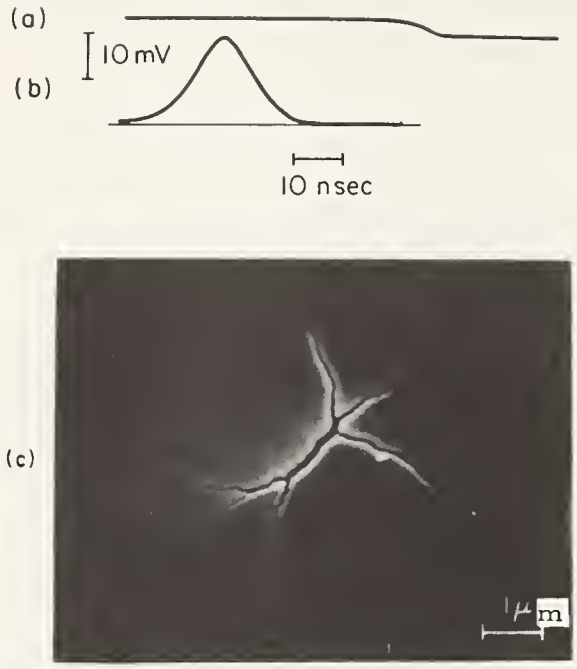

Figure 5. Exit site data set for λ/4 MgF_2 film damage of the "crack" type, site R11,5 (a) optical probe trace, (b) damaging ruby pulse, (c) SEM photograph. The incident peak field measured 0156 mV/cm.

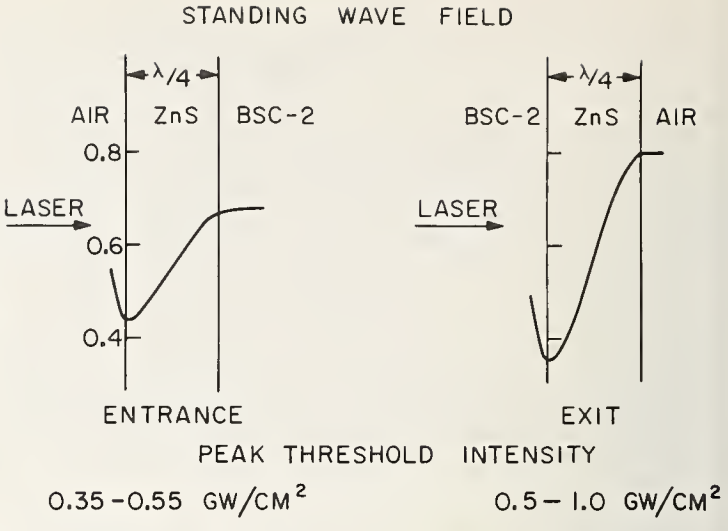

Figure 6. Measured peak threshold intensity at point of maximum standing wave field for λ/4 ZnS film.

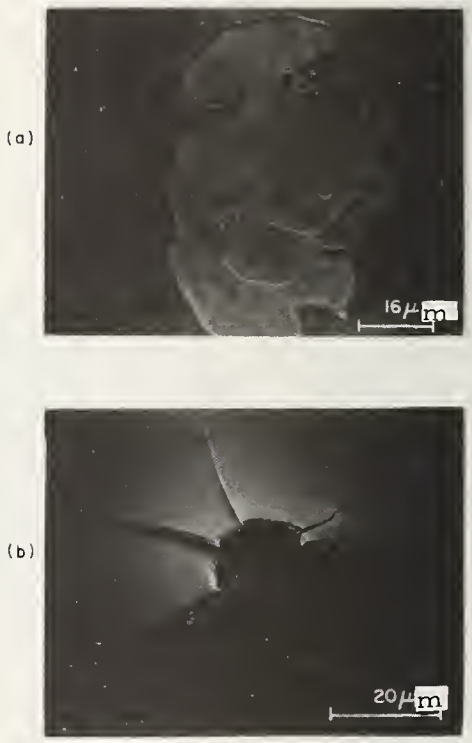

Figure 7. Effect of standing wave field on damage morphology in the 17-layer film for (a) entrance site (H1,7), (b) exit site (M12,5).

COMMENTS ON PAPER BY ALVASSINI, et al

In the discussion that followed this paper it was emphasized that the transmitted pulse shape is a very poor measure of damage near threshold, while the back-scattered light is very sensitive to the onset of the damage process.

5.9 The Importance of Refractive Index, Number Density, and Surface Roughness in the Laser-Induced Damage of Thin Films and Bare Surfaces

J. R. Bettis*, R. A. House, and A. H. Guenther
Air Force Weapons Laboratory
Kirtland AFB, NM 87117

and

R. Austin
Perkin-Elmer Corp.
Norwalk, Conn. 16851

Results of a laser-induced damage study to optical surfaces and thin-film coatings are reported. Ten different half wave films, placed on fused silica, sapphire, BK-7, and ZnSe, were subjected to 1.06 μm radiation in a 147 μm spot size. Nine different optical materials in bulk form including four glasses were also tested. The results were compared to a phenomenological equation relating threshold optical field to number density, refractive index, and root mean square surface roughness. The films were measured for inhomogeneity and were deposited by r.f. sputtering, electron beam heating, and thermal evaporation. Very good correlation was obtained between predicted and observed behavior.

Key words: Damage thresholds; laser damage; refractive index; surface damage; surface roughness; thin films.

1. Introduction

The research reported herein is a continuation of work reported at the 1974 Damage Symposium [1][1]. In that brief note a postulation of the expected behavior of the laser-induced damage threshold electric field as a function of the refractive index and number density of polarizable species in an optical material was given. At that time the thesis was tested against data on damage threshold values reported by a number of investigators on a variety of materials in various forms. The agreement was generally good for data from thin-films at surfaces and within bulk dielectric materials. This year a comprehensive examination of the working hypothesis was performed by damaging a set of coated and uncoated samples prepared especially for such tests. As noted last year, fluorides, as a class of materials, did not appear to obey the suggested relationship, thus a set of fluoride materials in bulk and thin film form ranging in refractive index from 1.38 to 1.62 was examined to determine whether fluorides behaved contrary to the expected behavior. In addition, the scatter inherent in thin-film coatings was investigated as a possible indicator of relative sensitivity to laser-induced damage, as well as a study to correlate substrate roughness with thin film threshold, compare surface threshold for bare surfaces to surface threshold for the material in thin-film form, and an evaluation of thin-film thresholds with deposition technique.

2. Experimental Method

For the experimental portion of this study the arrangement shown schematically in figure 1 was employed. The laser consists of a Nd^{+3} doped glass oscillator with a 16 mm in diameter by 300 mm long rod and one amplifier stage with 16 mm in diameter by 500 mm long rod.** The lowest order TEM mode was selected by an intracavity aperture of 1.9 mm diameter. The far field intensity distribution was measured with a 135 μm pinhole [2] and found to be Gaussian to within 13%. The laser was operated at a constant pump level with the target energy being controlled by a set of non-saturating Schott attenuating filters used in pairs for minimal beam steering. The temporal pulse shape was monitored by a pair of ITT biplanar photodiodes, one of which was supplied with an integrating circuit to monitor total energy and detect pre- or post-lasing caused by regenerative feedback. Over a series of 6000 shots the pulse width was stable at 40 ± 1 nsec. The target energy was monitored with a pyroelectric detector.*** Its digital output was correlated against a carbon-cone thermopile calorimeter as well as against an additional pyroelectric detector. The variation in measured energy for the thermopile calorimeter and integrating photodiode was $\pm$ 8.5 and 9% when compared to the two pyroelectric detectors

* Based upon portions of a PhD thesis submitted to the Graduate Engineering School of the Air Force Institute of Technology, Wright-Patterson AFB, Ohio 45433.

** Normal oscillator and first amplifier of a Compagnie General d'Electric VD 640 laser system.

*** Laser Precision Engineering model RPK 3230.

1. Figures in brackets indicate the literature references at the end of the paper.

while the pyroelectric detectors tracked each other to ± 4%. The specific filters employed served as an additional check on the credibility of the readout from the pyroelectric detector. The helium-neon lasers were used as aids in detecting damage through laser induced scatter (LIS) [3] and a phase-contrast method discussed in a separate paper presented at this symposium [4].

The spot size from the 503.5 mm focusing lens was 147 μm to the e^{-2} power points. This spot size was large enough to obviate any dependence of threshold on the spot size [5]. Total energy was 0.4 j nominal.

Two principal observations have become apparent as a result of this investigation. One is that the characterization of a substrate material is important in predicting both its damage threshold and the threshold of any film applied to it. The second is that without special control over more parameters than has been proposed, thin films may exhibit greatly different optical characteristics compared to the same material in bulk form, and as such, the careful determination of a variety of resultant film properties is needed. Partially because of these considerations each bare surface was measured for roughness by the total integrated scatter (TIS) [6] technique and a representative number were measured by the fringes of equal chromatic order (FECO) [7] technique. The films were measured for internal scatter by TIS, for physical thickness with a Tallystep weighted stylus depth gauge, and for spectral response to determine optical thickness and homogeneity with a Carey 14 spectrophotometer.

Results of the reflection spectra for four films are shown in figures 2 and 3. Figure 2 is the spectral response of a pair of good films, ZrO_2 and ThF_4 while figure 3 depicts the generally inhomogeneous films of LiF and MgF_2. The behavior observed in figure 3 can be adequately modeled by a refractive index variation of 7% increasing from the substrate outward. Although this variation in the refractive index is not sufficient in itself to lower the expected threshold to the values observed (figure 5), it is an indication that the film will behave in a less than ideal or predictable fashion from first principles (i.e., assuming that the material in thin-film form is identical to the bulk optical and physical properties).

Studies are continuing on the samples utilizing Auger spectroscopy, ellipsometry, SEM, and a possibly revealing study on the OH^- contamination on surfaces as it affects coating deposition and composition, and ultimately damage threshold.

The preparation of the bare substrates is described in a separate paper presented at this symposium [4]. For this portion of the report the films were deposited on samples prepared to best-finish specifications (typically $< \lambda/5$ wave flatness and $\sim$ 15 Å rms roughness). The dielectric films were deposited by one of three techniques: radio frequency sputtering, electron beam heating, and thermal evaporation. A set of MgF_2 deposition technique films were prepared by each of the three methods. The remainder of the films were applied by electron beam heating. For the majority of samples, each dielectric film was specified to be a half-wave in optical thickness at the 1.06 μm wavelength used in the study. This parameter was monitored by observing the reflectance of the film-substrate system as the film was being deposited. For films whose index is greater than the substrate index a minimum in reflectance at 1.06 μm is obtained when a half-wave optical thickness is reached. For homogeneous films this minimum corresponds to the reflectance of the substrate. The half wave thickness was chosen because this assured that the optical electric field at the substrate-film interface was the same as the optical electric field at the film-air interface. Because to an electric field a half-wave window is apparently not there, one would expect the character of the substrate to have a very great effect on the field at the surface of the film. Thus one would expect the roughness of the substrate to materially affect the threshold of the film. This may not be as critical in multilayer reflector films since the electric field tends to "pile up" in the first few (outer) layers of the stack. It is also the thickness which gives the least variation in the electric field of a standing wave pattern for slight variations in the thickness. For films whose index is less than the substrate index a reflectance maximum is obtained when a half-wave optical thickness is reached. For films whose index is the same as, or very near the index of the substrate, it is necessary to use a separate witness plate (substrate) with a different index varying as much as possible from that of the film to realize maximum sensitivity in the measurement of the optical thickness. In using a separate witness plate one should match the mechanical properties of the surface (e.g., coefficient of thermal expansion, roughness, crystallinity, if any, and orientation) so that such effects as different residual stress of the film on the sample and the film on the witness plate do not induce changes in film density and refractive index between the two films.

A total of 25 irradiations were taken on each sample-repositioning on a virgin site for each exposure. The sites were shielded from each other with an apertured face plate [4] so that plasma blowoff and ultraviolet radiation from any breakdown plasmas would not affect adjacent sites. The 25 shots were sufficient to determine electric field threshold to with ± 12%. An increase in the number of shots by a factor of four failed to significantly reduce the statistical limits of the value.

3. Theory

Dielectric systems respond to an electric field through their polarizability. A semi-classical approach to the problem of displacement of a bound electron in an alternating field of amplitude, E_ℓ, and frequency, ω, yields the following equation for the charge displacement x,

$$xe^{i\omega t} = \frac{n^2 - 1}{n^2 + 2} \frac{3\varepsilon_o}{Nq_e} E_\ell e^{i\omega t} \tag{3.1}$$

where the polarizability, x, has been related to refractive index, n, and number density, N, by the Clausius-Mosotti equation, and the subscript, ℓ, denotes the local electric field. In a more standard form one can relate the macroscopic electric field to the local electric field by the Lorentz local field correction. In terms of measurable quantities eq. (3.1) may be rewritten as

$$xe^{i\omega t} = \frac{n^2 - 1}{N} \frac{\varepsilon_o}{q_e} \left[\frac{2}{n + 1} \; 19.4\sqrt{Sw/m^2} \right] e^{i\omega t} \tag{3.2}$$

where S is the power density incident on the dielectric and the expression in brackets is the macroscopic field, E, within the dielectric. Upon inverting this expression one obtains an expression directly relating the macroscopic field to certain material parameters.

$$E = \frac{N}{n^2 - 1} \frac{q_e}{\varepsilon_o} x \; . \tag{3.3}$$

Because the damage symposium functions as a sounding board dedicated to the interchange of ideas, the authors do not think it inappropriate to suggest two ways in which eq. (3.3) can be interpreted to predict laser damage thresholds.

Equation (3.3) predicts a direct relationship between the displacement of the optical electron in a dielectric and the applied field. It is obvious that there exists a displacement beyond which this equation is not applicable. Assuming that such a critical displacement x_{cr} does exist the electron would be sufficiently liberated from the atom by action of this threshold field. In order to quantify this proposition, recourse is made to order of magnitude arguments advanced by Seitz [8] and Bloembergen [9]. Seitz states that it is safe to assume that breakdown by electron avalanche will occur if a primary electron produces one electron by collisional ionization for each 10^5 atoms which it encounters. For most solid dielectrics with atomic densities of 5 - 12 x 10^{22} cm^{-3} this requirement implies that electron densities of 5 x 10^{17} to 1.2 x 10^{18} cm^{-3} are required for breakdown. Bloembergen states that breakdown may be defined as occurring when the electron density exceeds 10^{18} cm^{-3}. It is interesting to note that Seitz was dealing with dc breakdown of dielectrics while Bloembergen was involved with laser-induced damage to dielectrics. It is also of interest to note that Alyassini and Parks [10] used the measured specular reflectivity decrease at the onset of surface damage in BSC-2 to calculate the free electron density as 10^{18} - 10^{19} cm^{-3}. Thus, not only is it assured that it is unnecessary to ionize every atom in the focal volume of a laser to achieve damage, but one is able to ascribe an order of magnitude estimate of that percentage which is required. To account for this in eq. (3.3) consider that the total energy delivered to the target volume is reduced by that fraction of atoms which when ionized will result in damage. Taking Seitz criteria eq. (3.3) becomes

$$E_{th} = \frac{N}{n^2 - 1} \frac{q_e}{\varepsilon_o} x_{cr} \sqrt{10^{-5}} \; . \tag{3.4}$$

For these orders of magnitude calculations one need not probe deeply into quantum theory to ascribe a critical displacement. From the work of Wunsch [11] the dipole moments of polarizable entities do not saturate until the displacement of an electron distribution of an atom in most optical dielectrics reaches about 0.75 - 1.0 Å. Thus it would seem that the distance x_{cr} must be greater than this amount in order for the electron to be "freed" from the atom. It is possible and perhaps reasonable to suppose that the critical displacement is of the order of half the molecular spacing in the solid. Since these distances tend to be 3.5 - 4.0 Å this gives a reasonable value for x_{cr} of the order of 1.75 - 2.0 Å which exceeds the limit for saturation of the polarizability. Using this for purposes of comparison with experimental work results in one final form of eq. (3.3) as

$$E_{th} = \frac{N}{n^2 - 1} \frac{q_e}{\varepsilon_o} \frac{sep}{2} \sqrt{10^{-5}} \; . \tag{3.5}$$

As an alternative statement of eq. (3.3) consider the energy expended in displacing an electron a distance x. For purposes of identification of the functional relation it is sufficient to claim that

$$\mathcal{E} = \frac{1}{2} m\dot{x}^2 \; , \tag{3.6}$$

and since x and $\dot{x}$ are related through

$$\dot{x} = \frac{d}{dt}\left\{xe^{i\omega t}\right\} \tag{3.7}$$

one obtains

$$E_{th} = \frac{N}{n^2 - 1} \frac{q_e}{\varepsilon_o} \frac{1}{\omega} \sqrt{\frac{2\mathcal{E}}{m}} \sqrt{10^{-5}} \tag{3.8}$$

where the Seitz criteria has again been applied. Since laser-induced damage disrupts the lattice and has been shown [12] to cause plasmas of electrons and ions to be ejected from surface damage sites, the authors suggest that the heat of formation (or cohesive energy) related to the ions of the species is a likely candidate for the energy necessary to impart to 1 in 10^5 of the atoms in a solid in order to cause damage.

It should be noted that the $\frac{N}{n^2-1}$ term is the dominant term in both eqs. (3.5 and 3.8). While this term varies by factors up to 15 in the materials tested for this report the molecular separation and the square root of the heats of formation vary by factors of only three.

4. Results

In testing the relationship given by eqs. (3.5 and 3.8), 10 different materials in half-wave films applied to four different substrates were subjected to damaging laser pulses in the experimental arrangement shown in figure 1. As a check on the quality of the thin films the surfaces of five of these materials in uncoated bulk form were also damaged. To observe the major factor in eqs. (3.5 and 3.8) four optical glasses were also tested. From the spectral response of the MgF_2 and LiF films shown in figure 3 one might expect that the film quality evidenced there would result in anomalous or lower than expected threshold fields. In table 1 the ratio of film to bare substrate thresholds is displayed and one should note that the LiF and MgF_2 exhibit the lowest ratio. The LiF is only a partial result since the effect of surface roughness is currently being assessed and its quite rough nature ($\sim$ 100Å) will lower the LiF ratio even more. It is of interest to note that ZnSe alone has a higher threshold in film than in bulk form. This result is not completely unexpected due to the difficulty in producing clear, unbanded, and homogeneous bulk ZnSe [13].

Table 1. Ratio of Film to Bare Surface Thresholds

Material	Bare Surface Threshold	Film Threshold $\sigma_r^{0.75}$	Ratio
FS on FS	1.55 MV/cm	0.892 MV/cm	0.575
MgF_2 on FS	2.365	0.899	0.38
LiF on FS	1.27*	0.516	0.41
Al_2O_3 on Sapphire	0.608	0.439	0.72
ZnSe on ZnSe	0.116	0.122	1.06

*Film substrate much smoother than bare surface which is uncorrected for roughness.

In figure 4 the threshold electric field for films versus $\sqrt{L}\,\frac{N}{n^2-1}$ is plotted. The fit is not unreasonable with three exceptions: namely, the low values of Al_2O_3 require further explanation. For the course of this research it has been found that a critical parameter in determining threshold fields for surface damage depends on the surface roughness value. In the paper by House et. al., [4] a relationship was presented between threshold electric field and a power of the root mean square surface roughness. Over a range of surface roughness from 13 Å rms to 335 Å rms as measured by FECO interferometry, the threshold field for a SiO_2 overcoated surface varied from 0.9 MV/cm to 0.24 MV/cm, or a ratio in energy density of 14. To account for this trend one simply modifies the threshold field by $(\sigma/13.75)^m$ where σ is the root mean square roughness and m was taken as 0.75, although post-symposium work indicates 0.5 is more appropriate. This factor has the effect of modifying each surface to an equivalent roughness of 13.75 Å rms. Since most of the films were placed on 13.75Å rms fused silica blanks the only values changed significantly are the Al_2O_3 on Sapphire (43 Å), the ZnSe on ZnSe (30 Å), and the SiO_2 on BK-7 (21 Å).

A final form of eq, (3.5) including the roughness correction is

$$\left(\frac{\sigma}{\sigma_s}\right)^m E_{th} = \frac{N}{n^2-1} \frac{q_e}{\varepsilon_o} \frac{sep}{2} \sqrt{10^{-5}}\ , \tag{4.1}$$

where σ_s is a standard roughness against which the measured roughness is ratioed.

To demonstrate the major trend for bare uncoated surfaces one must plot the threshold field modified for roughness against $\frac{N}{n^2-1}$. These results shown in figure 6 indicate that the bulk of eqs. (3.5 and 3.8) holds for materials ranging from ZnSe (n = 2.485) to MgF_2 (n= 1.38) when each surface is referenced to a standard surface roughness. Although not present here, LiF at $\frac{N}{n^2-1}$=13.356 has been damaged and is currently being measured for roughness. Preliminary indications are that LiF will fit the expected behavior.

Data is currently being analyzed to compare the full functional forms of eqs. (3.5 and 3.8) to the experimental results. Preliminary calculations indicate that LiF and $A\ell_2O_3$ may hold the key to which one, if either, of eqs. (3.5 and 3.8) represents an acceptable view.

To demonstrate the order of magnitude fit of these equations the predicted value for fused silica was calculated by each one. From eq. (3.5)the predicted value is 6.14 MV/cm while eq. (3.8)predicts 40.1 MV/cm. These values compare with 5.2 MV/cm measured for bulk SiO_2 by Fradin [14] and indicate that eq. (3.5)may more nearly approximate the true nature of the damage process.

The final data to be presented involves MgF_2 films deposited by three techniques. In retrospect, MgF_2 may not have been a good choice for this evaluation since the MgF_2 films generally appear to be inhomogeneous in form. The three techniques were: rf sputter, thermal evaporation, and electron beam heating. The results in table 2 are at best inconclusive. There simply are too many extrinsic variables present in film deposition to state with assurance which technique gives best films of MgF_2 or any other material. (It was a good idea to use MgF_2, however, because it does give anomalous results and this was a search, however unsuccessful.)

Work is continuing to analyze the data and the many variables as yet not fully considered. From the work of Guenther et. al., [15] it appeared that film stress was an important factor in determining film thresholds. The present work tends to substantiate that claim to some degree. From the data analyzed so far, and from the reanalysis of previously published data in terms of the hypothesis advanced in this paper, it appears that the major factor in determining a film's threshold is expressed by some form of eq. (3.3), whether the displacement is used explicitly or implicitly, while the stress in the film is a frequently secondary effect.

Table 2. Thresholds for MgF_2 Films Versus Deposition Technique

Technique	Threshold Electric Field
Electron Gun	0.737 MV/cm
Thermal Evaporation	0.797 MV/cm
R-F Sputter	0.899 MV/cm

Essentially the same comments apply to the use of scatter in the films as damage predictors. However, just as a poorly deposited film can have such bad stress characteristics so as to overcome the intrinsic effects so can a film possess enough scatter to overcome the intrinsic effects. It is important to observe that in film thicknesses other than $\lambda/2$, scatter, roughness, and stress can play a much greater role.

5. Conclusions

There are three major conclusions to draw from this study. It is obvious that the relationship expressed by eq. (3.3)is a major determining factor in the threshold of film surfaces, bare surfaces, and, from the work presented last year, bulk materials. Some form of the cohesive energy - whether expressed in relation to the free atoms, free ions, neutral gases, or standard form of the constituents is to be determined - may be important in the total functional form. Secondly, fluorides as a group do not exhibit anomalous behavior. Rather some fluorides make better films than other fluorides. An obvious sub-conclusion is that films with near theoretical spectral response (i.e., response similar to that exhibited in the bulk form) exhibit higher damage thresholds. A third major conclusion is that values for surface and thin film thresholds are not meaningful unto themselves unless the surface roughness is specified. Obviously other extrinsic factors such as stress, etc., will be important in certain cases. Note that although MgF_2 and LiF do not follow the predicted dependence in thin-film form they both, at least preliminarily, do fit when the surface of the bulk materials is damaged. It cannot be over stressed that the compelling reason for this behavior lies in the inhomogeneities of the thin films as revealed by figure 3.

6. Acknowledgments

The authors are indebted to the following people for the time and energy they spared: Norm Boling of Owens-Illinois shared some particularly fruitful discussions as did Alex Glass of Lawrence Livermore; Bryan Newnam of Los Alamos Scientific Laboratory helped design the experimental arrangement as did Del Owyoung of Sandia Laboratories; Hal and Jean Bennett and Jane Bruce performed various measurements for us; and Dr. Karl Mader of Schott Optical supplied impossible to find data on their optical glasses.

7. References

[1] Bettis, J. R., Guenther, A. H., and Glass, A. J., NBS Special Publication 414, U.S. GPO, Washington, D.C. (1974), p. 214

[2] Owyoung, A., NBS Special Publication 387, U.S. GPO, Washington, D.C. (1973), p. 11

[3] Newnam, Brian E. and DeShazer, L. G., NBS Special Publication 372, U.S. GPO, Washington, D.C. (1972), p. 123

[4] House, R. A., Bettis, J. R., Guenther, A. H., and Austin, R., This Symposium

[5] DeShazer, L. G., Newnam, B. E., and Leung, K. M., NBS Special Publication 387, U. S. GPO, Washington, D. C. (1973), p. 114

[6] Bennett, H. E. and Porteus, J. O., JOSA 51, No. 2 (1961), p. 123

[7] Holland, L., The Properties of Glass Surfaces, Chapman and Hall, London (1966), p. 113

[8] Seitz, F., The Modern Theory of Solids, McGraw Hill, N.Y. (1940)

[9] Bloembergen, N., IEEE J. of Quantum Electronics QE-10, No. 3, (Mar 1974), p. 375

[10] Alyassini, Nabil and Parks, Joel H., This Symposium

[11] Wunsch, Donald C., Doctoral Dissertation submitted to New Mexico State University (1969), p. 64

[12] Avizonis, P. V., and Farrington, T., Applied Physics Letters 7, (1965), p. 204

[13] Braunstein, M., Laser Window Surface Finishing and Coating Technology, ARPA Contract F19628-73-C-0234

[14] Fradin, D. W. and Bass, M., NBS Special Publication 387, GPO, Washington, D.C. (1973), p. 225

[15] Austin, R. Russel, Michaud, Raymond C., Guenther, Arthur H., Putnam, Joseph M., and Harniman, Richard, NBS Special Publication 372, GPO, Washington, D.C. (1972), p. 135

[Note added in proof: Further analysis of the surface roughness correction factor (σ^m) indicates that an exponent value m in eq. (4.1) of 0.5 is probably more appropriate than 0.75 as employed in figures 4, 5, and 6. Little of the discussion is changed except to make eq. (3.8) less likely than eq. (3.5) in modeling the behavior observed.]

8. Figures

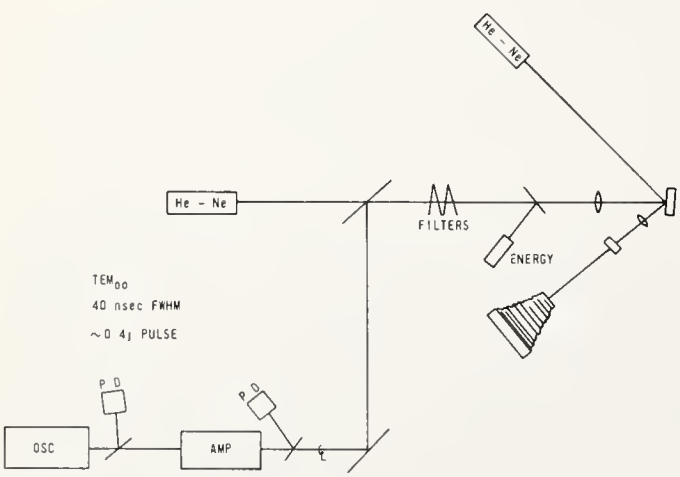

Figure 1. Experimental arrangement showing diagnostics and damage detection apparatus.

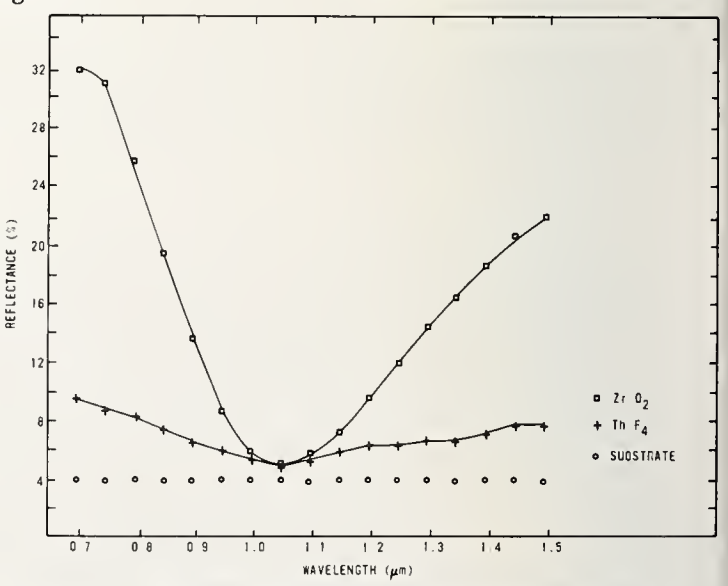

Figure 2. Percent reflectance versus wavelength for homogeneous half-wave ZrO_2 and ThF_4 compared to fused silica substrate. A systematic offset has the value of substrate reflectance at 4% rather than the true value of 3.36%.

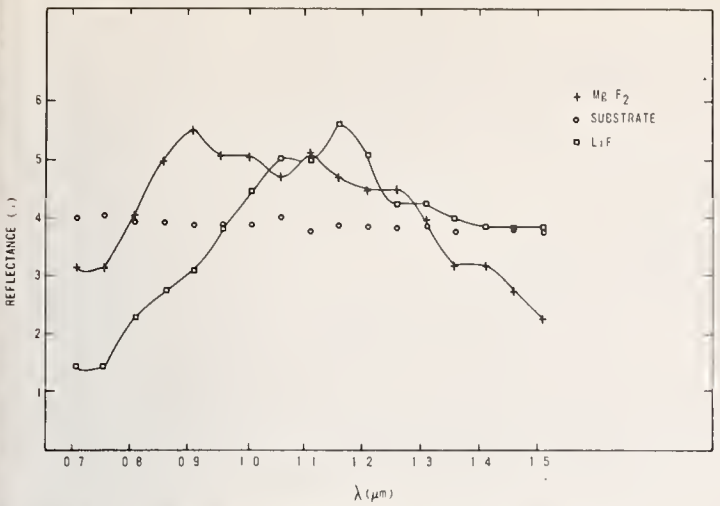

Figure 3. Percent reflectance versus wavelength for inhomogeneous half-wave LiF and MgF_2 compared to fused silica substrate. A systematic offset has the values of substrate reflectance at 4% rather than the true value of 3.36%.

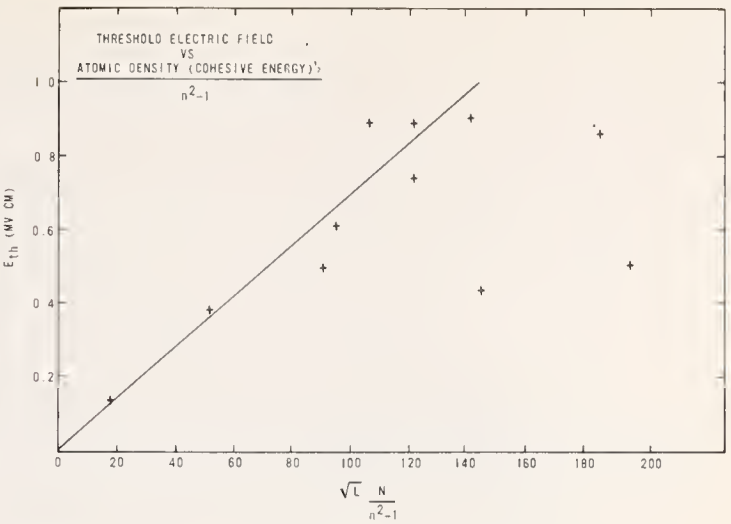

Figure 4. Threshold electric field versus $(\text{cohesive energy})^{0.5} \frac{N}{n^2-1}$ for half-wave films of 10 materials on four substrates. The materials in ascending order of the dependent variable are: ZnSe, ZrO_2, BaF_2, CeF_3, ThF_4, SiO_2(2), PrF_3, Al_2O_3, MgF_2, and LiF.

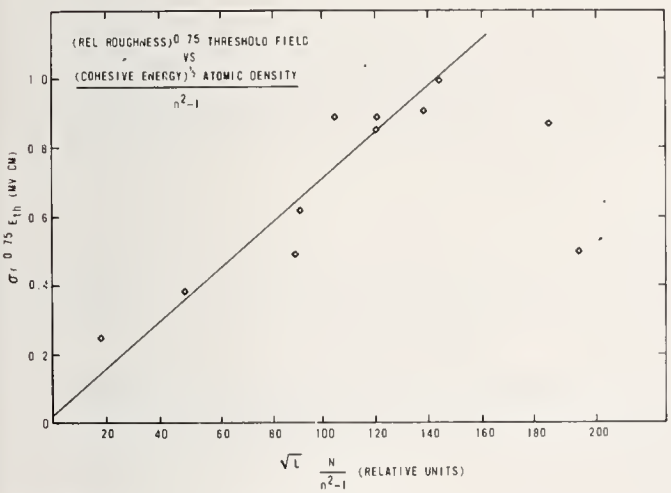

Figure 5. (Roughness relative to 13.75 Å rms)$^{0.75}$ x threshold field versus $(\text{cohesive energy})^{1/2} \frac{N}{n^2-1}$ for the 10 materials in figure 4.

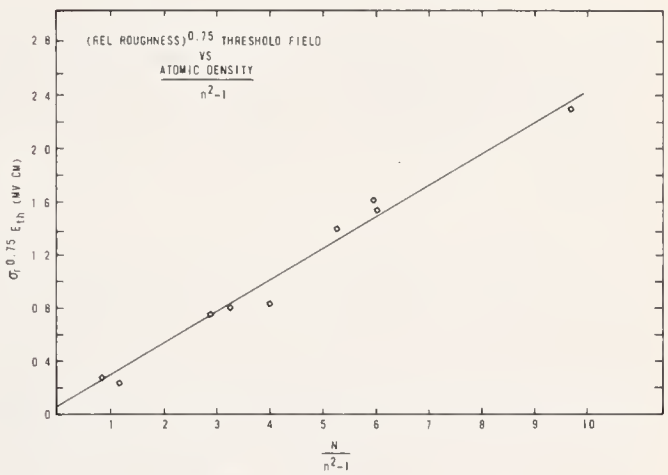

Figure 6. (Roughness relative to 13.75 Å rms)$^{0.75}$ x threshold field versus $\frac{\text{atomic density (N)}}{n^2-1}$ for (in ascending order of dependent variable) the bare surfaces of: ZnSe, ZnS, $LASF_6$, SF-14, SF-12, Al_2O_3, BK-7, SiO_2, and MgF_2.

COMMENTS ON PAPER BY BETTIS, *et al*

It was pointed out that sputtered films are not always the best and that for a given multilayer dielectric film composition and design one must choose the appropriate method of deposition whether it is sputtering, evaporated deposition, or electron beam deposition. It was further pointed out that the method of deposition is not sufficient to characterize the thin film process, but in addition the conditions of deposition including the preparation of the substrate must also be considered. A point was raised concerning electric field intensification in the presence of surface roughness and the authors indicated that that effect had not been explicitly considered. The listeners were referred to the subsequent paper by House, et al., for further details concerning this series of investigations.

5.10 Investigation of the Damage Properties of Multilayer Dielectric Coatings for Use in High Power Nd:Glass Lasers*

C. E. Thomas, B. Guscott, K. Moncur, S. Hildum, and R. Sigler

KMS Fusion, Inc.
P. O. Box 1567
Ann Arbor, Michigan 48106

The development of high-power Nd:glass laser systems has reached a point where the damage in multilayer dielectric coatings limits the available energy from the laser. KMSF has initiated a testing program to identify the parameters that affect the damage levels of dielectric coatings. We will report the measured damage levels as a function of predeposition substrate cleaning, the dielectric material used (TiO_2 vs ZrO_2), the substrate material (Pyrex vs BK-7 or quartz), and the laser pulse length (80 to 480 picoseconds). Damage levels will be compared with the light-scattering properties of the coatings.

Key words: Coating damage; laser damage; mirrors; multilayer dielectric coatings; polarizers.

1. Introduction

This paper presents experimental data on the laser damage levels of multilayer dielectric coatings. These coatings are considered critical to the operation of our high-power Nd:glass laser system since the coatings damage before any other component, and therefore, limit the energy which can be delivered to our laser-fusion targets. We will report on the current damage levels of commercial coatings on large substrates obtained from several vendors, as well as on sample coatings which have been manufactured under contract to KMS Fusion with controlled variation of parameters to test the influence of substrate cleaning, coating materials, substrate material, and laser pulse length.

2. The KMSF Laser

A block diagram of the current KMS Fusion Nd:glass laser system is shown in figure 1. Damage tests are run with this laser using the 90-mm-output beam from the spatial filter.

The pulse shape generated from this system is formed by stacking 30 picosecond Gaussian pulses with variable time separations. Unless otherwise noted, all damage testing reported here used six equal-amplitude pulses spaced by 40 picoseconds forming a square pulse envelope about 250 picoseconds long. There is temporal ripple on this pulse, however, so the peak power densities are somewhat higher than the quoted average power densities.

The importance of multilayer dielectric coatings to the KMSF system is illustrated by table 1, which summarizes the 91 coated surfaces which are in the main laser beam.

Table 1. Multilayer Dielectric Coatings in the KMS Fusion Laser System

Mirrors	31
Anti-Reflection (AR) Coated Surfaces	44
Beamsplitters	7
Polarizers	9
Total No. of Coatings	91

3. Damage Test Procedure

Dielectric coatings are damage tested by focussing the main laser onto the part as illustrated in figure 2. The parts are placed in one of three different positions corresponding to beam diameters of 20, 14, or 10 mm. Each part is oriented at the angle of incidence and polarization for which it was designed. If the part does not damage at the 20 mm position, it is moved to a higher-intensity position and a new portion of the surface until visible damage occurs on one shot. Based on the degree of damage at the lowest power density for which damage was observed, we estimate the maximum level at which no visual damage would be expected in a single shot. Using different beam diameters to vary the incident power density avoids the need for large changes in the laser output power which

* The work was supported in part by the United States Energy Research and Development Administration under Contract E(11-1) 2709.

could change the laser-beam spatial distribution.

A microdensitometer trace of a typical IR photographic plate which illustrates the laser-beam spatial distribution at the 90-mm-beam position is shown in figure 3. The "hot spots" seen in this photograph are characteristic of self-focussing, which occurs in high-power glass-laser beams. The spatial filter has removed the high-frequency fluctuations. Due to the relatively high intensity of the lower spatial frequencies in the Fourier transform plane, they cannot be blocked by conventional spatial filters without substantial erosion of the pinhole. The plasma generated by small pinholes affects the laser-beam temporal and spatial shape. Thus we currently operate with a relatively large pinhole and accept the intensity fluctuations shown in figure 3. Folding the density variation through the H & D curve for the IR plates (measured with 250 picosecond exposures), the peak-to-peak intensity variation is estimated at 7 dB.

The remaining self-focussing peaks have focal points tens of meters from the spatial filter. The 10-meter lens used in damage testing effectively shortens this focal distance and figure 4 shows that the intensity fluctuations at the 10 mm test position have increased slightly. From this trace we estimate that the intensity fluctuates about 9 dB over the beam at the test positions.

Quoted power densities are those calculated perpendicular to the beam axis. The power density on oblique surfaces will be lower than the quoted values by the cosine of the angle of incidence.

In summary, the laser beam which we use for damage testing has 8 to 10 dB spatial-intensity fluctuations and 20 to 50% temporal fluctuations. All power densities and energy densities quoted here are values averaged over the time and space of the laser beam. The peak power density in the hot spots where the damage invariably occurs in the coatings is higher than the quoted average values by 10 to 12 dB.

4. Damage Test Results

Damage measurements of mirrors, polarizers, and anti-reflection coatings are reported in the next three sections followed by damage measurements as a function of laser pulse length and the predamage scattering characterisitcs of the coatings.

4.1 Damage Measurements of High Power Mirrors

Our mirror-damage testing activity has been divided into two areas: first, the routine testing of full-sized purchased mirrors and mirror samples supplied periodically by various coating vendors, and secondly, the testing of a controlled set of mirror samples coated under contract from KMS Fusion.

In the controlled experiments 6 to 9 two-inch samples were included in each coating run. The substrate material, predeposition cleaning, and postdeposition processing were varied for each sample. In the case of the mirror-coating runs, some samples were BK-7 and some were Pyrex, some were cleaned with hydrofluoric acid, some with nitric acid, and some with boiling water before being coated. Finally, some of the substrates were baked after coating to increase oxidization.

The damage-testing measurements for two mirror-coating runs are presented in figure 5. The ordinate is our subjective estimation of the degree of damage after one shot. Medium (M) damage corresponds roughly to 50% of the damaged area being destroyed, very light (VL) damage corresponds to two or three hot-spot damage sites, and very, very light (VVL) damage means that only one faint blemish is visible to the eye. All damage measurements were made with "p" polarized light at 45° angle of incidence. The abscissa of figure 5 is the average power level calculated perpendicular to the beam axis, as previously discussed.

The data of figure 5 include samples from two coating runs. The first run (solid lines) used 35 layers of ZrO_2/SiO_2. The second run (dashed lines) used 11 layers of TiO_2/SiO_2. The general conclusions from these data are:

1) The eleven layers of TiO_2/SiO_2 (dashed lines) are consistently better than the 35 layers of ZrO_2/SiO_2.
2) The TiO_2/SiO_2 samples (replotted in figure 6) on pyrex substrates (dashed lines of figure 6) consistently show higher damage levels than similar samples on BK-7 substrates.
3) Baking the sample after deposition (a technique which previously was thought to improve damage level) had no effect of the BK-7 sample, and actually degraded the pyrex-sample damage level to the BK-7 levels.
4) Predeposition cleaning had no significant effect on mirror-damage level.

Prior to this experiment, our standard high powered mirrors incorporated ZrO_2 on either BK-7 or pyrex substrates with postdeposition baking. According to the data of figure 5, this combination of parameters would yield mirror-damage levels between 5 and 10 gigawatts/cm^2. We have now changed all our mirrors to TiO_2/SiO_2 on pyrex without any postdeposition baking with a corresponding increase in damage level up to 20 to 25 gigawatts/cm^2 in 250 picoseconds.

Damage levels for full-sized mirrors or vendor-supplied mirror samples are plotted in figure 7 as a function of delivery time over the last six months. Four different coating vendors have been used as indicated by the letters A through D. Each letter generally represents a batch of up to 12 mirrors. The circled letters denote normal-incidence mirrors; all the others denote 45° mirrors. The subscript "s" indicates a sample; all other mirrors are full-sized mirrors. The letters Z and T indicate whether ZrO_2 or SiO_2 was used in the mirror, although we do not always know the exact composition. There are several interesting trends in figure 7. First, if we exclude the samples and normal-incidence mirrors, there is a general trend toward higher damage level for the 45° mirrors actually used in our system. Thus in January none of our tested mirrors exceeded 20 GW/cm^2, but by June some of our mirrors were approaching 40 GW/cm^2.

Another interesting sequence involves vendor "C". In mid-February we tested several small, normal-incidence samples, which typically have higher damage levels than 45° mirrors. The best mirror survived over 60 GW/cm^2. Next, the vendor supplied a 45° sample and the damage level fell to 35 GW/cm^2. Finally, vendor "C" supplied a full-sized mirror on a 20 cm substrate and the damage level fell again to 18 GW/cm^2. Other vendors have exhibited similar sequences.

Notice also that the three ZrO_2 normal incidence mirror samples supplied by vendor "C" suffered damage between 45 and 65 gigawatts/cm^2, while the three TiO_2/SiO_2 mirrors shown in figure 7 suffered damage between 20 and 40 gigawatts/cm^2. This result (ZrO_2 better than TiO_2) is just the opposite of what our controlled experiments with vendor "A" show. Vendor "A's" production mirrors tested in May and June show that for their process TiO_2 is better than a composite ZrO_2 design. Thus a vendor's coating procedure may be more important at this point in time than the actual materials used.

4.2 Damage Measurements of Polarizers

In addition to achieving high damage levels, polarizer coating layers must be made more uniform than mirror layers to produce acceptable optical properties since polarizers operate at the edge of the absorption band. Our current optical specifications for polarizers include "p" transmission greater than 95% and "s" transmission less than 1%. The "p" transmission versus angle of incidence at the center of a typical 12-inch polarizer is shown in figure 8. At 58° angle of incidence, the above specification is met. However, the "p" reflection exceeds the maximum allowable 5% value over most of the polarizer outside a central 1-to-2-cm area as shown in figure 9. In the past, 50 to 60% of our polarizers have been rejected after not meeting the optical specifications.

Substantial improvements in coating uniformity have been made by three of our coating vendors. The transmission versus angle of one particularly good 18 x 36 cm polarizer is shown in figure 10, and its positional scan in figure 11. The entire part meets the specification of less than 5% "p" reflection, having less than 0.5% over almost all of the useful area.

Initial acceptance is not always sufficient, however. We have observed some aging on all polarizers which have been retested. The transmission curves consistently shift to longer wavelengths or larger angles of incidence as shown in figures 12 through 15. For the polarizer of figure 12, the "p" transmission at the initial optimum angle of 60° fell from 99% to only 78% after five months in our laser system. We subsequently found that the optimum angle shifted from 60° to 64°. Note that the "s" rejection actually improved by a factor of more than 10. The polarizers of figures 13, 14, and 15 were unused spares; their performance shifted without any exposure to laser radiation.

Returning to damage considerations, the measured damage levels of sample polarizers from our test program obtained in two different coating runs (all TiO_2/SiO_2 and composite TiO_2/SiO_2 plus ZrO_2/SiO_2) are summarized in figure 16. The damage levels are consistently low compared to mirror damage levels. None of the parameter variations, including a low coefficient of expansion substrate (quartz), predeposition cleaning, or postdeposition baking had any significant effect on damage level.

The damage levels of vendor-supplied samples and full-size polarizers over the last six months are shown in figure 17. Only one vendor has been able to supply polarizers with over 20 gigawatts/cm^2 damage levels at 240 psec; however, this vendor cannot currently achieve satisfactory uniformity for parts larger than about 25 cm due to the limited size of his coating chambers. Note that with only one exception over six months, even the sample polarizers on 2-inch-diameter substrates do not reach the 20 gigawatts/cm^2 level which we have found necessary for sustained operation in our laser system.

4.3 Damage Measurements on Anti-Reflection (AR) Coatings

The damage measurements for two AR coating runs are summarized in figure 18. The damage levels are consistently higher than for polarizers, presumably because fewer layers are used. The TiO_2/SiO_2 layers (dashed lines) tend to have higher damage levels than the ZrO_2/SiO_2, except for the ZrO_2 coating on the HF-cleaned substrate. In general, predeposition cleaning seems to raise the damage level, although the HF cleaning which significantly increased the ZrO_2 damage level

showed only a small improvement in the TiO_2 run. More data on the effects of acid cleaning are needed.

4.4 Damage Level versus Scattering

It would be desirable to be able to estimate the damage level of dielectric coatings by measuring some other property such as light scattering. This is particularly true for the coating vendors, since no vendor currently has the capability of damage testing his own product. Therefore, we measured the back-scattering characteristics of selected coatings which were subsequently damage tested.

The scattering-measurement apparatus is diagrammed in figure 19. Each part was illuminated with 3-mm-diameter helium-neon laser beam at 632.8 nm. A lens then imaged the dielectric layers via the 45° back-scattered light onto an RCA 931A photomultiplier tube. For each part we calculated the ratio of the measured back-scattered power to the ratio of the detected solid angle to 4π. For multilayer dielectric coatings, typically this back-scatter ratio is 10^{-4} at 45° compared to about 10^{-6} for a polished glass surface.

The damage level versus scattering for 45° mirrors is shown in figure 20. The sample pieces (X's) showed a strong correlation between low scatter and high damage levels. The scattering must be below 1.3×10^{-4} for damage levels above 10 gigawatts/cm^2. However, at least one full-sized mirror, (O's), made by "C" showed a high damage level with relatively high scattering.

There was no correlation between scattering and damage for polarizers (figure 21), although none of the samples tested had scattering less than 1.3×10^{-4}. On the other hand, all the AR coatings scattered less than 3×10^{-5} (figure 22) and all their damage levels were above 10 gigawatts/cm^2.

In summary, for three of our vendors a back-scattering level at 45° of less than 1.3×10^{-4} relative to an isotropic scatterer appears to be necessary, but not sufficient for damage levels above 10 gigawatts/cm^2. The fourth vendor is able to manufacture high power mirrors with scatter above 1.3×10^{-4} and yet with a damage level above 10 gigawatts/cm^2 at 250 psec.

4.5 Damage Levels versus Laser Pulse Length

Measurement of laser damage level versus pulse length is important both to improve laser operation whenever possible, and hopefully to better understand the damage mechanisms in the dielectric coatings. The results of damage measurements at three pulse lengths (80 psec, 240 psec, 480 psec) are summarized in figure 23. The increased power damage-level at shorter pulse lengths has important operational implications for our laser system. Assuming that polarizer damage limits the available power, we can increase the power delivered to our fusion targets by reducing laser pulse length.

The data of figure 23 are replotted in figure 24 as energy damage-level (instead of power damage-level) versus pulse length, showing that the damage levels are neither constant-power nor constant-energy phenomena in the 80 to 480 psec regime.

5. Summary

Figures 23 and 24 also serve as a summary of our current status with respect to damage of multilayer dielectric coatings. Polarizers are currently our limiting component. To date our experimental program with one vendor has shown no significant variation in polarizer damage level with the substrate material (quartz vs BK-7), the substrate cleaning process, the materials used, and the postdeposition baking process.

AR coatings are the next most susceptible component. As laser output energies increase, the pulse length should increase according to current laser fusion-scaling theories. At longer pulse lengths the AR coating power damage level will not be adequate, so improvements will be needed. Our program has shown that substrate cleaning may improve damage levels, although the data are inconclusive.

Finally, for the three different coating designs tested here, mirror coatings currently have the highest damage level. This work has shown ways in which these coatings may improved. Our materials study showed TiO_2 better than ZrO_2 with respect to damage for one vendor, while another had much better damage levels with ZrO_2. Furthermore, a pyrex substrate can yield higher damage levels than a BK-7 substrate, while cleaning has no significant effect.

6.0 Acknowledgments

We gratefully acknowledge the support of the following coating vendors who have supplied

samples and have improved the damage characteristics of multilayer dielectric coatings: Coherent Radiation, CVI Laser Corporation, Spectra Physics, and Optical Coating Laboratory, Inc. We also wish to thank Verne R. Costich, Gary W. DeBell, and Yu H. Hahn for many valuable technical discussions and guidance.

7. Figures

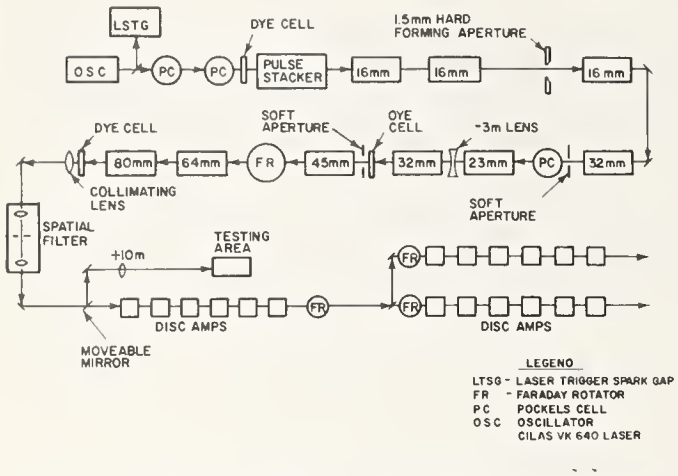

Figure 1. Block diagram of KMSF laser system, June 1975.

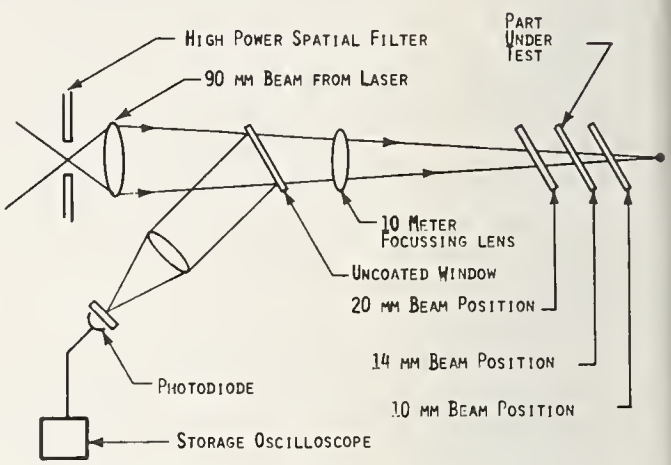

Figure 2. Block diagram of damage testing apparatus.

Figure 3. Microdensitometer trace across photographic plate of 90 mm beam.

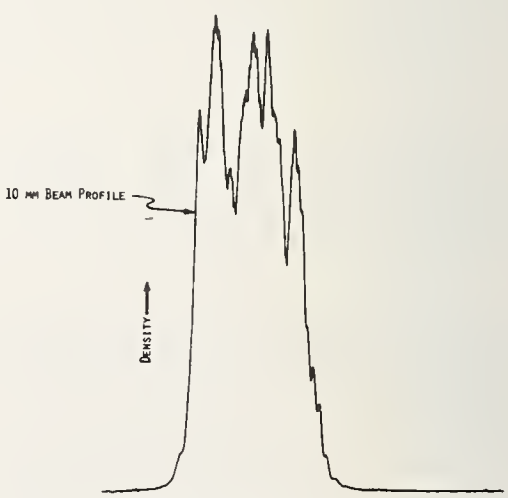

Figure 4. Microdensitometer trace across plate of the beam condensed to 10 mm.

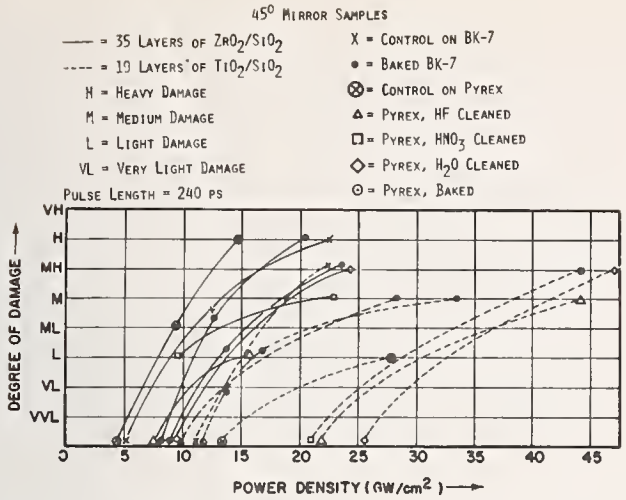

Figure 5. Damage levels of 45° mirror samples.

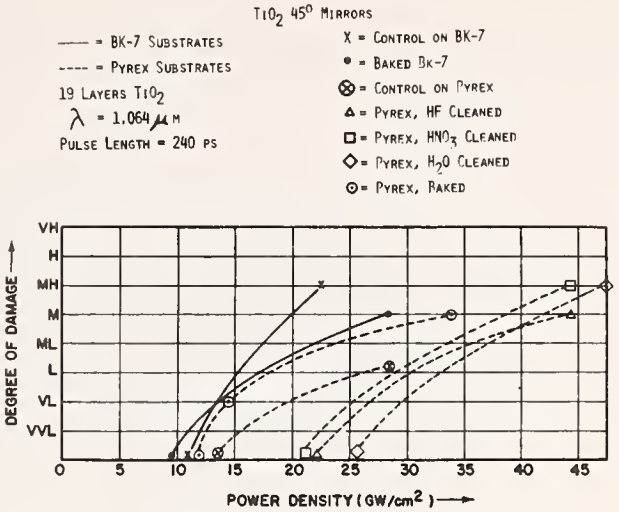

Figure 6. Damage levels of TiO_2 45° mirror samples.

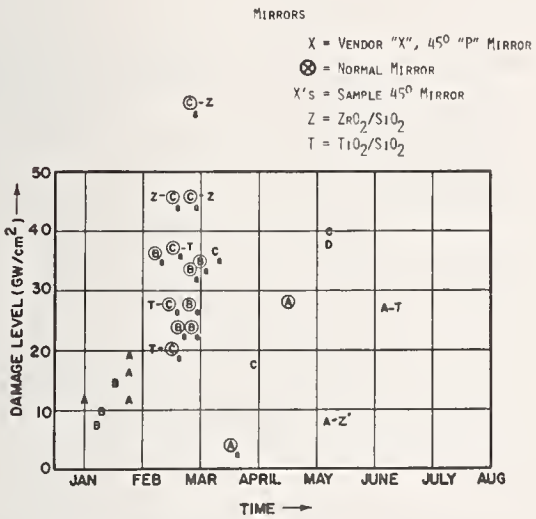

Figure 7. Mirror damage level versus time of manufacture.

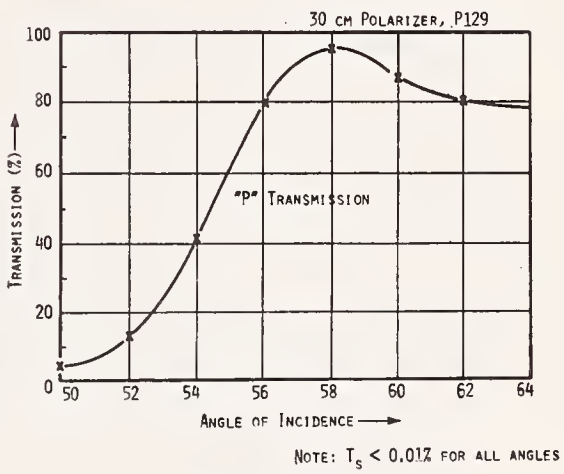

Figure 8. Transmission vs angle for 30 cm polarizer P129.

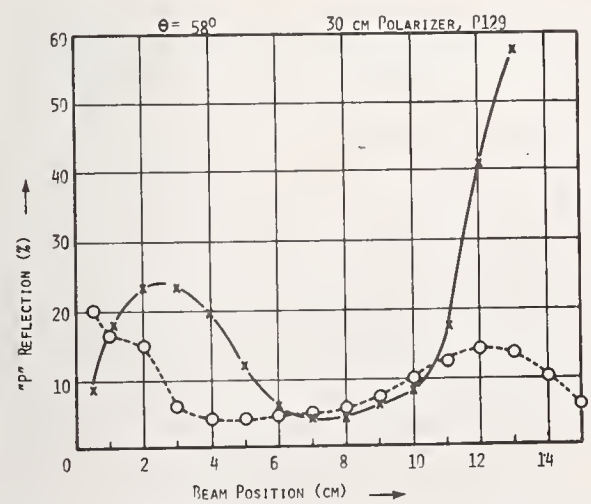

Figure 9. Positional variation across polarizer P129.

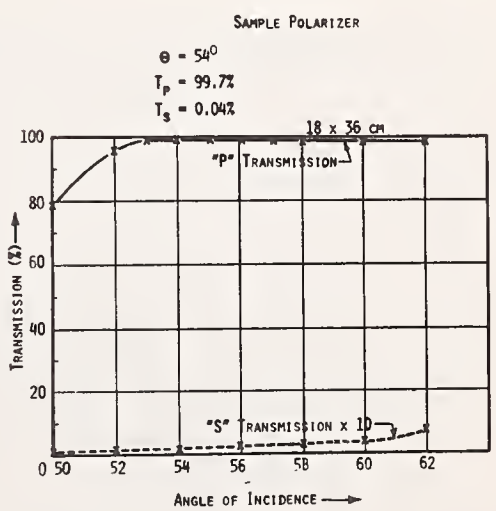

Figure 10. Transmission versus angle for 18 x 36 cm polarizer sample.

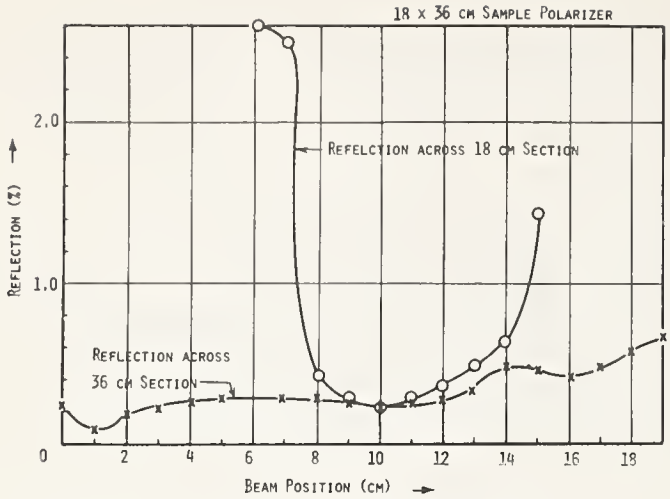

Figure 11. Positional variation across 18 x 36 cm polarizer sample.

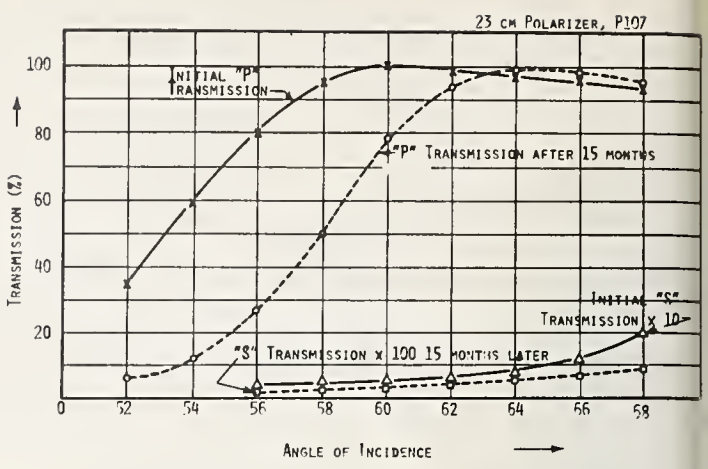

Figure 12. Transmission versus angle for polarizer P107.

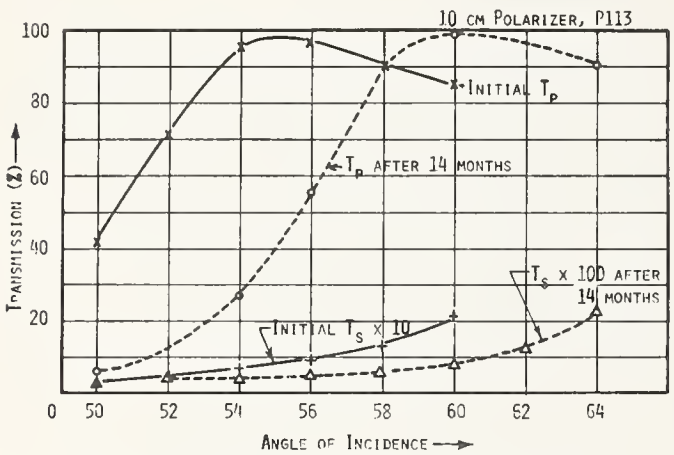

Figure 13. Transmission versus angle for polarizer P113.

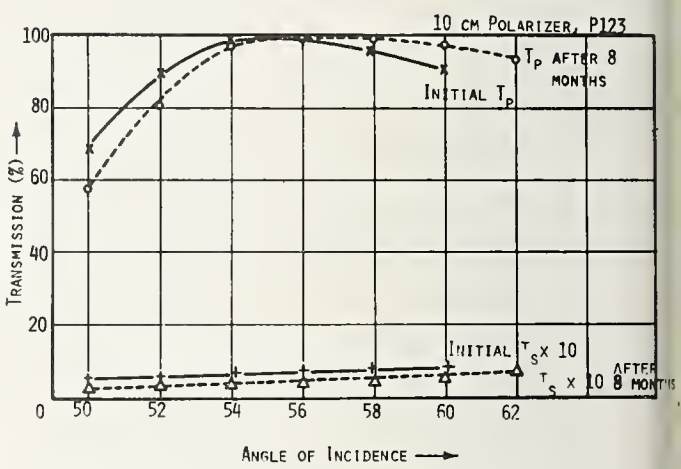

Figure 14. Transmission versus angle for polarizer P123.

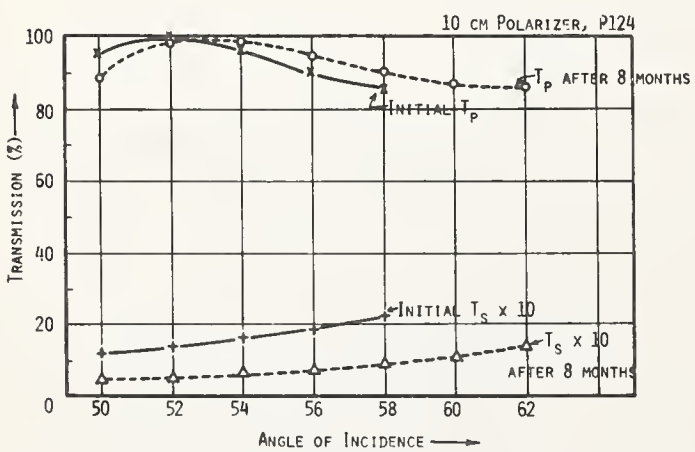

Figure 15. Transmission versus angle for polarizer P124.

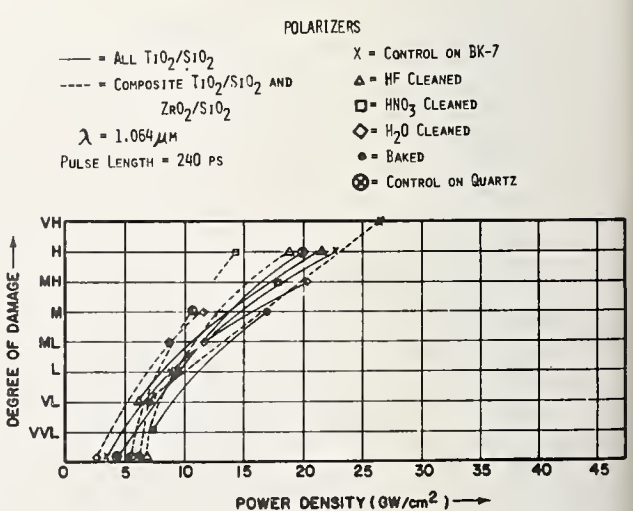

Figure 16. Damage levels of sample polarizers.

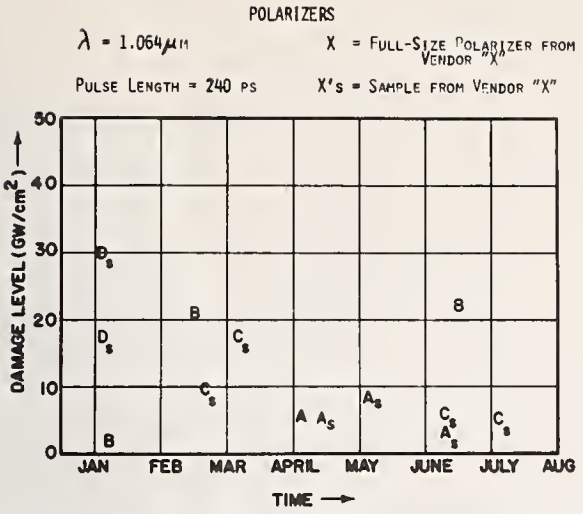

Figure 17. Polarizer damage level versus time of manufacture.

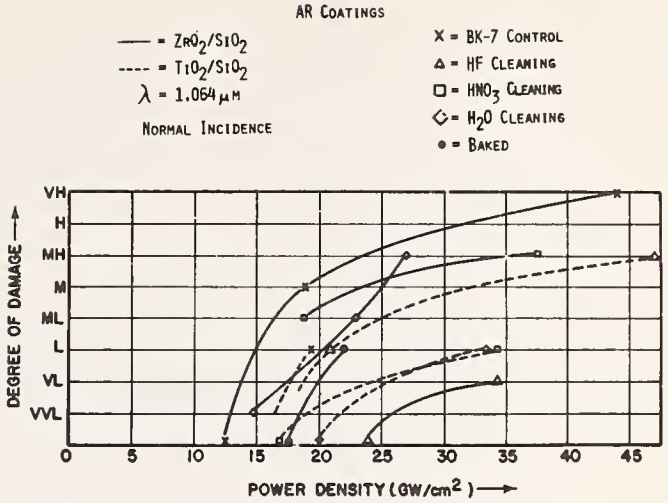

Figure 18. Damage levels of sample anti-reflection coatings.

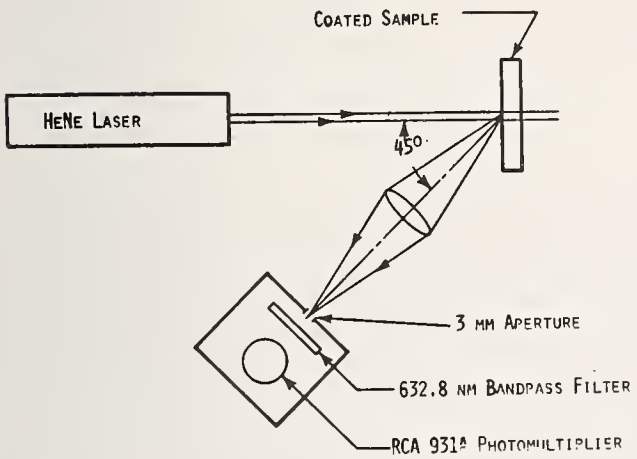

Figure 19. Apparatus for measuring coating backscatter.

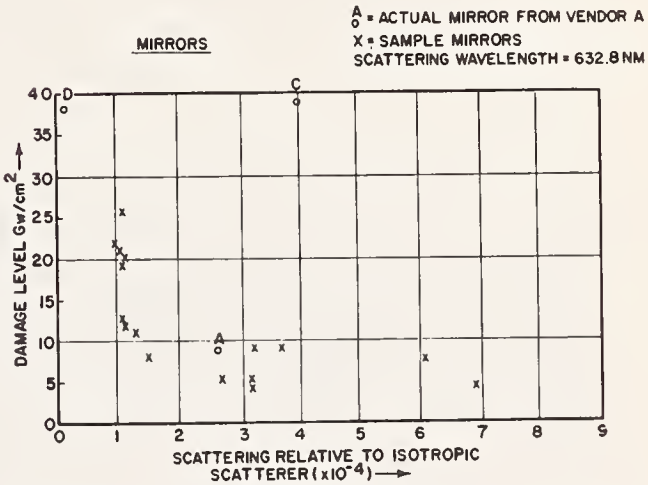

Figure 20. Damage level versus scattering for mirrors.

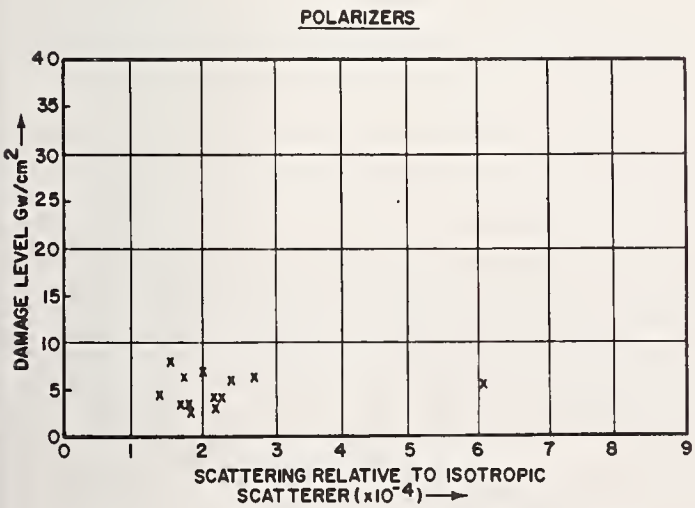

Figure 21. Damage level versus scattering for polarizers.

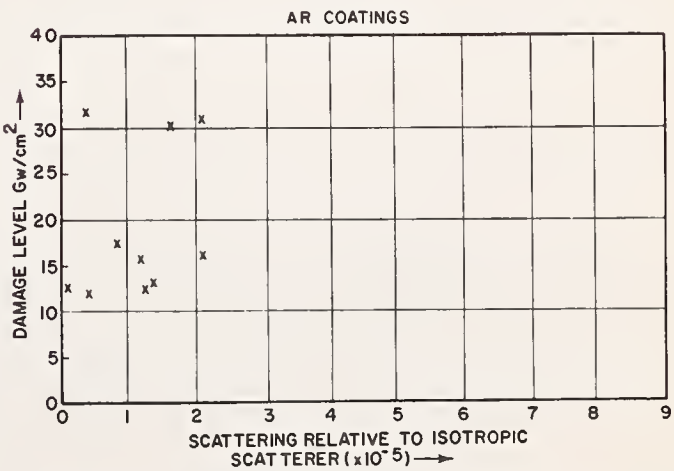

Figure 22. Damage level versus scattering for AR coatings.

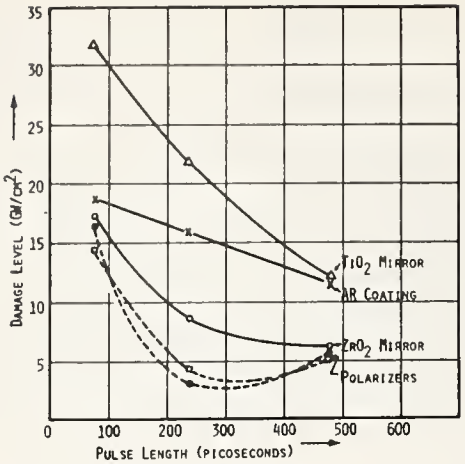

Figure 23. Power damage level versus pulse length.

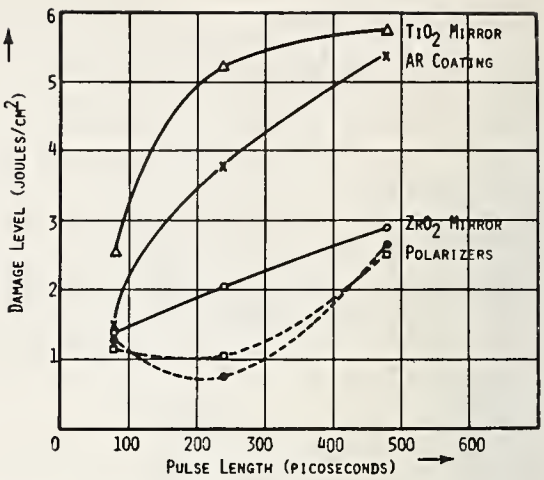

Figure 24. Energy damage level versus pulse length.

COMMENTS ON PAPER BY THOMAS, *et al*

The effects of the subsqrate finishing were considered to be negligible in all cases since in all cases substrate scattering was observed to be down by at least an order of magnitude below the level of scattering observed with the coating in place. There was some discussion of the possible causes of the long term aging effect which was observed in this research. Hypothesis which were put forward included oxidation of the film and the influence of absorbed water vapor on the film. The observed spectral shift seemed to be consistent with the hypothesis of water vapor influencing the film properties rather than oxidation, and therefore it was proposed that the films could be restored to their original design properties by baking out.

5.11 Correlation of Laser-Induced Damage with Surface Structure and Preparation Techniques of Several Optical Glasses at 1.06 μm

R. A. House*, J. R. Bettis, and A. H. Guenther
Air Force Weapons Laboratory
Kirtland AFB, NM 87117

and

R. Austin
Perkin-Elmer Corp.
Norwalk, Conn. 06851

An extensive experimental investigation has been conducted to correlate laser-induced surface damage with surface structural properties in a range of transparent dielectric materials. Materials investigated were Fused Silica (Corning and Optosil); BK-7 (Schott "P" quality); ED-2, ED-4, and Cervit (all Owens-Illinois). Samples were prepared using controlled grinding, conventional polishing, ion polishing, and bowl-feed polishing. Major parameters of interest were the polishing compound used, the rms surface roughness, the subsurface fracture zone, etching, flame polishing, overcoating with $\lambda/2$ of the substrate material, and the possibly deleterious effect of ultrasonic cleaning. The damaging radiation was a focused 1.06 μm laser beam of about 40 ns width in the TEM_{oo} transverse mode. Target sites on a given sample were shielded from each other against blowoff and UV radiation.

Key words: Damage thresholds; fused silica; ion polishing; surface damage; surface roughness; surface structure; thin films; ultrasonic cleaning.

1. Introduction

The subject of short-pulse laser damage at the surfaces of dielectric materials has received considerable attention in the last few years. Many experiments have been performed on a wide variety of coated and uncoated materials, and because of those experiments three ideas have become increasingly apparent. (1) There are many extrinsic variables affecting laser surface damage [1-7][1]. (2) The electric field is the primary initiator of the pulsed-damage process [8-12]. (3) There has been a growing tendency to discount surface topography as unimportant - if the substrates have the "best" optical finish, such as from superpolishing. This is perhaps partly due to a general misinterpretation of Bloembergen's hypothesis on surface flaws and their limiting sizes.

The purpose of the research reported in this paper is to correlate laser-induced surface damage with surface and near-surface (subsurface) structural properties in a variety of transparent dielectric materials. The material of emphasis, however, is fused silica. In order to perform a meaningful set of experiments, it was necessary to prepare a series of samples according to specific fabrication procedures. In addition, a large number of physical measurements had to be made, both before and after laser irradiation. This paper will concern itself primarily with correlations between damage threshold and roughness, subsurface disorder, and various finishing processes such as etching, overcoating, ion polishing, bowl-feed polishing, and ultrasonic cleaning. Complete details on sample preparations will be given, not because of their intrinsic value in fabricating optics, but because of the necessity to completely describe the samples and their resultant surface character.

2. Experiment

The experimental arrangement used in this research is shown in figure 1 and is described in detail elsewhere [13].

An important feature of this research and that of [13] was the use of a special target mask. Figure 2 shows the mask mounted on the sample holding ring. The purpose of the mask was to shield target sites from one another - both optically and physically. In preliminary experiments, it was found that even the smallest breakdowns produced effects to a range as much as 100 times the actual crater diameter. Each aperture in the mask was isolated by means of an annular-shaped piece of printed circuit design tape. These tape pads were forcibly pressed onto the target face. Use of the breath test (described below) on several preliminary samples damaged during use of the mask showed that indeed the various target sites were isolated.

---

*Based upon portions of a PhD thesis submitted to the Graduate Engineering School of the Air Force Institute of Technology, Wright-Patterson AFB, Ohio 45433

1. Figures in brackets indicate the literature references at the end of the paper.

Figure 3 shows the typical form of the raw data for a given sample. The standard experiment was 25 shots, with a new site for each shot. A ratio, R, was calculated for each sample, where

$$R = \frac{\text{lowest energy which produced damage}}{\text{highest energy at which there was no damage}} .$$

The reported energy threshold was obtained by joining the lowest damage energy with the highest non-damage energy and reading where the line crossed ordinate zero. Ratio R indicated how threshold-like the sample was, and it was used to derive error bars for the data.

Two comments are required concerning this method of data taking. Firstly, the described simple method of obtaining the threshold value was chosen because many other methods of analysis were tried and all of them were no more accurate or precise. In addition, they were all more time-consuming. Secondly, 25 shots seemed sufficient for accuracy to about ±20%. In a study such as this, one is not looking for small differences but rather major differences - factors of 2, for instance. For differences of this magnitude, a greater number of exposures is not necessary.

3. Damage Indicators

A recurrent problem in recent years has been what constitutes the onset of damage. With or without the appearance of a plasma, it is generally accepted that damage is an irreversible change in the physical properties of the surface. In this experiment we monitored the appearance of surface response in four independent ways: (a) direct visual observation of plasma by two observers; (b) a LIS/diffraction method; (c) a phase contrast method; and (3) the breath test.

a. Plasma observation. One observer watched through the sample from the back, just below the beam line. The other observer watched from the front, through the phase contrast focusing lens. Consensus on the appearance of a plasma was sufficient for a determination that damage occurred. Disagreement was decided by one of the other methods.

b. LIS/diffraction. This method made use of a He-Ne beam directed through the second turning mirror and focused on the target by the target lens. Damage was indicated by the appearance of laser-induced scatter - (LIS) - both forward and backward - and by the appearance of diffraction rings in the transmitted beam.

c. Phase Contrast. This method was developed by us specifically for the purpose of detecting surface damage. Used in conjunction with a photo-detector, the method can also be used to monitor the formation of damage in a time-resolved manner as well as the fact that it occurred. The phase contrast arrangement is shown in figure 4. The reflected He-Ne beam is focused onto the phase plate by the lens. The quarter-wave dot on the phase plate retards the zero-order diffracted light (specular component) relative to the higher-order diffracted, or scattered light, resulting in a diffraction/interference pattern.

Figures 5 and 6 show typical patterns for bare and overcoated samples. In each figure the pattern on the left is the virgin site and the pattern on the right is the damaged site. The overall elliptical pattern shape and background diffraction are due to the fact that the indicent He-Ne beam is vignetted at non-normal incidence by the target mask.

d. Breath test. This test consisted of steaming the damaged surface with one's breath. The breath test was used only after the various sample analyses were made and was not a real-time test. We employed this test because preliminary experiments showed it to be the most sensitive indicator of the presence of surface change. There was never an ambiguity about whether or not damage had occurred--even if one or more of the other indicators failed. We believe that a damage event alters surface bond and charge distributions, and hence, locally alters the contact angle for water.

After approximately 6000 shots, our judgment is that the four damage indicators rank in increasing sensitivity as follows: LIS/diffraction, phase contrast, visual observation of plasma, breath test.

4. Sample Preparations

Samples for this research were fabricated with eight types of surface preparation: conventional grinding and finishing, overcoating with SiO_2 and MgF_2, flame polishing, etching, subsurface disorder, ion polishing, bowl-feed polishing, and ultrasonic cleaning. Sample dimensions were 1.5 inches in diameter and either 0.375 or 0.300 inches in thickness. All samples, except those which were flame polished, were prepared to a flatness figure of $\lambda/5$ or better. Substrate materials used were (1) fused silica: Optosil I and Corning 7940; (2) BK-7: Schott "P" quality; (3) ED-2, ED-4, and Cervit: Owens-Illinois.

a. Conventional grinding/finishing. These were the samples used for the basic study of threshold vs. roughness. They were subjected to a controlled grinding procedure (see below) to minimize the possible effects of subsurface disorder. Then they were conventionally polished to the desired roughness values and overcoated in the center with a 0.5-inch diameter, opaque thin-film dot of molybdenum. A representative number of samples from each batch were measured for surface roughness by the fringes of equal chromatic order (FECO) technique, and all samples were measured for surface scatter by the total integrated scatter (TIS) technique.

The controlled grinding procedure was followed to minimize the final expected thickness of the subsurface disorder region. At each stage, a thickness of material at least three times the previous grit size was removed. The final grinding stage was a 3 μm grit stage. The rule of three derives from the empirical rule of thumb that a given grit size produces a fracture zone of thickness about three times the grit size. Hence, each stage in the controlled-grinding process attempts to remove the fracture zone produced by the previous stage. The last five grinding stages used alumina grits.

Following controlled grinding, conventional polishing was done on Swiss pitch using milled barnesite and distilled water. Normal cleaning procedure after polishing was a rinse in distilled water, followed by vapor degreasing in freon. All samples on which molybdenum was deposited were cleaned by a mild sputter-etch with argon before the molybdenum was sputtered on. The sputter etch conditions were 2 min., 20 μm argon, and 150 W. The molybdenum deposition conditions were 7 min., 20 μm argon, 1200 VDC target voltage, and 180 VDC substrate bias.

b. Overcoating. A set of samples with a range of surface roughness values was overcoated with half-wave thicknesses of SiO_2 and MgF_2. These samples were control ground, conventionally polished, overcoated with a molybdenum dot, and measured by FECO and TIS. Then they were overcoated at 250° C by E-gun deposition. For SiO_2 the vacuum was 5×10^{-6} torr and the deposition time was 5 min.; for MgF_2, the vacuum was 5×10^{-5} torr and the deposition time was 10 min. The starting materials were MgF_2 - new, Patinal, 99.9% pure; and SiO_2 - CERAC. Following the dielectric deposition, another TIS measurement was made. The difference in the two TIS measurements yielded information about film scatter. The half-wave thickness was chosen to facilitate comparison of breakdown intensities with those obtained for bare substrates.

c. Flame polishing. Following the controlled grinding and conventional polishing to desired roughness values (determined by FECO), the samples were cleaned and then flame-polished. This was done by spinning each sample in a glass-blower's lathe and playing an acetylene torch over the surface until the surface softened. Then the samples were overcoated with a molybdenum dot and measured by TIS. Obviously, this was not a very quantitative process and the resultant surface figure was poor. In addition, although the surface scatter and roughness were extremely low near the center, the scatter increased radially outward. Data were taken only on the inner ring of target sites for these samples. These samples were expected to exhibit higher thresholds than any of the other samples.

d. Etching. A series of samples identical to the surface roughness samples was subjected to an etching procedure after conventional polishing and FECO: (1) a wash in Solveno and acetone, (2) a wash in Orvus and a rinse with distilled water, (3) an ultrasonic cleaning in benzene, (4) a 10-minute etch in a 10% nitric acid solution and distilled water, (5) a rinse in distilled water, with the sample being blown dry. Then the samples were overcoated with a Molybdenum dot. These samples were expected to be higher in threshold than the surface roughness samples because of an expected reduction in surface contamination and disorder.

e. Subsurface disorder. These samples were fabricated to test the effect of the disorder region (caused by grinding) which lies below the Beilby polish layer. The samples were prepared by interrupting the controlled grinding procedure at given stages and then polishing to better than 20 Å surface roughness. Then the usual FECO, molybdenum dot, and TIS were done.

f. Ion-polishing. While the above samples were all fused silica, the ion-polished and bowl-feed polished samples were sets of five different materials: fused silica, ED-2, ED-4, BK-7, and Cervit. The ion-polished samples were control-ground and conventionally polished with rouge, with the conventional polishing removing about 10 μm of material. The ion polishing conditions were as follows: 70° angle of incidence; doses of 10^{17} /cm^2 and 10^{18} /cm^2; energies of 20KV and 30KV; and ions of H, Ar, and Xe. These samples were overcoated in the center with aluminum and measured by TIS.

g. Bowl-feed polishing. These samples were control ground and then bowl-feed polished using rouge. A total of four polishing times for each material type were used. Then the samples were coated with aluminum and measured by TIS.

h. Ultrasonic cleaning. Impelled by recent findings of Saito [14] and Gibbs and McLachlan [15] on the deleterious effects on surface topography produced by ultrasonic cleaning, a rudimentary

NOTE: 1 torr = $\frac{101\ 325}{760}$ Pa.

experiment on some samples of fused silica was performed. Two of the previous roughness samples, two samples provided by R. Austin (of Perkin-Elmer Corp.), and three samples provided by H. Bennett (of the Michelson Labs, NWC) were ultrasonically cleaned in two commercial solutions (Micro and Radiac) for varying periods of time. Then the thresholds of the controls and ultrasonically cleaned samples were determined. The ultrasonic cleaner was a 250W Bransonic 52.

5. Experimental Results

Figure 7 shows the results for the conventional grinding/finishing samples. $\mathcal{E}$ is the incident energy threshold, in mJ, and σ is the surface roughness. Because $\sqrt{\mathcal{E}}$ is proportional to the electric field (the irradiation geometry and material index of refraction were constant in each experiment), the plot shows the existence of a close log-log relationship between the electric field and the surface roughness.

This is not surprising since one may consider that surface scattering is a measure of the tendency of surfaces to "absorb" laser light - by field enhancement at surface flaws, plasmon excitation, etc. One assumes that

$$\mathcal{E} \sim I_{scat}^{-m} , \tag{5.1}$$

where $m>0$ and I_{scat} is the scattered light intensity. From scattering/roughness theory [16] it is known that for sufficiently small roughness, σ, one can write

$$\frac{R_{scat}}{R_o} \sim \frac{I_{scat}}{I_o} \cong \left(\frac{4\pi\sigma}{\lambda}\right)^2 , \tag{5.2}$$

where R_{scat} is the reflectance of the surface for scattered light

R_o is the reflectance of a completely smooth surface of the same material

I_o is the incident intensity.

For $\lambda = 1.06$ μm, the condition $\sigma < 250$ Å appears to be sufficient. This leads to

$$E \sim \sqrt{\mathcal{E}} \sim \frac{1}{\sigma^m} , \tag{5.3}$$

where E is the electric field in MV/cm. Hence, one expects

$$\sigma^m \sqrt{\mathcal{E}} \sim \text{const.} \tag{5.4}$$

In considering eq. (5.4), one can assume that the smoothest possible surface will have a limiting roughness of several Å (e.g., the average interatomic distance). Then the threshold should approach the bulk threshold. Fradin [17] has recently reported the bulk threshold of fused silica to be 5.2 MV/cm. From the density of fused silica, an average atomic spacing of 3.57Å is obtained. The lattice parameter for crystalline quartz is 4.9Å. Using these values, two data points are plotted as squares in figure 7. The straight-line fit is for the five roughness samples only. It is encouraging to note that both points for the bulk breakdown fit the surface data reasonably well.

The precise value of m for a given set of samples depends, of course, on the actual physical state of the surface. But the relationship should hold for a wide variety of surface types. In figure 8 are plotted the data for the SiO_2-overcoated samples, in figure 9 are the data for the M_gF_2-overcoated samples and in figure 10 are the data for the flame-polished samples. The line-fit in figure 9 includes only the E-gun films. The significant observation concerning figure 10 is that all four samples were well under Bloembergen's 100Å limit, and yet the thresholds were strikingly ordered by the roughness values. The result seems surprising since Bloembergen [10] pointed out that surface flaws and inclusions with typical dimension 100Å or less should not affect the damage threshold.

Unfortunately, the etched samples did not closely fit relationship eq. (5.4), although the overall trend of the data was similar. The results are presented in table 1. We do not yet know the explanation for the lack of a similar fit the simple relationship of eq. (5.4).

Table 1. Etched Samples: Breakdown field vs. Surface Roughness

σ(Å)	E(MV/cm)
42	1.11
82	0.34
243	0.41
325	0.29

In table 2 is presented a process vs. threshold correlation for various roughness ranges, using data from the conventionally-finished, overcoated, flame-polished, and etched samples. For the flame-polished samples, the indicated roughness range denotes the roughness before the flame-polishing stage was carried out. The final roughness values (inferred from TIS measurements) of the flame-polished samples are given in parentheses, after the breakdown field values.

Table 2. Process vs. Threshold (MV/cm) for Various Roughness Ranges

14Å Range	40Å Range	80Å Range
Conv.: 1.60	Flame: 2.12 (17.7Å)	Flame: 1.73 (60.6Å)
SiO_2 : 0.89	Etch : 1.11	SiO_2 : 0.42
MgF_2 : 0.64	Conv.: 0.98	Etch : 0.35
	SiO_2 : 0.66	MgF_2 : 0.26
	MgF_2 : 0.34	
140Å Range	**240Å Range**	**330Å Range**
Conv.: 0.36	Flame: 1.78 (56Å)	Flame: 2.24 (13.3Å)
MgF_2 : 0.23	Etch : 0.41	Etch : 0.29
	Conv.: 0.32	Conv.: 0.24
	SiO_2 : 0.29	SiO_2 : 0.24

Two sets of subsurface disorder samples were irradiated and the results are given in table 3. There is no obvious relation between threshold and roughness of the form eq. (5.4), nor is there an obvious relationship between threshold and grit size, g. There does seem to be a reasonable fit of the data to a relationship of the form

$$\sigma^m \; g^n \sqrt{\mathcal{E}} \sim \text{const.} \qquad (5.5)$$

Where m = 0.5, n = 0.023, however, the analysis has not proceeded sufficiently to warrant the assertion that eq. (5.5) is meaningful. Comparison of the breakdown values for the 20 μm grit samples with those for the other samples (and keeping in mind the general effect of roughness on threshold), it is seen that the 20 μm values are abnormally low.

Table 3. Results for the Subsurface Disorder Samples

g (μm)	σ(Å)	E(MV/cm)
3	15.9	1.60
5	10.1	1.87
5	10.1	1.76
12	9.15	1.85
12	9.15	2.19
20	10.9	1.23
20	10.9	1.42
30	8.87	2.10
30	8.87	1.76

The results for the ion-polished samples are given in table 4. The first five entries show the material effects, since all these samples were identically polished. The fifth through eighth samples show the effects of varying the dose and energy on the material fused silica. Samples five and eight through twelve show the effects on fused silica of varying the ion and of proceeding from low dose-low energy to high dose-high energy. Comparing only the electric field data for fused silica with the reference sample (conventional finish, barnesite polished, 1.60 MV/cm, and 13.75Å roughness), we see that samples 5, 6, 8, 11, and 12 all had slightly lower thresholds. Both argon-polished samples had slightly higher thresholds. The more interesting result is the comparison of the quantities $(\sigma^{0.5})(E)$ for the reference and ion-polished samples. These quantities constitute a "roughness correction," based on the results of figures 7,8, and 9. Only sample 5 is lower than the reference in this comparison. In fact, for each ion used, the progression from low dose-low energy to high dose-high energy leads to a decrease in the corrected field strength. The argon-polished samples showed an increase in corrected field strength of 88%, with the Xenon-polished samples having an increase of 36%,and the hydrogen-polished samples having an increase of 31%. These comments, however, are not conclusive yet, because we have not yet examined the samples for probable refractive index change [18, 19].

Table 4. Results for Ion Polishing. All Samples Were Previously Rouge Polished.

Sample	Material	Ion	Dose (cm^{-2})	Energy (KV)	σ (Å)	E(MV/cm)	$\sigma^{0.5}$ E
1	BK-7	H^+	10^{17}	20	18	1.43	-
2	Cervit	H^+	10^{17}	20	-	0.55	-
3	ED-4	H^+	10^{17}	20	47	1.18	-
4	ED-2	H^+	10^{17}	20	-	0.84	-
5	FS	H^+	10^{17}	20	14	1.32	4.94
6	FS	H^+	10^{17}	30	25	1.53	7.65
7	FS	H^+	10^{18}	20	11	2.34	7.76
8	FS	H^+	10^{18}	30	25	1.39	6.95
9	FS	Ar^+	10^{17}	20	31	2.00	11.14
10	FS	Ar^+	10^{18}	30	36	1.68	10.08
11	FS	Xe^+	10^{17}	20	36	1.34	8.04
12	FS	Xe^+	10^{18}	30	31	1.46	8.13
Ref. (FS)	FS	-	-	-	13.75	1.60	5.93

Table 5 shows the results for the bowl-feed polished samples. Except in the case of Cervit, the rouge-polished samples are significantly lower in threshold than the ion polished samples. Since roughness values for Cervit are not available, a much larger roughness for the ion-polished case could easily explain the apparent discrepancy. Note the absence of significant variation in threshold as a function of polishing time for the fused silica. Note also that the corrected values are significantly lower than the reference corrected value.

Table 5. Results for Bowl-Feed Polished Samples.
Samples were Polished with Rouge.

Sample	Time (hrs)	σ(Å)	E(MV/cm)	$\sigma^{0.5}$E
BK-7	40	30	0.93	-
Cervit	46.5	-	0.55	-
ED-4	45	40	0.77	-
ED-2	48	-	0.62	-
FS	48	13	0.86	3.10
FS	72	13	0.90	3.24
FS	96	11	0.87	2.88
FS	120	18	0.86	3.65
Ref. (FS)	-	13.75	1.60	5.93

Table 6 gives the results for the ultrasonic cleaning experiment. Sample PE#3 was originally cleaned for 3/4 hours, damaged, cleaned for an additional 16 3/4 hours, and damaged again. The rouge-polished PE samples showed no significant variation even for long cleaning times, even though the roughness variation was a factor of 5. The rouge contamination probably dominated. However, the two barnesite-polished samples showed a possible threshold reduction after only a short time in the cleaner. The dramatic threshold reduction occurred for the HB samples - 21% for Micro solution and 32% for Radiac solution. These reductions in electric field correspond to energy reductions of 38% and 54%.

Table 6. Ultrasonic Experiment on Fused Silica

Sample	Polishing	Time (hrs)	Solution	σ(Å)	E(MV/cm)
PE#1	C,R	0	-	25	0.73
PE#3	C,R	3/4	MI	∿25*	0.72
PE#3	C,R	17 1/2	MI	119	0.75
077	C,B	0	-	16	0.87
082	C,B	1/2	RA	∿16*	0.80
HB#5	C,B	0	-	∿20*	1.74
HB#6	C,B	16 3/4	MI	∿20*	1.37
HB#7	C,B	17	RA	∿20*	1.18

C = Conventional
B = Barnesite
R = Rouge
MI = Micro
RA = Radiac
* Approximate, not measured yet

Finally, figures 11-16 show the types of surfaces obtained for the conventionally finished, etched, flame-polished, subsurface, ion-polished, and bowl-feed polished samples. Note that on even the smoothest surfaces can often be found defects with dimensions greater than 100Å.

6. Conclusions

a. Roughness. The existence of a relationship of the form of eq. (5.4) is strong evidence of the importance of the electric field in surface breakdown and of the enhancement of the electric field at surface scattering sites. The relationship quite obviously holds over as much as two orders of magnitude in roughness, and in particular it holds as the roughness approaches zero. However, the fact that roughness may be small does not imply that Bloembergen's surface flaw model and its conclusions are necessarily wrong. This is because $\sigma \to o$ does not necessarily imply the absence of defects with typical dimensions more than 100Å (see figures 11-16).

b. Etching. The nitric acid etching procedure yielded an improvement in electric field threshold of about 21%, but the magnitude of the improvement could possibly have been adversely affected by the ultrasonic cleaning stage of the procedure.

c. Flame polishing. Although bad for general surface figure, flame polishing did drastically reduce surface roughness and yielded a dramatic increase of as much as 830% in electric field threshold. This occurred for the largest initial roughness values. At the low roughness end the increase was 115%. Possible explanations would include superficial smoothing by glass flow, defect annealing, and contaminant removal due to vaporization.

d. Overcoating. Both types of films, SiO_2 and MgF_2, generated significant reductions in threshold. SiO_2 showed an average reduction of 21% in electric field threshold and MgF_2 showed an average reduction of 54%. Correlations of the thin-film data with index inhomogeneity, film scatter, etc., have not yet been done. So the explanation for threshold reduction in these films has not yet been determined.

e. Subsurface disorder. There was only a weak correlation of threshold with roughness and grit size. The thresholds were generally higher than for the minimum disorder samples. Since measurements of the actual extent of the subsurface disorder region have not been completed, we conclude the following: If large subsurface zones of disorder do exist, then the effect of this disorder on threshold is secondary to the effect of the topography of the exposed finish layer.

f. Ion polishing. The results for ion-polishing at high energies were somewhat erratic, at least in terms of electric field breakdown strength only. Three of the hydrogen-polished samples and both of

the Xenon-polished samples showed a decrease in threshold compared to the reference samples. Making a roughness correction to the field strength values yielded a more ordered picture - as pointed out in the discussion of table 4. The corrected breakdown values showed that all three ions used resulted in improved damage thresholds. This is in keeping with Giuliano's results on sapphire [7] and with the expectation that ion-polished surfaces should have a reduced level of mechanical damage (due to previous grinding and abrasive polishing) and a reduced level of surface contamination. This last comment is especially telling when it is recalled that all of the ion-polished samples had previously been rouge polished. Rouge contamination is known to reduce the threshold for breakdown at 1.06 μm [1, and below].

g. Bowl-feed polishing. In general, a comparison of tables 4 and 5 shows that the presence of rouge contamination in the bowl-feed polished samples caused a reduction of threshold. For fused silica the reduction averaged about 45%, and there was no dependence on polishing time, within experimental accuracy, in the range from 48 to 120 hours.

h. Ultrasonic cleaning. The results were somewhat erratic, but generally did show that for some conditions of duration and type of cleaning solution considerable threshold reduction occurred. An interesting conclusion is suggested by comparison of corrected field values for the PE samples. The corrected fields are 3.65 MV/cm, for PE #1 (0 hours) and 8.18 MV/cm, for PE #3 (17.5 hours). The first value correlates with the results for rouge polished fused silica (table 5), and the second value correlates with the ion-polished fused silica (table 4). Not only did the ultrasonic cleaning in Micro solution lead to an increase in surface topography (i.e., an increase in roughness), but it apparently brought about a drastic reduction in contamination by rouge.

i. In general. The overall general conclusion of this research is that the electric field at breakdown is intimately related to the surface roughness - from large roughness values down to and including the smoothest surfaces. The corollary is that a complete statement of conditions in a surface damage experiment must include the value of the surface roughness.

Additional measurements, including Auger spectrometry, SEM, Nomarski microscopy, surface topography, ellipsometry, and damage morphology are currently being conducted on the samples. In addition, ultrasonic cleaning experiments of a more quantitative nature are being planned.

7. Acknowledgments

The authors would like to express their deep appreciation for fruitful discussions and various sample analyses to the Dr's. Bennett of the Michelson Labs, to Dr. Harold Posen and co-workers at AFCRL, to Dr. John Reichert of Texas Tech, and to Dr. Robert Hengehold of the Air Force Institute of Technology. In addition, we would like to acknowledge the technical support of Perkin-Elmer Corp. and the Materials Branch of the Air Force Weapons Laboratory.

8. References

[1] Boling, N. L., Dubé, G., and Crisp, M. D., NBS Special Publication No. 387 (U.S., GPO, Wash., D.C., 1973), p. 69.

[2] Ringlien, J. A., Boling, N. L., and Dubé, G., Appl, Phys. Lett. 25, #10, 598 (1974).

[3] Fersman, I. A. and Khazov, L. D., Sov. J. Opt. Tech. 37, 627 (1970).

[4] Khan, J. M., NBS Special Publication No. 372 (U.S. GPO, Wash., D.C., 1972), p. 75.

[5] Davit, J., J. Appl. Phys. 39, #13, 6052 (1968).

[6] Swain, J. E., ASTM Special Technical Publication No. 469 (ASTM, Phila., Pa., 1969), p. 69.

[7] Giuliano, C. R., NBS Special Publication No. 372 (U.S. GPO, Wash., D.C., 1972), p. 55.

[8] Crisp, M. D., IEEE J. Quant. Elect. QE-10, #1, 57 (1974).

[9] Newnam, B. E., NBS Special Publication No. 414 (U.S. GPO, Wash., D.C., 1974), p. 39.

[10] Bloembergen, N., Appl. Opt. 12, #4, 661 (1973).

[11] Bettis, J. R., Guenther, A. H., and Glass, A. J., NBS Special Publication No. 414 (U.S. GPO, Wash., D.C., 1974), p. 214.

[12] Fradin, D. W. and Bass, M., Appl. Phys. Lett. 23, #11, 604 (1973).

[13] Bettis, J. R., House, R. A., Guenther, A. H., and Austin, R., This Symposium.

[14] Saito, T. T., Private communication.

[15] Gibbs, W. E. K. and McLachlan, A. D., This Symposium.

[16] Bennett, H. E. and Porteus, J. O., JOSA 51, 123 (1961).

[17] Fradin, D. W. and Bass, M., Appl. Phys. Lett. 22, #4, 157 (1973).

[18] Bayly, A. R., Radiation Effects 18, 111 (1973).

[19] Presby, H. M. and Brown, W. C., Appl. Phys. Lett. 24, #10, 511 (1974).

[Note added in proof: Subsequent to the presentation of this paper at the symposium, results of further measurements of roughness on these samples became available. TIS measurements were made at Perkin-Elmer and at China Lake, FECO measurements were made at China Lake, and Tallystep measurements were made at AFWL. In general, the various methods of inferring roughness showed the trend exhibited in figure 7. However, there tended to be a wide variation in inferred roughness values for any given sample. The data for this paper made use of the original FECO (PE) numbers, except in the case of the flame-polished samples. For these samples, only the TIS values represented the final surface topography. The FECO measurements are the only ones considered to be consistent over our whole roughness range. TIS measurements were done in the visible and are not considered reliable above about 100 Å roughness. Tallystep measurements become suspect below about 100 Å. In any event, the important conclusion still holds. Surface breakdown does definitely correlate with at least some measure of surface scattering - be it TIS values or inferred roughness. However, because of the difficulty in determining and specifying the true roughness over the total range of values, the numerical slope ($\ln\sqrt{\varepsilon}$ vs $\ln\sigma$) should not be considered absolute. Recall that TIS and FECO estimates are in good agreement at low surface roughness. What obviously is called for are better scatter-roughness determinations together with auto-covariance measurements of each of the differently processed surfaces as well as a sensitive measure of their impurity content and a detailed determination of surface structure (crystallinity, etc.).]

9. Figures

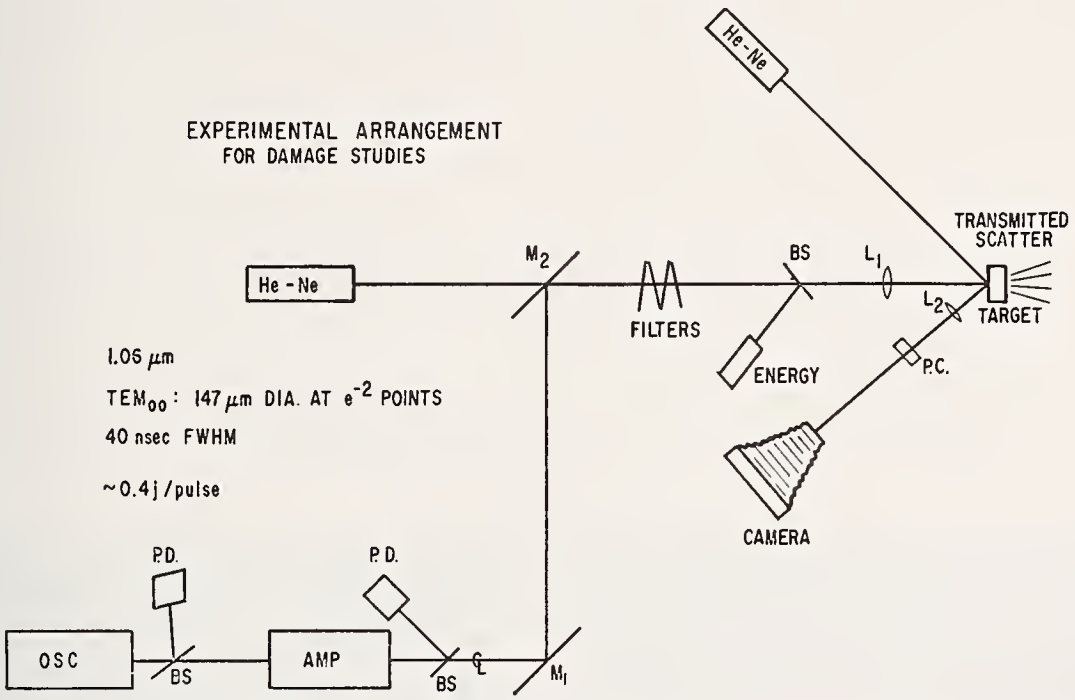

Figure 1. Experimental arrangement for damage studies. BS denotes beam splitters; M_1 and M_2 are dielectric turning mirrors, optimized at 45° incidence angle for 1.06 μm; L_1 is the target lens, of focal length 513.5 mm; L_2 is the phase-contrast focusing lens, of focal length 250 mm; PC is the phase contrast plate (see figure 4 for details).

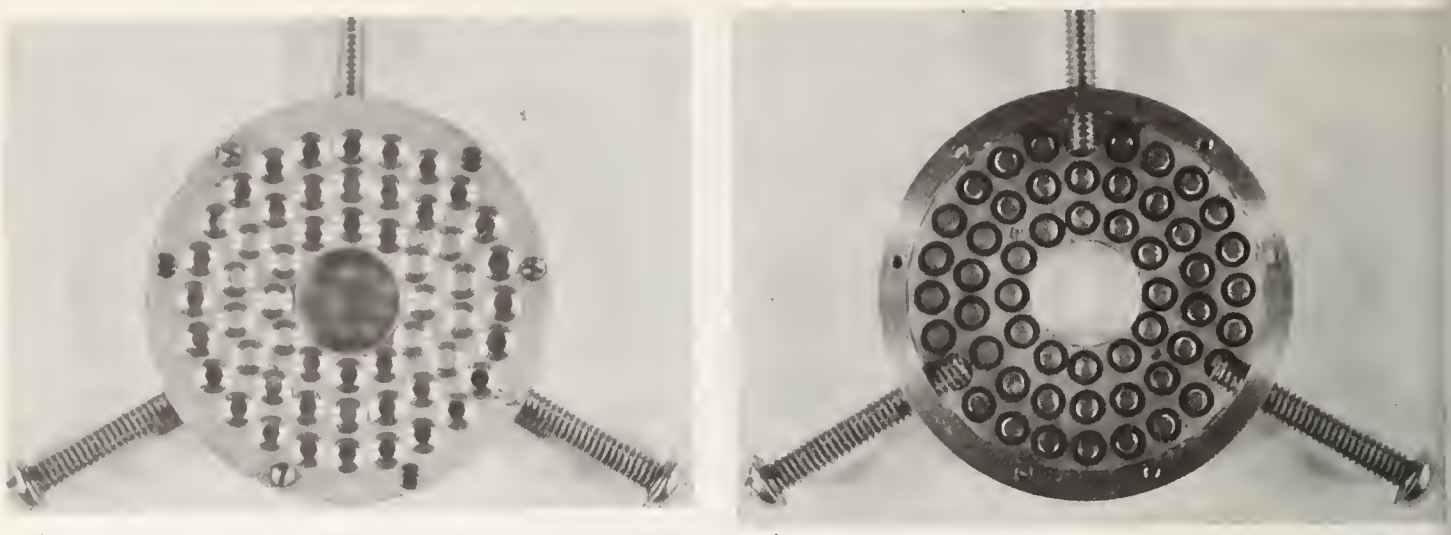

(a) (b)

Figure 2. Target mask, mounted on sample holder ring. In actual practice, the positioning screws are nylon - metal screws are shown for clarity. Small apertures (for target sites) are 2 mm in diameter. Large central aperture permits access to metal dot on sample. See figure 4 for view of mask on sample. Black rings around each aperture in (b) are sealing pads, described in text.

a. Front face - toward laser beam. b. Back face - pressed against sample surface.

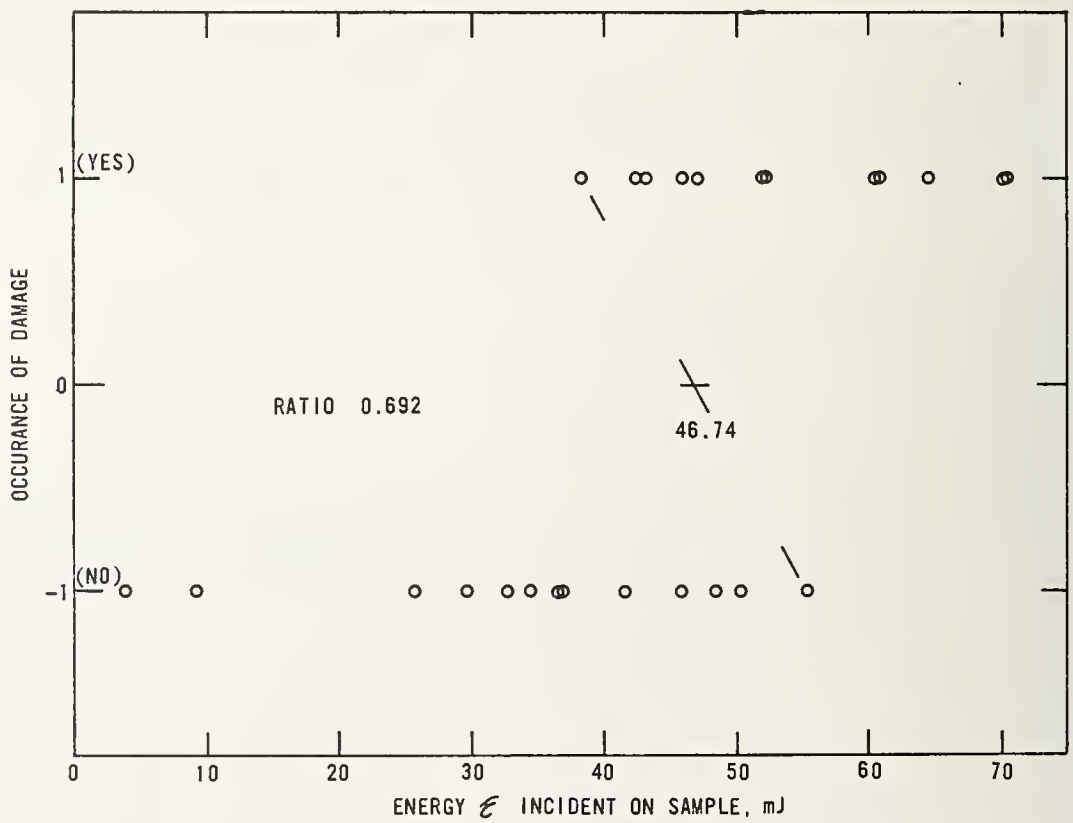

Figure 3. Typical raw data plot

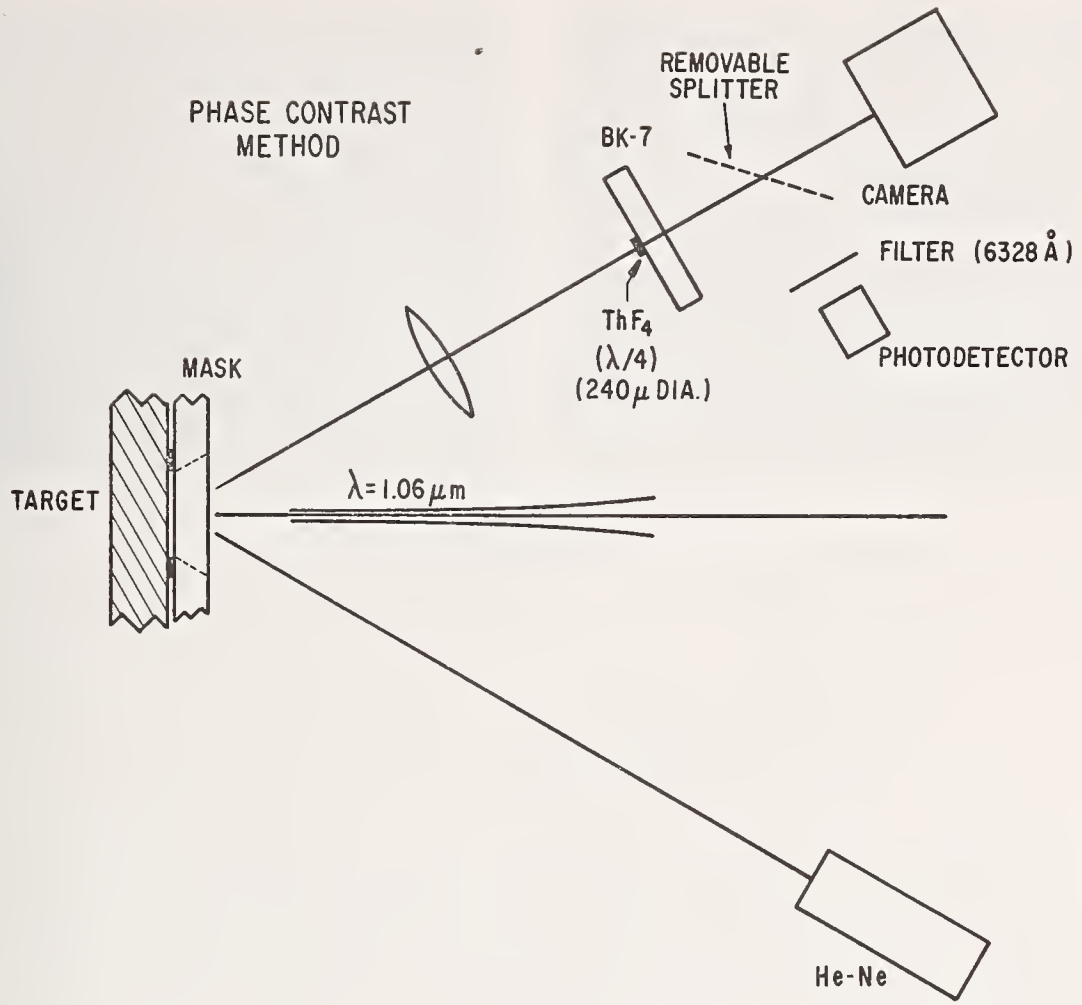

Figure 4. Phase contrast method. Photo detector/beam splitter option was not used in this study.

(a) (b)

Figure 5. Phase contrast for bare surface.
a. Before damage. b. After damage.

(a) (b)

Figure 6. Phase contrast for overcoated surface.
a. Before damage. b. After damage.

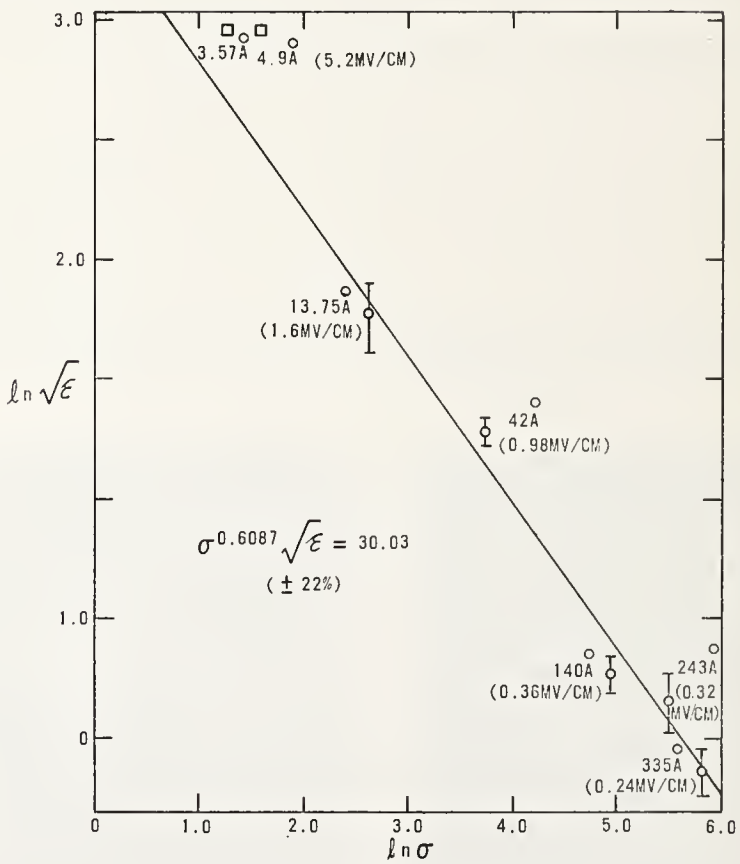

Figure 7. Electric field threshold vs roughness for the conventionally-finished samples. Circles with error bars denote our data. Squares denote Fradin's value for bulk breakdown, using assumed roughness values (see text). Data points are labeled by roughness values and breakdown electric fields (in parentheses). The equation is the fitted straight line - fitted only to our data. Electric fields are macroscopic (include the index of refraction).

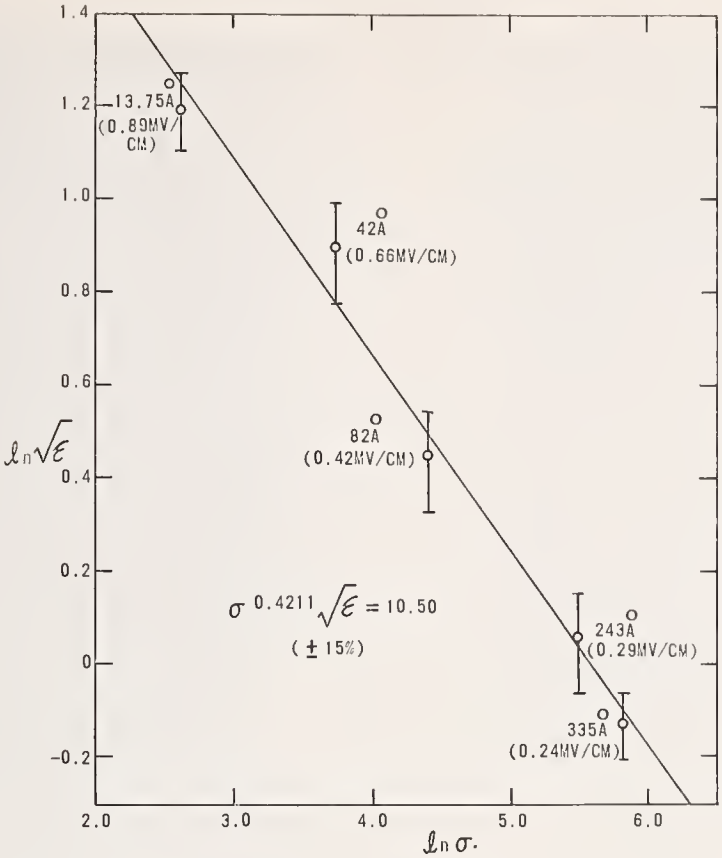

Figure 8. Electric field threshold vs roughness of the substrate, for the half-wave SiO_2-overcoated samples. Data points are labeled by roughness values and breakdown electric fields (parentheses). Electric fields are macroscopic (include the index of refraction). The equation is the fitted straight line.

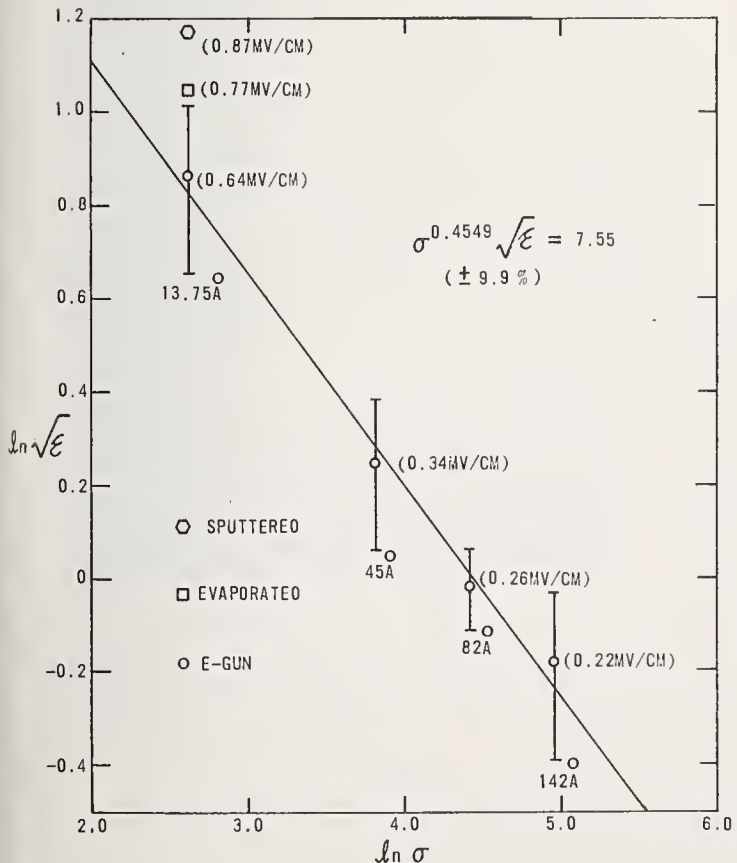

Figure 9. Electric field threshold vs roughness of the substrate, for the half-wave MgF_2-overcoated samples. Data points are labeled by roughness values and breakdown electric fields (parentheses). Electric fields are macroscopic (include the index of refraction). The equation is the straight-line fit to only the E-gun data points.

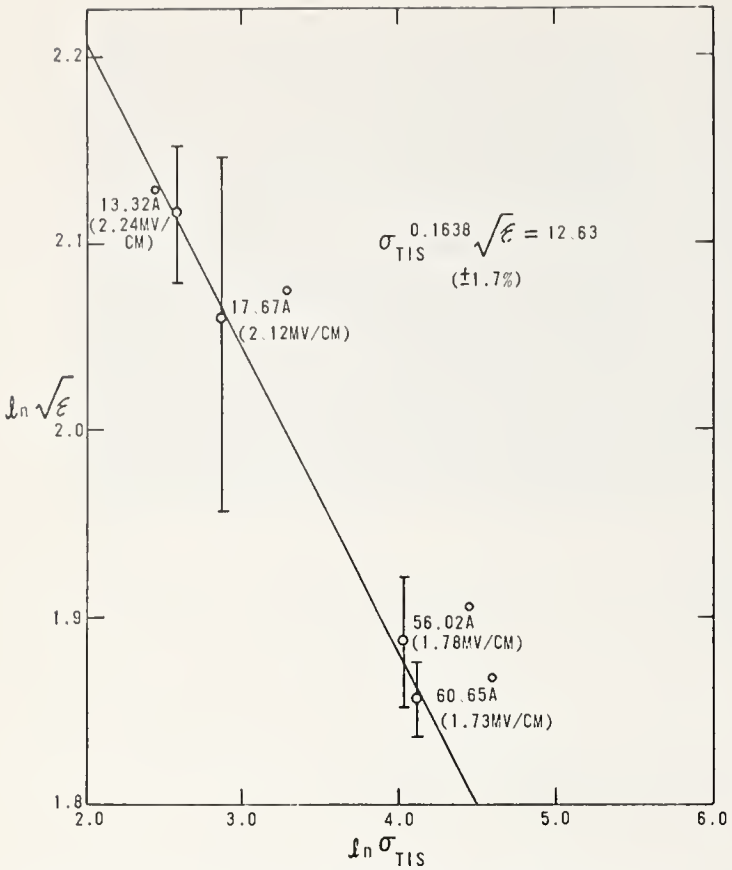

Figure 10. Electric field threshold vs roughness for the flame-polished samples. Data points are labeled by roughness values and breakdown electric fields (parentheses). Electric fields are macroscopic (include the index of refraction). The equation is the fitted straight line.

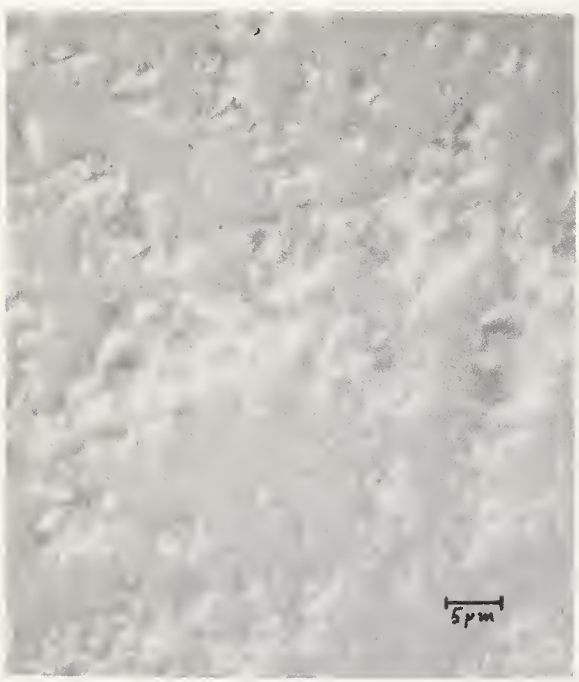

Figure 12. Fused silica, etched. σ = 82 Å.

Figure 11. Fused silica, conventionally finished. σ = 243 Å.

Figure 13. Fused silica, flame-polished. Before flame-polish, σ = 310 Å. After flame-polish, σ = 13.3 Å.

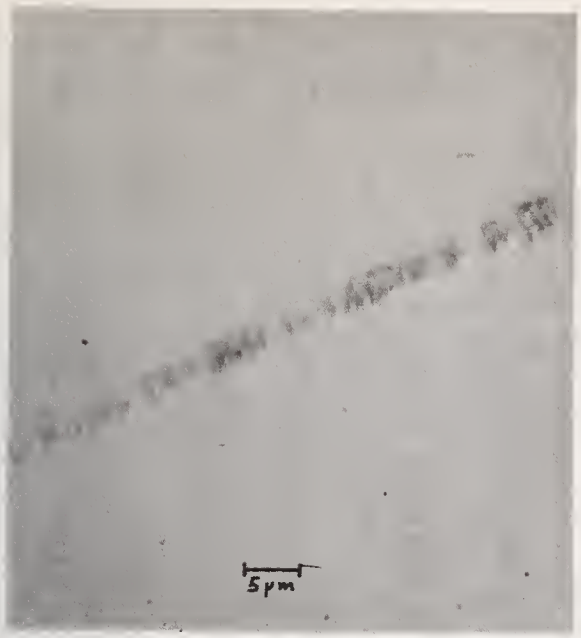

Figure 14. Fused silica, substrate disorder. 12 μm grit size. σ = 9.15 Å.

Figure 15. Fused silica, hydrogen-polished. 10^{17} ions/cm^2, 20 KV energy. σ = 14 Å.

Figure 16. Fused silica, bowl-feed polished. 48 hours polishing time, σ = 13 Å

COMMENTS ON PAPER BY HOUSE, et al

Norm Brown from the Lawrence Livermore Laboratory made some significant comments concerning the polishing process and its influence on observed damage thresholds. He pointed out that very often the polishing process tends to smooth over subsurface damage compacting the surface layer and this effect is most pronounced with coarser grits. He also cautioned the listeners to be careful in the use of small bowl-feed machines. In those machines with small reservoirs the polishing process proceeds too rapidly and there is a significant chance that the polishing compound will be fused into the surface. A way of getting around this is to increase the reservoir of the recirculating slurry and to circulate the slurry using a tubing pump so that when the slurry is changed the tubing also can be changed. He further emphasized the importance of the choice of polishing compound in determining the surface properties. It is of course well known that the use of jewelers' rouge leads to an easily damaged surface. Brown pointed out that he has observed a surface of better quality obtained with a zirconium oxide slurry than with a cerium oxide slurry, at least with the polishing compounds supplied from one manufacturer. Further discussion ensued concerning the degradation of optical figure in the flame polishing process. It was brought out in the discussion that flame polished glass surfaces are among the most damage resistant one can obtain, but that the typical flatness available, for example, in flame polished microscope slides which are commercially available is of the order of 5 to 10 microns flatness variation. There is further evidence that a surface roughness is the determinant in damage properties rather than the presence or absence of subsurface structure or damage in the material. This is consistent with the observation earlier reported that in ultrasonic cleaning the surface layer may be disrupted revealing subsurface structure, and thereby reducing the damage threshold. However, it is also important to remember that subsurface damage should be kept at a minimum in any optical surface in order to ensure good optical properties quite apart from questions of laser damage.

6.1 Picosecond Breakdown Studies: Threshold and Nonlinear Refractive Index Measurements and Damage Morphology*

W. L. Smith, J. H. Bechtel, and N. Bloembergen

Gordon McKay Laboratory
Harvard University
Cambridge, Mass. 02138

Single picosecond pulses from a well-calibrated Nd:YAG laser have been used to study the bulk dielectric properties of 14 transparent solids. Measured values of the breakdown thresholds and nonlinear refractive indices are presented. Photomicrographic data of the damage morphology yield information concerning spatial and temporal microplasma growth from initiating electrons, and concerning the spatial density of initiating sites. The data indicate avalanche ionization is the damage mechanism. Preliminary results from a breakdown study at 0.53 μm are discussed.

Key words: Avalanche ionization; dielectric breakdown; inclusions; laser damage threshold; morphology; nonlinear refractive index; picosecond laser pulses.

1. Introduction

We wish to present results which have been obtained in a study of laser-induced damage in transparent solids with picosecond pulses. Aspects of the 1.06 μm investigation which have been completed to date and which are discussed include breakdown threshold measurements, nonlinear refractive index measurements, and microscopic observations of the damage morphology [1]. In addition, comments concerning a similar study at the second-harmonic wavelength, 0.532 μm, are included.

2. Experiment

The experimental technique that we have used is one first mentioned by Zverev and Paskkov in 1969 [2], and later by Fradin in 1973 [3]. The rationale of the technique will now be described.

Consider a low power, diffraction-limited, Gaussian laser pulse of wavelength λ with an initial intensity e^{-1} radius ρ. A corrected lens of focal length f will focus this pulse, as shown in figure 1, to a spot having a radius w equal to $\lambda f/2\pi\rho$. If the pulse power is P and we define a focal area $A = \pi w^2$, then the focal plane intensity distribution is given by

$$I(r) = I_{max}\, e^{-(r/w)^2}. \tag{1}$$

I_{max} in the low power limit will equal P/A.

This simple picture is modified, however, for all bulk breakdown experiments at wavelengths shorter than roughly one micron by the effects of self-focusing. The characteristic quantity for this self-action, the critical power for self-focusing, is given by

$$P_{cr} = c\lambda^2/32\pi^2 n_2 , \tag{2}$$

where n_2 is the nonlinear refractive index. For an input pulse power less than P_{cr}, the focal situation is modified as shown in figure 2. The low-power focal area A is reduced to $A' = A(1-PP_{cr}^{-1})$, thereby increasing I_{max}. Thus we arrive at a relation for I_{max} which may be written

$$P^{-1} = I_{max}^{-1} A^{-1} + P_{cr}^{-1} , \tag{3}$$

of the form $y = ax + b$. Therefore, a plot of the reciprocal measured power necessary to cause breakdown, as a function of reciprocal focal area, should yield the breakdown electric field

$$E_b = [I_{max}/n_0\epsilon_0 c]^{1/2} \tag{4}$$

from the reciprocal slope I_{max}^{-1}. In addition, the vertical-axis intercept yields the nonlinear refractive index by eq. (2).

A diagram of the experimental apparatus is illustrated in figure 3 and will be described briefly. The Brewster-ended Nd:YAG mode-locked (Kodak 9860) oscillator is constrained to oscillate in the TEM_{00} mode by an intracavity aperture. A single pulse is excised from the train by a Pockels cell, and is amplified as needed up to approximately 300 MW by two single-pass Nd:YAG amplifiers. A Tektronix 519 scope (CRO-1) is used to insure that only data from clean, single pulses are used. The photodiode PD-3 measured the energy incident on the lens L, and was calibrated against two Eppley

1: Figures in brackets indicate the literature references at the end of the paper.

Laboratory thermopiles. The pulse spatial profile was measured exactingly and determined to be Gaussian to the e^{-2} points. The average temporal duration of the laser was carefully measured by two-photon absorption and second-harmonic autocorrelation techniques to be 30 ± 6 psec. The temporal profile fits well to a Gaussian shape. Because of inherent small fluctuations in the pulse duration of the laser, a nonlinear-optic monitor of pulse duration was devised and added to the laser system [4]. The fundamental pulse energy content signal, $\mathscr{E}_f$, from PD-3 in figure 3 is used in conjunction with the second-harmonic pulse energy content signal, $\mathscr{E}_{sh}$, from PD-2 to record the ratio

$$R \equiv \mathscr{E}_f^2 / \mathscr{E}_{sh} = q\tau \qquad (5)$$

for each laser pulse. This relation is easily derived by using the known Gaussian temporal profile of our laser output. The quantity q is a collection of constants for a given experiment, involving phase-matching angle, etc. After each breakdown experiment, involving about 150 shots, the average of the individual pulse R values was normalized to a 30 psec. FWHM duration, thereby providing individual pulse duration values. This technique was important in obtaining accurate breakdown threshold measurements.

Three lenses were used in the experiment for each material. The focal lengths were 0.5, 1.0, 1.5 inches, with focal areas of 34, 48 and 108 square microns, respectively. All aberrations were carefully considered and the focal area for the smallest focal length lens was measured to verify the calculated area. Each material was tested at least twice. The procedure involved firing pulses into each sample while recording various signals and visually monitoring damage spark occurrence as the pulse power was brought up through the threshold level. The sample was moved between shots so that each pulse sampled a new volume element. Coordinates of each probed site in the crystal were recorde and later a high-power microscopic examination was performed to verify uncertain sightings. The reproducibility of the data when probing different specimens and different volume elements in a single specimen indicates that a property characteristic of the bulk material is observed. Typically 50 shots were used with each lens. The data were then plotted as shown in figure 4, an example of KCl. The sharpness of the threshold is typical of the behavior encountered in these experiments. The observed uncertainty in the breakdown threshold field was less than or equal to the experimental uncertainty of ± 15%. Data from such graphs were then plotted as shown in figure 5, for this same material. The desired quantities are extracted as discussed above.

3. Breakdown Threshold Results

First let us consider the pulse duration dependence of the breakdown field in NaCl at 1.06 μm. Figure 6 displays measurements at four pulse durations made by other investigators and the measurement made in the present study at 30 psec. The solid curve in figure 6 is the result of an approximate theoretical calculation discussed in [5]. The present work verifies the behavior of the threshold in the picosecond region, and in addition, makes available similar data for five other alkali-halides, as shown. The reciprocal pulse duration can be related to the avalanche ionization rate as will be discussed later.

Next, let us examine the variation of the 1.06 μm breakdown threshold for picosecond pulses across the periodic table. Our results are presented in table 1. We have tested 14 materials: 9 alkal halides and 5 other materials of optical importance. The threshold field varies by a factor of over 6, from 3.4 MV/cm for RBl to 22.3 MV/cm for KDP. The latter value is so high as to approach the value thought necessary to induce multiphoton ionization [6]. Figure 7 displays the trend of the normalized thresholds across the periodic table. Previous data from DC [7], and Q-switched CO_2 [8], ruby [9], and Nd:YAG [10] laser damage studies are presented for comparison. Note that all the data from a single experiment are normalized to the NaCl threshold of that same data set. The systematic variation throughout the alkali-halides is the result of the systematic variation of the parameters of the avalanche: the band gap, phonon densities of states, and the deformation potential. The similar chemical dependence of the DC and optical thresholds is a compelling statement in favor of the intrinsic avalanche ionization nature of the data.

Table 1. Rms breakdown electric field strengths (E_b uncertainty, ± 15%; field ratio uncertainty, ± 10%).

	NaF	NaCl	NaBr	KF	KCl	KBr	KI
E_b(MV/cm)	10.77	7.34	5.67	8.34	5.86	5.33	5.87
E_b/E_b^{NaCl}	1.47	1.00	0.77	1.14	0.08	0.73	0.80
	LiF	RbI	ED-4 glass	YAG:Nd	Fused SiO_2	CaF_2	KDP
E_b(MV/cm)	12.24	3.40	9.90	9.82	11.68	14.44	22.28
E_b/E_b^{NaCl}	1.67	0.46	1.35	1.34	1.59	1.97	3.04

4. Nonlinear Refractive Index Results

For the breakdown measurements that we performed at 1.06 μm, the input power was typically a few tenths (but never greater than 0.9) of the critical power, P_{cr}. Due to the λ^2 dependence of P_{cr}, it is clear that accurate measurements of P_{cr} are of increasing importance to breakdown experiments for $\lambda < 1.06$ μm, which we are undertaking presently. We have measured n_2 for 12 materials and the data are presented in table 2. Due to our experimental conditions that the laser pulse duration is much shorter than the electrostrictive response time ($\sim 10^{-9}$ sec), and that the materials tested are ionic solids, our n_2 values are of electronic origin only. Values of n_2 obtained by others with different techniques and from theory are listed for comparison. The smallest value of n_2 we measured was that of NaF, a factor of 15 less than that of KBr. Agreement with the measurements of others is reasonable in almost all cases (LiF excepted), considering the rather large experimental uncertainties listed. The expected chemical-dependence in the alkali-halides is observed.

Table 2. Measured values of nonlinear refractive index (in units of 10^{-13} esu).

Mat'l	Present Work	Other Work							
		Experiment[a]						Theory[b]	
		I	II	III	IV	V	VI	I	II
	± 50%	± 300%	± 20%	± ~20%	± 7%	± 20%	± 10%		
NaBr	9.6								
NaCl	6.5	3.0	4.2					2.0	4.9
NaF	0.95	0.71						0.37	0.86
KI	11.2							7.1	20.7
KBr	14.2	6.8	7.3					3.2	9.0
KCl	3.3	3.1	4.8					2.3	4.8
LiF	2.4	0.82	0.54	0.92				0.76	0.82
CaF_2	2.8		0.92	1.13				1.1	1.1
SiO_2	1.4		1.8	1.82	1.00			3.6	2.9
KDP	3.6								
ED-4	2.1			2.60	1.73				
YAG:Nd[c]	3.5			4.51	4.10	3.16	3.47		

[a] I. Values from third-harmonic generation, Wang and Baardsen [11];
II. Values from three-wave mixing, Maker and Terhune [12];
III. Values from three-wave mixing, Levenson and Bloembergen [13];
IV. Values from intensity-dependent ellipse rotation, Owyoung [14];
V. Value from time-resolved interferometry, Bliss et al., [15];
VI. Value from time-resolved interferometry, Moren et al., [16].

[b] I. Calculated from generalized Miller's rule, Wang [17].
II. Calculated from Wang's rule, Wang [17].

[c] All experimental values in this row, with one exception, are for pulse propagation along a [111] direction, as in the usual laser rod configuration; in these cases the measured nonlinear susceptibility is

$$\frac{1}{2}\left(\chi^{(3)}_{1111} + \chi^{(3)}_{1221} + 2\chi^{(3)}_{1122}\right) .$$

The value in the column designated III is for the single element $\chi^{(3)}_{1111}$, however. The present work investigated a YAG:Nd crystal; all other values in the row pertain to undoped YAG crystal.

5. Damage Morphology

To date, not a great deal of use has been made of bulk damage morphology for obtaining data on damaging processes themselves, except in the area of inclusion damage. Early workers were quick to recognize inclusion damage by its vestige of specks randomly placed in the focal volume.

Regarding the needle-like tracks of more intrinsic origin, however, the morphology has been employed only as a simple yes-or-no indicator of the occurrence of damage. One reason for this situation is that a great degree of control and calibration of the laser source is necessary to produce damage very close to threshold. Precise control in prior years was not always achievable for reasons such as (even slight) mode beating. Damage tracks from TEA CO_2 laser pulses are of large (~ .5 mm) dimension even at threshold, due to plasma absorption of the energy in the long trailing edge of the TEA pulse. Information about the plasma growth mechanism is therefore obscured or lost by the severe disruption of the focal region.

An intriguing question is whether it is possible to capture information about plasma growth inside a solid material by allowing it to develop only through early stages, and not to the point of

excessive disruptive heating. Current estimates of the density of free or slightly bound electrons which may act as nucleation centers for the avalanche process are in the 10^8 - 10^{10} per cm^3 range [6]. Larger values due to bleachable F-center concentrations have been discussed [18]. If we assume a starting center density of $10^{12}/cm^3$, say, then we obtain a linear density ℓ^{-1} of one nucleation center per micron. Should an avalanche begin from such a center, it would need to produce a light scattering region of roughly 5000 Å ≡ d' diameter in order to be observed microscopically. If we use

$$d(t) = 2r(t) = 2\sqrt{4Dt} \tag{6}$$

as a simple random-walk spatial growth estimate, then we require

$$5 \times 10^{-5} \text{ cm} \sim d' \leq d \leq \ell \sim 10^{-4} \text{ cm} \tag{7}$$

in order for the individual microplasma remnants to be observable.

Using $D \sim 1$ to 10 cm^2-sec^{-1} under high electric fields [19], we conclude that for a pulse duration of a few tens of picoseconds, we perhaps would be able to see microscopically the vestiges of individual, resolved microplasmas. From such data we should be able to extract information regarding the actual density of starting sites, spatial and temporal plasma growth, etc.

Figure 8 is a high-resolution optical photomicrograph of a damage track produced in NaCl. The damaging pulse had a maximum electric field at the focal point, E_f, of 8.7 MV/cm, 18% greater than the measured threshold field of 7.3 MV/cm for NaCl. The total power in this pulse was 86.3 kW. It was focussed by a 1/2" focal length lens. The pulse propagation direction is from left to right. The photograph was taken with blue light using a Leitz Ortholux microscope with a 0.4 N.A. objective and 340 power total magnification. The calculated resolution (.61 λ/N.A.) is ~ 0.7 μm. The scale lines on the figure are 10 μm apart, and were transferred to this photograph from one of an objective micrometer which was made under identical magnification conditions.

One observes in the figure discrete specks, which are the vestiges of microplasmas resulting from avalanche ionization. We believe that each of the microspots originated from a single electron. From the linear density of microspots, one obtains a volume density of nucleation centers of about 2×10^{11} cm^{-3}, which is consistent with the estimates mentioned earlier. To our knowledge, this measurement technique represents the only way to determine the actual density of avalanche nucleation centers in a material. This density will, of course, be a function of incident pulse intensity and frequency [18].

The next feature of the damage track to be discussed is the diameter of the microspots. The largest diameter in figure 8 is about 1.5 μm; the smallest measurable diameter, limited by microscopic resolving power, is about 0.5 μm. We have not attempted a detailed calculation for an expected diameter. Several difficulties would beset such a program. In general, the same set of difficulties that at present prevent detailed calculations of other aspects of avalanche phenomena in solids also plagues this problem: incomplete knowledge of high-field collision rates, diffusion parameters, etc. In this preliminary report we simply note that the observed average diameter of about 1.0 μm is in agreement with the very crude diffusion model estimate of $2\sqrt{4Dt} \approx 0.8$ μm, taking 10 cm^2/sec for the diffusion coefficient and 38.7 psec, the 1/e duration of the intensity, for the diffusion duration.

The last feature of figure 8 to be discussed is the perimeter of the track. The results of several calculations, using the parameters of the pulse that produced the damage track of figure 8, are shown in figure 9. In this figure the point $z = r = 0$ corresponds to the focal point in the NaCl material. Distance away from the focal point in the laser pulse propagation direction is plotted on the horizontal axis, and distance away from the focal point, in the plane normal to the propagation axis, is plotted along the vertical axis. Therefore, the plane of figure 9 is also that of figure 8, but with modified z and r scales. Isothermal curves for a temperature of 1000°C are plotted for three heating mechanisms: joule heating by avalanche produced electrons, and metallic inclusion heating from spherical inclusions of two different radii a. The dashed curve is the actual damage track perimeter from figure 8.

The isotherms for inclusion heating cases are derived from work of Sparks and Duthler [20]. The curve designated by a = 100 Å represents a cross section of a three-dimensional surface, within which any sodium inclusions of radius 100 Å would heat the surrounding NaCl to a temperature of 1000°C. The calculation was performed using thermal and optical parameters of Na as the inclusion material, although the results would not differ greatly for other metals (Al, Ca, Fe, Mg, Cu) which are possible impurities in NaCl [21]. All temperature dependence of the thermal parameters was neglected. In the case of a 100 Å inclusion radius, the radius is of the order of magnitude as the 1.06μm absorption depth of ~ 150 Å in Na, and smaller than the radiation wavelength in the host. Therefore, a model assuming uniform heat generation within the inclusion is an appropriate approximation, and results in an inclusion temperature rise above ambient temperature [20] of

$$T_1 = \frac{3\sigma I t}{4\pi a^3 C_I}. \tag{8}$$

Here I is the incident laser intensity; t represents elapsed time from the beginning of the laser pulse at t = 0 when the temperature is taken as 0°C. C_I is the heat capacity per unit volume of Na

(1.23 J/cm^3 °C). The absorption cross section σ is derived from Mie scattering theory and is given by

$$\sigma = \frac{12\pi n_H^3 \omega^2 \Gamma a^3}{c\omega_p^2} \quad , \tag{9}$$

for metals with $2\pi n_H a/\lambda \ll 1$. In the above expressions c is the vacuum speed of light, n_H is the linear index of refraction of the host, λ is the vacuum wavelength, ω is laser angular frequency, ω_p is the Na plasma frequency ($\sim 9\times10^{15}$ sec^{-1} [22]). Γ is the electron relaxation frequency which is approximately 1.3×10^{14} sec^{-1} for an Na particle of 100 Å radius [20]. For the purpose of the inclusion heating calculations, the laser temporal profile was taken to be a square wave having duration equal to the 1/e duration of the actual intensity profile (2τ = 39.7 psec for the track under discussion) and having intensity equal to the actual peak intensity. Using the above expressions and that for the electric field in the focal region, one arrives at an equation for the temperature attained by an inclusion located at some point (r, z) in the focal volume:

$$T_1 = \frac{18 n_H^4 \epsilon_0 \tau \omega^2 \Gamma E_f^2 e^{-\{r^2/[\rho^2(1-PP_{cr}^{-1})(1+z^2 z_{RE}^{-2})]\}}}{C_I \omega_p^2 (1+z^2 z_{RE}^{-2})} \tag{10}$$

In this equation ϵ_0 is the free space permittivity, E_f is the maximum rms electric field at the focal point, ρ is the intensity 1/e spatial radius in the focal plane (3.3 μm), and z_{RE} is the focal Rayleigh distance of $2\pi\rho^2 n_H/\lambda$ for the electric field (98.5 μm). The curve in figure 9 for a = 100 Å was found by setting T_1 in eq. (10) equal to 1000°C and solving for r as a function of z. The melting temperature of NaCl and Na is 800°C. This curve, for a = 100 Å, is for the most easily damaging inclusion size for our experimental conditions [20].

The curve designated by a = 1000 Å in figure 9 was computed in a similar manner. However, because the radius a exceeds the skin depth, a model assuming a delta function source heating a slab of metal was employed. The quantity Γ is 5×10^{13} sec^{-1} in this case [20]. The equations for the case of a = 1000 Å which correspond to eqs. (9) and (10) are

$$T_2 = \frac{\sigma I t^{1/2}}{2\pi^{3/2} a^2 ((C_H K_H^{1/2} + (C_I K_I)^{1/2}} \quad , \tag{11}$$

and

$$T_2 = \frac{6\sqrt{2\tau}\, n_H^4 \epsilon_0 \omega^2 \Gamma E_f^2 e^{-\{r^2/[\rho^2(1-PP_{cr}^{-1})(1+z^2 z_{RE}^{-2})]\}}}{\pi^{1/2} \omega_p^2 ((C_H K_H)^{1/2} + (C_I K_I)^{1/2})(1+z^2 z_{RE}^{-2})} . \tag{12}$$

In the above equations C_H is the host heat capacity per unit volume (1.85 J/cm^3 °C) and K_I (1.34W/cm °C) and K_H (0.065W/cm °C) are the thermal conductivity of the inclusion and NaCl host, respectively. Equation (12) was likewise set equal to 1000°C and solved for r as a function of z to produce the curve for a = 1000 Å in figure 9.

The curve identified by avalanche ionization in figure 9 is from a calculation given by

$$T_3 = \frac{e^2 \tau E_f^2 e^{-\{r^2/[\rho^2(1-PP_{cr}^{-1})(1+z^2 z_{RE}^{-2})]\}}}{C_H m(1+\omega^2\tau_r^2)(1+z^2 z_{RE}^{-2})} \int_{-\infty}^{\infty} N(t')\, e^{-(t'/\tau)^2}\, dt' \quad , \tag{13}$$

where the number of electrons per unit volume is

$$N(t) = N_0 \int_{-\infty}^{t} e^{\eta\{E(t')\}}\, dt' \, . \tag{14}$$

The ionization rate $\eta\{E(t)\}$ above was obtained from the data in figure 6. The ionization rate is related to the pulse duration τ_{FWHM} by $\eta = 18\,\tau_{FWHM}^{-1}$, as discussed in [5]. For the numerical integration of eq. (13), $\eta\{E(t)\}$ was represented by the function

$$\text{Log}\ \eta\{E(t)\} = 3.97\ (\text{Log}\ E) - 15.62 \quad , \tag{15}$$

which fits the experimental data well for E between 1.0 and 9.0 MV/cm. In eq. (13), m and e are the electron mass and charge, and τ_r is the effective momentum-change relaxation time (taken here to be ω^{-1} [6]). The quantity N_0 in eq. (14) has before been taken to be the initial number of free or almost free electrons per unit volume, in a continuum approximation, and was found earlier from figure 8 to be about 2×10^{11} cm^{-3}. However, in light of the new data of figure 8 showing discrete microplasma structure, it is useful to interpret N_0 differently. The average volume of the single microspots in figure 8 is about 10^{-12} cm^3. Therefore, if we consider all the energy absorbed by the microplasma to be deposited into that volume of NaCl, neglecting all heat loss processes into the surrounding NaCl, then the temperature reached by that NaCl sphere is given by eq. (13). In this spirit, N_0 was given the value 10^{12} cm^{-3} in the computation for the avalanche ionization isotherm. That isotherm was produced by a numerical integration over time of eq. (13), at various values of the coordinates (r, z).

The agreement between the observed damage perimeter and the calculated avalanche ionization perimeter for a temperature rise of 1000°C is quite good, both in shape and extent. The two inclusion isotherms predict that any metallic inclusion of the appropriate size within the designated curve should have been melted along with the surrounding NaCl, and, therefore, should have produced a microscopically observable signature. However, in only one track in fifty in this sample was a speck sighted far outside the avalanche ionization curve. This observed fact, and the additional observed fact that the illustrated damage track appearance was observed in all the tested materials, lead us to believe that inclusion effects in these experiments are negligible. Certainly crystal imperfections in the form of inclusions with dimension of a few angstroms up to perhaps 1000 Å exist. Nevertheless, these experiments imply that their densities are small enough that their role is of no significance greater than perhaps as shallow traps for initial electrons.

6. Picosecond Breakdown at 0.53μm

Preliminary breakdown experiments have been performed at 0.532μm with picosecond pulses obtained by harmonic generation. The tested materials were LiF, NaF, NaCl, KCl, KBr, KDP CaF_2 and fused quartz. A great difficulty inherent in this experiment is the effect of self-focusing on the focal area. Analysis of the data has only begun. However, it appears certain that the breakdown thresholds at 0.532μm exceed those at 1.06μm, by a factor larger than that due to pulse duration dependence of the threshold alone. In terms of the familiar qualitative expression for the frequency dependence of the threshold [6],

$$E(\omega) = \sqrt{1 + \omega^2 \tau_r^2}\ E_{DC}\ , \tag{16}$$

it appears that at 0.532μm the breakdown threshold departs measurably from the DC limit. These remarks will be made quantitative in the near future. The threshold increase for the doubled frequency implies that multiphoton ionization does not take a dominant role in the 0.532μm damage, as that effect would produce decrease in the threshold. It is possible that multiphoton ionization plays an initial role in the avalanche process which goes undetected due to the avalanche process becoming dominant after the first electrons are produced [18]. The damage morphology at 0.532μm exhibits the same features as the 1.064μm morphology.

7. Summary

Dielectric breakdown threshold measurements have been presented for 14 transparent solids. The measurements were made with single, 30 psec average FWHM duration, 1.064μm laser pulses, in a manner which corrects for the effects of self-focusing. The threshold values are those of an avalanche ionization process. Nonlinear refractive index measurements, also obtained in the breakdown experiments, were presented. Photographic data from a microscopic study of the damage tracks in NaCl was presented. Information from this data regarding the number of initiation sites for plasma growth, approximately 10^{12} per cm^3 in the investigated sample, was discussed. The damage perimeter was also shown to indicate that avalanche ionization is the damage mechanism.

8. Acknowledgments

The authors are grateful to Patrick Heck of Owens-Illinois, Inc., for supplying a sample of ED-4 glass, and to S. Maurici for his skillful sample preparation. Helpful discussions with Prof. Eli Yablonovitch of Harvard are most appreciated. The authors are indebted to Prof. Lance Taylor of Harvard for his generous loan of photomicrographic equipment and collaboration.

*Research supported in part by the National Aeronautics and Space Administration (under contract NGR-22-007-117) and by the Joint Services Electronics Program (under contract N00014-67-A-0298-0006).

9. References

[1] A detailed account of the experiment reported here, except for material concerning damage morphology, is to be published in the Physical Review B-15, July (1975).

[2] G.M. Zverev and V.A. Pashkov, Zh. Eksp. Teor. Fiz. 57, 1128 (1969) [Sov. Phys. - JETP 30, 616 (1970)].

[3] D.W. Fradin, IEEE J. Quantum Electron. QE-9, 954 (1973). Note that Eq. (2) in this reference should read $l_d = I_0(1-P/P_{cr})^{-1}$.

[4] W.L. Smith and J.H. Bechtel, submitted for publication in J. App. Phys. The proportionality expressed by Eq. (5) was noted by M.J. Brienza [Appl. Phys. Lett. 10, 221 (1967)] and used by C.V. Shank and E.P. Ippen [Appl. Phys. Lett. 24, 373 (1974)] in conjunction with a cw mode-locked dye laser.

[5] D.W. Fradin, N. Bloembergen, and J.P. Letellier, Appl. Phys. Lett. 22, 635 (1973).

[6] N. Bloembergen, IEEE, J. Quant. Elect. QE-10, 375 (1974).

[7] A. von Hippel, J. Appl. Phys. 8, 815 (1937).

[8] E. Yablonovitch, Appl. Phys. Lett. 19, 495 (1971).

[9] D.W. Fradin and M. Bass, Appl. Phys. Lett. 22, 206 (1973).

[10] D.W. Fradin, E. Yablonovitch, and M. Bass, Appl. Opt. 12, 700 (1973).

[11] C.C. Wang and E.L. Baardsen, Phys. Rev. 185, 1079 (1969), and Phys. Rev. B1, 2827 (1970).

[12] P.D. Maker and R.W. Terhune, Phys. Rev. 137, A801 (1965).

[13] M.D. Levenson, IEEE, J. Quant. Elect. QE-10, 110 (1074), and M.D. Levenson and N. Bloembergen, Phys. Rev. B10, 4447 (1974).

[14] A. Owyoung, IEEE, J. Quant. Elect. QE-9, 1064 (1973).

[15] E.S. Bliss, D.R. Speck and W.W. Simmons, Appl. Phys. Lett. 25, 728 (1974).

[16] M.J. Moran, C. She, and R.L. Carman, IEEE, J. Quant. Electron QE-11, 259 (1975).

[17] C.C. Wang, Phys. Rev. B2, 2045 (1970).

[18] P. Bräunlich, A. Schmid, and P. Kelly, Appl. Phys. Lett. 26, 150 (1975).

[19] F. Seitz, Phys. Rev. 76, 1376 (1949).

[20] M. Sparks and C.J. Duthler, J. Appl. Phys. 44, 3038 (1973).

[21] Personal communication with D. Cope, Harshaw Chemical Co., Solon, Ohio.

[22] C. Kittel, "Introduction to Solid State Physics," 4th ed. (John Wiley and Sons, New York, 1971).

10. Figures

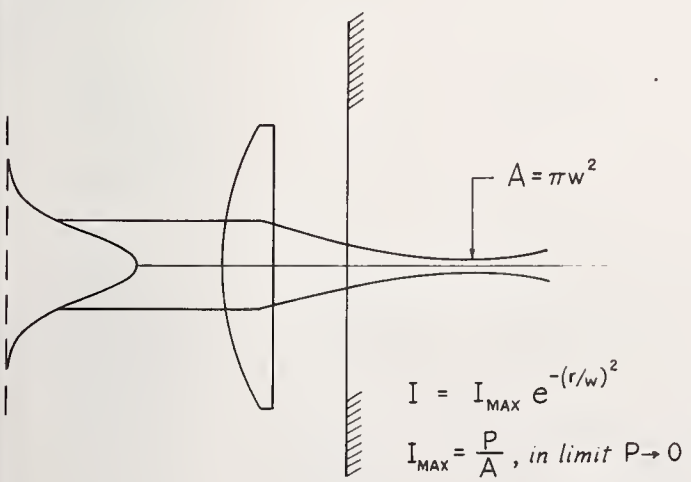

Figure 1. Illustration of the external focusing of a Gaussian laser pulse into a medium.

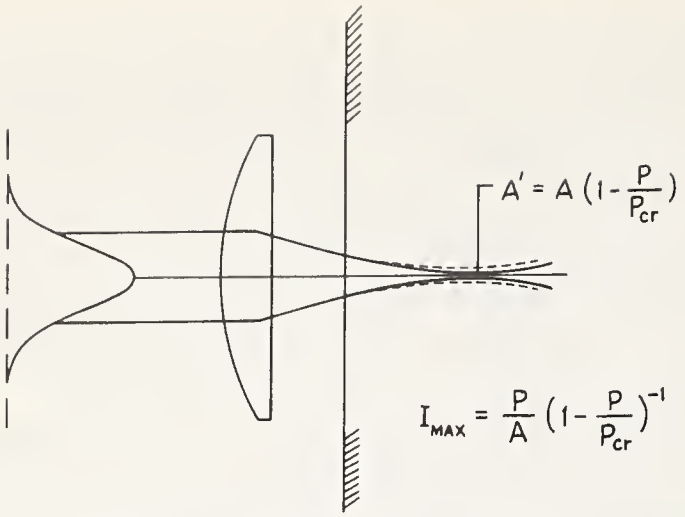

Figure 2. Illustration of the external focusing into a material of a Gaussian laser pulse having power P that is nonnegligible compared to P_{cr}. Self-focusing reduces the focal area from A to A', thereby increasing I_{max}.

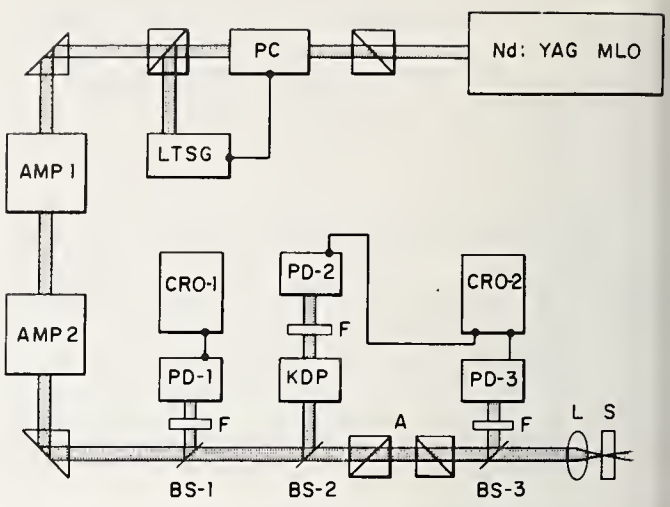

Figure 3. Schematic diagram of the experimental arrangement. MLO, mode-locked Nd:YAG oscillator; PC, Pockels cell; LTSG, laser-triggered spark gap; AMP, Nd:YAG amplifier; BS, beam splitter; F, filter PD, biplanar photodiode; CRO, oscilloscope; KDP, second-harmonic generation crystal; A, double Glan-prism variable attenuator, L, focusing lens; S, dielectric sample.

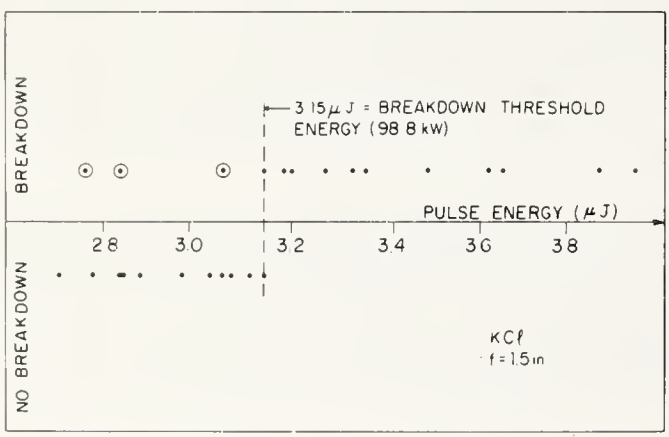

Figure 4. Results of breakdown experiment in KCL for f = 1.5" lens. The three circled points resulted from atypically short pulses.

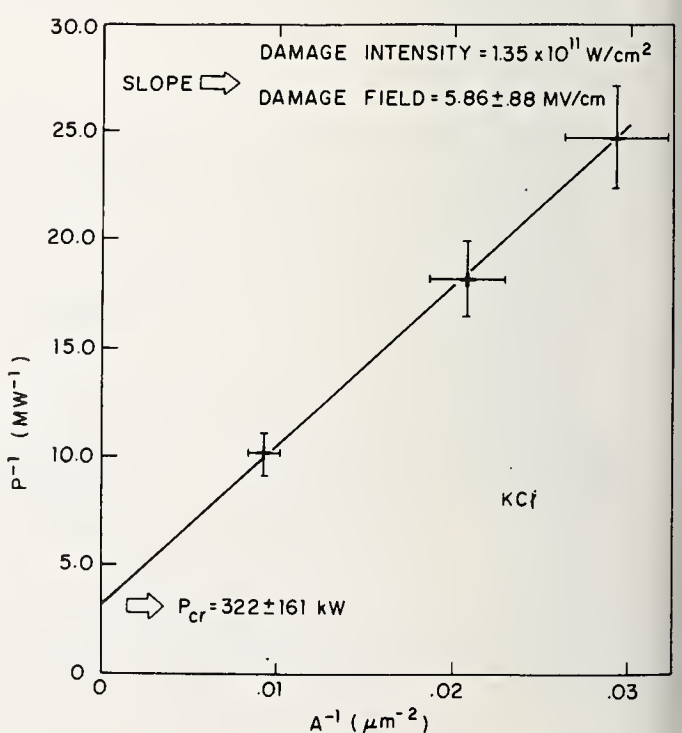

Figure 5. Results of breakdown experiments in KCl for three lenses. The solid line is a least-squares fit to the data. The slope equals the reciprocal threshold breakdown intensity and the vertical-axis intercept equals the reciprocal critical power for self-focusing.

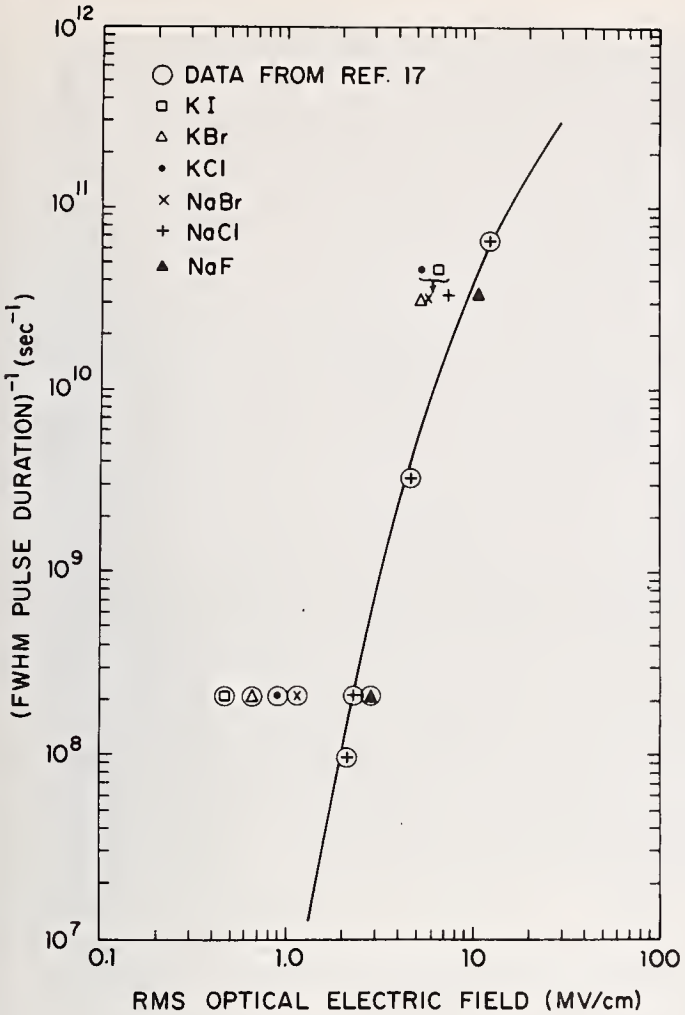

Figure 6. Functional relationship between the breakdown threshold electric field strength and the pulse duration. The solid curve is a semiempirical prediction for NaCl, discussed in [5].

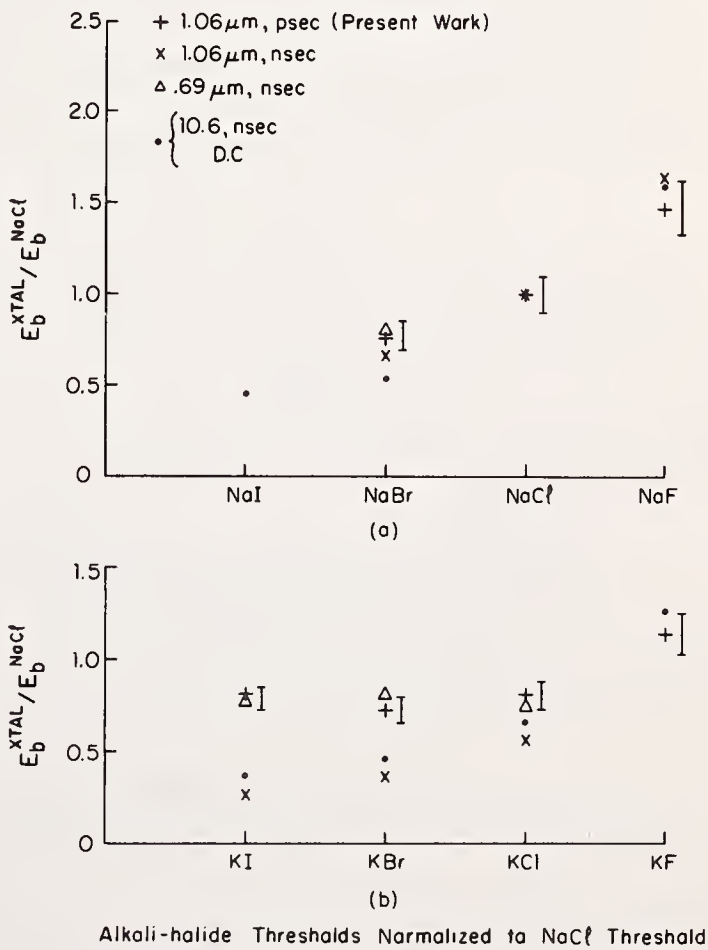

Figure 7. Experimental trend of the breakdown field through a) the Na-halides and b) the K-halides. Shown for comparison is data from previous studies: (x), [10]; (Δ), [9]; (•), dc data from [7], 10.6 μm data from [8]. In the figure, nsec denotes a pulse duration on the order of nanoseconds, and psec, picoseconds. Each set of data is normalized to the field for NaCl of that same data set. Error bars for the present work are shown displaced to the right.

Figure 8. Photomicrograph of a damage track in NaCl produced by a 32.2 psec (FWHM), 1.06 μm, 86.3 kW laser pulse. The pulse was focused to a 1/e intensity diameter in the focal plane of 6.6 μm. The maximum rms electric field reached at the focal point was 8.7 MV/cm, 18% above the threshold field. The pulse propagation direction is from left to right. The scale marks are spaced by a distance of 10.0 μm.

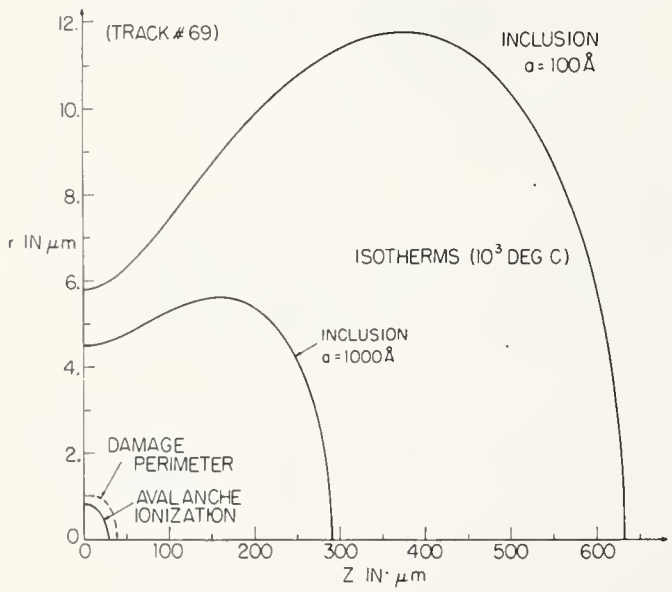

Figure 9. Calculated isothermal curves for three possible heating mechanisms for the damage track shown in figure 8. The z axis is laser propagation axis; the point z = r = 0.0 is the focal point. The actual damage perimeter is indicated by the dashed curve.

COMMENTS ON PAPER BY SMITH, et al

(See comments on paper by Sparks, which follows)

6.2 Current Status of Electron-Avalanche-Breakdown Theories*

M. Sparks

Xonics, Incorporated, Van Nuys, California 91406

Evidence is presented that current theories of electron-avalanche breakdown in dielectrics are inadequate to explain existing data or to be predictive. Specific difficulties include the following: (1) The theoretical value of the ionization frequencies are too small, by tens of orders of magnitude in some cases, to explain the experimental damage results even when the large initial conduction electron densities in (4) below are assumed. (2) The theoretical result for the frequency dependence of the breakdown electric field $E_B \sim (1 + \omega^2\tau^2)^{1/2}$ disagrees with experimental results. The explanation in terms of an anomalously small electron relaxation frequency is inconsistent with the value of τ required to explain the magnitude of E_B, with calculated values of τ (by two orders of magnitude), and with the difference between the dc and 10.6 μm experimental values of E_B. (3) The temperature dependence of E_B is incorrect. (4) The assumed value of the electron density $n_c = 10^8$-10^{10} cm^{-3} required to initiate the avalanche is in conflict with results of photoconductivity measurements. Bounds on n_c set by estimates of the value of the electronic conductivity indicate that the probability of finding an electron in the focal volume during the pulse is less than 10^{-6}, possibly much less, in some cases. (5) The theories are not predictive. Tentative new theoretical results hold promise of explaining existing experiments and being predictive.

Key words: Electron-avalanche breakdown; dielectrics; frequency dependence; magnitude.

1. Introduction

The motivation for the study of electron-avalanche breakdown was an attempt to predict the magnitude of the breakdown electric field, E_B, and its temperature and frequency dependence and to predict whether the effect would be intrinsic or extrinsic, all in the vacuum-ultraviolet region. It was found that current theories could not afford this information. The rather serious problems with current theories are discussed, and a tentative theory of avalanche breakdown that appears to alleviate the difficulties is presented briefly.

The practical importance of breakdown in limiting the performance of material in numerous applications and fundamental interest in the subject have stimulated enormous interest in electrical breakdown in dielectrics. The laser studies of avalanche breakdown in the last five years have supplied invaluable new experimental data. No attempt is made to review the literature on electron-avalanche breakdown, which extends from the early studies of A. von Hippel [1][1] in 1931 to the present. In fact, in the first volume of Annalen der Physik in 1799, A. Van Marum [2] reported the laboratory observation of electrical breakdown in glass. There are a number of textbooks and reviews. The newer of J. J. O'Dwyer's [3] books, the reviews by N. Bloembergen [4] and N. Klein [5], and the report by D. Fradin [6] should lead the reader into the literature.

At least part of an apparent disagreement in the literature and among investigators in the field as to how good the current theories of electrical breakdown in solids are, stems from what is expected of the theory. If the goal of the theory is to explain the magnitude of the breakdown field, E_B, within an order of magnitude or so, then any one of many theories that have been proposed will suffice. This is, in fact, to be expected since small changes

*This research was supported by the Advanced Research Projects Agency of the Department of Defense and was monitored by the Defense Supply Service, Washington, D. C.

[1]Figures in brackets indicate the literature references at the end of this paper.

in the value of the electric field give rise to large changes in the values of the physical quantities of interest, such as the ionization frequency. The electric field appears in an exponent in most theories, and even a factor-of-two change in E can change the probability for damage by tens of orders of magnitude in some cases. For example, see figure 2 in section 3. This situation is analogous to the fact that the value of the temperature must be known more accurately than within a factor of ten in most cases, as in thermal emission over a barrier or in the human environment, where a one percent change is large, a ten percent change is intolerable, and a factor of two is exocrematory.

If, on the other hand, the goal of the theory is to explain the magnitude of avalanche ionization frequency, ω_c, in the expression for the conduction-electron density, $n_c = n_{c0} \exp(\omega_c t)$, to within an order of magnitude at the observed value of E or to explain the dependence of E_B on the laser frequency ω, temperature T, laser-pulse duration t_p, or material parameters, or to be predictive, then current theories are inadequate. The problem is more serious than simply an inability to calculate the values of ω_c or E_B to within some required accuracy, as it was found in the early attempts to understand the existing experimental data that even in being overly generous with the values of all parameters, current theories still failed. If a theory cannot explain the experimental results to within the estimated errors of the experimental and theoretical results, the theory will be considered as unsatisfactory. A factor of three to ten difference in E_B is not sufficient.

2. The Avalanche Process

The simplest current explanation of electron-avalanche breakdown is as follows. In the presence of an electric field $\underset{\sim}{E}$ and electron-phonon collisions, an electron drifts in the direction of $\underset{\sim}{E}$ gaining energy $\mathcal{E}$ as it goes. The electron absorbs energy from the electric field, as illustrated schematically in figure 1a. The rate of energy gain from the field is given by the well known relation

$$\left(\frac{d\mathcal{E}}{dt}\right)_E = \frac{e^2 \tau_k E^2}{m(1+\omega^2 \tau_k^2)} , \qquad (2.1)$$

where ω is the frequency of the electric field and τ_k is the electron relaxation frequency for large-angle scattering. When the electron attains sufficient energy $\mathcal{E}_I$, it can excite another conduction across the electronic energy gap from the valence band. Repetition of this multiplication process continues to increase the number of electrons until breakdown occurs. Breakdown has been assumed to occur when this process increases the energy density, n_c, from an initial value of $10^8 - 10^{10}\ cm^{-3}$ to $10^{18}\ cm^{-3}$, as discussed at the end of section 3.

For the dc case illustrated in figure 1, electron-phonon collisions prevent the electron from accelerating very rapidly to high energies by changing its direction of travel every τ_k seconds on the average. If the electron were to go without suffering a collision for a long time, its energy would be increased more efficiently. Such a "lucky" event, shown at L in figure 1a, is discussed in section 6. Small-angle collisions are less effective in inhibiting the rapid build up of energy. However, both small-angle and large-angle collisions reduce the electron energy since phonons (having energies $\hbar\omega_q$) are excited in the scattering process. In figure 1, the build-up of energy impeded by the large-angle scattering and the energy loss, are visualized individually in the (a) and (b) parts of the figure. In passing, notice that the electron drift velocity $v_d = \mu E$, where $\mu = e\tau_k/m$ is the mobility, is determined by the increase in the component k_z of wave vector $\underset{\sim}{k}$ in the direction of $\underset{\sim}{E}$, which is related to the curvature of the trajectory in figure 1a.

The rate of loss of energy to the lattice phonons is

$$(d\mathcal{E}/dt)_L = \hbar\omega_p/\tau_L , \qquad (2.2)$$

where $\hbar\omega_p$ is an average phonon energy and τ_L is the time constant that includes small- and large-angle scattering. The time constants τ_k and τ_L are calculated in [7]. Equating (2.1) and (2.2) and solving for $E = E_{EL}$ gives the value

$$E_{EL} = \left(\frac{m\hbar\omega_p}{e^2} \frac{1 + \omega^2\tau_k^2}{\tau_k\tau_L} \right)^{1/2} \tag{2.3}$$

of E at which the net rate of change of $\mathcal{E}$ is zero. For $E > E_{EL}$, the electron gains energy on the average, and vice versa. If the electron gains energy on the average at each collision, it will accelerate until $\mathcal{E} = \mathcal{E}_1$. Thus, the simplest criterion for breakdown is that $E \geq E_B$ with

$$E_B = E_{EL} \quad . \tag{2.4}$$

The energy dependence of the relaxation frequencies will be considered in section 8. Values of E_B calculated from (2.4) and (2.3) typically are a factor of three to ten times greater than observed values. For example, at 1.06 μm with [7] $\tau_k = 1.36 \times 10^{-15}$ sec and $\tau_L = 8.77 \times 10^{-16}$ sec for sodium chloride at room temperature, (2.3) and (2.4) give

$$E_B = 9.0 \text{ MV/cm} ,$$

which is a factor of 4.3 times greater than the experimental value [6] of 2.1 MV/cm.

3. Ionization Frequency

Current theories do not explain the experimentally determined values of the ionization frequency ω_c, as will now be shown. The ionization frequency can be obtained from the model in section 2 by integrating

$$\frac{d\mathcal{E}}{dt} = \left(\frac{d\mathcal{E}}{dt}\right)_E - \left(\frac{d\mathcal{E}}{dt}\right)_L \quad , \tag{3.1}$$

for $\mathcal{E} = 0$ to $\mathcal{E}_I$, which corresponds to $t = 0$ to t_I, where t_I is the time required for the electron to gain energy $\mathcal{E}_I$ in the presence of the field and of phonon collisions. The values of $(d\mathcal{E}/dt)_E$ and $(d\mathcal{E}/dt)_L$ in (3.1) are given by (2.1) and (2.2). Assuming that τ_k and τ_L are constants, the integration gives

$$\mathcal{E}_I = \frac{e^2\tau_k}{m(1+\omega^2\tau_k^2)} (E^2 - E_{EL}^2) t_I \quad . \tag{3.2}$$

Since the number of conduction electrons doubles every t_I seconds, n_c is equal to

$$n_c = n_{c0}(2)^{t_p/t_I} \quad ,$$

which can be written as

$$n_c = n_{c0} e^{\omega_c t_p} \quad , \tag{3.3}$$

with

$$\omega_c = 0.693 \frac{\hbar\omega_p}{\mathcal{E}_I \tau_L} \frac{E^2 - E_{EL}^2}{E_{EL}^2} \quad , \qquad \text{for } E > E_{EL} \ , \tag{3.4}$$

and $\omega_c = 0$ for $E < E_{EL}$. For [7] $\hbar\omega_p = 1/40$ eV, $\mathcal{E}_I = 8$ eV, $\tau_L = 8.77 \times 10^{-16}$ sec, $\tau_k = 1.36 \times 10^{-15}$ sec (see figure 5 below), and $\lambda = 1.06\,\mu$m, (2.3) gives $E_{EL} = 9.04$ MV/cm. With these values and $E = 1.1\, E_{EL}$, (3.4) gives $\omega_c = 5.19 \times 10^{11}$ sec^{-1}. The agreement with experiment is poor, as illustrated in figure 2 and discussed below.

In comparing the result (3.4) for ω_c with experimental results of the dependence of E_B on the laser-pulse duration t_p, the relation between ω_c and t_p is needed. This is commonly obtained [6] by assuming that n_c is increased from an initial value of 10^8–10^{10} cm^{-3} to a final value of 10^{18} cm^{-3}, as already mentioned. Taking the logarithm of (3.3) with $n_{c0} = 10^9$ cm^{-3} and $n_c(t_p) = 10^{18}$ cm^{-1} gives the required expression

$$\omega_c = t_p^{-1} \ln (n_c / n_{c0}) \cong 20.7\, t_p^{-1} \ . \tag{3.5}$$

The experimental values [6] of t_p^{-1} for sodium chloride at room temperature and 1.06 μm are shown in figure 2. The dc results, which will be discussed in section 6, are included here for comparison with the 1.06 μm results. The theoretical result for t_p^{-1} from (3.4) and (3.5) is plotted as a solid curve. The theoretical results of Holway and Fradin [8] obtained from a numerical solution of a transport equation, with one parameter adjusted, also are shown on figure 2. The agreement between experiment and either theory is poor. At $E_B \cong 2$ MV/cm, (3.4) gives $t_p^{-1} = 0$, compared with the experimental value of $\sim 10^8$ sec^{-1}. Extrapolating the Holway-Fradin curve to $E = 2$ MV/cm (which surely gives an inaccurate value for such a great extrapolation) gives a value of t_p^{-1} that is 18 orders of magnitude smaller than the experimental value. The relatively smaller factor of ~ 3.7 between the lowest experimental point and the theoretical curve illustrates the assertion made in section 1, that order-of-magnitude accuracy in the value of E_B is very weak testimony at best for the validity of a theory of avalanche breakdown. It is perhaps worth mentioning that ω_c appears in an exponent, and a factor of 10^{18} error in ω_c makes a factor of

$$(10^9)^{10^{18}}$$

error in n_c.

Finally, consider the criterion for damage. The one used above [6]

$$n_c / n_{c0} = 10^9 \tag{3.6}$$

is one of the commonly used criteria. Seitz [9] introduced the "40 generation" criterion in which an electron starting at the cathode must undergo 40 multiplications before reaching the anode. This corresponds to

$$n_c / n_{c0} = (2)^{40}$$

on the average. With

$$(2)^{30} = 10^9 \ ,$$

the criterion (3.6) corresponds to 30 generations during the laser-pulse duration. Another commonly used criterion [5, 10, 11] is that the sample temperature must be raised to the melting temperature. There are many other possible criteria, some of which are discussed in [7].

4. Frequency Dependence of the Breakdown Field

It will be shown in this section that current theories give a much stronger frequency dependence of E_B than observed experimentally. It is currently believed that the frequency dependence of E_B should be given by

$$E_B \sim (1 + \omega^2 \tau_k^2)^{1/2} , \tag{4.1}$$

which follows from (2.4) and (2.3). The increase in the value of E_B from the first 10.6 μm laser experiments over the dc values was attributed to this frequency factor in (4.1). It was then surprising that there was little additional increase in E_B, first at 1.06 μm, then at 0.694 μm.

At $\lambda = 0.694$ μm, the value of $1/\omega$ is 3.69×10^{-16} sec. According to (4.1) and the experimental result that E_B changes little between 10.6, 1.06, and 0.694 μm, the value of τ would have to satisfy

$$\tau_k < 2.10 \times 10^{-16} \text{ sec} \tag{4.2}$$

(even for a 15-percent increase in E_B from 10.6 to 0.694 μm) for values of $\mathcal{E}$ between ~1/40 eV and ~8 eV. It is extremely unlikely that τ_k is this small. The calculations in [7] indicate that τ_k is an order-of-magnitude greater than 2×10^{-16} sec for all values of $\mathcal{E}$ on this range, and that τ_k is two orders of magnitude greater than the value in (4.2) at $\mathcal{E} \cong 8$ eV. See figure 5 below.

Furthermore, the values of τ_k required to explain the observed values of E_B are inconsistent with (4.2). At 10.6 μm, the experimental value of E_B is [12] 1.95 MV/cm for NaCl. From (2.4) and (2.3) with $\tau_k = \tau_L$ and $\hbar\omega_p = 1/40$ eV, the value of τ_k required to give this experimental value of E_B is

$$\tau_k = 2.00 \times 10^{-15} \text{ sec}^{-1} . \tag{4.3}$$

The frequency dependence of E_B calculated from (2.3) with this value of τ_k is in poor agreement with experiment, as seen in figure 3. For example, even though the theoretical curve was fit to the experimental result at 10.6 μm, the theoretical value of $E_B = 11.1$ MW/cm at 0.694 μm is much greater than the experimental value of 2.3 MV/cm. If the difference between τ_k and τ_L is included, the agreement is even poorer. Including the energy dependence of τ_k and τ_L makes little difference in this result.

5. Initial Electron Density

In this section it will be shown that the initial density of conduction electrons is so small that the probability of finding an electron in a typical focal volume is much less than unity. This is in disagreement with current theories, in which the initial density of electrons n_{c0} in (3.3) required to start the avalanche is usually assumed to have the value

$$n_{c0} = 10^8 - 10^{10} \text{ cm}^{-3} . \tag{5.1}$$

It is also assumed that the avalanche process must increase the value of n_c to 10^{18} cm^{-3}. From (3.3), the ionization frequency $\omega_c = t_p^{-1} \ell n (n_c / n_{c0})$ is rather weakly dependent on the initial electron density n_{c0}. With

$n_c = 10^{18}\,cm^{-1}$, changing the value of n_{c0} from $10^9\,cm^{-3}$ to $10^4\,cm^{-3}$ changes ω_c by 56 percent. However, there is the more serious problem with small electron densities that the probability of an electron being in the focal volume during the pulse becomes negligibly small for the small values of n_{c0}, as discussed below.

The assumed value of n_{c0} in (5.1) would at first appear to be a reasonable density, which could result from thermal ionization of impurity levels, for example. Under closer examination, this density is seen to be unreasonably large. First, with 10^8–10^{10} conduction electrons per cubic centimeter, previous observations of photocurrents would have been impossible.

It is not difficult to see why lower densities are expected. For F centers in sodium chloride for the best case of the chemical potential having the value $\frac{1}{2}\,\mathcal{E}_F$ (below the conduction band), where $\mathcal{E}_F \cong 2\,eV$ is the energy of the F center below the conduction band, the theoretical value of n_c at room temperature is [13]

$$n_c = (5 \times 10^{13}\, 2.41 \times 10^{19})^{1/2} \exp\left[-\tfrac{1}{2}(2)(40)\right]$$

$$= 10^{-1}\,cm^{-3}\ ,$$

which is negligibly small. The density $5 \times 10^{13}\,cm^{-3}$ of F centers is the greatest value the crystal can have without being colored, as shown in [7]. Shallower imperfection levels could contribute more electrons, but it is currently believed that there is not a sufficient density of shallow levels, and 10^8–$10^{10}\,cm^{-3}$ from shallow levels is inconsistent with photoconductivity experiments.

Measurements of the dc conductivity σ would afford sufficiently accurate estimates of the value of n_c. However, room-temperature values of σ were not found in the literature. In the absence of experimental values, a simple estimate further suggests that $n_c = 10^8$–$10^{10}\,cm^{-3}$ is unlikely. Values of σ in $(ohm\,cm)^{-1}$ are [13] 10^6 for a good conductor, 10^2 to 10^9 for semiconductors, 10^{-14} to 10^{-22} for insulators, and 10^{-26} for extrapolation from high-temperature ionic conductivity values [3]. For $n_c = 10^8$–$10^{10}\,cm^{-3}$, σ lies in the semiconductor range rather than the insulator range, which is not reasonable for alkali halides.

For σ in the insulator range, that is $\sigma \leq 10^{-14}\,(ohm\,cm)^{-1} = 9 \times 10^{-3}\,sec^{-1}$, the conductivity relation [13]

$$n_c = m\sigma/e^2\tau_k$$

gives

$$n_c \leq 2 \times 10^4\,cm^{-3}\ . \tag{5.2}$$

For this limit of n_c, the probability of finding an electron in the focal volume can be estimated as follows. Since the electron-avalanche process is highly nonlinear, only the region of the focal volume with E near the maximum is effective, and the diameter d_f and length ℓ_f of the high-field region are less than the $1/e^2$ or $1/e$ values. Reasonable values for 1.06 μm experiments [14], which also correspond to the damage volume, are $d_f = 2\,\mu m$ and $\ell_f = 50\,\mu m$. With $V_f \cong 2 \times 10^{-10}\,cm^3$ and (5.2), the value of $n_c V_f$ is

$$n_c V_f < 4 \times 10^{-6}\ .$$

This negligibly small probability of finding an electron in the focal volume indicates that there is not a sufficient electron density to initiate the avalanche. Furthermore, the value of n_c from (5.2) is at least eight orders of magnitude too small to explain the number of nucleation centers reported by Smith, Bechtel, and Bloembergen in the following paper in these proceedings.

This problem of an insufficient prepulse electron density is one of the less serious difficulties with current theories, since there are mechanisms for generating the starting electrons as discussed in section 9. However, the source of the starting electrons can determine the value of E_B; then assuming that $n_{c0} = 10^8 - 10^{10}\,cm^{-3}$ would give an incorrect value of E_B.

6. Lucky-Electron Avalanche at dc

Several of the attempts to alleviate the difficulties in the simple theory discussed in the previous sections will be considered here and in the following two sections. In the present section it will be shown that current lucky-electron theories do not explain the experimental values of E_B. The value of τ_k is the average time between collisions, with each individual time between collisions being different from τ_k in general. Seitz [9] and Shockley [15] considered the effects of the deviations from the average in dc experiments. In the discussion of figure 1 in section 2, it was pointed out that collisions limit the rate of energy absorption from the field in the dc case. Thus, a few "lucky" electrons that have collision times much greater than the average value can gain energy $\mathcal{E}_I$ even when $(d\mathcal{E}/dt)_E < (d\mathcal{E}/dt)_L$ is satisfied on the average. Thus E_B can be less than the value of E_{EL} in (2.3).

A simple demonstration of the large energy gained by the lucky electrons is obtained from the equation of motion between collisions for the component k_z of the electron wave vector $\underset{\sim}{k}$ along the direction of the dc field $\underset{\sim}{E} = \hat{z}E$

$$dk_z/dt = eE/\hbar \quad . \tag{6.1}$$

The solution between collisions is

$$k_z = k_{z0} + eEt/\hbar \quad .$$

The corresponding electron energy is

$$\mathcal{E} = \frac{\hbar^2}{2m}\left[k_x^2 + k_y^2 + \left(k_{z0} + \frac{eEt}{\hbar}\right)^2\right],$$

which shows that the greater the value of t between collisions, the greater the value of $\mathcal{E}$. In passing, notice that the energy gained

$$\Delta\mathcal{E} = \frac{\hbar eEt}{m}\left(k_{z0} + \frac{eEt}{2\hbar}\right) \tag{6.2}$$

is large for small-angle collisions, for which k_{z0} is large on the average. Also, for isotropic scattering, for which $k_{z0} = 0$ on the average, (6.2) with $t = \tau_{iso}$ and $(d\mathcal{E}/dt)_E = \Delta\mathcal{E}/\tau_{iso}$ give

$$\left(\frac{d\mathcal{E}}{dt}\right)_E = \frac{e^2\tau_{iso}E^2}{2m} \quad , \tag{6.3}$$

in agreement with (2.1) for $\frac{1}{2}\tau_{iso} = \tau_k$ and $\omega = 0$.

It is not difficult to show that the probability that the electron goes for time t without undergoing a collision is [9,7]

$$P_\tau(t) = e^{-t\langle 1/\tau_k\rangle} \quad , \tag{6.4}$$

where $\langle 1/\tau_k \rangle$ is the time average of $1/\tau_k$. The time t_{nc} required for an electron to gain energy $\mathcal{E} \cong 8\,eV$ in the absence of collisions is from (6.2) with k_{z0} negligible

$$t_{nc} = \frac{(2\,m\,\mathcal{E}_I)^{1/2}}{e\,E} = \left(\frac{1\,MV/cm}{E}\right) 9.54 \times 10^{-14}\ sec \quad . \tag{6.5}$$

The time average $\langle 1/\tau_k \rangle$ can be approximated by the average over the electron wave vector k [7]. From figure 5 below, the average from $\mathcal{E} = k_B T = 1/40\ eV$ to $\mathcal{E} = \mathcal{E}_I = 8.1\,eV$ is $\langle 1/\tau_k \rangle = 3 \times 10^{14}\ sec^{-1}$. Thus, (6.4) and (6.5) give

$$P_\tau(t_{nc}) = \exp\left[-28.6\left(\frac{1\,MV/cm}{E}\right)\right] \quad . \tag{6.6}$$

This small probability of ionization per "try" of 3.8×10^{-13} for $E = 1\,MV/cm$ must be multiplied by the number of "tries," which can be estimated as follows. Seitz [9] has argued that 40 multiplications, which results in $(2)^{40} = 10^{12}$ electrons in a small volume is a typical value for breakdown. In other words, the electron must undergo 40 multiplications before being swept into the anode by the field. Thus, for a sample 3.2×10^{-2} cm thick [16] and electrons with average drift velocity [3] $v = \mu E = 20\ (cm^2/V\,sec)\ 10^6\ V/cm$, the electron energy must reach $\mathcal{E}_I$ (in the presence of collisions) in time

$$t_I = \frac{1}{40}\ \frac{3.2 \times 10^{-2}\,cm}{2 \times 10^7\,cm/sec}\ \left(\frac{1\ MV/cm}{E}\right) = \left(\frac{1\ MV/cm}{E}\right) 4.00 \times 10^{-11}\ sec \quad .$$

During this time t_I, the electron makes $t_I/\tau_k = 2.93 \times 10^4$ collisions on the average. After each collision, it has another try to accelerate without a collision. Thus, the number of tries is t_I/τ_k. The probability of ionization P_I is the product of the probability of ionization per try times the number of tries:

$$P_I = \frac{t_I}{\tau_k}\ P_\tau(t_{nc}) = 1.1 \times 10^{-8} \ll 1 \quad . \tag{6.7}$$

This small value of P_I at the experimental value of $E = 1\,MV/cm$ shows that the lucky-electron mechanism of avalanche is clearly inadequate in this example.

The ionization frequency, ω_c, is approximately equal to the product of the number of tries per unit time $1/\tau_k$ and the probability of ionization per try

$$\omega_c \cong \frac{1}{\tau_k}\ e^{-t_{nc}/\langle 1/\tau_k \rangle} \quad , \tag{6.8}$$

where the coefficient $1/\tau_k$ is the thermal equilibrium value. Thus, from (6.6) and (6.8)

$$\omega_c = 7.33 \times 10^{14} \exp\left[-28.6\left(\frac{1\,MV/cm}{E}\right)\right] sec^{-1} \quad . \tag{6.9}$$

The comparison in figure 4 of this ionization frequency, ω_c, in (6.9) with experimental values [16] illustrates the poor agreement. The experimental dc results are obtained by converting the sample length ℓ to the time τ_ℓ required for the electron to drift across the sample by using the expression

$$t_\ell = \ell/\mu E \quad ,$$

where μ is the electron mobility. The ionization frequency, ω_c, is then obtained from (3.5) with $t_p = t_\ell$. Values of t_ℓ for the curve marked "μ const" were calculated using the constant, low field experimental value [3] of $\mu = 20\,\mathrm{cm}^2/\mathrm{V\,sec}$ for the mobility. For the $\mu = \mu(E)$ curve, the theoretical expression for the field dependence mobility is given on p. 122 of [3]. In the variable-μ result used in [17] it was assumed that the mobility decreases with increasing field, as it should for nonpolar solids. In the theoretical result used here, the mobility increases with increasing field. The physical reason is that $\mu = e\tau_k/m$ and increasing the field increases the average value of τ_k in polar solids by forcing the electrons into the higher k region in figure 5 of section 8 where the relaxation frequency $1/\tau_k$ is smaller. Thus, the lower curve in (d) of figure 1 in ref. [17] appears to be a reasonable lower limit in general, but it apparently is not approached in the alkali halides. In figure 2, only the constant μ curve was shown for clarity in comparing the dc and 1.06 μm results.

7. Lucky Reversing-Electron Avalanche at Laser Frequencies

It will be shown that the lucky reversing-electron theory [18] cannot explain the 0.694 μm breakdown results. The mechanism probably is important only at frequencies below the CO_2-laser frequency, and then only with the modifications discussed in section 9.

If an electron in an ac electric field does not undergo collisions, its wave vector oscillates with some peak value k_{pk}, rather than increasing continuously as in the dc case. Thus, the wave vector can be increased between two collisions by the peak-to-peak value $2k_{pk}$, at most. The value of

$$2k_{pk} = \frac{2\sqrt{2}\,eE}{\hbar\omega} = \frac{E}{2.2\,\mathrm{MV/cm}^{-1}}\ \frac{\lambda}{0.694\,\mu\mathrm{m}}\ 3.50\times10^6\,\mathrm{cm}^{-1} \tag{7.1}$$

is easily obtained by integrating (6.1) with $E(t) = E_{pk}\exp(i\omega t)$ and using $E_{pk} = \sqrt{2}\,E_{RMS}$ with $E \equiv E_{RMS}$.

According to the lucky-reversing-electron theory, the electron must suffer a backscattering collision during the time the value of k is near k_p. Then the electron is traveling in the same direction as $\underset{\sim}{E}$ during two successive half-cycles. It is, therefore, accelerated rather than deaccelerated as it would be if its direction had not been reversed. This process must be repeated until $k = k_I$, where k_I is the value of k required to generate a second electron, as before. The sequence is so unlikely that a very rough estimate is sufficient to demonstrate that it is negligible.

For an electron that has a lucky reversing collision when $k_z = -k_{pk}$, the next lucky reversing collision must occur at $k = +k_{pk}$. For the case of $\omega\tau_k \gg 1$, the electron makes several oscillations before suffering a collision, on the average. Thus the probability of a collision during the time $t_{pk} - \frac{1}{2}\Delta t$ to $t_{pk} + \frac{1}{2}\Delta t$, where $t = t_{pk}$ at $k = +k_{pk}$, is approximately equal to $\nu\Delta t \equiv \omega\Delta t/2\pi$. Here $1/\nu$ is the period of oscillation. For $\omega\tau_k \ll 1$ it can be shown that the probability is even lower.

Selecting Δt to make $k = 0.8\,k_{pk}$ at the two ends of the time interval Δt and using $2\cos^{-1}0.8 = 73.7°$ gives $\nu\Delta t = 0.205$. A generous estimate of the effective fractional solid angle $\Delta\Omega/4\pi$ for backscatter near 180° is 1/5, which gives

$$P_B = \frac{1}{5}\nu\Delta t = 4\times10^{-2}$$

for the probability of the backscattering collision.

The number N_C of such collisions required to make $k = k_I$ is greater than $k_I/2k_{pk}$. The inequality results from the fact that the change in k between the reversing collision is less than $2k_{pk}$, since the collisions were assumed to occur at $|k| > 0.8k_{pk}$ and collisions with scattering angle $\theta \neq 180°$ are less effective. Thus an

overestimate is obtained by using $N_C = k_I / 2k_{pk}$. The value of k_I is $\sim 1.46 \times 10^8\ cm^{-1}$ for $\mathcal{E} \cong 8$ eV, and $2k_p \cong 3.50 \times 10^6\ cm^{-1}$ according to (7.1). Thus $N_C = 41.9$.

The probability for k reaching k_I is therefore

$$\left(P_B\right)^{N_C} = \left(4 \times 10^{-2}\right)^{41.9} = 2.67 \times 10^{-59} \quad . \tag{7.2}$$

Multiplying by the number of tries $t_p / \tau_k = 5 \times 10^6$ during the pulse duration t_p, which is again an overestimate, since $\omega \tau_k \gg 1$ gives $P_s = 1.3 \times 10^{-52}$ for the probability of success of attaining $k = k_I$, which is negligible as stated.

A previous estimate [18] used much smaller values of the number of reversing collisions N_C (M in the reference), which appears in the exponent in (7.2). Values of $N_C = 1$ to 7 for various materials, apparently obtained from a fit to experimental results, are much smaller than our lower limit of $N_C = 42(0.694/1.06) = 27$. Also, the tacit assumption that $\omega \tau_k \ll 1$ is satisfied appears to have been made in one part of the previous calculation. These two differences account for tens of orders of magnitude difference in the two results.

8. Energy Dependence of Electron Relaxation Frequencies

At the early stages of the electron-avalanche-breakdown investigation reported in [7], a number of modifications of the existing theories were tried in hopes of solving the problems of these theories. Only slight improvements could be made. For example, consider the effects of including the energy dependence of the relaxation frequencies. A calculation in [7] of the values of τ_k and τ_L gives the results in figure 5.

Including this energy dependence of τ_k and τ_L in (2.1) and (2.2) gives the results sketched in figure 6. Increasing the value of E raises the curve $(d\mathcal{E}/dt)_E \sim E^2$ and leaves $(d\mathcal{E}/dt)_L$ unchanged. For sufficiently great values of E, the curve $(d\mathcal{E}/dt)_E$ lies above $(d\mathcal{E}/dt)_L$ at all values of k as marked "greater E" on figure 6, and breakdown surely would occur in most cases of interest.

For the value of E in figure 6, electrons with $k_\ell < k < k_{EL}$ lose energy on the average, while those with $k < k_\ell$ and $k > k_{EL}$ (for $\omega\tau \ll 1$) gain energy on the average. Thus, the lucky-electron process must take the electron across the barrier between k_ℓ and k_{EL}, shown shaded in figure 6. This is considerably more probable in general than making $k = k_I$ as was required in sections 6 and 7. However, even this easier process has a probability that is too low to explain experiments. In [7] it is shown that <u>if</u> the electrons generated in the avalanche process have $k > k_{EL}$, then the lucky-electron mechanism, with the starting electrons supplied by cathode or impurity emission, can explain the <u>dc</u> data.

For the case of laser frequencies, the factor $(1 + \omega^2 \tau_k^2)^{-1}$ in (2.1) reduces the value of $(d\mathcal{E}/dt)_E$, the reduction being especially great at large k where τ_k is large. There is typically another barrier, or region of $(d\mathcal{E}/dt)_E < (d\mathcal{E}/dt)_L$, at high values of k, as illustrated in figure 6. At 10.6 μm with E = 2 MV/cm, this second barrier starts at $k \cong k_I = 1.6 \times 10^8\ cm^{-1}$. At higher frequencies, the value of $(1 + \omega^2 \tau_k^2)^{-1}$ becomes so small that the two barriers merge, and all electrons with $k > k_\ell$ lose energy on the average. The lucky-electron process then must carry k all the way to k_I, which is very unlikely as already shown.

9. Preliminary New Theory

The difficulties of the current theories discussed in the previous sections are removed by a new theory that includes mechanisms for generating starting electrons and for initiating and sustaining an avalanche. The major new mechanisms at laser frequencies are the photon-electron-phonon process illustrated schematically in

figure 7 and inter-conduction-band transitions. The photon-electron-phonon process was considered for acoustical phonons in 1954 by Holstein in studies of metals.

The significance of these processes is that the electron can absorb the large energy $\hbar\omega$ of the photon, which is not possible for a single-vertex intra-band electron-photon process (first vertex in figure 7) because energy and momentum cannot be conserved. In the Holstein process, an electron interacts with both a phonon and a photon. The large wave vector of the phonon allows wave vector to be conserved so that the large energy of the photon can be absorbed by the electron. A schematic illustration of the increase in the energy of an electron by the combined effects of the Holstein process H, the electron-phonon scattering P, and the vertical interband process V is shown in figure 8.

In the dc experiments on sodium chloride at room temperature, the starting electrons are supplied principally by thermionic emission from the cathode. The lucky-electron process accelerates the electron to the top of the barrier at $\mathcal{E} = \mathcal{E}_{EL}$, after which the average-electron acceleration raises the energy to $\mathcal{E} = \mathcal{E}_I + \mathcal{E}_{exc}$. An important factor is that the excess energy $\mathcal{E}_{exc}$ above the minimum $\mathcal{E}_I$ required for ionization must be sufficiently great that the ionized electrons will have $\mathcal{E} > \mathcal{E}_{EL}$ so that they will in turn be accelerated from initial energy $\mathcal{E} > \mathcal{E}_{EL}$ to $\mathcal{E}_I$ by the average-electron process. Thus, it is necessary to obtain only one or a few electrons with $\mathcal{E} > \mathcal{E}_{EL}$. By contrast, in the laser experiments every ionizing electron must be accelerated to $\mathcal{E} > \mathcal{E}_{EL}$.

At 10.6 μm the starting electrons are excited from F centers by multiphoton absorption or tunnel emission. The Holstein process is sufficient to accelerate the electron to $k_{EL} \cong \frac{1}{2} k_{BZ}$ (or $\mathcal{E}_{EL} \cong 1.5$ eV). The threshold appears to be determined by the condition that $(\mathcal{E}_{EL})_{upper} = \mathcal{E}_I$. That is, for $E < E_B$, the barrier at high electron energies in figure 6 extends to such low energies that the electrons are not accelerated to $\mathcal{E} = \mathcal{E}_I$. However, the value of E required to obtain $\mathcal{E} > (\mathcal{E}_{EL})_{lower}$ is approximately equal to the value of E at which $(\mathcal{E}_{EL})_{upper} = \mathcal{E}_I$. Thus, either condition could control since both give the same value of E_B to within the accuracy of the calculations.

At 1.06 μm the starting electrons are generated by two-photon absorption by the F centers, and these electrons gain energy $\mathcal{E} > \mathcal{E}_I$ by a series of three Holstein processes plus approximately ten vertical inter-conduction-band transitions as in figure 8.

At 0.694 μm the starting electrons are generated by five-photon absorption across the gap, which is a faster process than two-photon absorption by F centers. The starting electrons are accelerated to $\mathcal{E} \cong 3$ eV by the Holstein process acting twice. Then the vertical inter-conduction-band process accelerates the electrons to $\mathcal{E} = \mathcal{E}_I$, as at 1.06 μm.

Finally, at 0.172 μm (xenon laser, with $\hbar\omega = 7.21$ eV), the starting electrons are generated by two-photon absorption across the gap. The electron energy is increased to $\mathcal{E} > \mathcal{E}_I$ by one Holstein event plus one vertical inter-conduction-band transition. These processes for generating the starting electrons and for accelerating them to $\mathcal{E} = \mathcal{E}_I$ are summarized in figure 9.

In all cases the electron density at time zero when the electric field is turned on was assumed to be zero, and the criterion for damage was that the temperature was raised to the melting point. A square pulse of duration equal to one-third the full-width-half-power pulse width was used since only the high-intensity region of the pulse is effective in the highly nonlinear processes. The electric field values quoted are the RMS values at the maximum intensity of the pulse. The intensity I is related to the RMS electric field E by the relation $I = c n_r E^2 / 4\pi$.

The results of the calculations that have been completed to date are shown in figures 2-4. The dependence of the breakdown field on the laser-pulse duration at 1.06 μm is shown in figure 2. The agreement is excellent, especially in view of the facts that no parameters were adjusted and that previous theories with parameters adjusted disagreed with experiment by many orders of magnitude in t_p^{-1} over most of the curve. Such good

agreement in likely to be fortuitous, as discussed below. It is important that no parameters have been adjusted. Adjusting the value of parameters to improve agreement between theory and experiment reduces the credibility of any theory. This is especially relevant in the present case in which the results are so sensitive to small changes in the value of E.

The comparison between the theoretical and experimental frequency dependence of the breakdown field in figure 3 for 10 nsec pulses shows good agreement. The experimental point at the ruby-laser frequency is the 10 nsec-pulse value of 2.1 MW/cm rather than the 4.7 nsec-pulse value of 2.3 MV/cm as in Fradin's [6] original comparison of the experimental values of E_B at different frequencies. In figure 4 the theoretical result for the single point calculated to date lies on the experimental curve.

The agreement with experiment of all the theoretical results obtained to date is better than had been expected in view of the possible inaccuracies in the calculated values of τ_k, τ_L, and the frequency ω_H for the Holstein process, and in view of the rather gross approximations used at this early stage in the theory.

The theory presented here removes all the difficulties of previous theories and the tentative results obtained to date are encouraging. However, additional results from a number of other studies in progress are needed in order to further evaluate the theory.

10. Acknowledgments

I am indebted to many people who kindly discussed electron-avalanche breakdown. It was realized that the electron-phonon-optical-phonon process was one of the missing keys to the theory while discussing the Joule heating aspect of the problem with Dr. Norton Moise. Dr. Douglas Mills pointed out that the electron-photon-acoustical-phonon process had been studied by Dr. Theodore Holstein in studies of metals. Dr. Holstein subsequently became involved in the present program. He suggested that the inter-conduction-band processes should be investigated, developed a transport theory to include the effect of large-energy transfer processes, and contributed in numerous discussions. Several helpful discussions with Dr. David Fradin are gratefully acknowledged. Discussions with Drs. M. Bass, N. Boling, P. Braunlich, C. J. Duthler, F. Luty, and J. Marburger are appreciated.

11. References

[1] von Hippel, A., Z. Physik 67, 707 (1931); J. Appl. Phys. 8, 815 (1937).

[2] Van Marum, M., Ann. Physik 1, 68 (1799).

[3] O'Dwyer, J. J., The Theory of Electrical Conduction and Breakdown in Solid Dielectrics (Clarendon, Oxford, 1973).

[4] Bloembergen, N., IEEE J. Quantum Elect. QE-10, 375 (1974).

[5] Klein, N., Adv. in Elect. and Elect. Phys. 26, 309 (1969).

[6] Fradin, D. W., Harvard Univ. Technical Report No. 643, Contract N00014-67-A-0298-0006, May (1973); Fradin, D. W., Yablonovitch, E., and Bass, M., Appl. Opt. 12, 700 (1973).

[7] Sparks, M. and Duthler, C. J., Xonics Fifth Technical Report, Contract DAHC15-73-C-0127, June (1975).

[8] Holway, L. H. and Fradin, D. W., J. Appl. Phys. 46, 279 (1975).

[9] Seitz, F., Phys. Rev. 76, 1376 (1949).

[10] Braunlich, P. F., Bendix Research Labs Final Report, Contract F19628-73-C-0032, August (1974); Braunlich, P., Schmid, A., and Kelly, P., Appl. Phys. Lett. 26, 150 (1975).

[11] Sparks, M. and Duthler, C. J., J. Appl. Phys. 44, 3038 (1973).

[12] Yablonovitch, E., Appl. Phys. Lett. 19, 495 (1971).

[13] Kittel, C., Introduction to Solid State Physics, 4th ed. (Wiley, New York, 1971).

[14] Smith, W. L., Bechtel, J. H., and Bloembergen, N., Phys. Rev., in press.

[15] Shockley, W., Czech. J. Phys. B11, 81 (1961) and Sol. St. Elect. 2, 35 (1961).

[16] Watson, D. B. and Heyes, W., J. Phys. Chem. Solids 31, 2531 (1970).

[17] Yablonovitch, E. and Bloembergen, N., Phys. Rev. Lett. 29, 907 (1972).

[18] Bass, M. and Barrett, H. H., IEEE J. Quant. Elect. QE-8, 338 (1971).

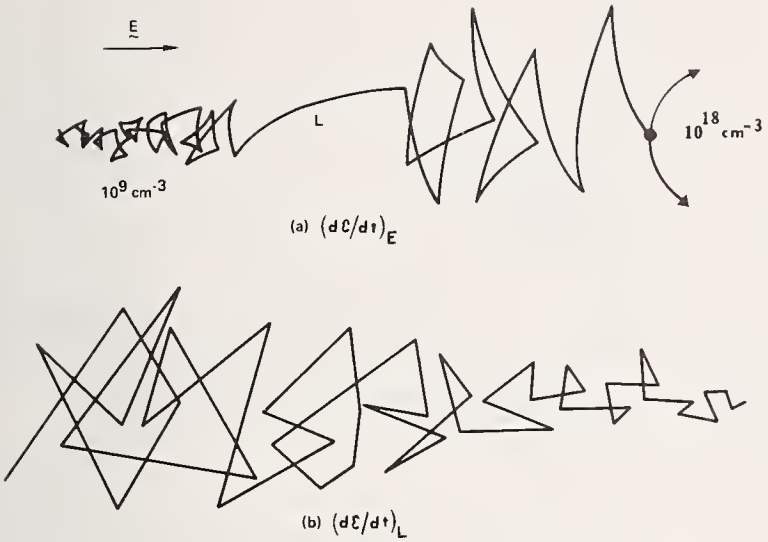

Figure 1. Schematic representation of an electron's path in the presence of an electric field $\underset{\sim}{E}$ and collisions with phonons: Part (a) illustrates the increase in the electron's energy by a dc electric field and (b) shows the energy loss to phonons. At L in (a) the electron is "lucky," that is it does not suffer a collision for a long time, thereby gaining great energy from the field.

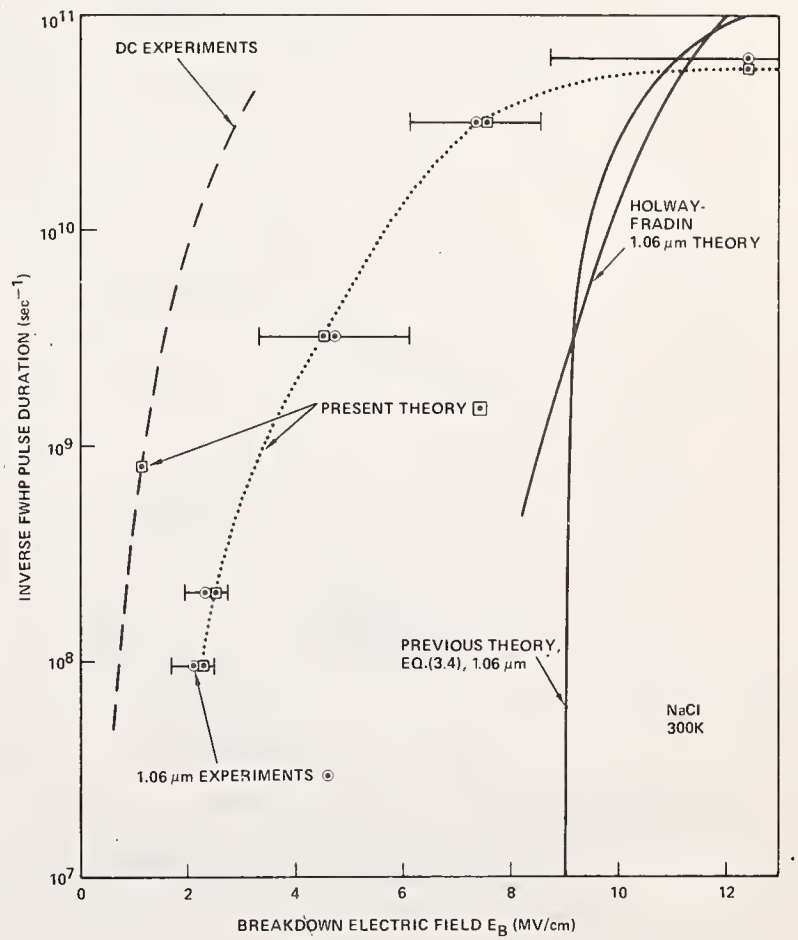

Figure 2. Comparison of 1.06 μm [6] (points ◉) and dc [16] (dashed curve) ⊡ experimental values of the inverse pulse duration t_p^{-1} with two solid theoretical curves showing poor agreement for both. The preliminary new theoretical results (points and dotted curve) are discussed in section 9.

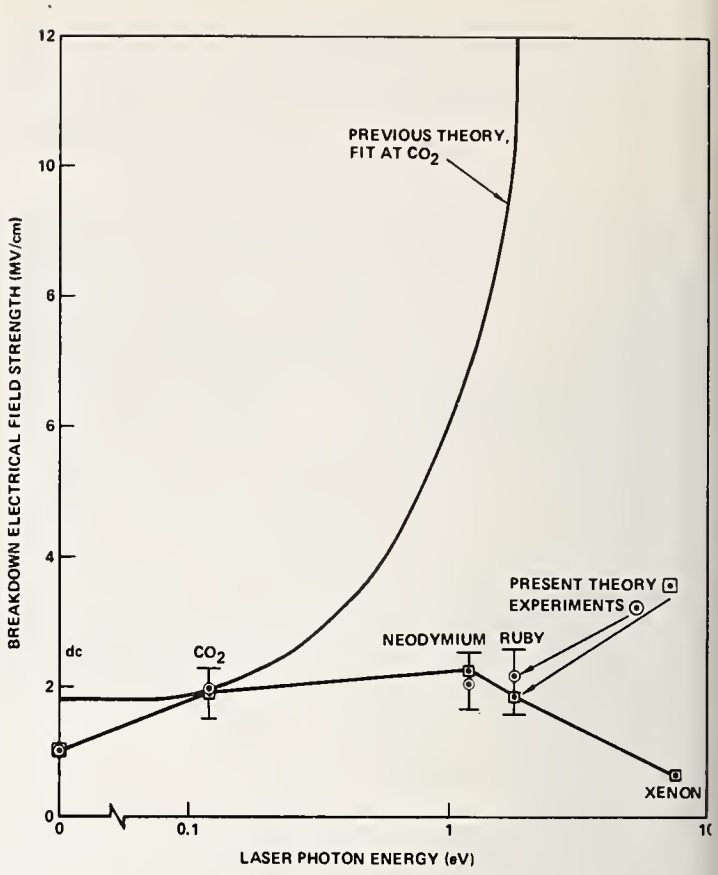

Figure 3. Comparison of the experimental results [6] with the theoretical results (2.4) and (2.3) fit at 10.6 μm showing poor agreement for the frequency dependence of the breakdown electric field.

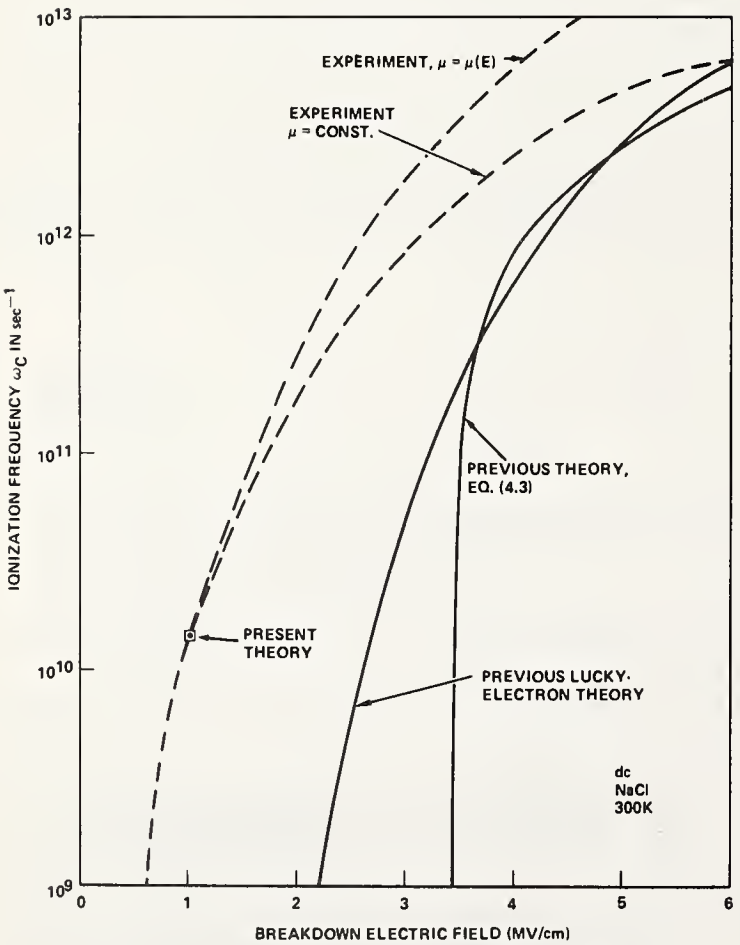

Figure 4. Comparison of the experimental results [16] with the result eq. (6.9) of the lucky-electron theory. The agreement is improved from that of eq. (3.4) for the average electron, but is still poor.

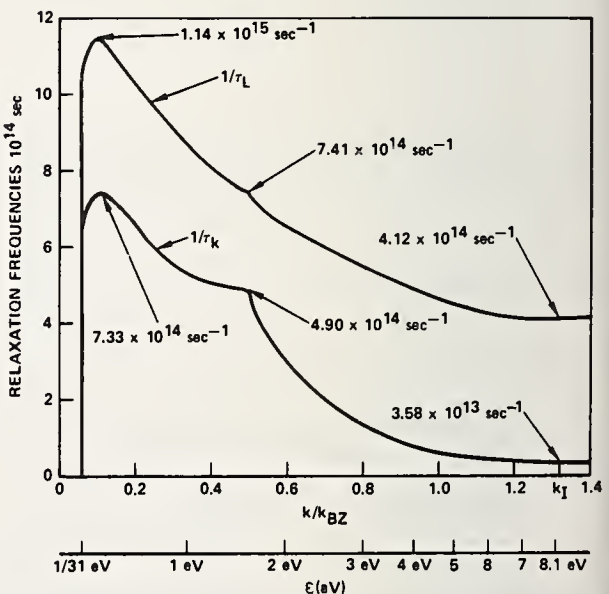

Figure 5. Dependence of electron relaxation frequencies on electron energy.

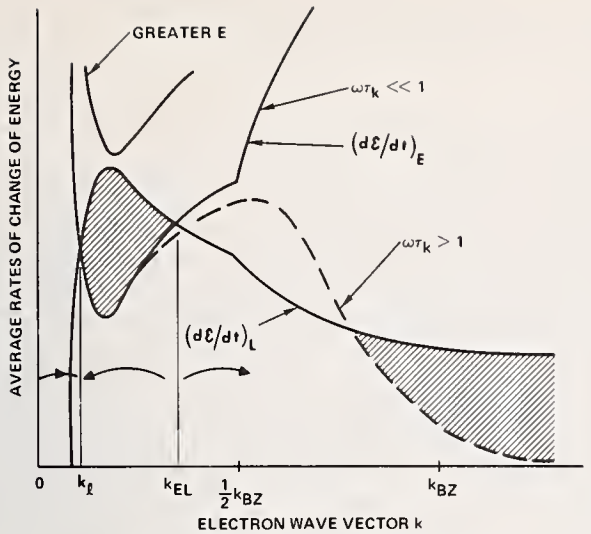

Figure 6. Wave-vector dependence of the electron energy gain and loss showing the shaded energy barriers of net average loss.

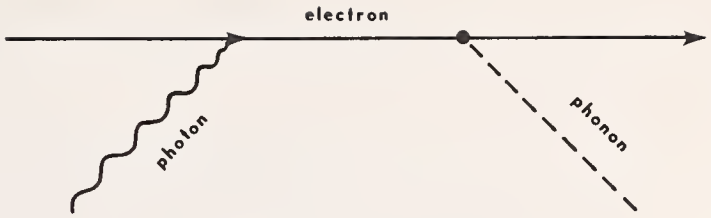

Figure 7. Schematic illustration of the Holstein process in which an electron gains energy $\hbar\omega$ in an interaction with a photon and a phonon.

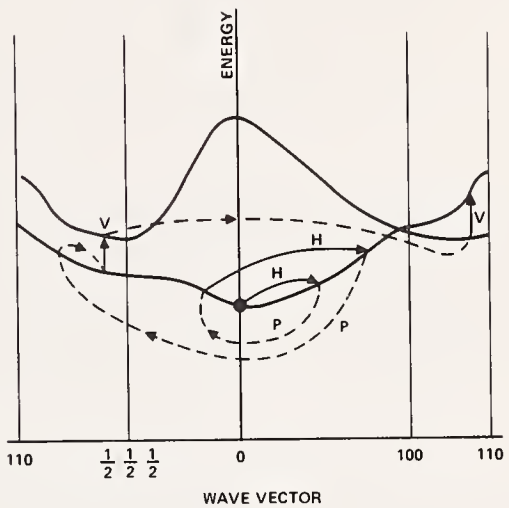

Figure 8. Schematic illustration of the processes in which an electron gains energy $\xi > \xi_I$ by Holstein collisions H, vertical inter-conduction-band collisions V, and phonon collision P.

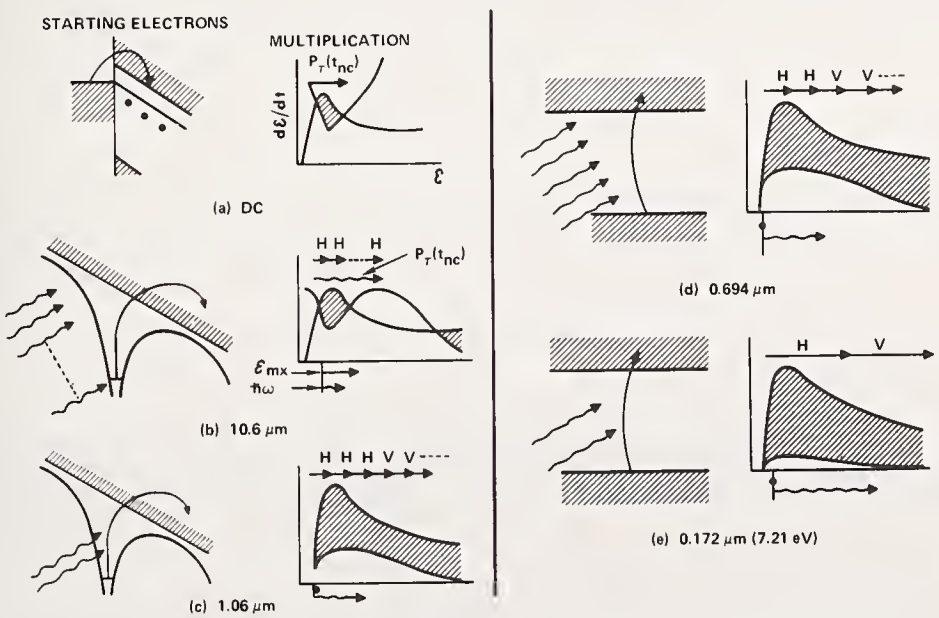

Figure 9. Summary of the processes of generating the starting electrons and increasing their energies to the ionization value.

COMMENTS ON PAPERS BY SPARKS and SMITH, et al

It was pointed out that the observed value of the threshold for damage is not a very sensitive detector of the process of initiation of the damage, as for example, multiphoton ionization, but that the damage morphology is a much more sensitive indicator of the nature of the damage process. This point will be discussed further in the next paper in this proceedings. The visual inspection technique used by Smith to determine damage threshold was found to be extremely sensitive. If the amount of stray light present in the laboratory was kept to a minimum and the observation was made with a dark adapted eye, Smith found that he could see visible evidence of damage processes which were very difficult and in some cases impossible to detect by subsequent microscopic investigation. In the general discussion a point was raised concerning the apparent discrepancy between laser damage data and the somewhat older data on dc breakdown. The sense of the discussion was that the dc breakdown data was put in question by uncertainties in electrode effects, impurity effects, and characterization of the samples. In all probability modern laser breakdown data is much more reliable than the old dc data.

6.3 A Statistical Analysis of Laser Induced Gas Breakdown - A Test of the Lucky Electron Theory of Avalanche Formation*

D. Milam†

Lawrence Livermore Laboratory, University of California
Livermore, California 94550

and

R. A. Bradbury and R. H. Picard

Air Force Cambridge Research Laboratories
Hanscom Field, Bedford, Massachusetts 91730

It is shown that the statistical distribution of breakdown times of gas volumes irradiated with square waveform ruby laser pulses can be explained by accounting for the probability that initial electrons are reliably produced by photoionization. Furthermore, the nature of the statistics of gas breakdown are closely related to those predicted by the lucky electron theory, and to the experimentally observed statistics of breakdown in solid dielectrics. It is suggested, therefore, that the statistics of intrinisic breakdown in both gases and solids may be related to the probability of obtaining initial charge rather than purely a manifestation of the lucky electron statistical process.

Key words: Electron avalanche; laser-induced gas breakdown; photoionization.

1. Introduction

The lucky-electron theory of avalanche formation assumes that free electrons of unspecified origin are forced to undergo repetitive accelerations and lattice collisions under the driving influence of the incident laser field. The average free electron gains little energy from the applied field since collisions are, in general, frequent and lossy. Occasionally, a free electron obtains ionizing energy through a sequence of "lucky" momentum-reversing collisions and accelerations. Avalanche breakdown is assumed to be virtually assured once a single electron in the focal volume is capable of ionizing its surround. In this paper we describe an experimental test of the lucky-electron theory.

2. Statement of the Lucky-Electron Theory

Since most collisions are lossy, the forced motion of a free electron in an applied field can be visualized as a sequence of trials, each with some small but finite probability of resulting in an ionizing electron energy. A typical trial will last only until the first collision. The probability per trial that an individual electron will reach ionization energy ε has been stated [1][1] as

$$\phi_1 = A_o f^m e^{-K/E}, \tag{1}$$

where f is the fraction of all collisions that are "lucky", m is the number of half-cycles required to produce ionizing energy, K is a material constant, and E is the applied field. The number m is itself inversely dependent on E, so that we can restate eq. (1) in the form,

$$\phi_1 = A_o e^{-K'/E} \quad . \tag{2}$$

On a particular focal site there will be n_s free electrons each independently undergoing trials at a rate approximately equal to the collision rate τ_c^{-1}. The probability $P_{ND}(t)$ of avoiding damage by avalanche breakdown until time t is simply the cumulative probability that all trials preceeding time t are unsuccessful;

*This work was performed at Air Force Cambridge Research Laboratories with support from both the Air Force and the Advanced Projects Research Agency.

†Employed by AFCRL while this research was performed.

1. Figures in brackets indicate the literature references at the end of the paper.

$$P_{ND}(t) = (1 - \phi_1)^{n_s t/\tau_c} \quad . \tag{3}$$

Operationally one envisions irradiating N_o sites, and determining the number $N(t)$ still undamaged at time t, so that

$$P_{ND}(t) = \lim_{N_o \to \infty} \frac{N(t)}{N_o} \quad . \tag{4}$$

For convenience we shall chose to use logarithmic plots, and rewrite $P_{ND}(t)$ in the form

$$P_{ND}(t) = e^{-\Gamma t}, \quad \Gamma = \frac{n_s}{\tau_c} \left| \ell n(1 - \phi_1) \right| \quad . \tag{5}$$

We observe that when n_s, τ_c, and ϕ_1 are constant, the logarithmic plots of P_{ND} will be linear curves. Since ϕ_1 is very small, the dependence of the slope Γ upon the applied field strength E is given to high accuracy by the expanded form,

$$\Gamma \cong \frac{n_s}{\tau_c} \{\phi_1 - \frac{1}{2} \phi_1^{\,2} + \text{------}\}, \tag{6}$$

when only the first term is retained. Relative slopes, found at different values of E, should therefore, be calculable from the equation,

$$\Gamma \cong \frac{n_s}{\tau_c} e^{-K'/E} \tag{7}$$

Logarithmic plots of $P_{ND}(t)$ will be nonlinear if n_s or E varies in time or space due to any of the following situations:

a. Spatial variation of E due to field enhancement on some focal sites.

b. Spatial variation in n_s due to electron traps or easily ionizable impurities.

c. Variation of n_s in time at all sites due to ionization of the basic dielectric itself.

Cases a and b produce functions $\ell n\, P_{ND}(t)$ which are more steeply sloped at early times than at later times, due to the larger damage rates present on some sites. Note that the factor Γ is in fact a damage rate since

$$\frac{N(t)}{N_o} = e^{-\Gamma t}, \tag{8}$$

where we have used eqs. (3) and (5). Condition c above will result in functions $\ell n\, P_{ND}$ which slope more steeply at later times due to the constantly increasing damage rate.

3. Experimental Test of the Lucky-Electron Theory

It is possible to test the above hypotheses by experimentally generating the functional forms $P_{ND}(t) = \frac{N(t)}{N_o}$, using a technique described [2] at the preceeding Boulder Conference. That technique is illustrated in figure 1. A large number N_o of small sites are irradiated using square-waveform ruby laser pulses of strength E_o. The survival time of each site is observed by recording the damage-induced termination of the laser pulse transmitted through the site. A table of survival times is then organized to allow plotting of $N(t)/N_o$. All data is sorted after the experiment to eliminate firings for which E_o varied significantly during the pulse; all remaining data are included in the analysis.

Data for Transparent Dielectrics

We have applied this technique to record functions $P_{ND}(E, t)$ for a wide range of dielectric films and polished surfaces, and for the bulk of such materials as fused quartz, sapphire, ED-2, ED-4, BK-7, CaF_2, KCL, KBr, and other randomly chosen glasses. In only two instances do we observe functions P_{ND} which are closely related to the predictions of the lucky-electron theory: namely, bulk fused quartz and sapphire. For even these cases, the agreement is incomplete unless one allows selected variations of n_s in both time and space. Consider data shown for fused quartz in figure 2. The functions $P_{ND}(t)$ found at 34.5 and 39 kW are reasonably linear in time, indicating potential agreement with lucky-electron theory. Using an effective avalanche constant K' computed from the slopes of data at those two power levels, one can calculate the slope expected for data at 42.5 kW. The third data set exhibits two problems: the slope is too large to agree with the curve predicted by the lucky-electron theory, and many of the sites irradiated at 42.5 kW damaged during the rise of the pulse. These early damages are most likely due to inclusions or to a large spatial variation in ionizability. Field enhancement by defects or a time-constant spatial variation of n_s cannot explain the early damages since we must assume that similiar sites were sampled at the two lower power levels, and that their effects were incorporated into the effective K'. As a result, the slope can change with changes in E only predicted by $e^{-K'/E}$ when damage is due to such time constant spatial variations. The second problem, too large a slope for those sites not damaged during the risetime can be explained by the lucky-electron theory, only by assuming that n_s, and therefore the damage rate, are increasing in time.

Three data sets generated in fused quartz all yield the same result.

The reader should be aware that we have in the past erroneously identified [2] a combination of lucky-electron avalanche breakdown and electric field enhancement at defects as the cause of data such as that in figure 2. For reasons stated above, it is clear that that combination of mechanisms will not totally explain the data.

In sapphire the agreement between data and the lucky-electron theory is excellent within restricted time intervals, as shown in figure 3. Initial damages at each power level lie on linear curves whose slopes are related by $e^{-K'/E}$. However, all sites surviving an initial irradiation interval damaged at a well defined time, which again demands that n_s be increasing in time if the lucky-electron effect is invoked to describe damages.

4. Introduction to Gas Breakdown

Based on the failure to find close general agreement with the lucky-electron theory when solid dielectrics were studied, we decided to investigate the statistical nature of laser-induced gas breakdown. The arguments used to formulate the lucky-electron model are equally applicable to breakdown in gases. Indeed, the concept of an electron traveling under the influence of the applied field, and suffering collisions in which the duration of the interaction is small relative to the mean time τ_c between collisions, is perhaps more applicable to a gas. Furthermore, the gas pressure, and therefore the collision rate can be varied at will, so that the relationship between breakdown characteristics and collision time can be determined.

Laser-induced gas breakdown has been extensively studied and review papers are available [3,4]. Since it is not our purpose to survey the field of laser breakdown in gases, we shall rely on these reviews for the few facts needed here. The accomplishments of individual workers in the field are acknowledged in the extensive bibliographies attached to the reviews.

Theoretical treatments of gas breakdown assume that the plasma development is well described by the solution of rate equations. The increase in the free electron population, n_e, is assumed to result from multiphoton ionization and from collision-assisted ionization, with the latter rate taken to have the functional form found in microwave breakdown. Losses in the electron population are due to diffusion, recombination, and attachment. Solutions have been found to describe the growth in n_e under a variety of assumptions concerning the relative contributions of the various gains and losses. These solutions adequately account for the functional dependencies of the threshold breakdown fields, and generally account for the magnitude of such fields. Ready [4] notes, for example, that even the simplest assumptions result in an expression for the threshold flux F_{th},

$$F_{th} = \frac{10\ mc}{\pi e^2 \tau_p} I\ \omega^2 \tau_c \quad , \tag{9}$$

which agrees with the experimental dependences found for pulse duration τ_p, laser frequency ω, ionization potential I, and the pressure of the gas which is inversly porportional to τ_c. These dependencies hold when collision assisted ionization is dominant.

5. Statistics in Gas Breakdown

Stastical arguments have not been used to describe laser-induced gas breakdown. It is assumed that time independent average rates are observed for each process, resulting in a precisely defined time of damage for each precisely defined incident laser intensity. For moderate gas pressures, in the range 10 torr < p < 10^4 - 10^5 torr, the collision-assisted cascade growth process dominates plasma formation for Q-switched pulsed having durations of tens of nanoseconds. As the pressure or pulse duration is reduced, direct photoionization becomes important. In the transition region, the cascade process is richly seeded with starting electrons, so that any statistical effects resulting from a lack of initial electrons for the cascade process, or in the photoionization process itself, are unlikely.

One can, therefore, from the most general principals predict several features that should be observable in the statistics of laser-induced breakdown. If the rate equations with time constant rates are an adequate representation of plasma growth, the time of breakdown will be precisely related to the pulse intensity. Since some rates are very nonlinear in intensity, significant spread can be expected in the breakdown times even if stringent precautions are taken to include only data taken at a preselected field strength E. The spread in breakdown times should have a predictable dependence on the average time of breakdown. If all rates involved are all sufficiently large to be adequately represented by time averages, the least experimental scatter will be obtained by insuring that damage, on the average, occurs at early times during the square-pulse irradiation. Larger scatter in breakdown time will be observed at lower intensities where lesser rates are allowed to compete over long times.

The spread in breakdown times will also have a predictable dependence on pressure, since the threshold for collision-assisted breakdown is inversely dependent on pressure [4] while the photoionization rate is only very weakly pressure dependent [4]. As a result, the threshold irradiation field increases as the pressure is decreased. The number of electrons created by direct photoionization will increase very rapidly as the irradiation level increases, since photoionization is proportional to the intensity raised to some large power. Photoionization in argon, for example, should be proportional to the ninth power of intensity. One can, therefore, predict a pressure dependence in the scatter of breakdown times. At low pressures, approximately one torr, photoionization predominates over collision-assisted ionization, with the result that the accumulation of electrons will depend critically on intensity, so that even with careful selection of irradiation levels, a large scatter in breakdown times will be observed. As the pressure is increased, both the field necessary to produce breakdown and the photoionization rate will be reduced until one begins to see the statistical features associated with single photoionization events. At that point, one again expects to see a large scatter in breakdown times associated with a small spread in irradiation intensity.

Based on the arguments above, one should be able to find breakdown occurring at a well defined time at intermediate pressure levels ($\sim 10^3$ torr). As the pressure is increased, the time of breakdown will become less well determined at each intensity level. One should eventually reach the situation corresponding to observation of actual atomic statistics in the production of starting electrons. Since the photoionization rate for individual atoms is constant in time, the breakdown can occur at any time during irradiation. This latter state is then closely related to the statistics predictable for the lucky-electron process.

6. Measurement of the Distribution of Breakdown Times in Gas Using a Ruby Laser

Using the technique described above, we have measured the distribution of breakdown times in argon at several pressures and in nitrogen at one pressure. The gas was contained in a high pressure housing designed for use as a laser-triggered spark gap. Filling was accomplished in a series of evacuation-flush steps to furnish a reasonable assurance that the gas was at the maximum purity level possible. A controlled leak was used to move the gas so that each gas volume was irradiated only once. The lens used to focus the beam produced a beam waist of approximately Gaussian profile which was ≈ 6.0 μm in diameter at half-maximum. A detailed reduction [5] of magnified images of the beam profile indicate that the peak on-axis intensity was 2.3 Gw/cm^2 for each kW into the system. The time of breakdown in each focal volume was monitored in the same fashion as described for dielectrics in section 3.

7. Data and Conclusions

Plots of $N(t)/N_o$, the fractional number of gas volumes which have not suffered breakdown, are shown in figures 4,5,6, and 7 for argon at pressures of 1820, 2810, 8510, and 26,600 torr, respectively. The data, taken as a whole, shows exactly those trends associated with the assumption that gas breakdown is adequately described by rate equations. Breakdown at 1820 torr was deterministic, occurring at a well-defined time at each power level. The spread in breakdown times became greater

NOTE: 1 torr = $\frac{101\ 325}{760}$ Pa.

when breakdown occurred later during the laser pulse. We recall that the collision-assisted impact ionization process dominates breakdown [4] at this pressure. Photoionization, with its strong intensity dependence, must have served only to furnish a copious supply of initial free electrons, since breakdown occurs at a sharply defined time. It is evident that we did not, at this pressure, observe the large fluctuations in breakdown time predicted if photoionization were furnishing a major portion of the breakdown plasma, or if the photoionization rate were so low that free charge was not reliably produced.

The statistics of breakdown in argon at 2810 torr as shown in figure 5 were essentially the same as those at 1800 torr. Breakdown was largely deterministic; both the average breakdown time and the time jitter were slightly increased by decreasing the beam intensity.

By making a significant pressure change from 2810 torr to 8510 torr, the statistical characterists of breakdown in argon were markedly altered as shown in figure 6. The time of breakdown was poorly defined with $N(t)/N_o$ having the approximate form predicted for lucky-electron avalanche breakdown. Data at 103 Gw/cm^2 does not, however, have the slope predicted by the factor $e^{-K'/E}$, although the data may be too few to serve as an adequate test.

Data taken at 26,600 torr as shown in figure 7 confirms the trend toward less deterministic behavior at higher pressures and lower intensities. Ample data was obtained at each of four intensity levels to show that the probability of breakdown per unit time, or the breakdown rate, was constant over at least the 14 nsec interval investigated. Two possible explanations are available, but the relative slopes still do not agree with the exponential factor related to the lucky-electron theory. Agreement with that theory could be found by assuming that the lucky-electron damage rate had increased more rapidly than $e^{-K'/E}$ due to a power dependent change in the number of electrons undergoing trials. Such charge, if produced by photoionization, must accumulate in time except under a very carefully chosen balance of gains and losses which could not exist at all power levels. It would seem, therefore, that an argument which assumed that the lucky-electron rate increased faster than $e^{-K'/E}$ due to intensity dependent photoionization, also would demand that the rate increase in time at some intensity levels. Since this combination of events did not occur, we must assume that the statistics of breakdown probably did not result directly from the lucky-electron effect.

An alternate explanation for data in figure 7 is to simply assume that the photoionization was so improbable that an initial free electron population was not reliably established in each focal volume. Since the photoionization of individual atoms is described by a constant probability per unit time, the linear curves in figure 7 would result if we had been producing only a few charges in each focal volume. Alternatively, if the photoionization was improbable, a large experimental jitter in breakdown time would be predicted due to the intensity nonlinearity of photoionization. These two effects, while conceptually different, are probably very difficult to separate experimentally.

If one assumes that the collision-assisted ionization rate has the form of eq. 9, so that the breakdown threshold is inversely proportional to pressure, one can make a rough estimate of the fractional ionization occurring by photoionization at 26,600 torr. To accomplish the estimate, we assume that we are able to directly ionize $\approx .1$ the neutral atoms in the focal volume when the pressure is 1 torr. The number of ionizations, $.1\ N_oV$, is related to the breakdown intensity at 1 torr by an equation of the form [4],

$$.1\ N_oV = C\ (N_oV)\ F_{th}^{9} \quad , \tag{10}$$

where N_o is the density of neutrals, V is the effective volume for a ninth order process, and F_{th} is the breakdown intensity which is assumed to expressible as an inverse function of pressure,

$$F_{th} = \delta/P,\ \delta = \text{constant}, \tag{11}$$

if only pressure is allowed to vary. The constant C in eq.(10)is a product of the pulse duration and the ionization rate. Using this form, the fraction X of the atoms which would be ionized at a higher pressure p_2 is calculable from the fraction ionized at $P_1 = 1$ torr;

$$\frac{.1}{X} = \frac{C\ F_{th,1}^{9}}{C\ F_{th,2}^{9}} = \left(\frac{P_2}{P_1}\right)^{9} \quad , \tag{12}$$

so that $X \approx .1(P_1/P_2)^9$ in order of magnitude. Using eq. (12), the fractional ionization at 26,600 torr is $X = 1.8 \times 10^{-40}$. More conservative estimates that .1 the focal volume is directly ionized at P_1 = 10 torr or at P_1 = 100 torr lead to estimates $X = 1.5 \times 10^{-31}$ and $X = 1.5 \times 10^{-22}$ respectively. One may, therefore, reasonably expect to have trouble producing starting electrons in a focal volume of approximately 10^{-9} cm^3 which contains only 10^{12} atoms at a pressure of 26,600 torr.

We also measured the distribution of breakdown times in nitrogen at 8,210 torr. That data is shown in figure 8. Again we observed a constant probability per unit time for breakdown, and in this instance the slopes were in rather close agreement with the predictions of the lucky-electron theory. We note, however, that there seems to be no apriori reason to assume that we cannot use the argument concerning a lack of consistent photoionization to describe the breakdown data in figure 8.

Finally, we measured the distribution of breakdown times with dc electric fields of various magnitude applied to the gas volume. The dc field should have two effects [6]. It should sweep naturally occurring electrons from the focal volume, and it should furnish a forced one-way drift loss during plasma build-up. The field could also possibly remove charged dirt, but we have no evidence that dirt contributed to our measurements is such small volumes. The distribution of breakdown times in nitrogen in the presence of a strong dc field is shown in figure 9. The data again is explicable by assuming that the starting charge density is unreliably produced by photoionization and that some of the electrons produced are lost by one-way drift.

8. Final Conclusions

The simple damage rate associated with the lucky-electron theory, $\Gamma = e^{-K'/E}$, is closely related to the observed aspects of damage in a limited class of high-quality, solid, transparent dielectrics. The expression does not, however, account in detail for the statistics of the total breakdown process unless special assumptions are made concerning spatial and temporal variations of the free electron population.

In laser-induced gas breakdown, statistical results similiar to those found in solid dielectrics are found at pressures above a few thousand torr. The statistical fluctuation in the time of breakdown in high pressure gases can be understood as a result of a low probability for photoionization at the breakdown field strengths associated with those pressures. The form of the breakdown statistics in gas at high pressure is, however, identical with that predicted for the lucky-electron effect in some cases and closely related in other cases.

The data suggests that statistics observed in laser damage are a real phenomena, and that they may be more closely associated with the production of starting electrons than with the statistical model predicted by the lucky-electron effect.

9. Acknowledgments

The authors acknowledge extensive discussions with Dr. Norman Boling of Owens Illinois, Dr. Michael Bass of the Center for Laser Studies at the University of Southern California, and Dr. Alex Glass of Livermore Laboratories, during which the ramifications and formulations of the lucky-electron theory were discussed at length. Dr. David C. Smith of United Aircraft Research Laboratories furnished significant discussion concerning the gas breakdown data. We are further grateful to the secretarial and photographic personnel at Livermore who aided in preparation of the manuscript.

10. References

[1] Bass, M., and H. H. Barrett, IEEE J. Quantum Electron., QE-8, 338 (1972).

[2] Milam, D., R. A. Bradbury, R. H. Picard, and M. Bass., Laser Induced Damage in Optical Materials: 1974, edited by A. J. Glass and A. H. Guenther (U. S. Govt. Printing Office, Washington, 1974), p. 169.

[3] deMichelis, C., IEEE J. Quantum Electron., QE-5, 188 (1969).

[4] Ready, J. F., Effects of High-Power Laser Radiation, Chapter 5, Academic Press, New York, 1971.

[5] Weaver, H. J., G. E. Sommargren, and E. S. Bliss, Proc. of SPIE, 48 63, (1974).

[6] Tulip, J., and H. Seguin, Appl. Phys. Lett., 23, 135 (1973).

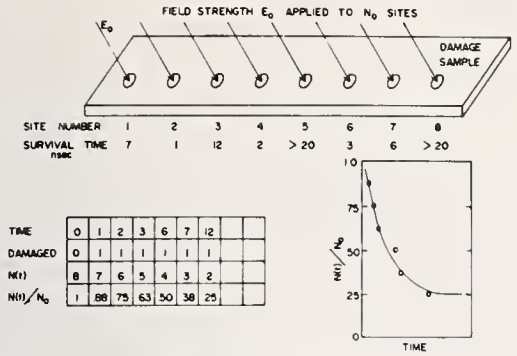

Figure 1. Schematic representation of the experiment used to measure $P_{ND}(t)/N_o$, the probability of avoiding damage until time t. Survival time is measured for each of N_o sites.

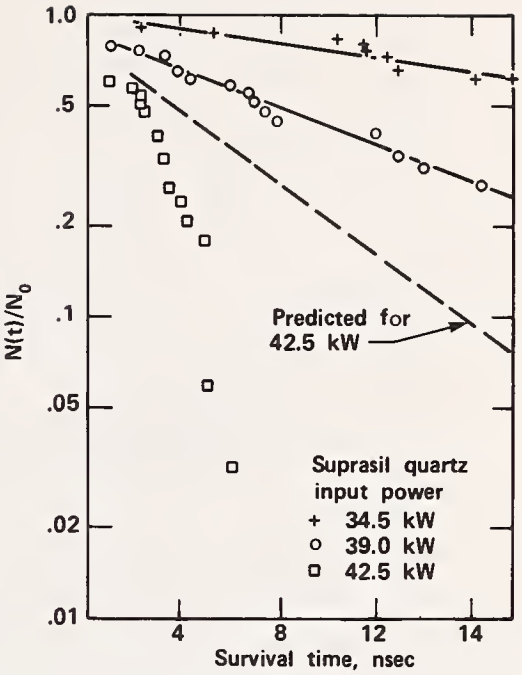

Figure 2. Survival curves for suprasil fused quartz. Data for t > 2 nsec is reasonably linear, but the slope increases more rapidly than predicted by $e^{-K'/E}$. The slopes predicted by the exponential factor for data at 42.5 kW is shown by the dashed curve.

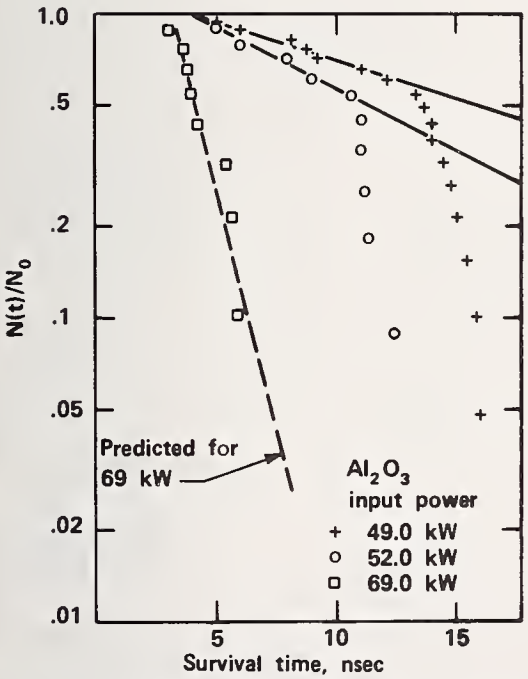

Figure 3. Survival curves for single crystal sapphire. Initial data agrees with the lucky-electron slope factor as shown by agreement between data at 69 kW and the dashed curve.

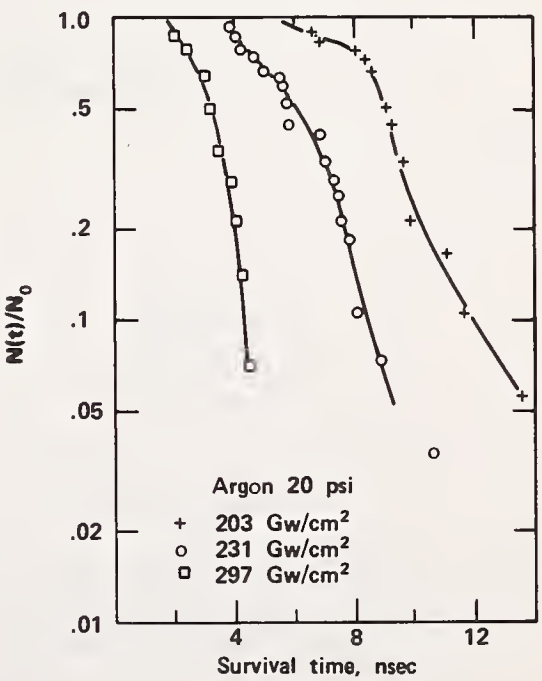

Figure 4. Survival curves for argon at a pressure of 1820 torr (20 psi over-pressure) at three irradiation levels.

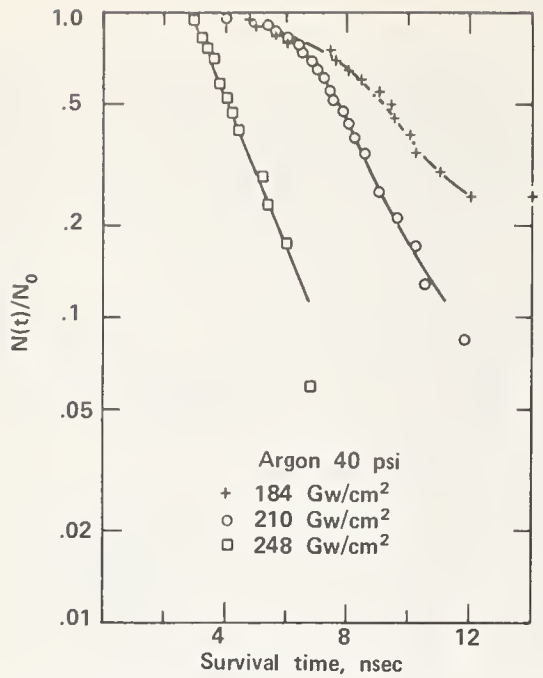

Figure 5. Survival curves for argon at a pressure of 2810 torr (40 psi overpressure) at three irradiation levels.

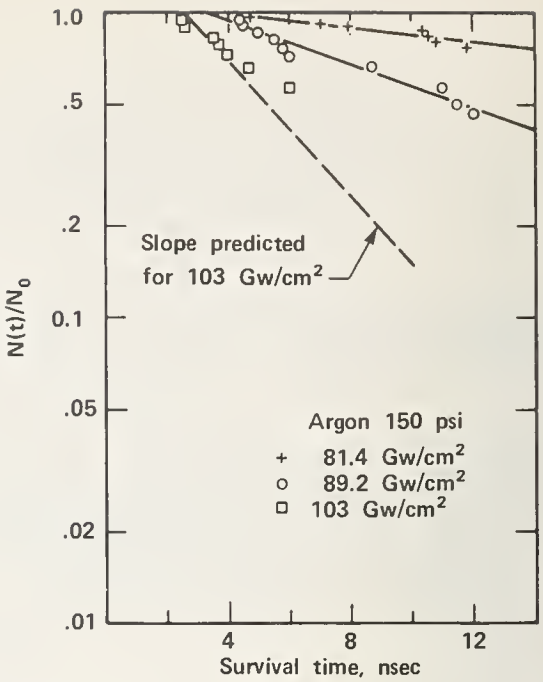

Figure 6. Survival curves for argon at a pressure of 8510 torr (150 psi overpressure) at three irradiation levels. Slope predicted by the lucky-electron factor $e^{-K'/E}$ for data at 103 Gw/cm^2 is shown by a dashed line.

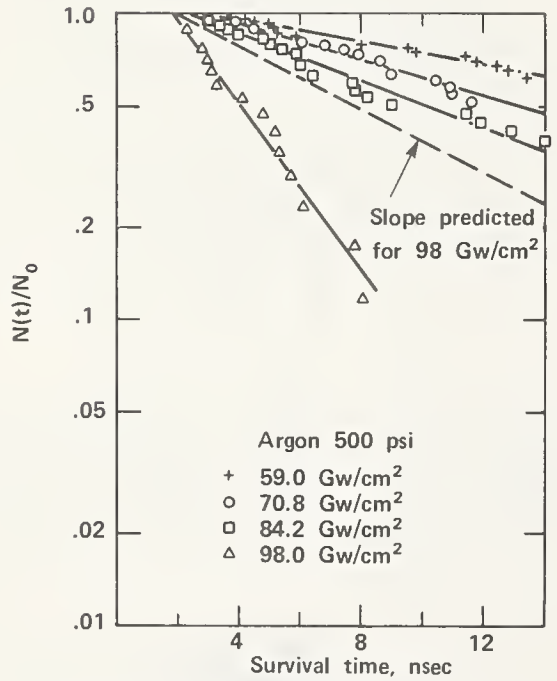

Figure 7. Survival curves for argon at a pressure of 26600 torr (500 psi overpressure) at three irradiation levels. Slope predicted by the lucky-electron factor $e^{-K'/E}$ is shown by a dashed line.

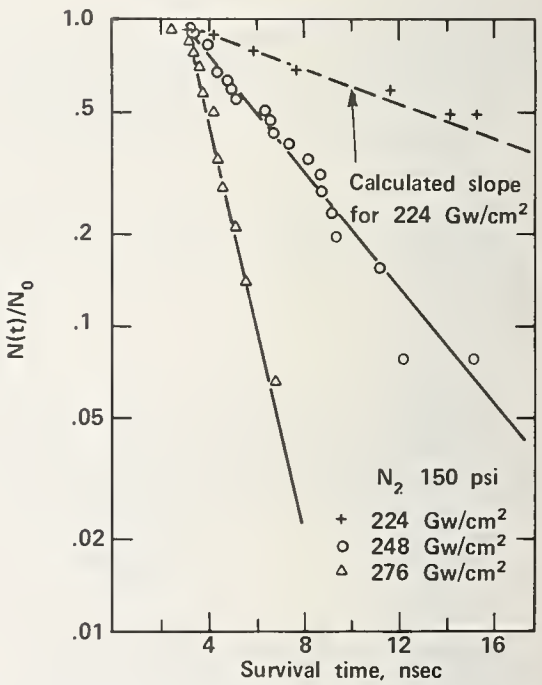

Figure 8. Survival curves for N_2 at a pressure of 8210 torr (150 psi overpressure) for three irradiation levels. The data is in close agreement with the lucky-electron slope factor $e^{-K'/E}$ as shown by agreement between the dashed curve and data at 224 Gw/cm^2.

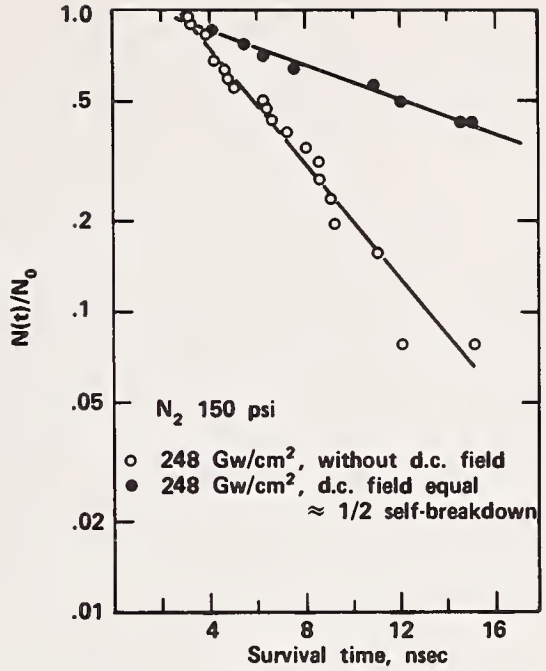

Figure 9. Survival curves for N_2 at a pressure of 8210 torr (150 psi overpressure), both with and without the presence of a transverse dc electric field applied to the gas volume.

NO COMMENTS ON PAPER BY MILAM, et al

6.4 Measurement of Free Electron Density at the Onset of Laser-Induced Surface Damage in BSC-2*

Nabil Alyassini and Joel H. Parks

Departments of Physics and Electrical Engineering
University of Southern California
Los Angeles, California 90007

A study of transient processes which occur during laser induced surface damage to BSC-2 glass was conducted. An optical probe technique was employed in this study which used a He-Ne laser to internally probe the surface at the critical angle. The variations in the detected He-Ne beam revealed a decrease in the site specular reflectivity which precedes structural damage by as much as 2.4 nsec. This is shown to be the result of a laser induced increase in the free electron density at the irradiated surface site with a measured average build up time of 1.6 nsec, resulting in a detectable decrease in the site refraction index ($\Delta n=10^{-5}$-10^{-3}). From the measured specular reflectivity decrease, a calculation of the free electron density at the onset of damage indicates a density of 10^{18}-$10^{19}/cm^3$. It is shown that the resulting free electron absorption can transfer a damaging amount of energy from the laser pulse to the sample causing at least melting of the irradiated surface site.

Key words: Damage electron density; electron density transient; free electron absorption; laser induced surface damage; optical probe technique; refractive index variation.

1. Introduction

Presently, it is widely accepted that free electrons are the cause of laser induced damage to intrinsically transparent dielectrics in a self focusing free situation and in absence of absorbing inclusions. Although there is not broad agreement [1-8][1] on the process by which the free electron density increases in the presence of an intense laser field, it has been suggested [6] that the free electron density must reach 10^{18}-10^{19}/cc in order to cause damage to the dielectric by heating due to free electron absorption.

Such a density of free electrons will induce a detectable decrease in the refractive index of the dielectric in addition to making it lossy. This paper reports on the successful measurement of the decrease in specular reflectivity of a BSC-2 surface site which was subjected to a damaging Q-switched ruby laser pulse. This reflectivity change was observed to occur a few nanoseconds prior to the onset of catastrophic damage. It is shown that the specular reflectivity decrease is due to a decrease in refractive index of the irradiated surface site which was caused by a laser induced increase in the free electron density. A measure of the free electron density at onset of damage was calculated, and the amount of energy transferred by such a density of free electrons from the damaging laser pulse to the lattice was found to be sufficient to at least cause melting of the site. This study also provides a measure of the free electron build up time.

2. Experimental Technique

Figure 1 shows the optical probe technique previously discussed [9-11] which was used to monitor the specular reflectivity decrease of a BSC-2 surface site during the presence of an intense Q-switched TEM_{oo} single mode Gaussian ruby pulse. The surfaced site to be damaged was probed internally at its critical angle by a 3 mW unpolarized He-Ne laser. The reflected probe intensity was measured with a photodiode detector which had a measured rise time of less than 1 nsec, and which was synchronized to the damaging ruby pulse with a measured accuracy of better than ±0.25 nsec [11]. Entrance and exit surface damage were studied and each site was irradiated only once. The measured ruby spot size and the calculated probe spot size at the irradiated sample surface were 34μm and less than 4μm, respectively.

---

* Partially supported by Advanced Research Projects Agency and the Joint Services Electronics Program at USC.

1. Figures in brackets indicate the literature references at the end of this paper.

One of the reasons for probing the BSC-2 surface internally at its critical angle is shown in figure 2. As can be seen, the absolute decrease in the BSC-2 sample reflectivity due to a decrease in its index is maximum at the critical angle for both polarizations. That is, the sensitivity of the reflected probe intensity to a decrease in the index of the site is maximum at the critical angle. Also, since reflected probe intensity is maximum at critical angle, the sensitivity of the optical probe detection is also maximum at this angle. In addition, perturbation of the probe by the spark that was found to always accompany surface damage in BSC-2 is eliminated when probing internally.

3. Experimental Results

Figures 3 and 4 show typical data sets for BSC-2 entrance and exit surface sites damage, respectively. These traces have been copied from the original photographs for clarity of presentation. The values shown in the figures were measured from the original photographs. An important finding of this study was the observation in over half the damaged sites of a time delay Δt between the start of the dip in the optical probe trace and the start of the dip in the transmitted damaging ruby pulse, with the ruby trace delayed relative to the probe trace. During this interval of time the probe trace dropped ΔV(mV).

The point in time at which the transmitted damaging ruby pulse started its dip is the point at which the free electron density reached a critical value (10^{18}-$10^{19}/cm^3$) causing sharp attenuation of the damaging ruby pulse [6,11,12]. The onset of damage apparently occurs at this point, since the resulting Joule heating of the irradiated site becomes appreciable at this density, eventually leading to irreversible damage.

At the start of the dip in the reflected probe intensity, the free electron density at the irradiated site was too low to cause any appreciable heating of the site ($\sim 10^{16}/cm^3$). However, this density was enough for the resulting decrease in the refractive index to cause a detectable decrease in the site reflectivity when probed at the critical angle, as will be shown. The damaging ruby pulse is relatively insensitive to such a decrease in the index since it was normally incident at the sample surface (see figure 2). The delay Δt ranged in value between 0.5 - 2.4 nsec (lower value is limit of our measurement accuracy) with an average value of 1.6 nsec. The detected probe signal ΔV ranged in value between 0-6 mV with an average value of 3.3 mV.

4. Analysis

An originally lossless dielectric of index n plus a free electron density N_o can be described by an "extrinsic" index n_1 and extinction coefficient k_1. It can be shown [11,13] using Maxwell's equations for a wave of radian frequency ω and the classical free electron model [14] that n_1 and k_1 are given by (MKS units):

$$k_1^2 = \frac{B}{2}\left[\sqrt{1 + \left(\frac{A/B}{\omega\tau_c}\right)^2} - 1\right] \tag{1}$$

$$n_1 = \sqrt{n^2 + k_1^2 - A} \tag{2}$$

where

$$A = \frac{\omega_p^2 \tau_c^2}{1 + \omega^2 \tau_c^2}$$

$$B = n^2 - A$$

$$\omega_p^2 = \frac{N_o e^2}{\varepsilon_o m},$$

and τ_c is the free electron lattice collision time. The plasma frequency ω_p depends on the electron charge and mass e and m, respectively, and ε_o the free space dielectric constant ($\varepsilon_o = 8.854 \times 10^{-12}$ F/m).

For the case of interest here $N_o < 10^{20}/cm^3$, thus at the ruby or He-Ne radian frequency $\omega_p << \omega$ and

$A \ll 1$. Therefore, even for a collision time as small as 10^{-16} sec., eqs. (1) and (2) are accurately approximated by:

$$k_1 \simeq \frac{A}{2\omega\tau_c n} \cdot \tag{3}$$

and

$$n_1 \cong 1 - \frac{A}{2n} \cdot \tag{4}$$

Thus, the refractive index variation is simply

$$\Delta n = \frac{A}{2n} \cdot \tag{5}$$

It can be shown that the reflectivity of a substrate having an index $(n - \Delta n)$ at the angle of total internal reflection, $\theta = \sin^{-1}(1/n)$ is given by:

$$R_{||} = \left[\frac{(n^2 - 1)^{\frac{1}{2}} - \Delta n^2 \left(\frac{n}{\Delta n} - 1\right)\left(\frac{2n}{\Delta n} - 1\right)^{\frac{1}{2}}}{(n^2 - 1)^{\frac{1}{2}} + \Delta n^2 \left(\frac{n}{\Delta n} - 1\right)\left(\frac{2n}{\Delta n} - 1\right)^{\frac{1}{2}}} \right]^2$$

$$R_{\perp} = \left[\frac{\left(\frac{n}{\Delta n} - 1\right)(n^2 - 1)^{\frac{1}{2}} - \left(\frac{2n}{\Delta n} - 1\right)^{\frac{1}{2}}}{\left(\frac{n}{\Delta n} - 1\right)(n^2 - 1)^{\frac{1}{2}} + \left(\frac{2n}{\Delta n} - 1\right)^{\frac{1}{2}}} \right]^2$$

for a beam polarized parallel or perpendicular to the plane of incidence, respectively. These can be approximated in the case of BSC-2 glass ($n = 1.513$) for $\Delta n < 10^{-3}$ by:

$$R_{||} \cong 1 - \frac{4n\sqrt{2n}\,\Delta n^{\frac{1}{2}}}{\sqrt{n^2 - 1}} \tag{6}$$

$$R_{\perp} \cong 1 - \frac{4\sqrt{2n}\,\Delta n^{\frac{1}{2}}}{n\sqrt{n^2 - 1}} \cdot \tag{7}$$

Since the time constant of the polarization fluctuations of the unpolarized probe beam is much smaller than the probe detector rise time, the measured reflectivity of the sample R is given by the average value

$$R = \tfrac{1}{2}(R_{||} + R_{\perp}).$$

After algebraic manipulation of eqs. (6) and (7) we obtain,

$$\Delta n = \frac{n(n^2 - 1)(1 - R)^2}{8(n^2 + 1)^2} \cdot \tag{8}$$

Where the measured value of R at onset of damage is given by:

$$R = \frac{V - \Delta V}{V} \quad , \tag{9}$$

V being the initial reflected probe signal before irradiation (V = 33-34 mV).

Hence from the measured value of ΔV, R is calculated using eq. (9), which is then used to obtain an estimate of Δn from eq. (8). Values of the parameter A are then calculated using eq. (5). The values of R, Δn, and A are all based on measured and known quantities. Assuming a value for the electron lattice collision time, an estimate for the free electron density N_o and extinction coefficient k_1 at the onset of damage can finally be obtained from the analytical expression for A.

Table 1 lists the measured and calculated values of R, Δn, N_o, and k_1 for site D64,9 and P7,8, whose data sets are shown in figures 3 and 4, respectively. The value of ω used in calculating k_1 was that of the ruby laser ($\omega = 2.71 \times 10^{15}$ rps), and the frequency used in calculating N_o was that of the He-Ne laser ($\omega = 2.98 \times 10^{15}$ rps). Values of the electron-lattice collision time have been taken from the literature [6].

Table 1.

			$\tau_c = 10^{-15}$ sec		$\tau_c = \frac{1}{\omega} \cong 3.3 \times 10^{-16}$ sec	
Site	R	Δn	N_o (cm^{-3})	k_1	N_o(cm^{-3})	k_1
D64,9	0.888	2.8×10^{-4}	2.7×10^{18}	1.0×10^{-4}	5.0×10^{18}	3.2×10^{-4}
P7,8	0.918	1.6×10^{-4}	1.5×10^{18}	5.9×10^{-5}	2.7×10^{18}	1.8×10^{-4}

For the sites that showed a delay $\Delta t > 0.5$ sec, Δn varied in value between 1.2×10^{-5} and 6.8×10^{-4} with a mean value of 2.7×10^{-4}. Using a collision time of $\tau_c = 10^{-15}$ sec, N_o varied between 1.1×10^{17} and 6.7×10^{18}(cm^{-3}) with a mean value of 2.6×10^{18} (cm^{-3}), while k_1 range was 4.3×10^{-6} - 2.6×10^{-4} with a mean value of 1.0×10^{-4}. For $\tau_c = \omega^{-1} \cong 3.3 \times 10^{-16}$ sec, N_o was in the range 2.0×10^{17} - 1.2×10^{19}(cm^{-3}) with a mean value of 4.8×10^{18}, and the k_1 range was 1.3×10^{-5} - 7.8×10^{-4} with a mean value of 3.1×10^{-4}. Note that using a shorter collision time in these calculations results in higher values for the free electron density N_o and the extinction coefficient k_1.

The measured value of Δn, the calculated values of the free electron density, and extinction coefficient are all lower estimates. First, due to the morphology of the BSC-2 entrance and exit surface damage, it was difficult to exactly observe the location of the probe beam relative to the damaged region using the 40X telescope. If the probe beam was slightly displaced from the central portion of the ruby laser pulse, the probe sampled a lower field site area with a lower free electron density. Second, it is also probable that the probe beam was incident at an angle slightly off the critical angle, and hence was less sensitive to changes in the index of the irradiated site (see figure 2). Finally, the free electron could have continued increasing for one or two nanoseconds beyond the start of the dip in the transmitted damaging ruby pulse.

We have solved the one dimensional heat equation with a heat source that is Gaussian in time [11], and found that the values of k_1 calculated for each damaged site at onset of damage was more than enough to subsequently cause at least melting of most of the sites that showed a time delay Δt.

5. Conclusions

The ability of the optical probe technique to measure time dependent index variations in the range $\Delta n = 10^{-5} - 10^{-3}$ on the nanosecond timescale provides a sensitive, non-destructive method of examining the transient properties of materials.

The utility of the probe technique to obtain detailed temporal data of laser induced damage has resulted in the observation of the buildup of a free electron density several nanoseconds prior to the onset of surface damage in BSC-2 glass. The magnitude of the density, in the $10^{18} - 10^{19}/cm^3$ range, is consistent with measured index variation and the Joule heating necessary to cause melting at the surface site. The buildup time, in the 1-2 nanosecond range, is interesting in view of recent publications [7,8] which are critical of current theories of electron-avalanche breakdown as the mechanism for this buildup. Sparks [7] suggests a collision process requiring several nanoseconds to establish an electron density sufficient to initiate damage.

6. Acknowledgments

We would like to acknowledge valuable discussions with Prof. J. Marburger and Prof. R. W. Hellwarth.

7. References

[1] Hellwarth, R. W., "Role of photo-electrons in optical damage," Damage in Laser Materials, NBS Spec. Pub. 341, 67 (1970).

[2] Wasserman, A., "A mechanism for damage in solids by intense light," Appl. Phys. Lett. 10, 132 (1967).

[3] Keldysh, L. V., "Ionization in the field of a strong electromagnetic wave," Sov. Phys. JETP 20, 1307 (1965).

[4] Bass, M. and H. H. Barrett, "Avalanche breakdown and the probabilistic nature of laser-induced damage," IEEE J. QE 8, 338 (1972).

[5] Holway, L. H., Jr., "High frequency breakdown in ionic crystals," J. Appl. Phys. 45, 677 (1967).

[6] Bloembergen, N., "Laser-induced electric break down in solids," IEEE J. QE 10, 375 (1974).

[7] Sparks, M., "Current status of electron-avalanche-breakdown theories," this publication.

[8] Boling, N. L., et al., "Statistics in laser-induced dielectric breakdown," Appl. Phys. Lett. 27, 191 (1975).

[9] Parks, J. H. and N. Alyassini, "Time resolved damage studies of thin film and substrate surfaces," Laser-Induced Damage in Optical Materials, NBS Spec. Pub. 372, 104 (1972).

[10] Alyassini, N., J. H. Parks and L. G. DeShazer, "Time resolution of laser-induced damage to thin films," Laser-Induced Damage in Optical Materials, NBS Spec. Pub. 387, 133 (1973).

[11] Alyassini, N., "A study of laser-induced damage to dielectric surfaces and thin films," Ph.D. Dissertation, U. of So. California, 1975 (University Microfilm, Ann Arbor, Mich.).

[12] Giuliano, C. R., "The dynamics of transmitted, reflected and scattered laser pulses above and below damage threshold: The search for pre-catastrophic damage," NBS Spec. Pub. 414, 179 (1974).

[13] Galkin, G. N., L. M. Blinov, V. S. Vavilov and A. G. Golovashkin, "Plasma resonance on nonequilibrium carriers in semiconductors," JETP Lett. 7, 69 (1968).

[14] Kittel, C., Introduction to Solid State Physics (John Wiley & Son, 3rd ed. 1968).

8. Figures

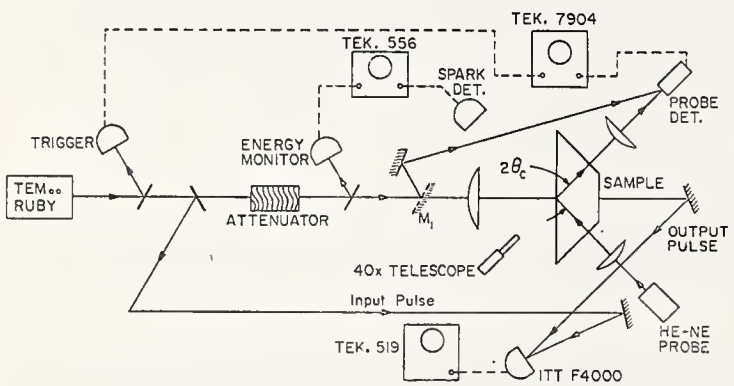

Figure 1. Schematic of experimental arrangement and optical probe technique for study of surface damage in scilicate glass BSC-2.

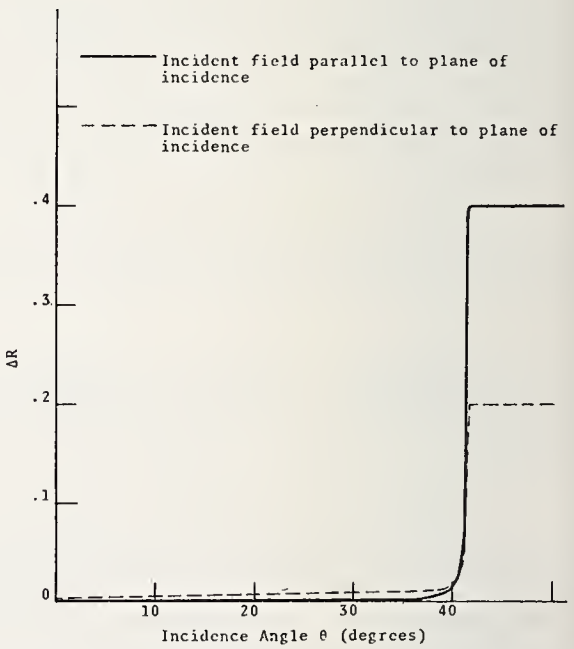

Figure 2. Absolute change in reflectivity ΔR of a BSC-2 sample of index n = 1.513 due to a decrease of .003 in its index, versus the incidence angle θ. At each angle of incidence θ, a decrease in the index will cause a change in the reflectivity; ΔR is the absolute magnitude of this change.

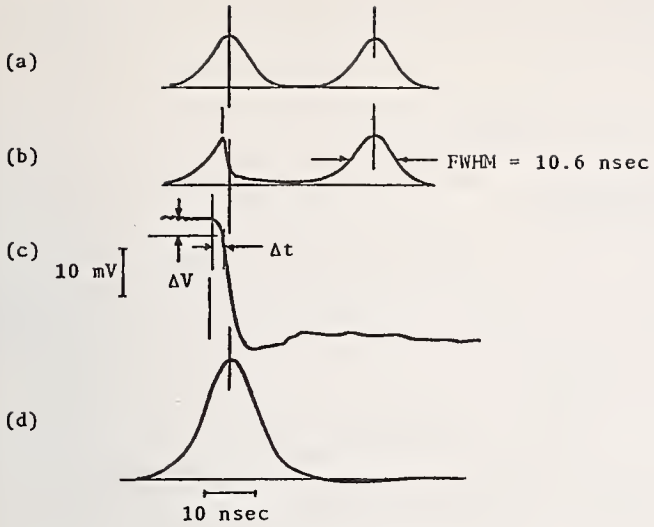

Figure 3. Entrance surface damage data, site D64,9. (a) output (left) and input pulse traces of a non-damaging pulse, (b) output and input pulse traces of the damaging pulse, (c) optical probe trace, (d) damaging ruby pulse. The time scale for traces (a) and (b) is 10 nsec/8.5 mm. Measured values for this data site are Δt = 1.5 nsec, ΔV = 3.5-4.0 mV.

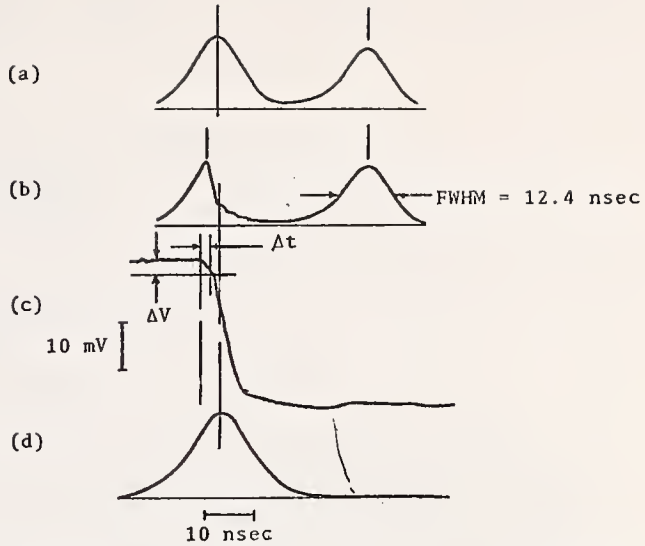

Figure 4. Exit surface damage data, site P7,8. (a) output (left) and input pulse trace of a non-damaging pulse, (b) output and input pulse traces of the damaging pulse, (c) optical probe trace, (d) damaging ruby pulse. The time scale for traces (a) and (b) is 10 nsec/8.5 mm. The measured values for this site are Δt = 2.4 nsec and ΔV = 2.5-3.0 mV.

NO COMMENTS ON PAPER BY ALYASSINI and PARKS

6.5 Multi-pulse Optical Damage of NaCl*

P. Bräunlich
Bendix Research Laboratories
Southfield, Michigan 48076

and

Research Institute for Eng. Sciences
College of Engineering
Wayne State University
Detroit, Michigan 48202

and

P. Kelly
Physics Division
National Research Council
Ottawa, Canada KIA OS1

Single-shot intrinsic laser damage of NaCl at 1.06 μm is caused by avalanche ionization. The reduction of the damage threshold of an order of magnitude in case the sample is exposed to a mode-locked train of ten pulses, observed by Penzkofer, was assumed to be caused by absorbing inclusions [1][1]. In this paper we show that the dependence of the damage threshold on the number of pulses in a mode-locked train can be satisfactorily explained by the avalanche breakdown mechanism.

Key words: Avalanche breakdown; intrinsic damage; mode-locked pulse trains.

Recently Penzkofer [1] reported intrinsic damage thresholds for NaCl that is exposed to a train of up to 10 mode-locked pulses of 6 psec FWHM duration from a Nd: Yag laser. He measures the following damage thresholds.

i)	1.5×10^{12} W/cm^2	for a single pulse
ii)	4×10^{11} W/cm^2	for damage occurring in the second pulse
iii)	1.5×10^{11} W/cm^2	for damage occurring in the 10th pulse

In agreement with recent work by the Raytheon-Harvard group [2], the single pulse damage is interpreted as avalanche breakdown; however, the multi-pulse thresholds as due to inclusion heating [1]. This inconsistency is unacceptable in view of the fact that in both cases the probability for hitting an absorbing inclusion is identical. A closer examination of the problem appears therefore warranted. We will show in this paper that the dependence of the damage threshold on the number of pulses in the pulse train can be explained quite adequately by the avalanche breakdown mechanism [2,3,4].

For the computation of the damaging photon fluxes, we employed the same electron kinetic approach as used in [3,4,8]. A detailed discussion of this computational procedure was given in [4]. While this type of analysis does not permit to calculate absolute value of the damage threshold with high accuracy, it is well suited to study the change of a threshold with parameters such as the pulse width, etc., or, as in the present case, with the number of pulses in the mode-locked train. The calculations reported here were performed with 15 psec FWHM individual pulses having a pulse separation of 300 nsec. All pulses in the train are of equal height A^* (peak photon flux) and are given by

$$F = A^* \sin^2 (\pi t/t_p) \tag{1}$$

where t_p = 30 psec is the full pulse duration.

The electron kinetic equations used for this purpose were described in [4]:

$$dT/dt = n_c e^2 \tau E^2/m\rho k \ (1 + \omega^2\tau^2) \tag{2}$$

$$dn_c/dt = n_v\omega_{vc} + n_c\omega_i + n_t\omega_{tc} - n_c (N_t - X - n_t)\omega_{ct} + X\omega_{Fc} \tag{3}$$

$$dn_t/dt = -n_t\omega_{tc} + n_c(N_t - X - n_t)\omega_{ct} \tag{4}$$

$$dX/dt = -X\omega_{Fc} \tag{5}$$

where m is the effective electron mass, τ the electron-phonon collision time, ω the laser frequency, e the electron charge, E the rms optical field strength, ρ the sample density, and k its heat capacity.

The temperature increases during the laser pulse, and when the melting point T_m = 1074 K is reached, irreversible damage occurs [4,7].

* supported by the Division of Materials Research of the National Science Foundation

1. Figures in brackets indicate the literature references at the end of the paper.

The ω_{ik}'s are electron transition rates in appropriate units. The subscripts designate the type of transition. X and n_t are the density of F-centers in the ground level and in the excited level, respectively. N_t is the density of Cl^--vacancies which we assume to be $5 \times 10^{+16}$ cm^{-3}. The best crystals available have at least 1×10^{16} cm^{-3} Cl^- vacancies.

The avalanche ionization rate is given by [4,5,6]

$$\ln \omega_i(E) = 8.17 + 4.22 \ln E - 0.823 (\ln E)^2; \quad 1 \leq E \leq 50 \qquad (6)$$

from which ω_i (sec^{-1}) is obtained by using the rms optical field strength E in the units MV/cm.

At the ruby wavelength conduction electrons (n_c) are generated from valence electrons (n_v) by five-photon absorption (transition rate ω_i), by two-photon absorption (ω_{Fc}) from F-centers in the ground level (X), and by single-photon absorption (ω_{tc}) from excited F-centers (n_t).

The numerical values of the involved transition rates are listed in table 1.

We have considered three different cases

- λ = 1.06 µm; here all multi-photon terms in eq. (3)-(4) are neglected
- λ = 6943 Å; we have calculated two mechanisms in this case, (a) avalanche ionization only, no five-photon photo carrier generation, and (b) five-photon assisted avalanche ionization.

On first sight the avalanche breakdown mechanism apparently cannot account for the one order of magnitude reduction in the damaging photon flux when the damage occurs in the 10th pulse of the train as compared to single pulse damage. That this is not so will be shown in the following section.

Single-pulse damage is commonly observed at around $t = t_p/2$, and we assume this was the case in Penzkofer's experiments also. For two-pulse damage, the probability for it to occur around $t_p/2$ of the second pulse is also very high [7]. In both cases, damage may also occur at considerably smaller peak fluxes than those producing breakdown at $t_p/2$; however, the probability for damage to occur late in the pulse decreases accordingly [7]. As the peak flux of the pulses in a train is reduced, damage occurs later in the train. The temperature of the exposed spot in the crystal increases from pulse to pulse. It may either rise up to the melting point, T_m, and result in irreversible material modifications (damage), or it may reach a steady-state equilibrium at which temperature losses (e.g., by diffusion) and carrier recombination prevent further increase of T during the duration of the train.

In order to establish the relation between the peak flux A^* and the time of damage occurrence in a multi-pulse train, we have calculated $T_m(t)$ as a function of A^*. The chosen pulse trains (up to 10 pulses of 15 psec FWHM, 300 nsec pulse separation) have a duration of up to .3 µsec. Carrier relaxation (the life time of free electrons and of excited F-centers is 10^{-6} sec. [8]) effects the results somewhat. However, smaller separation times (≤100 nsec) between pulses result in negligible decay of n_c and n_f during the duration of the pulse train. Temperature diffusion as well as electron diffusion is negligible for pulse trains of <1 µsec duration [3] provided the laser spot radius is larger than 10 µm.

Some results are compiled in table 2. Clearly, Penzkofer's results can be explained by avalanche breakdown alone. Our "avalanche only" data clearly indicate that at A*/10, ten pulses produce breakdown where A^* is one shot damage threshold at $t_p/2$. No alternate damage mechanism appears necessary to account for the large difference in the breakdown threshold for simple pulse damage as compared to multi-pulse damage. For completeness, some results for "avalanche only" and for multi-photon assisted avalanche breakdown at the ruby frequency are listed as well. The decrease in A^*_{dam} with the number of pulses in the train is again significant.

Figure 1 shows the relation between the damaging peak flux A^* and the time of damage occurrence in the pulse train. Since no damage occurs between pulses, the separation times between pulses have been neglected in this graph.

In view of these results it appears appropriate to re-examine the classic experiment by Yablonovitch [9] who found a systematic correlation between dc breakdown and laser breakdown at 10.6µm. He used a train of short pulses from a CO_2 laser having a total length of 100 nsec, which is short enough to neglect relaxation effects. The width of the individual pulses was a few nsec. The thresholds he measures are multi-pulse values. Typically, damage appeared to have occurred in the fourth pulse. In view of the above calculations we expect the single-pulse damage thresholds for all alkali halides to be higher than the values reported in [11] and thus appreciably higher than the dc thresholds. The correlation with the dc results, however, is expected to be unaltered.

References

[1] A.Penzkofer; Optics Com. 11, 265 (1975).

[2] N. Bloembergen; IEEE Quant. Electron. QE-10, 375 (1974)

[3] P. Bräunlich; Final Report for Air Force Cambridge Research Lab, AFCRF-TR-0266, 1974 (unpublished)

[4] P. Bräunlich, A. Schmid, P. Kelly; Appl.Phys. Lett 26, 150 (1975).

[5] E. Yablonovitch and N. Bloembergen; Phys. Rev. Lett 29, 907 (1972).

[6] D. Fradin, Harvard University Technical Report No. 643, 1973 (ONR-372-0012) (unpublished)

[7] P. Kelly, P. Bräunlich and A. Schmid; Appl. Phys. Lett 26, 233 (1975).

[8] I. M. Catalano, A. Cingolani, and A.N. Minafra, Phys. Rev. B5, 1620 (1972).

[9] E. Yablonovitch, Appl. Phys. Lett 19, 495 (1971).

Tables and Figures

Table 1. Values of transition rates. The superscript o denotes the optical and th the thermal part of the transition rate.

Photon-induced transitions	
$\lambda = 0.694\mu$	
	$\sigma_5 = 0.5 \times 10^{-141}(cm^{10}sec^4)$
	$n_v\omega_{vc} = 1.12 \times 10^{-118}F^5(sec^{-1}cm^{-3})$
	$\omega^o_{tc} \leq 10^{-16}F(sec^{-1})$
	$\omega^o_{FC} \approx 1.6 \times 10^{-48}F^2(sec^{-1})$

Thermally-induced transitions
$\omega^{th}_{tc} \approx 7 \times 10^9 T^{3/2} \exp(-0.11eV/kT)$ (sec^{-1})
$\omega^{tc}_{FC} \leq 7 \times 10^8 T^{3/2} \exp(-1.94eV/kT)$ (sec^{-1})
$\omega_{ct} \approx 1.45 \times 10^{-6}(sec^{-1}cm^3)$

Table 2. Laser peak photon flux A^*_{dam} required for pulse train damage of NaCl

No. of pulses in train	Avalanche Nd(1.17 eV) A^*_{dam} 10^{30}(photon/sec cm^2)	Avalanche Nd(1.17 eV) t_{dam} (psec)	Avalanche Ruby(1.78 eV) A^*_{dam} 10^{30}(photon/sec cm^2)	Avalanche Ruby(1.78 eV) t_{dam} (psec)	five-photon assisted Avalanche A^*_{dam} 10^{30}(photon/sec cm^2)	five-photon assisted Avalanche t_{dam} (psec)
1	11.9	15	7.77	15	1.44	13.7
2	5.95 4.75 3.60	7.4 14 24	3.9 3.1 2.4	7.8 14 24	.72 .665	17.1 23
10	1.19	17.5	.777	24	.359 .360	22.7 23.2

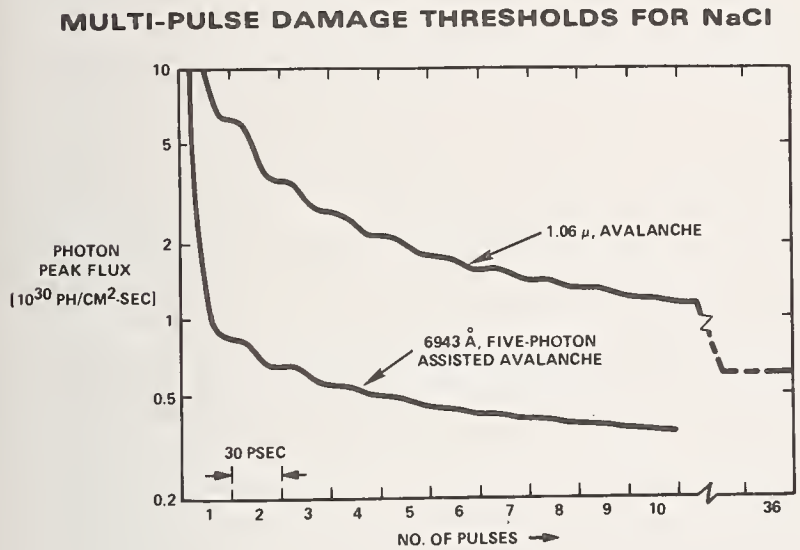

Figure 1. The relation between the damaging peak flux Å and the time of damage occurrence in the pulse train.

COMMENTS ON PAPER BY BRAUNLICH and KELLY

The speaker emphasized the fact that the critical parameters in determining multipulse damage are diffusion times, both electron diffusion in the case of avalanche ionization, and thermal diffusion. For inclusion damage the absorbing inclusion integrates over the pulse train so that damage can occur under multipulse illumination at inclusions that will not lead to damage under single pulse illumination. A similar effect can occur in the case of avalanche ionization. If the separation time between successive pulses is short compared with the electron diffusion time out of the volume or electron trapping time, then the plasma will continue to increase in density from pulse to pulse. However, even if this condition is not satisfied there will still be an integration effect. Each electron avalanche process heats the lattice and if the pulse separation is short compared to the thermal diffusion time the lattice temperature will continue to rise from pulse to pulse even though the electron avalanche process is the cause of the damage, so that in avalanche damage both effects are actually present. Whatever means leads to the heating of the lattice, whether it is via electron avalanche heating or inclusion heating, once a critical temperature is arrived at the lattice is disrupted and irreversible damage occurs.

6.6 Do Multi-photon Induced Collision Chains Lead to Pre-breakdown Material Modifications in Alkali Halides?*

A. Schmid and P. Bräunlich
Research Institute for Engineering Sciences
College of Engineering
Wayne State University
Detroit, Michigan 48202

and

Bendix Research Laboratories
Southfield, Michigan 48076

and

P. K. Rol
Research Institute for Engineering Sciences
College of Engineering
Wayne State University
Detroit, Michigan 48202

Experiments are described that indicate the existence of a new phenomenon in certain alkali halides: the multi-photon induced collision chain along [211] and [110] directions of the halide sublattice at power densities below the one-shot damage threshold. A preliminary model description of the involved physical processes is given. The sequence of events starts with the multi-photon generation of self-trapped excitons and leads, via nonradiative exciton-decay, to the formation of new color centers and/or to the ejection of atomic species from the surface. Possible implications which these pre-breakdown material modifications may have on intrinsic optical breakdown are discussed.

Key words: Alkali halides; collision chains; halogen emission; intrinsic damage; multi-photon absorption.

Laser damage reveals itself through one or more of the following phenomena, all of which indicate an irreversible modification of the damaged material [1][1]:

i) a sudden decrease of the transmitted laser power
ii) the formation of a hot plasma
iii) the formation of bubbles and cracks (or craters on the surface).

If none of these phenomena is observed, the material is believed to be uneffected aside from some temporary increase in temperature, possible electric charging (due to emission of photoelectron), or evaporation of contaminants from the surface, etc.

Boling et al [2] have recently investigated the formation of color centers which may be formed by electron or hole trapping in existing point defects; e.g., the formation of F-centers in NaCl by trapping of conduction electrons in Cl^--vacancies. These color centers represent an electronic material modification which can reduce the damage threshold in repeated shot experiments. This is, of course, one of the reasons why studies of intrinsic laser damage should be performed on sample sites which were not previously exposed to intense laser photon fluxes. Also, color center formation may be one of the origins of the statistical character of laser damage[2]. Nevertheless, repeated-shot damage thresholds are of considerable practical interest for they provide information on the susceptibility of optical components to laser damage under repetitive use.

In the present paper we discuss experimental evidence for another type of pre-breakdown material modification that we believe may have a profound effect on the damage characteristics of certain optical materials. This laser induced change of the sample is not electronic in character (such as electron trapping in Cl^--vacancies), but rather consists of laser induced formation of new or additional absorbing defects by removing lattice constituents from their normal sites. The removal of lattice constituents can be particularly efficient on the surface as we have found in the case of NaCl, KCl, and KBr that are exposed to intense fluxes from a Q-switched ruby laser. The range of fluxes for which we were able to detect this phenomenon extends from the one-shot damage threshold down to about one-tenth of this value.

The experimental arrangement which we used is shown in figure 1. Inside a vacuum chamber ($\leq 2 \times 10^{-6}$ Torr) the crystal is mounted on a sample holder. The beam from a Q-switched ruby laser is focused onto the sample and the emitted species are analyzed with a minature Mattauch-Herzog mass spectrometer[3] which is positioned such that it receives atoms and ions being emitted from the fcc alkali-halide in the [110] direction. The halogen atom signals increase with A^N, where A is the peak laser flux and N is an integer, which depends on the particular alkali halide and is larger than two. For KCl we find N=4.

*Supported by the Division of Materials Research of the National Science Foundation
1. Figures in brackets indicate the literature references at the end of the paper.

A preliminary calibration of the detection system showed that at the highest flux, just below the damage threshold, up to 10^{16} halogen atoms may be emitted per laser shot.

The directionality of the halogen emission was established with the aid of microchannel plates in conjunction with a phosphor screen or with specially modified detectors having high spatial resolution. A typical result from an undistorted surface region of KCl is shown in figure 2. Emission occurs in four [211] directions and the four [110] directions that penetrate the sample surface. Only four of the twelve possible [211] spots are observed because of geometrical detector limitation. The center hole in the detector is required for passage of the laser beam.

We believe the following simple model describes the physical processes that occur in the sample. During exposure to the laser pulse, self-trapped excitons are formed by multi-photon absorption. In alkali halides this self-trapped exciton may also be regarded as a V_k color center plus one electron [4]. Since this in itself is an excited state, it will decay radiatively or non-radiatively to the ground state. The multi-photon excitation is expected to lead to the same final state of the exciton as observed by electron bombardment[5], x-ray[6] or UV-excitation[7]. At room temperature the probability for non-radiative decay is high. It was shown that the non-radiative decay of the V_k^- center leads to the formation of separated F and H centers via a halogen atom replacement collision sequence[8]. If we apply this model to our experiment, and if we assume that the crystal surface intercepts the replacement collision sequence, then not only the emission of halogen ions and neutrals can be explained, but also its structural directionality.

In summary, the following sequence of events appears to occur:

1) Multi-photon excitation of an electron from the valence band during the duration of the laser pulse.
2) The resulting Cl-ion which has the excited electron only weakly bound finds its energetic saddle point in the formation of a Cl_2^- molecule-ion or a V_k center with an orbital electron attached. This V_k^- center can also be understood as a self-trapped exciton.
3) At room temperature the lifetime of the self-trapped exciton is very short and two options of exciton decay are open:
    a) radiative decay: results in luminescence
    b) non-radiative decay: results in kinetic energy for the Cl partners of the original Cl_2^- molecule-ion.
4) Non-radiative decay may launch a Pooley-Hersh collision chain[9] along [211] and [110] direction in fcc alkali halides.
5) If the laser excitation occurs close enough to the surface ($\sim$ 40 Å) the crystal surface may intercept the collision chain and Cl is released into the mentioned specific crystallographic directions in ionized and neutral form.

In the bulk, the formation of new Cl^--vacancies and Cl-interstials as a result of the collision chain is expected to reduce the damage threshold from shot to shot. However, we have not yet incorporated a color center creation rate in our kinetic damage model, and a dynamic description [2,10] of this effect is not available at this time.

On the surface a pit is eventually formed after one or more shots, and according to Bloembergen[1], the threshold flux for avalanche ionization is reduced as soon as the dimensions of this groove reach a few hundred A. At sufficiently high fluxes this may occur even during one shot of 30 nsec duration so that ablation in conjunction with avalanche ionization, in fact, appears to be the damage mechanism at least in KCl, KBr, and NaCl at the ruby frequency. With a laser spot radius of .1 mm, we calculate the area affected by collision chains to be .015 mm^2. A fourth-order excitation process is assumed in this case. In KCl we have 2.5×10^{12} lattice cells per mm^2 or $.5 \times 10^{13}$ Cl-ions per mm^2 of surface area. Therefore, the measured emission corresponds to more than 1000 ablated layers per laser shot at the upper pre-breakdown flux limit. The effected areas may not be detected with the usual optical methods used to detect the occurrence of breakdown until the dimensions of the pit approach 1 μm or more.

Finally, we want to point out that a new mechanism appeared to be effective in some of the observed damage events. Figure 3 shows a damage site in the [110] plane of KCl. The emission pattern observed during that particular event was very similar to the one in figure 2. We must conclude from the symmetric appearance of the damage site that no plasma was formed which would have caused deposition of material in a circular pattern[11]. Rather, we believe that damage occurred due to a dense flux of simultaneously propagating collision chains with no indication of avalanche breakdown. The latter process would have resulted in melting and plasma formation.

References

[1] N. Bloembergen, IEEE Quant.Electron. QE-10, 375, (1974).

[2] N. Boling, P. Braunlich, A. Schmid and P. Kelly, Appl. Phys. Lett. (Aug. 15, 1975) to be published.

[3] J. P. Carrico, S. Booker, J. Rice and E. Schaefer; J. Phys. E. Sci. Instrum., 7, 471 (1974).

[4] R. G. Fuller, R. T. Williams, and M. N.Kabler; Phys. Rev. Letter 25, 446 (1970).

[5] See, for example: R. T. Williams, and M. N. Kabler; Phys. Rev. B9, 1897 (1974) and Solid State Comm. 10, 49, (1972).

[6] A. Wasiela, G. Ascarelli, and Y. Merle d'Aubigne; Phys. Rev. Lett. 31, 993 (1973).

[7] V. V. Bichevin, KL. F. Käambre, Ch. B. Lushchik, and E. S. Tiisler, Soviet Physics - Solid State 12, 2332, (1971).

[8] Y. Al Jammal, and P. D. Townsend; J. Phys. C. Solid State 6, 955 (1973)

[9] R. Smoluchowski, O. W. Lazareth, R. D. Hatcher and G. J. Dienes; Phys. Rev. Lett 27, 1288, (1971).

[10] P. Bräunlich, A. Schmid and P. Kelly, Appl. Phys. Lett 26, 150 (1975) and Appl. Phys. Lett. 26, 253 (1975).

[11] N. Boling, G. Dubé, and M. D. Crisp; Appl. Phys. Lett. 21, 487 (1972 and references therein.

Figures

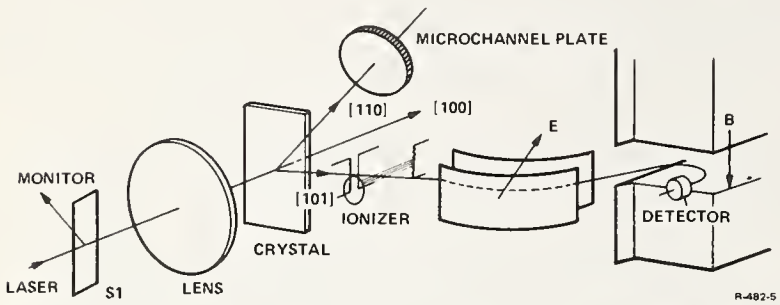

Figure 1. Schematic of experimental arrangement.

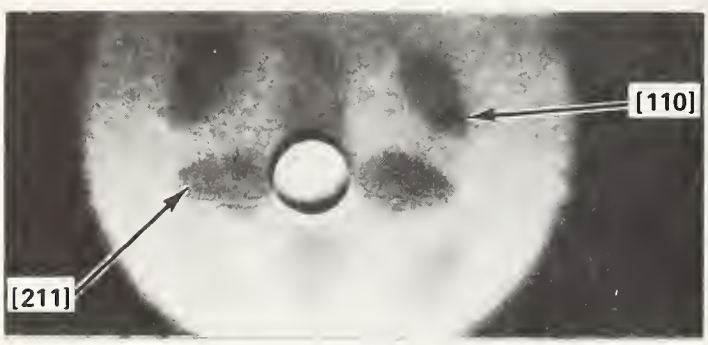

Figure 2. Cl-emission pattern during exposure of KCl to an intense pulse from a Q-switched ruby laser.

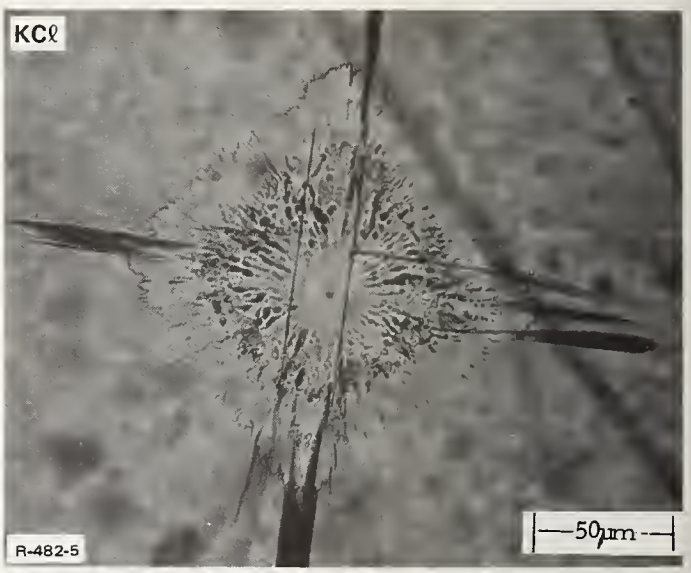

Figure 3. Damage site on exit surface of KCl after exposure to one pulse from a Q-switched ruby laser.

COMMENTS ON PAPER BY SCHMIDT, *et al*

There is a clear implication in this work that a sample would damage at a significantly lower threshold on the second shot after it had been irradiated once and the color center formation proposed in this research had taken place. The speaker indicated that that experiment had not been carried out. He further indicated that F-centers are thought to be formed in this process no coloration of the crystal could be seen because of the fact that all the F-centers would be formed in a very small volume of the crystal and therefore the net absorption induced by the F-centers is very small. The speaker further indicated that a series of experiments more extensive than those indicated in the paper have been carried out including the irradiation of potassium chloride, potassium bromide, sodium chloride, and lithium flouride. The particle emission has been observed in potassium chloride and potassium bromide, but not in lithium fluoride. The sodium chloride results obtained at the time of the presentation of the paper were still ambiguous. The lack of observation of particle emission in the case of lithium flouride is consistent with the very large energy gap of that material.

6.7 Multiphoton Absorption Coefficients in Compound Semiconductors from Ruby to CO_2 Laser Wavelengths

R. A. Shatas. S. S. Mitra,* and L. M. Narducci†

Quantum Physics, Physical Sciences Directorate
U. S. Army Missile Command
Redstone Arsenal, Alabama 35809

A critical review of multiphoton absorption coefficients for direct band semiconductors of interest in laser optical applications is presented. The two-photon nonlinear absorption coefficients have been calculated in the second order perturbation employing interconduction band transition model of Braunstein and Ockman, two-valence band intraconduction or intravalence band transition model of Basov et al., and the Keldysh electromagnetic field "dressed" valence and conduction band wavefunction model. In all models, corrections to the original calculations were needed to account for effective masses, dielectric constants and the energy band dispersion relations. Comparison of theoretical predictions at 0.694, 1.06, 1.318, and 10.6 μm laser wavelengths shows that, in general, the Basov model slightly over-estimates, the Braunstein model substantially under-estimates the nonlinear absorption, and the Keldysh model yields second order nonlinear absorption about three times larger than Braunstein. It is shown that the second order nonlinear absorption coefficient in the photon energy range $E_g/2 < \hbar\omega < E_g$ where E_g is the forbidden gap width, can be as high as 10^{-5} cm W^{-1} and therefore under certain circumstances can exceed the linear absorption at laser flux intensities as low as 10^5 W cm^{-2}. In addition, nonlinear absorption coefficients up to the fifth order have been estimated from the Keldysh model. The utility of the Keldysh model is demonstrated by the surprisingly good prediction of the band-edge absorption in GaAs and InSb without any adjustable parameters.

Key words: Multiphoton processes; nonlinear absorption; nonlinear optical properties; semiconductor optical properties; two-photon absorption coefficients.

1. Introduction

Under illumination by intense coherent infrared radiation sources presently available, many optoelectronic materials are driven into a nonlinear response region. In this paper, we analyze processes contributing to the nonlinear absorption of light by electronic transitions taking place as a result of a multiquantal process in a dielectric or a semiconductor material usually transparent to low intensity radiation. We also show that the absorbance at high radiation fluxes is describable by a nonlinear differential equation. For the case of a weak radiation field, this equation can be linearized and its solution yields the Lambert-Beer law. At high intensities, however, nonlinear terms dominate, and consequently, a general analytic solution is not available. Physical arguments must be invoked to separate terms in powers of intensity. For each particular ratio of materials properties to radiation flux parameters, one particular term dominates the absorption. Electronic transition rates induced by photon processes of appropriate multiplicity enter as coefficients in the nonlinear differential equation describing the absorption. Their calculation can be undertaken in the framework of the time-dependent perturbation theory of wave mechanics; also, a semiphenomenological approach employing the rudiments of the "dressed state" concept of the quantum field theory is parametrized in terms of the one-electron effective mass approximation. In the perturbation-theoretic approach, a semiclassical treatment of the interaction operator is undertaken in which the vector potential of the Maxwell field is used to describe the optical radiation, and the oscillating electron in the momentum representation accounts for the electronic motion. The description is complicated by the need to employ the effective mass parametrization of the energy band theory of the solid state. Within the limits imposed by these fundamental difficulties, numerical methods were developed to calculate multiphoton absorption for a number of technologically important semiconductors. Because of a rather unsatisfactory state of the fundamental knowledge in the nonlinear quantum optics from both the physical and the mathematical points of view, a deeper insight through the employ of methods leaning towards the axiomatic quantum field theory was sought. One significant aspect of this approach is that the dynamic eigenlevel shifts of the originally quasi-

---

*Permanent address: Department of Electrical Engineering, University of Rhode Island, Kingston, RI.

†Permanent address: Department of Physics, Worcester Polytechnic Institute, Worcester, MA.

stationary states caused by the turn-on of the radiation field can be incorporated at the beginning of calculations. This fast-varying modulation of the eigenfunction of a discrete state of the matter field is not usually accessible by the perturbation expansion of the first-quantized wave mechanics simply because the order of perturbation expansion usually is not carried out beyond the first-nonzero contribution. Computerized numerical solutions for transition probabilities in various approaches are given and compared with experimental data; disagreements between theory and experiment are shown to arise from certain inadequacies of the theoretical approach. Suggestions with respect to the further development of the nonlinear quantum optics of solids are offered. In reviewing the research literature on the multiphoton absorption processes in gases, we note extensive investigations in recent years [1-3].[1] Unfortunately, despite numerous theoretical and experimental contributions, there is a wide scatter between both the measured and the predicted values of multiphoton absorption. Because of the many applications of pulsed lasers, there is a need to identify theoretical approaches which are suitable to predict at least the order of magnitude of multiphoton absorption in optically transparent materials. In the case of gases, the ratio of the ionization potential to the photon energy of a typical pulsed laser is rather high; therefore, atomic photoionization experiments are not suitable to test theories constructed for optical electromagnetic fields of moderate intensity. Specifically in what follows, we compare two low-order perturbation treatments with a semiclassical procedure in which the band distortion due to the electromagnetic field is taken into account. Within the context of models proposed by Keldysh [4], Braunstein and Ockman [5], and Basov et al. [6,7], we calculate second order absorption coefficients for a number of direct-bandgap semiconductors and compare theoretical predictions with available experimental results. In section 2, we consider the rate equations describing the nonlinear absorption. In section 3, we outline a general formulation of the multiphoton absorption within the semiclassical radiation theory in the electric dipole approximation. Section 4 deals with the Keldysh "exact" model which employs conduction and valence band electronic wavefunction "dressed" by the radiation field. Section 5 contains the perturbation-theoretic approaches of Braunstein and Ockman. Comparison between the theoretically predicted and the experimentally determined values of nonlinear absorption coefficients is given in section 6.

2. Attentuation of Light by Nonlinear Absorption

In a transparent material, residual absorption of light may be related to a number of independent processes such as multiphoton and -phonon excitations, presence of residual free carriers or impurities, creation of excitonic states, and perhaps phonon parametric amplification. At sufficiently high intensities of the optical field, free carriers created through the elementary excitation processes enumerated above, may contribute to the time dependence of the absorption through the free carrier interaction with the electromagnetic field (so-called inverse Bremsstrahlung). The time dependence of this part of absorption follows from the rate equations describing the free carrier density and shows typically transients of 10^{-12} to 10^{-8} sec duration reflecting the trapping and recombination rates in solid materials. In these considerations, we will neglect these transient contributions.

For the steady-state description of the nonlinear absorption, we argue that for a given material with a fixed bandgap between the valence and conduction bands E_g and a given incident photon energy $\hbar\omega$, the photon absorption on ν-th order dominates. Here ν denotes the ratio $\langle E_g/\hbar\omega + 1\rangle$, and the brackets $\langle\ \rangle$ stand for the integer part of this ratio. Although linear energy losses caused by nonresonant processes will always be present even in the purest materials, low-intensity measurements can yield reliable values of the linear absorption coefficient. Hence observed intensity loss due to multiphoton absorption should be satisfactorily described by the phenomenological rate equation

$$\frac{dI}{d\ell} = -\left(\alpha_1 I^1 + \alpha_2 I^2 + \ldots + \alpha_n I^n\right) = -\sum_{\nu=1} \alpha_\nu I^\nu \ , \tag{2.1}$$

where ℓ represents the spatial coordinate along the direction of travel of the light in the material, and α_ν is the ν-photon absorption coefficient. The total experimentally observed intensity attenuation should be corrected for the contribution due to nonresonant losses. The corrected value provides the rate of intensity loss $dI/d\ell$ due to nonlinear absorption processes.

In the above rate equation, I denotes the incident intensity (light flux in units of W cm^{-2}). The dimension of the ν-th order absorption coefficient α_ν is $(\text{length})^{2\nu-3}/(\text{power})^{\nu-1}$. If the multiphoton process of order ν dominates, we can express the attenuation rate of the light flux as

$$\frac{dI}{dt} = -\frac{c}{\sqrt{\varepsilon_\infty}} \sum_{\nu} \alpha_\nu I^\nu \ ,$$

---

[1] Figures in brackets indicate the literature references at the end of this paper.

where c is the velocity of light in vacuum, and ϵ_∞ is the high-frequency dielectric constant of the material. The relation between the flux in the material I [W cm^{-2}] and the peak electric field amplitude E_o [V cm^{-1}] in practical electromagnetic units is given by $I = \frac{1}{2}(E_o^2 \sqrt{\epsilon_\infty}/R_o)$, where R_o is the vacuum impedance (377 Ω). The relation between the flux I [W cm^{-2}] and the photon number density N_{ph} [cm^{-3}] is given by $I = (c/\sqrt{\epsilon_\infty})\, \hbar\omega\, N_{ph}$. Accordingly, the rate of photon absorption per unit volume is expressed by

$$\frac{dN_{ph}}{dt} = \frac{\alpha_\nu}{\hbar\omega} I^\nu = -\nu \frac{dN_e}{dt} \quad ,$$

where N_e designates the number density of free carriers created by across the gap ionization through the ν-photon absorption. The right-hand side of the above equation is also a consequence of the energy balance condition since the rate of the photon absorption must be ν-times larger than the rate of the free carrier creation; hence $dN_{ph}/dt + \nu(dN_e/dt) = 0$. We also designate

$$\frac{dN_e}{dt} = w(E_o^{2\nu}) \quad ,$$

where w is the multiphoton transition rate; consequently, the multiphoton absorption coefficient for the ν-th order process is given by

$$\alpha_\nu = \frac{2\nu\, \hbar\omega\, (2R_o)^\nu\, w(E_o^{2\nu})}{\epsilon_\infty^{\nu/2}\, E_o^{2\nu}} \quad . \tag{2.2}$$

In eq. (2.2) ϵ_∞ is the high frequency dielectric constant, and the factor of 2 is introduced to account for the free carrier spin degeneracy. Note that despite the apparent dependence of the absorption coefficient upon E_o, the actual calculated numerical values of α_ν given in section 6 are field independent.

3. Multiphoton Absorption by the Semiclassical Time-Dependent Perturbation

The theoretical description of multiphoton absorption is based on the employ of second- and higher-order time-dependent quantum mechanical perturbation theory. In the case of the two-photon process, it has been first shown by M. Goeppert-Mayer [8] that the interaction term coupling the momentum of the electron $\vec{p}$ with the vector potential of the Maxwell field $\vec{A}$, given by $(e/mc)\, \vec{p} \cdot \vec{A}$, can be canonically transformed to $\vec{P} \cdot \vec{E}$. This transformation is valid when the linear extent of the interacting electron-ion system is small with respect to the wavelength of the radiation field (this condition is readily satisfied for the electric dipole mediated transitions into far ultraviolet wavelengths); subsequently, either of these interaction terms can be used in perturbation expansion. Here P denotes the polarization of the medium.

At first we shall review the salient features of the perturbation theory. Let there be two eigenstates of energy E_i and E_f; we are concerned with an electric dipole transition between them induced by photons of energy $\hbar\omega < E_f - E_i$. Such transitions can then only take place by the participation of more than one photon. The order of the photon process is obviously given by $\langle 1 + (E_f - E_i)/\hbar\omega \rangle$ where $\langle\ \rangle$ indicates the integer part. The probability of such transitions will depend on the number density of photons or the electric field intensity of the radiation. Large field intensities will also introduce level shifts.

Let us consider the time-dependent Schrödinger equation

$$\mathcal{H}\psi = i\hbar \frac{\partial \psi}{\partial t} \quad . \tag{3.1}$$

The Hamiltonian $\mathcal{H}$ consists of the unperturbed time-independent Hamiltonian $\mathcal{H}^o$ and a time-dependent perturbation term $\mathcal{H}'(\vec{r},t)$. If $\psi_n^o(\vec{r})$ defined by

$$\mathcal{H}^o \psi_n^o(\vec{r}) = E_n \psi_n^o(\vec{r}) \tag{3.2}$$

are the eigenstates of $\mathcal{H}^o$, $\psi_n^o(\vec{r},t)$ is given by

$$\psi_n^o(\vec{r},t) = \psi_n^o(\vec{r}) \exp\left[-i \frac{E_n}{\hbar} t\right] \quad . \tag{3.3}$$

The general state function, which is the solution of eq. (3.1), can be expressed as a superposition of states

$$\psi(\vec{r},t) = \sum_n a_n(t)\ \psi_n^o(\vec{r},t) \quad . \tag{3.4}$$

The probability that at any time t the system is in a state with energy E_n is given by $|a_n(t)|^2$. Substituting eq. (3.4) in eq. (3.1), and making use of eqs. (3.2) and (3.3), one obtains

$$\dot{a}_n(t) = \frac{1}{i\hbar} \sum_{n'} a_{n'}(t) \langle \psi_n | \mathcal{H}' | \psi_{n'} \rangle \quad . \tag{3.5}$$

Equation (3.5) may be used to solve a_n to any order. The zeroth order coefficients $a_n^{(o)}(0)$ at the time $t = 0$ are zero except for the initial state, for which

$$a_i^{(o)}(0) = 1 \quad .$$

The first order coefficient $a_n^{(1)}(t)$ is therefore

$$a_n^{(1)}(t) = \frac{1}{i\hbar} \int_o^t \langle \psi_n | \mathcal{H}' | \psi_i \rangle\ dt' \quad . \tag{3.6}$$

To obtain the second order correction to the coefficient $a_n(t)$, one substitutes the above value of $a_n^{(1)}(t)$ in the right-hand side of eq. (3.1) and solves for $a_f^{(2)}(t)$. Continuing this iterative process, one can write for a general n-th-order correction (the summation over all repeated indices is implied)

$$a_f^{(n)}(t) = \left(\frac{1}{i\hbar}\right)^n \int_o^t \langle \psi_f | \mathcal{H}' | \psi_n \rangle\ dt' \int_o^{t'} \langle \psi_n | \mathcal{H}' | \psi_m \rangle\ dt'' \ldots$$

$$\times \int_o^{t^{n-1}} \langle \psi_s | \mathcal{H}' | \psi_i \rangle\ dt^{(n)} \quad . \tag{3.7}$$

The repeated indices of the wave functions are the so-called intermediate states. With the use of eq. (3.3), eq. (3.7) may be rewritten in terms of the unperturbed wave functions as

$$a_f^{(n)}(t) = \left(\frac{1}{i\hbar}\right)^n \left[\frac{\langle \psi_f^o | \mathcal{H}' | \psi_n^o \rangle}{E_n - E_r \pm \hbar\omega_1 \ldots \pm \hbar\omega_n} \cdots \right.$$

$$\left. \times \frac{\langle \psi_s^o | \mathcal{H}' | \psi_i^o \rangle}{E_s - E_i \pm \hbar\omega_1}\right] \int_o^t \exp\left\{\frac{i(E_f - E_i \pm \hbar\omega_1 \ldots \pm \hbar\omega_n)\, t'}{\hbar}\right\} dt' \quad . \tag{3.8}$$

For the sake of generality, every one of the n-photons has been assigned a different frequency $\omega_n \neq \omega_m$.

The transition probability rate may be readily obtained from eq. (3.8) and is given by

$$w_{if}(\omega) = \frac{d}{dt} |a_{if}(t)|^2 \quad . \tag{3.9}$$

So w_{if} will contain square of the expression in the square bracket of eq. (3.8), and the integral in eq. (3.8) will introduce a δ-function

$$\delta(E_f - E_i \pm \hbar\omega_1 \ldots \pm \hbar\omega_n)$$

to satisfy the energy conservation requirement.

For optical transitions in a crystalline solid, the initial and final states are obviously the valence and the conduction bands, respectively. The choice of the intermediate states accounts for different results in different calculational schemes. The order of the transition equals the number of quanta of the perturbing field absorbed or emitted. The intermediate states do not appear in the δ-function, but in the denominator of the square of the pre-integral terms of eq. (3.8). Therefore the contribution of the intermediate states to the transition probability becomes significant when they are located close to the initial or final states.

In the presence of a radiation field described by the vector potential $\vec{A}$, the kinetic energy of the electron is modified to

$$\frac{1}{2m}\left(\vec{p} - \frac{e}{c}\vec{A}\right)^2$$

which as a result introduces a perturbation Hamiltonian in eq. (3.1) of the type

$$\mathcal{H}' = \frac{e}{mc}\vec{p} \cdot \vec{A} \tag{3.10}$$

where $\vec{A} = A_o \hat{e}_1 \exp[i\vec{k} \cdot \vec{r} - \omega t]$. Here, $\vec{k}$ and ω are photon wave vector and frequency, respectively, and $\hat{e}$ its unit polarization vector. In eq. (3.10) we have neglected the $|\vec{A}|^2$ term, which is usually very small at the wavelengths and intensities in question. The amplitude $\hat{e}A_o$ of the vector potential is related to the photon density N_{ph} by

$$A_o^2 = \frac{2\pi N_{ph} \hbar c^2}{\omega \epsilon_\infty} \quad \text{(c.g.s.)} \tag{3.11}$$

where ϵ_∞ is the dielectric constant. The calculation of the transition probability rate then boils down to the calculation of the matrix elements of $\vec{p} \cdot \vec{A}$ between the valence band (or bands). the chosen intermediate levels and the conduction band. This is essentially what Braunstein et al., [5] and Basov et al., [6,7] models pertain to do.

Keldysh treatment [4], however, differs from the above scheme as it also includes the level shifts caused by the perturbing electric field $\vec{E}$, which was neglected by Braunstein and Basov. The energy shift of a level induced by the field $\vec{E} = \mathcal{R}\vec{E}_o \exp[i(\vec{k} \cdot \vec{r} - \omega t)]$ is given by

$$\Delta E_n = \frac{1}{4}\sum_m \left\{ \frac{|\vec{p}_{mn} \cdot \vec{E}_o|^2}{E_n - E_m - \hbar\omega} + \frac{|\vec{p}_{mn} \cdot \vec{E}_o|^2}{E_n - E_m + \hbar\omega} \right\} . \tag{3.12}$$

where the summation extends to all other states of the system. In the case of a semiconductor, these level shifts account for the change in bandgap in the presence of a field, which in the case of static fields is fairly well known, and is termed the Franz-Keldysh [9] effect. Keldysh's treatment for the multiphoton transition probability between shifted levels incorporates the dynamic Franz-Keldysh effect, and will be described in section 4.

4. The Keldysh "Dressed State" Model

Keldysh [4] treated the multiphoton absorption as the high frequency limit of the time-dependent tunneling induced by the oscillatory electric field of the laser radiation. In other words, a unified description is available for the autoionization process under the influence of a strong low-frequency field and for the multiphoton ionization induced by a strong high-frequency field. Keldysh's treatment applies to both isolated atoms and crystalline solids (e.g., semiconductors). In both cases Keldysh calculates the probability of direct electron excitation from the ground state (or valence band) to the continuum (or conduction band) and the excitation probability through intermediate states of the discrete spectrum. The intermediate states could be higher excited states of the Coulomb field of isolated atoms, or impurity levels and excitonic states in crystalline solids.

Keldysh considers a system described by a Hamiltonian of the form

$$\mathcal{H} = \mathcal{H}_o + \mathcal{H}_C + \mathcal{H}_F \tag{4.1}$$

where $\mathcal{H}_o$ is the kinetic energy term, $\mathcal{H}_C$ is the Coulomb contribution to the potential energy (or the crystal field in solids), and $\mathcal{H}_F$ is the interaction energy of the bound charge in a periodic electric field $E(t) = E_o \cos \omega t$. The electron is assumed to be initially in the unperturbed Coulomb ground state given by the wave function

$$\psi_o(r,t) = \psi_o(r) \exp(-i\mathcal{E}_o t/\hbar)$$

$$= \frac{1}{(\pi a_o^3)^{\frac{1}{2}}} \exp(-r/a_o) \exp(-i\mathcal{E}_o t/\hbar) \tag{4.2}$$

where $a_o = \hbar^2/(me^2 z)$ is the z-charged atom Bohr radius and $\mathcal{E}_o$ its ionization potential.

In the case of a crystalline solid, the Bloch wave function is modified by the presence of the electromagnetic field as follows. (In a sense, the bare electron state is "dressed" by the electric field component of the e.m. field.)

$$\psi_p^{(v)}(\vec{r},t) = u_{p(t)}^{(v)}(\vec{r}) \exp\left\{\frac{i}{\hbar}\left(\vec{p}(t) \cdot \vec{r} - \int_o^t d\tau E_v[p(\tau)]\right)\right\} \tag{4.3}$$

where

$$\vec{p}(t) = \vec{p} + \frac{e\vec{E}_o}{\omega} \sin \omega t \quad . \tag{4.4}$$

The amplitude functions $u_{p(t)}^{(v)}(\vec{r})$ correspond to a valence electron with momentum $\vec{p}(t)$ and have the translational symmetry of the $p(t)$ lattice. The principal difference between the traditional treatment of this problem and the Keldysh approach is that he recognizes the modification of the unperturbed bands under the influence of the field. This modification amounts to a replacement of the unperturbed momentum p with the time-dependent momentum given by eq. (4.4). The excited electronic states associated with the continuum of an atom or in the conduction band of a solid are assumed to be unaffected by the electrostatic Coulomb energy, but are modified by the perturbing effect of the electromagnetic field. Thus, in the case of isolated atoms, the ionized electron is described by the solution of the Schrödinger equation

$$i\hbar \frac{\partial \psi}{\partial t} = -\left(\frac{\hbar^2}{2m}\nabla^2 + e\vec{E}(t) \cdot \vec{r}\right)\psi \tag{4.5}$$

which is given by

$$\psi_p(\vec{r},t) = \exp\left\{\frac{i}{\hbar}\left(\vec{p} + \frac{e\vec{E}_o}{\omega} \sin \omega t\right) \cdot \vec{r}\right\}$$

$$\times \exp\left\{-\frac{i}{\hbar}\int_o^t d\tau \frac{1}{2m}\left(\vec{p} + \frac{e\vec{E}_o}{\omega} \sin \omega\tau\right)^2\right\} \quad . \tag{4.6}$$

For the case of a solid, the conduction electron is described by the Bloch function

$$\psi_p^{(c)}(r,t) = u_{p(t)}^{(c)}(r) \exp\left\{\frac{i}{\hbar}\left[\vec{p}(t) \cdot \vec{r} - \int_o^t d\tau E_c[p(\tau)]\right\}\right. \quad . \tag{4.7}$$

One again notices that the wave function of the final state is also dressed by the perturbing action of the field. As a consequence, the electronic transition does not occur between unperturbed states, but rather between nonstationary states in which the electron acceleration due to the field is taken into

account. Finally, the transition probability rate is calculated according to first order perturbation theory. The calculated transition probability is then summed over all possible final momenta of the quasi-free electron.

In order to arrive at an explicit expression for the transition probability, Keldysh used the following parabolic energy-band relation for a solid

$$E(k) = E_g \left(1 + \frac{\hbar^2 k^2}{m^* E_g}\right)^{\frac{1}{2}} \tag{4.8}$$

where m^* designates the reduced effective mass of the electron-hole pair $1/m^* = 1/m_e^* + 1m_h^*$, E_g denotes the width of the bandgap, and the momentum and k-space representations are connected by the relation $\vec{p} = \hbar\vec{k}$.

In the limiting case when the parameter

$$\gamma = \frac{\omega}{eE_o} (2m^* E_g)^{\frac{1}{2}} \tag{4.9}$$

is much larger than unity (a condition which is readily satisfied for most of crystalline solids), Keldush's transition rate (electronic transition probability per unit volume and per unit time) is given by

$$w = \frac{2}{9\pi}\omega \left(\frac{m^*\omega}{\hbar}\right)^{\frac{3}{2}} \Phi\left[\left(2\langle x+1\rangle - 2x\right)^{\frac{1}{2}}\right] \times \left(\frac{e^2E_o^2}{16m^*\omega^2E_g}\right)^{\langle x+1\rangle} \exp\left[2\langle x+1\rangle\left(1 - \frac{e^2E_o^2}{4m^*\omega^2E_g}\right)\right] . \tag{4.10}$$

The meaning of symbols in eqs. (4.9) and (4.10) is given below: $\gamma = 6.45 \times 10^3 (m^*E_g)^{\frac{1}{2}}/(\lambda E_o)$, where m^* is given in units of electron mass, E_g in eV, λ-wavelength of incident light in vacuum (in μm), E_o is the electric field amplitude in the material in units of MV m^{-1}, $\Phi(z) = e^{-z^2}\int_o^z e^{y^2} dy$ is the Dawson integral, $x = E_g/\hbar\omega\left(1 + e^2E_o^2/(4m^*\omega^2E_g)\right)$, and $\langle \ldots \rangle$ is the integer of the argument.

Up to five photon transition probability rates have been calculated by means of relation (4.10) for a number of semiconductors as function of wavelength of light at a given field intensity of 10 MV m^{-1} in the material. The relevant band masses and bandgaps used in these calculations are listed in table 1.

Table 1. Material parameters used in calculation of multiphoton transition rates as function of energy of incident laser light shown in figures 1 to 6.

Semiconductor	Bandgap (eV)	Effective mass ratio		
		Electron	Hole	Reduced pair mass
GaAs	1.53	0.068	0.5	0.06
GaSb	0.8	0.047	0.5	0.043
InAs	0.46	0.02	0.41	0.019
PbS	0.34	0.66	0.5	0.364
InSb	0.26	0.013	0.6	0.0127
PbTe	0.24	0.22	0.29	0.125

The log w vs photon energy plots are given in figures 1 to 6. Numbers written above each plateau of the transition rate indicate the integer value of $\langle E_g/\hbar\omega + 1\rangle$. Apart from quantitative differences, the qualitative functional dependence in figures 1 to 6 is strinkingly similar in that a quasi-resonant behavior at integer $E_g/\hbar\omega$ values is displayed. This reminds us of one of the most obvious features of the multiphoton transition probability calculated by Bebb and Gold [10] for hydrogen-like atoms which shows the distinctly resonant dependence of the excitation probability as a function of the incident photon energy. While the energy levels of isolated atoms are clearly quite different from the bands of

semiconductors considered in Keldysh's model, a quasi-resonant dependence of the transition rate on the incident photon energy seen in our calculations is qualitatively correct.

It should be also remarked that Weiler et al.,[11] have extended Keldysh's calculation to include the effects of longitudinal or transverse magnetic fields on the interband electronic transition. Weiler's conclusions are in agreement with Keldysh's results for zero applied magnetic field. One expects a series of edge absorptions of the form $\sim (\nu\hbar\omega - E_g)^{\frac{1}{2}}$ where ν is the photon multiplicity. Such a behavior is indeed found in the negative slope of the transition rate after each quasi-resonant "peak" as seen in figures 1 to 6. It has been argued that, at best, Keldysh's theory should provide acceptable results only for processes of fairly high photon multiplicity and that its application to two-photon absorption processes should not yield more than qualitative agreement with the experimental data. Recent experiments [12] involving four-photon transition in ZnS are at variance with Keldysh's prediction, while they are in fair agreement with perturbative semiclassical calculations [13]. However, a good agreement with three-photon absorption in CdS has been found. C. H. Lee measured [14] the three-photon absorption coefficient $\alpha_3 = 1.3 \cdot 10^{-2}$ cm^3/GW^2 for single-crystal CdS. Our calculations based on the evaluation of eqs. (2.2) and (4.10) yielded a value of $\alpha_3 = 0.2 \cdot 10^{-2}$ cm^3/GW^2. We have used $E_g = 2.42$ eV, $\epsilon_\infty = 5.32$ and $m^* = 0.192$ as CdS material parameters in this calculation. A more systematic comparison for the two-photon absorption coefficient is presented in section 6. An additional feature of the Keldysh model was found (which was rather unexpected) that it predicts very well the one-photon absorption coefficient near the band edge for two thus far analyzed semiconductors, GaAs and InSb. It is known that near the fundamental absorption edge, the one-photon absorption coefficient can be expressed as

$$\alpha_1 = A(\hbar\omega - E_g)^{\gamma} \tag{4.11}$$

where $\hbar\omega$ is the photon energy, and γ is a constant which equals 1/2 and 3/2 for allowed direct transitions and forbidden direct transitions, respectively. We specialize eq. (4.11) for the case $\hbar\omega > E_g$. In addition, the exponent γ equals 2 for indirect phonon assisted transitions and 1/2 for allowed indirect transitions to exciton states.

Near the absorption edge, where the values of $(\hbar\omega > E_g)$ become comparable to the binding energy of the exciton, the Coulomb interaction between the free hole and the electron must be taken into account. For $\hbar\omega < E_g$ the absorption merges continuously into that due to the higher excited states of the exciton; where $\hbar\omega \gg E_g$, higher energy bands will participate in the transition process and complicated band structures will be reflected in the absorption coefficient. The least square fit of absorbance vs photon energy curves for photon energies near the band edge of GaAs yields the following values for A and γ : $A = 44 \cdot 10^3$, $\gamma = 0.499$, and $A = 44.7 \cdot 10^3$, $\gamma = 0.505$ from Moss and Hawkins' [15] and from Sturge's [16] measurements, respectively. Numerical evaluation of eqs. (2.2) and (4.10) for the one-photon transition case $\nu = 1$ can be expressed by the functional dependence shown in eq. (4.11) with $A = 44 \cdot 10^3$ and $\gamma = 1/2$. Hence, the Keldysh model besides giving the correct value of the absorption coefficient at the band edge of GaAs describes very well its wavelength dependence also. This agreement is seen in figure 7 where unadjusted calculated absorption coefficients are compared with Moss and Hawkins' experimental values for photon energies between 1.42 to 1.48 eV. GaAs parameters used in calculating the theoretical absorption coefficient of figure 7 are listed in table 2.

Table 2. List of parameters for GaAs used in the theoretical fit of figure 7. The values for reduced effective mass m* and dielectric constant ϵ_∞ have been obtained from [18] and [19], respectively.

Data source	E_g[eV]	m*	ϵ_∞
[15]	1.403	0.059	10.9
[16]	1.521	0.059	10.9
[16]	1.435	0.059	10.9

For the comparison of theoretical and experimental one-photon absorption coefficient of InSb, the experimental data points have been taken from figure 3 of [20]. The empirical equation which fits the data around the band edge is listed in table 3 together with the reduced effective mass and the high frequency dielectric constant which are needed for the theoretical comparison.

Table 3. Empirical relation for the absorption coefficients of InSb reported in [20]. The bandgap energy E_g has been calculated by a least square fitting procedure. The reduced effective mass m^* and the high-frequency dielectric constant ε_∞ have been obtained from [19] and [21], respectively.

$$\alpha = 2.026 \cdot 10^4 (\hbar\omega - E_g)^{\frac{1}{2}} \ [cm^{-1}]$$

$\hbar\omega, E_g$ in eV

$E_g = 0.2248$ [eV]

$m^* = 0.0113\ m$; $m = 9.108 \cdot 10^{-28}$ [g]

$\varepsilon_\infty = 15.7$

In fig. 8 we have plotted the experimental data together with the results of the numerical evaluation of eqs. (2.2) and (4.10). We note that the quantitative agreement between the Keldysh theory and the measured data is rather good, particularly if we consider the large range of incident photon energies included in the comparison. A further discussion on the agreement of Keldysh model with the second-order perturbation theory is given in section 6.

5. Second-Order Perturbation Models.

In this section, we consider two second-order perturbation models first proposed by Braunstein and Ockman [5] and by Basov et al., [6,7]. As explained in section 3, in the second-order perturbation an intermediate state is required to complete the transition from the initial to the final state of the system perturbed by the radiation field. A proper accounting of intermediate states becomes important when their energy eigenstates are close to initial or final states of the system, or if they coincide with other real states encountered in practical materials such as exciton or impurity states. Therefore, the agreement between the calculated and the observed nonlinear absorption coefficients will depend largely upon the inclusion of the appropriate details of the energy band structure.

Braunstein and Ockman [5] consider vertical transitions between unperturbed parabolic bands. They assume that the only significant intermediate state is a higher conduction band designated with n in figure 9.

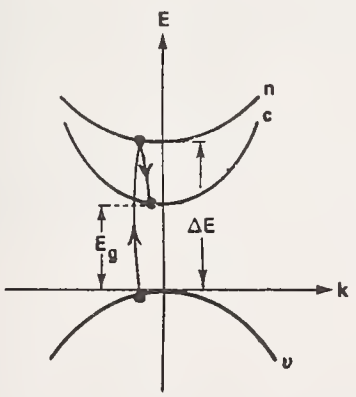

Figure 9. The interconduction band transition model of Braunstein; v , c , and n refer to the valence, lowest conduction, and intermediate conduction bands, respectively. All energy bands are taken to be parabolic in the k-space.

Second-order perturbation theory yields the transition rate per unit volume for vertical transitions at a given value of k ; subsequently, the k-dependent probability is integrated over all values of k . For allowed-allowed transitions, the result is

$$w = \frac{|\mathcal{K}_{nc}|^2 |\mathcal{K}_{vn}|^2}{8\pi\hbar^4} \frac{m^{\frac{3}{2}}}{\sqrt{2}} \frac{(2\hbar\omega - E_g)^{\frac{1}{2}}}{(a_c + a_v)^{\frac{3}{2}}} \left(\Delta E - \hbar\omega + \frac{a_n + a_v}{a_c + a_v} (2\hbar\omega - E_g) \right)^{-2} \tag{5.1}$$

In eq. (5.1), $\mathcal{H}_{nc}$ and $\mathcal{H}_{vn}$ are the matrix elements of the interaction Hamiltonian between the conduction c and the valence v bands, and the intermediate conduction band n, respectively. The free electron mass is designated with m, and a_i (i = c,v,n) is the reciprocal effective mass ratio m/m_i^*. The energy gap ΔE is the energy difference between the top of the heavy hole band (the only valence band included in this calculation) and the bottom of the intermediate conduction band.

The interaction Hamiltonian is taken to be of the form

$$\mathcal{H} = \frac{e}{mc} \vec{p} \cdot \vec{A} \quad .$$

We will evaluate the matrix elements of the interaction term by the so-called $\vec{k} \cdot \vec{p}$ method [22]. In this method, the matrix elements of the effective Hamiltonian are given by

$$\mathcal{H}_{j,\ell} = [E_j(\vec{k}_o) + \frac{\hbar^2}{2m} (\vec{k}^2 - \vec{k}_o^2)] \delta_{j,\ell} + \frac{\hbar}{m} (\vec{k} - \vec{k}_o) \cdot \vec{p}_{\ell,j} \quad . \tag{5.2}$$

Consider a solid consisting of two energy bands denoted by 0 and 1 each having an extremum in the reciprocal lattice space at $\vec{k}_o = 0$ and at corresponding momenta $\vec{p}_{01} = \vec{p}_{10}^* = \vec{p}$ taken to be isotropic. We choose the zero of energy axis to be at the top of the lower band 0 such that $E_o(\vec{k}_o) = 0$ and $E_1(\vec{k}_o) = E_g$ for the upper band, E_g being equal to the forbidden gap width. These assumptions restrict our treatment to solids with allowed direct transitions between the two bands. The Hamiltonian operator is then given by a 2 x 2 matrix shown below

$$\mathcal{H} = \begin{vmatrix} \frac{\hbar^2 k^2}{2m} & \frac{\hbar}{m} \vec{k} \cdot \vec{p} \\ \frac{\hbar}{m} \vec{k} \cdot \vec{p} & E_g + \frac{\hbar^2 k^2}{2m} \end{vmatrix} \quad . \tag{5.3}$$

Its diagonalization yields the following eigenvalues of the matrix (5.3)

$$E_{0,1}(k) = E_g/2 + \hbar^2 k^2/2m \pm \sqrt{E_g^2/4 + \hbar^2 k^2 p_{0,1}^2/m^2} \quad . \tag{5.4}$$

For small values of k, the square root in eq. (5.4) can be expanded in a power series about $E_g/2$. Retention of the first-term only yields the following expression for the lower energy band

$$E_o(k) = \frac{\hbar^2 k^2}{2m} \left[1 - \frac{2p^2}{mE_g}\right] \quad , \tag{5.5}$$

and

$$E_1(k) = E_g + \frac{\hbar^2 k^2}{2m} \left[1 + \frac{2p^2}{mE_g}\right] \tag{5.6}$$

for the upper energy band. The effective reciprocal mass tensor of the carrier in n-th band is defined by

$$(m/m_n^*)_{\alpha\beta} = \frac{m}{\hbar^2} \frac{\partial^2 E_n(k)}{\partial k_\alpha \partial k_\beta} \quad . \tag{5.7}$$

Because of the assumption of isotropic matrix elements in the Hamiltonian (5.3) of the two-band model, eqs. (5.5) to (5.7) yield scalar reciprocal effective masses for free carriers, $[m/m^*_o]_o = 1 - 2p^2/(mE_g)$, and $[m/m^*_1]_1 = 1 + 2p^2/(mE_g)$ for the lower and the upper energy bands, respectively. We take the lower band 0 to be the highest valence band and the upper band 1 the lowest conduction band of a solid with a direct energy bandgap. The effective reciprocal masses of holes h in the valence v and electrons e in the conduction c bands are thus given by the scalar relations

$$[m/m^*_h]_v = 1 - 2p^2/(mE_g) \tag{5.8}$$

and

$$[m/m^*_e]_c = 1 + 2p^2/(mE_g) \quad , \tag{5.9}$$

respectively.

The band curvatures of the valence and the conduction bands are of opposite signs which accounts for the opposite signs of the p^2 term in the eqs. (5.8) and (5.9). Keeping in mind the opposite curvatures, we can rewrite eqs. (5.8) and (5.9) in absolute values to yield

$$|m/m^*_h| = 2p^2/(mE_g) - 1 \tag{5.8a}$$

and

$$|m/m^*_e| = 2p^2/(mE_g) + 1 \quad . \tag{5.9a}$$

From (5.8a) and (5.9a), one readily obtains $m/m^* = 4p^2/(mE_g)$. The energy-momentum relation needed to evaluate the matrix elements of the interaction Hamiltonian in terms of the one-electron effective mass approximation of the solid state theory is therefore given by

$$\frac{p^2}{2m} = \frac{E_g}{8}\left(\frac{m}{m^*}\right) \quad , \tag{5.10}$$

which is quite satisfactory for small values of k. We proceed in evaluating the matrix elements of eq. (5.1) with the help of eq. (5.10) and substitute the transition rate into eq. (2.2) for the case $\nu = 2$. The second-order nonlinear absoprtion coefficient is given by

$$\alpha_2 = \frac{\sqrt{2}\,\pi e^4}{c^2 \hbar\omega \epsilon_\infty} \frac{(\Delta E - E_g)\,\Delta E}{(\hbar\omega)^2} f_{nc}\, f_{vn}$$

$$\times \frac{(2\hbar\omega - E_g)^{\frac{1}{2}}}{\sqrt{m^*}} \left[\Delta E - \hbar\omega + \frac{a_n + a_v}{a_c + a_v}(2\hbar\omega - E_g)\right]^{-2} \quad . \tag{5.11}$$

The f_{nc} and f_{vn} denote the oscillator strengths for the transitions mediated by $\mathcal{H}_{vn}$ and $\mathcal{H}_{nc}$, respectively. In numerical calculations given in section 6, it is taken that $f_{nc} = f_{vn} = 1$. All parameters in eq. (5.11) are expressed in c.g.s. electrostatic units.

Equation (5.11) has been specialized for the case of single photon beam of frequency ω in the material (rather than two beams at two different frequencies ω_1 and ω_2). Braunstein and Ockman's expression for the nonlinear absorbance given by eq. (7) of [5] must be multiplied by a factor of $1/(\epsilon_\infty^2)\left(m/(2m^*)\right)^2$ to obtain our eq. (5.11). The first term in the corrective factor is due to the different formulation of absorption coefficient in our eq. (2.2) as compared with eq. (2) of [5], and the second term arises because we evaluated the matrix elements of allowed transitions in the

$\vec{k} \cdot \vec{p}$ approximation rather than by employing eq. (4) of ref. 5. Our eq. (5.11) includes appropriate factors for spin orientation and photon multiplicity.

A generalization of Braunstein's calculation for anisotropic energy bands has been given by Hassan [23]. His results agree with our eq. (5.11) in the limit of zero anisotropy.

In Basov et al.,[6,7] model, the two highest valence bands v_1 and v_2 and the lowest conduction band c are coupled by the radiation field. Furthermore, the intermediate states are conduction (or valence) intraband states as shown in figure 10.

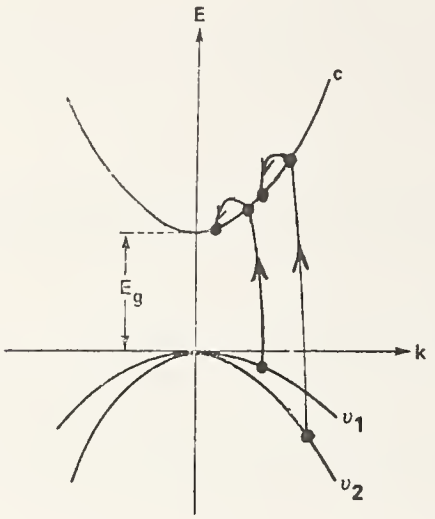

Figure 10. The energy band model employed by Basov et al. Parabolic energy bands v_1, v_2 refer to the bound electrons in valence band, and c is the conduction band. Intermediate levels are provided by intraconduction and intravalence states. Only intraconduction band transitions are explicitly indicated.

Second order perturbation calculation of this model leads to the following expression for the second order absorption coefficient

$$\alpha_2^{(i)} = \frac{2 \cdot 2^9 \sqrt{2}\,\pi\, e^4 (m^*)^{\frac{1}{2}} (2\hbar\omega - E_g)^{\frac{3}{2}}}{\varepsilon_\infty c^2 (\hbar\omega)^5} \frac{\left| (\hat{e} \cdot \vec{p})_{cv_i} \right|^2}{m^2} \qquad (5.12)$$

where $\hat{e}$ is the unit polarization vector of the incident radiation, $\vec{p}$ is the momentum operator of the electron and the index i = 1,2 refers to the initial state of the electron in the valence bands. Contrary to Basov et. al., we use eq. (5.10) to evaluate the momentum matrix elements, and furthermore we average over all directions in the k-space. The total absorption coefficient must contain summation over both valence band contributions, $\alpha_2 = \Sigma_i \alpha_2^{(i)}$. Since each valence band contributes about equally, we need to calculate only $\alpha_2^{(1)}$. Therefore, values listed in table 7 of section 6 must be multiplied by a factor close to 2 to obtain the total second-order absorption coefficient in this model.

In our eq. (5.12), factor of 2 has been introduced to account for the spin degeneracy. This factor has been omitted in the original work by Basov et al. Further differences between our eq. (5.12) and Basov et al., expressions arise because of an incorrect numerical factor used in relating the flux intensity with the magnitude of vector potential in [6]. This gives a multiplicative correction of 1/16. Averaging the scalar product $|\hat{e} \cdot \vec{p}|^2$ over all directions in the k-space yields another multiplicative correction of 1/3. Hence, Basov et al., expression for the second-order absorbance in the context of eq. (6) of [6] must be multiplied by a factor of 1/48.

This has been noted previously by Lee and Fan [24] and Fossum and Chang [21]. The need for this correction does not arise in connection with our eq. (5.12) because our absorption coefficient α_2 is intensity-independent and it was calculated from our eq. (2.2) rather than eqs. (6) and (8) of [6], and the averaging over the k-space has been also performed in the calculations listed in section 6. A further difference between Basov et al., work and our eq. (5.12) arises from our use of the $\vec{k} \cdot \vec{p}$ method in evaluating the matrix elements of the interaction operator. Because of eq. (5.10), we evaluate

$$\frac{|(\hat{e}\cdot\vec{p})_{c\text{-}v_i}|^2}{m^2} = E_g/4m^* \quad ,$$

whereas Basov et al., use the relation $p^2/2m = E_g\, m^*/m$ in connection with eq. (5) and the relation $p^2/2m = 3E_g/4m_e^*$ in the experimental results section of [6]. In section 6, we report the numerical evaluation of eq. (5.12).

6. Comparison Between Calculated and Measured Absorption Coefficients

In this section, we compare absorption coefficients calculated from eq. (2.2) with available experimental data for the second-order nonlinear absorption. First, we evaluate the transition rates for photon multiplicities $\nu = 1$ to 3 in the perturbed valence and conduction band wavefunction model of Keldysh, eq. (4.10). For the second-order calculation, we also use the perturbation-theoretic approaches for the two different band models, eqs. (5.11) and (5.12).

In the Keldysh model calculation, it is necessary to evaluate the Dawson integral numerically by using the trapezoidal rule of integration. In general, the accuracy of the numerical integration is of the order of a few parts in 10^5. If it is desired to increase the accuracy of the integration, increase the number of intervals N in the program line 260. The computation time will increase accordingly.

The computer program listed in table 4 has been written in a modified BASIC programming language for the HP 9830A calculator equipped with ROM's containing the mathematics package and the plotter control. This program (less lines 1000 and above, which contain the calculation of the absorption coefficient), with an appropriate modification of the plotting routine, has also been employed in plotting figures 1 to 6 of section 2.

Table 4. HP 9830A computer program used to calculate and to plot the wavelength dependence of absorption coefficients of the order 1 to 3 from eqs. (4.10) and (2.2). The computer system consists of extended memory core HP 9830A, built-in mathematics and plotter control ROM's, the HP 9866A printer and the HP 9862A plotter. Instructions for use are contained in lines 30 to 255.

```
30 REM THIS PROGRAM CALCULATES THE TRANSITION RATE PREDICTED BY KELDYSH
40 REM AND PLOTS VS PHOTON ENERGY IN ELECTRON VOLTS; KEY IN RUN AND FOLLOW INSTRUCTIONS
42 REM IT ALSO PLOTS ABSORPTION COEFF. VS PHOTON ENERGY IN ELECTRON VOLTS
50 REM NOTE· AT LEAST ONE INCREMENT MUST BE ASSIGNED
70 PRINT "INPUT PLOTTER SCALE  XMIN, XMAX, YMIN, YMAX"
71 PRINT
72 PRINT
80 INPUT S1, S2, S3, S4
90 SCALE S1, S2, S3, S4
95 XAXIS S3, S2/10, S1, S2
100 YAXIS S1, S4/2, S3, S4
115 FLOAT 3
120 PRINT "ENTER GAP IN EV, LAMBDA IN MICRONS"
130 PRINT "ENTER EL. FIELD IN UNITS OF MEGAVOLTS/M, MASS IN EL. MASS"
140 PRINT
150 INPUT G, L, E, M
160 PRINT
170 PRINT "IF YOU WANT TO INCREMENT GAP, KEY IN DELTAGAP; IF NOT KEY IN ZERO"
180 PRINT
190 INPUT G1
200 PRINT "IF YOU WANT TO INCREMENT LAMBDA, KEP IN DELTALAMBDA; IF NOT, KEY IN ZERO"
210 PRINT
220 INPUT L1
230 PRINT "IF YOU WANT TO INCREMENT EL. FIELD, KEY IN DELTAFIELD; IF NOT, ZERO"
240 PRINT
250 INPUT E1
252 PRINT "TO PLOT ABSORPTION COEFF. INPUT DIELECTRIC CONST (E2); IF NOT, ZERO"
253 PRINT
254 PRINT
255 INPUT E2
260 N=20
270 PRINT "GAP="; G,"LAMBDA=";L
280 PRINT "EL. FIELD=";E,"MASS=";M
```

```
290 PRINT "G1=G1;"L1="L1;"E1="E1
295 PRINT "S1="S1;"S2="S2;"S3="S3;"S4="S4
297 PRINT "E2="E2
300 PRINT
210 PRINT
320 A=8.76057E+36*(M/L)↑1.5/L
330 B=1.23752E-08*(E*L)↑2/ (M*G)
340 X=0.806015*G*L*(1+B)
350 R1=INT(X+1)
360 Z=(2*R1-2*X)↑0.5
370 W1=A*(B/4)↑R1*EXP(2*R1*(1-B)-Z*Z )
380 Y=Z/N
390 P=(1+EXP(Z*Z))*Z/(2*N)
400 F=0
410 FOR I=1 TO N-1
420 F=F+EXP((I*Z/N)↑2)
430 NEXT I
440 W2=P+F*Z/N
450 W=W1*W2
460 IF G1=0 THEN 520
470 PLOT G,LGTW
490 IF G>5 THEN 630
500 G=G+G1
510 GOTO 320
520 IF L1=0 THEN 570
524 IF E2#0 THEN 530
525 PLOT 1.2395/L,LGTW
527 IF E2=0 THEN 540
530 GOSUB 1000
540 IF L>21 THEN 630
550 L=L+L1
560 GOTO 320
570 IF E1=0 THEN 630
580 PRINT E,LGTW
600 IF E>50 THEN 630
610 E=E+E1
620 GOTO 320
630 END
1000 X=INT(G/(1.2395/L))+1
1010 A=2*X*1.2395/L*1.602E-19*754↑X*W/(SQRE2↑X*(E*1E+04)↑(2*X))
1020 PLOT 1.2395/L,LGTA
1030 RETURN
```

GaAs absorption coefficient for photon processes from 1 to 4 order calculated with the program listed in table 4 is shown in figure 11. The material parameters used in this calculation are listed in table 5. Experimental data for the absorption coefficient of GaAs are available for the first-order and second-order transitions only; they are entered as a dot, a vertical bar, and a circle in figure 11. It is seen that the agreement at 1.5 eV (one-photon linear absorption) and 0.94 eV (two-photon nonlinear absorption) between the Keldysh model prediction and the experiment is quite good. The sharp decline in absorption at the increase of the order of the photon multiplicity will be moderated by the contribution from the excitonic states. Since the calculation does not include exciton effects, one can expect that the experimental values will not agree with the predictions in the range of photon energies up to 0.1 eV less than that of the absorption edge for a particular order of photon multiplicity. Furthermore, impurities giving rise to energy levels within the forbidden gap would also increase the absorption coefficient. Undoubtedly, they also contribute to the large scatter of experimental values seen at 1.17 eV in figure 11. Because none of these contributions are accounted for in the Keldysh model, the predicted values of the absorption coefficients should be regarded as lower limits expected in the case of very pure materials. By inspection of fig. 11, one can estimate that the second-order absorption will be significant at light fluxes above 10^6 W cm^{-2} and the third order - above 10^8 W cm^{-2} for the intrinsic nonlinear electronic transition processes in direct-bandgap materials. Absorption coefficients for several semiconductors of this type are listed in tables 5 and 6 for fixed laser wavelengths of doubled Nd^{3+} -glass (0.53 μm), ruby (0.694 μm), Nd^{3+}-glass (1.06 μm), Nd^{3+}-YAG (1.318 μm), HF (2.8 μm), DF (3.9 μm), CO (5.3 μm), and CO_2 (10.6 μm).

Since the order of the transition is the dominant factor in determining the magnitude of the absorption, a large variation in the bandgap with the temperature implies a very large temperature dependence of the absorption coefficient. This is demonstrated in the last entry of table 6 by listing absorption coefficients of PbS calculated at 300 K and 0 K. Because the perturbative methods have been

Table 5. Absorption coefficients of order (1) to (3) calculated from the Keldysh model for direct bandgap semiconductors of 2.6 to 1.2 eV bandgap. Material parameters listed in [18] and [31] were used; m* denotes the reduced effective pair mass and ε_∞ is the high frequency dielectric constant.

Material specifications				Absorption coefficient of order (ν) in units $cm^{2\nu-3}/W^{\nu-1}$ at a given wavelength λ in μm			
Material	Bandgap	m*	ε_∞	λ=0.530	λ=0.694	λ=1.06	λ=1.318
ZnSe	2.58 (300 K)	0.132	5.9	$5 \cdot 10^{-9}$ (2)	$6.4 \cdot 10^{-9}$ (2)	$2.6 \cdot 10^{-21}$ (3)	$4.7 \cdot 10^{-21}$ (3)
CdS	2.53 (300 K)	0.192	5.32	$4.7 \cdot 10^{-9}$ (2)	$6.1 \cdot 10^{-9}$ (2)	$1.8 \cdot 10^{-21}$ (3)	$3.4 \cdot 10^{-21}$ (3)
CdSe	1.74 (300 K)	0.124	6.1	$6.5 \cdot 10^{4}$ (1)	$1.9 \cdot 10^{4}$ (1)	$1.7 \cdot 10^{-8}$ (2)	$1.65 \cdot 10^{-8}$ (2)
CdTe	1.50 (300 K)	0.084	7.21		$3.4 \cdot 10^{4}$ (1)	$2.3 \cdot 10^{-8}$ (2)	$2.7 \cdot 10^{-8}$ (2)
GaAs	1.435	0.063	10.9		$2.7 \cdot 10^{4}$ (1)	$1.9 \cdot 10^{-8}$ (2)	$2.3 \cdot 10^{-8}$ (2)
InP	1.28 (300 K)	0.062	9.56		$3.4 \cdot 10^{4}$ (1)	$2.6 \cdot 10^{-8}$ (2)	$3.17 \cdot 10^{-8}$ (2)

Table 6. Absorption coefficients of order (1) to (3) calculated from the Keldysh model for direct bandgap semiconductors of 0.8 to 0.15 eV bandgap. Material parameters listed in [18] and [31] were used; m* denotes the reduced effective pair mass and ε_∞ is the high frequency dielectric constant.

Material specifications				Absorption coefficient of order (ν) in units $cm^{2\nu-3}/W^{\nu-1}$ at a given wavelength λ in μm			
Material	Bandgap	m*	ε_∞	λ=2.8	λ=3.9	λ=5.3	λ=10.6
GaSb	0.8 (0 K)	0.043	14.4	$8.7 \cdot 10^{-8}$ (2)	$3.4 \cdot 10^{-18}$ (3)		
GaSb	0.69 (300 K)	0.043	14.4	$1.3 \cdot 10^{-7}$ (2)	$4.9 \cdot 10^{-18}$ (3)	$6.5 \cdot 10^{-18}$ (3)	
InAs	0.46 (0 K)	0.019	11.8	$4.6 \cdot 10^{-7}$ (2)	$6.3 \cdot 10^{-7}$ (2)	$3.5 \cdot 10^{-7}$ (2)	
InSb	0.228	0.014	15.68			$1.4 \cdot 10^{3}$ (1)	$2.1 \cdot 10^{-6}$ (2)
PbTe	0.19 (0 K)	0.011	3.69			$3.4 \cdot 10^{3}$ (2)	$1.6 \cdot 10^{-6}$ (2)
PbS	0.34 (300 K)	0.36	18.5	$2.7 \cdot 10^{4}$ (1)	$1.5 \cdot 10^{-7}$ (2)	$2 \cdot 10^{-7}$ (2)	$1.1 \cdot 10^{-17}$ (3)
PbS	0.15 (0 K)	0.034	18.5			$6.5 \cdot 10^{3}$ (1)	$3.2 \cdot 10^{-6}$ (2)

carried out to the second order only, comparison of the second-order nonlinear absorption coefficient calculated for the three models of sections 4 and 5 is given in table 7. For material parameters used in these calculations and comparison with the available experimental data, the reader is referred to [32]. We note that the absorption coefficient calculated from the Keldysh model generally falls in-between that of the two perturbation models of Braunstein and Basov. However, the Basov model usually ove estimates the absorption coefficient; therefore, the Keldysh model values yield currently the best estimate of the lower limit of the nonlinear absorption coefficients.

7. Conclusions

Comparison of theoretical models of Keldysh, Braunstein, and Basov in calculating the nonlinear absorption coefficients for direct band semiconductors with forbidden energy bandgaps between 2.6 to 0.15 eV show that the second order perturbation models of Braunstein and Basov differ in their prediction for α_2 by almost three orders of magnitude. The Keldysh model prediction for α_2 lies between the two perturbation models and is usually slightly lower than the experimental value. A large scatter in reported experimental values of α_2 (perhaps attributable to the presence of impurities in real materials) hinders in selecting the best theoretical approach. However, generally it can be stated that if the interference terms in calculating transition rates are neglected, the absorption constants are underestimated (Braunstein and Ockman). Calculations allowing transitions from several bands (Basov) generally overestimate the absorption. The Keldysh method in which the effect of the optical electromagnetic field on the eigenfunctions of the unperturbed system is incorporated at the beginning of the calculation gives a slight underestimate of the two-photon absorption. It describes very well the band edge absorption of the one-photon process. Intuitively, one would concede that the perturbation of the eigenstates of the noninteracting system by the light intensities of interest is significant and that the perturbed eigenfunctions should be introduced at the onset of calculations as it is done in the Keldysh model. In addition, the Keldysh model is the only one currently available to calculate absorption coefficients higher than second order since there has been no published work carrying perturbation theory to a higher than second order in semiconductors.

Table 7. Comparison of calculated two-photon absorption coefficient α_2 [cm W^{-1}] for direct bandgap semiconductors. Absorption coefficients were calculated from eqs (2.2), (4.10), (5.11), and (5.12) for Keldysh, Braunstein, and Basov models, respectively. Contribution from only one valence band is listed under Basov; the total absorption coefficient should include transitions from both valence bands and should be nearly twice as large.

Material	Wavelength in μm	α_2 [cm W^{-1}] calculated from model of		
		Keldysh	Braunstein	Basov
ZnSe	0.694	$6.4 \cdot 10^{-9}$	$2.2 \cdot 10^{-9}$	$4.5 \cdot 10^{-7}$
CdS	0.694	$6.1 \cdot 10^{-9}$	$2.2 \cdot 10^{-9}$	$4.4 \cdot 10^{-7}$
CdSe	1.06	$1.7 \cdot 10^{-8}$		$1.2 \cdot 10^{-6}$
	1.318	$1.65 \cdot 10^{-8}$		10^{-6}
CdTe	1.318	$2.7 \cdot 10^{-8}$	$9.6 \cdot 10^{-9}$	$1.8 \cdot 10^{-6}$
GaAs	1.06	$1.9 \cdot 10^{-8}$	$6.7 \cdot 10^{-9}$	$1.4 \cdot 10^{-6}$
	1.318	$2.3 \cdot 10^{-8}$	$8.25 \cdot 10^{-9}$	$1.5 \cdot 10^{-6}$
InP	1.06	$2.6 \cdot 10^{-8}$	$8.4 \cdot 10^{-9}$	$1.8 \cdot 10^{-6}$
InSb	10.6	$2.1 \cdot 10^{-6}$	$0.72 \cdot 10^{-6}$	$1.8 \cdot 10^{-5}$

However, because intensities above 10^9 W cm^{-2} are required to attain a signficant absorption in the third order in pure materials, such calculations may be superfluous for practical applications because of the onset of Drude absorption by free carriers created through the avalanche multiplication induced by the optical electric field. In fact, the notion that a single physical process can explain the effects of an intense laser pulse on a given optical material is too simplistic to hold because, for example, the multiphoton absorption and the avalanche ionization are two competing processes having a different time dependence.

On the other hand, this contribution demonstrates that it is important to include properly the band parameters of the solid state into the calculation. In particular, if contributions from excitonic states and impurity levels should be included, a summation over all corresponding elements of the interaction Hamiltonian must be incorporated into the calculation of absorption coefficients. The outline of such a procedure is given in [33]. Furthermore, up to the third order, it is sufficient to use the $\vec{P} \cdot \vec{A}$ interaction term in the electric dipole approximation.

8. Acknowledgments

The authors are thankful to Dr. C. C. C. Lee for pointing out inconsistencies in the original Basov et al., work and for his comments on the contributions of excitonic states to the nonlinear absorption. Also, thanks are due to Mr. J. E. Williams who has programmed several calculations reported in this work.

9. References

[1] V. I. Bredikhin, M. D. Galanin, and V. N. Genkin, Usp. Fiz. Nauk 110, 3 (1973) [Sov. Phys.-Usp. 16, 299 (1973)].

[2] J. M. Worlock, Two-photon Spectroscopy, in Laser Handbook, Vol. 2, Arecchi and Schulz-DuBois, eds. (North-Holland, 1972).

[3] S. Bakos, Multiphoton Ionization of Atoms, Adv. in Electronics and Electron Physics, Vol. 36, L. Marton, ed., (Academic Press, 1974).

[4] L. V. Keldysh, Zh. Eksp. Teor. Fiz. 47 (1964) [Sov. Phys.-JETP 20, 1307 (1965)].

[5] R. Braunstein and N. Ockman, Phys. Rev. 134, A499 (1964).

[6] N. G. Basov, A. Z. Grasyuk, I. G. Zubarev, V. A. Katulin, and O. N. Krokhin, Zh. Eksp. Teor, Fiz. 50, 551 (1966) [Sov. Phys.-JETP 23, 366 (1966)].

[7] N. G. Basov, A. Z. Grasyuk, V. F. Efimkov, I. G. Zubarev, V. A. Katulin, and J. M. Popov, Proceedings of the International Conference on the Physics of Semiconductors, Kyoto 1966, J. Phys. Soc. Japan 21 Suppl., 277 (1966).

[8] M. Goeppert-Mayer, Naturwissenschaften 17, 932 (1929); Annalen der Physik 9, 273 (1931).

[9] W. Franz, Zeitschr.f. Naturforschg. 13a, 484 (1958).
L. V. Keldysh, Zh. Eksp. Teor. Fiz. 34, 1138 (1958) [Sov. Phys.-JETP 7, 768 (1958)].

[10] H. B. Bebb and A. Gold, Phys. Rev. 143, 1 (1966).

[11] M. H. Weiler, M. Reine, B. Lax, Phys. Rev. 171, 949 (1968).

[12] I. M. Catalano, A. Cingolani, and A. Minafra, Solid State Comm. 16 (1975).

[13] J. H. Yee, Phys. Rev. B3, 355 (1971).

[14] C. H. Lee, "Interaction of Intense Picosecond Light Pulse with Materials," Progress Reports, Defense Documentation Center #AD741391 and AD750414 (1972).

[[15] T. S. Moss and T. D. F. Hawkins, Infrared Phys. 1, 111 (1961).

[16] M. D. Sturge, Phys. Rev. 127, 768 (1962).

[17] I. Kudman and T. Seidel, J. Appl. Phys. 33, 771 (1962).

[18] D. Long, Energy Bands in Semiconductors (J. Wiley, N.Y., 1968).

[19] E. Kartheuser, in Polarons in Ionic Crystals and Polar Semiconductors, ed., J. T. Devreese (North-Holland Publ., 1972).

[20] G. W. Gobeli and H. Y. Fan, Phys. Rev. 119, 613 (1960).

[21] H. J. Fossum and D. B. Chang, Phys. Rev. B8, 2842 (1963).

[22] J. Callaway, Quantum Theory of the Solid State, Part A, pp. 248-252 (Academic Press, New York, 1974).

[23] A. R. Hassan, Il Nuovo Cimento 70B, 21 (1970).

[24] C. C. Lee and H. Y. Fan, Appl. Phys. Letters 20, 18 (1972).

[25] Y. A. Oksman, A. A. Semenov, V. N. Smirnov, and O. M. Smirnov, Fiz. Tekh. Poluprov. 6, 731 (1972) [Sov. Phys. Semicond. 6, 629 (1972).

[26] C. C. Lee and H. Y. Fan, Phys. Rev. B9, 3502 (1974).

[27] A. Z. Grasyuk, I. G. Zubarev, V. V. Lobko, Yu. A. Matveets, A. B. Mironov, and O. B. Shatberashvili, ZhETF Pis. Red. 17, 584 (1973) [Sov. Phys. JEPT Lett. 17, 416 (1973)].

[28] S. Jayaraman and C. H. Lee, Appl. Phys. Letters 20, 392 (1972).

[29] D. A. Kleinman, R. C. Miller, and W. A. Nordland, Appl. Phys. Letters 23, 243 (1973).

[30] J. M. Ralston and R. K. Chang, Appl. Phys. Letters 15, 164 (1969).

[31] J. I. Pankove, Optical Processes in Semiconductors (Prentice Hall, Englewood Cliffs, N.Y., 1971).

[32] S. S. Mitra, L. M. Narducci, R. A. Shatas, Y. F. Tsay, and A. Vaidyanathan, Applied Optics, 1975, in press.

[33] C. C. C. Lee, "Two Photon Absorption and Second Harmonic Generation in Semiconductors," Doctoral Dissertation, Purdue University (May 1974) (unpublished).

10. Figures

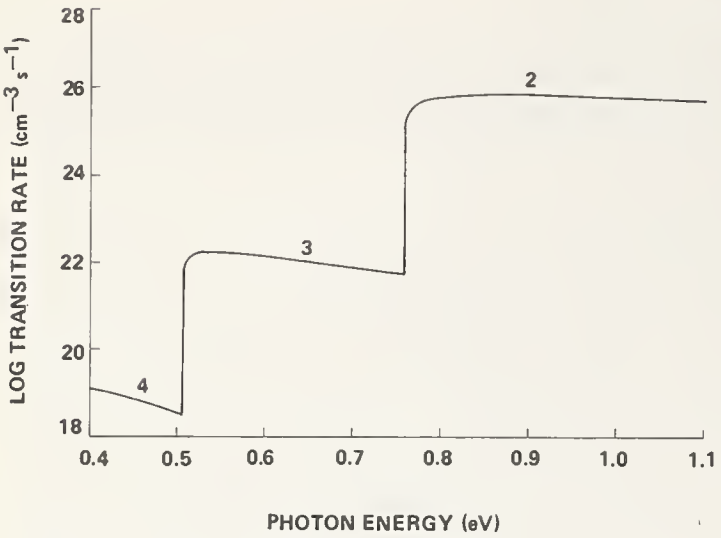

Figure 1. GaAs multiphoton transition rate (2-nd to 4-th order) in cm^{-3} s^{-1} induced by a constant optical electric field of 10^4 V cm^{-1} amplitude and varied frequency.

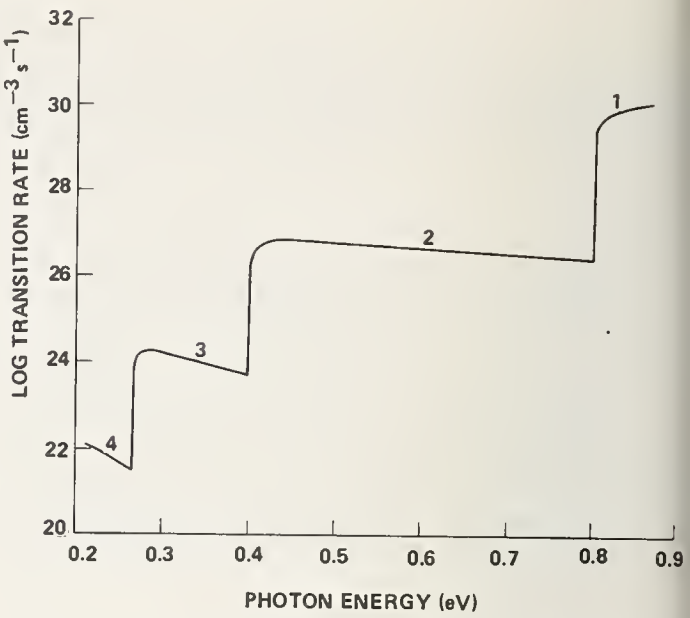

Figure 2. GaSb multiphoton transition rate (1-st to 4-th order) in cm^{-3} s^{-1} induced by a constant optical electrical field of 10^4 V cm^{-1} amplitude and varied frequency.

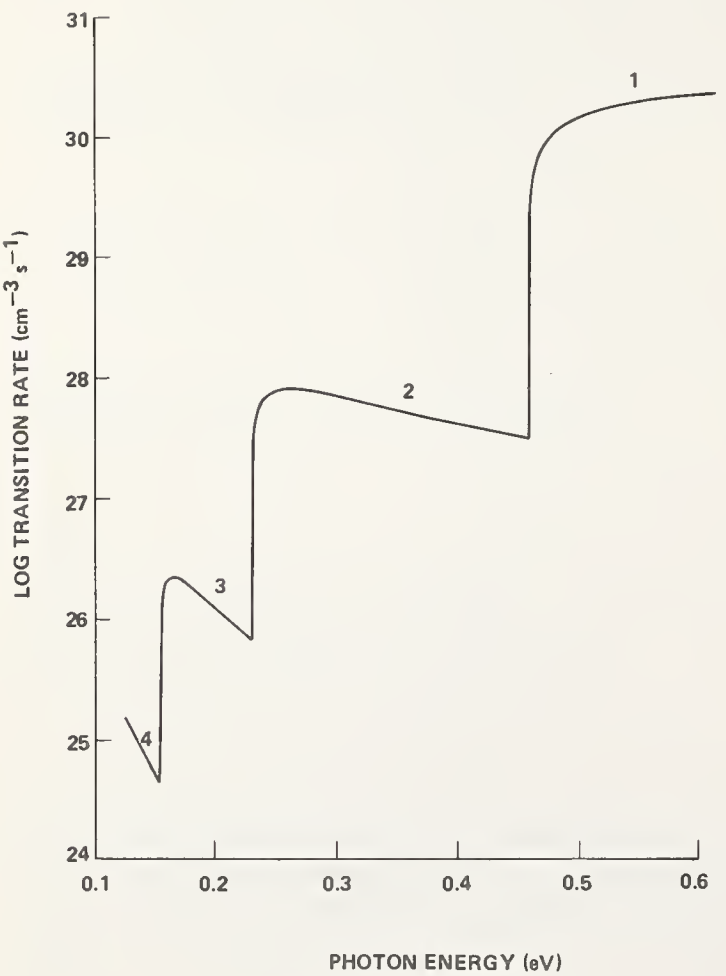

Figure 3. InAs multiphoton transition rate (1-st to 4-th order) in cm^{-3} s^{-1} induced by a constant optical electrical field of 10^4 V cm^{-1} amplitude and varied frequency.

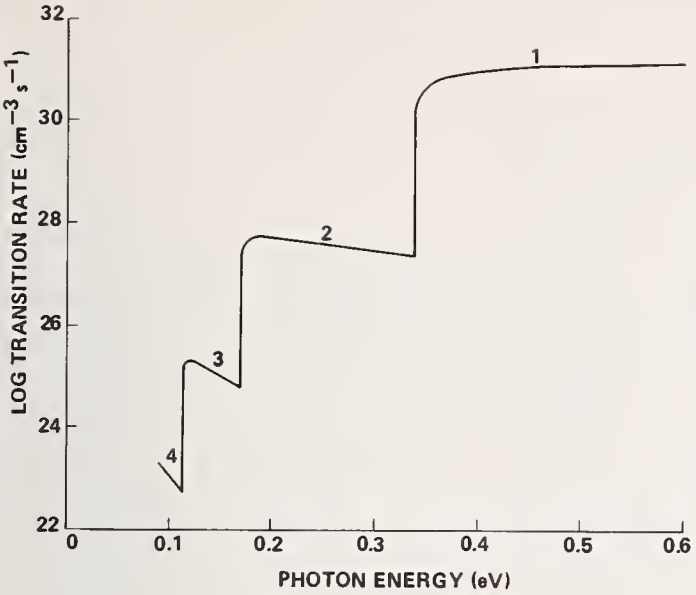

Figure 4. PbS multiphoton transition rate (1-st to 4-th order) in cm^{-3} s^{-1} induced by a constant optical electric field of 10^4 V cm^{-1} amplitude and varied frequency.

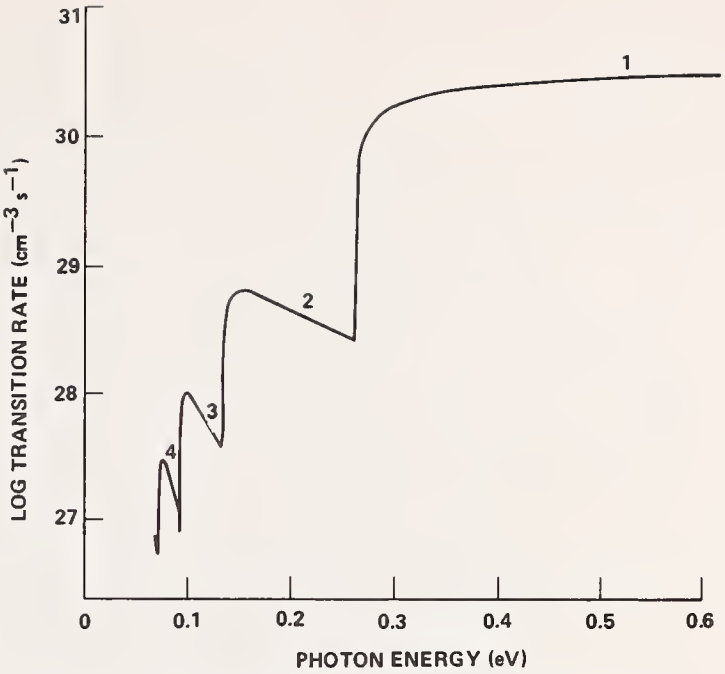

Figure 5. InSb multiphoton transition rate (1-st to 4-th order) in cm^{-3} s^{-1} induced by a constant optical electric field of 10^4 V cm^{-1} amplitude and varied frequency.

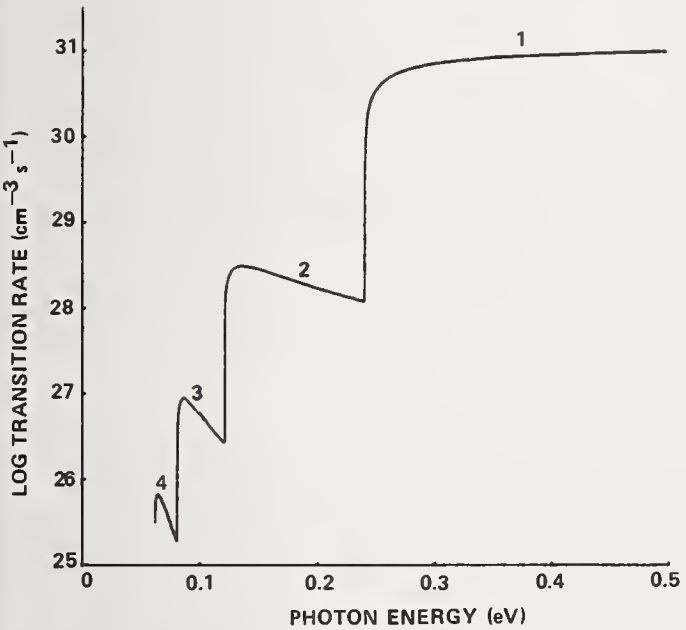

Figure 6. PbTe multiphoton transition rate (1-st to 4-th order) in cm^{-3} s^{-1} induced by a constant optical electric field of 10^4 V cm^{-1} amplitude and varied frequency.

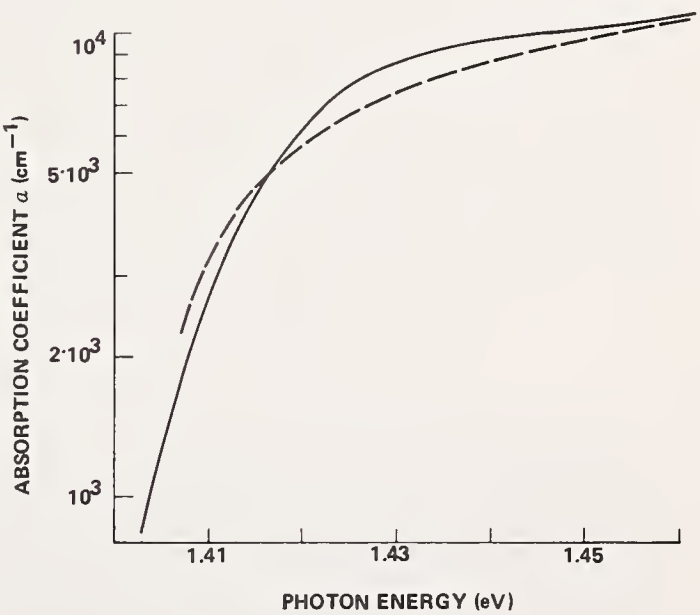

Figure 7. Comparison between the experimental values of the absorption coefficient of GaAs at room temperature [15] (solid curve) and the Keldysh model calculation (dashed curve).

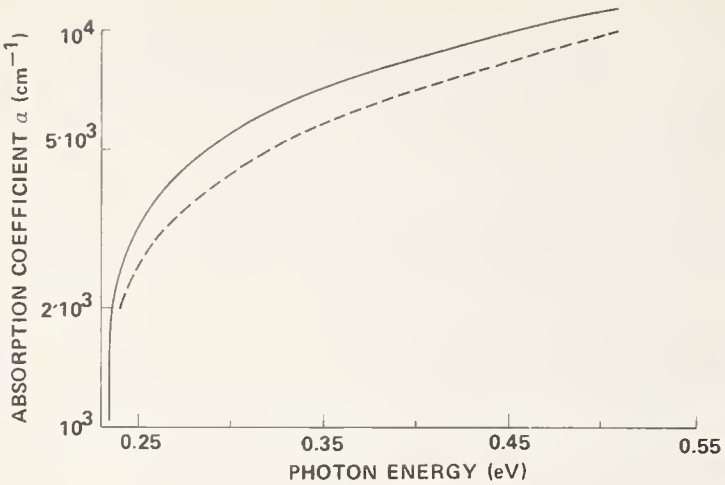

Figure 8. Comparison between the experimental values of the absorption coefficient of pure InSb taken from [20] (solid curve) and the Keldysh model calculation (dashed curve).

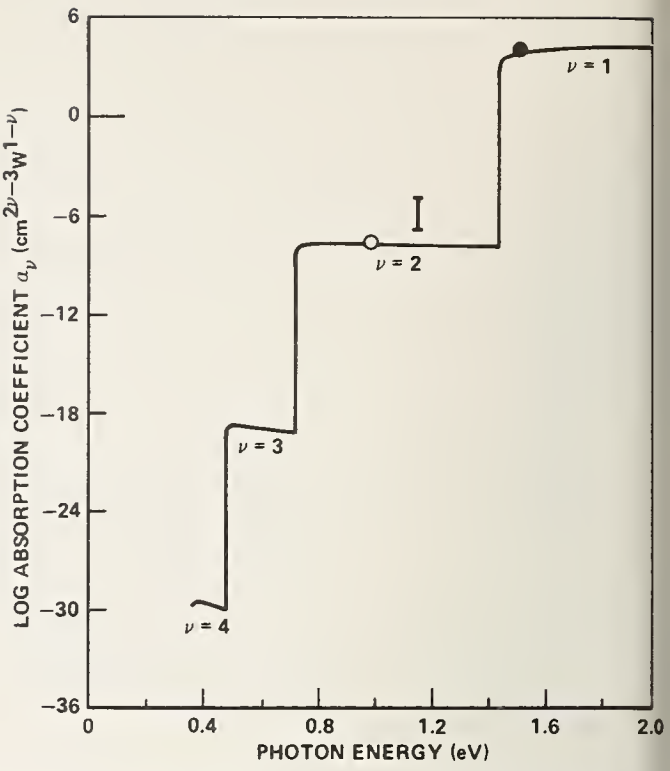

Figure 11. Multiphoton absorption coefficient of GaAs at room temperature calculated from eqs. (4.10 and 2.2). See table 5 for material parameters used in the calculation. The dimension of the absorption coefficient is given in units of $cm^{2\nu-3}\ W^{1-\nu}$, with ν designating the order of the absorption process. Experimental data are shown for 1.5 eV photon energy [16] (dot), 1.17 eV photon energy [6, 25, 28] (vertical bar), and 0.94 eV [29, 30] (circle).

COMMENTS ON PAPER BY SHATAS, et al

The speaker commented that the reason no comparison was given between theory and experiment for large gap materials such as alkali-halides was that the absence of high-power short-wavelength lasers limited the availability of experimental data. He pointed out that for significant two-photon absorption to occur even when it was energetically allowed fluxes of the order of megawatts per square centimeter were required. Peter Braunlich of the Bendix Research Laboratories pointed out that two-photon data on alkali-halides are available and in fact abundant in the literature, but that these were obtained using one intense source such as an infrared or visible laser and an incoherent source of ultra-violet light. It was further pointed out in the discussion that with the advances of short-wavelength laser technology data on two-photon absorption in a variety of materials would be forthcoming.

6.8 Electroabsorption: A Possible Damage Consideration

Rettig P. Benedict* and Arthur H. Guenther

Air Force Weapons Laboratory
Kirtland AFB, NM 87117

Electroabsorption, also known as photon-assisted tunneling or the Franz-Keldysh effect, is the phenomenon in which the application of a large electric field produces a change in the absorption coefficient of a solid material. This effect has been proposed as a possible laser damage mechanism since the effective absorption coefficient will be dependent upon the laser intensity (optically related electric field) rather than the constant it is usually taken to be. The constant value is normally determined from low laser intensity calorimetric or emittance measurements.

A theoretical investigation of the interaction of an EM field with a material shows that the dc field limit is a tunneling effect and the high-frequency limit is multiphoton absorption so that electroabsorption is closely related to the latter. The result being that one should primarily consider multiphoton absorption rather than electroabsorption for potential damage implications in most situations. Calculations are presented that indicate the relative importance of multiphoton absorption for window materials for both visible and IR lasers. The results indicate that multiphoton absorption will usually be unimportant for IR materials except in cases of extremely high fields and no other competing damage mechanisms. For materials used with visible lasers, the phenomenon must be considered as a potential cause of damage.

Key words: Electroabsorption; IR optics; laser damage; multiphoton processes; uv.

1. Introduction

The question has been raised recently whether the Franz-Keldysh effect (also known as electroabsorption or photon-assisted tunneling) could affect the damage thresholds of laser window materials [1][1]. As shown theoretically by Franz [2] and Keldysh in 1958 [3], a uniform dc electric field applied to a crystal will change the optical absorption coefficient significantly in the neighborhood of the energy gap. Subsequently, the existence of the "Franz-Keldysh" effect has been confirmed experimentally not only at dc but also at fields with frequencies to 10^{10} Hz. At optical frequencies ($\sim 10^{14}$ Hz) the existence of this phenomenon could result in an intensity-dependent absorption coefficient thereby possibly invalidating the extrapolation of absorption measurements made at low power. It will be shown that this is unlikely for lasers operating at frequencies far below the gap. At these frequencies, the interaction of the electric field with the medium is characterized by multiphoton absorption, which will be seen to be the high frequency limit of the Franz-Keldysh effect [4]. The theory and previously published experimental results are discussed as well as some calculations pertaining to multiphoton absorption in IR, visible, and uv window materials.

2. Theory

Using an elementary model, one can assess the differences between electric field induced tunneling at low and high frequencies. The width (ℓ) of the barrier through which the valence electron must tunnel can be characterized by $\ell = E_g/Fe$ from a consideration of the distance it takes an electron to acquire E_g of energy under a field F, ignoring collisions. During this acceleration by the field, the average electron velocity can be written as $v = \sqrt{E_g/2m}$. Using these expressions, we can associate a tunneling frequency $\omega_t = Fe/\sqrt{2mE_g}$. At low frequencies ($\omega << \omega_t$), the electron has sufficient time to tunnel in less than one cycle; however, at very high frequencies ($\omega >> \omega_t$) the electron does not acquire E_g of energy in a single cycle. The effect now is more one of the simultaneous absorption of several photons. Keldysh developed the initial theory in this area and concluded that dc photon-assisted tunneling and multiphoton absorption were the low and high frequency limits of the same interaction.

In his 1965 paper, Keldysh examined the transition probability of a valence electron to the conduction band continuum as the result of the interaction with a sinusoidally time varying uniform

*Presently completing the thesis requirements for the PhD degree at the Air Force Institute of Technology, Wright-Patterson AFB, Ohio 45433.

[1]Figures in brackets indicate the literature references at the end of the paper.

electric field. The initial state was described by a Bloch wave function for a valence electron. The final state was a non-stationary conduction band state that directly accounts for the electric field effects. This allows intraband and interband transitions to be considered. The Houston wave functions for an electron in a solid under the influence of an electric field were employed with the inclusion of a time varying field. First-order perturbation theory was then used to determine the interband transition probability from the valence band to all possible final states in the conduction band. In the process, Keldysh made the approximation that $\hbar\omega << E_g$ so that for the multiphoton case, several photons are required. Keldysh's results usually are assumed to apply for five or more photons only. The result is given in his paper as follows [4]:

$$W = \frac{2\omega}{9\pi}\left(\frac{\sqrt{1+\gamma^2}}{\gamma}\,\frac{m^*\omega}{\hbar}\right)^{3/2} Q\left(\gamma, \frac{\tilde{\Delta}}{\hbar\omega}\right)\exp\left\{-\pi\left\langle\frac{\Delta}{\hbar\omega}+1\right\rangle x\left[K\left(\frac{\gamma}{\sqrt{1+\gamma^2}}\right)-E\left(\frac{\gamma}{\sqrt{1+\gamma^2}}\right)\right]\right\} E\left(\frac{1}{\sqrt{1+\gamma^2}}\right) \tag{1}$$

where $\gamma = \sqrt{mEg}/eF$ (note 1).

$$\tilde{\Delta} = \frac{2}{\pi} E_g \,\frac{\sqrt{1+\gamma^2}}{\gamma}\, E\left(\frac{1}{\sqrt{1+\gamma^2}}\right)$$

$\langle x\rangle$ denotes the integer part of x

m* is the effective electronic mass

K, E are complete elliptic integrals of the first and second kind

$$Q(\gamma, x) = \left[\pi \Big/ 2K\left(1\Big/\sqrt{1+\gamma^2}\right)\right]^{1/2} x \sum_{n=o}^{\infty}\exp\left\{-\pi\left[K\left(\gamma\Big/\sqrt{1+\gamma^2}\right)-E\left(\gamma\Big/\sqrt{1+\gamma^2}\right)\right]n\Big/ E\left(1\Big/\sqrt{1+\gamma^2}\right)\right\} x\, \Phi\left\{\left[\pi^2\,(2\langle\chi+1\rangle-2\chi+n)\Big/ 2K\left(1\Big/\sqrt{1+\gamma^2}\right) x\, E\left(1\Big/\sqrt{1+\gamma^2}\right)\right]^{1/2}\right.$$

$$\Phi(x) = e^{-x^2}\int_o^x e^{z^2}\,dz\,.$$

Keldysh examined two limiting cases: $\gamma<<1$ and $\gamma>>1$ where $\gamma\sqrt{mE_g/eF} = \omega/\omega_t$. The former case corresponds to low frequencies (and strong fields) and his results reduce to the standard equation for dc photon-assisted tunneling (electroabsorption). For $\gamma>>1$, high frequencies, the transition probability is given by Keldysh as

$$W = \frac{2}{9\pi}\,\omega\left(\frac{m^*\omega}{\hbar}\right)^{3/2}\Phi\left[\left(2\left\langle\frac{\tilde{\Delta}}{\hbar\omega}+1\right\rangle-\frac{2\tilde{\Delta}}{\hbar\omega}\right)^{1/2}\right]\exp\left[2\left\langle\frac{\tilde{\Delta}}{\hbar\omega}+1\right\rangle\left(1-\frac{1}{4\gamma^2}\right)\right]\left(\frac{1}{4\gamma}\right)^{2\left\langle\frac{\tilde{\Delta}}{\hbar\omega}+1\right\rangle}. \tag{2}$$

This approach of calculating multiphoton transition probabilities was also followed by Weiler, et al., [5] who extended the analysis to include magnetic fields. Her results for zero magnetic field are essentially the same as those of Keldysh.

Kovarskii and Perlin [6] follow Keldysh's path, but did not constrain themselves to a two-band approximation; that is, the matrix elements for the transitions using the actual crystal energy bands were calculated and used. Again the results are similar to those of Keldysh, with some small corrections. They are also valid for fewer than five photons, a region where the Keldysh result could be significantly in error. (Bychov and Dykhne also looked at this problem with no substantial differences --[7].)

The second approach to calculating N-photon transition probabilities is to use N^{th} order perturbation theory between stationary initial and final states. Several people have done this such as Basov [8], Braunstein [9] and Yee [10] for two, two and four-photon absorption, respectively. To date, no one has published calculations of this type for more than four photons that we discovered. Direct comparisons between these results and those of Keldysh et al are questionable since Keldysh's results are only valid for large N, at least five, but it does give some measure of consistency. In the case of four-photon absorption, Yee calculated the transition probabilities for ZnS(E_g = 3.8eV) and Nd:YAG laser light (1.06μm) and got $W = 10^{18}$ cm^{-3} sec^{-1} by his perturbation

theory and $W = 10^{16}$ cm^{-3} sec^{-1} from eq. (2). He also states that if the average lifetime is on the order of 10^{-9} sec then his results of 10^{9} e/cm^3 agree favorably with photoconductivity experiments. Others have made numerical calculations for two photon absorption and in most cases also found Keldysh's equation gave a result that was about a factor of one hundred low, not too surprising for this small an N.

3. Experimental Results

Experimental measurements of multiphoton absorption have been made almost since the discovery of the laser. Usually, only two or three photon processes are observed. Some of the earliest work was by Hopfield and Worlock [11] looking at two-photon absorption in KI and CsI with a ruby laser. The ruby was used to apply the high frequency field (1.8 eV) and the change in absorption from 4eV up to 6.5eV (the gap energy) was examined with a Xenon arc lamp. The theory for this two-beam experiment was later developed by Yacoby--[12]. Two-photon absorption has also been observed in several IR window materials such as Si, GaAs, CdTe, and, CdSe [13]. Specifically for ZnSe, an intensity dependent absorption coefficient was measured to be 0.04 cm/MW in the neighborhood of 10^8 watts/cm^2 [14]. Thus at 100 MW/cm^2, we expect an absorption coefficient due to two-photon absorption of 4cm^{-1}. Since this is for an electric field of 1.1×10^5v/cm in the material, we can compare it with the prediction, based on Keldysh's work of 0.5 cm^{-1}. The absorption coefficient for N-photon absorption is given by $\alpha_N = (8\pi N\hbar\omega/nc\langle F^2\rangle)W$ where $\langle F^2\rangle$ is the average value of the square of the local field, taken to be the square of the external field (not exactly correct) [15].

One paper presented breakdown experiments, which involved N-photon absorption for N as high as eleven [16]. The experiments were performed in air and KDP at 1.06 μm and 0.533 μm using picosecond pulses given in table 1. In most cases, the Keldysh predictions are in good agreement. This stems both from the fact that this theory fits rather better for high N, and that multiphoton absorption is important as a breakdown mechanism for short pulse widths where electron avalanche rate effects become important.

Table 1. Breakdown Threshold (10^{12} watts/cm^2)
(After Orlov--[16])

	∿ N	Keldysh	Exp
AIR			
1.06μm	11	23	70
0.533μm	6	40	30
KDP			
1.06μm	5	7.6	7 - 10
0.533μm	3	6.8	4 - 6

The primary conclusion from the experimental work to date is that Keldysh's theory seems to give a fair approximation for N-photon absorption for N>2, and no worse than a factor of one hundred low for two-photon absorption.

4. Implications for High Power Laser Windows

Generally, materials considered for high power IR laser windows have large band gaps so that the laser frequency is far below the fundamental absorption edge. This will also reduce any possible problems from multiphoton absorption because of the large number of photons required. For example, we look at ZnSe at 10.6μm and 4μm at 10^6 volts/cm

at 10.6μm:

N = 22 Eg = 2.6ev m* = 0.133m

W = 5.4×10^3/cm^3 sec [γ = 1.76 so one uses the exact expression rather than eq. (1)]

$\alpha \simeq 7 \times 10^{-25}$/cm^{-1}

at more 4μm:

$N = 8$ all else the same

$W = 3 \times 10^{16}/cm^3$ sec

$\alpha = 3 \times 10^{-12}$ cm^{-1}

These numbers are extremely small and uninteresting from a practical point of view, even at 10^6v/cm. The magnitude is not surprising if we examine eq. (2) again:

$$W = \text{const}\ \omega^{5/2} \left(\frac{1}{4\gamma}\right)^{2N} \exp\left[2N\left(1 - \frac{1}{4\gamma^2}\right)\right]$$

or for $\gamma >> 1$ $W = \text{const}\ \omega^{5/2} \left(\frac{1}{4\gamma}\right)^{2^N} e^{2^N}$

and since $(1/4\gamma) << 1$, W depends on a small number to a large power. We do notice, however, that upon substituting for $\gamma\sqrt{mEg}/eF$

$$W \sim F^{2^N} \quad \text{or} \quad \alpha \sim F^{2^{(N-1)}}$$

therefore, everything is strongly field dependent, if $\gamma >> 1$.

The field strength of 10^6v/cm corresponds to about 6GW/cm^2 in ZnSe. At this level other damage mechanisms such as avalanche ionization would be very important in intrinsic material failure [1]. For example, short laser pulse intrinsic breakdown in alkali halides occurs about 2×10^6v/cm at 10.6μm and is caused primarily by an electron avalanche [17]. In ZnSe to date, typical failure levels are near 200-300MW/cm^2 or at fields of about 2.3×10^5v/cm. The damage observed has frequently been associated with inclusions [18]. With the strong field dependence of W, the transition probabilities at this field strength are significantly lower than the already calculated low values at 10^6v/cm.

Clearly, it does not appear that multiphoton absorption will contribute noticeably to damage levels in IR materials due to direct absorption. Another consideration might be whether this phenomenon could produce enough carriers to initiate an electron avalanche, i.e., would multiphoton absorption produce more carriers than are already there by other means. In the case of intrinsic material, photoionization is probably the major source of carriers in ZnSe at 300 K. For example, direct sunlight could produce 10^{15}-10^{17} e/cm^3 sec, about the same as that produced by 4 μm radiation at 10^6 volts/cm. Again multiphoton absorption appears insignificant. However, for low temperature high purity windows, shielded from photoionization production, multiphoton absorption could contribute the first few carriers.

The calculations given above have been specifically for ZnSe; however, the effect is even smaller for other IR window materials such as the alkali halides as the energy gap is much wider in these materials. Bloembergen completely discounts multiphoton absorption in these materials since N∿100 [19]. Other materials such as Ge and Si could possibly experience problems, but they are not being actively considered for high average power applications. Overall multiphoton absorption should be considered negligible for high average power IR windows, with large band gaps.

In the visible and especially the uv range of the spectrum, multiphoton absorption can become extremely important at high laser powers. This follows, of course, since the number of photons which must be simultaneously absorbed is reduced considerably. Two materials that are heavily used in the visible and near uv are quartz and MgF_2. Taking the energy gaps to be 7.3 eV and 11 eV, for 5000Å radiation we are concerned with three- and five-photon absorption, respectively. Using Keldysh's frequency approximation ($\gamma >> 1$) we get for the transition probability and absorption coefficient at 5000Å

	Quartz	MgF_2
W	$6 \times 10^{-26}\ E^6 \left(\frac{m}{m^*}\right)^{3/2}$	$3 \times 10^{-68}\ E^{10} \left(\frac{m}{m^*}\right)^{7/2}$
α (cm^{-1})	$4 \times 10^{-37}\ E^4 \left(\frac{m}{m^*}\right)^{3/2}$	$3 \times 10^{-79}\ E^8 \left(\frac{m}{m^*}\right)^{7/2}$
γ	$1.7 \times 10^{10} \left(\frac{m^*}{m}\right)^{1/2} E^{-1}$	$2.1 \times 10^{10} \left(\frac{m^*}{m}\right)^{1/2} E^{-1}$
		(E in volts /m).

Again using 10^6 v/cm α (quartz) $\sim 10^{-5}$ cm^{-1} and α (MgF_2) $\sim 10^{-15}$ cm^{-1} assuming an $m^* = m$. These are still not large contributions, but if the effective mass is small and considering Keldysh's estimates are usually two orders of magnitude small, at high power levels, this effect may become important. If

we look more toward the uv, e.g., 2500 Å, the contribution from multiphoton absorption becomes much more pronounced. For the same 10^6 v/cm, we get α (MgF_2) $\sim 10^{-7}$ cm^{-1} ($m^* = m$) and α (quartz) $\sim$ 0.5 cm^{-1} ($m^* = m$). Thus, as higher power lasers become available in the visible and near uv, where the energy gap of the materials to be used as optical components is at best only a few times that of the photon energy, multiphoton absorption will become an extremely important damage consideration.

5. Summary

We have seen how the photon-assisted tunneling in a dc electric field, otherwise denoted electro-absorption or the Franz-Keldysh effect, is the low frequency limit of the same phenomenon that gives rise to multiphoton absorption in high frequency electric fields, such as those associated with a high power laser. The magnitude of this multiphoton absorption has been computed by several theories and to some extent checked by experiment. Agreement is good for many photon absorption and within a factor of one-hundred for two photon absorption. Calculations of the change in absorption in IR window materials were presented and the results shown to be negligible even if one allowed a factor of one hundred increase. The primary reason is the large number of photons required. For lasers operating at frequencies within factors of 2 or 3 of the energy gap of the window material, multiple photon absorption will become significant, especially for very short pulse lasers (picoseconds) where normal avalanche breakdown is highly rate dependent. In the future, as very high power pulsed lasers are developed in the visible and uv, multiphoton absorption must be considered as a contributor to laser induced damage.

6. Acknowledgments

The first author would like to acknowledge his appreciation for the hours of consultation given him by his professors, Dr R. H. Hengehold and Maj. K. Jungling at AFIT.

7. References

(1) Bettis, J. R., Guenther, A. H., and Glass, A. J., "The Influence of the Optical Electric Field on Pulsed Laser Induced Damage Processes," IEEE '74 Region Six Conference.

(2) Franz, W., "The Effect of an Electric Field on an Optical Absorption Edge," Z. Naturforschung 13a:484 (1958).

(3) Keldysh, L. V., "The Effect of a Strong Electric Field in the Optical Properties of Insulating Crystals," Soviet Physics JETP 7:788 (1958).

(4) Keldysh, L. V., "Ionization in the Field of a Strong Electromagnetic Wave," Soviet Physics - JETP 20:1307 (1965).

(5) Weiler, M., Reine, M., and Lax, B., "Theory of Multiphoton Magnetoabsorption in Semiconductors," Physical Review 171:949 (1968).

(6) Kovarskii, V. A. and Perlin, E. Yu, "Multiphoton Interband Optical Transitions in Crystals," Physica Status Solidi 45:47 (1971).

(7) Bychov, Yu A. and Dykhne, A. M., "Breakdown in Semiconductors in an Alternating Electric Field," Soviet Physics JETP 31:928 (1970).

(8) Basov, N. G. et al, "Semiconductor Quantum Generator with Two-Photon Optical Excitation," Soviet Physics JETP 23:366 (1966).

(9) Braunstein, R., "Optical Double-Photon Absorption in CdS," Physical Review 134:A499 (1964).

(10) Yee, J. H., "Four-Photon Transition in Semi-Conductors," Physical Review B 3:355 (1971).

(11) Hopfield, J. J. and Worlock, J. M., "Two-Quantum Absorption Spectrum of KI and CsI," Physical Review 137:A1455 (1965).

(12) Yacoby, Y., "High-Frequency Franz-Keldysh Effect," Physical Review 169:610 (1968).

(13) Ralston, J. M. and Chang, R. K., "Optical Limiting in Semiconductors," Applied Physics Letters 15:164 (1969).

(14) Arsen'ev, V. V. et al, "Nonlinear Absorption and Limitation of Light Intensity in Semiconductors," Soviet Physics JETP 29:413 (1969).

(15) Wooten, F., Optical Properties of Solids, Academic Press, New York, Chapter 3, 1972.

(16) Orlov, R. Yu, et al, "Investigation of Breakdown Produced in Dielectrics by Ultra Short Laser Pulses," Soviet Physics JETP 34:418 (1972).

(17) Yablonovitch, E., "Optical Dielectric Strength of Alkali Halide Crystals Obtained by Laser-Induced Breakdown," Applied Physics Letters 19:495 (1971).

(18) Fradin, D. W. et al, "Optical Damage in Laser Material," Conference on High Power IR Laser Window Materials, ed. C. A. Pitha, A. Armington and H. Posen, Vol III, p 1047, 1974.

(19) Bloembergen, N., "Laser-Induced Electric Breakdown in Solids," IEEE Journal of Quantum Electronics, QE-10:375 (1974).

NOTE 1: Keldysh originally defines γ for gases and includes the $\sqrt{2}$ as given on the first page. However, he later redefines γ without the $\sqrt{2}$ for solids.

NOTE 2: In this paper F refers to the peak field strength and E the rms field strength. All numerical values are rms values.

6.9 Irradiance Limits for Vacuum Ultraviolet Material Failure*

C. J. Duthler and M. Sparks

Xonics, Incorporated, Van Nuys, California 91406

Calculated values of irradiance I at which materials fail in 7.2 eV pulses of 10 nsec duration by various mechanisms indicate that metallic mirrors melt at very low values, typically I ≅ 20 MW/cm. Improving the aluminum, which is the only good metallic vuv reflector, would increase I by a factor of only three. The lowest of the thresholds for transparent materials are ~140 MW/cm^2 for the intrinsic reversible process of optical distortion caused by the conduction electrons generated by two-photon absorption and ~200 MW/cm^2 for the intrinsic irreversible process of thermal fracture by two-photon absorption. Other thresholds are: ~1 GW/cm^2 for fracture from enhanced stimulated Raman scattering in Raman-active materials; ~1.6 GW/cm^2 for melting from two-photon absorption; ~2 GW/cm^2 for optical distortion from the nonlinear refractive index (bound electrons); and ~100 GW/cm^2 for thermal fracture from extrinsic one-photon absorption with β = 0.1 cm^{-1}. Included in the calculations are the Joule heating by the generated electrons, which is greater than the direct heating by the absorption process, and electron-avalanche multiplication. Thermally induced optical distortion has a higher threshold than that for the optical distortion by generated conduction electrons.

Key words: Nonlinear index of refraction; optical distortion; thermal fracture; two-photon absorption.

1. Introduction

Our theoretical studies of materials damage by high-power, vacuum-ultraviolet (vuv) radiation were motivated by the successful operation of lasers in this wavelength region [1][1]. High output powers have been achieved from the rare-gas excimer lasers with wavelengths of 174 nm ($\hbar\omega$ = 7.2 eV) for the xenon laser [2], 146 nm (8.5 eV) for the krypton laser [3], and 126 nm (9.8 eV) for the argon laser [4]. At the present time there have been no experiments on materials damage in the vuv, other than that observed with the first lasers, which were materials limited [2,5].

The laser cavity-mode pattern was burned into the thin-film aluminum mirrors in these first lasers. The threshold irradiance (intensity) for this damage was I ≅ 20 MW/cm^2. Since orders-of-magnitude greater power would be feasible if suitable mirrors were available, there is great interest in obtaining improved reflectors. Transparent materials for high-power use as windows, lenses, reflecting devices, and other optical components are of even greater interest.

Consider the intrinsic limit for metallic reflectors in the vuv. For a metal to be a good reflector it must have a plasma frequency large compared to the frequency of interest, and it must not have interband transitions in the region of interest. These conditions are best satisfied in the vuv by aluminum. Silver and gold, which are commonly used in the visible and infrared, are transparent in the vuv since their plasma wavelengths are greater than 200 nm.

---

*This research was supported by the Advanced Research Projects Agency of the Department of Defense and was monitored by the Defense Supply Service, Washington, D. C.

[1]Figures in brackets indicate the literature references at the end of this paper.

The reflectance of aluminum as a function of frequency is shown in figure 1. In the infrared, values of the reflectance as large as 99 percent are obtained. Aluminum is somewhat anomalous in that it has interband transitions in the near infrared. With extreme care in sample preparation under exacting laboratory conditions, values of reflectance approaching 92 percent have been obtained from the visible to the vuv [6]. Below the plasma wavelength of 81.4 nm (15.2 eV), aluminum is transparent except for interband transitions.

Chow and Sparks [7] have shown that the 92 percent reflectance, observed with the best samples at 174 nm, is within two percent of the intrinsic limit. In commercially available mirrors the absorptance in the vuv typically is 20 percent or greater, as denoted by the dashed curves in figure 1. Mills and Maradudin [8] have studied these greater values of absorptance, which result from enhanced coupling to aluminum surface plasmons caused by a rough surface or rough Al_2O_3 or MgF_2 overcoating.

In view of the extreme difficulty of achieving the intrinsic reflectance limit of aluminum and considering the large absorptance at the intrinsic limit, significant improvements in the failure thresholds of metallic reflectors do not seem possible. Improved reflectance has been obtained using a stack of very thin aluminum layers separated by approximately one-quarter wave layers of MgF_2 [9]. The damage threshold of these multilayer structures remains to be investigated. However, even greater damage thresholds should be attainable from the use of transparent materials as multilayer dielectric reflectors, or as total internal reflection devices.

Problems of transparent materials for high-power vuv use also are severe. There are few materials with sufficiently great electronic band gap E_g to avoid the great linear absorption above the absorption edge. Those having the largest band gaps are ionic materials composed of light ions from the edges of the periodic table. Materials having E_g greater than 7.2 eV include: LiF ($\sim$13), MgF_2 ($\sim$11), KF (10.9), NaF ($>$10.5), RbF (10.4), CsF (10), LiCl ($\sim$10), CaF_2 ($\sim$10), SrF_2 ($>$9), BaF_2 ($>$9), NaCl (8.6), KCl (8.5), LiBr ($\sim$8.5), Al_2O_3 (8.3), RbCl (8.2), KBr (7.8), NaBr (7.7), SiO_2 ($\sim$7.7), and MgO (7.3). All transparent materials will suffer the effects of two-photon absorption at the xenon laser frequency. The 13 eV band gap of LiF, which is the largest band gap of all transparent solids, is less than twice the photon energy of the xenon laser with $2\hbar\omega_L = 14.4$ eV.

Many of these materials are not expected to be useful as practical high-power vuv windows. The alkaline-earth halides are superior to the alkali halides with respect to hygroscopic properties and fracture strengths. Sapphire and quartz have highly desirable chemical and mechanical properties, but their band gaps of 8.3 eV and 7.7 eV, respectively, are very close to the xenon laser photon energy of 7.2 eV. The steepness of the electronic absorption edge appears to allow their use as xenon laser windows unless further study reveals such effects as anomalous frequency dependence of the absorption coefficient or a large nonlinear refractive index.

For construction of dielectric reflectors, there is a paucity of large index materials so that it may be necessary to use moderately absorbing materials. The absorption coefficient of such materials as NdF_3 and LaF_3 needs further investigation.

Aged LiF can suffer increased absorption from vuv induced color centers. It is not yet known if two-photon absorption at 7.2 eV will result in similar creation of color centers in LiF or other materials.

The frequency dependence of the linear absorption coefficient β of such ionic materials as alkali halides is shown schematically in figure 2. In the infrared, the intrinsic absorption mechanism is the creation of phonons which results in a large peak in β at the reststrahl frequency followed by a broad, exponentially decreasing multiphonon tail. At the CO_2 laser frequency many materials are impurity limited with absorption coefficients as low as 10^{-4} cm^{-1} being obtained. In the ultraviolet the intrinsic absorption mechanism is the excitation of electrons from the valence band to the conduction band. In contrast to the infrared, the electronic "Urbach tail" is relatively sharp (typically $\sim 10^8$ cm^{-1}/eV for the rate of reduction of the absorption coefficient β) so that materials can be used close to the edge without suffering excessive linear intrinsic absorption.

Presently available materials have extrinsic absorption coefficients ranging from 0.1 to 1 cm^{-1} for vuv frequencies below the intrinsic absorption edge [10]. Even though these values are quite large, improving the

materials to reduce the linear absorption will not result in a greater threshold for the case of a single 10 nsec pulse, unless the one-photon induced optical-distortion mechanism of section 3D is operative. Even then, the threshold would be increased from ~60 MW/cm^2 to only ~140 GW/cm^2, which is set by the two-photon induced electron optical distortion. However, in cw or repeated pulse systems it is expected that lowering the value of β should increase the threshold substantially. If such systems become of interest, the present analyses could be extended easily to include these cases.

2. Metallic Reflectors

Materials damage in the first xenon lasers occurred with the laser cavity-mode pattern being burned into the thin-film aluminum mirrors. The mechanism for damage in this case can be understood with the aid of figure 3, where a cross section of one of the laser-cavity mirrors is sketched. The mirror consists of a coating of aluminum approximately 100 A thick on a magnesium fluoride substrate. At the xenon-laser wavelength of 174 nm, commercially available aluminum reflectors typically have 20 percent absorptance, and the intrinsic limit is approximately 6 percent.

In order to determine the threshold for metallic-reflector damage, the surface temperature T of the mirror is calculated by dividing the energy absorbed $IA\mathcal{A}t$ by the volume of heated material $\mathcal{A}d$. Here I is the incident irradiance, A the absorptance, $\mathcal{A}$ the surface area that is irradiated, t is the pulse duration, and $d = (\pi K t/4C)^{1/2} = 2 \times 10^{-5}$ μm (for a 10 nsec pulse in MgF_2) is the thermal diffusion depth. Also, K is the thermal conductivity and C the heat capacity per unit volume. Equating this energy density IAt/d to CT gives

$$T = (4t/\pi CK)^{1/2} IA \quad . \tag{1}$$

Notice that the energy is absorbed in the thin aluminum film, while the volume of heated material is determined by the thermal diffusion into the magnesium fluoride.

For short pulse durations, failure occurs by melting of the aluminum film since aluminum has a lower melting point than MgF_2, and thermal stresses in the small volume of heated material are insufficient to cause fracture. Using A = 0.2, K = 0.11 W/cm K, and C = 4.1 J/cm^{3}K in eq. (1) yields a failure intensity of 20 MW/cm^2. The failure intensity decreases as the square root of the pulse duration, while the power density increases as $t^{1/2}$.

3. Transparent Materials

In addition to use in thin-film dielectric reflectors, transparent materials are of course needed for windows, lenses, and other optical components. Single-shot thresholds are calculated in the following for failure of bulk transparent materials by various mechanisms. These bulk thresholds can be used as a guide for thin films or for multiple shots.

A. Two-Photon Absorption

The two-photon absorption coefficient β_2 can be calculated using golden-rule perturbation theory which yields the formal expression [11, 12]

$$\beta_2 = \frac{4\pi\epsilon^{1/2}}{\hbar c\, n_L} \sum_i \sum_f \delta(E) \left| \sum_h \frac{\mathcal{H}_{fh}\mathcal{H}_{hi}}{E_f - E_h - \hbar\omega} \right|^2 , \tag{2}$$

where ϵ is the dielectric constant, n_L is the laser-photon occupation number, and $\delta(E)$ is an energy-conserving delta function. In eq. (2), $\mathcal{H}_{fh}$ and $\mathcal{H}_{hi}$ are matrix elements of the interaction Hamiltonian (which can be written

in terms of dipole matrix elements) between the initial state i (valence band) or the final state f (conduction band) and an intermediate state h. The matrix elements are summed over all possible initial, final, and intermediate states that conserve over-all energy. Possible intermediate states are higher conduction bands, exciton levels, lower valence bands, and the conduction band itself with intra-band transitions.

Present knowledge of the band structure of large-band-gap insulators, even LiF, is insufficient to predict which intermediate states are dominant or to calculate the two-photon absorption coefficient to better than an order-of-magnitude accuracy. Tentatively, it appears that a lower valence band may be the dominant intermediate state for LiF at the xenon-laser frequency. Simple arguments indicate that two-photon absorption is parity forbidden at the absorption edge in LiF. For slightly larger energies, two-photon absorption is allowed. Neglecting the wave-vector dependence of the transition matrix elements gives the frequency dependence $\beta_2 = \beta_{20} (\omega - \omega_g/2)^{1/2}$, where β_{20} is constant and $\hbar\omega_g$ is the band gap. This approximate frequency dependence, which is obtained from the joint density of states of parabolic conduction and valence bands, agrees qualitatively with experimental results for two-photon absorption coefficient in heavier alkali halides [13].

The two-photon absorption coefficient is proportional to the intensity and can be written formally as

$$\beta_2 = (I/I_0)\, 1\ \mathrm{cm}^{-1} \quad . \tag{3}$$

At the xenon-laser frequency in LiF, an order-of-magnitude estimate of the characteristic intensity at which $\beta = 1\ \mathrm{cm}^{-1}$ is $I_0 = 1.2\ \mathrm{GW/cm}^2$ [12].

B. Optical Distortion

There are two nonlinear mechanisms for optical distortion in the vacuum ultraviolet. First, the process of two-photon absorption creates conduction electrons, which in turn, can scatter incident radiation. The second mechanism is the usual nonlinear index, n_2, of the bound electrons in the solid, which is the dominant mechanism for optical distortion and catastrophic self focusing in infrared Nd-glass lasers. In the vicinity of two-photon absorption bands, the nonlinear index can be resonantly enhanced. The two mechanisms are not independent since n_2 is obtained from the real part of the third-order susceptibility, and two-photon absorption from the imaginary part.

The change in the refractive index from conduction electrons created by two-photon absorption is estimated using the Drude-theory result

$$\delta_n = -\omega^2/2 n_0 \omega_p^2 \quad , \tag{4}$$

where

$$\omega_p^2 = 4\pi N e^2/m \quad .$$

In eq. (4), ω_p^2 is the plasma frequency, e is the electronic charge, m is the reduced effective mass of the electrons, and n_0 is the linear refractive index. At the threshold for optical distortion, the number of free carriers is approximately equal to the integrated number of photons absorbed, neglecting relaxation, although the number is slightly larger as a result of electron-avalanche creation of additional pairs.

Our criterion for optical distortion is that the change in the optical path length at the center of the beam is 1/8 wave:

$$\lambda/8 = (\delta n)\, z \quad , \tag{5}$$

where z is the thickness of the material, which is taken to be 1 cm. Using the absorption coefficient in eq. (3) for LiF yields the free carrier threshold intensity $I = 160\ \mathrm{MW/cm}^2$ for a 10 nsec duration xenon-laser pulse.

The change in the refractive index from the nonlinear index of bound electrons is $\delta n = n_2 E^2$, where E is the rms electric field. The typical value of $n_2 = 10^{-13}$ esu, observed in the visible and infrared, yields a threshold of I = 7 GW/cm^2 for optical distortion. However, resonant enhancement of n_2 by two-photon absorption in the vuv reduces this threshold.

A simple model of the nonlinear index that preserves much of basic physics has been considered by Fournier and Snitzer. [14] This model considers a solid composed of noninteracting molecules having three electronic levels. The nonlinear index in this case is

$$n_2 = \frac{4\pi N}{n_0} \left(\frac{n_0+1}{3}\right)^4 \frac{e^4}{\hbar^3} \left(\frac{\hbar}{2m}\right)^2 \frac{f_{01} f_{12}}{\omega_{12}(\omega^2 - \omega_0^2)^2} \left[\frac{(\omega_0^2 + 5\omega^2)}{(\omega_0^2 - 4\omega^2)} + 2\right] , \tag{6}$$

where n_0 is the linear refractive index, $\hbar\omega_0$ is the energy of the electronic excited states, $\hbar\omega_{12}$ is the energy difference of the excited states, and f_{01} and f_{12} are the oscillator strengths for the transitions between subscripted levels. Since our primary interest is in the frequency dependence of n_2, eq. (6) is written in terms of the low frequency nonlinear index n_{20}:

$$n_2 = \frac{1}{3} n_{20} \frac{\omega_0^4}{(\omega^2 - \omega_0^2)^2} \left[\frac{(\omega_0^2 + 5\omega^2)}{(\omega_0^2 - 4\omega^2)} + 2\right] . \tag{7}$$

Methods of estimating n_{20} from linear optical constants have been proposed [14, 15].

The first term within the square brackets of eq. (7) has a resonance at one-half the one-photon absorption frequency ω_0. The nonlinear index is plotted as a function of frequency from eq. (7) in figure 4. In the absence of damping very large values of n_2 would be obtained near $\omega_0/2$. To keep n_2 finite, a small amount of damping has been added, which leads to a broadened two-photon absorption line at $\omega_0/2$ shown by the dashed curve in figure 4.

The molecular model is not realistic for solids such as alkali halides, which have broad two-photon absorption bands. For LiF, two-photon transitions from the valence band to the lowest conduction band extend from $\omega_g/2$ to approximately ω_g. To estimate the frequency dependence of n_2 in this case, eq. (7) is integrated over a distribution of oscillator frequencies having density $(\omega - \omega_g)^{1/2}$, which yields

$$n_2 = n_{20} \frac{1}{2(\omega_m - \omega_g)^{3/2}} \int_{\omega_g}^{\omega_m} \frac{\omega'^4 (\omega' - \omega_g)^{1/2}}{(\omega^2 - \omega'^2)^2} \left[\frac{(\omega'^2 + 5\omega^2)}{(\omega'^2 - 4\omega^2)} + 2\right] d\omega' . \tag{8}$$

This integral is approximated by replacing ω' in the slowly varying terms of the integrand by ω_g, which gives

$$n_2 = \frac{2}{3} n_{20} \frac{\omega_g^4}{(\omega^2 - \omega_g^2)^2} + \frac{1}{2} n_{20} \frac{\omega_g^4 (\omega_g^2 + 5\omega^2)}{(\omega_m - \omega_g)^{3/2} (\omega^2 - \omega_g^2)^2} \int_{\omega_g}^{\omega_m} \frac{(\omega' - \omega_g)^{1/2} d\omega'}{(\omega'^2 - 4\omega^2)} . \tag{9}$$

Notice that eq. (9) has the form of a Kramers-Kronig integral over the two-photon absorption band. Even though the individual oscillators diverge at one-half the resonant frequency, the integral over the oscillators remains finite, except at ω_g, and has the value

$$\mathcal{I}(\omega < \omega_g/2) = \frac{1}{2\omega}(\omega_g + 2\omega)^{1/2} \tan^{-1}\left[\left(\frac{\omega_m - \omega_g}{\omega_g + 2\omega}\right)^{1/2}\right]$$

$$- \frac{1}{2\omega}(\omega_g - 2\omega)^{1/2} \tan^{-1}\left[\left(\frac{\omega_m - \omega_g}{\omega_g + 2\omega}\right)^{1/2}\right]$$

and

$$\mathcal{I}(\omega_g/2 < \omega < \omega_g) = \frac{1}{2\omega}(\omega_g + 2\omega)^{1/2} \tan^{-1}\left[\left(\frac{\omega_m - \omega_g}{\omega_g + 2\omega}\right)^{1/2}\right]$$

$$- \frac{1}{2\omega}(2\omega - \omega_g)^{1/2} \ln\left|\frac{(2\omega - \omega_g)^{1/2} + (\omega_m - \omega_g)^{1/2}}{(2\omega - \omega_g)^{1/2} - (\omega_m - \omega_g)^{1/2}}\right| \qquad (10)$$

The nonlinear index obtained from eqs. (9) and (10) is plotted as a function of frequency in figure 5. The maximum positive value of $n_2 \cong 3n_{20}$ occurs at $\omega_g/2$. As the frequency increases, n_2 passes through zero (no optical distortion) and attains large negative values near ω_g. However, close to ω_g, one-photon effects will dominate. The xenon-laser frequency equals $0.55\omega_g$ in LiF. Using $n_2 = 3n_{20}$ with $n_{20} = 10^{-13}$ esu yields a threshold of $I = 2\,GW/cm^2$ for optical distortion in LiF. This is a factor of 12 greater than the estimated threshold for optical distortion from conduction electrons.

Although optical distortion from the nonlinear index of bound electrons is negligible at the xenon-laser frequency in LiF, there are other cases for which it may be important. The degree of resonance enhancement at $\omega_g/2$ increases with decreasing two-photon absorption band width. If a material has a strong sharp two-photon absorption band with the laser frequency adjacent to, but not within, the band, two-photon creation of free carriers will not occur, and the nonlinear index will be considerably enhanced. Large negative values of n_2 are predicted for ω just below ω_g for broad-band materials. This negative value of n_2 could yield strong nonlinear defocusing, but the three-band model used may not be valid in this frequency range. Then a more realistic model including effects of higher bands is needed for accurate predictions.

The frequency dependence of the nonlinear index has not been measured experimentally. A factor of 100 resonant enhancement of three-wave mixing (also obtained from the third-order susceptibility) has been observed in diamond by Levenson et al., [16] when the difference frequency was resonant with the Raman frequency.

Optical distortion from heating of the material by absorbed radiation, which is the dominant mechanism for distortion in cw 10.6 μm lasers, is negligible on the 10 nsec time scale of the xenon laser (except for rapidly repeated pulses). The lack of thermal distortion results from the fact, that, first, recombination of the electron-hole pairs is negligible on this time scale. Even if the pairs degraded rapidly into heat, there would be no optical distortion since the thermal expansion of the lattice (which dominates dn/dT) is slow.

C. Irreversible Damage Thresholds

Heat generated by two-photon absorption will result in thermal fracture of transparent materials. This will occur on a time scale of microseconds during which the thermal stresses in the material approach their equilibrium values. The previous analysis of Sparks and Chow [17] indicates that a LiF window fractures when the temperature at the center of the window is 7 K greater than at the edge. Using the two-photon absorption coefficient in eq. (3), and allowing for electron-avalanche creation of additional conduction electrons, and Joule heating of these electrons yields a fracture threshold of $I = 1.6\,GW/cm^2$ for LiF.

The electron-avalanche creation of conduction electrons and Joule heating of these carriers is highly nonlinear [18]. A factor of only three greater irradiance will result in two orders of magnitude greater heating in LiF.

Local fracture from absorbing inclusions, if present, will have the lowest permanent damage threshold. Since absorbing inclusions are expected to absorb at least as much energy in the vuv as in the infrared, the failure power density of $2\,J/cm^2$ ($200\,MW/cm^2$ with a 10 nsec pulse) observed for many materials in the infrared, is expected to apply in the vuv [19]. This failure mechanism, being extrinsic, can be removed by materials improvement, in principle.

D. Other Failure Mechanisms

In Raman-active crystals, enhanced stimulated Raman scattering can lead to materials damage from heating by phonons created in the scattering process. Sparks has estimated the threshold irradiance of $2\,GW/cm^2$ for thermal fracture by this mechanism [20]. Of the candidate 7.2 eV window materials, Raman scattering is symmetry allowed in the alkaline-earth halides, but not in the alkali halides.

Another form of optical distortion is nonlinear generation of harmonic frequencies in transparent materials. Frequency doubling occurs in materials lacking a center of inversion which, of the candidate materials, includes only crystalline SiO_2. Frequency tripling can occur in materials having a center of inversion, but the effects of frequency tripling are expected to be less severe than those from two-photon absorption.

Linear, extrinsic absorption can lead to optical distortion and thermal fracture, as with intrinsic two-photon absorption. The efficiency of generation of conduction electrons by linear, extrinsic absorption is not known. If each photon absorbed generates a conduction electron, it is estimated that an impurity absorption coefficient of $\beta = 0.15\ cm^{-1}$ will yield an optical distortion threshold of $60\,MW/cm^2$. At higher intensities nonlinear mechanisms dominate. An irradiance of $I = 30\,GW/cm^2$ is required for thermal fracture from extrinsic one-photon heating with $\beta = 0.15\ cm^{-1}$, compared to $I = 2\,GW/cm^2$ for two-photon heating.

Such crystalline defects as F centers have been observed to be created by light absorption [21]. It is possible that unavoidable two-photon absorption will create defects,which in turn yield an increasing extrinsic absorption coefficient at 7.2 eV. This remains to be investigated.

4. Summary and Conclusions

The various failure thresholds are presented graphically in figure 6. Unless otherwise noted, these thresholds are most appropriate for a single, 10 nsec duration, xenon-laser pulse in LiF. The mechanism having the lowest threshold of $I = 20\,MW/cm^2$ is melting of thin-film aluminum mirrors. With transparent materials, the lowest reversible threshold is $I = 140\,MW/cm^2$ for optical distortion by free carriers created by intrinsic, two-photon absorption. Depending on the efficiency for the creation of free carriers, extrinsic absorption coefficients greater than approximately $\beta = 10^{-1}\ cm^{-1}$ are required for lower optical distortion thresholds. Light absorption is known to create crystalline defects. Two-phonon creation of defects may lead to unacceptably large linear absorption coefficients in aged materials.

The lowest irreversible damage threshold of $200\,MW/cm^2$ occurs for localized fracture from absorbing inclusions. This mechanism being extrinsic, can be eliminated in principle. The lowest intrinsic threshold results from thermal fracture from two-photon heating and has the threshold of $1.6\,GW/cm^2$ for LiF. Assuming a comparable two-photon absorption coefficient for other materials, the threshold for thermal fracture is expected to be greater for the materials having greater fracture strengths. The threshold in MgF_2 is estimated as 4 GW/cm^2. Thermal fracture from an extrinsic absorption coefficient of $\beta = 0.1\ cm^{-1}$ is negligible compared to that from two-photon absorption.

The threshold of $2\,GW/cm^2$ for optical distortion from the nonlinear index of bound electrons in LiF is negligible compared to the distortion from free carriers. This mechanism may be dominant in other materials if the laser frequency is adjacent to, but not within, a sharp, strong two-photon absorption line. Another nonlinear mechanism that can lead to failure is enhanced stimulated Raman scattering. In materials with allowed Raman scattering (includes alkaline-earth halides), heating from Raman-created phonons results in fracture at $I = 2\,GW/cm^2$.

An accuracy of only one order of magnitude is expected for the above thresholds because of an order-of-magnitude uncertainty in the two-photon absorption coefficient. Our present efforts are directed toward a better understanding of the linear optical properties of wide-band-gap materials so that better estimates of two-photon absorption and other nonlinear effects can be made.

5. References

[1] Rhodes, C. K., IEEE J. Quant. Elect. QE-10, 153 (1974).

[2] Hughes, W. M., Shannon, J., Kolbi, A., Ault, E., and Bhaumik, M., Appl. Phys. Lett. 23, 385 (1973).

[3] Hoff, P. W., Swingle, J. C., and Rhodes, C. K., Appl. Phys. Lett. 23, 245 (1973).

[4] Hughes, W. M., Shannon, J., and Hunter, R., Appl. Phys. Lett. 24, 488 (1974).

[5] Laser Focus, p. 10, May (1973).

[6] Feuerbacher, B. P. and Steinmann, W., Opt. Commun. 1, 81 (1969).

[7] Chow, H. C. and Sparks, M., J. Appl. Phys. 46, 1307 (1975).

[8] Maradudin, A. A. and Mills, D. L., Phys. Rev. B 11, 1392 (1975); Mills, D. L. and Maradudin, A. A., Phys. Rev., in press.

[9] Spiller, E., Optik 39, 118 (1973).

[10] Tomiki, T. and Miyata, T., J. Phys. Soc. Japan 27, 658 (1969).

[11] Braunstein, R., Phys. Rev. 125, 475 (1962).

[12] Sparks, M. and Sham, L. J., to be published.

[13] Hopfield, J. J. and Worlock, J. M., Phys. Rev. 137, A1455 (1965); Frölich, D. and Staginnus, B., Phys. Rev. Lett. 19, 496 (1967).

[14] Fournier, J. T. and Snitzer, E., IEEE J. Quant. Elect. QE-10, 473 (1974).

[15] Wang, C. C., Phys. Rev. B 2, 2045 (1970).

[16] Levenson, M. D., Flytzanis, C., and Bloembergen, N., Phys. Rev. B 6, 3962 (1972).

[17] Sparks, M. and Chow, H. C., J. Appl. Phys. 45, 1510 (1974).

[18] Sparks, M., these proceedings, and to be published.

[19] Sparks, M. and Duthler, C. J., J. Appl. Phys. 44, 3038 (1973); Duthler, C. J., Appl. Phys. Lett. 24, 5 (1974).

[20] Sparks, M., J. Appl. Phys. 46, 2134 (1975).

[21] Warneck, P., J. Opt. Soc. Am. 55, 921 (1965).

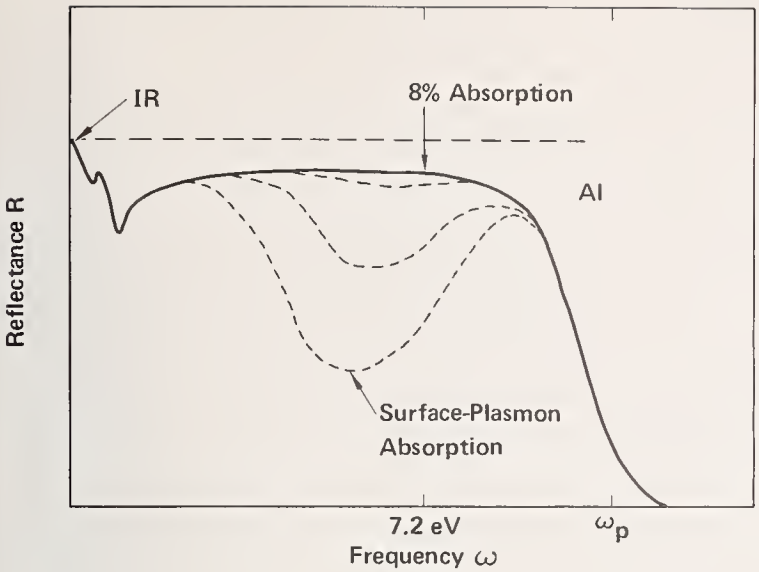

Figure 1. Reflectance of aluminum as a function of frequency. At 7.2 eV, the intrinsic absorptance is 8%. More typically, the absorptance is limited by surface plasmons as shown by dashed curves.

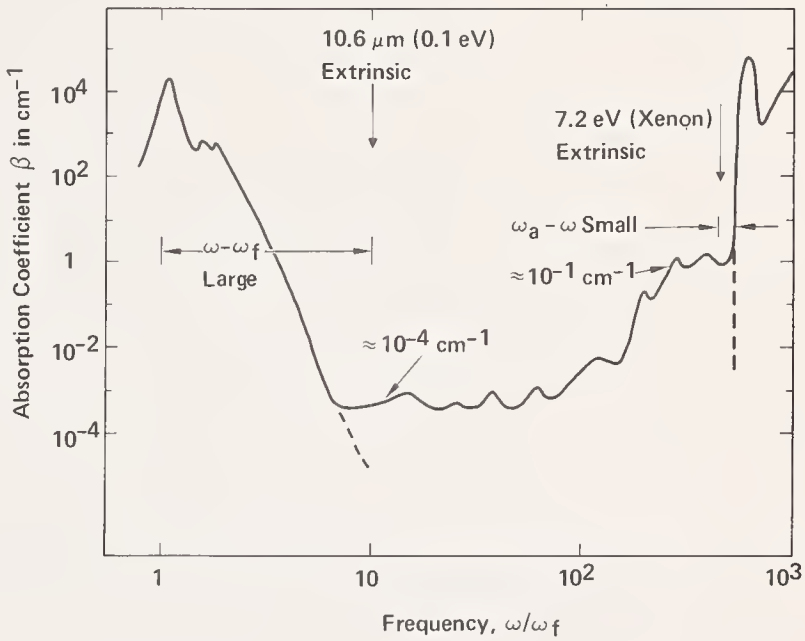

Figure 2. Absorption coefficient of an ionic solid as a function of frequency.

Figure 3. Sketch of aluminum-film laser-cavity mirror. The heat diffusion dept is δ.

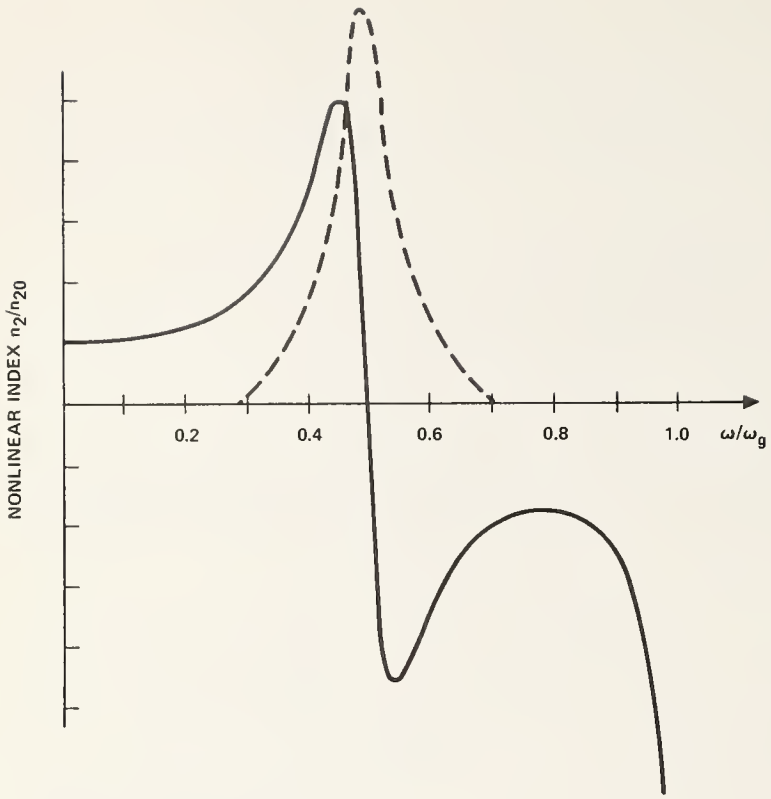

Figure 4. Frequency dependence of the nonlinear refractive index for a solid consisting of molecular oscillators. Two-photon absorption is denoted by dashed curve.

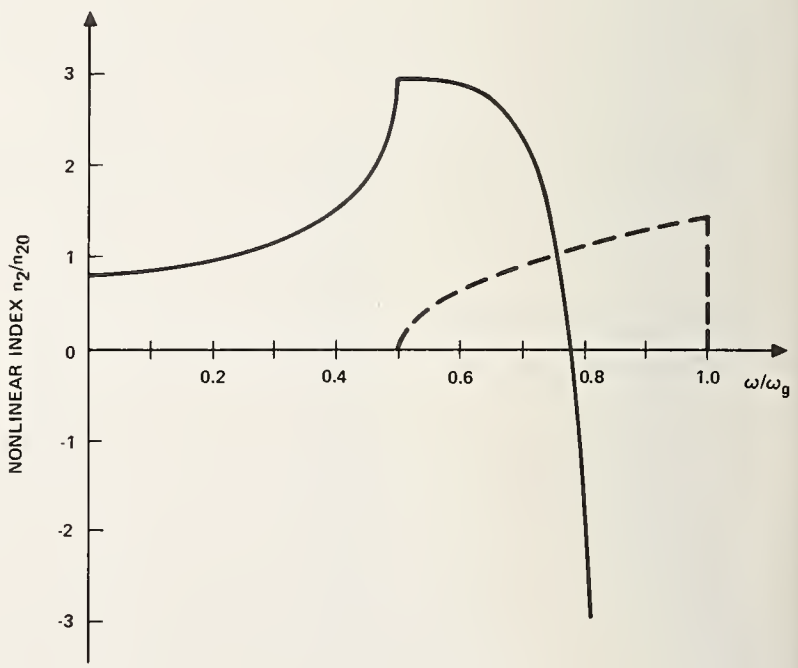

Figure 5. Frequency dependence of the nonlinear refractive index for a broad-band solid, such as LiF. Two-photon absorption is denoted by dashed curve.

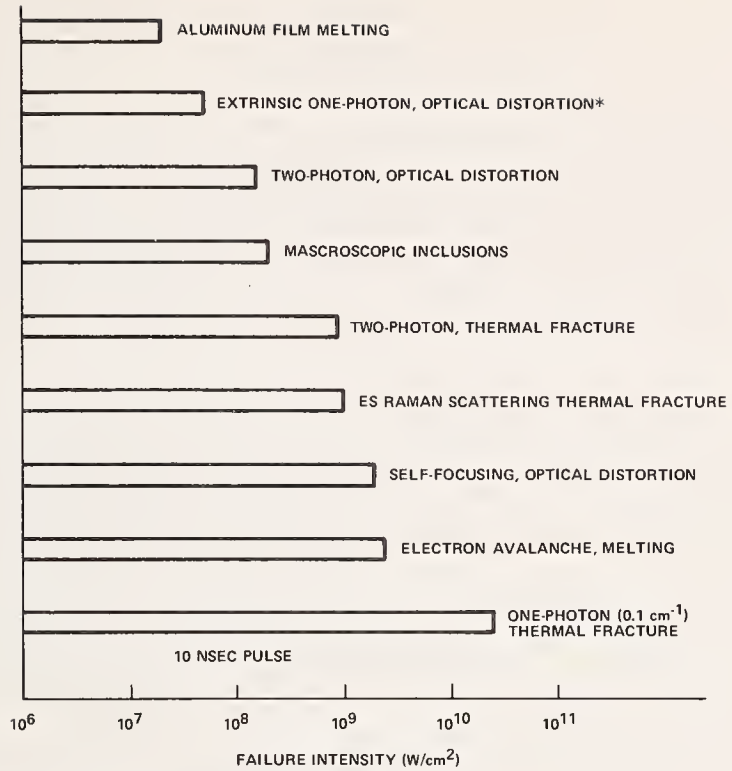

*ONLY IF ELECTRONS GENERATED; SEE TEXT.

Figure 6. Failure irradiances for various mechanisms. Except for mirror melting and Raman scattering fracture, these thresholds are most appropriate for a single 7.2 eV xenon-pulse incident on LiF.

COMMENTS ON PAPER BY DUTHLER and SPARKS

In response to a question from the audience the speakers indicated that stimulated brillouin scattering was considered as a potential damage mechanism and not found to be significant.

APPENDIX I

PARTICIPANTS

A

C. M. Allred	Electromagnetics Division, National Bureau of Standards, Boulder, CO 80302
N. Alyassini	Phys. Dept., SSC, USC, Los Angeles, CA 90024
L. J. Aplet	Hughes Aircraft Co., M.S. E119, Centinela & Teale Sts., Culver City, CA 90230
J. B. Arnold	Union Carbide Corporation, P.O. Box Y, Oak Ridge, TN 37830
D. M. Aspinwall	Lockheed Missiles & Space Co., D52-01 - B201, 3251 Hanover St., Palo Alto, CA 94304
R. R. Austin	Perkin-Elmer Corp. Main Ave., Norwalk, CT 06897
D. G. Aviv	Aerospace Corporation, P.O. Box 92957, Los Angeles, CA 90009

B

A. D. Baer	Naval Weapons Center, Code 6018, China Lake, CA 93555
W. P. Barnes, Jr.	ITEK Corporation, 10 Maguire Road, Lexington, MA 02173
M. Bass	Univ. of Southern Calif. Center for Laser Studies, Los Angeles, CA 90007
H. E. Bennett	Michelson Lab. Naval Weapons Center, Code 6018, China Lake, CA 93555
E. Bernal G.	Honeywell Corp. Res. Ctr., 70701 Lyndale Ave. So., Bloomington, MN 55420
J. R. Bettis	USAF, Kirtland AFB, NM 87117
A. L. Bloom	Coherent Radiation, Inc., 3210 Porter Drive, Palo Alto, CA 94304
L. C. Bobb	Frankford Arsenal, L5000, Bridge & Tacony Sts., Philadelphia, PA 19137
N. Boling	Owens-Illinois, 1700 N. Westwood Ave., Toledo, OH 43666
W. T. Boord	Honeywell Systems and Res. Center, R2340, 2600 Ridgway Parkway, Minneapolis, MS 55413
R. J. Bouchard	Rockwell International, Box 464, Golden, CO 80401
H. S. Boyne	Electromagnetics Division, National Bureau of Standards, Boulder, CO 80302
R. A. Bradbury	Air Force Cambridge Res. Labs., Hanscom AFB, MA 01731
P. Braunlich	Engineering Physics Dept., Bendix Research Labs, Southfield, MI 48076
M. Braunstein	Chem. - Physics, Hughes Research Labs, 3011 S. Malibu Canyon Rd., Malibu, CA 90291
N. J. Brown	Lawrence Livermore Lab., Box 808, Livermore, CA 94550
J. Bruce	AFCRL/LQO, Hanscom AFB, MA 01730
J. R. Buckmelter	Air Force Weapons Lab., Optical Systems Branch (LRE), Kirtland AFB, NM 87117

C

A. B. Callender	AFWL/LRE, Kirtland AFB, NM 87117
A. Carlson	Cleveland Crystals, Inc., Box 17157, Euclid, OH 44117
G. E. Chamberlain	Electromagnetics Division, National Bureau of Standards, Boulder, CO 80302
C. F. Cline	Lawrence Livermore Lab., L-401, P.O. Box 808, Livermore, CA 94500
A. R. Cook	Electromagnetics Division, National Bureau of Standards, Boulder, CO 80302
V. Costich	Coherent Radiation, Inc., 3210 Porter Dr., Palo Alto, CA 94304

D

B. L. Danielson	Electromagnetics Division, National Bureau of Standards, Boulder, CO 80302
G. W. Day	Electromagnetics Division, National Bureau of Standards, Boulder, CO 80302
D. L. Decker	Naval Weapons Center, Code 6018, China Lake, CA 93555
R. K. DeLong	TRW Systems, One Space Park, Mail Station 01/2070, Redondo Beach, CA 90278
J. A. Detrio	University of Dayton, Research Institute, 300 College Park, Dayton, OH 45469
M. J. Dodge	National Bureau of Standards, U.V. Physics Sec., A251 Physics Bldg., Washington, D.C. 20234
R. Doussain	Laboratoire National D'Essais, 1, Rue Gaston Boisseir, Paris, France
C. E. Durbin	Rockwell International, Machining R&D, P.O. Box 464, Golden, CO 80401
C. J. Duthler	Xonics Inc., 6837 Hayvenhurst Ave., Van Nuys, CA 91406

E

D. F. Edwards	Los Alamos Scientific Lab, MS 564, Los Alamos, NM 87545
R. R. Esposito	International Laser Systems, 729 Sagebrush Trail, Albuquerque, NM 87123
W. S. Ewing	AFCRL, LQO/30, Bedford, MA 01739

F

J. Feldman	Electro-Optics Dept., EM Labs, 500 Executive Blvd., Elmsford, NY 10523
J. R. Fenter	Air Force Materials Lab., Wright-Patterson AFB, OH 45433
A. M. Frank	Lawrence Livermore Lab., Optics Group, Box 808, Livermore, CA 94550
D. L. Franzen	Electromagnetics Division, National Bureau of Standards, Boulder, CO 80302

G

D. H. Gill	Los Alamos Scientific Laboratory, Los Alamos, NM 87544
C. R. Giuliano	Hughes Res. Labs, 3011 Malibu Canyon Road, Malibu, CA 90265
A. J. Glass	Univ. of Calif., P.O. Box 808, Livermore, CA 94550
A. T. Glassman	ME Dept. Optics-Group, Lawrence Livermore Lab., Box 808, Livermore, CA 94550
I. Goldstein	Raytheon Missile Systems Div., Huntwell Rd., Bedford, MA 01730
A. Golubovic	AFCRL, LQO, Hanscom AFB, MA 01730
W. V. Goodell	Optical Sciences Div., NRL, Washington, D.C.
P. M. Gruzensky	Electromagnetics Division, National Bureau of Standards, Boulder, CO 80302
A. H. Guenther	Air Force Weapons Lab./CA, Kirtland AFB, NM 87117
A. Gundjian	McGill University, Sherbrooke Street, Montreal P. Q. Canada

H

Y. Hahn	CVI Laser Corp., 200 Dorado Pl. SE., Albuquerque, NM 87123
T. Harris	Raytheon Company, 130 Second Avenue, Waltham, MA 02154
G. L. Hennessey	Valpey Corp. 1244 Highland St., Holliston, MA 01746
R. Hilton	Texas Instruments Inc., P.O. Box 6015, MS 406, Dallas, TX 75222
R. A. Hoffman	Westinghouse Electric Corp., R&D Center, Beulah Road, Pittsburgh, PA 15235
S. J. Holmes	Northrop Research & Technology, 3401 W. Broadway, Hawthorne, CA 90250
D. Horowitz	National Bureau of Standards, Bldg. 223, Rm. A-259, Washington, D.C. 20234
R. A. House II	AFWL, DYX, Kirtland, AFB, NM 87117
C. A. Huguley	Laser Div./LRE, Air Force Weapons Lab., Kirtland AFB, NM 87117

I

J

R. H. Johnson	Northrop Research & Technology, 3401 W. Broadway, Hawthorne, CA 90250

K

T. Kardos	Broomer Research, 23 Sheer Plaza, Plainview, NY 11803
J. C. Kershenstein	U.S. Naval Research Lab., Code 5503, Washington, D.C. 20234
J. M. Khan	Lawrence Livermore Lab., L-503, P.O. Box 808, Livermore, CA 94550
G. E. Kuhl	USAF, AFML/LPO, Wright Patterson AFB, OH 45433
J. Kurdock	Perkin-Elmer Corp., 77 Danbury Road, So. Wilton, CT 06897

L

J. Lancelot	CEA/CEL, B.P. 27, Villeneuvi St. Georges 94, France
J. K. Larin	Laser Optics Inc., P.O. Box #3, Danbury, CT 06476
R. A. Lawton	Electromagnetics Division, National Bureau of Standards, Boulder, CO 80302
M. Le Bodo	Laboratoire National D'Essais, 1, Rue Gaston Boisseir, Paris, France
K. M. Leung	U. of So. Calif., Center for Laser Studies, University Park, Los Angeles, CA 90007
R. L. Lewis	Electromagnetics Division, National Bureau of Standards, Boulder, CO 80302
D. H. Liebenberg	Los Alamos Scientific Lab., P.O. Box 1663, Los Alamos, NM 87544
R. M. Linford	Dept. E457, McDonnell Douglas, P.O. Box 516, St. Louis, MO 63166
H. G. Lipson	Air Force Cambridge Res. Lab. LQS, Hanscom AFB, MA 01731
J. D. Lytte	Dept. 62-30, Lockheed Missiles & Space Co., Bldg. 151, P.O. Box 504, Sunnyvale, CA 95014

M

R.W. MacPherson	Electro-Optics Div., DREV/CRDV, P.O. Box 880, Courcellette, Quebec, Canada GOA IRO
I. H. Malitson	Optical Physics Div., National Bureau of Standards, A 251 Physics Bldg., Washington, D.C. 20234
G. E. Marx	Westinghouse Elect. Corp., Adv. Tech. Labs, P.O. Box 1521, M.S. 3714, Baltimore, MD 21203
F. J. McClung	Adaptive & High Power Optics Dept., Laser Div., Hughes Aircraft, Culver City, CA 90230
D. Milam	Y-Div., Lawrence Livermore Lab., Livermore, CA 94550
P. Miles	Raytheon Co., Hartwell Road, Bedford, MA 01730
K. Moncur	KMS Fusion, 3941 Research Park Drive, Ann Arbor, MI 48106
M. Monsler	Science Applications Inc., 3 Preston Ct., Bedford, MA 01730
D. Morelli	Optical Coating Lab., Inc., 2789 Giffen Ave., Santa Rosa, CA 95403

N

N. S. Nahman	Electromagnetics Division, National Bureau of Standards, Boulder, CO 80302
B. E. Newnam	Los Alamos Scientific Lab., L-2, P.O. Box 1663, MS 552, Los Alamos, NM 87544
T. E. Norwood	U.S. Army High Energy Laser Proj., AMCPM-HEL, U.S. Army Missile Command, Redstone Arsenal, AL 35809

O

D. F. O'Brien	USAF, Materials Lab/LPO, Wright-Patterson AFB, OH 45433
R. W. O'Neil	Optics Div., MIT Lincoln Laboratory, P.O. Box 73, Lexington, MA 07179

P

J. H. Parks	Physics Dept., Univ. Southern Calif., University Park, Los Angeles, CA 90007
R. H. Picard	AF Cambridge Research Labs., OPL, Hanscom AFB, MA 01731
H. S. Pilloff	Office of Naval Res., Code 421, 800 N. Quincy St., Arlington, VA 22217
J. O. Porteus	Naval Weapons Center, Code 6017, China Lake, CA 93555
H. Posen	USAF Cambridge Research Labs., Solid State Sci/LQO, Hanscom AFB, MA 01731
R. F. Prater	AFWL/LRE, Kirtland AFB, NM 87117

Q

R

W. L. Ramer	Rockwell Int., Rocky Flats Plant, P.O. Box 464, Golden, CO 80401
D. W. Readey	U.S. ERDA/DPR, Materials Sciences Program, Washington, D.C. 20545
W. Reichect	Univ. of Calif., LASL, L-1, Los Alamos, NM 87545
D. K. Rice	Northrop Research & Technology Center, 3401 W. Broadway, Hawthorne, CA 90250

S

T. Saito	U.S. Air Force, Lawrence Livermore Labs, L-140, P.O. Box 808, Livermore, CA 94550
A. A. Sanders	Electromagnetics Division, National Bureau of Standards, Boulder, CO 80302
A. Schmid	Bendix Corp. -- Research Labs, Southfield, MI 48076
R. A. Shatas	Physical Sciences Div., U.S. Army Missile Comm., Bldg. 77770, AMSML-RRD, Redstone Arsenal, AL 35802
G. H. Sherman	II-VI, Inc., 207 Garden Lane, Glenshaw, PA 15116
R. E. Sladky	Union Carbide Corp, Y-12 Plant, P.O. Box Y, Bldg. 9998, Oak Ridge, TN 37830
D. H. Sliney	U.S. Army Environmental Hygiene Agency, Aberdeen Proving Ground, MD 21010
R. L. Smith	Electromagnetics Division, National Bureau of Standards, Boulder, CO 80302
W. L. Smith	Div. Engineer & Applied Physics, Harvard Univ., 321 McKay Lab, Cambridge, MA 02138
M. J. Soileau	Naval Weapons Center, Code 6018, China Lake, CA 93555
M. Sparks	Xonics, Inc., 6837 Hayvenhurst Ave., Van Nuys, CA 91406
W. J. Spawr	Spawr Optical Research, Inc., 1521 Pomona Rd., Corona, CA 91720
J. L. Stapp	USAF Weapons Lab., LRE, Kirtland AFB, NM 87108
J. Starling	Ceramics Dept. -- V1864, Honeywell Inc., 1885 Douglas Dr. N., Golden Valley, NM 55422
D. L. Stierwalt	Naval Electronics Laboratory Center, Code 4600, 271 Catalina Blvd., San Diego, CA 92152
J. C. Stover	Rockwell International, R&D, Bldg. 881, P.O. Box 464, Golden, CO 80401
R. Strandlund	Optical Coating Lab., Inc., 2789 Giffen Ave., Santa Rosa, CA 95403

T

A. Takenouche	Electrical Eng., Colo. State Univ., 719 S. Washington St., Apt. 119, Fort Collins, CO 80521
C. E. Thomas	KMS Fusion, P.O. Box 1567, Ann Arbor, MI 48106

U

V

K. Vedam	Penn. State Univ., 276 Materials Res. Lab, University Park, PA 16802

W

F. B. Waldrop	Develop. Div., Union Carbide Nuclear, P.O. Box Y, Bldg. 9202, Oak Ridge, TN 37830
E. P. Wallerstein	Laser Div., L-543, Lawrence Livermore Labs., P.O. Box 808, Livermore, CA 94550
V. Wang	Hughes Research Lab., 30-25-00, 3011 Malibu Canyon Rd., Malibu, CA 90265
S. W. Warren	Electrical Products Div., ITT Component, Edinburgh Way, Harlow, Essex, England
R. Webb	Holobeam Laser, Inc., 560 Winters Ave., Paramus, NJ 07652
C. B. Willingham	Research Div., Raytheon Co., 28 Seyon St., Waltham, MA 02154
T. D. Wise	Ball Bros. Res. Corp, P.O. Box 1062, Boulder, CO 80302
R. M. Wolff	Valpey Corp., Box 2311, Newport Beach, CA 92663
S. M. Wong	Rockwell International, Bldg. 779, P.O. Box 464, Golden, CO 80401
D. L. Wright	Dept. of EE, Colorado State University, Fort Collins, CO 80523

X

Y

Yu Chung	EE Dept., North Carolina A&T State Univ., Greensboro, NC 27411

Z

J. L. Zar AVCO Everett Res. Lab., Everett, MA 02149
R. W. Zimmerer Scientech, Inc., 5649 Arapahoe, Boulder, CO 80303

NBS-114A (REV. 7-73)

U.S. DEPT. OF COMM. BIBLIOGRAPHIC DATA SHEET	1. PUBLICATION OR REPORT NO. Special Publication 435	2. Gov't Accession No.	3. Recipient's Accession No.

4. TITLE AND SUBTITLE.

Laser Induced Damage in Optical Materials: 1975

5. Publication Date April 1976

6. Performing Organization Code

7. AUTHOR(S)
Edited by Alexander J. Glass and Arthur H. Guenther

8. Performing Organ. Report No.

9. PERFORMING ORGANIZATION NAME AND ADDRESS

NATIONAL BUREAU OF STANDARDS
DEPARTMENT OF COMMERCE
WASHINGTON, D.C. 20234

10. Project/Task/Work Unit No. 2769569

11. Contract/Grant No.

12. Sponsoring Organization Name and Complete Address *(Street, City, State, ZIP)*
Electromagnetics Division, National Bureau of Standards, Boulder, CO 80302
American Society for Testing & Materials, Phila., PA 19103
Dept. of the Navy, Office of Naval Research, Arlington, VA 22217
~~Energy Research & Development Admin., Washington, D. C. 20234~~

13. Type of Report & Period Covered Final

14. Sponsoring Agency Code

15. SUPPLEMENTARY NOTES

Library of Congress Catalog Card Number: 76-4985

16. ABSTRACT *(A 200-word or less factual summary of most significant information. If document includes a significant bibliography or literature survey, mention it here.)* The Seventh ERDA-ASTM-ONR-NBS Symposium on Laser Induced Damage in Optical Materials was held at the National Bureau of Standards in Boulder, Colorado, on July 29-31 of this year. These Symposia are held as part of the activities in Subcommittee II on Lasers and Laser Materials, of the ASTM. Subcommittee II is charged with the responsibilities of formulating standards and test procedures for laser materials, components, and devices. The Chairman of Subcommittee II is Haynes Lee, of Owens-Illinois, Inc. Co-chairmen for the Damage Symposia are Dr. Arthur Guenther, Chief Scientist of the Air Force Weapons Laboratory, and Dr. Alexander J. Glass, Head, Theoretical Studies, Y Division, Lawrence Livermore Laboratory.

Over 150 attendees at the Symposium heard 42 papers on topics relating fabrication procedures to laser induced damage in optical materials; on metal mirrors; in infrared window materials; the multipulse, wavelength and pulse length dependence of damage thresholds; damage in dielectric films and at exposed surfaces; as well as theoretical discussions on avalanche ionization and multiphoton processes of importance at shorter wavelengths. Of particular importance was the sealing relations developed from several parametric studies relating fundamental properties (refractive index, surface roughness, etc.) to the damage threshold. This year many of the extrinsic influences tending to reduce a material damage resistance were isolated such that a measure of its egregious nature could be quantified. Unfortunately, it was evident that much still needs to be accomplished to improve processing and fabrication procedures to allow a measurable approach to a materials intrinsic strength to be demonstrated.

17. KEY WORDS *(six to twelve entries; alphabetical order; capitalize only the first letter of the first key word unless a proper name; separated by semicolons)*
Avalanche ionization; IR windows and mirrors; laser damage; laser materials; multiphoton processes; self-focusing; thin films.

18. AVAILABILITY

[X] Unlimited

[ ] For Official Distribution. Do Not Release to NTIS

[X] Order From Sup. of Doc., U.S. Government Printing Office Washington, D.C. 20402, SD Cat. No. C13 · 10:435

[ ] Order From National Technical Information Service (NTIS) Springfield, Virginia 22151

19. SECURITY CLASS (THIS REPORT) UNCLASSIFIED

21. NO. OF PAGES 437

20. SECURITY CLASS (THIS PAGE) UNCLASSIFIED

22. Price $5.60

USCOMM-DC 29042-P74

☆U.S. GOVERNMENT PRINTING OFFICE: 1976 210-801/225 1-3

NBS TECHNICAL PUBLICATIONS

PERIODICALS

JOURNAL OF RESEARCH reports National Bureau of Standards research and development in physics, mathematics, and chemistry. It is published in two sections, available separately:

• **Physics and Chemistry (Section A)**

Papers of interest primarily to scientists working in these fields. This section covers a broad range of physical and chemical research, with major emphasis on standards of physical measurement, fundamental constants, and properties of matter. Issued six times a year. Annual subscription: Domestic, $17.00; Foreign, $21.25.

• **Mathematical Sciences (Section B)**

Studies and compilations designed mainly for the mathematician and theoretical physicist. Topics in mathematical statistics, theory of experiment design, numerical analysis, theoretical physics and chemistry, logical design and programming of computers and computer systems. Short numerical tables. Issued quarterly. Annual subscription: Domestic, $9.00; Foreign, $11.25.

DIMENSIONS/NBS (formerly Technical News Bulletin)—This monthly magazine is published to inform scientists, engineers, businessmen, industry, teachers, students, and consumers of the latest advances in science and technology, with primary emphasis on the work at NBS. The magazine highlights and reviews such issues as energy research, fire protection, building technology, metric conversion, pollution abatement, health and safety, and consumer product performance. In addition, it reports the results of Bureau programs in measurement standards and techniques, properties of matter and materials, engineering standards and services, instrumentation, and automatic data processing.

Annual subscription: Domestic, $9.45; Foreign, $11.85.

NONPERIODICALS

Monographs—Major contributions to the technical literature on various subjects related to the Bureau's scientific and technical activities.

Handbooks—Recommended codes of engineering and industrial practice (including safety codes) developed in cooperation with interested industries, professional organizations, and regulatory bodies.

Special Publications—Include proceedings of conferences sponsored by NBS, NBS annual reports, and other special publications appropriate to this grouping such as wall charts, pocket cards, and bibliographies.

Applied Mathematics Series—Mathematical tables, manuals, and studies of special interest to physicists, engineers, chemists, biologists, mathematicians, computer programmers, and others engaged in scientific and technical work.

National Standard Reference Data Series—Provides quantitative data on the physical and chemical properties of materials, compiled from the world's literature and critically evaluated. Developed under a world-wide program coordinated by NBS. Program under authority of National Standard Data Act (Public Law 90-396).

NOTE: At present the principal publication outlet for these data is the Journal of Physical and Chemical Reference Data (JPCRD) published quarterly for NBS by the American Chemical Society (ACS) and the American Institute of Physics (AIP). Subscriptions, reprints, and supplements available from ACS, 1155 Sixteenth St. N. W., Wash. D. C. 20056.

Building Science Series—Disseminates technical information developed at the Bureau on building materials, components, systems, and whole structures. The series presents research results, test methods, and performance criteria related to the structural and environmental functions and the durability and safety characteristics of building elements and systems.

Technical Notes—Studies or reports which are complete in themselves but restrictive in their treatment of a subject. Analogous to monographs but not so comprehensive in scope or definitive in treatment of the subject area. Often serve as a vehicle for final reports of work performed at NBS under the sponsorship of other government agencies.

Voluntary Product Standards—Developed under procedures published by the Department of Commerce in Part 10, Title 15, of the Code of Federal Regulations. The purpose of the standards is to establish nationally recognized requirements for products, and to provide all concerned interests with a basis for common understanding of the characteristics of the products. NBS administers this program as a supplement to the activities of the private sector standardizing organizations.

Federal Information Processing Standards Publications (FIPS PUBS)—Publications in this series collectively constitute the Federal Information Processing Standards Register. Register serves as the official source of information in the Federal Government regarding standards issued by NBS pursuant to the Federal Property and Administrative Services Act of 1949 as amended, Public Law 89-306 (79 Stat. 1127), and as implemented by Executive Order 11717 (38 FR 12315, dated May 11, 1973) and Part 6 of Title 15 CFR (Code of Federal Regulations).

Consumer Information Series—Practical information, based on NBS research and experience, covering areas of interest to the consumer. Easily understandable language and illustrations provide useful background knowledge for shopping in today's technological marketplace.

NBS Interagency Reports (NBSIR)—A special series of interim or final reports on work performed by NBS for outside sponsors (both government and non-government). In general, initial distribution is handled by the sponsor; public distribution is by the National Technical Information Service (Springfield, Va. 22161) in paper copy or microfiche form.

Order NBS publications (except NBSIR's and Bibliographic Subscription Services) from: Superintendent of Documents, Government Printing Office, Washington, D.C. 20402.

BIBLIOGRAPHIC SUBSCRIPTION SERVICES

The following current-awareness and literature-survey bibliographies are issued periodically by the Bureau:

Cryogenic Data Center Current Awareness Service

A literature survey issued biweekly. Annual subscription: Domestic, $20.00; foreign, $25.00.

Liquefied Natural Gas. A literature survey issued quarterly. Annual subscription: $20.00.

Superconducting Devices and Materials. A literature survey issued quarterly. Annual subscription: $20.00. Send subscription orders and remittances for the preceding bibliographic services to National Bureau of Standards, Cryogenic Data Center (275.02) Boulder, Colorado 80302.

Electromagnetic Metrology Current Awareness Service Issued monthly. Annual subscription: $24.00. Send subscription order and remittance to Electromagnetics Division, National Bureau of Standards, Boulder, Colo. 80302.

U.S. DEPARTMENT OF COMMERCE
National Bureau of Standards
Washington, D.C. 20234

OFFICIAL BUSINESS

Penalty for Private Use, $300

POSTAGE AND FEES PAID
U.S. DEPARTMENT OF COMMERCE
COM-215

SPECIAL FOURTH-CLASS RATE
BOOK